Springer Tracts in Electrical and Electronics Engineering

Trupti Ranjan Lenka
Hieu Pham Trung Nguyen *Editors*

HEMT Technology and Applications

Springer

Springer Tracts in Electrical and Electronics Engineering

Springer Tracts in Electrical and Electronics Engineering (STEEE) publishes the latest developments in Electrical and Electronics Engineering - quickly, informally and with high quality. The intent is to cover all the main branches of electrical and electronics engineering, both theoretical and applied, including:

- Signal, Speech and Image Processing
- Speech and Audio Processing
- Image Processing
- Human-Machine Interfaces
- Digital and Analog Signal Processing
- Microwaves, RF Engineering and Optical Communications
- Electronics and Microelectronics, Instrumentation
- Electronic Circuits and Systems
- Embedded Systems
- Electronics Design and Verification
- Cyber-Physical Systems
- Electrical Power Engineering
- Power Electronics
- Photovoltaics

- Energy Grids and Networks
- Electrical Machines
- Control, Robotics, Automation
- Robotic Engineering
- Mechatronics
- Control and Systems Theory
- Automation
- Communications Engineering, Networks
- Wireless and Mobile Communication
- Internet of Things
- Computer Networks

Within the scope of the series are monographs, professional books or graduate textbooks, edited volumes as well as outstanding PhD theses and books purposely devoted to support education in electrical and electronics engineering at graduate and post-graduate levels.

Review Process

The proposal for each volume is reviewed by the main editor and/or the advisory board. The books of this series are reviewed in a single blind peer review process.

Ethics Statement for this series can be found in the Springer standard guidelines here https://www.springer.com/us/authors-editors/journal-author/journal-author-helpdesk/before-you-start/before-you-start/1330#c14214

More information about this series at https://link.springer.com/bookseries/16799

Editors
Trupti Ranjan Lenka and Hieu Pham Trung Nguyen

HEMT Technology and Applications

Editors
Trupti Ranjan Lenka
Department of Electronics and Communication Engineering, National Institute of Technology Silchar, Silchar, Assam, India

Hieu Pham Trung Nguyen
Department of Electrical and Computer Engineering, New Jersey Institute of Technology, Newark, New Jersey, USA

ISSN 2731-4200 e-ISSN 2731-4219
Springer Tracts in Electrical and Electronics Engineering
ISBN 978-981-19-2164-3 e-ISBN 978-981-19-2165-0
https://doi.org/10.1007/978-981-19-2165-0

Contents

Editors and Contributors

About the Editors

Trupti Ranjan Lenka is an Assistant Professor in the Department of Electronics and Communication Engineering, National Institute of Technology Silchar, India. He received a B.E. degree in Electronics and Communication Engineering from Berhampur University, Odisha, in 2000, M.Tech. degree in VLSI Design from Dr. A. P. J. Abdul Kalam Technical University, Lucknow, in 2007 and a Ph.D. degree in Microelectronics Engineering from Sambalpur University, Odisha, in 2012. He was a Visiting Researcher at Helen and John C. Hartmann Department of Electrical and Computer Engineering, New Jersey Institute of Technology (NJIT), Newark, New Jersey, the USA, in 2019, and Solar Energy Research Institute of Singapore (SERIS), National University of Singapore (NUS), Singapore, in 2018. He received Distinguished Faculty Award by NIT Silchar in 2019. He has supervised 12 Ph.D. and 23 M.Tech. students under his guidance. He has published 105 journal research papers, 17 book chapters, and 58 conference papers to his credit and delivered 21 invited talks. His research interests include nanoelectronics: III-nitride heterojunction devices (HEMT, NW LED), solar photovoltaics, energy harvesting using MEMS, and nanotechnology.

Hieu Pham Trung Nguyen received his Ph.D. degree in Electrical Engineering from McGill University, Canada, in 2012. He joined the New Jersey Institute of Technology in 2014 and currently is an Associate Professor in the Department of Electrical and Computer Engineering. He is a recipient of the 2020 NSF CAREER Award, the 2019 Saul K Fenster Innovation in Engineering Education Ward, the SPIE Scholarship in Optics and Photonics 2012 (for his potential long-range contributions to the field of optics, photonics, or related field), the Best Student Paper Award 2011 (Second Place) at the IEEE Photonics Conference 2011, and the Outstanding Student Paper Award at the 28th North American Molecular Beam Epitaxy Conference, 2011. He is

serving as a reviewer for over 70 journals. His research areas are electronic and photonic devices.

Contributors

Lucky Agarwal
School of Electronics Engineering, Vellore Institute of Technology, Chennai, Tamil Nadu, India

G. Amarnath
Department of ECE, Marri Laxman Reddy Institute of Technology and Management, Hyderabad, India

Kalyan Biswas
ECE Department, MCKV Institute of Engineering, Liluah, Howrah, WB, India

G. Chatterjee
Department of Electronics and Communication Engineering, The LNM Institute of Information Technology, Jaipur, Rajasthan, India

Meenakshi Chauhan
Department of Electronics and Communication Engineering, The LNM Institute of Information Technology, Jaipur, Rajasthan, India

M. C. Chinnaiah
Department of ECE, B.V. Raju Institute of Technology, Narsapur, India

Rachita Ghoshhajra
CSE Department, MCKV Institute of Engineering, Liluah, Howrah, WB, India

Manisha Guduri
Department of ECE, KG Reddy College of Engineering and Technology, Hyderabad, India

Mridula Gupta

Senior Professor and Head, Department of Electronic Science, University of Delhi South Campus, New Delhi, India

Santosh Kumar Gupta
Department of Electronics and Communication Engineering, Motilal Nehru National Institute of Technology, Allahabad, Uttar Pradesh, India

Kanjalochan Jena
Department of Electronics and Communication Engineering, The LNM Institute of Information Technology, Jaipur, Rajasthan, India

Sneha Kabra
Associate Professor, Department of Instrumentation, Shaheed Rajguru College of Applied Sciences for Women, University of Delhi, New Delhi, India

Mousiki Kar
Department of Electronics and Communication Engineering, Heritage Institute of Technology, Kolkata, India

Abdul Naim Khan
Department of Electronics and Communication Engineering, The LNM Institute of Information Technology, Jaipur, Rajasthan, India

Atanu Kundu
Department of Electronics and Communication Engineering, Heritage Institute of Technology, Kolkata, India

Trupti Ranjan Lenka
Microelectronics and VLSI Design Group, Department of Electronics and Communication Engineering, National Institute of Technology Silchar, Silchar, Assam, India

S. N. Mishra
School of Electronics Engineering, KIIT (Deemed to be University), Bhubaneswar, Odisha, India

Varun Mishra

Department of Electronics and Electrical Engineering, Graphic Era (Deemed to be University), Dehradun, Uttarakhand, India

P. Murugapandiyan
Department of Electronics and Communication Engineering, Anil Neerukonda Institute of Technology & Sciences, Visakhapatnam, Andhra Pradesh, India

Hieu Pham Trung Nguyen
Department of Electrical and Computer Engineering, New Jersey Institute of Technology, Newark, New Jersey, USA

Deepak Kumar Panda
Microelectronics and VLSI Design Group, School of Electronics, VIT-AP University, Amaravati, Andhra Pradesh, India

G. Purnachandra Rao
Department of Electronics and Communication Engineering, National Institute of Technology Silchar, Silchar, Assam, India

N. Ramkumar
Department of Electronics and Communication Engineering, Anil Neerukonda Institute of Technology & Sciences, Visakhapatnam, Andhra Pradesh, India

Samriddhi Raut
Department of ECE, Maharaja Surajmal Institute of Technology, Guru Gobind Singh Indraprastha University, New Delhi, India

S. Ravi
Department of Electronics and Communication Engineering, Seshadri Rao Gudlavalleru Engineering College, Gudlavalleru, Andhra Pradesh, India

D. S. Rawal
MMIC Fabrication Division, Solid State Physics Laboratory, Defence Research & Development Organization, New Delhi, India

Angsuman Sarkar
ECE Department, Kalyani Government Engineering College, Kalyani, Nadia, WB, India

Manoj Saxena
Department of Electronics, Deen Dayal Upadhyaya College, University of Delhi, New Delhi, India

Khushwant Sehra
Department of Electronic Science, University of Delhi South Campus, New Delhi, India

Laxman Singh
Department of Electronics and Communication Engineering, Noida Institute of Engineering and Technology, Greater Noida, India

Rajan Singh
Microelectronics and VLSI Design Group, Department of Electronics and Communication Engineering, National Institute of Technology Silchar, Silchar, Assam, India

Raghunandan Swain
Department of Electronics and Telecommunication Engineering, Parala Maharaja Engineering College, Berhampur, Odisha, India

Raghuvir Tomar
Department of Electronics and Communication Engineering, The LNM Institute of Information Technology, Jaipur, Rajasthan, India

Yogesh Kumar Verma
School of Electronics and Electrical Engineering, Lovely Professional University, Jalandhar, Punjab, India

T. R. Lenka, H. P. T. Nguyen (eds.), *HEMT Technology and Applications*, Springer Tracts in Electrical and Electronics Engineering
https://doi.org/10.1007/978-981-19-2165-0_1

Ultrawide Bandgap AlGaN-Channel-Based HEMTs for Next-Generation Electronics

P. Murugapandiyan[1] ✉, N. Ramkumar[1] and S. Ravi[2]
(1) Department of Electronics and Communication Engineering, Anil Neerukonda Institute of Technology & Sciences, Visakhapatnam, Andhra Pradesh, 531162, India
(2) Department of Electronics and Communication Engineering, Seshadri Rao Gudlavalleru Engineering College, Gudlavalleru, Andhra Pradesh, 521356, India

✉ **P. Murugapandiyan**
Email: murugavlsi@gmail.com

Abstract
This chapter reviews the recent progress in ultrawide bandgap AlGaN-channel-based high electron mobility transistors. AlGaN channel is the alternate substitute for the conventional GaN channel. In order to enhance the power handling capability of III-nitride-based heterostructure devices, improving the breakdown performance of the device without reduction in the current density is one of the simplest techniques. AlGaN-channel-based HEMTs favorably increase the critical electric field of the device. For the next-generation RF application, further improving the power handling capabilities of RF modules, AlGaN channel HEMT is the most optimistic applicant and it delivers four times larger GaN HEMT's power performance and thus becoming the possible substitute to the GaN channel for the next generation power as well as RF devices and circuits. This chapter describes the

polarization details of $Al_xGa_{1-x}N/Al_yGa_{1-y}N$ heterostructure, and various device structure of AlGaN channel HEMTs and their static and dynamic characteristics.

Keywords GaN – HEMT – Heterostructure – Polarizations – RF – Ultra-wide Bandgap

1 Introduction

Since the III-nitride semiconductor materials offer a wide range of bandgap spectrum, III-nitride-based devices are widely used in optoelectronics, RF, and power electronics applications. Due to the existence of stronger polarization, high critical breakdown field, and higher carrier velocity, the GaN-channel-based HEMTs are used in high-power RF amplification and switching. Because of the existence of polarization effects, the AlGaN/GaN heterostructure interface has a high density of electron density with high carrier mobility and many researchers demonstrated the potential of AlGaN/GaN HEMTs. Several GaN-channel-based commercial HEMTs are developed and available in the market for high-power microwave applications, low-noise RF circuit design, DC–DC converters, electric vehicles, motor drivers, etc.

Further increasing the power density of the III-nitride devices for next-generation electronics and enhancing the breakdown voltage of the HEMTs are most important. Table 1 shows the compound semiconductor material properties. The AlN material properties dominate the GaN in terms of 2 × bandgap, 4 × breakdown field, high Johnson figure of merit (JFoM), good thermal conductance, and high Baliga figure of merit (BFoM). Due to these outstanding properties, $Al_xGa_{1-x}N$ ultrawide bandgap ternary material is used as the channel instead of a conventional GaN channel for improving the breakdown field of the HEMTs. Therefore, high Al composition AlGaN-channel-based HEMTs are expected to exhibit extremely large blocking voltage and high-temperature operation in modern power electronics era. Aside from power electronics applications, AlGaN channel HEMTs are promising candidates for millimeter-wave applications because of their high Johnson figure of merit ($V_{\mathrm{BR}} \times F_T = \frac{E_{\mathrm{BR}} V_{\mathrm{sat}}}{2\pi}$) and expected to

deliver high RF power density at millimeter wave. In evaluating AlGaN channel HEMT technologies for millimeter-wave high-power applications, the cutoff frequencies (F_T, and F_{MAX}) of the HEMTs are important device parameters in addition to breakdown voltage and high drain current density. The improvement in the device cutoff frequency was achieved through scaling techniques.

Table 1 Semiconductor material properties

	Si	GaAs	SiC	GaN	AlN
Bandgap (eV)	1.12	1.42	3.26	3.40	6.20
Breakdown field (MV/cm)	0.3	0.4	3.0	3.3	12
Electron mobility (cm^2/Vs)	1500	8500	1000	2000	1090
Electron saturation velocity (cm/s) × 10^7	1	2	2	2.5	2.2
Dielectric constant	11.9	12.9	10	8.9	8.5
JFoM	1	7	400	760	7800
BFoM	1	9	11	39	67

2 Spontaneous and Piezoelectric Polarization of $Al_xGa_{1-x}N/Al_yGa_{1-y}N$ Heterostructure

The III-nitride-based heterostructure-based devices are widely used in various electronic applications including high power switching, high power microwave, and optoelectronics. The asymmetry of wurtzite crystal structure induces spontaneous polarization (SP) and piezoelectric polarization (PZ) effect in III-nitride semiconductors-based heterostructure devices. Due to the polarization difference between a wide bandgap and a narrow bandgap semiconductor, a high density of 2DEG is existing at the interface. The spontaneous polarization difference between the materials and strain-induced piezoelectric polarization is the major source of creation of 2DEG [1]. This property of III-nitride heterostructure devices is attractive for power electronics and microwave applications. The $Al_xGa_{1-x}N/Al_yGa_{1-y}N$ heterostructure polarization details are illustrated

in Fig. 1 for Ga-face crystal structure by considering relaxed, and tensile strain.

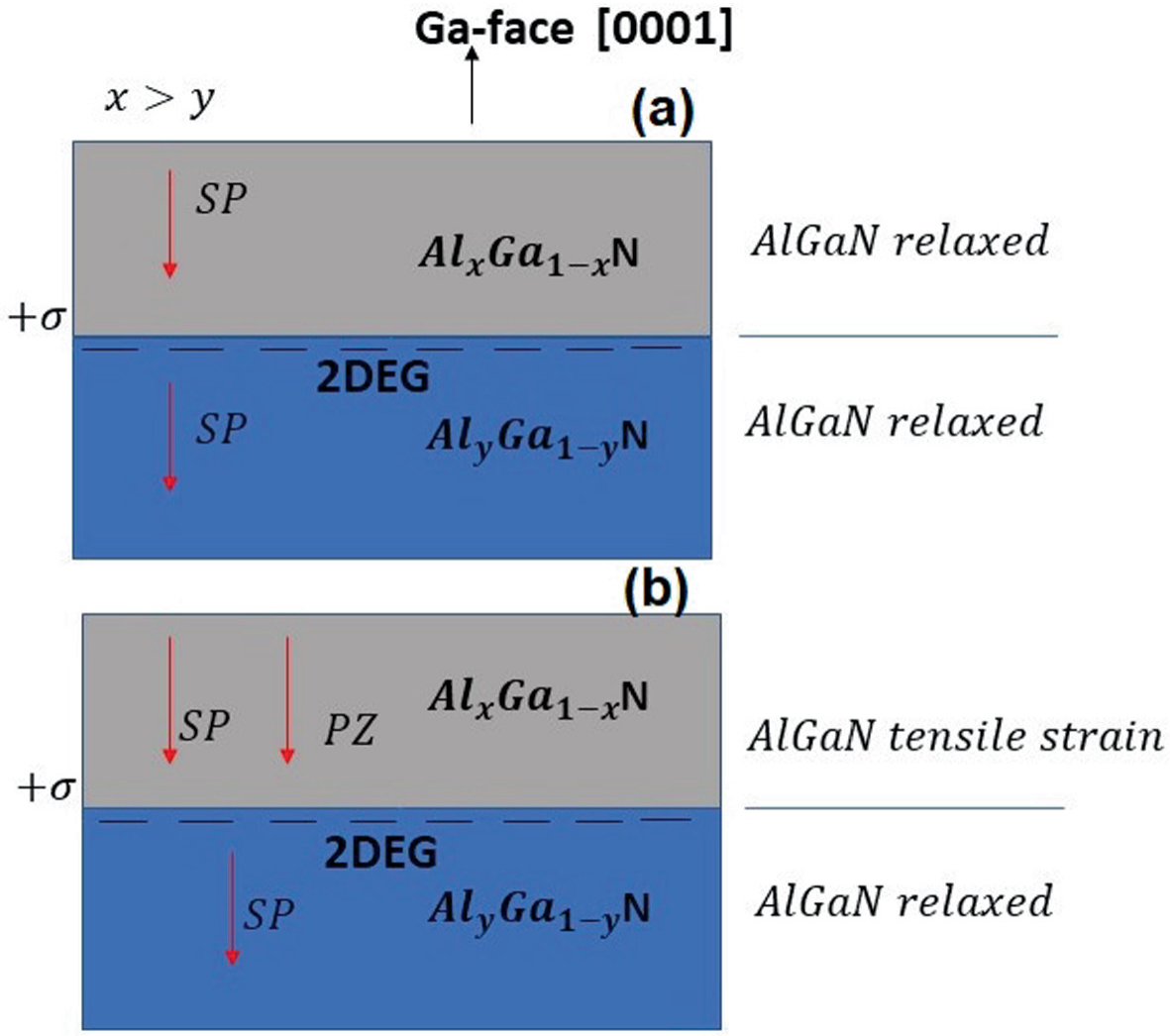

Fig. 1 Spontaneous and piezoelectric polarization details of $Al_xGa_{1-x}N/Al_yGa_{1-y}N$ heterostructure

The polarization sheet charge density was obtained from the following equation:

$$\sigma = P\,(\text{top}) - P\,(\text{bottom}) = \{\text{SP}\,(\text{top}) + \text{PZ}\,(\text{top})\} - \{\text{SP}\,(\text{bottom}) + \text{PZ}\,(\text{bottom})\} \quad (1)$$

The polarization induced charges depend on Al composition and surface roughness. As shown in Fig. 1a and b, to neutralize the polarization induced positive charges ($+\sigma$), the free electrons from

donor-like surface trap states come and occupy the quantum well when the $Al_xGa_{1-x}N/Al_yGa_{1-y}N$ band offset is reasonably high. Assume the heterostructure was grown in pseudomorphic (Fig. 1b), the tensile strain $Al_xGa_{1-x}N$ piezoelectric polarization will improve the $P_{AlxGa1-xN}$– $P_{AlyGa1-yN}$ polarization difference. In the absence of stain-induced PZ also, electrons are accumulated in the quantum well due to the SP difference of $Al_xGa_{1-x}N/Al_yGa_{1-y}N$. The PZ of wurtzite III-nitride materials are described as follows:

$$\mathrm{PZ} = 2\frac{a\left(\mathrm{Al}_x\mathrm{Ga}_{1-x}\mathrm{N}\right) - a\left(\mathrm{Al}_y\mathrm{Ga}_{1-y}\mathrm{N}\right)}{a\left(\mathrm{Al}_y\mathrm{Ga}_{1-y}\mathrm{N}\right)}\left(e_{31(\mathrm{Al}_x\mathrm{Ga}_{1-x}\mathrm{N})} - e_{33(\mathrm{Al}_x\mathrm{Ga}_{1-x}\mathrm{N})}\frac{c_{13(\mathrm{Al}_x\mathrm{Ga}_{1-x}\mathrm{N})}}{c_{33}\left(\mathrm{Al}_x\mathrm{Ga}_{1-x}\mathrm{N}\right)}\right) \quad (2)$$

where c_{13}, and c_{13} are elastic constants, a is lattice constant, and c_{13} and c_{13} are elastic coefficient. The elastic coefficient parameter, elastic constant, and lattice constant of $\mathrm{Al}_x\mathrm{Ga}_{1-x}\mathrm{N}$ ternary alloy are as follows:

$$C_{13} = 5x + 103 \quad (3)$$

$$C_{33} = -32x + 405 \quad (4)$$

$$e_{13} = -11x - 0.49 \quad (5)$$

$$e_{33} = 0.73x + 0.73 \quad (6)$$

$$a = (3.189 - 0.077x)\,10^{-10}\mathrm{m} \quad (7)$$

The spontaneous polarization of $\mathrm{Al}_x\mathrm{Ga}_{1-x}\mathrm{N}$ ternary alloys is calculated from the following equation:

$$\mathrm{SP}\left(\mathrm{Al}_x\mathrm{Ga}_{1-x}\mathrm{N}\right) = -0.090x - 0.034\,(1-x) + 0.021x\,(1-x) \quad (8)$$

The total carrier density in the 2DEG region for undoped device configuration is as follows;

$$n_S(x) = \frac{\sigma(x)}{\mathrm{e}} - \left(\frac{\varepsilon_0 \varepsilon(x)}{d_{\mathrm{Al}x\mathrm{Ga1}-x\mathrm{N}} \cdot \mathrm{e}^2}\left(\mathrm{e}\phi_b(x) + E_f(x) - \Delta E_c\right)\right) \quad (9)$$

The carrier density in the channel depends on the relative dielectric constant $\varepsilon(x)$, thickness of the barrier layer $d_{\mathrm{Al}x\mathrm{Ga1}-x\mathrm{N}}$, Schottky barrier $\phi_b(x)$, Fermi energy level $E_f(x)$, and conduction band offset ΔE_c. Therefore, the sheet charge density can be controlled by Al composition in the AlGaN barrier and the thickness of the barrier. The bandgap of AlGaN ternary material and conduction band offset is calculated from the following:

$$\varepsilon(x) = (-0 \cdot 5x) + 9 \cdot 5 \quad (10)$$

$$\mathrm{e}\phi_b(x) = (1 \cdot 3x + 0.84)\,\mathrm{e}V \quad (11)$$

$$E_g(\mathrm{AlN}) = 6.13\mathrm{e}V \quad (12)$$

$$E_g(\mathrm{GaN}) = 3.42\mathrm{e}V \quad (13)$$

$$E_g(\mathrm{Al}_x\mathrm{Ga}_{1-x}\mathrm{N}) = xE_g(\mathrm{AlN}) + (1-x)E_g(\mathrm{GaN}) - x(1-x)\,1.0eV \quad (14)$$

$$\Delta E_C = 0.7\left(E_g(\mathrm{Al}_x\mathrm{Ga}_{1-x}\mathrm{N}) - E_g\left(\mathrm{Al}_y\mathrm{Ga}_{1-y}\mathrm{N}\right)\right)eV \quad (15)$$

3 AlGaN-Channel-Based HEMTs for High-Frequency Electronics Application

In recent years, ultrawide bandgap semiconductors (AlGaN, Ga2O3, and diamond) have attracted enormous research interest as key

components for high-power switching applications [1–10]. Particularly, $Al_xGa_{1-x}N$-channel-based HEMTs are optimistic devices for future electronics because of their wide bandgap relative to the GaN channel ($E_c = E_g^n; n \sim 2.5 to 2.7$), strong polarization, high saturation velocity, ultrahigh breakdown field. The Monte Carlo simulation showed the Al-rich AlGaN material is favorable for high-power RF performance because the saturation velocity is on par with GaN [11]. Recently, Al-rich $Al_xGa_{1-x}N/Al_yGa_{1-y}N$-based HEMTs have proven their potential, which is exceeded the $Al_xGa_{1-x}N$ /GaN-based HEMTs performances [12–15]. And therefore, $Al_xGa_{1-x}N/Al_yGa_{1-yN}$-based HEMTs are suitable for realizing solid-state power amplifiers (PAs) with high power, wide operational bandwidth, and high efficiency for 5G and 6G wireless communications. The maximum RF power delivered to a load of a basic amplifier circuit is as follows:

$$P_{\max} = I_{\max}\left(\frac{V_{\text{br}} - V_{\text{knee}}}{8}\right) \tag{16}$$

The high RF current ($I_{\max}$), and breakdown voltage (V_{br}) of the transistor will improve the output power density of a solid-state power amplifier. Due to the virtue of high critical electric field (c_{13}), large breakdown field, and a high Johnson figure of merit ($\text{JFOM} = E_C\frac{v_{\text{sat}}}{2}$), the AlGaN channel HEMTs are highly desirable for high-power RF electronics. Further, the c_{13} enhanced by Al-rich $Al_xGa_{1-x}N/Al_yGa_{1-y}N$ ($x > y$) heterostructures. High output current density (I_{DS}) and high V_{BR} are the important factors for improving the power density of solid-state power amplifier. The $Al_yGa_{1-y}N$ channel HEMT with high Al composition enables the critical field ~4 × higher than GaN-channel-based devices. The low carrier mobility (μ) and alloy scattering degrade the on-state current ($J = qn_sE$) for long AlGaN channel devices. However, at a high electric field, the saturation velocity of AlGaN channel HEMTs is on par with GaN-channel devices [11]. Therefore, the

current density ($J = qv_{sat}n_s$) of Al-rich AlGaN channel HEMTs majorly depends on 2DEG electron density (n_s).

3.1 Device Scaling for High-Frequency Application

Figure 2 shows the small-signal model of HEMT and Fig. 3. indicates the extraction of the cutoff frequency of the transistors from its small-signal characteristics. The device's parasitic capacitances $(C_{GS} + C_{GD})$ and parasitic resistances such as gate (R_G), drain (R_D), source (R_S), and drain to source (R_{DS}) limit the high-frequency operation of HEMTs. Among all these components, device transconductance (G_M), and gate to source capacitance (C_{GS}) has more influence on the high-speed operation of the HEMTs [16]. The cutoff frequency of the device can be written as the following equations [16]:

$$F_T = \frac{G_m}{2\pi\,(C_{GS} + C_{GD})} \tag{17}$$

$$F_{MAX} = \frac{F_T}{2\,(R_G + R_{DS})^{1/2}} \tag{18}$$

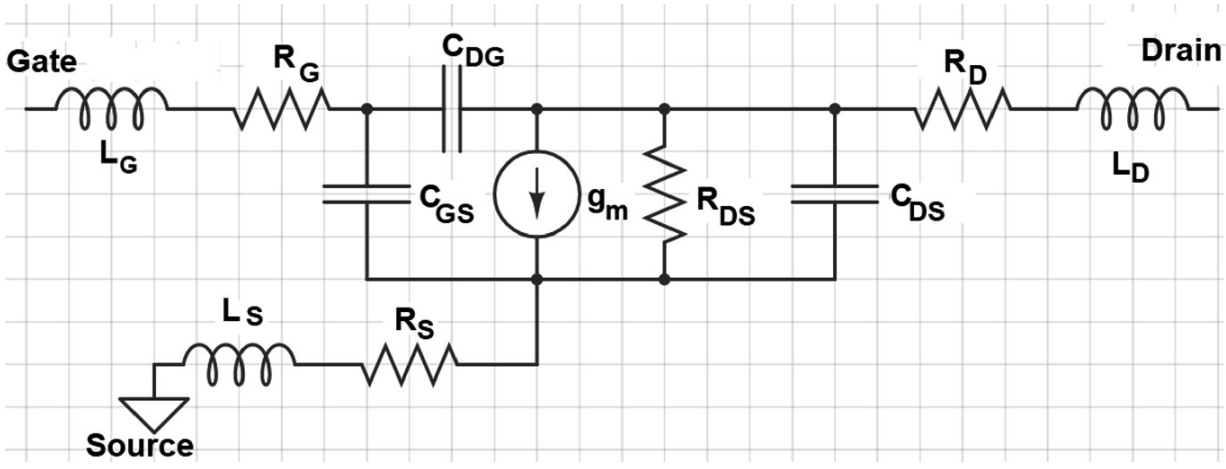

Fig. 2 Small signal model of HEMT

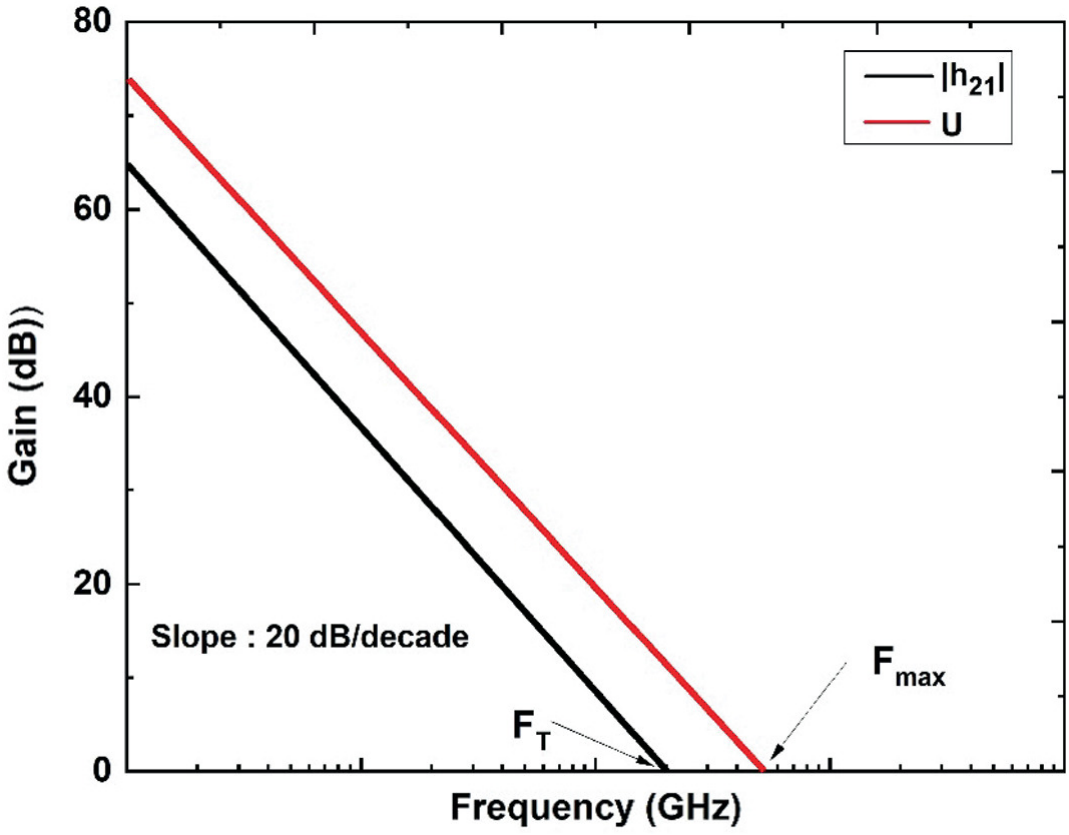

Fig. 3 Extraction of F_T and F_{MAX} from small signal characteristics

For obtaining maximum oscillation frequency F_{MAX}, the gate capacitances, gate resistance, and transconductance of the HEMT need to be optimized. Reduction in the channel length L_G will increase the current gain cut-off frequency $F_T = \frac{v_{sat}}{2\pi L_G}$ by reducing the electron transit time. A T-shaped gate structure minimizes the gate resistance by offering a wide gate area for carrier transport with a smaller footprint as shown in Fig. 4.

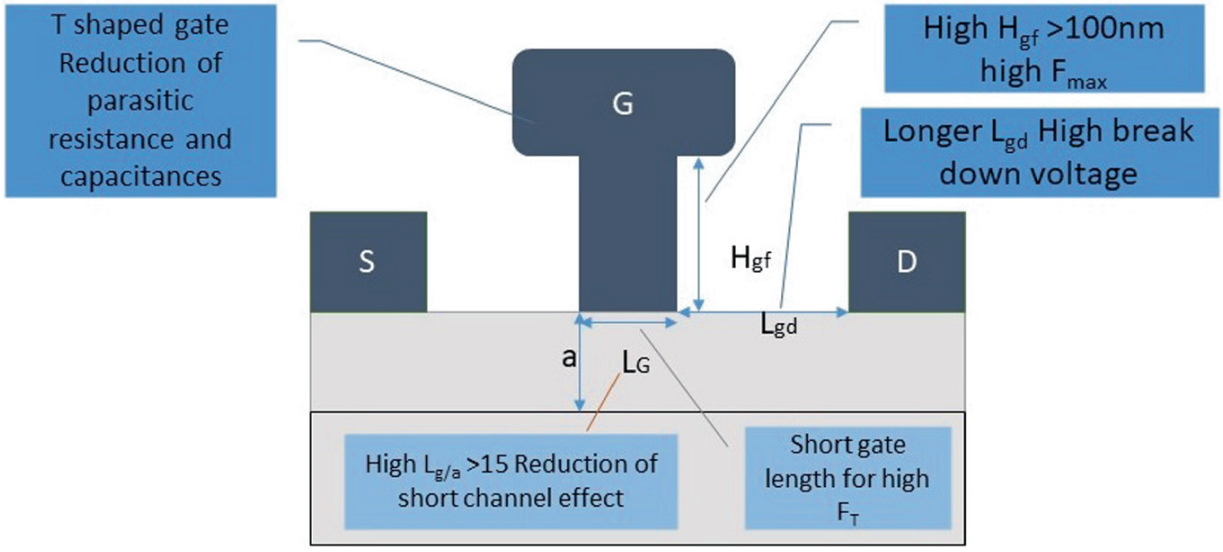

Fig. 4 T-gate HEMT structure

3.2 Device Configuration of AlGaN Channel HEMTs

Figure 5 shows a typical AlGaN channel HEMTs. The HEMT consists of a 30 nm Si-doped (~3.5×10^{18} cm^{-3}) $Al_{0.85}Ga_{0.15}$ N barrier, 400 nm $Al_{0.7}Ga_{0.3}$ N channel layer, and 50 nm graded buffer [17]. The doped barrier layer enhances the carrier density (n_s) in the channel up to 7.2 $\times 10^{12}$ cm^{-2}. The Hall measurement shows 2200 Ω/square of sheet resistance and 390 cm^2/V.s of carrier mobility. SiN-passivated device surface with L_G = 80 nm exhibited 80 mA/mm drain current density, and breakdown voltage of 493 V for L_{GD} = 2 μm. The device shows F_T/F_{MAX} of 28.4/18.5 GHz. Moreover, the large-signal measurements showed 11% power-added efficiency at 3 GHz operational frequency.

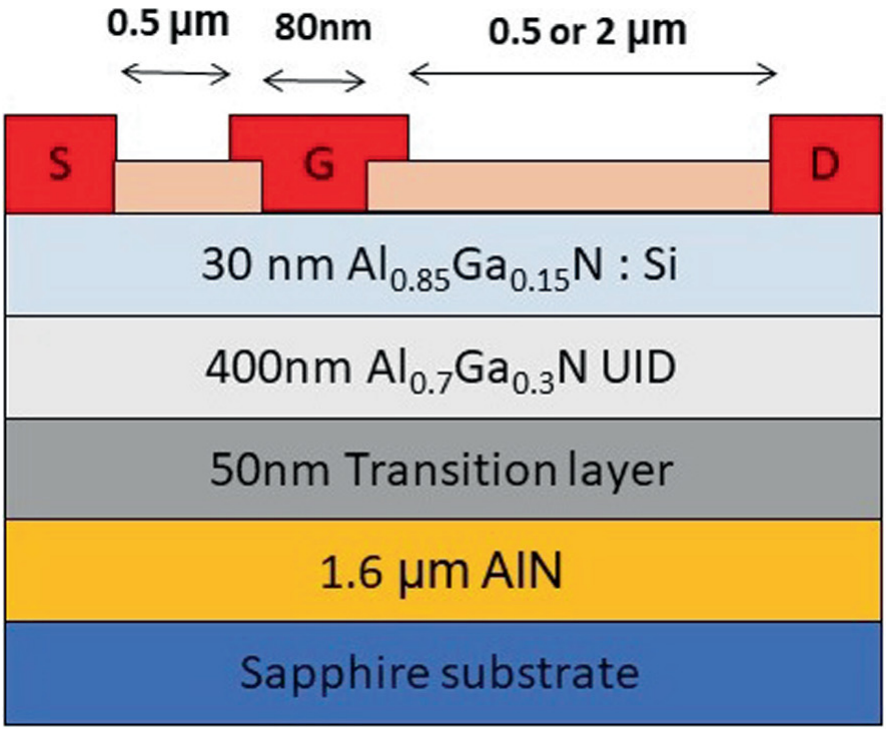

Fig. 5 L_G 80 nm AlGaN channel HEMT

The main challenge in AlGaN channel HEMT is making good ohmic contact for Al-rich channel devices. A low-contact resistance device is achieved by a linearly graded contact layer using MBE or MOCVD [18, 19]. Several contact engineering has been adopted [12–15] for improving the performance of the device. Generally, the ohmic contacts are realized by regrown or alloyed ohmic contacts. Low contact resistance of 2.6×10^{-4} Ω.cm^2 was reported for $Al_{0.3}Ga_{0.7}$ N channel HEMT [14] by using Zr-based alloy contact.

A Si-doped barrier ($Al_{0.65}Ga_{0.35}$ N) MOSHEMT with Zr/Al/Mo/Au-based ohmic contact is shown in Fig. 6 and TLM (transmission line measurement) measurement result is plotted in Fig. 7. The HEMT has shown a minimum contact resistance of 1.64 Ω.mm and recorded 0.6 A/mm peak current density and the Hall mobility measurements result showed μ_n of 430 cm^2/V.s [14]. For a high breakdown field, Al mole fraction must be in both the barrier and channel layers. Heterostructure with $Al_xGa_{1-x}N/Al_yGa_{1-y}N$, where $x > y > 0.65$, increases the breakdown voltage 3 × better than the GaN channel. At the same time, ohmic contact resistance of the wideband gap heterostructure

increases, which limits the high-frequency operation of the HEMTs. The regrown ohmic contact technology achieved a low ohmic contact resistivity of 5×10^{-3} Ω.cm^2 [20].

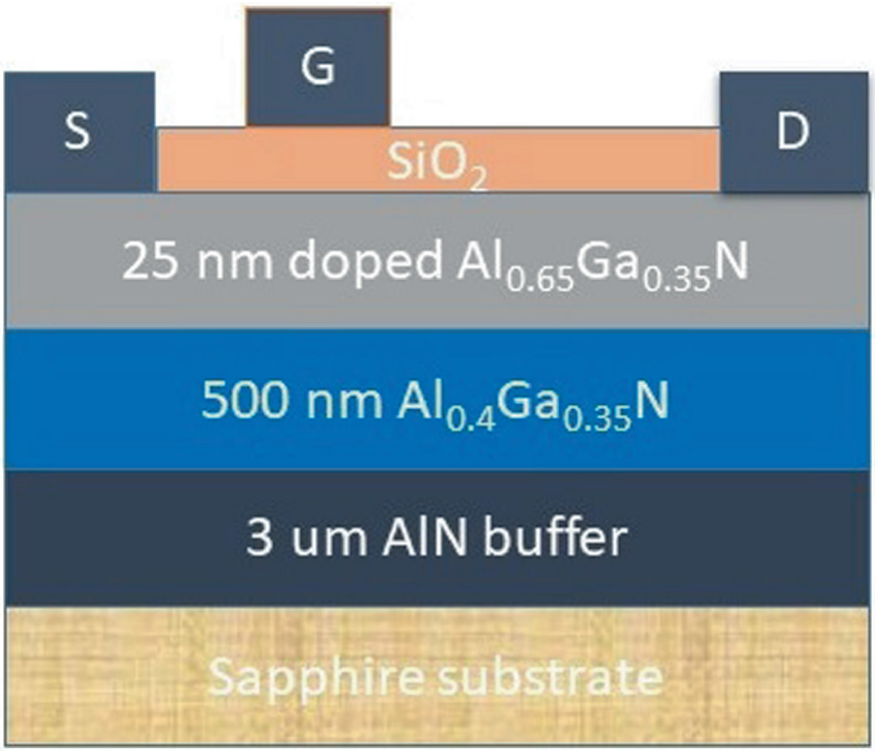

Fig. 6 AlGaN channel MOSHEMT

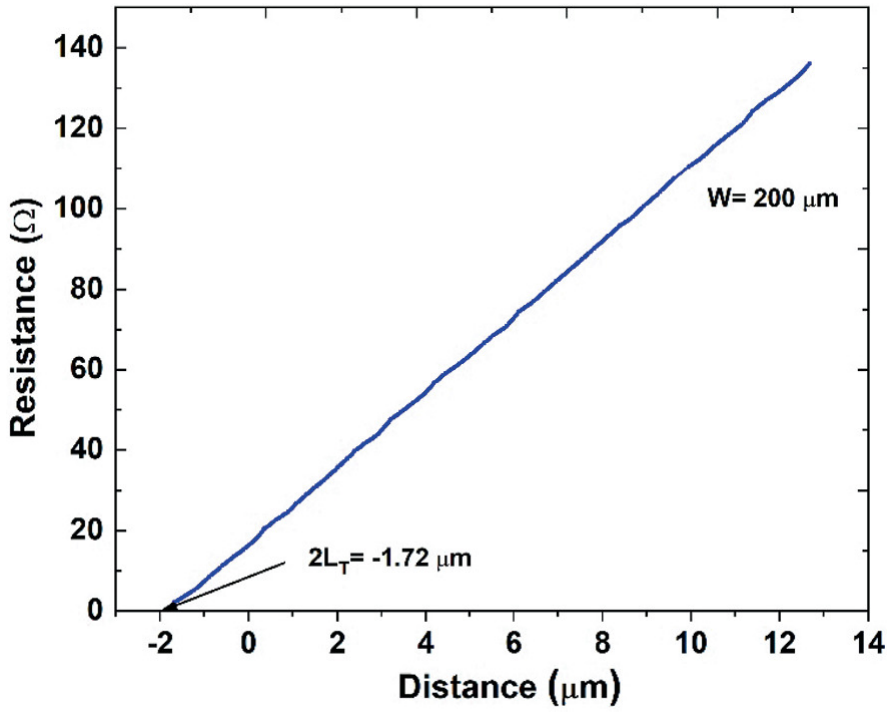

Fig. 7 TLM measurement

The schematic view of *n* + regrowth AlGaN channel HEMT is shown in Fig. 8. The energy band profile through $Al_{0.85}Ga_{0.15}$ N/$Al_{0.66}Ga_{0.34}$ N is displayed in Fig. 9. The 2DEG is presented just below the heterostructure interface and the conduction band energy level is below the Fermi level. The energy band profile through *n* + GaN/$Al_{0.66}Ga_{0.34}$ N is displayed in Fig. 10. The conduction band energy level exactly overlapped with the Fermi level (0 eV). Therefore, the regrown ohmic contact has a low electron density [20]. Another method to minimize the contact resistance, the graded AlGaN contact layer is used. $Al_{0.7}Ga_{0.3}$ N/$Al_{0.5}Ga_{0.5}$ N HEMT with graded *n* + AlGaN source/drain region is depicted in Fig. 11 and the energy band diagram of heterostructure is displayed in Fig. 12. The graded AlGaN region consists of 40 nm *n* + doped (Si ~ 6 × 10^18 cm^{-3}) graded AlGaN layer with the Al composition from 70 to 50% and 30 nm *n* + doped (Si ~ 5 × 10^18 cm^{-3}) AlGaN grading from 50 to 30%.

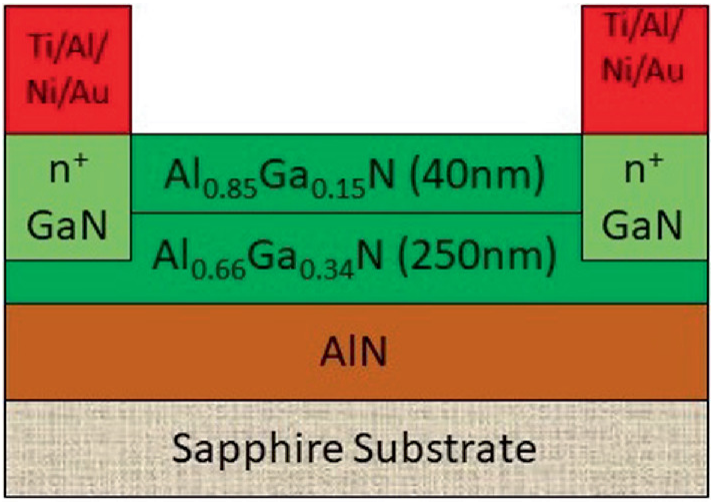

Fig. 8 Schematic view of *n* + GaN regrown AlGaN channel HEMT

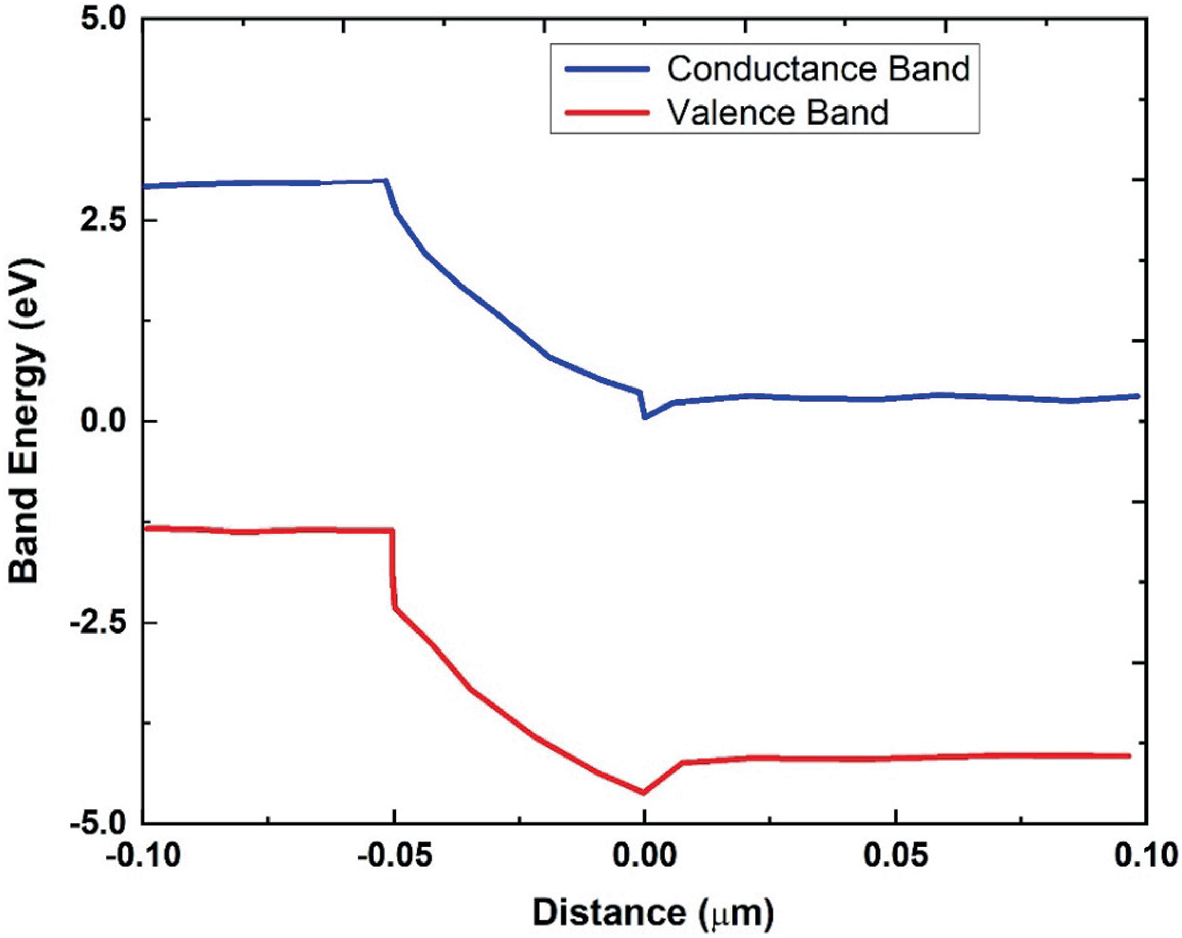

Fig. 9 Energy band diagram of $Al_{0.85}Ga_{0.15}$ N/$Al_{0.66}Ga_{0.34}$ N heterostructure

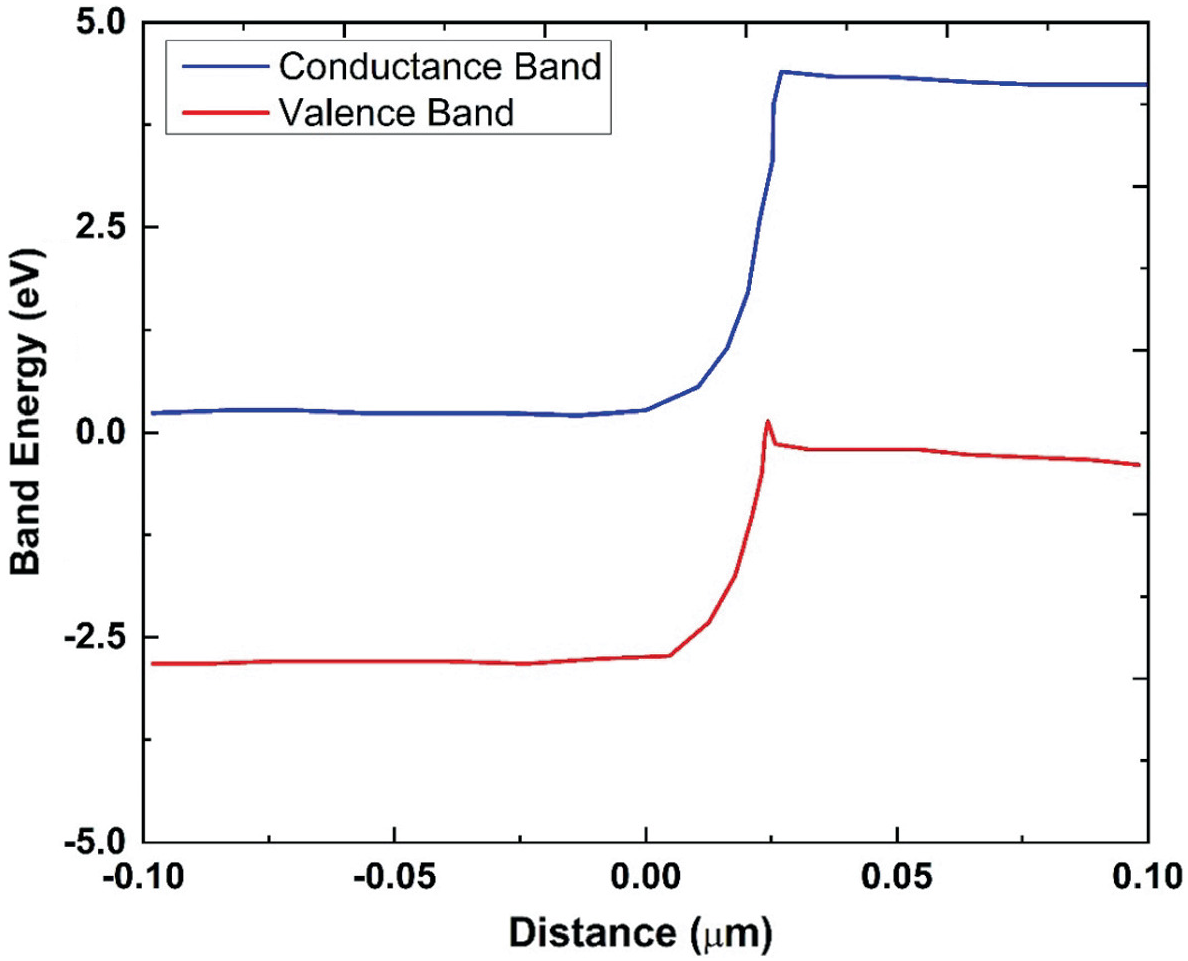

Fig. 10 Energy band diagram of *n* + GaN/$Al_{0.66}Ga_{0.34}$ N heterostructure

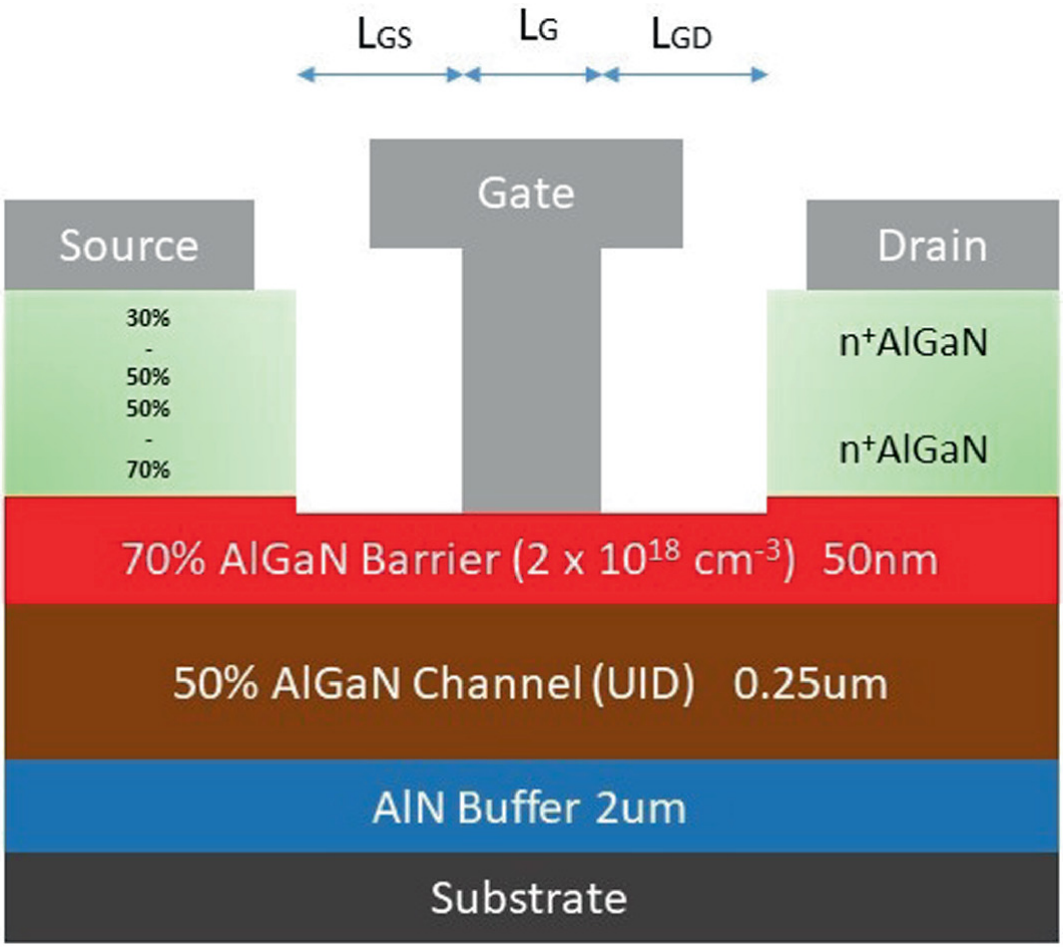

Fig. 11 Schematic view of *n* + AlGaN source/drain region HEMT

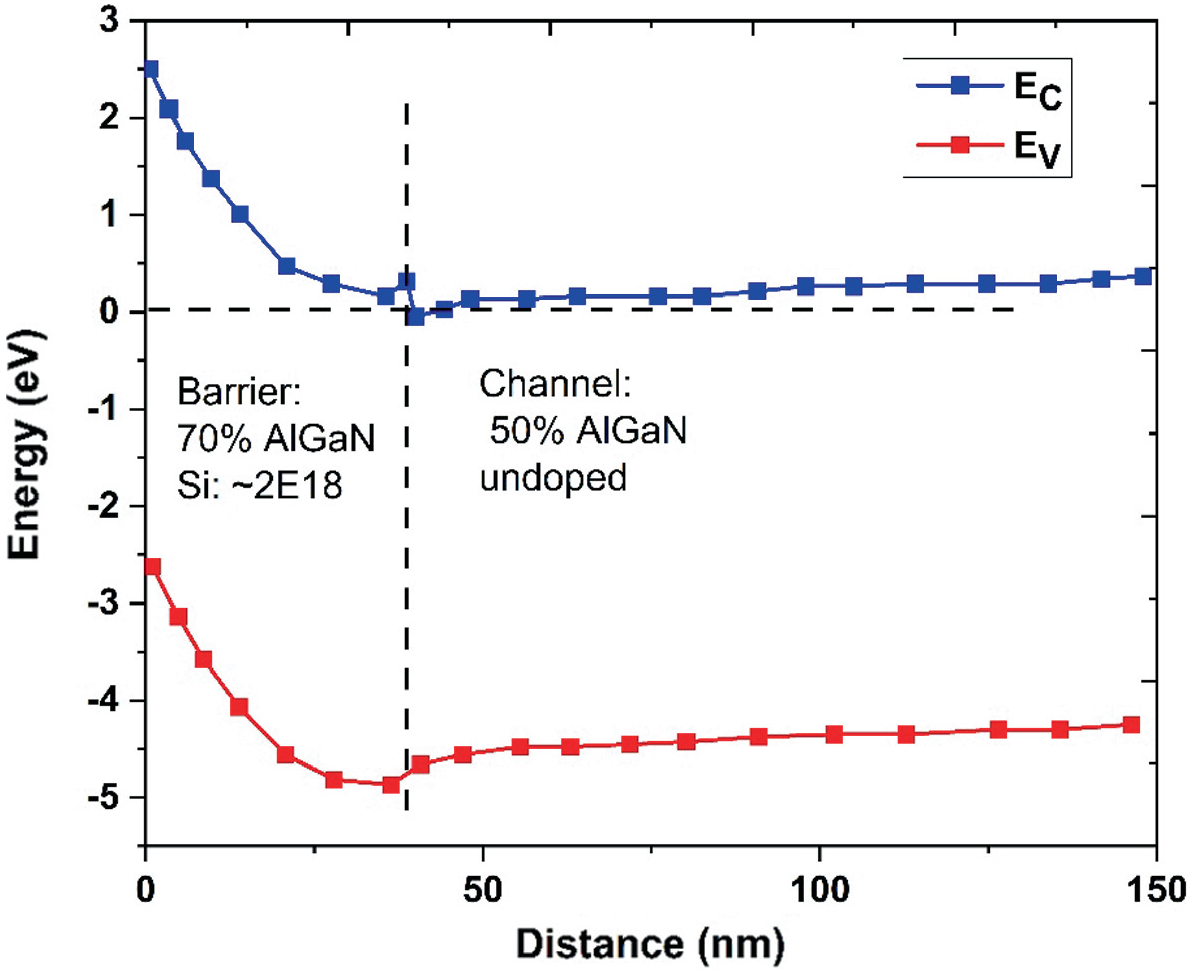

Fig. 12 Energy band diagram of $Al_{0.7}Ga_{0.3}$ N/$Al_{0.5}Ga_{0.5}$ N heterostructure

Figure 13 displays the energy band profile of the source/drain region. The *n* + AlGaN graded region maintains a flat conduction band between the surface and channel which enables tunneling-based ohmic contacts. The HEMT showed 120 cm^2/V.s of electron mobility and 8.8 × 10^{12} cm^{-2} of 2DEG density. Figure 14a shows the very good ohmic behavior and Fig. 14b displays the resistance variations with contact spacings [21]. L_G = 160 nm HEMT showed a F_T/F_{MAX} of 20/40 GHz. And the cutoff frequency dependence on drain current is plotted in Fig. 15, where V_{GS} swept from 0 to −10 V and V_{DS} kept at 13 V. Moreover, the device had shown 170 V of V_{BR}.

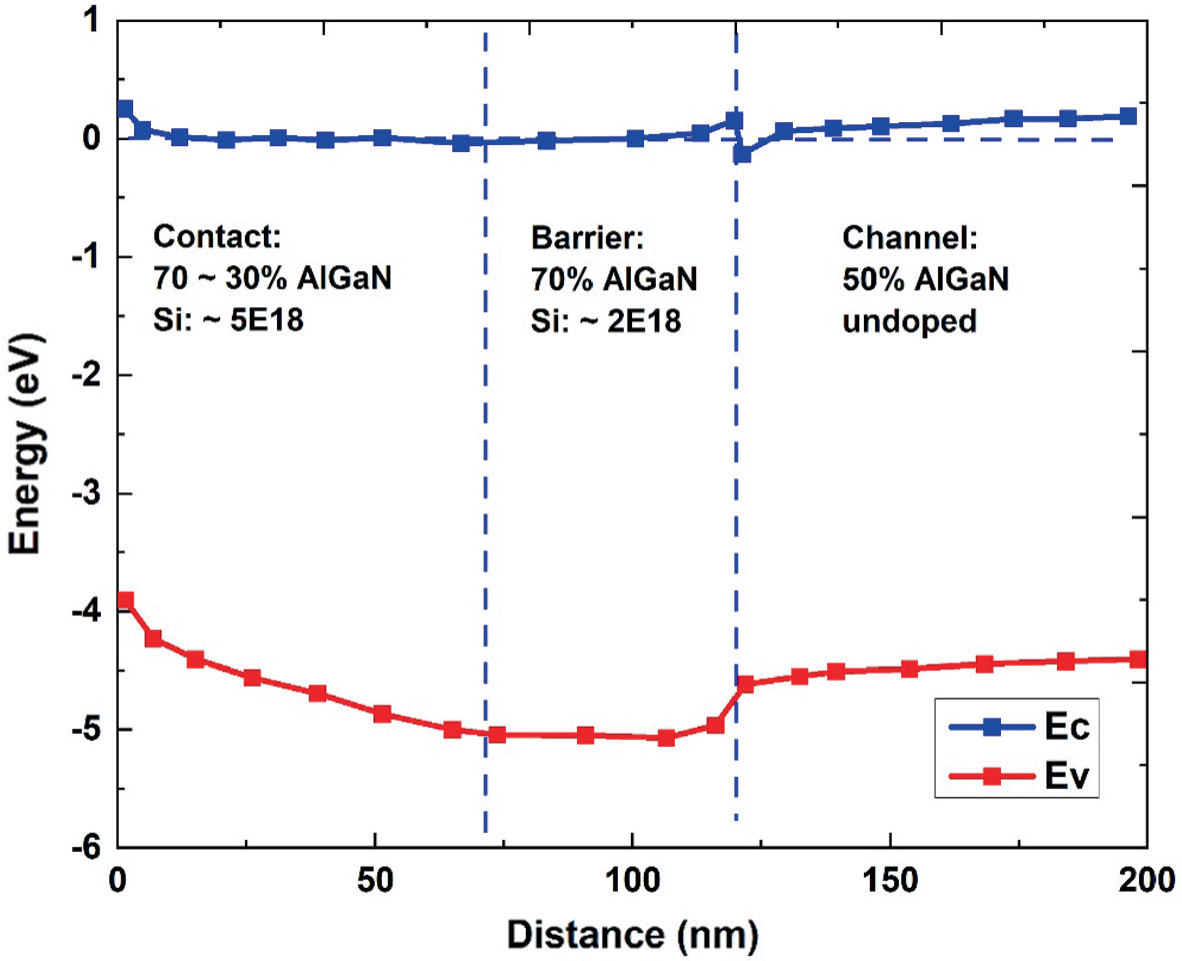

Fig. 13 Energy band diagram of access region

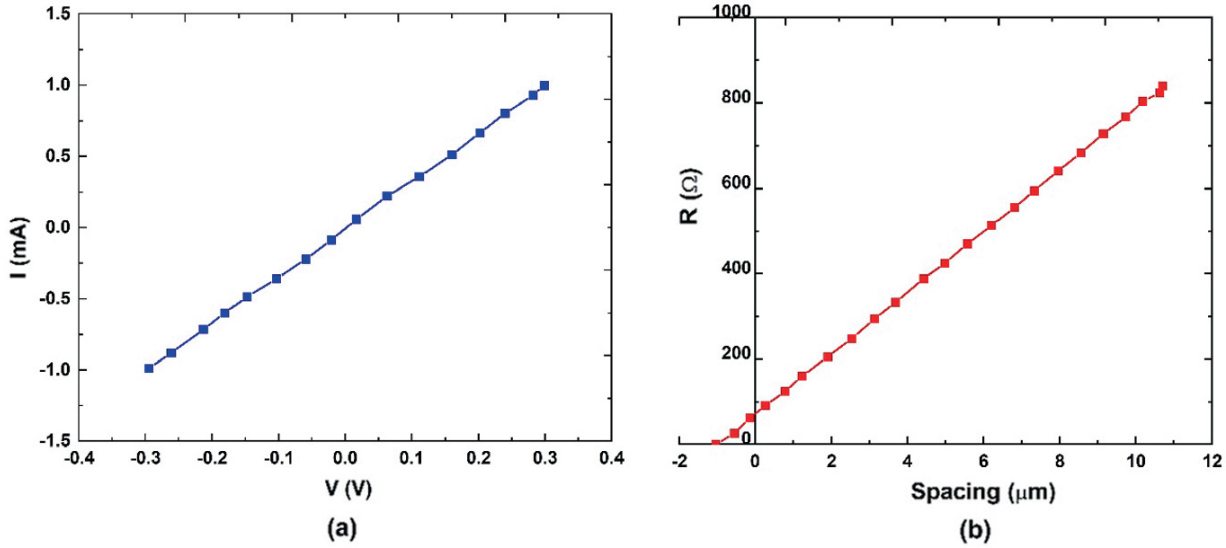

Fig. 14 **a** Two terminal V–I characteristics **b** Resistance variations with contact spacings

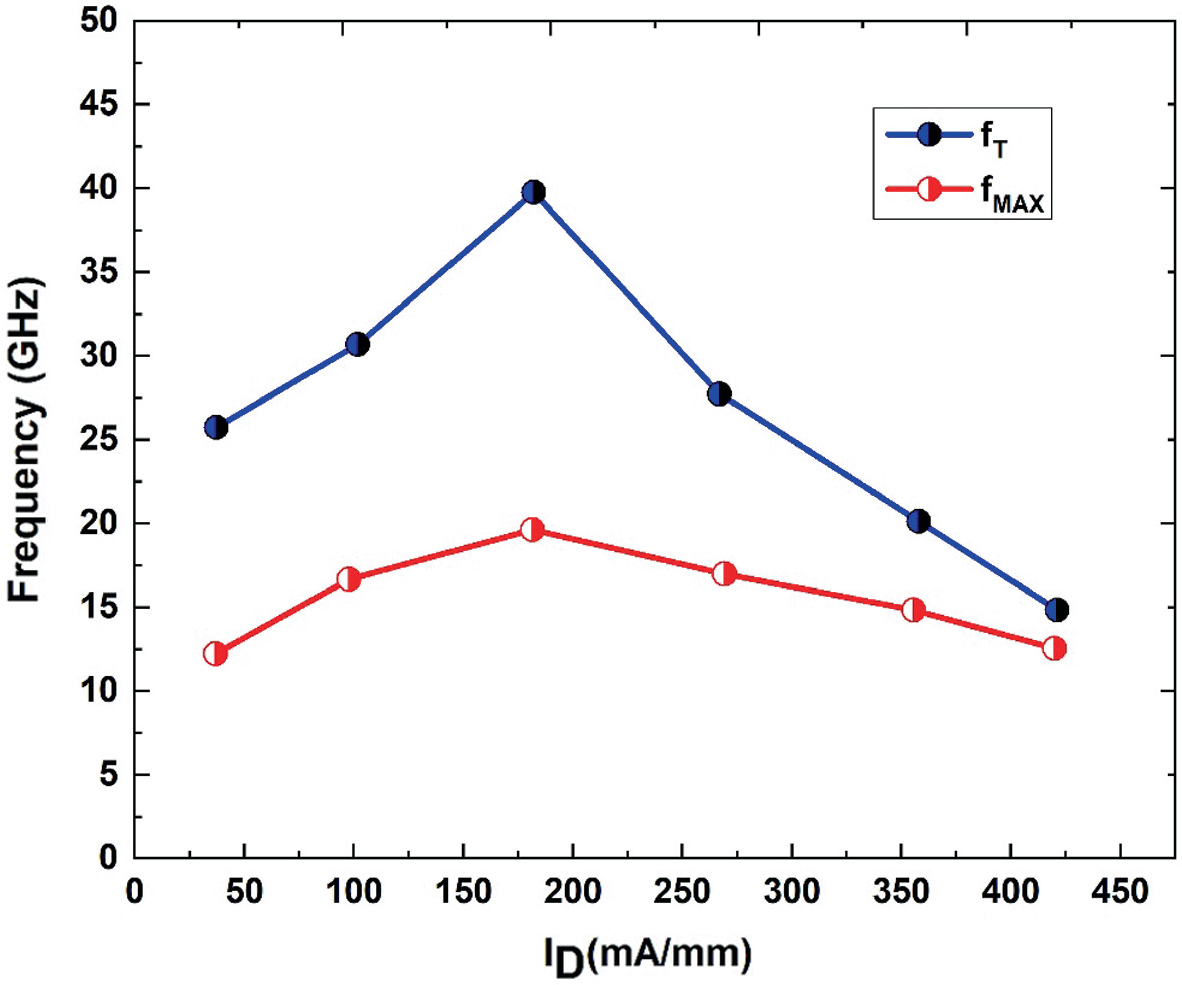

Fig. 15 Cutoff frequency as a function of drain current

Polarization-graded AlGaN channel HEMT (PolFETs) introduces a three-dimensional electron slab by polarization effects and further the carrier density enhanced by impurity doping [22]. This three-dimensional electron slab, PolFETs, showed flatter g_m, which improves the device linearity. And also, the doped PolFETs devices experience less current collapse. A Si-doped ($\sim 1 \times 10^{18}$ cm^{-3}) graded Al-composition (~65% to 82%) AlGaN channel with n++ AlGaN ($\sim 1 \times 10^{20}$ cm^{-3}) regrown ohmic contact shown in Fig. 16. The PolFETs showed an F_T/F_{MAX} of 5.4/14.2 GHz [22].

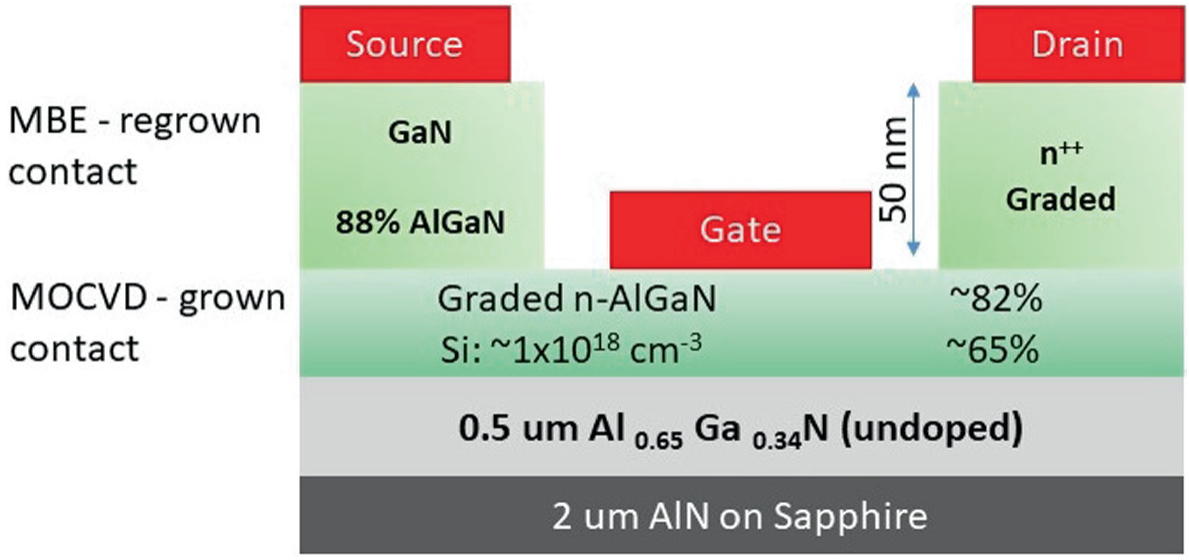

Fig. 16 Schematic view of PolFET

L_G = 130 nm HEMT with reverse graded AlGaN source/drain contact layer [23] shown in Fig. 17. The graded AlGaN ohmic region is grown by molecular beam epitaxy (MBE). The Ti/Al/Mo/Au ohmic contact metal stack with Si_3N_4 passivation device showed F_T/F_{MAX} of 40/58 GHz. The doped $Al_{0.75}Ga_{0.25}$ N barrier layer (~2×10^{18} cm-3)/$Al_{0.6}Ga_{0.4}$ N channel heterostructure enables μ_n of 175 cm^2/V.s and n_s of 8.5×10^{12} cm^{-2}. The device showed 45 V of breakdown voltage. A good aspect ratio (L_G/gate to channel distance (d)) and further scaling of the device dimensions will improve the saturation velocity of the 2DEG carrier.

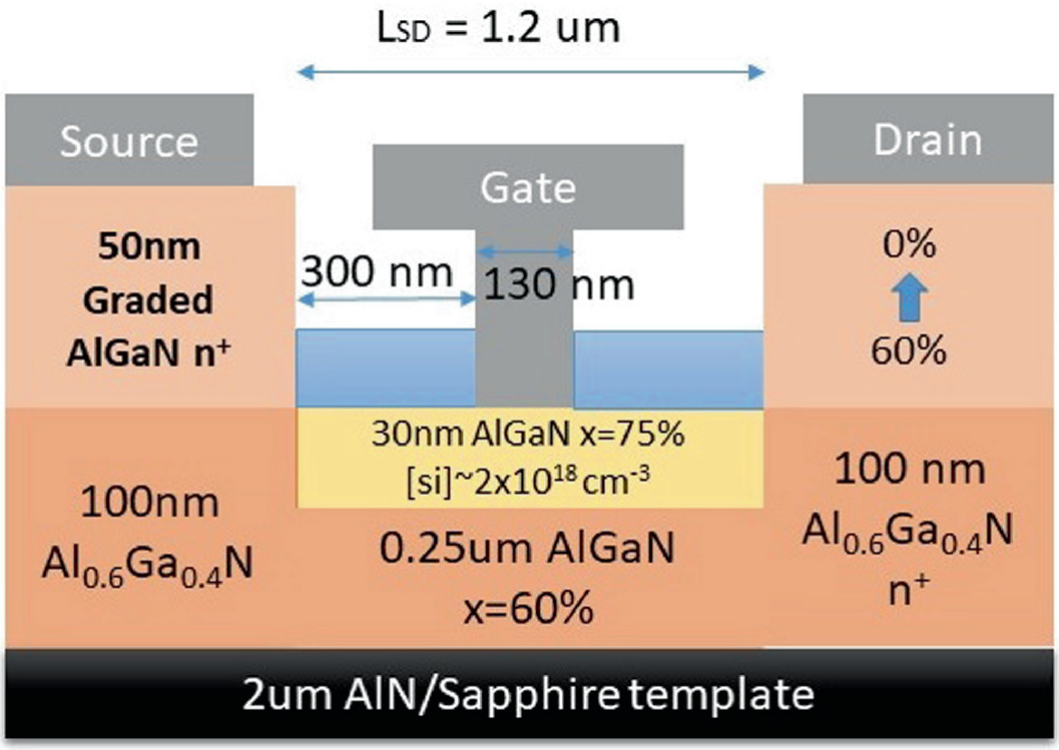

Fig. 17 Device structure of $Al_{0.75}Ga_{0.25}$ N/$Al_{0.6}Ga_{0.4}$ N HEMT

Conventional Si-based MOSFET technology used up to 3 GHz RF applications and GaN-based HEMTs are widely used in 5G communication systems. 5G communication protocols demand high linear power amplifiers to avoid eliminating leaking into adjacent cells and reduce the bit error rate, which reduces the digital pre-distortion [24]. Despite remarkable power density at high frequencies, GaN-based HEMTs suffer from the nonlinear operation. Nonlinear source resistance and transconductance (G_m) drop-off at high gate bias are the major source of nonlinear device behavior [25, 26]. Transconductance drop-off mainly because of decreased saturation velocity of the carrier with increased carrier density at high V_{GS}. One simple strategy to enhance the linearity of the device is to replace 2DEG (two-dimensional electron gas) with 3DEG (three-dimensional electron gas) by linear grading of Al content in the AlGaN barrier [27]. The linearly graded barrier layer enables almost a constant charge density of electrons in the channel due to the polarization charge gradient. In such a PolFET device, the depletion width only changes when the gate bias increases and the volumetric electron density remain nearly constant and hence

there is no significant change in saturation velocity of electrons in the channel leading to flatter transconductance (G_m). The flat G_m is highly desirable for high-linear applications. Figure 18 shows the AlGaN channel PolFET. The device has a 20 nm graded (0–30%) AlGaN channel and a thick $Al_{0.2}Ga_{0.8}$ N (70 nm) cap layer. The thick AlGaN cap layer ensures enough surface-to-channel distance so that the fringing field between the surface and channel is suppressed. The energy band diagram of the access region heterostructure interface is plotted in Fig. 19. A 2DEG region at the $Al_{0.2}Ga_{0.8}$ N/GaN epitaxial passivation layer enables more negative pinch-off voltage in the access region than the gate region, which eliminates the virtual gate effects. A deep recessed 0.7 μm gate length Ni/Au/Au metal stack Schottky contact was deposited and the gate terminal extended 0.3 μm towards the drain region to further enhance the breakdown voltage and reduce the dispersion. The PolFETs showed 860 cm^2/V.s electron mobility and 9.6 × 10^{12} cm^{-2} 2DEG density. Moreover, the device showed an I_{DS} of 0.5 A/mm, a flat $G_{m,max}$ of 160 mS/mm, minimum current collapse, V_{BR} of 110 V, and F_T/F_{MAX} of 14/22 GHz. The F_T and F_{MAX} variation with gate bias are displayed in Fig. 20. The PolFET showed a stable RF behavior for a wide range of gate biases. Load pull measurement results of the device exhibited 50% power-added efficiency at 4 GHz operation [27].

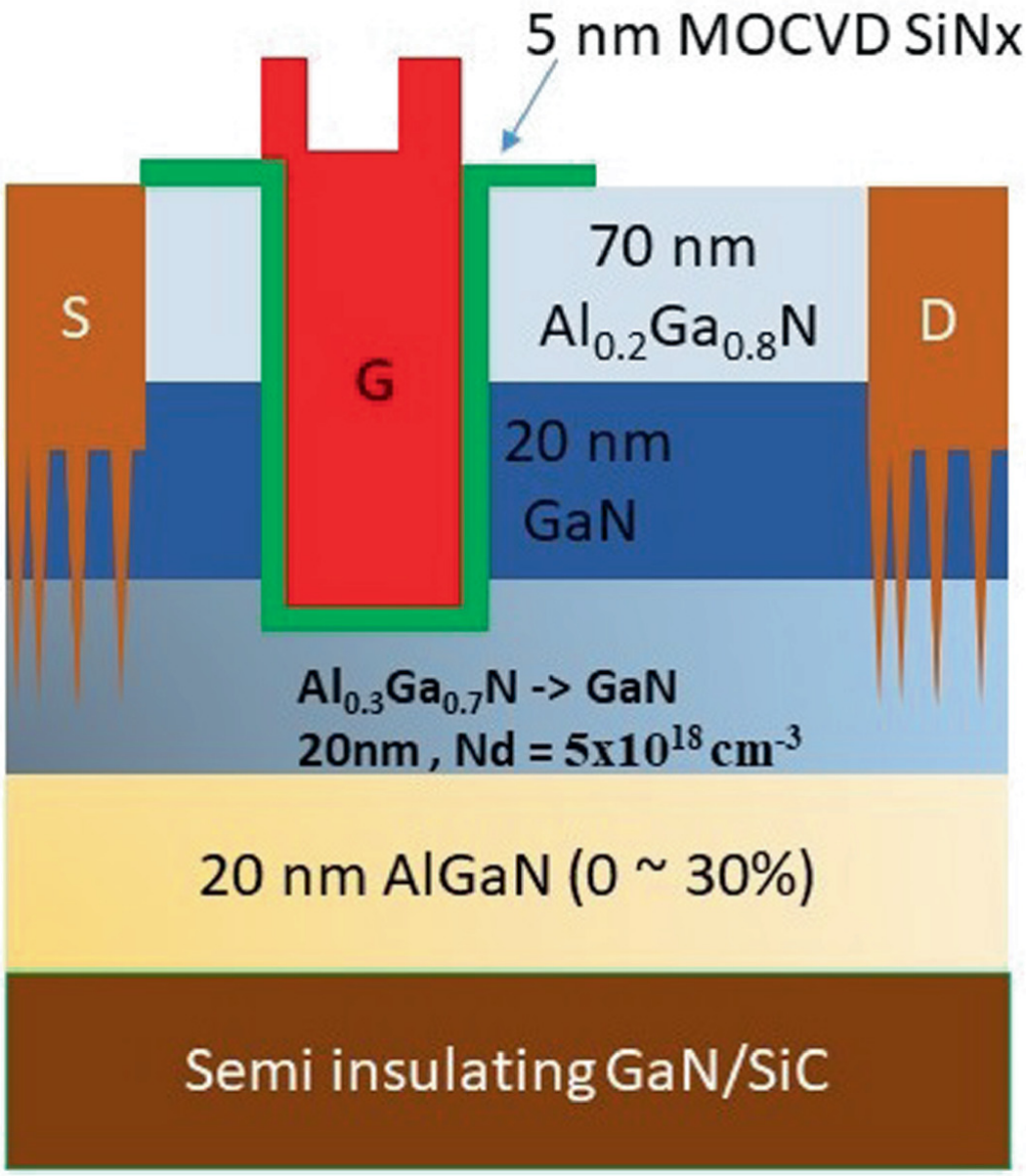

Fig. 18 Device structure

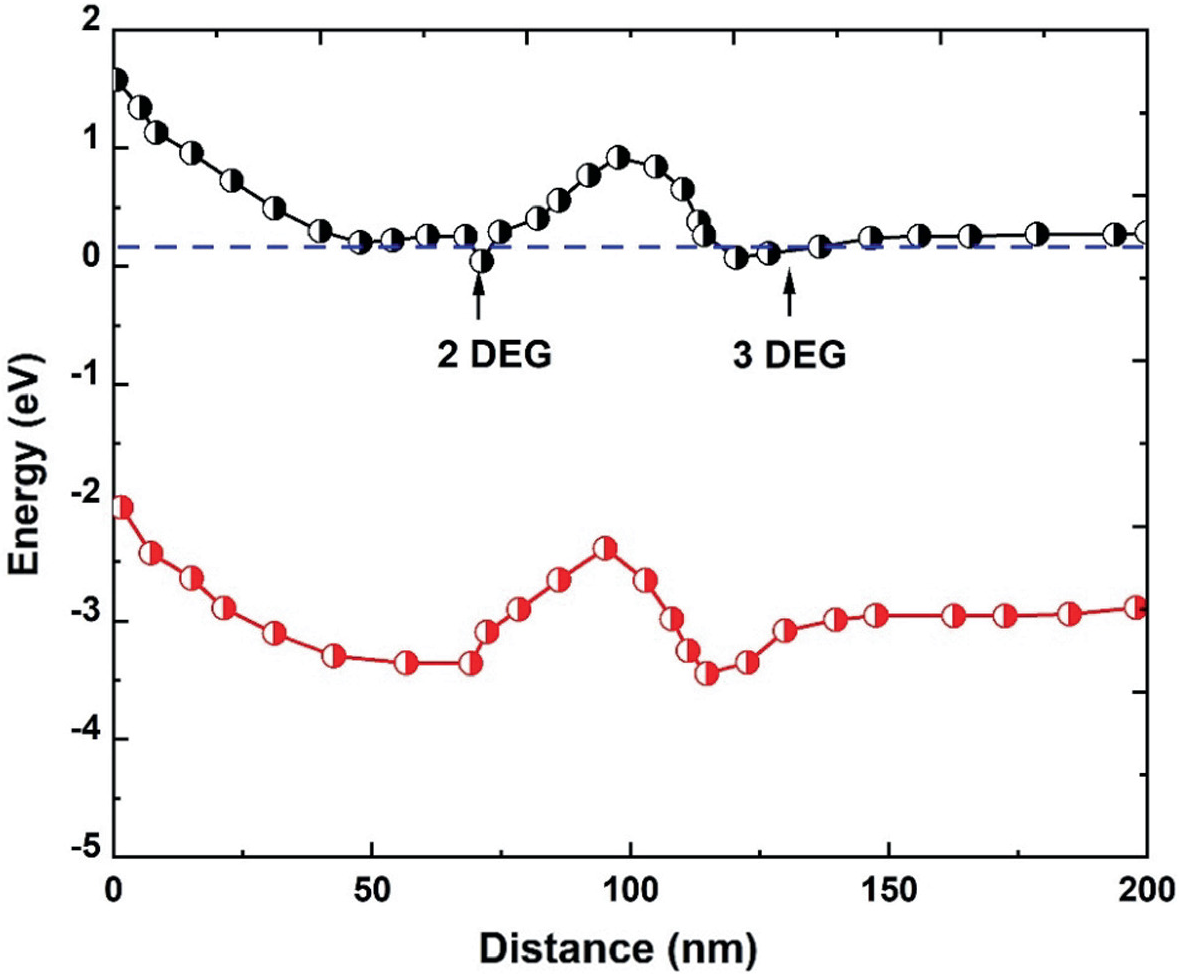

Fig. 19 Band diagram

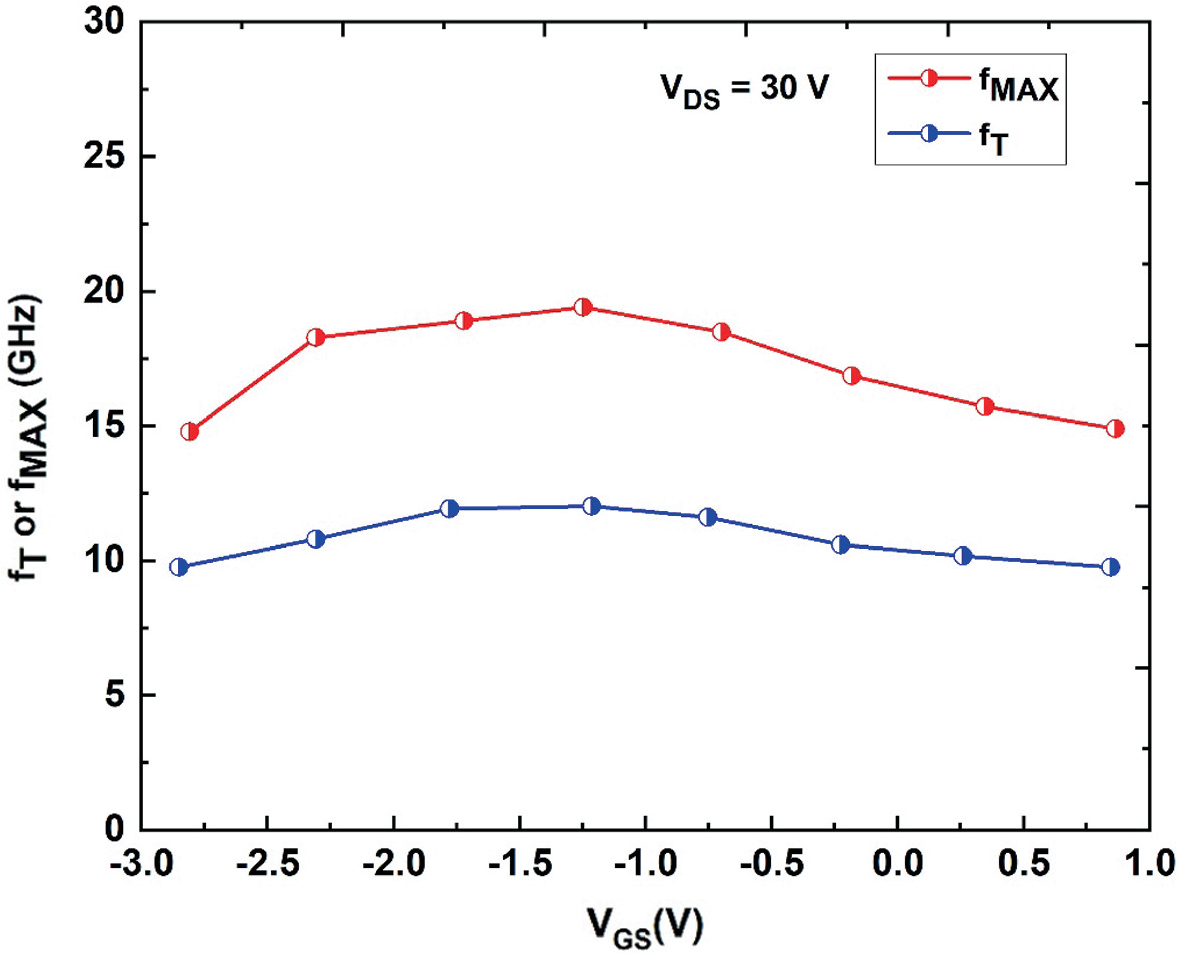

Fig. 20 F_T/F_{MAX} dependence on V_{GS}

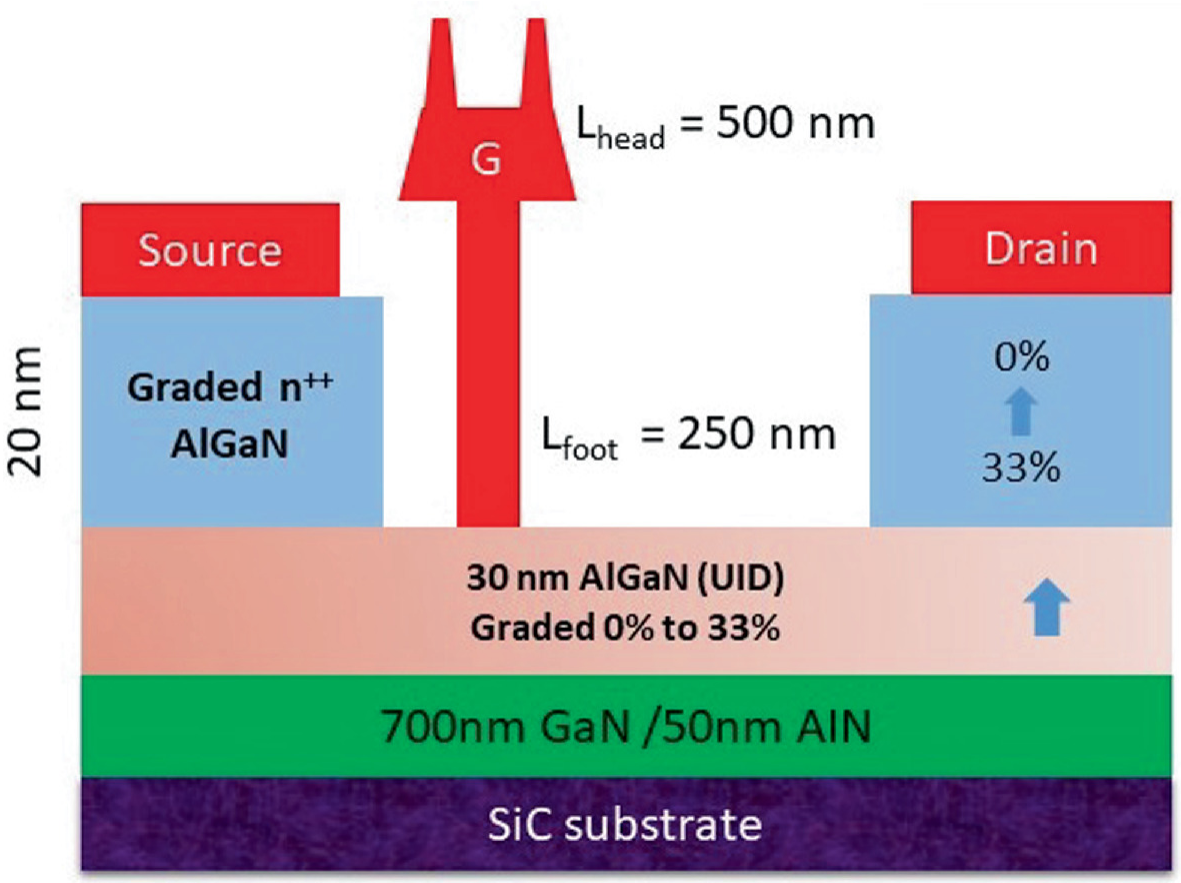

Fig. 21 Device structure of PolFET

L_G = 250 nm PolFET on SiC substrate is shown in Fig. 21. A 20 nm graded (33% to 0%) n + AlGaN (Si ~ 10^{20} cm^{-3}) regrown source/drain contact showed a very low ohmic contact resistance 0.1 Ω.mm. Graded AlGaN channel (0–33%) HEMT showed an on-state current density of 0.9 A/mm recorded by a 250 nm gate length device along with 240 mS/mm transconductance. The device RF demonstrated an F_T/F_{MAX} of 52/67 GHz and also a flat g_m and RF performance was measured for a wide range of gate biases [28]. The F_T/F_{MAX} dependence on drain current is plotted in Fig. 22. The PolFET exhibited a stable RF behavior for a wide range of gate biases. Table 2 presents the state-of-the-art of $Al_yGa_{1-y}N$-channel-based HEMTs for high-frequency applications.

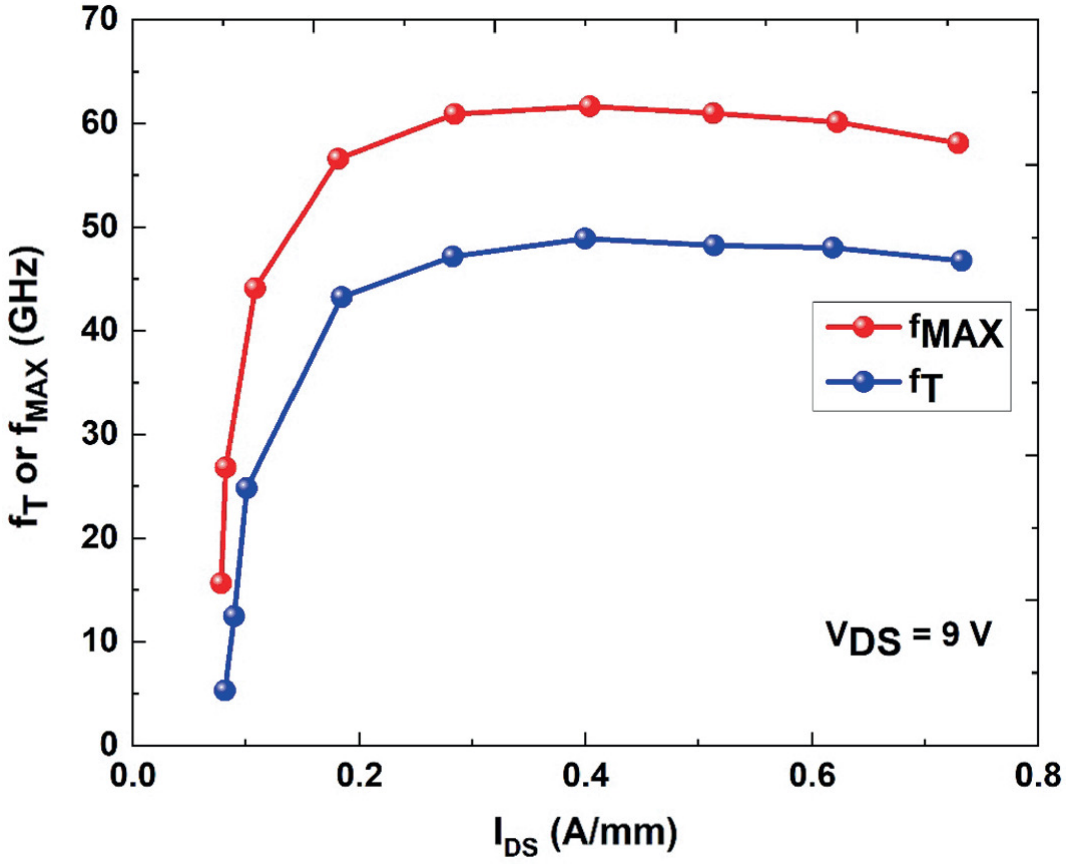

Fig. 22 F_T/F_{MAX} dependence on drain current

Table 2 High-frequency performance of $Al_yGa_{1-y}N$-channel-based HEMTs

Reference, Year	L_G in nm	Barrier/Channel	I_{DS} in A/mm	$G_{m,max}$ in mS/mm	V_{BR} in V	F_T/F_{MAX} In GHz
[1], 2014	1000	$Al_{0.4}Ga_{0.6}$ N/$Al_{0.15}Ga_{0.85}$ N	0.6	190	–	7/10
[17], 2018	60	$Al_{0.85}Ga_{0.15}$ N/$Al_{0.70}Ga_{0.30}$ N	1.2	24	92	18.5/28.4
[21], 2019	160	$Al_{0.7}Ga_{0.3}$ N/$Al_{0.5}Ga_{0.5}$ N	0.42	38	170	20/40
[22], 2018	800	Graded (Al 82→65%) AlGaN/$Al_{0.65}Ga_{0.35}$ N	0.15	34	35	5.4/14.2
[23], 2019	130	$Al_{0.75}Ga_{0.25}$ N/$Al_{0.60}Ga_{0.40}$ N	0.46	450	45	40/58
[27], 2020	300	Graded (Al 30→0%) AlGaN/GaN	0.5	150	110	14/22
[28], 2017	250	Graded (Al 33 →0%) AlGaN/GaN	0.95	230	–	52/67

4 AlGaN Channel HEMTs in Power Switching Applications

Despite the high breakdown performance of the ultrawide bandgap AlGaN channel, due to significant lattice and thermal mismatches between the Al-rich AlGaN channel and buffer heterostructure, the crystalline quality is very poor [29, 30]. Therefore, the Al-rich AlGaN channel HEMT cannot meet the theoretical electric field strength. A simple approach to improve the breakdown voltage of high-quality crystalline $Al_{0.1}Ga_{0.9}$ N channel HEMT is hybrid ohmic/Schottky drain contacts [31] without modifying the conventional device fabrication steps. The hybrid ohmic/Schottky drain contact $Al_{0.3}Ga_{0.7}$ N/$Al_{0.1}Ga_{0.9}$ N HEMT fabricated structure is shown in Fig. 23. The device shows 9.2×10^{12} cm^{-2} of sheet charge density and 2070 cm^2V^{-1} s^{-1} of carrier mobility due to improved polarization and the alloy disorder scattering mechanism is majorly reduced by the low Al-mole fraction AlGaN device. $L_G = 3$ μm, and $W_G = 50$ μm device exhibited a remarkable breakdown voltage of 2200 V for $L_{GD} = 22$ μm. This hybrid technology anticipated uniform breakdown characteristics due to improved surface metal morphology.

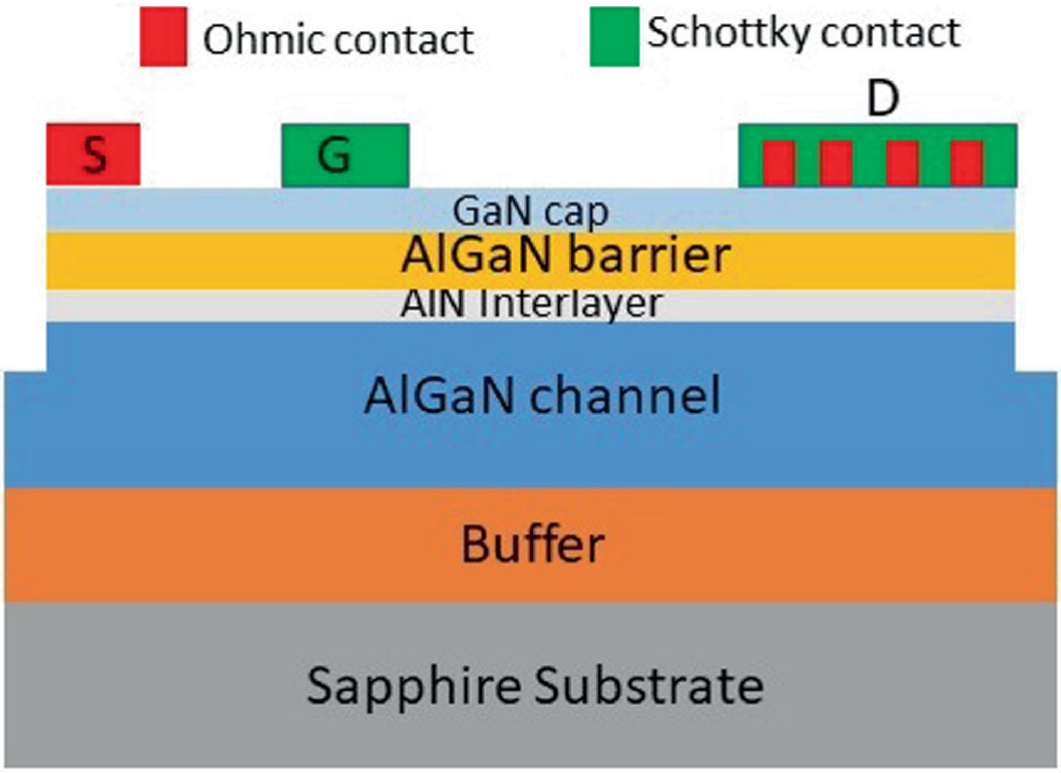

Fig. 23 Device structure of hybrid ohmic/Schottky contact HEMT

The AlGaN channel HEMTs demonstrated superior breakdown performance to GaN channel. However, the carrier mobility is a bit lower than the GaN channel because of alloy disorder scattering. It affects the basic characteristics of the HEMTs. Graded AlGaN buffer HEMT technology enhances the carrier of the channel [32]. Graded AlGaN buffer and GaN buffer HEMT device are depicted in Fig. 24. The device consists of a 200 nm AlGaN channel, a 500 nm graded AlGaN channel, and a 1 μm GaN buffer. The graded buffer HEMT shows I_{DS} of 849 mA/mm and g_m of 108. The breakdown characteristics of graded AlGaN buffer HEMT recorded a 408 V breakdown voltage for 5 μm L_{GD} [32].

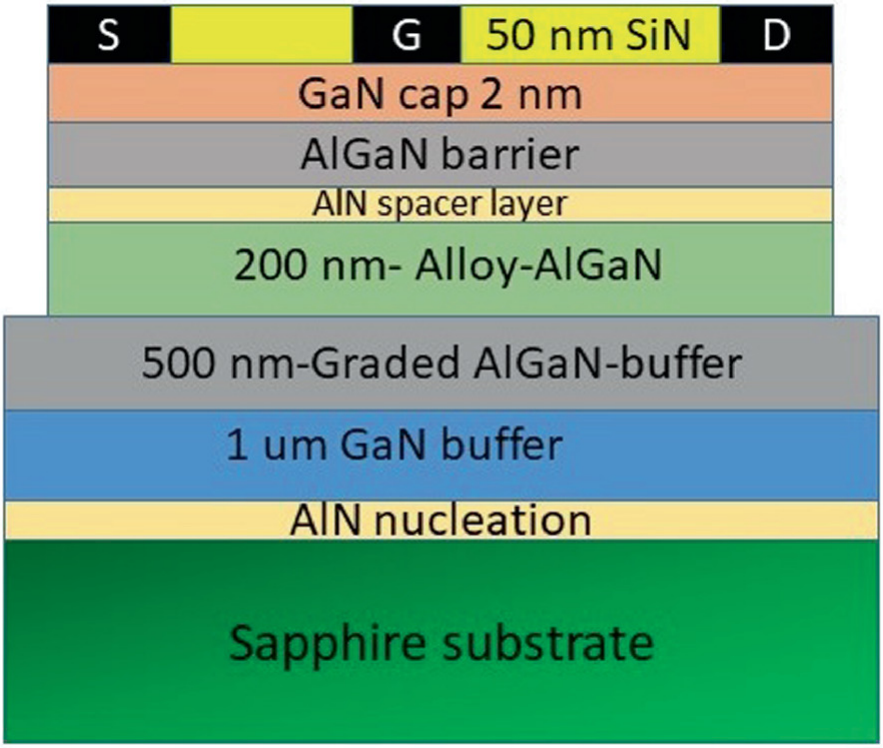

Fig. 24 Graded AlGaN channel HEMT

Enhancing the electron mobility of Al-rich AlGaN channel HEMTs is very important for both high-power switching and microwave electronics. Enabling simultaneous improvement in both mobility and career density is a challenge in Al-rich AlGaN HEMTs. High Al-mole fraction AlGaN channel enhances the sheet charge density but channel mobility is reduced. To overcome this problem, polarization-induced doping of AlGaN PolFETs is used [33]. The polarization property of the III-nitride material is the major source for AlGaN PolFETs to offer free electrons with reduced ionized scattering, which improves the mobility of Al-rich AlGaN channels. Usually, in conventional AlGaN HEMTs, the 2DEG is created below the abrupt heterojunction interface between the Al-rich barrier and channel. And the Al-rich barrier impacts the mobility of the channel directly. Whereas, in AlGaN PolFETs, a graded AlGaN barrier is used to create a three-dimensional electron slab (3DES), which enables high μ in the channel due to the PolFETs channel being very close to the surface. Which will cause high-frequency dispersion and this problem may be solved by a suitable passivation technique. $Al_xGa_{1-x}N$ PolFET with Al composition graded from 0.6 to 1

is shown in Fig. 25. The measured Hall mobility of the HEMT is 320 $cm^2/V.s$ and n_s of 1.3×10^{13} cm^{-2}. The PolFET shows an I_{DS} of 188 mA/mm and a breakdown voltage of 620 V for L_{GD} = 2.7 µm.

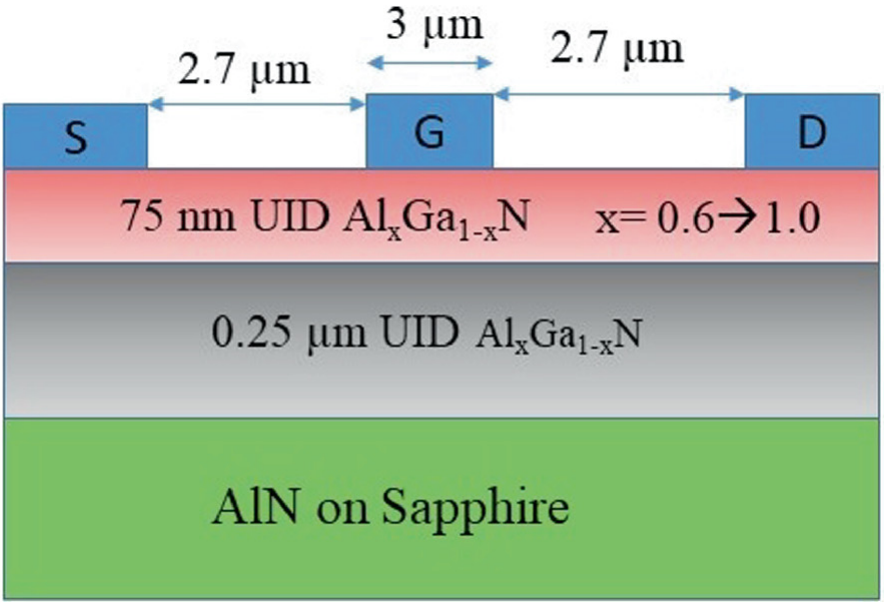

Fig. 25 PolFET device geometry

In many power switching applications [34–36], the high reverse blocking voltage of the transistor is essential. AlGaN/GaN HEMTs with Schottky drain contact achieved a maximum of −900 V reverse blocking voltage by adopting a trigate field plate technique [37], which effectively modulates the electric field. However, beyond −1000 V reverse blocking voltage AlGaN/GaN HEMTs is a critical one due to technological limitation. Because of the high critical electric field of AlGaN than the GaN, further improving the reverse blocking voltage of III-nitride-based devices, the ultrawide bandgap AlGaN material is the attractive alternate channel to GaN. AlGaN channel HEMT with Schottky drain contact is illustrated in Fig. 26. The device is passivated by Al_2O_3. The Hall measurements show 3.9×10^{12} cm^{-2} of 2DEG density and 801 cm^2V^{-1} s^{-1} of electron mobility. The AlGaN channel HEMT exhibited a reverse breakdown voltage V_{RB} > −3000 V [38].

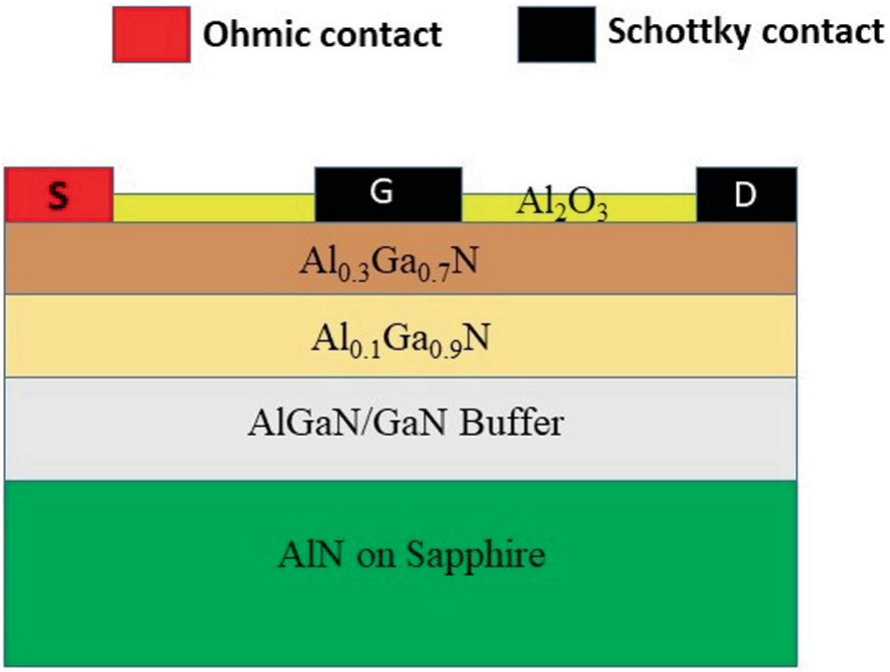

Fig. 26 Schottky drain AlGaN channel HEMT

5 Conclusion

In recent years, the $Al_xGa_{1-x}N$ channel HEMTs are becoming emerging devices for high-power and high-frequency electronics due to ultrawide bandgap, high-temperature operation, higher cutoff frequency, and high critical electric field. And also, the advancement of AlGaN channel HEMTs enhanced the linearity performance. Therefore, the Al-rich AlGaN channel devices are suitable candidates for next-generation power electronics.

References

1. T. Nanjo, K. Kurahashi, A. Imai, Y. Suzuki, M. Nakmura, M. Suita, E. Yagyu, High-frequency performance of AlGaN channel HEMTs with high breakdown voltage. Electron. Lett. **50**(22), 1577–1599 (2014)

2. A.G. Baca, B.A. Klein, A.A. Allerman, A.M. Armstrong, E.A. Douglas, C.A. Stephenson, T.R. Fortune, R.J. Kaplar, $Al_{0.85}Ga_{0.15}N/Al_{0.70}Ga_{0.30}N$ high electron mobility transistors with schottky gates and large on/off current ratio over temperature. ECS J. Solid State Sci. Technol. **6**(12), 161–165 (2017)

3. A.G. Baca, A.M. Armstrong, A.A. Allerman, B.A. Klein, E.A. Douglas, C.A. Sanchez, T.R. Fortune,

High temperature operation of $Al_{0.45}Ga_{0.55}N/Al_{0.30}Ga_{0.70}N$ high electron mobility transistors. ECS J. Solid State Sci. Technol. **6**(11) S3010-S3013 (2017)

4. S.J. Pearton, J. Yang, P.H. Cary IV, F. Ren, J. Kim, MJ. Tadjer, M.A. Mastro, A review of Ga_2O_3 materials, processing, and devices. Appl. Phys. Rev. **5**, 011301 (2018)

5. T. Oishi, Y. Koga, K. Harada, M. Kasu, High-mobility β-Ga2O3($\bar{2}$01) single crystals grown by edge-defined film-fed growth method and their Schottky barrier diodes with Ni contact. Appl. Phys. Express **8**, 031101 (2015)
[Crossref]

6. Z. Xia, C. Joishi, S. Krishnamoorthy, S. Bajaj, Y. Zhang, M. Brenner, S. Lodha, S. Rajan, Delta doped β-Ga_2O_3 field effect transistors with regrown ohmic contacts. IEEE Electron Device Lett. **39**(4), 568–571 (2018)
[Crossref]

7. Y. Zhang, C. Joishi, Z. Xia, M. Brenner, S. Lodha, S. Rajan, Demonstration of β-$(Al_xGa_{1-x})_2O_3/Ga_2O_3$ double heterostructure field effect transistors. Appl. Phys. Lett. **112**, 233503–233505 (2018)
[Crossref]

8. A.J. Green et al., β -Ga2O3 MOSFETs for radio frequency operation. IEEE Electron Device Lett. **38**(6), 790–793 (2017). https://doi.org/10.1109/LED.2017.2694805
[Crossref]

9. K. Ueda, M. Kasu, Y. Yamauchi, T. Makimoto, M. Schwitters, D.J. Twitchen, G.A. Scarsbrook, S.E. Coe, Diamond FET using high-quality polycrystallinediamond with f_T of 45 GHz and f_{max} of 120 GHz, IEEE Electron Device Lett. **27**(7), 570–572 (2006)

10. M. Kasu, K. Ueda, H. Ye, Y. Yamauchi, S. Sasaki, T. Makimoto, 2 W = mm output power density at 1 GHz fordiamond FETs, Electron. Lett. **41**(22), 1249–1250 (2005)

11. M. Farahmand, C. Garetto, E. Bellotti, K.F. Brennan, M. Goano, E. Ghillino, G. Ghione, J.D. Albrecht, P. Paul Ruden, Monte Carlo simulation of electron transport in Theiii-nitride Wurtzite phase materials system: Binariesand ternaries. IEEE Trans. Electron Device **48**(3), 535–542 (2001)

12. H. Tokuda, M. Hatano, N. Yafune, S. Hashimoto, K. Akita, Y. Yamamoto, M. Kuzuhara, High Al composition AlGaN-channel high-electron-mobility transistor on AlN substrate. Appl. Phys. Express **3**, 121003, 1–3 (2010)

13. T. Nanjo, A. Imai, Y. Suzuki, Y. Abe, T. Oishi, M. Suita, E. Yagyu, Y. Tokuda, AlGaN Channel HEMT With Extremely High Breakdown Voltage. IEEE Trans. Electron Device **60**(3), 1046–1053 (2013)

14. X. Hu, S. Hwang, K. Hussain, R. Floyd, S. Mollah, F. Asif, G. Simin, A. Khan, Doped Barrier Al0.65Ga0.35N/Al0.40Ga0.60N MOSHFETwith SiO2 Gate-insulator and Zr-based ohmic contacts.IEEE Electron Device Letters. **39**(10):1–4 (2018)

15. E.A. Douglas, S. Reza, C. Sanchez, D. Koleske, A. Allerman, B. Klein, A.M. Armstrong, R.J. Kaplar,

A.G. Baca, Ohmic contacts to Al-rich AlGaNheterostructures.Phys. Status Solidi A **214**(8), 1600842, 1–7 (2017)

16. K. Harrouche, F. Medjdoub, GaN-Based HEMTs for millimeter-wave applications. Wiley Online Library, Chapter **3**(Book Chapter), 99–135 (2020)

17. A.G. Baca, B.A. Klein, J.R. Wendt, S.M. Lepkowski, C.D. Nordquist, A.M. Armstrong, A.A. Allerman, E.A. Douglas, R.J. Kaplar, RF Performance of Al0.85Ga0.15N/Al0.70Ga0.30N high electron mobility transistors with 80 nm gates. IEEE Electron Device Lett. **40**(1), 17–20 (2019)

18. S. Bajaj, F. Akyol, S. Krishnamoorthy, Y. Zhang, S. Rajan, AlGaN channel field effect transistors with graded heterostructure ohmic contacts. Appl. Phys. Lett. **109**(13), 133508 (2016)

19. T. Razzak, S. Hwang, A. Coleman, H. Xue, S.H. Sohel, S. Bajaj, Y. Zhang, W. Lu, A. Khan, S. Rajan, Design of compositionally graded contact layers for MOCVD grown high Al-content AlGaN transistors. Appl. Phys. Lett. **115**(4), 043502 (2019)

20. E.A. Douglas, S. Reza, C. Sanchez, D. Koleske, A. Allerman, B. Klein, A.M. Armstrong, R.J. Kaplar, A.G. Baca, Ohmic contacts to Al-rich AlGaN heterostructures. Phys. Status Solidi A **214**(8), 1600842, 1–7 (2017)

21. H. Xue, S. Hwang, T. Razzak, C. Lee, G. C. Ortiz, Z. Xia, S.H. Sohel, J. Hwang, S. Rajan, A. Khan, Wu Lu, All MOCVD grown Al0.7Ga0.3N/Al0.5Ga0.5N HFET: An approach to makeohmic contacts to Al-Rich AlGaN channel transistors. **164**, 30534–30539 (2020)

22. T. Razzak, S. Hwang, A. Coleman, S. Bajaj, H. Xue, Y. Zhang, Z. Jamal-Eddine, S. H. Sohel, W. Lu, A. Khan, S. Rajan, RF operation in graded AlxGa1-xN (x=0.65 to 0.82) Channel Transistors. IET—Inst. Eng. Technol. **54**(23), 1351–1353 (2018)

23. H. Xue, C.H. Lee, K. Hussian, T. Razzak, M. Abdullah, Z. Xia, S.H. Sohel, A. Khan, S. Rajan, W. Lu, $Al_{0.75}Ga_{0.25}N/Al_{0.6}Ga_{0.4}N$ heterojunction field effect transistor with f_T of 40 GHz. Appl. Phys. Express **12**(6), 066502 (2019)

24. P. Choi, U. Radhakrishna, C.C. Boon, L.-S. Peh, D. Antoniadis, Linearity enhancement of a fully integrated 6-GHz GaN power amplifier. IEEE Microwave Wireless Compon. Lett. **27**(10), 927–929 (2017)

25. S. Bajaj, Z. Yang, F. Akyol, P.S. Park, Y. Zhang, A.L. Price, S. Krishnamoorthy, D.J. Meyer, S. Rajan, Graded AlGaN Channel Transistors for Improved Current and Power Gain Linearity. IEEE Trans. Electron Devices **64**(8), 3114–3119 (2017)

26. J.B. Khurgin, S. Bajaj, S. Rajan, Amplified spontaneous emission of phonons as a likely mechanism for density-dependent velocity saturation in GaN transistors. Appl. Phys. Express **9**, 094101 (2016)

27. S.H. Sohel, A. Xie, E. Beam, H. Xue, T. Razzak, S. Bajaj, S. Campbell, D. White, K. Will, Y. Cao, W. Lu, S. Rajan, Improved DC-RF dispersion with epitaxial passivation for high linearity graded AlGaN channel field effect transistors. Appl. Phys. Express **13**, 036502 (2020)

28. V. Sandeep, J. Charles Pravin, Influence of Graded AlGaN sub-channel over the DC and breakdown characteristics of a T-gated AlGaN/GaN/AlInN MOS-HEMT, superlattices and

microstructures, vol. 156 (2021). https://doi.org/10.1016/j.spmi.2021.106954

29. A.G. Baca, A.M. Armstrong, A.A. Allerman, E.A. Douglas, C.A. Sanchez, M.P. King, M.E. Coltrin, T.R. Fortune, R.J. Kaplar, An AlN/$Al_{0.85}Ga_{0.15}N$ high electron mobility transistor, Appl. Phys. Lett. **109**, 033509 (2016)

30. S. Muhtadi, S. Mo Hwang, A. Coleman, F. Asif, G. Simin, M.V.S. Chandrashekhar, A. Khan, High electron mobility transistors with Al0.65Ga0.35N channel layers on thick AlN/sapphire templates. IEEE Electron Device Lett. **38**(7), 914–917 (2017)

31. W. Zhang, J. Zhang, M. Xiao, L. Zhang, Y. Hao, High breakdown-voltage (>2200 V) AlGaN-channel HEMTs with Ohmic/Schottky hybrid drains. IEEE J. Electron Devices Soc. **6**, 931–935 (2018)
[Crossref]

32. M. Xiao, J. Zhang, X. Duan, W. Zhang, H. Shan, J. Ning, Y. Hao, High performance Al0.10Ga0.90N channel HEMTs. IEEE Electron Device Lett. **39**(8), 1149–1151 (2018)

33. A.M. Armstrong, B.A. Klein, A.G. Baca, A.A. Allerman, E.A. Douglas, A. Colon, V.M. Abate, T.R. Fortune, AlGaN polarization-doped field effect transistor with compositionally graded channel from Al0.6Ga0.4N to AlN, Appl. Phys. Lett. **114** 052103 (2019)

34. J.-K. Kang, H. Hara, A.M. Hava, E. Yamamoto, E. Watanabe, T. Kume, The matrix converter drive performance under abnormal input voltage conditions. IEEE Trans. Power Electron. **17**(5), 721–730 (2002)
[Crossref]

35. P.W. Wheeler, J. Rodriguez, J.C. Clare, L. Empringham, A. Weinstein, Matrix converters: A technology review. IEEE Trans. Ind. Electron. **49**(2), 276–288 (2002)
[Crossref]

36. T. Morita, S. Tamura, Y. Anda, M. Ishida, Y. Uemoto, T. Ueda, T. Tanaka, D. Ueda, *99.3% Efficiency of Three-Phase Inverter for Motor Drive Using GaN-Based Gate Injection Transistors*. Conference Proceedings -Annual IEEE Applied Power Electronics Conference and Exposition (APEC), pp. 481–484 (2011)

37. J. Ma, M. Zhu, E. Matioli, 900 V reverse-blocking GaN-on-Si MOSHEMTs with a hybrid tri-anode Schottky drain. IEEE Electron Device Lett. **38**(12), 1704–1707 (2017)
[Crossref]

38. Y. Wu et al., More Than 3000 V reverse blocking Schottky-drain AlGaN-channel HEMTs with >230 MW/cm2 power figure-of-merit. IEEE Electron Device Lett. **40**(11), 1724–1727 (2019)
[Crossref]

T. R. Lenka, H. P. T. Nguyen (eds.), *HEMT Technology and Applications*, Springer Tracts in Electrical and Electronics Engineering
https://doi.org/10.1007/978-981-19-2165-0_2

Breakdown Mechanisms and Scaling Technologies of AlGaN/GaN HEMTs

Sneha Kabra[1] ✉ and Mridula Gupta[2] ✉
(1) Associate Professor, Department of Instrumentation, Shaheed Rajguru College of Applied Sciences for Women, University of Delhi, Vasundhara Enclave, New Delhi, 110096, India
(2) Senior Professor and Head, Department of Electronic Science, University of Delhi South Campus, Benito Juarez Road, New Delhi, 110021, India

✉ **Sneha Kabra (Corresponding author)**
Email: sneha.kabra@rajguru.du.ac.in
Email: snehakabra@ieee.org

✉ **Mridula Gupta**
Email: mridula@south.du.ac.in

Abstract
Breakdown mechanisms play a significant role in determining the performance of AlGaN/GaN HEMTs in high-power circuit applications. This chapter presents a brief overview of various factors, which cause an early breakdown in AlGaN/GaN HEMT at high drain voltage. The chapter also covers technological advancements proposed so far by various research groups to enhance the breakdown voltage of the device. Further, scaling technologies are discussed to improve the high-frequency performance of the device.

Keywords Breakdown mechanisms – Field plates – Double-channel HEMT – Scaling technologies

1 Introduction

AlGaN/GaN HEMTs are primarily used in high-power, high-frequency switching applications because of the low on-resistance, high drain current density, and high breakdown voltage offered by these devices [1]. Breakdown voltage for GaN device is defined as the voltage level at which drain current of the pinched off transistor exceeds a normalized value of 1 mA/mm of device width. It is also defined as a nonlinear increase of subthreshold drain current with an increase in drain voltage. Vertical leakage current from GaN to silicon limits the maximum breakdown voltage in AlGaN/GaN HEMTs grown on silicon. Breakdown also depends on the specific epitaxial design of the buffer layer along with its material quality, lateral geometrical design of the device, and passivation technique [2]. The physical properties of various materials used for designing HEMTs are listed in Table 1. A large bandgap of GaN ensures a high breakdown field. The critical electric field of GaN is almost ten times higher than Si, thus making GaN, a suitable choice for making high-power devices. The breakdown voltage of AlGaN/GaN HEMT grown on silicon is lesser than those grown on SiC substrate. Different figures of merit have been proposed for quantifying the high power handling capability of material used for fabricating HEMT. These include Johnson's figure of merit for microwave performance, Baliga's figure of merit for a low frequency that reflects resistive losses, and Baliga's high-frequency figure of merit, which signifies switching losses.

Table 1 Material properties of commonly used semiconductors at room temperature

Material	**Si**	**4H-SiC**	**GaN**	**GaAs**
Energy bandgap, (eV)	1.1	3.3	3.42	1.4
Electron mobility, (cm^2/V-s)	1350	900	2000 (2DEG)	8500
Relative dielectric constant, ε_r	11.9	10.1	9	
Breakdown electric field, E_c($\times 10^6$ V/cm)	0.3	2.2	3.3	0.4
v_{sat} ($\times 10^7$ cm/s)	1.0	2.0	3.0	1.0
Johnson figure of merit ($E_c.v_{sat}/2\pi$)	1	180	760	7.1

Material	Si	4H-SiC	GaN	GaAs
Baliga's figure of merit for low frequency ($\varepsilon\mu E_c^3$)	1	130	650	15.6
Baliga's figure of merit for high frequency (μEc^2)	1	22.9	77.8	10.8

The aim of this chapter is to present a brief overview of various physical and technological factors responsible for breakdown in AlGaN/GaN HEMTs and different methods which have been proposed by various research groups to enhance the breakdown voltage of these devices for high-power applications. Section 2 of this chapter describes the causes of breakdown in AlGaN /GaN HEMTs. Breakdown strength and commonly used methods for improvement of breakdown voltage reported to date are explained in detail in Sects. 3 and 4, respectively. Finally, scaling technologies that are currently being explored for high-frequency applications of HEMTs are discussed in Sect. 5.

2 Causes of Breakdown in AlGaN/GaN HEMTs

At high drain bias, the electric field increases at the drain edge of the gate, which accelerates the breakdown. In order to have a high current density and large breakdown voltage, it is essential to confine electrons in 2DEG formed at the interface of AlGaN/GaN by maintaining sufficient potential height. There are many mechanisms that limit the high voltage capability of AlGaN/GaN HEMT. These include.

1.2.1 Leakage currents originating from the gate structure

1.2.2 Punch-through effect

1.2.3 Breakdown along the channel region

1.2.4 Breakdown through the buffer layer

1.2.5 Breakdown due to impact ionization.

2.1 Leakage Currents Originating from the Gate Structure

As shown in Fig. 1, surface leakage current at the passivation layer interface, leakage current through the barrier, and strain-induced leakage current adversely affect the breakdown voltage of AlGaN/GaN HEMT. Leakage current which originates from the gate reduces device efficiency and degrades the reliability [3, 4]. It can be seen from Fig. 2 that as device width is increased, gate leakage current increases. AlGaN back-barrier can be used to minimize the leakage current. It has also been found that if a thin layer of SiO_2 is deposited by plasma-enhanced chemical vapor deposition (PECVD) under the gate, it can reduce gate leakage by six orders of magnitude [5].

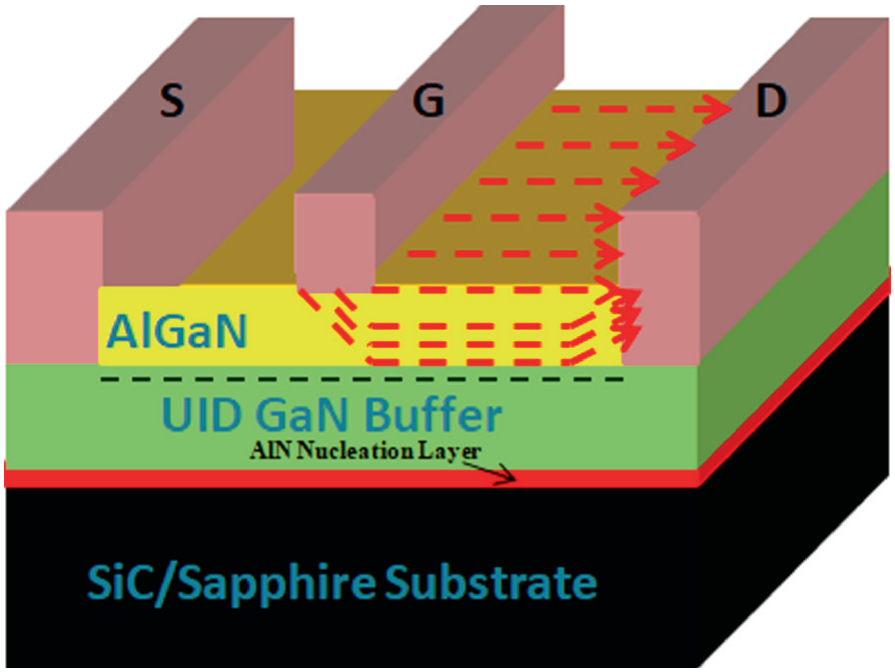

Fig. 1 Leakage current originating from the gate

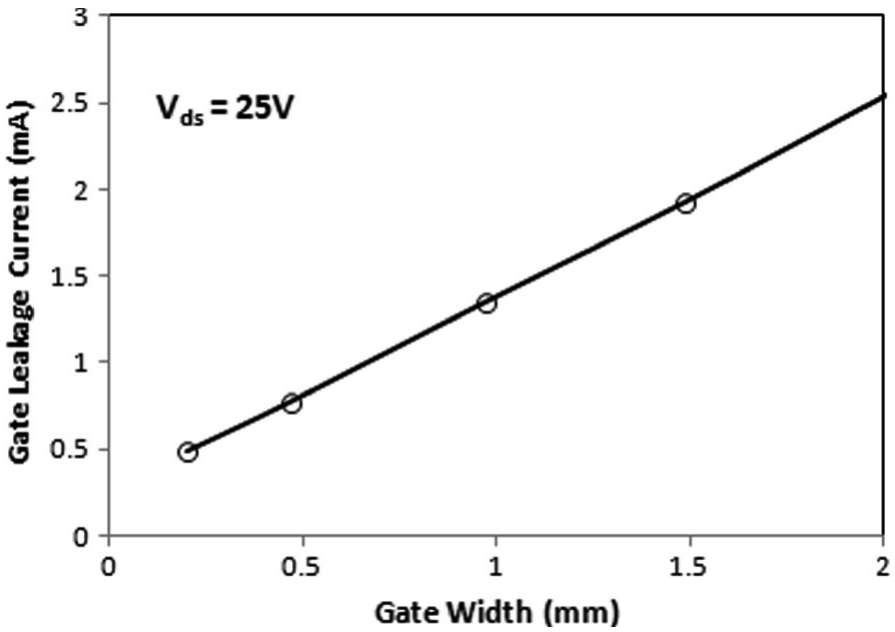

Fig. 2 Variation of gate leakage current with gate width

2.2 Punch-Through Effect

In conventional AlGaN/GaN HEMTs, at high drain bias, electrons present in the 2DEG get spilled over to the buffer layer thereby causing a sudden increase in subthreshold drain current and reducing the breakdown voltage. This phenomenon is called as punch-through effect. At high drain voltage, when a sufficiently high negative gate voltage closes the channel, electrons bypass the gate control region and flow to drain through the buffer as shown in Fig. 3. Thus, an increase in subthreshold and punch-through currents leads to an increase in dissipation of thermal energy thereby hindering the operation of the device at high bias [6].

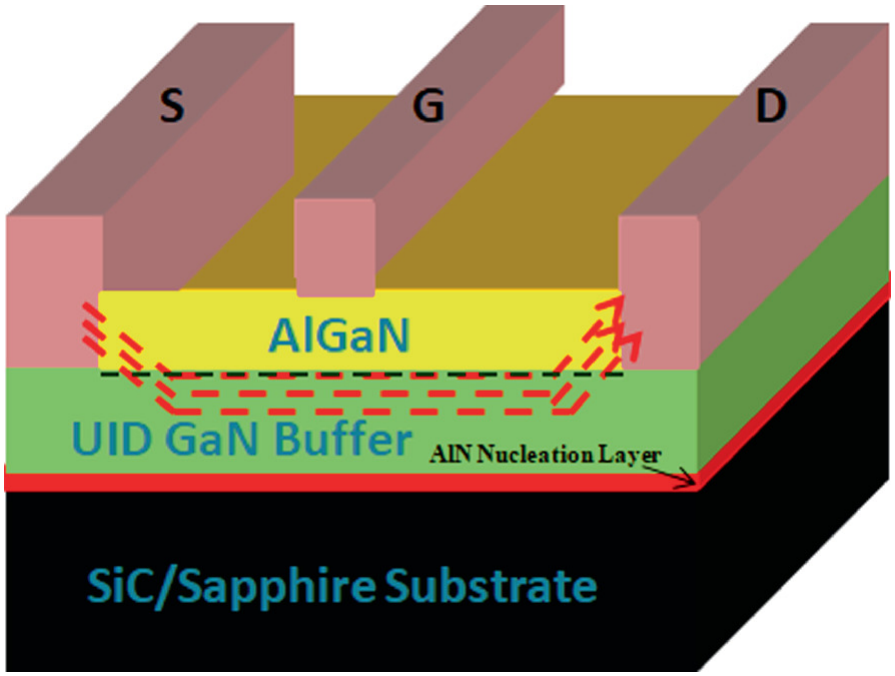

Fig. 3 Punch through in AlGaN/GaN HEMT on SiC or sapphire substrate

2.3 Breakdown Along the Channel Region

If leakage currents are suppressed, the breakdown voltage of AlGaN/GaN HEMTs increases as the gate to drain separation, $d_{GD.}$ increases. Thus, d_{GD} determines the maximum allowable operating voltage. At the breakdown state, the drain current rises rapidly and is mainly taken up from the gate. This indicates that electron flow from gate to drain primarily because of electron injection across the Schottky gate barrier. A schematic representation of the breakdown which occurs along the channel is depicted in Fig. 4.

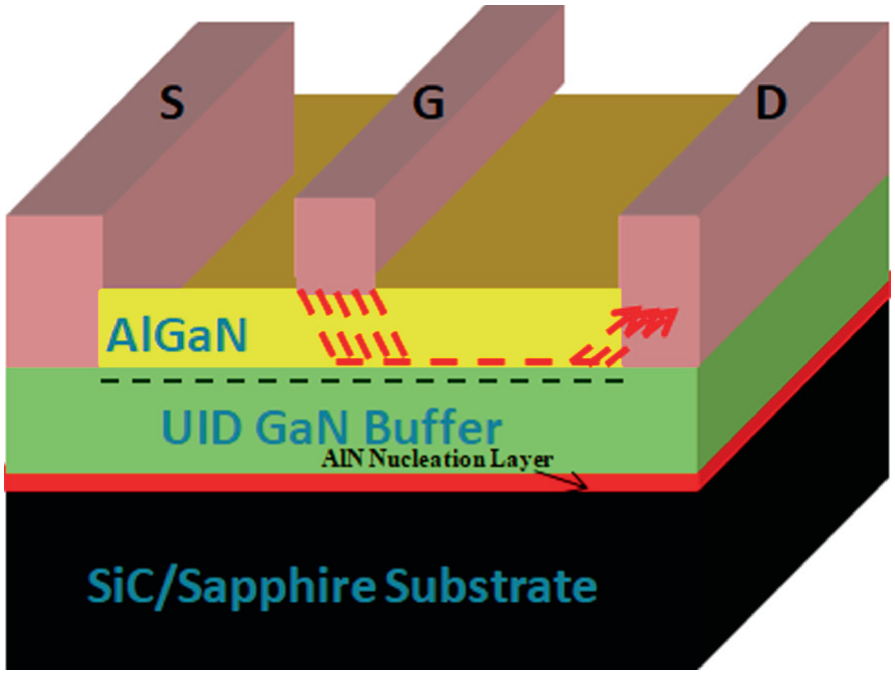

Fig. 4 Breakdown along the channel region

2.4 Breakdown Through the Buffer Layer

One of the major drawbacks of using Si or SiC substrate in AlGaN/GaN HEMTs is the vertical device breakdown that occurs across epitaxial layers. As the bias voltage increases, the electric field between the active regions that is source, drain, gate, channel area, and the conductive substrate increases more and more until the breakdown strength of the buffer layer is reached. Figure 5 shows the pictorial representation of the creation of a new leakage path bypassing the whole device. Thus breakdown voltage depends on buffer thickness, buffer technology, and surface contact technology [7].

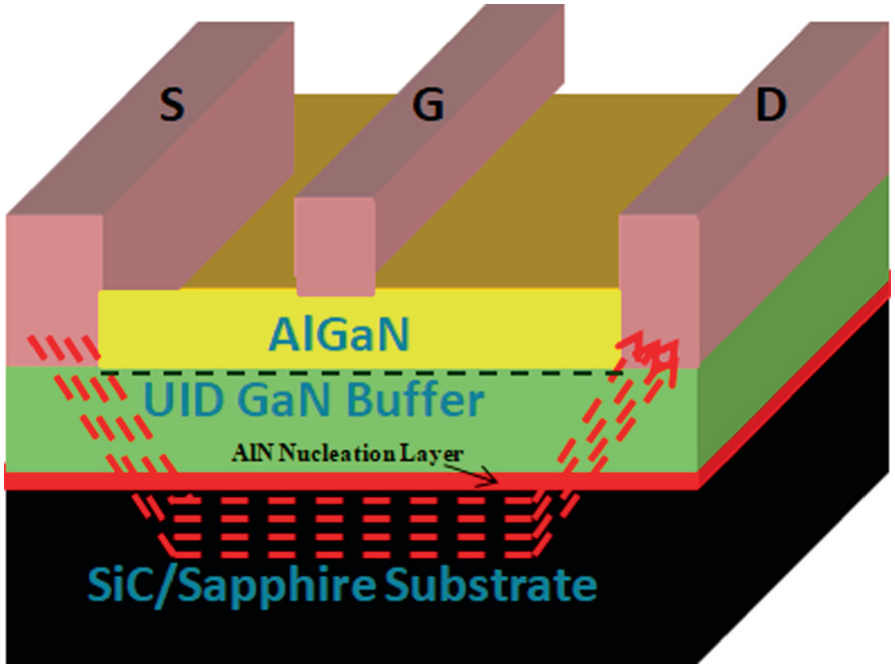

Fig. 5 Breakdown through the buffer layer

2.5 Breakdown Due to Impact Ionization

It has been observed that the holes generated due to impact ionization also cause breakdown in AlGaN/GaN HEMTs. These holes flow into the buffer layer and get captured by donors, which may lead to a reduction of the negative space charge region in the buffer layer [8]. Impact ionization is initiated in the off state due to the injection of electrons from the source to the high electric field regions near the drain side of the gate thereby accelerating the breakdown by increasing the electric field [2].

3 Breakdown Strength

The slope at which drain voltage increases on the increasing gate to drain distance is referred to as the breakdown strength of the device. It strongly depends on the selected buffer composition. Breakdown properties of AlGaN/GaN HEMTs can be studied using a bias stress test and TCAD simulations to ensure high reliability. The high breakdown strength of AlGaN/GaN HEMTs results in high breakdown voltage capability. As gate-to-drain spacing in GaN HEMTs increases, the breakdown voltage saturates at a particular drain voltage.

4 Methods of Increasing the Breakdown Voltage

In order to improve the breakdown voltage of AlGaN/GaN HEMTS, often a compromise is made in its cut-off frequency and resistance. Thus, it is imperative to use the appropriate device configuration and device engineering techniques to enhance breakdown voltage, power density, and cut-off frequency for high-frequency and high-power applications. The electric field in the vicinity of the gate should be reduced to delay premature breakdown and reduce dispersion effects. Some of the methods used for this purpose are as follows.

1.4.1. Field-plate Approach

1.4.2. Designing of potential barriers in the epitaxial buffer layer to confine electrons in the channel

1.4.3. Epitaxial layer engineering: Pre-Epitaxy Implantation (Increase of vertical breakdown)

1.4.4. Schottky source/drain contact HEMT

1.4.5. Use of high K dielectric passivation layer in HEMT

1.4.6. Use of electron blocking layer

1.4.7. Optimization of the gate to drain spacing

1.4.8. Modulation of electric field using partial GaN cap layer

1.4.9. Double-channel AlGaN HEMT.

4.1 Field-Plate Approach

Field plate approach reduces the electric fields inside critical regions of the device, which is useful for S-band high-power FETs. Crowding of the electric field near the drain side of gate edge results in a reduction in

breakdown voltage of AlGaN/GaN HEMTs. Therefore, different field-plate approaches have been proposed to mitigate drain field crowding to enhance breakdown voltage and reduce dispersive effects [9]. It consists of an asymmetric gate with an extension of the gate-to-drain edge.

It has been observed that the electric field is maximum near the gate in AlGaN/GaN HEMTs. It has to be reduced to reduce the probability of electrons spilling from the gate into the AlGaN layer or into the passivation to prevent premature breakdown. Field plates near the gate or drain have been extensively used to solve this issue. Dimensions of the field plates and thickness of passivation and metallization layers may be optimized to effectively smoothen the electric field near the gate. Some of the field-plate designs which have been reported so far are as follows:

a. Multiple grading field plates: Different voltages can be applied to the multiple grading field plates that can efficiently spread out the electric field to less critical regions of the device. This is because the drain access region of AlGaN/GaN HEMT is of the order of a few microns so it is easy to design tiny metal lines in the middle of the gate and drain as shown in Fig. 7.

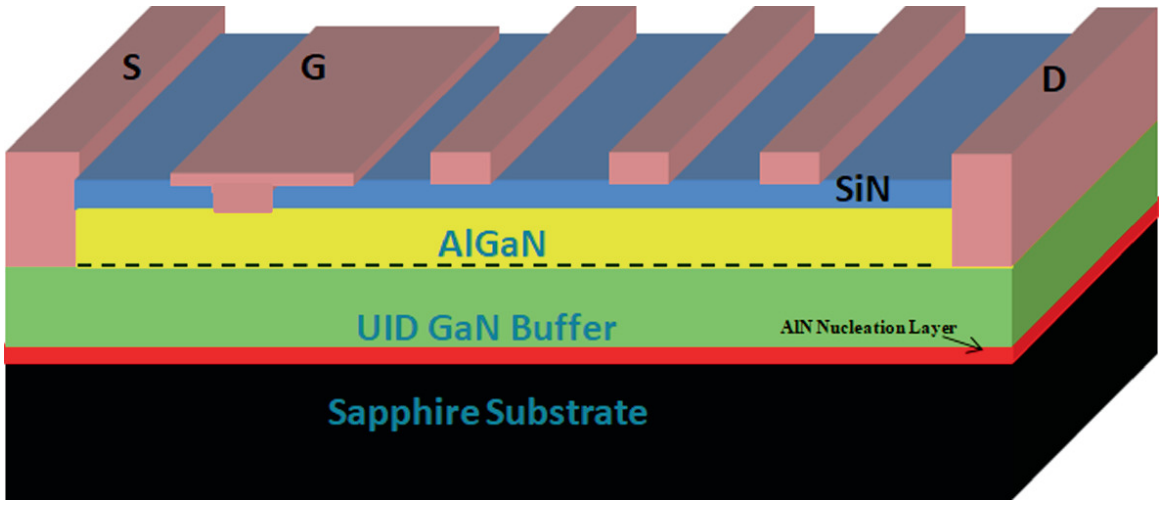

Fig. 7 Multiple grading field plates

b. Stack of source connected field plates: A stack of field plates connected to the source, combined with the T-gate is depicted in

Fig. 8. Although field plates that are connected to the source increase drain to source capacitance, they are found to have a marginal adverse impact on device instability.

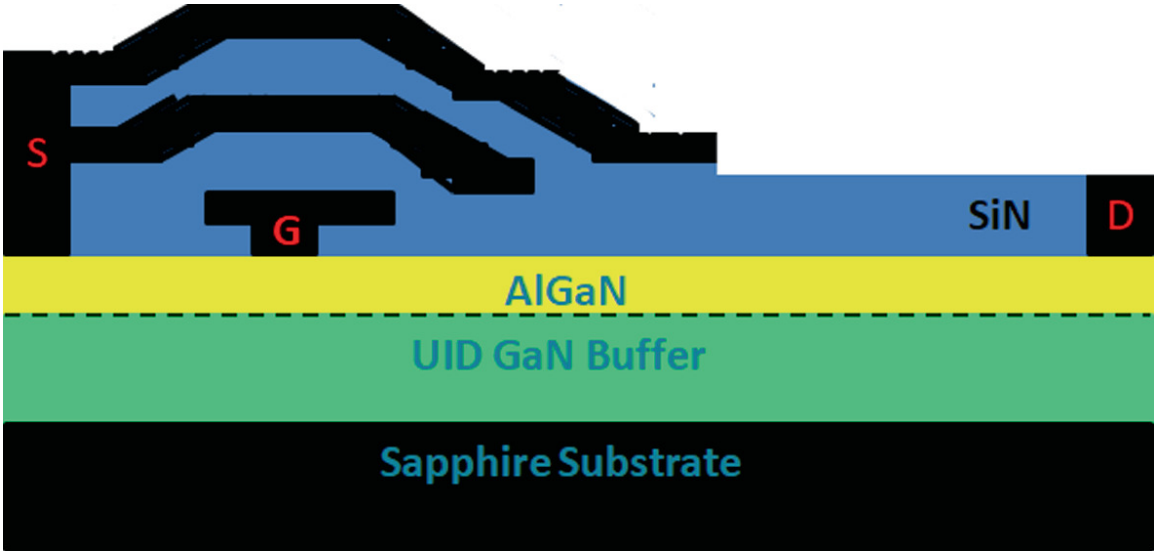

Fig. 8 A stack of source connected field plates

c.

Slanted field-plate structure: Slanted field plate represented in Fig. 9 reduces electric field crowding at the end of the field plate because the geometrical distance between the field plate and channel region increases slowly.

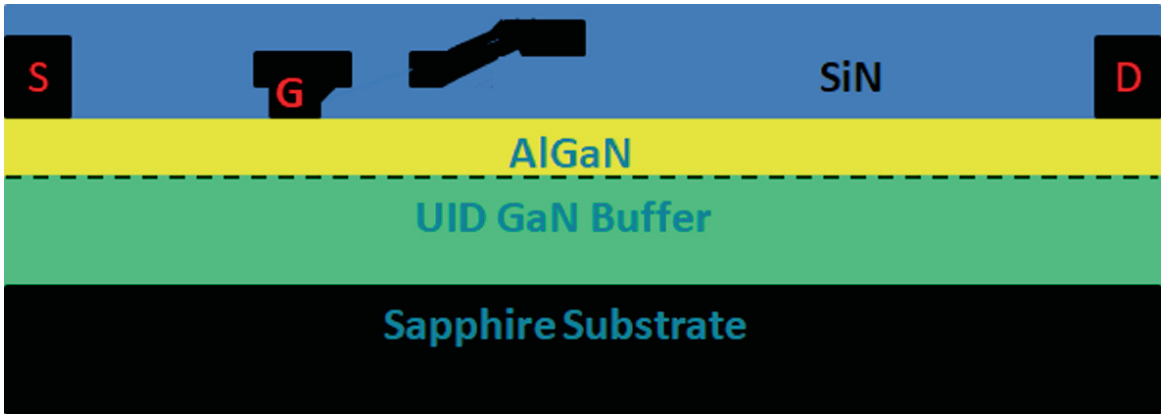

Fig. 9 Slanted field-plate structure

4.2 Designing of Potential Barriers in the Epitaxial Buffer Layer

Avoids the punch-through effect, therefore increasing high-voltage operation capability. It prevents electrons from punching through the gate control region. AlGaN barrier layers, carbon-or-iron-doped buffer layers, and a combination of these layers build up a repelling potential barrier for channel electrons and thus avoid punch through or shifting it to higher voltage levels. The structure of AlGaN/GaN HEMT with a potential barrier in the buffer layer is shown in Fig. 10.

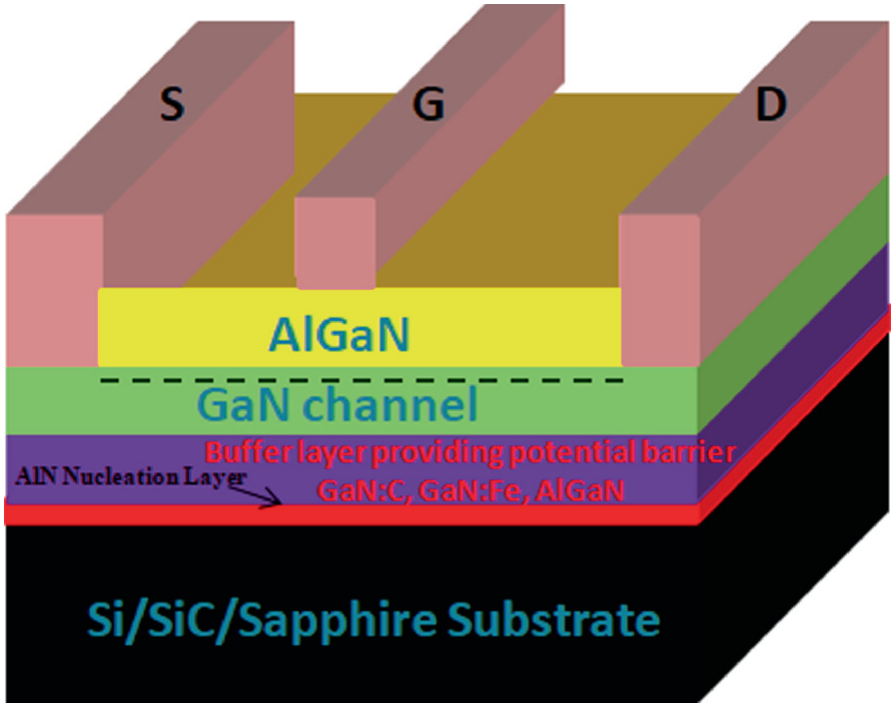

Fig. 10 AlGaN/GaN HEMT with a potential barrier in the buffer layer

4.3 Epitaxial Layer Engineering: Pre-epitaxy Implantation

Vertical buffer leakage can be decreased by providing isolation implantation into the conductive SiC substrate before epitaxial growth of AlGaN/GaN structures. Depending on actual implantation depth as well as the selection of ion species and implantation dose, the vertical breakdown can be significantly increased.

4.4 Schottky Source–Drain Contacts

Researchers have demonstrated that the use of Schottky source–drain contacts formed using high-temperature annealing prevents electric field spikes and leads to enhancement of breakdown voltage in AlGaN/GaN HEMTs. Metal stack of Ti/Au has been successfully used to validate suppression of source carrier injection-induced breakdown [10].

4.5 Use of High *K* Dielectric Passivation Layer in HEMT

High *k* passivation layer can be used to produce a uniform electric field and potential distribution between the gate and drain. Devices having a SiO_2 passivation layer offer improved breakdown voltage as compared to devices having a SiN passivation layer [11]. Yang et al. [12] have recently reported that implantation of fluorine ions in a thick SiN passivation layer can lead to a reduction in ON resistance and an increase in breakdown voltage of AlGaN/GaN HEMTs. They experimentally obtained a breakdown voltage of 803 V for AlGaN/GaN HEMT with fluorine ion implantation in the passivation layer, which is much higher than the breakdown voltage achieved for conventional AlGaN/GaN HEMT.

4.6 Use of Electron-Blocking Layer

It has been found that the breakdown voltage of AlGaN/GaN HEMT can be significantly enhanced by using the AlGaN/GaN/AlGaN layer which forms a quantum well and suppress the spilling of electrons outside the 2DEG channel thus also referred to as electron-blocking layer (EBL) [13]. Better confinement of electrons in 2DEG raises conduction band edge thereby increasing the potential barrier which results in suppression of subthreshold drain leakage current and enhancement in the device breakdown voltage. Figure 11 shows the structure of HEMT with an electron-blocking layer of AlGaN/GaN/AlGaN.

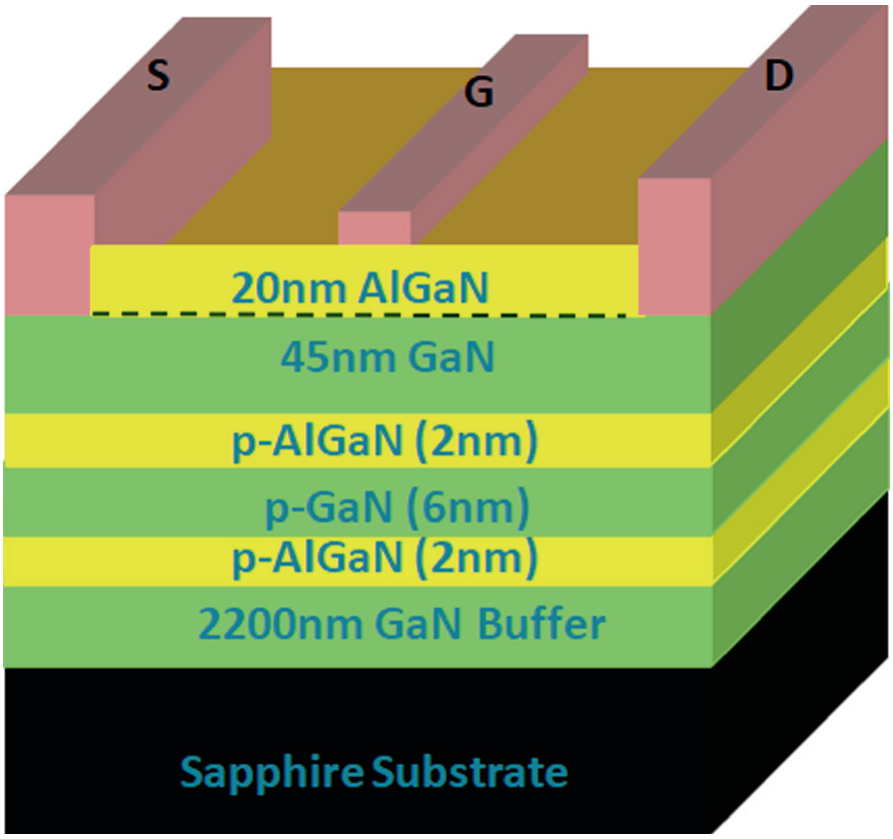

Fig. 11 AlGaN/GaN HEMT with electron-blocking layer [13]

4.7 Optimization of the Gate to Drain Spacing

A high k dielectric passivation layer in conjunction with optimized gate to drain spacing can be effectively used to reduce the electric field toward the drain edge of the gate [14]. Figure 12 clearly illustrates an increase in breakdown voltage with an increase in permittivity for a higher gate to drain spacing.

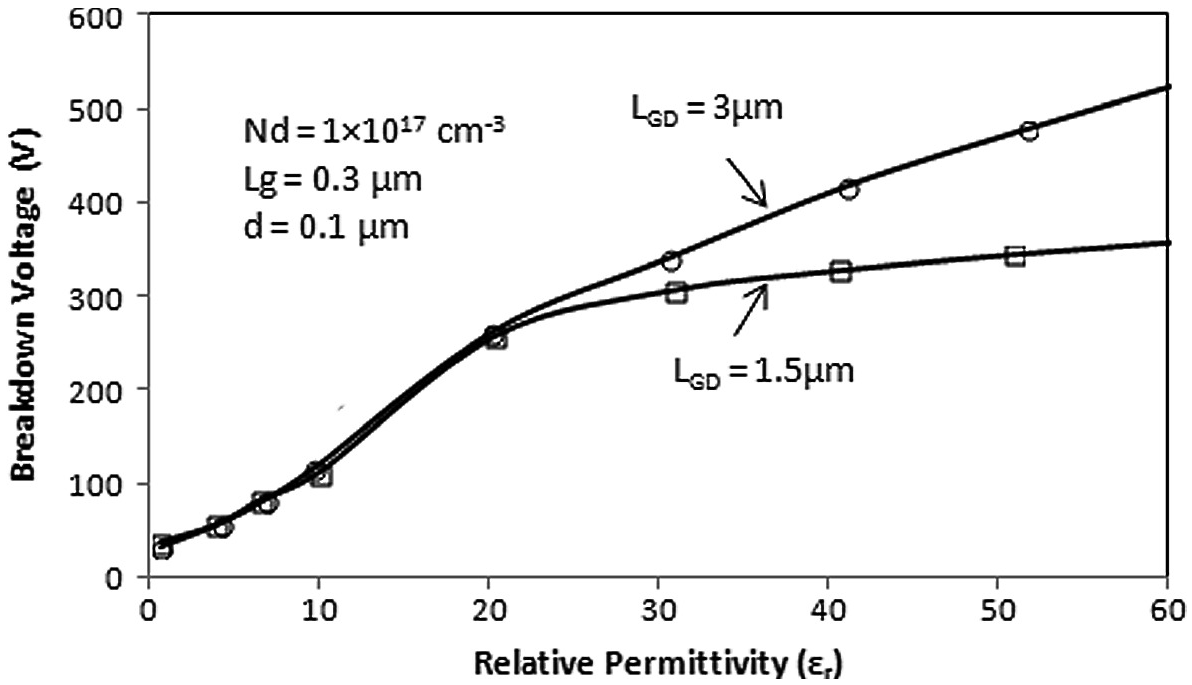

Fig. 12 Variation of breakdown voltage with relative permittivity [14]

4.8 Modulation of Electric Field Using Partial GaN Cap Layer

Duan et al. [15] proposed that the growth of a partial cap layer of GaN can reduce the peak electric field near the gate thus modulating the surface electric field distribution. It was also observed that as the length of the cap layer is increased, the electric field peak shifts toward the drain because of the elongated 2DEG region, thereby decreasing the electric field near the gate which eventually increases the breakdown voltage. The structure of AlGaN/GaN HEMT with a partial GaN cap layer is shown in Fig. 13.

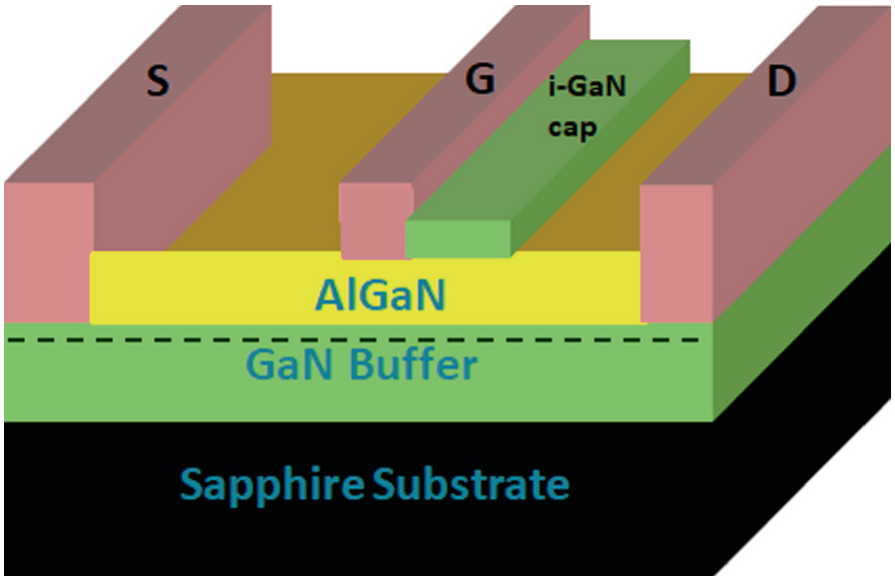

Fig. 13 AlGaN/GaN HEMT with a partial GaN cap layer

4.9 Double-Channel HEMT

In a recent research carried out by Zhang et al. [16], it has been found that the 2DEG current conduction capability and breakdown performance of HEMTs can be significantly enhanced by using a double-channel approach. Figure 14 depicts the 3D structure of double-channel HEMT.

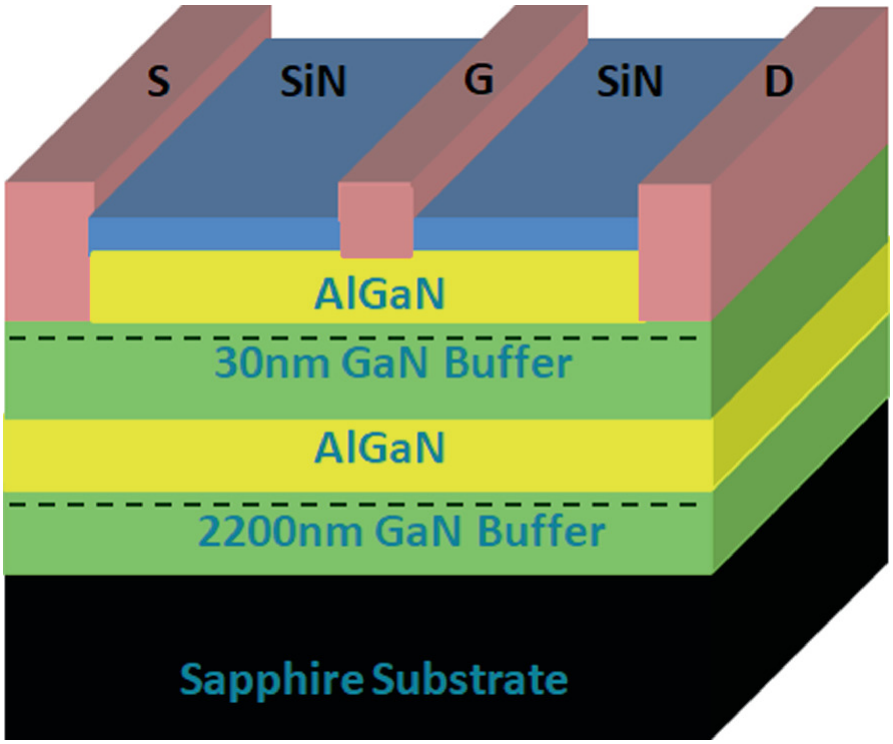

Fig. 14 Double-channel HEMT

Besides these methods, AlGaN/GaN HEMTs with magnesium-doped GaN layer also exhibits very low leakage current thereby increasing the breakdown voltage [17]. A high lateral breakdown voltage of about 10 kV has recently been obtained by Abid et al. [18] for thin channel AlGaN/GaN HEMTs fabricated on AlN/sapphire template.

5 Scaling Technologies of AlGaN/GaN HEMTs

A distinct deviation from linear scaling behavior is observed in AlGaN/GaN HEMTs for gate length less than 100 nm, which clearly indicates that parasitic elements begin to control the total delay time at small gate lengths. Thus all intrinsic, extrinsic, and parasitic elements need to be scaled proportionately for effective scaling of AlGaN/GaN HEMT to sub-50 nm gate length. Vertical scaling is required to suppress the short-channel effects whereas lateral scaling reduces electron transit time. Device scaling technologies have been explored to suppress the short channel effects, reduce parasitic resistances and capacitances, and improve the breakdown voltage [19].

Self-aligned-gate double-heterojunction AlGaN/GaN HEMT with heavily doped regrown *n*+-GaN ohmic contacts offer low R_{ON}, high maximum drain current, high transconductance, and high linearity with a broad transconductance curve [20]. Highly doped source/drain can drastically enhance the performance of the device by increasing electron concentration in the source region [21]. Regrown *n*+ -GaN ohmic contacts have also proved to decrease parasitic access resistances [22]. In order to obtain a high cutoff frequency, aggressive dimensional scaling (L_g and L_{sd}) is required, maintaining high breakdown voltage.

Lateral scaling using self-aligned gate (SAG) technology can be explored to reduce parasitic capacitance in highly scaled devices [23]. When gate length is reduced to a sub-50 nm range and becomes smaller than the source to drain distance (L_{ds}), cutoff frequency and maximum frequency of oscillation of HEMT are restricted by an extrinsic delay related to depletion of the 2DEG channel at the drain edge of the gate. This is referred to as drain delay and is directly related to the transit time of electrons through the depleted region. Therefore, it can be minimized by reducing gate to drain distance (L_{gd}), which can be achieved by developing a self-aligned gate process, through which precise dimension control along with high device yield and uniformity can be obtained.

References

1. F. Zeng et al., A comprehensive review of recent progress on GaN high electron mobility transistors: Devices, fabrication and reliability, Electron. **7**, (12) (2018). https://doi.org/10.3390/electronics7120377

2. G. Meneghesso, M. Meneghini, E. Zanoni, Breakdown mechanisms in AlGaN/GaN HEMTs: An overview, Jpn J. Appl. Phys. **53**(10). Japan Soc. Appl. Phys. (2014). https://doi.org/10.7567/JJAP.53.100211

3. A. Goswami, R.J. Trew, G.L. Bilbro, Modeling of the gate leakage current in AlGaN/GaN HFETs. IEEE Trans. Electron Devices **61**(4), 1014–1021 (2014). https://doi.org/10.1109/TED.2014.2302797
[Crossref]

4. A. Wang, L. Zeng, W. Wang, Simulation of gate leakage current of AlGaN/GaN HEMTs: Effects of the gate edges and self-heating. ECS J. Solid State Sci. Technol. **6**(11), S3025–S3029 (2017).

https://doi.org/10.1149/2.0031711jss
[Crossref]

5. R. Chu et al., 1200-V normally off GaN-on-Si field-effect transistors with low dynamic on -resistance. IEEE Electron Device Lett. **32**(5), 632–634 (2011). https://doi.org/10.1109/LED.2011.2118190
[Crossref]

6. M. Baeumler et al., Investigation of leakage current of AlGaN/GaN HEMTs under pinch-off condition by electroluminescence microscopy. J. Electron. Mater. **39**(6), 756–760 (2010). https://doi.org/10.1007/s11664-010-1120-9
[Crossref]

7. B. Lu, E. L. Piner, T. Palacios, *Breakdown Mechanism in AlGaN/GaN HEMTs on Si Substrate*, in Device Research Conference—Conference Digest, DRC, pp. 193–194 (2010). https://doi.org/10.1109/DRC.2010.5551907

8. W. Saito, T. Suwa, T. Uchihara, T. Naka, T. Kobayashi, Breakdown behaviour of high-voltage GaN-HEMTs. Microelectron. Reliab. **55**(9–10), 1682–1686 (2015). https://doi.org/10.1016/j.microrel.2015.06.126
[Crossref]

9. T. Asano, N. Yamada, T. Saito, H. Tokuda, M. Kuzuhara, *Breakdown Characteristics in AlGaN/GaN HEMTs with Multi-field-plate Structure*, in IMFEDK 2012—2012 International Meeting for Future of Electron Devices, Kansai, pp. 100–101 (2012). https://doi.org/10.1109/IMFEDK.2012.6218601

10. Q. Zhou et al., Schottky-contact technology in InAlN/GaN HEMTs for breakdown voltage improvement. IEEE Trans. Electron Devices **60**(3), 1075–1081 (2013). https://doi.org/10.1109/TED.2013.2241439
[Crossref]

11. S. Chander, S. Gupta, Ajay, M. Gupta, Enhancement of breakdown voltage in AlGaN/GaN HEMT using passivation technique for microwave application, Superlattices Microstruct. 120, 217–222 (2018). https://doi.org/10.1016/j.spmi.2018.05.039

12. C. Yang et al., High breakdown voltage and low dynamic ON-resistance AlGaN/GaN HEMT with fluorine ion implantation in SiNx passivation layer, Nanoscale Res. Lett. **14** (2019). https://doi.org/10.1186/s11671-019-3025-8

13. Y.J. Lee et al., High breakdown voltage in AlGaN/GaN HEMTs using AlGaN/GaN/AlGaN quantum-well electron-blocking layers. Nanoscale Res. Lett. **9**(1), 1–9 (2014). https://doi.org/10.1186/1556-276X-9-433
[Crossref]

14. R. Tomita, S. Ueda, T. Kawada, H. Mitsuzono, K. Horio, Analysis of dependence of breakdown voltage on gate-drain distance in AlGaN/GaN HEMTs with high-k passivation layer. IEEE Trans. Electron Devices **68**(4), 1550–1556 (2021). https://doi.org/10.1109/TED.2021.3060353
[Crossref]

15. B. Duan, L. Yang, Y. Wang, Y. Yang, Experimental results for AlGaN/GaN HEMTs improving

breakdown voltage and output current by electric field modulation. IEEE Trans. Electron Devices **68**(5), 2240–2245 (2021). https://doi.org/10.1109/TED.2021.3067865 [Crossref]

16. Y. Zhang et al., High-performance AlGaN double channel HEMTs with improved drain current density and high breakdown voltage, Nanoscale Res. Lett. **15**(1) (2020). https://doi.org/10.1186/s11671-020-03345-6

17. T. Liu et al., Suppression of the regrowth interface leakage current in AlGaN/GaN HEMTs by unactivated Mg doped GaN layer, Appl. Phys. Lett. **118**(7) (2021). https://doi.org/10.1063/5.0034584

18. I. Abid et al., High lateral breakdown voltage in thin channel AlGaN/GaN high electron mobility transistors on AlN/Sapphire Templates, Micromachines **10**(10) (2019). https://doi.org/10.3390/mi10100690

19. Y. Dai, J. Zhou, J. Chen, M. Han, *Scaling technologies for millimeter-wave GaN-HEMTs*, in 2012 IEEE MTT-S International Microwave Workshop Series on Millimeter Wave Wireless Technology and Applications, 2012, pp. 1–3,https://doi.org/10.1109/IMWS2.2012.6338180

20. K. Shinohara et al., Scaling of gan hemts and schottky diodes for submillimeter-wave mmic applications. IEEE Trans. Electron Devices **60**(10), 2982–2996 (2013). https://doi.org/10.1109/TED.2013.2268160 [Crossref]

21. K.C. Sahoo, C.-I. Kuo, Y. Li, E.Y. Chang, Novel metamorphic HEMTs with highly doped InGaAs source/drain regions for high frequency applications. IEEE Trans. Electron Devices **57**(10), 2594–2598 (2010). https://doi.org/10.1109/TED.2010.2062521 [Crossref]

22. A.G. Baca et al., An AlN/Al<inf>0.85</inf>Ga<inf>0.15</inf>N *High Electron Mobility Transistor with a Regrown Ohmic Contact*, in 2016 74th Annual Device Research Conference (DRC), Jun. 2016, pp. 1–2. https://doi.org/10.1109/DRC.2016.7548395

23. N.S. Garigapati, F. Lindelöw, L. Södergren, E. Lind, Capacitance scaling in $In_{0.71}Ga_{0.29}As$/InP MOSFETs with self-aligned a: Si spacers. IEEE Trans. Electron Devices **68**(8), 3762–3767 (2021). https://doi.org/10.1109/TED.2021.3092299 [Crossref]

T. R. Lenka, H. P. T. Nguyen (eds.), *HEMT Technology and Applications*, Springer Tracts in Electrical and Electronics Engineering
https://doi.org/10.1007/978-981-19-2165-0_3

Influence of Al_2O_3 Oxide Layer Thickness Variation on PZT Ferroelectric $Al_{0.3}Ga_{0.7}N/AlN/GaN$ E-Mode GR-MOSHEMT

Abdul Naim Khan[1] ✉, S. N. Mishra[2], Meenakshi Chauhan[1] ✉, Kanjalochan Jena[1] ✉ and G. Chatterjee[1] ✉

(1) Department of Electronics and Communication Engineering, The LNM Institute of Information Technology, Jaipur, Rajasthan, 302031, India

(2) School of Electronics Engineering, KIIT (Deemed to be University), Bhubaneswar, Odisha, 751024, India

✉ **Abdul Naim Khan (Corresponding author)**
Email: abdulnaimkhan.y19@lnmiit.ac.in

✉ **Meenakshi Chauhan**
Email: 20pec006@lnmiit.ac.in

✉ **Kanjalochan Jena**
Email: kanjalochan.jena@lnmiit.ac.in

✉ **G. Chatterjee**
Email: gaurav.chatterjee@lnmiit.ac.in

Abstract

The dielectric oxide Al_2O_3 induced gate recessed PZT ferroelectric $Al_{0.3}Ga_{0.7}N$/AlN/GaN MOSHEMT device behavior with different oxide thicknesses is analyzed in this work. The stack of different layers $Al_2O_3/Al_{0.3}Ga_{0.7}N$/AlN/GaN is grown on a silicon (Si) substrate. Gate recessed technique is used for achieving the normally off operation in the MOSHEMT. Normally off devices provide better control in gate leakage current and stability of threshold voltage (V_{th}). The ferroelectric material of lead zirconate titanate $Pb(Zr,Ti)O_3$ (PZT) is induced between the gate and oxide layer to obtain the enhancement type (E-Mode) operation to improve the device performance due to the strong polarization effect. The AlN spacer layer is introduced between the $Al_{0.3}Ga_{0.7}N$ barrier and GaN Channel to increase mobility and 2-DEG confinement. For controlling the GaN channel layer, the AlN nucleation layer is inserted between GaN/Si–substrate interfaces by producing better surface morphology. Furthermore, silicon-based substrates are used to achieve excellent thermal characteristics. Due to the polarization effect, a two-dimensional electron gas (2-DEG) is created at the $Al_{0.3}Ga_{0.7}N$/GaN interface. The analog performance parameters like drain current (I_d), output characteristics ($I_d - V_d$), transconductance (gm), cutoff frequency (f_T), and gate-to-source capacitance (C_{gs}) except maximum frequency of oscillation (F_{max}) show an improvement for 3 nm oxide layer thickness of Al_2O_3. The results of the proposed device $Al_{0.3}Ga_{0.7}N$/AlN/GaN PZT GR-MOSHEMT shows an impact on high power and RF-based devices. All the simulations are done by the commercial Silvaco Atlas Technology Computer-Aided Design (TCAD) tool.

Keywords $Al_{0.3}Ga_{0.7}N$/AlN/GaN – Al_2O_3 – 2-DEG – PZT – GR-MOSHEMT – E-Mode – TCAD

1 Introduction

Recently, gallium nitride-based devices are favorable ones over the GaAs and Si-based devices due to their superior material properties

such as large bandgap [1], high breakdown field [2], and high breakdown voltage [3]. AlGaN/GaN-based HEMT devices show better trade-off ON-Resistance (R_{ON}) and high breakdown voltage enabling the work device at higher frequencies. But GaN-based HEMTs provide negative threshold voltage due to work in normally on mode. For converting the normally on to normally off operation [4], a stack of metal oxide is needed with some modification in the gate electrode. MOS-HEMT-based devices show switch-off current at zero bias gate voltage [5]. Gate recessed-MOSHEMT (GR-MOSHEMT) provides low leakage gate current [6, 7], higher breakdown voltage [8, 9], and positive threshold voltage[10] as compared to HEMT-based devices, which show more impact in the system-based high-frequency applications [11]. Ferroelectric materials have been used as oxide gate dielectrics to perform E-mode [12] operations due to the impact of polarization to achieve two-dimensional electron gas (2-DEG) and generate the positive cutoff voltage. Different types of insulators are used for AlGaN/GaN MOSHEMTs such as Al_2O_3 [13], SiO_2 [14], SiNx [15], HfO_2 [16], etc. The major drawback of MOSHEMT-based devices is that they provide low transconductance compared to HEMT-based devices due to an increase in the AlGaN barrier layer thickness [17, 18], which limits the high RF performance [19]. The improvement in the gate transconductance [20, 21] is done by using a recessed gate methodology with a thin oxide layer. To operate the device in DC and high-frequency microwave application [22], AlN spacer layer is inserted between the barrier and the channel layer. The spacer layer increases the charge concentration and mobility near the interface, which is helpful in generating 2-DEG. The AlN nucleation layer was introduced to reduce the tensile stress and the lattice mismatch [23] between GaN and silicon substrate. Also, it provides better surface properties [24] for the deposition of nitride-based material on AlN. Silicon substrate provides better thermal properties to the proposed device structure.

To overcome the issues related to low transconductance, gate leakage, and negative threshold voltage, this work makes the following contributions:

- The proposed device structure suggests a ferroelectric dielectric oxide layer insertion between the gate and the Al_2O_3 oxide layer to

improve the 2-DEG.
- The AlN spacer layer inclusion helps to improve the AlGaN layer quality as well as remove the strain.
- This work searches Al_2O_3 oxide layer optimal thickness at which the proposed device shows better drain current, gate transconductance, and cutoff frequency. Investigation findings show that oxide layer thickness is an essential parameter for the realization of the device in DC and high-power applications.

In this work, we demonstrated the performance of the dielectric Al_2O_3 oxide layer by varying the thickness for ferroelectric $Al_{0.3}Ga_{0.7}N$/AlN/GaN GR-MOSHEMT to investigate the different figures of merit. Section 2 represents the behavior of the ferroelectric $Al_{0.3}Ga_{0.7}N$/AlN/GaN PZT GR-MOSHEMT device structure with device material properties. The simulated results are generated with the help of Silvaco atlas TCAD in Sect. 3. At last, the conclusion is drawn in Sect. 4.

---

2 Device Model Description and Material Properties

2.1 Device Structure

The proposed device structure for $Al_{0.3}Ga_{0.7}N$/AlN/GaN gate recessed E-mode MOSHEMT is shown in Fig. 1. A stack of epitaxial layers consists of a GaN cap layer, $Al_{0.3}Ga_{0.7}N$ barrier layer, AlN spacer layer, GaN channel layer, AlN nucleation layer, and silicon as a substrate layer from top to down approach with a thickness of 2 nm, 20 nm, 1 nm, 1.47 µm, 30 nm, and 20 nm, respectively. The AlGaN barrier layer is doped with a charge concentration of 1e17 cm^{-3} to increase the charge carriers at the $Al_{0.3}Ga_{0.7}N$/GaN interface to make 2-DEG rich in terms of electron concentration. The AlN spacer layer is used to increase electron mobility and make 2-DEG more confined. The nucleation layer is used between GaN and substrate to reduce lattice mismatch and provide smooth surface morphology to the device. The ferroelectric PZT with 3 nm layer thickness is used in this simulation. The dielectric

oxide layer of Al_2O_3 thicknesses varies from 2 to 4 nm by keeping all device parameters constant. In this device, gate length, gate-to-source distance, and gate-to-drain distance are considered as 2.5 µm each. The work function (ϕ) for gate, source, and drain contacts are 5.1, 3.9, and 3.9 eV, respectively. In this work, Different analog performance parameters like drain current (I_d), gate transconductance (g_m), cutoff frequency (f_T), gate-to-source capacitance (C_{gs}), and a maximum frequency of oscillations (F_{max}) are analyzed by varying the oxide thickness (2–4 nm) in the dielectric Al_2O_3 layer.

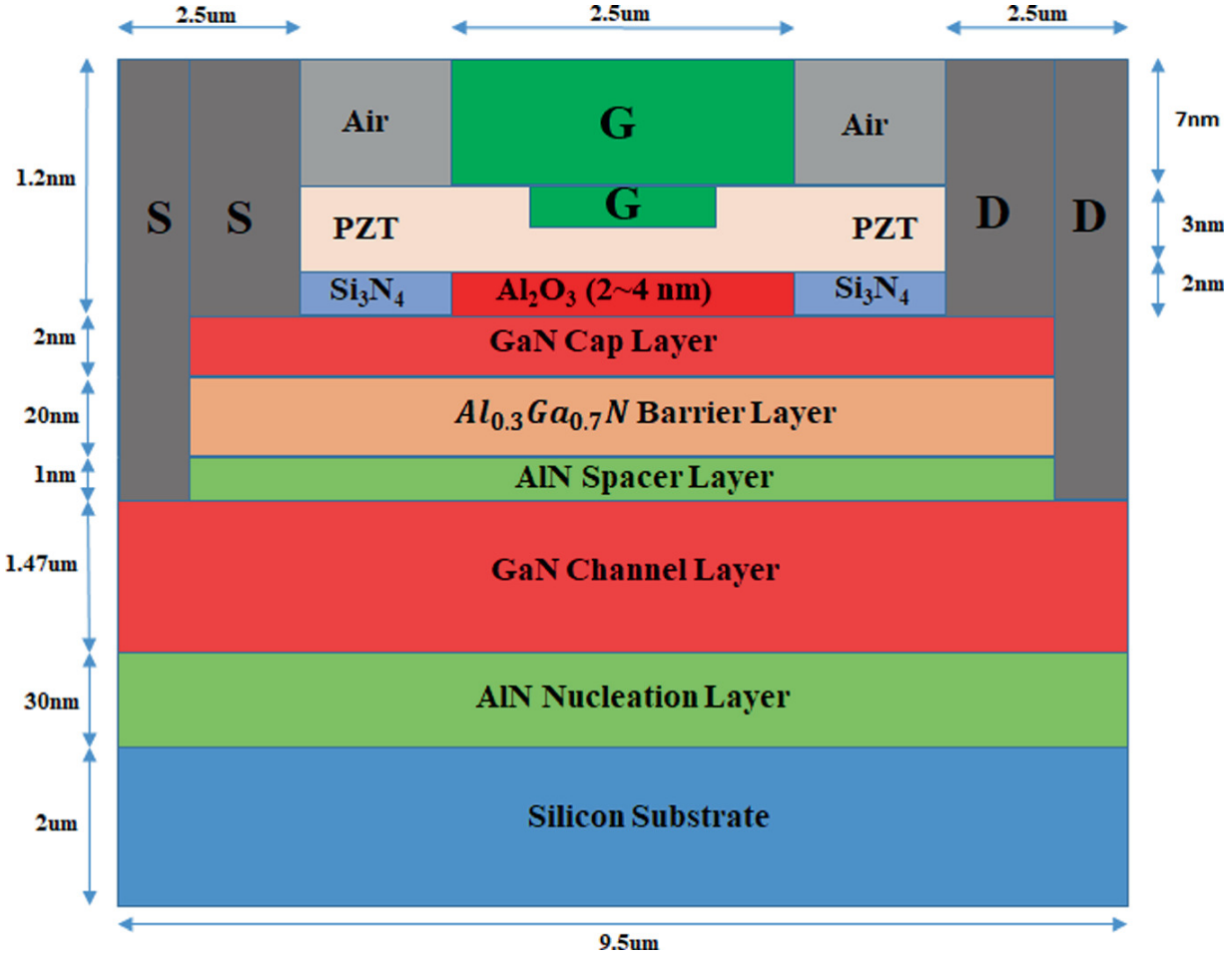

Fig. 1 Cross-sectional layout of the $Al_{0.3}Ga_{0.7}N$ /AlN/GaN gate recessed E-mode MOSHEMT

2.2 Material Properties and Equations

Two-dimensional simulations are performed using commercial Silvaco atlas TCAD software [25]; the material properties of $Al_{0.3}Ga_{0.7}N$ /AlN/GaN and silicon are listed in Table 1 and are used for simulation purposes.

Table 1 Material Properties of proposed $Al_{0.3}Ga_{0.7}N$/AlN/GaN E-mode gate recessed PZT structure [23, 26, 27]

Material properties	Unit	AlGaN	GaN	AlN	Silicon
Electron mobility	$cm^2/V\,s$	985.5	1350	1280	1350
Bandgap (E_g)	eV	3.87	3.42	6.2	1.12
Density of states (N_C)	cm^{-3}	2.07×10^{18}	1.07×10^{18}	2.07×10^{18}	3.2×10^{19}
Density of states (N_C)	cm^{-3}	1.16×10^{19}	1.16×10^{19}	1.16×10^{19}	1.8×10^{19}
Permittivity		9.55	9.5	8.5	11.8

The energy bandgap, electron affinity, permittivity, and state mass density of hole and electrons of AlGaN nitride-based ternary compound semiconductors are depended on the aluminum mole fraction in the material. Different equations are used for finding the specific parameter value according to their mole fractions are given below.

Now, Vegard's law is used for finding the energy bandgap of the ternary compound semiconductor as follows:

$$E_g\left(Al_{0.3}Ga_{0.7}N\right) = 0.3 * E_g\left(AlN\right) + \left(0.7 * E_g\left(GaN\right) - 0.21 * b\right) \quad (1)$$

where b is the bowing parameter and the value of b is 1.3 [23]

Electron affinity and permittivity of $Al_xGa_{1-x}N$ material are computed as

$$\chi\left(Al_{0.3}Ga_{0.7}N\right) = \chi\left(GaN\right) - 0.3759 \quad (2)$$

$$\varepsilon\left(Al_xGa_{1-x}N\right) = 8.5x + 8.9\left(1 - x\right) \quad (3)$$

The electron and hole mass density of $Al_xGa_{1-x}N$ ternary compound material can be calculated by linear interpolations [28]:

$$m_e\,(Al_xGa_{1-x}N) = 0.314x + 0.2\,(1 - x) \tag{4}$$

$$m_h\,(Al_xGa_{1-x}N) = 0.417x + 1.0\,(1 - x) \tag{5}$$

where *me* and *mh* are the electron and hole mass density of $Al_xGa_{1-x}N$ material and *x* is the mole fraction of $Al_xGa_{1-x}N$.

For achieving the maximum gain in the high linearity, devices transconductance should be high. Generally, AlGaN HEMT and MOSHEMT-based devices generate bell-shaped transconductance due to thermal effects and nonlinearity effects of source and drain resistances. The gate-to-source/drain capacitances are a function of gate charge variation concerning gate-to-source and drain-to-source voltages. The amount of net charge to apply voltage to gate bias is denoted by gate charge. The following equations can calculate transconductance, gate-to-source, and gate-to-drain capacitances [29]:

$$g_{\mathrm{m}} = \left.\frac{\partial I_D}{\partial V_{\mathrm{GS}}}\right| V_{\mathrm{DS}} = \mathrm{const} \tag{6}$$

$$C_{\mathrm{gs}} = \frac{\partial Q}{\partial V_{\mathrm{gs}}} \tag{7}$$

$$C_{\mathrm{gd}} = \frac{\partial Q}{\partial V_{\mathrm{ds}}} \tag{8}$$

where g_{m}, C_{gs}, and C_{gd} are denoted gate transconductance, gate-to-source capacitance, and gate-to-drain capacitance, respectively.

Generally, AlGaN/GaN-based MOSHEMT characterized its dynamics for high-frequency-related devices in two crucial parameters––cutoff frequency (f_{T}) and the maximum frequency of oscillations (F_{max}). These parameters are depended on the gate and output transconductance as

well as gate-to-source/drain capacitances. Expression for cutoff frequency and frequency of oscillations is given as [27, 30]

$$f_T = \frac{g_{\mathrm{m}}}{\left(2 \times \pi \times C_{\mathrm{gg}}\right)} \tag{9}$$

where C_{gg} is the summation of gate-to-source and gate-to-drain capacitances.

$$C_{\mathrm{gg}} = C_{\mathrm{gd}} + C_{\mathrm{gs}} \tag{10}$$

$$f_{\max} = \frac{f_T}{\left(2 \times \sqrt{g_{\mathrm{ds}} \times \left(R_g + R_s\right) + 2\pi \times f_T \times R_g \times C_{\mathrm{gd}}}\right)} \tag{11}$$

The ferroelectric model should be used in the simulation for setting the ferro material parameters. The permittivity for the ferroelectric material is given by the following Eqs. (12)–(13) [31]:

$$\varepsilon(E) = \mathrm{ferro.epsf} + \frac{\mathrm{ferro.ps}}{2\delta}.\mathrm{sech}^2\left[\frac{E - \mathrm{ferro.ec}}{2\delta}\right] \tag{12}$$

where E is the electric field, $\mathrm{ferro.ec}$ is the coercive field, $\mathrm{ferro.ec}$ is the spontaneous polarization, $\mathrm{ferro.pr}$ is the Remnant polarization, and $\mathrm{ferro.epsf}$ is the permittivity of the ferroelectric material.

$$\delta = \mathrm{ferro.ec}\left[\log\left[\frac{1 + \frac{\mathrm{ferro.pr}}{\mathrm{ferro.ps}}}{1 - \frac{\mathrm{ferro.pr}}{\mathrm{ferro.ps}}}\right]\right]^{-1} \tag{13}$$

Ferroelectric material parameters like $\mathrm{ferro.ec}$, $\mathrm{ferro.ec}$, $\mathrm{ferro.pr}$, and $\mathrm{ferro.epsf}$ can be specified in an atlas during simulation. The polarization effect is generated at the boundary of the ferroelectric

material and $Al_{0.3}Ga_{0.7}N$/GaN interface. Ferroelectric polarization related to dielectric constant and electric field is given by Eq. (14) [32]:

$$\varepsilon_1\varepsilon_0 E_1 + P_1 = \varepsilon_2\varepsilon_0 E_2 + P_{\text{ferro}} \tag{14}$$

where

ε_1: Linear dielectric constant of the semiconductor

ε_1: Linear dielectric constant of ferroelectric material

E_g and E_g: Electric field in semiconductor and ferroelectric material layer

P_1: Total Polarization of the device

P_{ferro}: Polarization of the ferroelectric material.

---

3 Simulation Results and Discussions

The ferroelectric $Al_{0.3}Ga_{0.7}N$/AlN/GaN PZT GR-MOSHEMT is simulated in TCAD by variation in Al_2O_3 oxide layer thickness from 2 to 4 nm with a step size of 1 nm. The electrical behavior of the proposed E-mode GR-MOSHEMT device with its energy bandgap at different oxide layer thicknesses is demonstrated in Fig. 2. The energy band diagram shows that the energy bandgap level shifts upward due to reducing the oxide layer thickness. $Al_{0.3}Ga_{0.7}N$, AlN, and GaN conduction and valence band energies are constant but show a positional shift for distance due to increment in the oxide layer thickness.

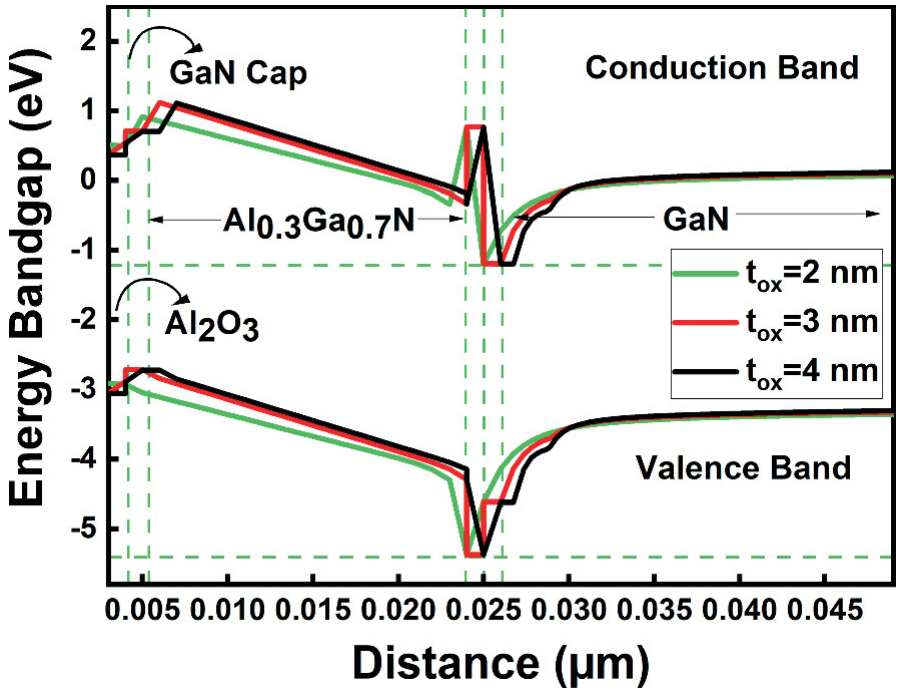

Fig. 2 Variation of energy bandgap (E_g) of PZT GR-MOSHEMT for Al_2O_3 oxide layer thickness t_{ox} = 2, 3, and 4 nm

The transfer characteristics of the proposed device are shown in Fig. 3. It is observed that the device shows a positive threshold voltage for gate-recessed MOSHEMT, and the maximum current is achieved for the oxide layer thickness of 2 nm. Generally, threshold voltage decrease may be due to the Al_2O_3 oxide layer having a positive charge and increased film stress in the device. When the gate to AlGaN barrier layer distance is increased, the current decreases due to less charge carrier's concentration at the interface. Charge carrier concentration is maximum at the interface. The proposed device shows a maximum drain current of 1.17 A/mm at 2 nm, higher than 19.4% and 21.5% of the oxide layer thickness of 3 and 4 nm, respectively.

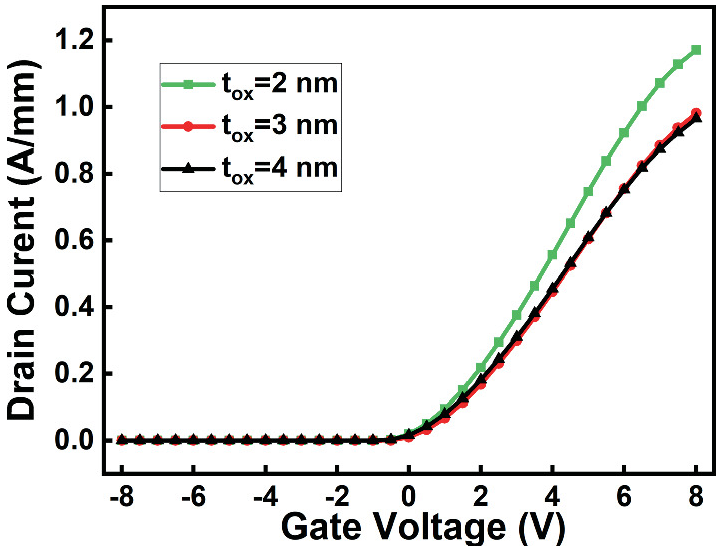

Fig. 3 Transfer characteristics of PZT GR-MOSHEMT for Al_2O_3 oxide layer thickness t_{ox} = 2 nm, 3 nm, and 4 nm

Figure 4 shows the output characteristics of the PZT ferro $Al_{0.3}Ga_{0.7}N$/AlN/GaN gate-recessed MOSHEMT for different oxide thicknesses. The higher drain voltage range for the gate-recessed MOSHEMT devices shows superior results in terms of drain current. The proposed device exhibited excellent drain current and pinch-off characteristics for the oxide layer thickness of 2 nm. This device achieves a maximum drain current of 0.22 A/mm at V_{gs} = 2 V.

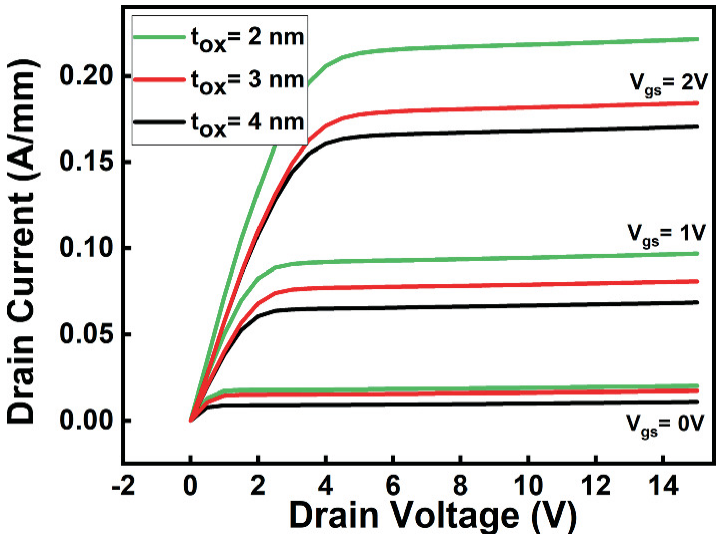

Fig. 4 Variation of output characteristics of PZT GR-MOSHEMT for Al_2O_3 oxide layer thickness t_{ox} = 2 nm, 3 nm, and 4 nm

Figure 5 illustrates the transconductance behavior of the proposed device with different oxide layer thicknesses. Transconductance increases with a decrease in oxide layer thickness. The high peak of gate transconductance for GR-MOSHEMT was 190 mS/mm, which is higher than 3 and 4 nm oxide layer thicknesses. As the distance between the gate and the $Al_{0.3}Ga_{0.7}N$ barrier increases due to changes in oxide layer thicknesses, as much gate controlling ability decreases. The threshold voltage, drain current, and gate transconductance strongly impacts the device due to the insertion of the Al_2O_3 dielectric oxide layer.

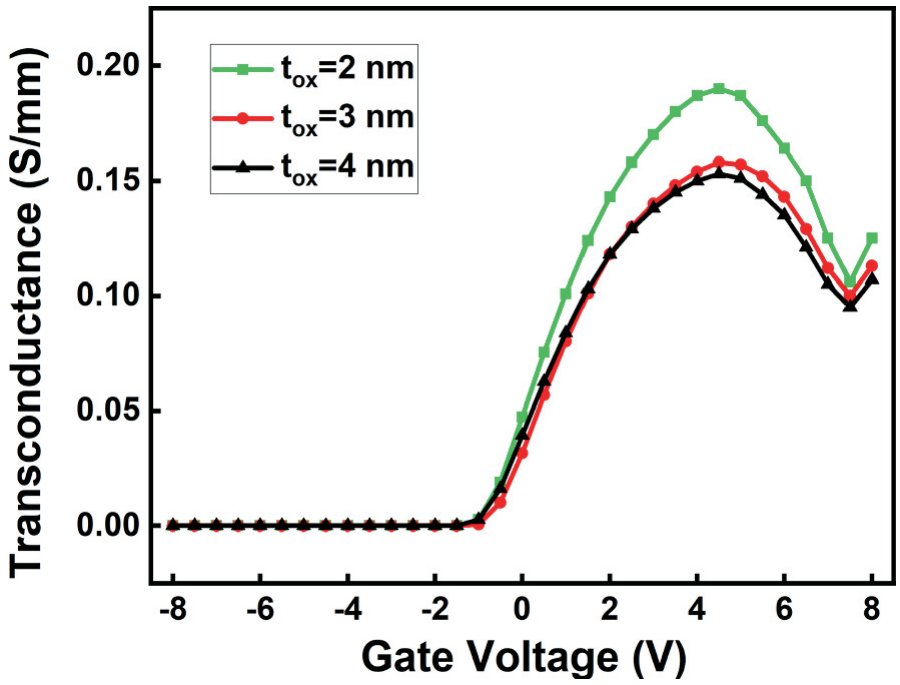

Fig. 5 Variation of gate transconductance (g_m) of PZT GR-MOSHEMT for Al_2O_3 oxide layer thickness t_{ox} = 2 nm, 3 nm, and 4 nm

Free charge carriers are the critical point for finding the intrinsic as well extrinsic capacitances. Gate-to-source/drain capacitances value depends on the number of charge carriers stored at the source/drain. Generally, gate-to-source capacitances show higher capacitances due to the accumulation of charge carriers near the source end. Gate-to-source capacitance–voltage (CV) measurement was carried out in Fig. 6 to investigate the interface quality and effective capacitance of the PZT ferro GR-MOSHEMT device. The effective gate-to-source capacitance

employed a series connection of the $Al_{0.3}Ga_{0.7}N$ barrier layer and Al_2O_3 oxide layer. Capacitance increases with a decrease in the oxide layer. The proposed device shows a higher capacitance of 28 pF at the 2 nm oxide layer, approximately 14.47% higher on the 3 nm oxide layer.

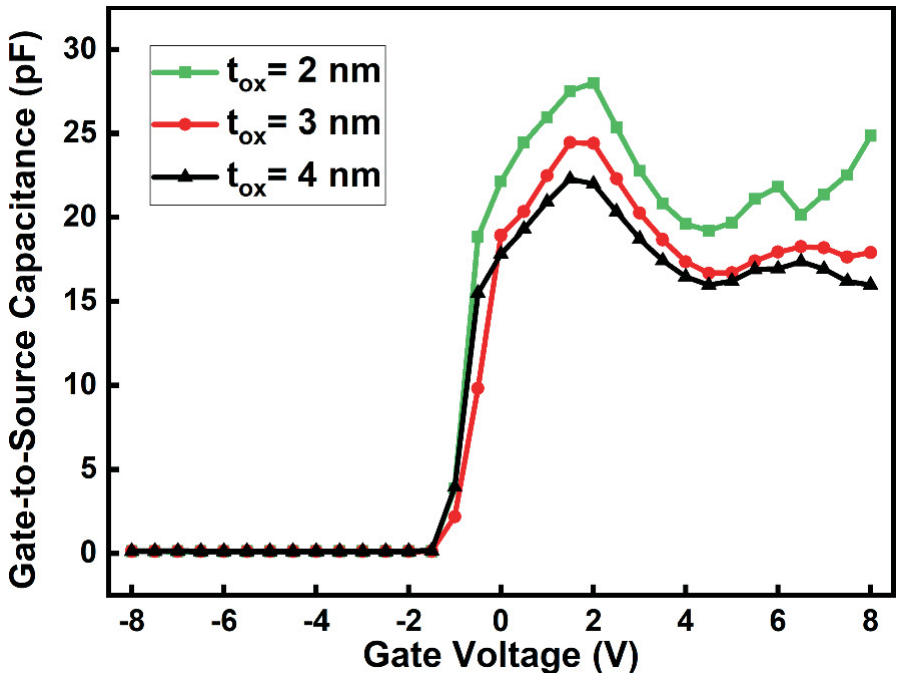

Fig. 6 Variation of gate-to-source capacitance (C_{gs}) of PZT GR-MOSHEMT for Al_2O_3 oxide layer thickness t_{ox} = 2 nm, 3 nm, and 4 nm

The cutoff frequency concerning the gate voltage for PZT ferro GR-MOSHEMT with different oxide layer thicknesses is shown in Fig. 7. The cutoff frequency (f_T) is proportional to the transconductance. As transconductance increases, the cutoff frequency also increases. Cutoff frequency rises abruptly with the rise in gate voltage but attaining maximum peak decreases due to inversion. The unit gain cutoff frequency shows slightly better improvement when the oxide layer thickness is decreased. The graph shows that the maximum peak of cutoff frequency is obtained at approximately 142 GHz for 2 nm oxide thickness.

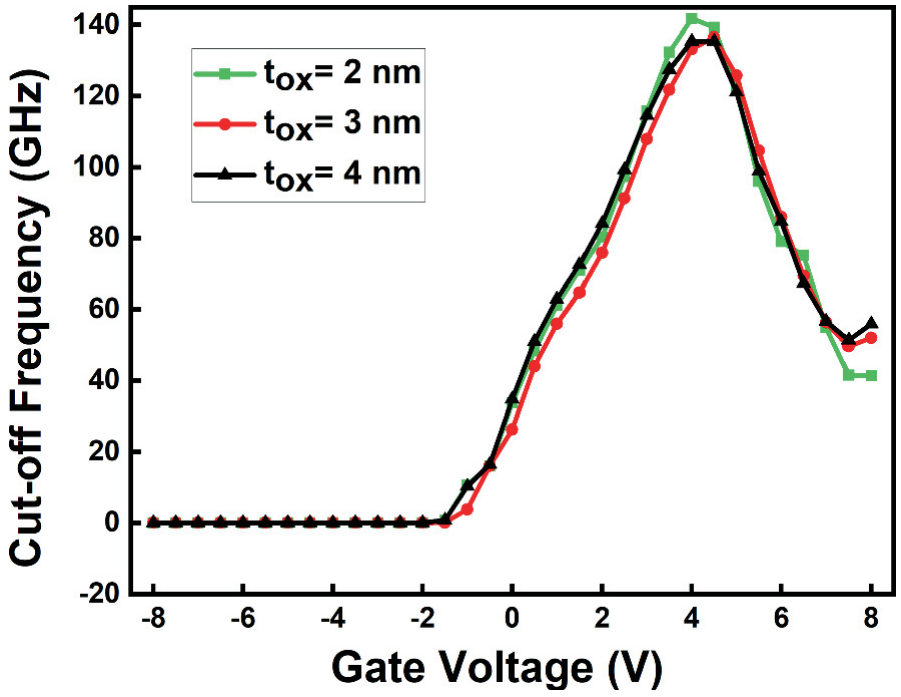

Fig. 7 Variation of cutoff frequency (f_T) of PZT GR-MOSHEMT for Al_2O_3 oxide layer thickness t_{OX} = 2 nm, 3 nm, and 4 nm

Below the threshold region, there are a fewer number of electrons in the channel. As gate bias voltage is increased, electrons accumulate in the GaN channel, therefore, intrinsic capacitances show a sharp increment. After the threshold region, capacitance shows saturation with increasing voltage. In this region, more charge carriers are accumulated toward the drain end and increase the drain capacitances. Gate-to-source/drain capacitances and transconductance are the factors that limit the frequency of oscillations. Figure 8 shows the maximum frequency of oscillation behavior to applied gate bias voltage at different oxide layer thicknesses. The variation in the plot depends on the cutoff frequency and the gate-to-source/drain capacitances. For oxide layer thickness of 3 nm, the maximum frequency is achieved by 18.39 GHz, which shows a slightly better peak than the 2 nm.

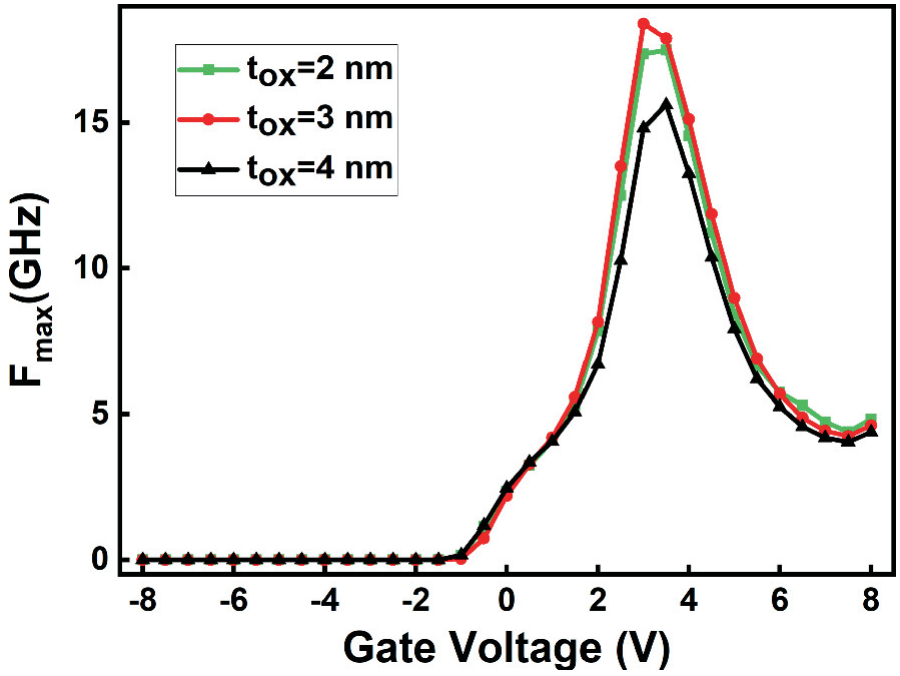

Fig. 8 Variation of maximum frequency of oscillation (F_{max}) of PZT GR-MOSHEMT for Al_2O_3 oxide layer thickness t_{ox} = 2 nm, 3 nm, and 4 nm

The comparative analysis of $Al_{0.3}Ga_{0.7}N$/AlN/GaN E-mode gate recessed PZT MOSHEMT of different Al_2O_3 oxide thicknesses is shown in Table 2. The table quickly shows that different parameters like drain current, transconductance, the gate-to-source voltage, and cutoff frequency show better results for the 2 nm thickness of the oxide layer as compared to 3 and 4 nm.

Table 2 $Al_{0.3}Ga_{0.7}N$/AlN/GaN E-mode PZT GR-MOSHEMT simulation results for different Al_2O_3 oxide layer thicknesses

S. No.	Parameters	Unit	t_{ox} = 2 nm	t_{ox} = 3 nm	t_{ox} = 4 nm
1	Threshold voltage	V	1.08	1.19	1.03
2	Drain current	A/mm	1.172	0.981	0.964
3	Transconductance	S/mm	0.190	0.158	0.152
4	Gate-to-source capacitance	pF	28.03	24.46	22.28
5	Cutoff frequency	GHz	141.9	136.5	135.4
6	Max. frequency of oscillations	GHz	17.89	18.39	15.61

4 Conclusion

This article proposes a ferroelectric PZT $Al_{0.3}Ga_{0.7}N$/AlN/GaN GR-MOSHEMT structure with the variation in the Al_2O_3 oxide layer. The variation in oxide layer thickness with ferroelectric material insertion just below the gate electrode shows an improvement in the transfer and output characteristics of the device. GR-MOSHEMT achieved the maximum cutoff frequency of 141.9 GHz at 2 nm oxide layer thickness due to the tradeoff relationship between gate transconductance and gate capacitance. The maximum frequency of oscillation shows upward and downward variation for oxide layer thickness. The findings of different parameters like I_d, g_m, $f_{T,}$ and C_{gs} conclude that the device PZT ferro $Al_{0.3}Ga_{0.7}N$/AlN/GaN GR-MOSHEMT shows overall better responses for the Al_2O_3 oxide layer thickness of 2 nm as compared to 3 nm and 4 nm. The proposed device shows better optimal results in terms of cutoff frequency for high-frequency-related applications.

References

1. F. Husna, M. Lachab, M. Sultana, V. Adivarahan, Q. Fareed, A. Khan, High-temperature performance of AlGaN/GaN MOSHEMT with SiO_2 gate insulator fabricated on Si (111) substrate. IEEE Trans. Electron Devices **59**(9), 2424–2429 (2012)

2. N.M. Shrestha, Y.Y. Wang, Y. Li, E.Y. Chang, Simulation study of AlN spacer layer thickness on AlGaN/GaN HEMT. Himalayan Phys. **4**, 14–17 (2013)

3. T. Hashizume, K. Nishiguchi, S. Kaneki, J. Kuzmik, Z. Yatabe, State of the art on gate insulation and surface passivation for GaN-based power HEMTs. Mater. Sci. Semicond. Process. **78**, 85–95 (2018)

4. H. Chandrasekar, S. Kumar, K.L. Ganapathi, S. Prabhu, S.B. Dolmanan, S. Tripathy, S. Raghavan et al., Dielectric engineering of HfO_2 gate stacks towards normally-ON and normally-OFF GaN HEMTs on Silicon. arXiv preprint arXiv:1708.03811 (2017)

5. E. Acurio, F. Crupi, P. Magnone, L. Trojman, G. Meneghesso, F. Iucolano, On recoverable behavior of PBTI in AlGaN/GaN MOS-HEMT. Solid-State Electron. **132**, 49–56 (2017)

6. V. Adivarahan, M. Gaevski, W.H. Sun, H. Fatima, A. Koudymov, S. Saygi, G. Simin et al., Submicron gate Si_3N_4/AlGaN/GaN-metal-insulator-semiconductor heterostructure field-effect transistors. IEEE Electron Device Lett. **24**(9), 541–543 (2003)

7. D. Kikuta, J.P. Ao, Y. Ohno, Gate leakage and electrical performance of AlGaN/GaN MIS-type HFET with evaporated silicon oxide layer. Solid-State Electron. **50**(3), 316–321 (2006)

8. S. Yagi, M. Shimizu, M. Inada, Y. Yamamoto, G. Piao, H. Okumura, Y. Yano, N. Akutsu, H. Ohashi, High breakdown voltage AlGaN/GaN MIS–HEMT with SiN and TiO_2 gate insulator. Solid-State Electron. **50**(6), 1057–1061 (2006)

9. J. LaRoche, W. Hoke, D. Altman, J. McClymonds, P. Alcorn, K. Smith, E. Chumbes, J. Letaw, T. Kazior, Performance and reliability of GaN MISHEMTs and MMICs fabricated from GaN grown on high resistance <111> Si substrates by molecular beam epitaxy, in *Digest of the 2013 International Conference on Compound Semiconductor Manufacturing Technology (2013 CS MANTECH)* (2013)

10. M. Ťapajna, L. Válik, F. Gucmann, D. Gregušová, K. Fröhlich, Š. Haščík, E. Dobročka, L. Tóth, B. Pécz, J. Kuzmík, Low-temperature atomic layer deposition-grown Al_2O_3 gate dielectric for GaN/AlGaN/GaN MOS HEMTs: impact of deposition conditions on interface state density. J. Vac. Sci. Technol. B Nanotechnol. Microelectron. Mater. Process. Meas. Phenom. **35**(1), 01A107 (2017)

11. S.-H. Yi, D.-B. Ruan, S. Di, X. Liu, Y.H. Wu, A. Chin, High performance metal-gate/high-κ GaN MOSFET with good reliability for both logic and power applications. IEEE J. Electron Devices Soc. **4**(5), 246–252 (2016)

12. D.K. Panda, T.R. Lenka, Linearity improvement in E-mode ferroelectric GaN MOS-HEMT using dual gate technology. Micro Nano Lett. **14**(6), 618–622 (2019)

13. T. Hashizume, S. Ootomo, H. Hasegawa, Al_2O_3-based surface passivation and insulated gate structure for AlGaN/GaN HFETs. Phys. Status Solidi (C) **7**, 2380–2384 (2003)

14. M.A. Khan, X. Hu, A. Tarakji, G. Simin, J. Yang, R. Gaska, M.S. Shur, AlGaN/GaN metal–oxide–semiconductor heterostructure field-effect transistors on SiC substrates. Appl. Phys. Lett. **77**(9), 1339–1341 (2000)

15. X. Hu, A. Koudymov, G. Simin, J. Yang, M.A. Khan, A. Tarakji, M.S. Shur, R. Gaska, Si_3N_4/AlGaN/GaN–metal–insulator–semiconductor heterostructure field–effect transistors. Appl. Phys. Lett. **79**(17), 2832–2834 (2001)

16. A. Kawano, S. Kishimoto, Y. Ohno, K. Maezawa, Takashi Mizutani, H. Ueno, T. Ueda, T. Tanaka, AlGaN/GaN MIS-HEMTs with HfO_2 gate insulator. Phys. Status Solidi C **4**(7), 2700–2703 (2007)

17. K.-Y. Park, H.-I. Cho, H.-C. Choi, Y.-H. Bae, C.-S. Lee, J.-L. Lee, J.-H. Lee, Device characteristics of AlGaN/GaN MIS-HFET using Al_2O_3–HfO_2 laminated high-*k* dielectric. Jpn. J. Appl. Phys. **43**(11A), L1433 (2004)

18. M.A. Khan, X. Hu, G. Sumin, A. Lunev, J. Yang, R. Gaska, M.S. Shur, AlGaN/GaN metal oxide semiconductor heterostructure field effect transistor. IEEE Electron Device Lett. **21**(2), 63–65 (2000)

19. M. Marso, G. Heidelberger, K.M. Indlekofer, J. Bernát, A. Fox, P. Kordos, H. Luth, Origin of

improved RF performance of AlGaN/GaN MOSHFETs compared to HFETs. IEEE Trans. Electron Devices **53**(7), 1517–1523 (2006)

20. D.P. Nguyen, X.-T. Tran, N.L.K. Nguyen, P.T. Nguyen, A.-V. Pham, A wideband high efficiency Ka-band MMIC power amplifier for 5G wireless communications, in *2019 IEEE International Symposium on Circuits and Systems (ISCAS)* (IEEE, 2019), pp. 1–5

21. S. Maroldt, C. Haupt, W. Pletschen, S. Müller, R. Quay, O. Ambacher, C. Schippel, F. Schwierz, Gate-recessed AlGaN/GaN based enhancement-mode high electron mobility transistors for high frequency operation. Jpn. J. Appl. Phys. **48**(4S), 04C083 (2009)

22. K. Jena, T.R. Lenka, Effect of AlN spacer thickness on device characteristics of AlInN/AlN/GaN MOSHEMT, in *2016 IEEE Region 10 Conference (TENCON)* (IEEE, 2016), pp. 3253–3256

23. T. Zine-Eddine, H. Zahra, M. Zitouni, Design and analysis of 10 nm T-gate enhancement-mode MOS-HEMT for high power microwave applications. J. Sci. Adv. Mater. Devices **4**(1), 180–187 (2019)

24. J.J. Freedsman, A. Watanabe, Y. Yamaoka, T. Kubo, T. Egawa, Influence of AlN nucleation layer on vertical breakdown characteristics for GaN-on-Si. Phys. Status Solidi (A) **213**(2), 424–428 (2016)

25. Silvaco: ATLAS user's manual: device simulation software (Silvaco, Santa Clara, CA, USA, 2013)

26. M. Verma, A. Nandi, DC analysis of GaN-capped AlGaN/GaN HEMT for different gate-drain spacing, in *2018 2nd International Conference on Inventive Systems and Control (ICISC)* (IEEE, 2018), pp. 1337–1340

27. N. Braga, R. Mickevicius, R. Gaska, X. Hu, M. S. Shur, M.A. Khan, G. Simin, J. Yang, Simulation of hot electron and quantum effects in AlGaN/GaN heterostructure field effect transistors. J. Appl. Phys. **95**(11), 6409–6413 (2004)

28. I. Vurgaftman, J.R. Meyer, L.R. Ram-Mohan, Band parameters for III–V compound semiconductors and their alloys. J. Appl. Phys. **89**(11), 5815–5875 (2001)

29. K. Jena, R. Swain, T.R. Lenka, Effect of thin gate dielectrics on DC, radio frequency and linearity characteristics of lattice-matched AlInN/AlN/GaN metal–oxide–semiconductor high electron mobility transistor. IET Circuits, Devices Syst. **10**(5), 423–432 (2016)

30. M. Farahmand, C. Garetto, E. Bellotti, K.F. Brennan, M. Goano, E. Ghillino, G. Ghione, J.D. Albrecht, P.P. Ruden, Monte Carlo simulation of electron transport in the III-nitride Wurtzite phase materials system: binaries and ternaries. IEEE Trans. Electron Devices **48**(3), 535–542 (2001)

31. M.H. Sani, A.A. Shakeri, *Design and Analysis of High-Power Device Based on PZT/AlGaN/GaN by Ferroelectric-Gate Heterojunction* (2020)

32. Y.C. Kong, F.S. Xue, J.J. Zhou, L. Li, C. Chen, Y.R. Li, Ferroelectric polarization-controlled two-dimensional electron gas in ferroelectric/AlGaN/GaN heterostructure. Appl. Phys. A **95**(3), 703–706 (2009)

T. R. Lenka, H. P. T. Nguyen (eds.), *HEMT Technology and Applications*, Springer Tracts in Electrical and Electronics Engineering
https://doi.org/10.1007/978-981-19-2165-0_4

Study of Different Transport Properties of MgZnO/ZnO and AlGaN/GaN High Electron Mobility Transistors: A Review

Yogesh Kumar Verma[1] ✉, Varun Mishra[2] ✉, Lucky Agarwal[3] ✉, Laxman Singh[4] and Santosh Kumar Gupta[5] ✉

(1) School of Electronics and Electrical Engineering, Lovely Professional University, Jalandhar, Punjab, 144411, India
(2) Department of Electronics and Electrical Engineering, Graphic Era (Deemed to be University), Dehradun, Uttarakhand, 248002, India
(3) School of Electronics Engineering, Vellore Institute of Technology, Chennai, Tamil Nadu, 600127, India
(4) Department of Electronics and Communication Engineering, Noida Institute of Engineering and Technology, Greater Noida, 201310, India
(5) Department of Electronics and Communication Engineering, Motilal Nehru National Institute of Technology, Allahabad, Uttar Pradesh, 211004, India

✉ **Yogesh Kumar Verma (Corresponding author)**
Email: yogesh.25263@lpu.co.in

✉ **Varun Mishra**
Email: varunmishra.ece@geu.ac.in

✉ **Lucky Agarwal**
Email: rel1408@mnnit.ac.in

✉ **Santosh Kumar Gupta**

Email: skg@mnnit.ac.in

Abstract
ZnO material exhibits superior properties required for several electronic applications. It has been noticed that the different temperature-based models of conventional AlGaN/GaN HEMTs have been widely studied; however, physics-based analytical models including the effect of temperature for MgZnO/ZnO HEMT are not sufficiently explored much as of now in the literature. Accordingly, in this brief, the different transport properties and Fermi energy levels of AlGaN/GaN and MgZnO/ZnO HEMT are studied with respect to different temperatures. Further, we have also comparatively reviewed the important transport properties including 2DEG density, internal electric field, and optical gain of AlGaN/GaN and MgZnO/ZnO quantum well structures having identical dimensions.

Keywords Temperature – 2DEG density – Fermi energy level – HEMT – Quantum well

1 Introduction

The study of the 2-DEG region at the heterojunction conferred the researchers with a new idea to fabricate heterostructure-based field-effect transistor [1–5]. Morkoc et al. [6] revealed that the modulation doping technique adopted in HFET reduces the ionized donor scattering. Anderson et al. [7] reported the presence of an inversion or accumulation layer of charge carriers (electrons) at the heterointerface of certain materials caused due to the electrons originating from the dopant impurities in wider bandgap material. These electrons turn out to accumulate in the lower bandgap region from the material of the wider bandgap and form 2 DEG at the heterointerface [8, 9]. Mimura et al. [1] reported the fabrication of GaAs/n-AlGaAs HEMT for the first time, with improved electrical performance. T. Mimura revealed the high-speed performance of the GaAs/n-AlGaAs HEMT to be three times superior to that of the MESFET at the temperature of 77 Hiyamizu et al. [10] reported enhanced mobility of the 2DEG at low temperatures in MBE-grown GaAs/n-AlGaAs heterojunction, and Witkowski et al. [11]

reported high electron mobilities in AlGaAs–GaAs modulation-doped heterojunction. Wang et al. [12] reported the growth of GaAs–AlGaAs modulation-doped multilayer structures using MBE with very high electron mobilities at 77 K. Delagebeaudeuf et al. [13] revealed that heterojunction 2-DEG Metal–Semiconductor Field-Effect Transistor (MESFET) is a promising candidate as low noise Field-Effect Transistor (FET). Drummond et al. [14] proposed a model describing electrical characteristics of modulation-doped FET. Lee et al. [15] developed a model describing current–voltage characteristics of HEMT. Weiler et al. [16] developed a model for DC *I*–*V* characteristics of the AlGaAs/GaAs HEMT. Sadwick et al. [17] presented a model for electrical characteristics of AlGaAs/GaAs HEMT using the quantum mechanical triangular potential well model. Majewski et al. [18] introduced a novel analytical model for MODFET to predict its electrical performance. Salmer et al. [19] discussed the properties of 2DEG. Shey et al. [20, 21] developed an analytical model for AlGaAs/GaAs HEMT.

ZnO is one of the ideal semiconductors having many attractive properties that would make it suitable for fabricating electronic and optoelectronic devices [22]. ZnO inherits n-type conductivity and transparent nature in its pure form [23–25]. Over the previous decades, worldwide researchers explored the possibility of ZnO as a supplement or other option to GaN for optoelectronics [26–30]. Thus, attempts have been concentrated on exploring the semiconductor properties of ZnO. Further, emphasis has been on obtaining p-type conductivity by controlling unintentional n-type conductivity in ZnO [31, 32]. Regardless of several attempts, stable p-nature in ZnO is still a challenge. Undoped ZnO shows n-type conductivity due to unintentional hydrogen incorporation and native point defects [33–37]. In nature, ZnO can exist in three types of crystal structure: wurtzite, zinc-blend, and cubic rock salt [38, 39]. The stable zinc blend phase exists only when ZnO is grown over the cubic substrate [40]. The huge difference in the electronegativity values of Zn^{2+} (1.65) and O^{2-} ion (3.44) results in stronger ionic bonding between Zn and O [41].

The work in this chapter is presented in five sections. The first section represents the introduction. The second section presents the review of electrical characterization of ZnO. The third section explains the effect of temperature on 2DEG density and the Fermi energy level of

AlGaN/GaN and MgZnO/ZnO HEMT. The study of optical gain and internal electric field in AlGaN/GaN and MgZnO/ZnO quantum well structures is given in the fourth section. Finally, the fifth section presents the conclusions highlighting the scope of the present work.

---

2 Electrical Characterization of ZnO

Figure 1 illustrates the wurtzite crystal lattice structure of ZnO. Figure 2 shows the band diagram of Schottky contact for n and p-type semiconductors. The Fermi-level energy band diagram before contact and after contact between the heterojunction has been shown in Fig. 3. Lee et al. [42] performed a study on the electrical characteristics of MgZnO/ZnO. Figure 4 represents the transmission electron microscope (TEM) image of MgZnO/ZnO. Figure 5 represents the band structure of hexagonal ZnO.

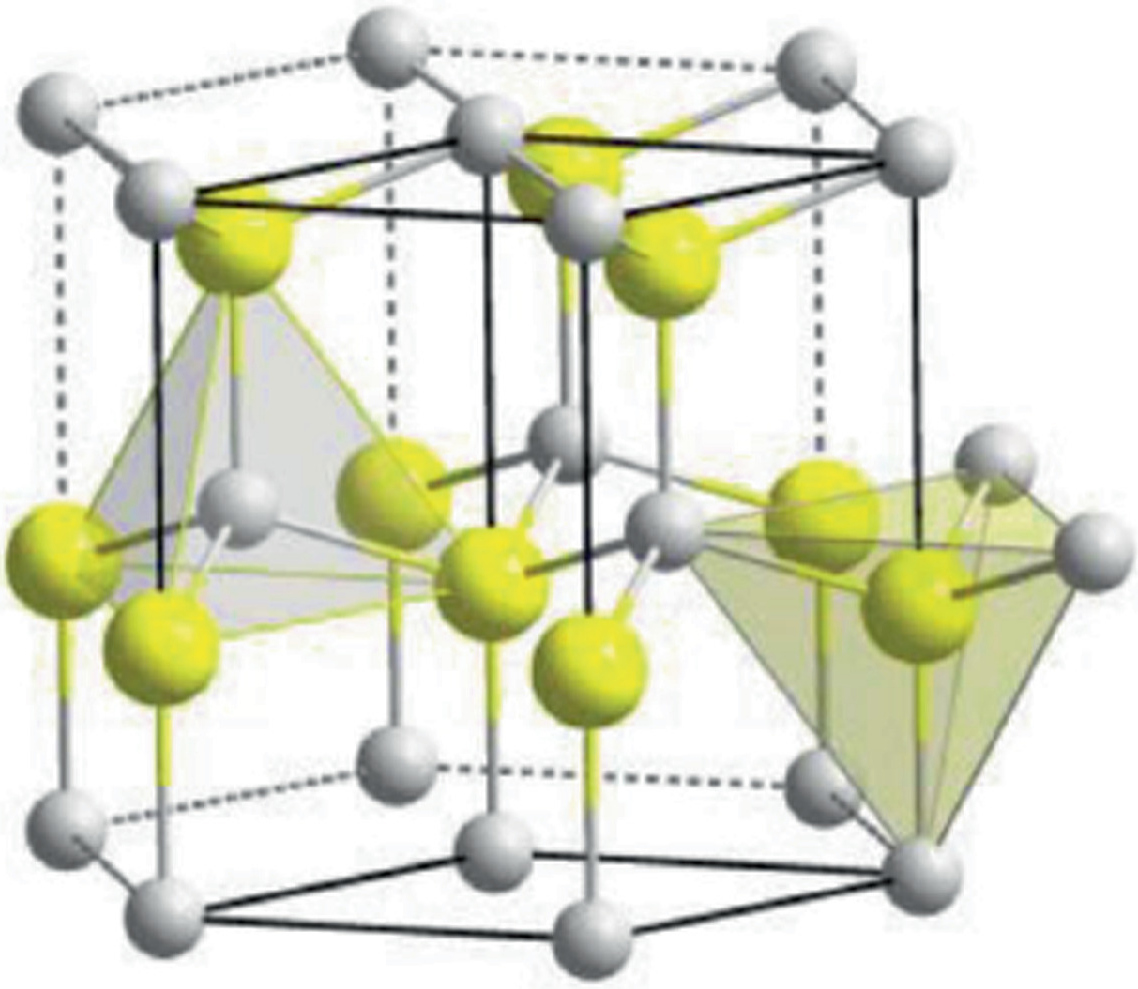

Fig. 1 Wurtzite crystal structure of ZnO (Zn––yellow spheres, O atoms––gray spheres); Ref. [24]

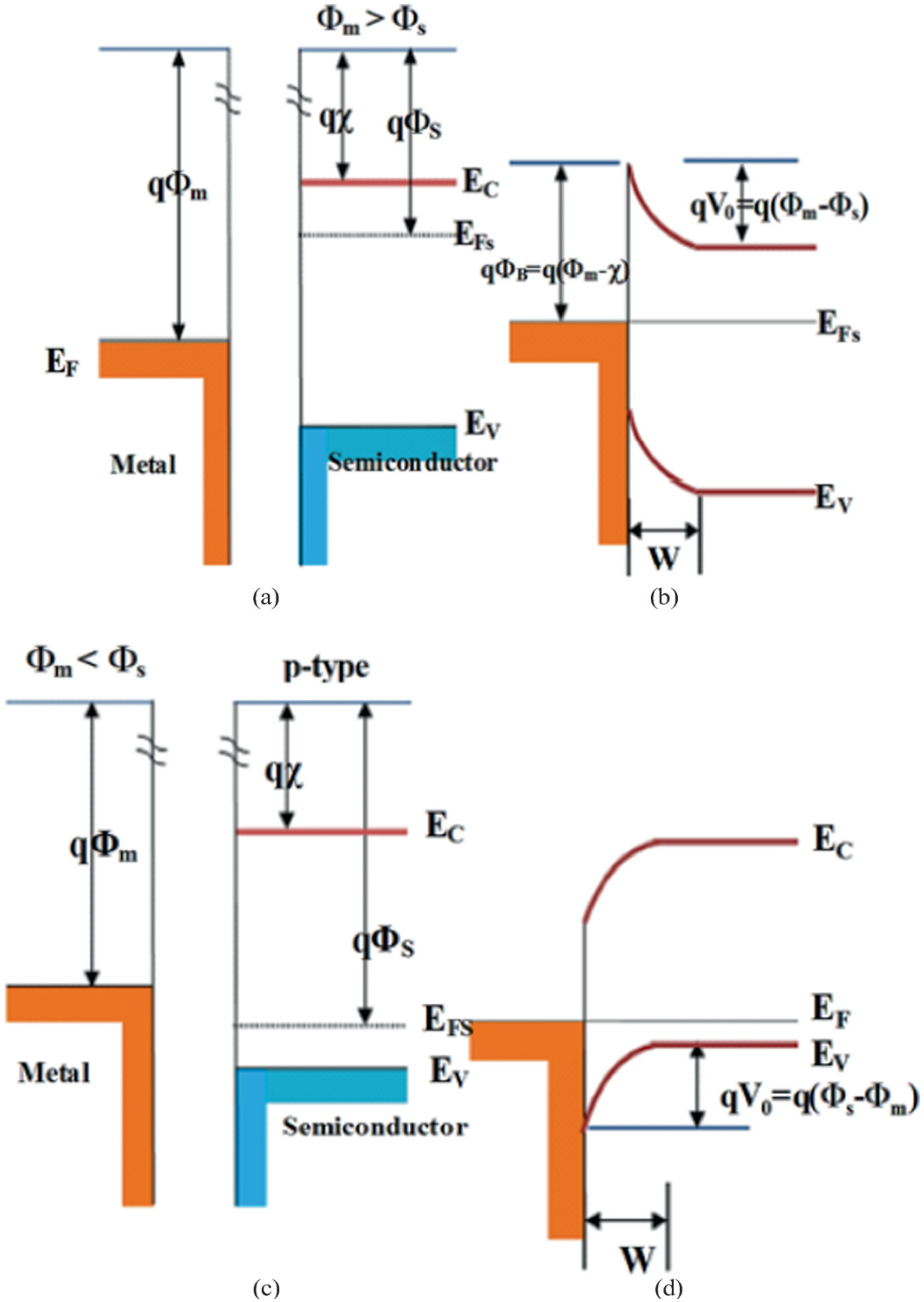
Φm > Φs
qχ
qΦS
qΦm
EC
EFs
EF
EV
Metal
Semiconductor
qV0=q(Φm-Φs)
qΦB=q(Φm-χ)
W
(a)
(b)
Φm < Φs
p-type
qχ
qΦm
EC
qΦS
EFS
EV
Metal
Semiconductor
EF
qV0=q(Φs-Φm)
W
(c)
(d)

Fig. 2 Schottky contact **a** n-type semiconductor and isolated metal, **b** metal/n-type semiconductor junction at equilibrium, **c** p-type semiconductor and isolated metal, **d** metal/p-type semiconductor junction at equilibrium; Ref. [43]

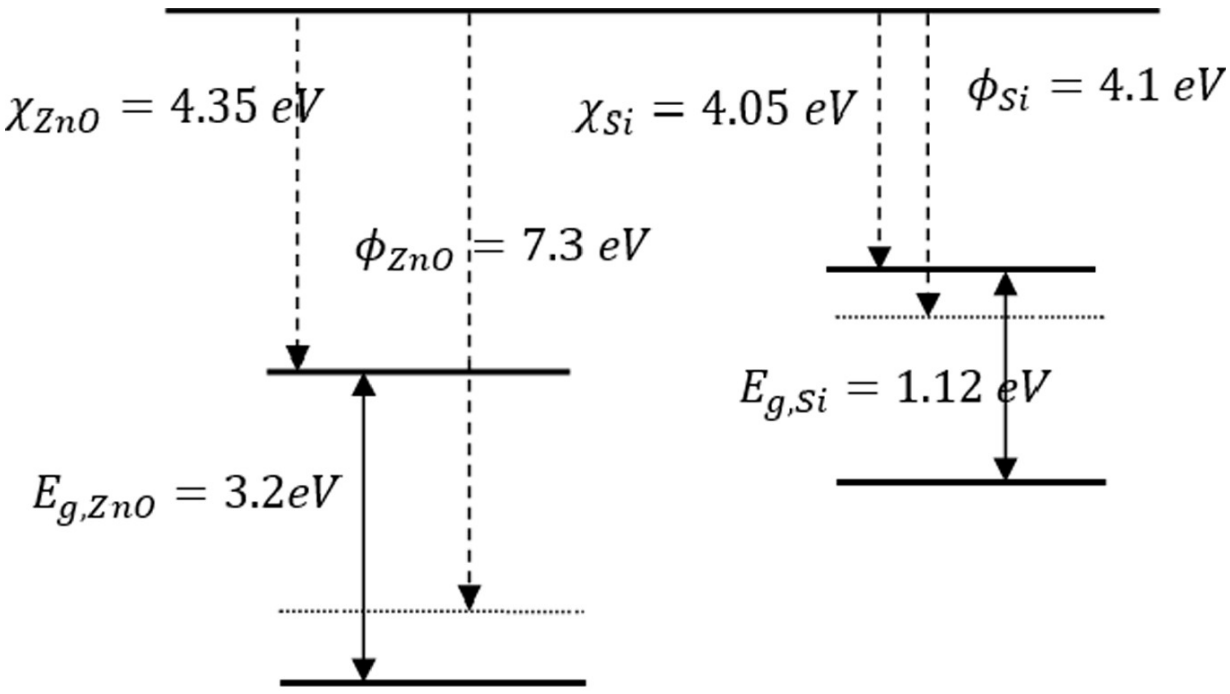

(a)

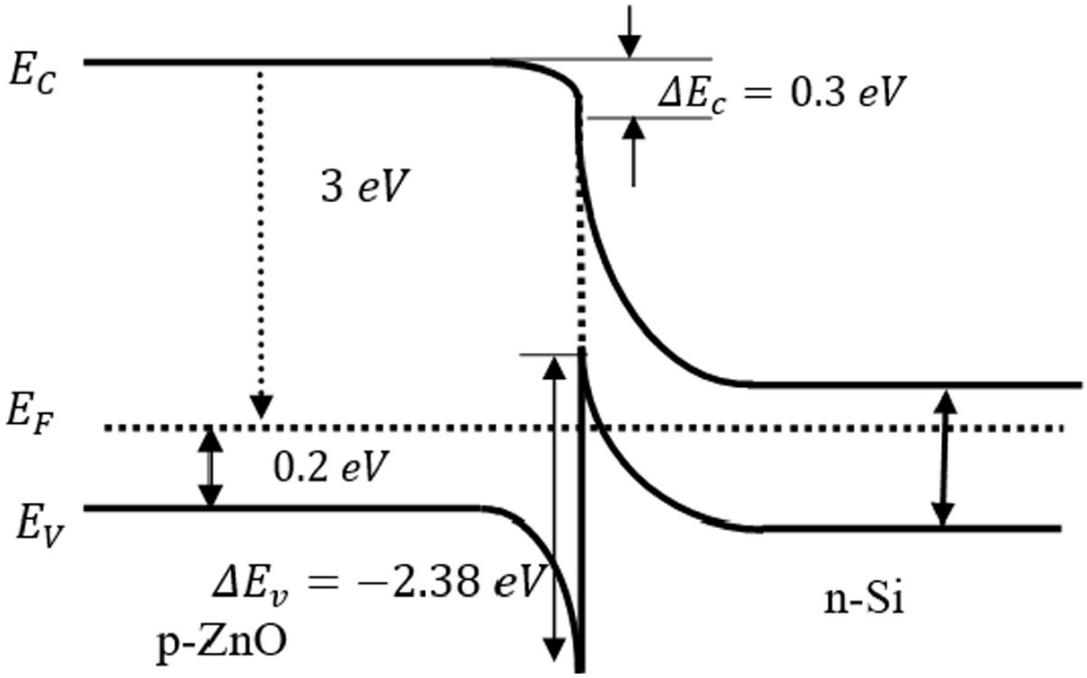

(b)

Fig. 3 Band diagram of the heterojunction **a** before contact, **b** after contact at equilibrium; Ref. [31]

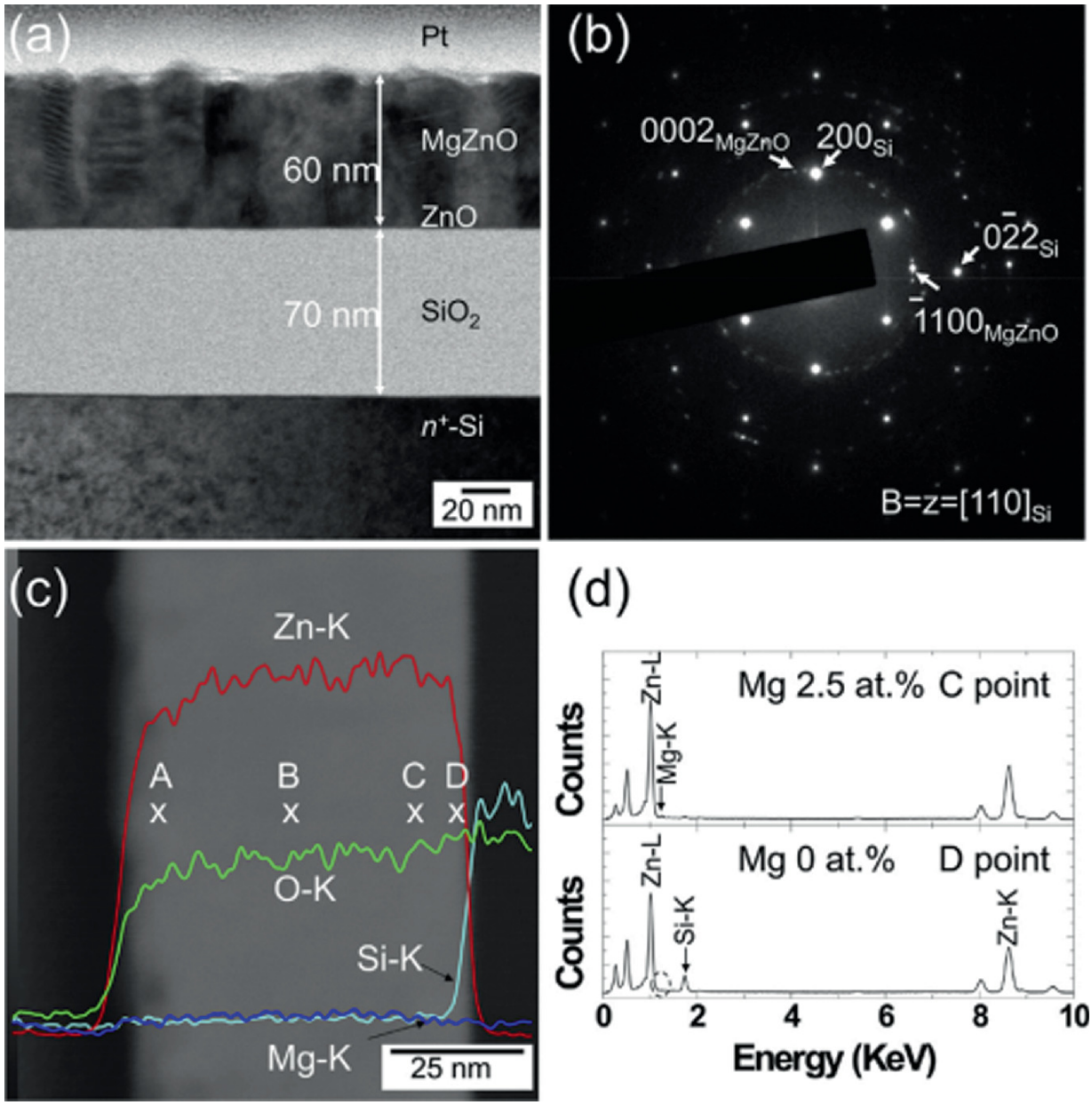

Fig. 4 **a** TEM image, **b** SAED pattern, **c** high-angle annular dark field TEM image and EDX-line scan, **d** EDX-spot spectrum of MgZnO/ZnO (12 nm); Ref. [42]

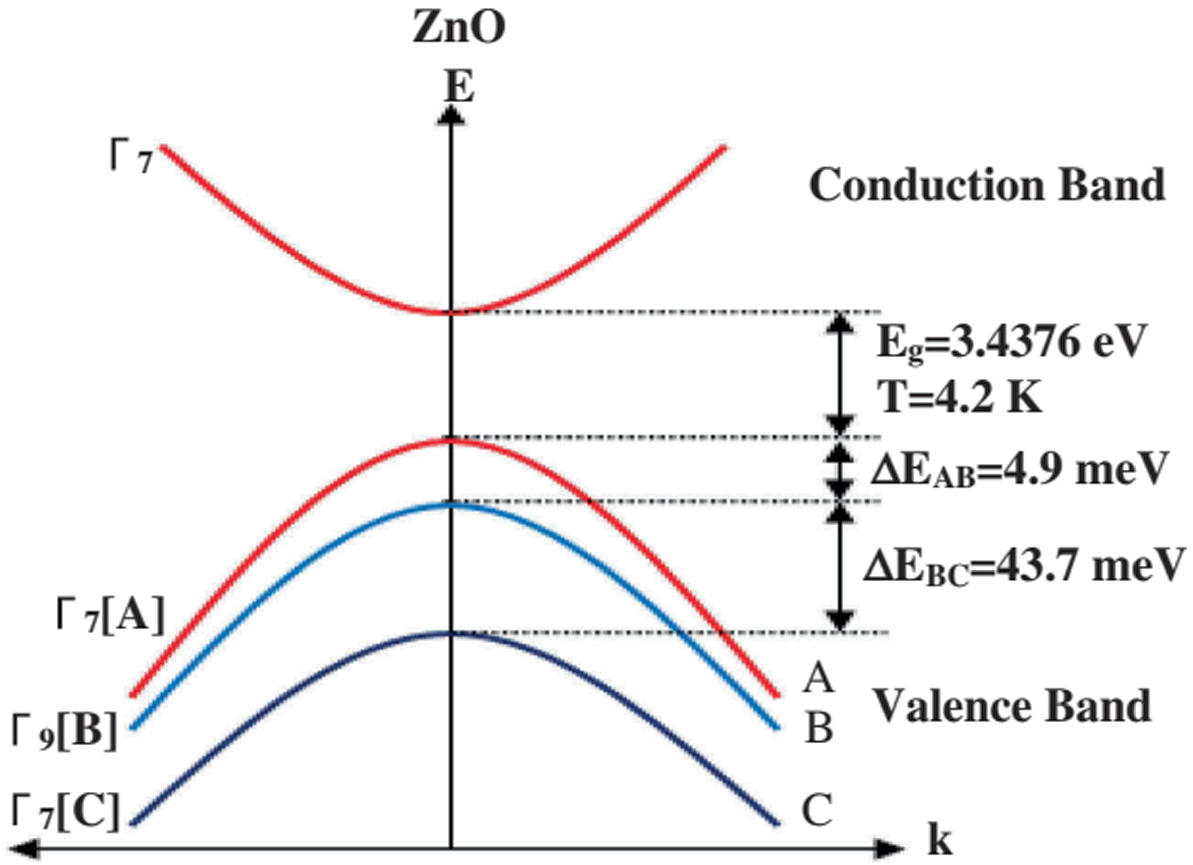

Fig. 5 Band structure of hexagonal ZnO; Ref. [44]

3 Effect of Temperature on 2DEG Density (n_S) and Fermi Energy Level (E_F) of AlGaN/GaN and MgZnO/ZnO HEMT

(a)

Effect of Temperature on 2DEG Density for AlGaN/GaN HEMT

Khan et al. [45] performed the analysis of the GaN/AlGaN heterostructure-based system and attributed the increased electron mobility in the 2DEG region. Shur et al. [46] calculated electron mobility for GaAs and GaN with respect to different values of temperature, as represented in Fig. 6.

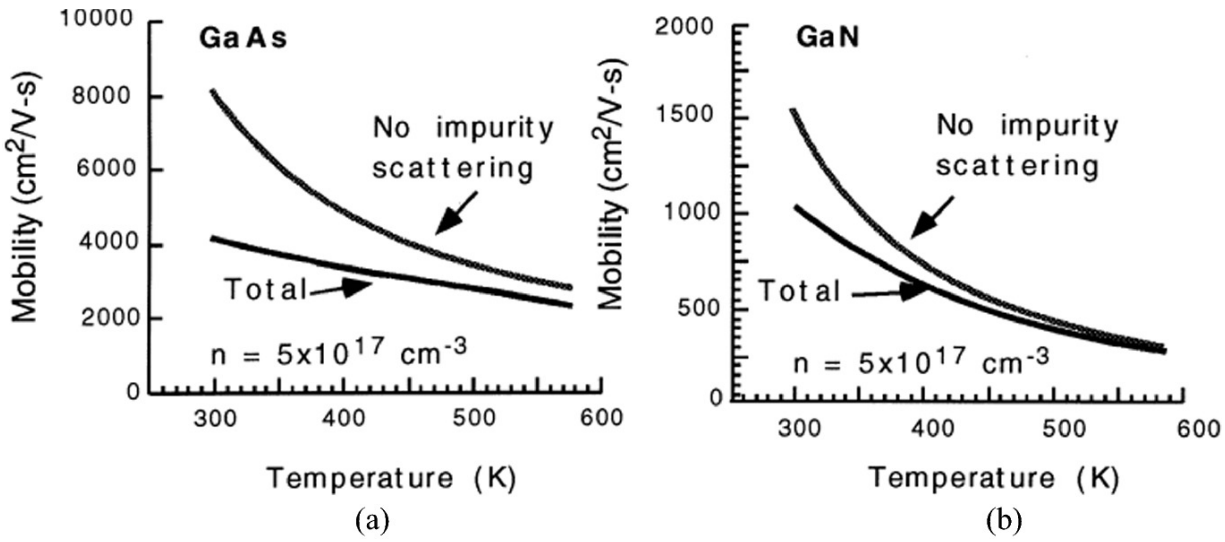

Fig. 6 Electron mobility with respect to Temperature (*K*) with and without accounting for impurity scattering [46]. **a** GaAs. **b** GaN

Khan et al. [47] fabricated AlGaN HFET and calculated its different performance parameters. Khan et al. [48] reported the DC characteristics and microwave performance of AlGaN/GaN HFET in the temperature range from 25 to 300 °C. Redwing et al. [49] fabricated high-quality $Al_{0.15}Ga_{0.85}$ N/GaN heterostructures on 6H-SiC and Sapphire substrates by metal–organic vapor phase epitaxy (MOVPE). Redwing et al. [49] confirmed the presence of 2DEG. Binari et al. [50] described the fabrication of 1 μm gate length AlGaN/GaN HEMT grown on SiC substrate and calculated transconductance, gate breakdown voltage, and pinch-off voltage [46]. Tan et al. [51] and Daumiller et al. [52] demonstrated in Fig. 7 that the 2DEG density remains relatively unchanged from 25 to 250 °C. Smorchkova et al. [53] revealed that 2DEG density is almost constant at low temperatures, however, it increases with an increase in temperature (i.e., at high temperature). Arulkumaran et al. [54] revealed that the 2DEG mobility and electron velocity decreases with increase in temperature. It is also revealed using Fig. 8 that 2DEG density increases with temperature (i.e., at high temperature).

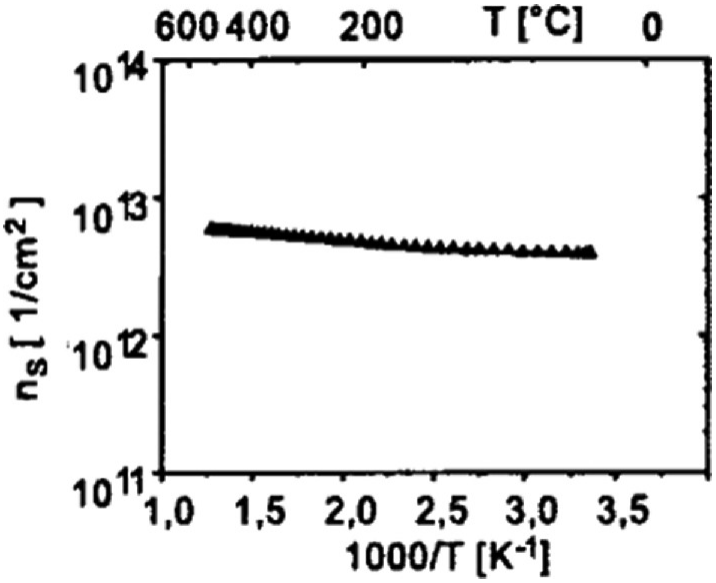

Fig. 7 Effect of temperature on 2DEG density; Ref. [52]

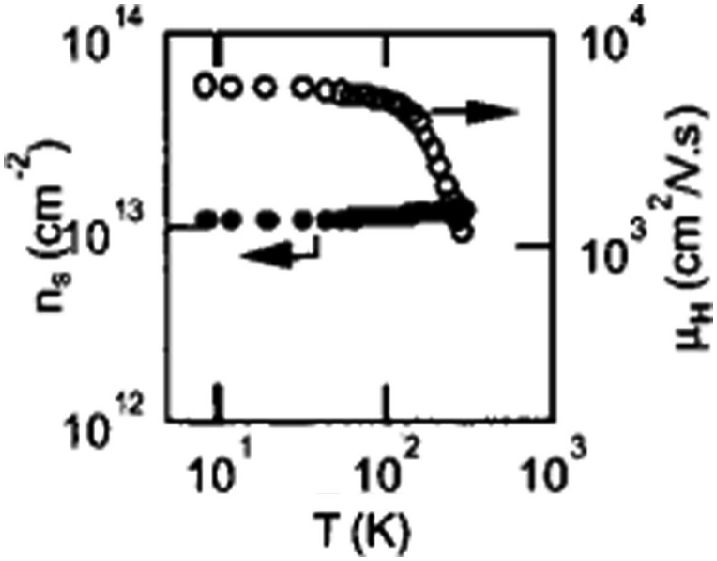

Fig. 8 Effect of temperature on 2DEG density; Ref. [54]

Maeda et al. [55] calculated the electron occupation ratio with respect to temperature, followed by the Fermi distribution function to account for the effect of temperature as represented in Fig. 9.

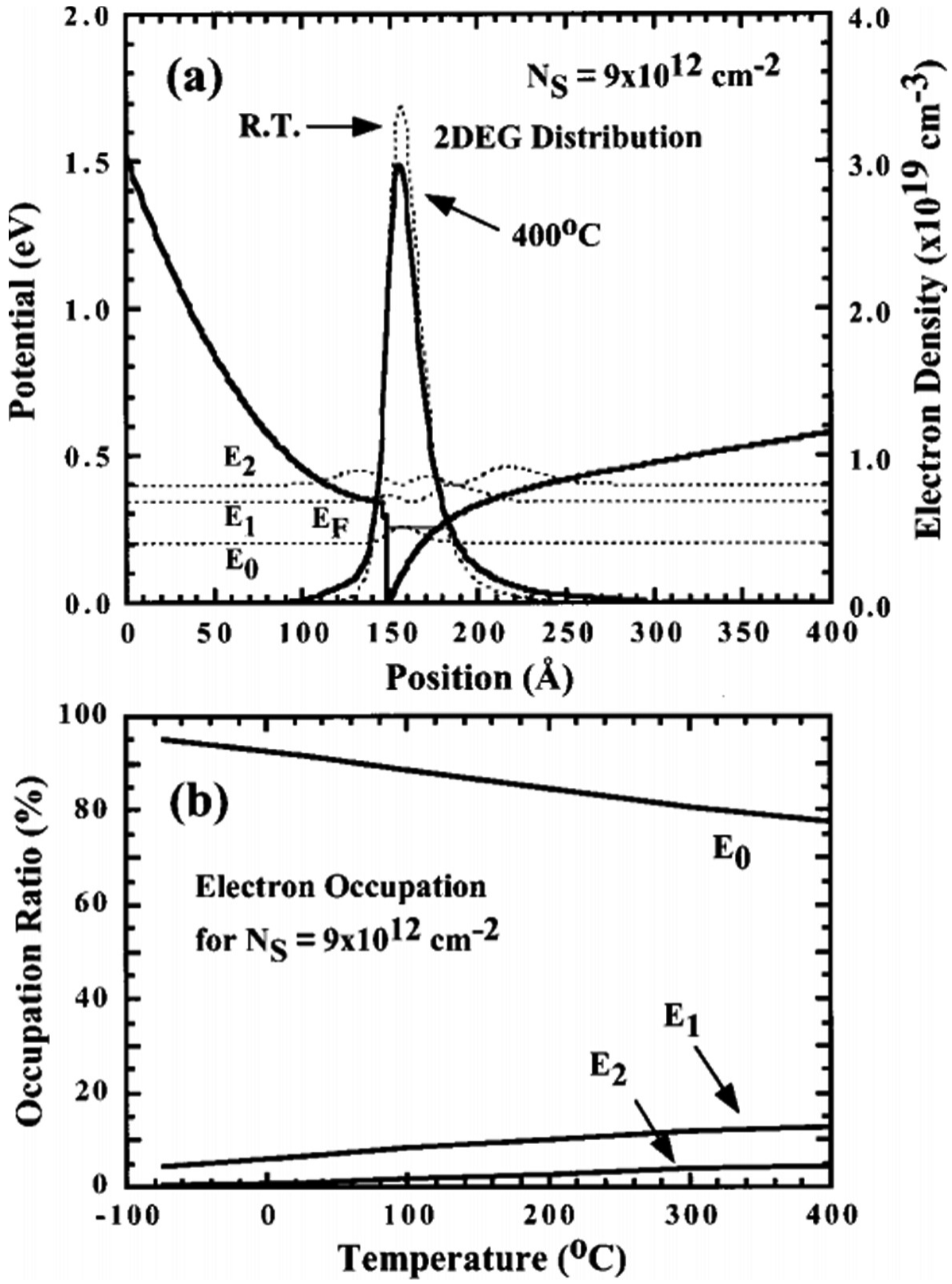

Fig. 9 **a** Potential and electron density with respect to position, **b** occupation ratio with respect to temperature; Ref. [55]

(b)

Effect of Temperature on Fermi Energy Level for AlGaN/GaN HEMT

Shur et al. [46] calculated the 2DEG density at the AlGaN/GaN heterointerface. Wu et al. [56] proposed the use of a high Al-content in the AlGaN/GaN MODFET structure for better device performance. Zhang et al. [57] developed a charge control model and a mobility model for AlGaN/GaN HEMT. Agrawal et al. [58] developed a model of AlGaN/GaN MODFET and reported the superiority of GaN-based devices over AlGaAs devices. Wu et al. [59] reported better electrical performance of GaN HEMTs over GaAs, similar to [60]. In addition to it, AlGaN/GaN HFET does not require modulation doping which is mandatory in AlGaAs/GaAs HFET to create 2DEG at the heterointerface [61]. Wu et al. [62] calculated the effect of temperature on E_F for AlGaN/GaN HEMT and revealed its magnitude as 0.092 eV and 0.052 eV at 300 K and 500 K, respectively, at a 2DEG concentration of 1.8×10^{12} cm^{-2}. Accordingly, E_F reduces with an increase in temperature for AlGaN/GaN HFET. Figure 10 represents the calculation of E_F as a function of n_s for different temperatures, as revealed by Wu et al. [62].

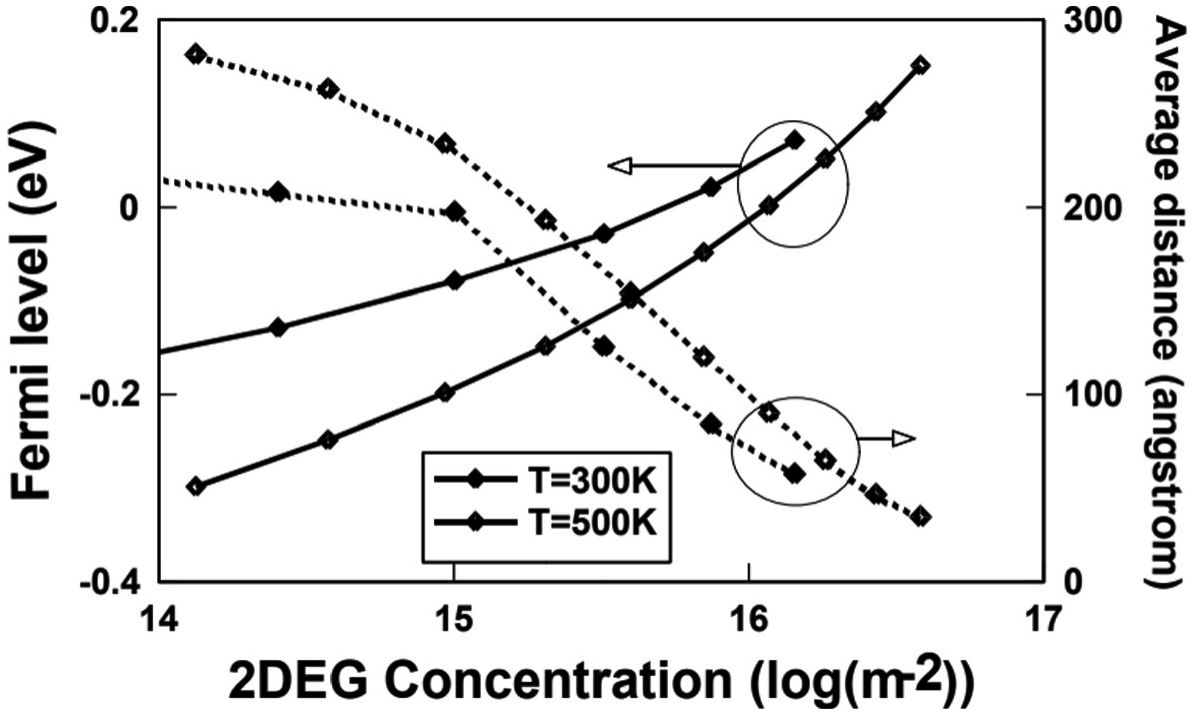

Fig. 10 E_F as a function of n_S for different temperatures, Ref. [62]

(c) Effect of Temperature on 2DEG Density for MgZnO/ZnO HEMT

The II–VI group oxide semiconductor ZnO possesses several merits over GaN including higher exciton binding energy (60 meV for ZnO and 21–25 meV for GaN) and a wide energy bandgap (3.37 eV for ZnO and 3.36 eV for ZnO) [63]. Edahiro et al. [64] revealed the formation of 2DEG at the heterointerface of zinc–magnesium oxide (ZnMnO) and zinc–oxide (ZnO). Koike et al. [65] revealed the formation of 2DEG density in $ZnO/Zn_{0.6}Mg_{0.4}$. Koike et al. [66] performed the characterization of a $Zn_{0.7}Mg_{0.3}O/ZnO$ HFET and examined the I–V characteristics. Tampo et al. [67] revealed the formation of 2DEG density at the heterointerface of Zn polar MgZnO/ZnO. Nause et al. [63] analyzed the electrical performance of MgZnO/ZnO HEMT. Tampo et al. [68] revealed the importance of determining and controlling the Mg composition in ZnMgO.

Tampo et al. [70] investigated the electrical properties of 2DEG for ZnMgO/ZnO heterostructure and revealed that the origin of 2DEG is the surface of the ZnMgO layer. Brandt et al. [71] compared the properties of ZnO/MgZnO heterostructures. Brandt revealed the formation of 2DEG in these heterostructures by temperature-dependent Hall effect measurements. Chin et al. [72] computed the 2DEG density with respect to different thicknesses of MgZnO. Tampo et al. [69] revealed in Fig. 11 that n_s remains almost constant for different values of temperature. Similarly, Chin et al. [72] reported almost constant sheet carrier concentration with respect to temperature using Fig. 12.

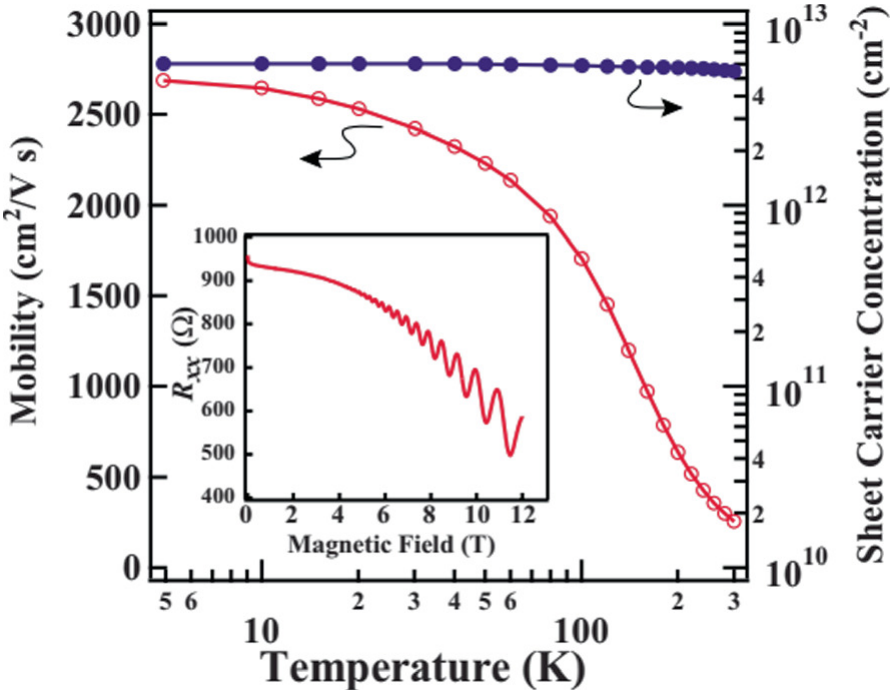

Fig. 11 Temperature-dependent Hall measurement for ZnMgO/ZnO heterostructure, Ref. [69]

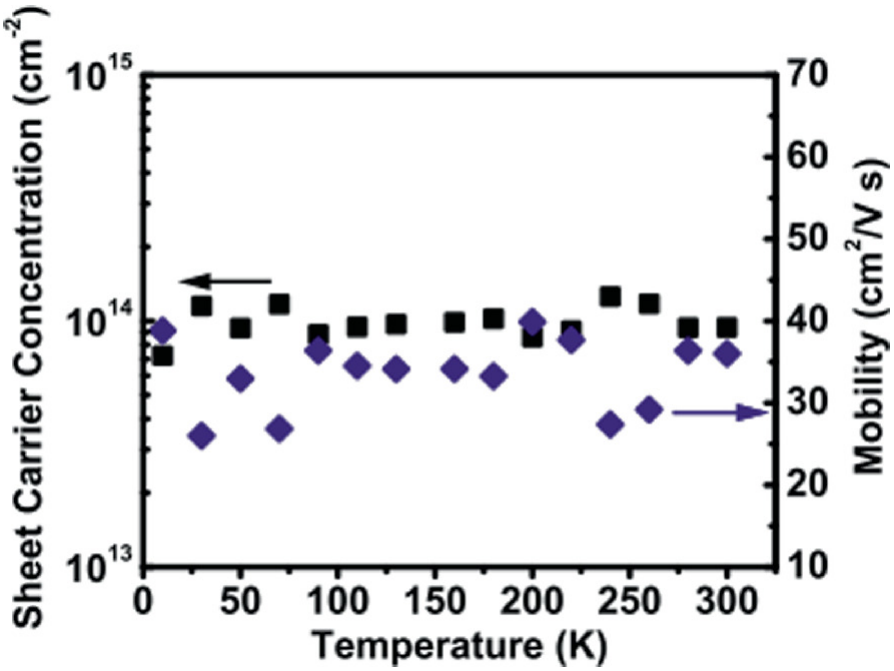

Fig. 12 Hall mobility and n_S of MgZnO/ZnO heterostructure; Ref. [72]

(d)

Effect of Temperature on Fermi Energy Level for MgZnO/ZnO HEMT

Ye et al. [69] analyzed the performance of ZnMgO/ZnO interface. Sasa et al. [73] reported the microwave performance of ZnO/ZnMgO HFET having a 15-nm-thick ZnO channel layer and 1–2 μm gate length. He et al. [74] analyzed the effect of temperature on Fermi energy level (E_F) for MgZnO/ZnO heterostructure using Fig. 13. He et al. [74] revealed that at a certain bias, E_F diminishes with the increase of the temperature.

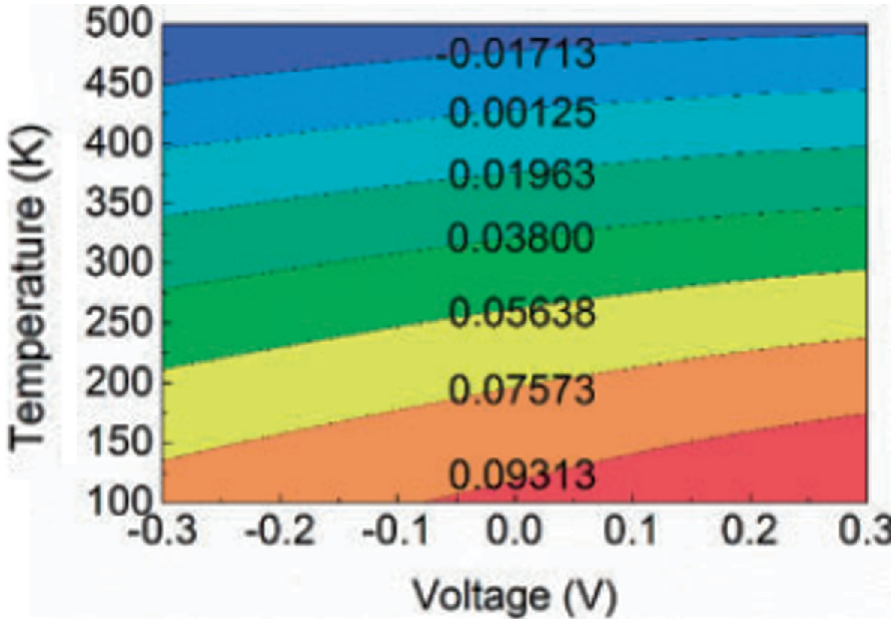

Fig. 13 Contour map of the E_F with respect to the bias voltage and temperature, Ref. [74]

4 Optical Gain and Internal Electric Field in AlGaN/GaN and MgZnO/ZnO Quantum Well

Jang et al. [75] performed Ab-initio calculations to predict different properties of wurtzite–MgO and wurtzite–MgZnO alloy; and predicted that the Vegard's law is not followed in $Mg_xZn_{1-x}O$ alloy to determine elastic stiffness constant C_{33}. S.-H. Jang calculated the ground-state properties for both wurtzite–ZnO and Wurtzite–MgO pseudopotential-plane wave method. Park et al. [76] calculated optical gain for MgZnO/ZnO and AlGaN/GaN and revealed that MgZnO/ZnO quantum well has a larger optical gain than the identical AlGaN/GaN, as evident from Fig. 14. Park et al. [76] revealed that the optical gain of

MgZnO/ZnO is larger due to negligible internal field in these quantum well structures, as evident from Fig. 15.

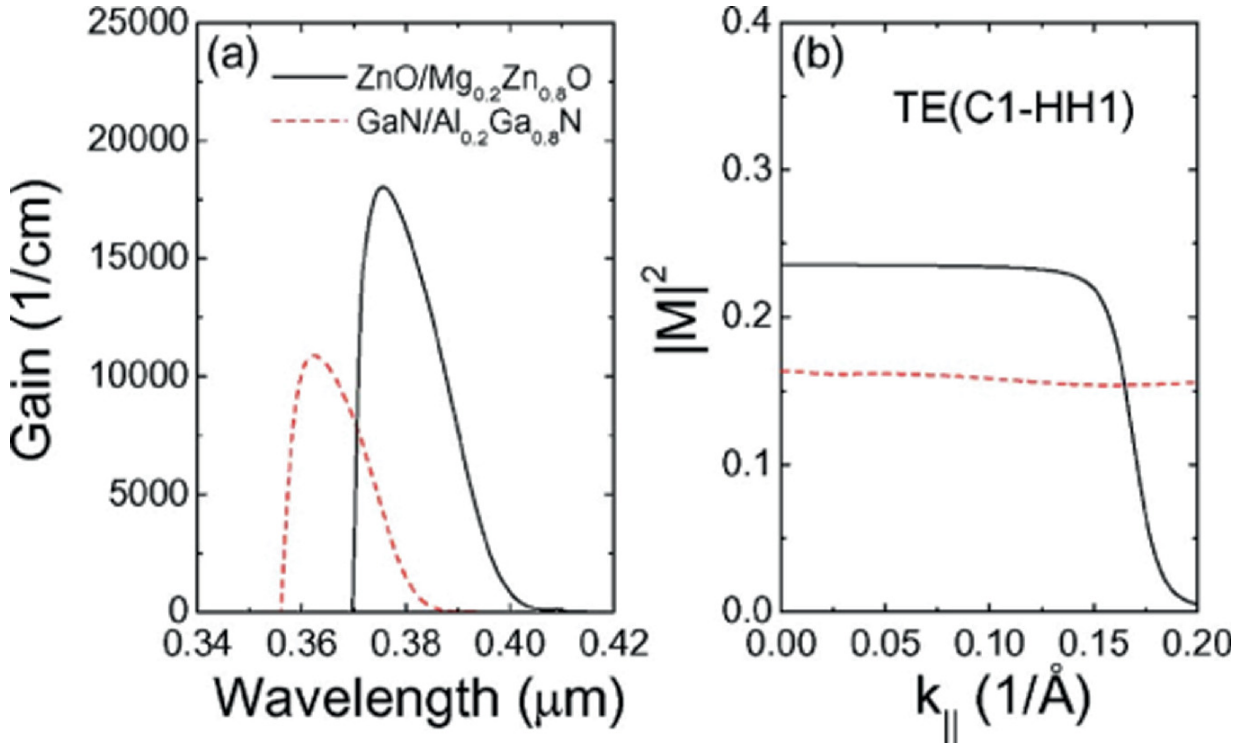

Fig. 14 **a** Optical gain, **b** optical matrix elements; Ref. [76]

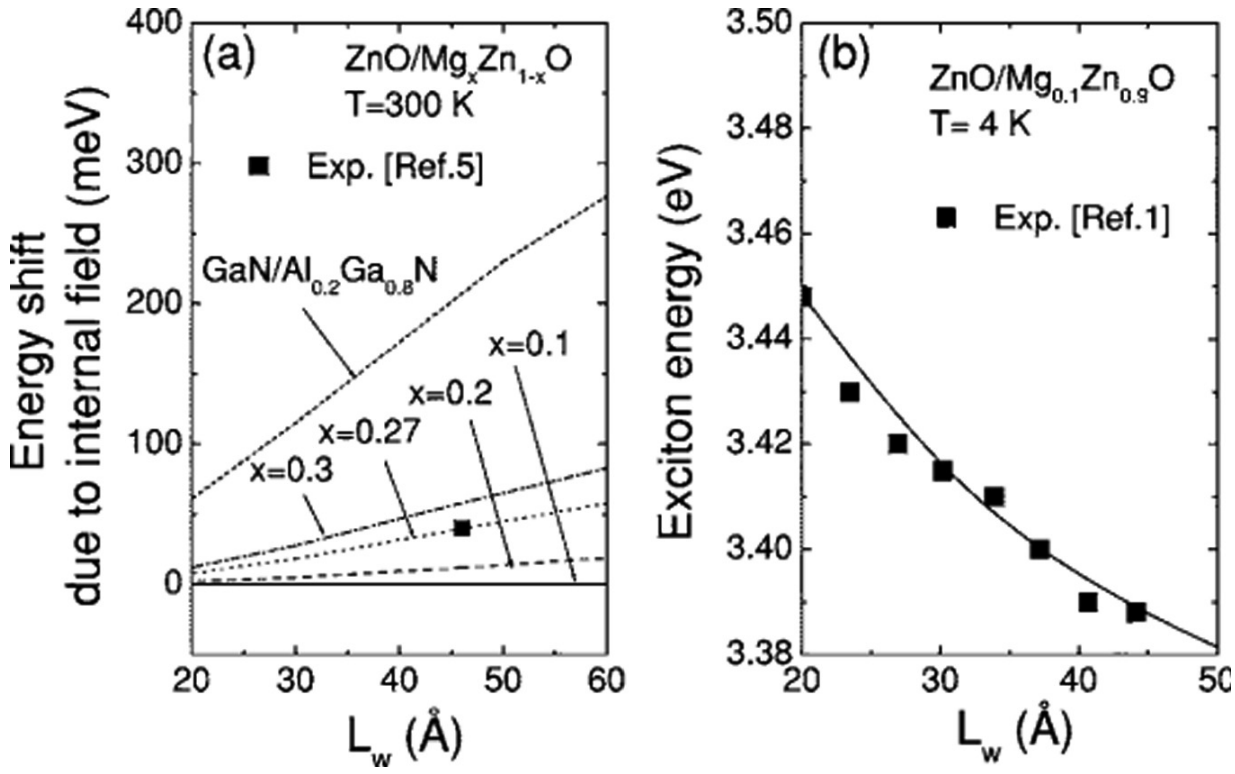

Fig. 15 **a** Energy shift due to internal field, **b** exciton energy; Ref. [76]

5 Conclusion

It is worth noting that for AlGaN/GaN HEMT 2DEG mobility and electron velocity decrease with an increase in temperature. The 2DEG density remains relatively unchanged at low temperatures; however, at high temperatures, it increases with an increase in temperature. On the other hand, the 2DEG density is found almost constant with respect to temperature for MgZnO/ZnO HEMT. It has also been noticed that the Fermi energy level reduces with an increase in temperature for AlGaN/GaN HEMT. Similarly, the Fermi energy level diminishes with the increase of the temperature in MgZnO/ZnO HEMT. Further, the optical gain of MgZnO/ZnO is noticed to be larger than AlGaN/GaN due to the larger internal electric field in AlGaN/GaN.

References

1. T. Mimura, S. Hiyamizu, T. Fujii, K. Nanbu, A new field-effect transistor with selectively doped GaAs/n–Al$_x$Ga$_{1-x}$As heterojunctions. Jpn. J. Appl. Phys. **19**(5), L225 (1980)

2. Y.-F. Wu et al., Very high breakdown voltage and large transconductance realized on GaN heterojunction field effect transistors. Appl. Phys. Lett. **69**(10), 1438–1440 (1996)

3. M.A. Khan et al., AlGaN/GaN metal oxide semiconductor heterostructure field effect transistor. IEEE Electron Device Lett. **21**(2), 63–65 (2000)

4. P.M. Solomon, H. Morkoc, Modulation-doped GaAs/AlGaAs heterojunction field-effect transistors (MODFET's), ultrahigh-speed device for supercomputers. IEEE Trans. Electron Devices **31**(8), 1015–1027 (1984)

5. K. Lee, M.S. Shur, T.J. Drummond, H. Morkoc, Parasitic MESFET in (Al, Ga) As/GaAs modulation doped FET's and MODFET characterization. IEEE Trans. Electron Devices **31**(1), 29–35 (1984)

6. H. Morkoc, P.M. Solomon, The hemt: A superfast transistor: an experimental GaAs–AlGaAs device switches in picoseconds and generates little heat. This is just what supercomputers need. IEEE Spectr. **21**(2), 28–35 (1984)

7. R.L. Anderson, Germanium-gallium arsenide heterojunctions. IBM J. Res. Dev. **4**(3), 283–287 (1960)

8. L. Esaki, R. Tsu, Superlattice and negative conductivity in semiconductors. IBM Res. Note RC **2418** (1969)

9. R. Dingle, H.L. Störmer, A.C. Gossard, W. Wiegmann, Electron mobilities in modulation-doped semiconductor heterojunction superlattices. Appl. Phys. Lett. **33**(7), 665–667 (1978)

10. S. Hiyamizu, T. Mimura, T. Fujii, K. Nanb, High mobility of two-dimensional electrons at the GaAs/n-AlGaAs heterojunction interface. Appl. Phys. Lett. **37**(9), 805–807 (1980)

11. L.C. Witkowski, T.J. Drummond, C.M. Stanchak, H. Morkoc, High mobilities in $Al_xGa_{1-x}As$–GaAs heterojuntions. Appl. Phys. Lett. **37**(11), 1033–1035 (1980)

12. W.I. Wang, C.E.C. Wood, L.F. Eastman, Extremely high electron mobilities in modulation-doped GaAs–$Al_xGa_{1-x}As$ heterojunction superlattices. Electron. Lett. **17**(1), 36–37 (1981)

13. D. Delagebeaudeuf, N.T. Linh, Metal-(n) AlGaAs–GaAs two-dimensional electron gas FET. IEEE Trans. Electron Devices **29**(6), 955–960 (1982)

14. T.J. Drummond, H. Morkoç, K. Lee, M. Shur, Model for modulation doped field effect transistor. IEEE Electron Device Lett. **3**(11), 338–341 (1982)

15. K. Lee, M.S. Shur, T.J. Drummond, H. Morkoc, Current-voltage and capacitance-Voltage characteristics of modulation-doped field-effect transistors. IEEE Trans. Electron Devices **30**(3), 207–212 (1983)

16. M.H. Weiler, Y. Ayasli, DC and microwave modeis for $AI_xGa_{1-x}As$/GaAs high electron mobility transistors. IEEE Trans. Electron Devices **31**(12), 1854–1861 (1984)

17. L.P. Sadwick, K.L. Wang, A treatise on the capacitance voltage relation of high electron mobility transistors. IEEE Trans. Electron Devices **33**(5), 651–656 (1986)

18. M.L. Majewski, An analytical DC model for the modulation-doped field-effect transistor. IEEE Trans. Electron Devices **34**(9), 1902–1910 (1987)

19. G. Salmer, J. Zimmermann, R. Fauquembergue, Modeling of MODFETs. IEEE Trans. Microw. Theory Tech. **36**(7), 1124–1140 (1988)

20. A.J. Shey, W.H. Ku, On the charge control of the two-dimensional electron gas for analytic modeling of HEMT's. IEEE Electron Device Lett. **9**(12), 624–626 (1988)

21. A.-J. Shey, W.H. Ku, An analytical current-voltage characteristics model for high electron mobility transistors based on nonlinear charge-control formulation. IEEE Trans. Electron Devices **36**(10), 2299–2306 (1989)

22. S.S. Shinde, P.S. Shinde, C.H. Bhosale, K.Y. Rajpure, Optoelectronic properties of sprayed transparent and conducting indium doped zinc oxide thin films. J. Phys. D. Appl. Phys. **41**(10) (2008)

23. Y.K. Verma, V. Mishra, S.K. Gupta, A physics based analytical model for MgZnO/ZnO HEMT. J. Circ. Syst. Comput. **29**(1), 2050009-1 (2020)

24. Ü. Özgür et al., A comprehensive review of ZnO materials and devices. J. Appl. Phys. **98**(4), 11 (2005)

25. P. Wang et al., Monte Carlo investigation of high-field electron transport characteristics in ZnMgO/ZnO heterostructures. IEEE Trans. Electron Devices **63**(1), 517–523 (2016)

26. Y.K. Verma, V. Mishra, P.K. Verma, S.K. Gupta, Analytical modelling and electrical characterisation of ZnO based HEMTs. Int. J. Electron. **106**(5), 707–720 (2019)

27. M. Rouchdi, E. Salmani, B. Fares, N. Hassanain, A. Mzerd, Synthesis and characteristics of Mg doped ZnO thin films: experimental and ab-initio study. Results Phys. **7**, 620–627 (2017)

28. M. Caglar, Y. Caglar, S. Ilican, Investigation of the effect of Mg doping for improvements of optical and electrical properties. Phys. B Condens. Matter **485**, 6–13 (2016)

29. S.S. Shinde, A.P. Korade, C.H. Bhosale, K.Y. Rajpure, Influence of tin doping onto structural, morphological, optoelectronic and impedance properties of sprayed ZnO thin films. J. Alloys Compd. **551**, 688–693 (2013)

30. S.S. Shinde, C.H. Bhosale, K.Y. Rajpure, Size dependent electron-phonon coupling in N, Li, In, Ga, F and Ag doped ZnO thin films. Spectrochim. Acta Part A Mol. Biomol. Spectrosc. **98**, 453–456 (2012)

31. L. Agarwal, B.K. Singh, S. Tripathi, P. Chakrabarti, Fabrication and characterization of Pd/cu doped ZnO/Si and Ni/cu doped ZnO/Si Schottky diodes. Thin Solid Films **612**, 259–266 (2016)

32. B.K. Singh, S. Tripathi, pn homojunction based on Bi doped p-type ZnO and undoped n-type ZnO for optoelectronic application in yellow–red region of visible spectrum. J. Lumin. **198**, 427–432 (2018)

33. Z.R. Dai, Z.W. Pan, Z.L. Wang, Novel nanostructures of functional oxides synthesized by

thermal evaporation. Adv. Funct. Mater. **13**(1), 9–24 (2003)

34. Y.K. Verma, V. Mishra, S.K. Gupta, Analog/RF and linearity distortion analysis of MgZnO/CdZnO quadruple-gate field effect transistor (QG-FET). Silicon, 1–17 (2020). https://doi.org/10.1007/s12633-020-00406-4

35. J.H. Campbell et al., NIF optical materials and fabrication technologies: an overview, in *Optical Engineering at the Lawrence Livermore National Laboratory II: The National Ignition Facility*, vol. 5341 (2004), pp. 84–101

36. S.S. Shinde, P.S. Shinde, S.M. Pawar, A.V. Moholkar, C.H. Bhosale, K.Y. Rajpure, Physical properties of transparent and conducting sprayed fluorine doped zinc oxide thin films. Solid State Sci. **10**(9), 1209–1214 (2008)

37. M.A. Khan et al., Enhanced sheet charge density in DIBS grown CdO alloyed ZnO buffer based heterostructure. IEEE Electron Device Lett. **39**(6), 827–830 (2018)

38. F. Benharrats, K. Zitouni, A. Kadri, B. Gil, Determination of piezoelectric and spontaneous polarization fields in $Cd_xZn_{1-x}O$/ZnO quantum wells grown along the polar 〈0001〉 direction. Superlattices Microstruct. **47**(5), 592–596 (2010)

39. A. Ashrafi, C. Jagadish, Review of zincblende ZnO: stability of metastable ZnO phases. J. Appl. Phys. **102**(7), 4 (2007)

40. V. Bilgin, S. Kose, F. Atay, I. Akyuz, The effect of substrate temperature on the structural and some physical properties of ultrasonically sprayed CdS films. Mater. Chem. Phys. **94**(1), 103–108 (2005)

41. K. Li, D. Xue, Estimation of electronegativity values of elements in different valence states. J. Phys. Chem. A **110**(39), 11332–11337 (2006)

42. J.H. Lee et al., A study of electrical enhancement of polycrystalline MgZnO/ZnO bi-layer thin film transistors dependence on the thickness of ZnO layer. Curr. Appl. Phys. **15**(9), 1010–1014 (2015)

43. B.K. Singh, S. Tripathi, Fabrication and characterization of Au/p-ZnO Schottky contacts. Superlattices Microstruct. **85**, 697–706 (2015)

44. B.K. Meyer et al., Bound exciton and donor-acceptor pair recombinations in ZnO. Phys. Status Solidi Basic Res. (2004). https://doi.org/10.1002/pssb.200301962 [Crossref]

45. M.A. Khan, J.M. Van Hove, J.N. Kuznia, D.T. Olson, High electron mobility GaN/$Al_xGa_{1-x}N$ heterostructures grown by low-pressure metalorganic chemical vapor deposition. Appl. Phys. Lett. **58**(21), 2408–2410 (1991)

46. M.S. Shur, GaN based transistors for high power applications. Solid. State. Electron. **42**(12), 2131–2138 (1998)

47. M.A. Khan, J.N. Kuznia, D.T. Olson, W.J. Schaff, J.W. Burm, M.S. Shur, Microwave performance of a 0.25 μm gate AlGaN/GaN heterostructure field effect transistor. Appl. Phys. Lett. **65**(9),

1121–1123 (1994)

48. M.A. Khan, M.S. Shur, J.N. Kuznia, Q. Chen, J. Burm, W. Schaff, Temperature activated conductance in GaN/AlGaN heterostructure field effect transistors operating at temperatures up to 300 °C. Appl. Phys. Lett. **66**(9), 1083–1085 (1995)

49. J.M. Redwing et al., Two-dimensional electron gas properties of AlGaN/GaN heterostructures grown on 6H–SiC and sapphire substrates. Appl. Phys. Lett. **69**(7), 963–965 (1996)

50. S.C. Binari, J.M. Redwing, G. Kelner, W. Kruppa, AlGaN/GaN HEMTs grown on SiC substrates. Electron. Lett. **33**(3), 242–243 (1997)

51. W.S. Tan, M.J. Uren, P.W. Fry, P.A. Houston, R.S. Balmer, T. Martin, High temperature performance of AlGaN/GaN HEMTs on Si substrates. Solid. State. Electron. **50**(3), 511–513 (2006)

52. I. Daumiller, C. Kirchner, M. Kamp, K.J. Ebeling, E. Kohn, Evaluation of the temperature stability of AlGaN/GaN heterostructure FETs. IEEE Electron Device Lett. **20**(9), 448–450 (1999)

53. I.P. Smorchkova et al., Polarization-induced charge and electron mobility in AlGaN/GaN heterostructures grown by plasma-assisted molecular-beam epitaxy. J. Appl. Phys. **86**(8), 4520–4526 (1999)

54. S. Arulkumaran, T. Egawa, H. Ishikawa, T. Jimbo, High-temperature effects of AlGaN/GaN high-electron-mobility transistors on sapphire and semi-insulating SiC substrates. Appl. Phys. Lett. **80**(12), 2186–2188 (2002)

55. N. Maeda, K. Tsubaki, T. Saitoh, N. Kobayashi, High-temperature electron transport properties in AlGaN/GaN heterostructures. Appl. Phys. Lett. **79**(11), 1634–1636 (2001)

56. Y.-F. Wu et al., High Al-content AlGaN/GaN MODFETs for ultrahigh performance. IEEE Electron Device Lett. **19**(2), 50–53 (1998)

57. Y. Zhang, J. Singh, Charge control and mobility studies for an AlGaN/GaN high electron mobility transistor. J. Appl. Phys. **85**(1), 587–594 (1999)

58. A. Agrawal, S. Sen, S. Haldar, R.S. Gupta, Analytical model for dc characteristics and small-signal parameters of AIGaN/GaN modulation-doped field-effect transistor for microwave circuit applications. Microw. Opt. Technol. Lett. **27**(6), 413–419 (2000)

59. Y.-F. Wu, D. Kapolnek, J.P. Ibbetson, P. Parikh, B.P. Keller, U.K. Mishra, Very-high power density AlGaN/GaN HEMTs. IEEE Trans. Electron Devices **48**(3), 586–590 (2001)

60. A. Kranti, S. Haldar, R.S. Gupta, An accurate charge control model for spontaneous and piezoelectric polarization dependent two-dimensional electron gas sheet charge density of lattice-mismatched AlGaN/GaN HEMTs. Solid State Electron. **46**, 621–630 (2002)

61. F.A. Marino, P. Menegoli, High performance multigate transistor. Google Patents (2015)

62. S. Wu, R.T. Webster, A.F.M. Anwar, Physics-based intrinsic model for AlGaN/GaN HEMTs. Mater. Res. Soc. Internet J. Nitride Semicond. Res. **4**, 775–780 (1999)

63.

J. Nause, S. Ganesan, High-electron mobility transistor with zinc oxide. Google Patents (2006)

64. T. Edahiro, N. Fujimura, T. Ito, Formation of two-dimensional electron gas and the magnetotransport behavior of ZnMnO/ZnO heterostructure. J. Appl. Phys. **93**(10), 7673–7675 (2003)

65. K. Koike et al., Piezoelectric carrier confinement by lattice mismatch at ZnO/$Zn_{0.6}Mg_{0.4}O$ heterointerface. Jpn. J. Appl. Phys. **43**, L1372 (2004)

66. K. Koike, I. Nakashima, K. Hashimoto, S. Sasa, M. Inoue, M. Yano, Characteristics of a $Zn_{0.7}Mg_{0.3}O$/ZnO heterostructure field-effect transistor grown on sapphire substrate by molecular-beam epitaxy. Appl. Phys. Lett. **87**(11), 7–10 (2005)

67. H. Tampo et al., Two-dimensional electron gas in Zn polar ZnMgO/ZnO heterostructures grown by radical source molecular beam epitaxy. Appl. Phys. Lett. **89**(13), 67–70 (2006)

68. H. Tampo et al., Strong excitonic transition of $Zn_{1-x}Mg_xO$ alloy. Appl. Phys. Lett. **91**(26), 261907 (2007)

69. J.D. Ye et al., Two-dimensional electron gas in Zn-polar ZnMgO/ZnO heterostructure grown by metal-organic vapor phase epitaxy. Appl. Phys. Lett. **97**(11), 2010–2012 (2010)

70. H. Tampo et al., Polarization-induced two-dimensional electron gases in ZnMgO/ZnO heterostructures. Appl. Phys. Lett. **93**(20), 11–14 (2008)

71. M. Brandt, H. von Wenckstern, G. Benndorf, H. Hochmuth, M. Lorenz, M. Grundmann, Formation of a two-dimensional electron gas in ZnO/MgZnO single heterostructures and quantum wells. Thin Solid Films **518**(4), 1048–1052 (2009)

72. H.A. Chin et al., Two dimensional electron gases in polycrystalline MgZnO/ZnO heterostructures grown by RF-sputtering process. J. Appl. Phys. **108**(5), 2–5 (2010)

73. S. Sasa et al., Microwave performance of ZnO/ZnMgO heterostructure field effect transistors. Phys. Status Solidi **208**(2), 449–452 (2011)

74. J. He, P. Wang, H. Chen, X. Guo, L. Guo, Y. Yang, Study on temperature effect on properties of ZnO/MgZnO based quantum cascade detector in mid-infrared region. Appl. Phys. Express **10**(1), 11101 (2016)

75. S.-H. Jang, S.F. Chichibu, Structural, elastic, and polarization parameters and band structures of wurtzite ZnO and MgO. J. Appl. Phys. **112**(7), 73503 (2012)

76. S.-H. Park, D. Ahn, Spontaneous and piezoelectric polarization effects in wurtzite ZnO/MgZnO quantum well lasers. Appl. Phys. Lett. **87**(25), 253509 (2005)

T. R. Lenka, H. P. T. Nguyen (eds.), *HEMT Technology and Applications*, Springer Tracts in Electrical and Electronics Engineering
https://doi.org/10.1007/978-981-19-2165-0_5

Analytical Modeling of Electric Field and Breakdown Voltage Characteristics of AlInN/GaN HEMT with Field Plates

G. Amarnath[1] ✉, Manisha Guduri[2] and M. C. Chinnaiah[3]
(1) Department of ECE, Marri Laxman Reddy Institute of Technology and Management, Hyderabad, India
(2) Department of ECE, KG Reddy College of Engineering and Technology, Hyderabad, India
(3) Department of ECE, B.V. Raju Institute of Technology, Narsapur, India

✉ **G. Amarnath**
Email: amarnath.nits@gmail.com

Abstract
An analytical modeling of electric field and breakdown voltage characteristics of AlInN/GaN HEMT with field plate at drain and gate regions is presented. In the model development, GaN buffer and Si substrate regions are treated as depletion regions. The developed model gives a deep physical understanding of the electric field and breakdown voltage characteristics of AlInN/GaN HEMT devices. The avalanche breakdown of a device appears in the vertical interface or edges of lateral field-plate structures. The relationship between vertical and lateral breakdown with respect to analytical modeling is presented. The breakdown characteristics are analyzed with device parameters including the thickness of regions, the length of field plate, and the distance between gate and drain. These analytical model characteristics are verified by matching with numerical simulations and are found in

good agreement. The developed model can be used as an effective direction for the optimization of the device to accomplish better performance.

Keywords GaN – HEMT – Field plate – Electric field – Breakdown voltage

1 Introduction

III–V wide bandgap GaN material is achieving consideration for its routine in high-power and high-frequency applications owing to its greater material properties [1–3]. The two-dimensional electron gas (2DEG) is created at the interface of AlInN and GaN due to the polarization present in the materials. The high 2DEG density and mobility give the high routine of AlInN/GaN High Electron Mobility Transistors (HEMTs) [4]. An analytical model of these HEMT devices is required to give physical understanding with easy approaches and effective results. The analytical model for heterostructure with GaN was introduced in [5], and electric-field dependent on drain voltage was explored in [6]. These analytical models are utilized for the optimization of the device.

Even though these models are related to numerical simulation curve fitting instead of analytical Poisson's solutions. With this method, modeling critical devices are becoming challenging, and needs simulation results to be acquired before analytical modeling. The analytical models are proposed by using Poisson’s expressions for AlInN/GaN HEMTs [7–9]. The electric field and channel potential are calculated by taking boundary conditions at the surface of the passivation layer. An analytical model was proposed with partial silicon doping in [10]. With this model, compromised analytical and simulation results are obtained. AlInN/GaN HEMT device is suitable for high-power application due to its high breakdown voltage capacity and it is considered for the analysis. These models are obtained by electric field and potential at the heterointerface. There are some critical challenges in analyzing the breakdown voltage with their model limitations. An analytical model was present by taking the potential at the surface of the passivation layer to calculate the breakdown voltage in [11]. However, the breakdown voltage in the vertical field is not incorporated. So, a two-

dimensional analytical model of AlInN/GaN with drain and gate field plates is proposed by considering substrate and buffer regions as depletion regions to analyze electric field and breakdown voltage characteristics.

2 Device Structure

The cross-sectional schematic view of AlInN/GaN HEMT with gate and drain field plates is given in Fig. 1. The AlInN barrier is recessed below the gate region to operate the device in an enhancement mode. Si_3N_4 material is used as the passivation and gate dielectric layer [12]. This Metal–Insulator–Semiconductor structure is considered to accomplish less gate leakage current in HEMT structures [12]. It is commonly identified that the electric field at drain or gate edges becomes high and it causes significant avalanche breakdown in the device. To overcome this effect, field plate technology is employed at the drain and gate regions [13] and is used for this structure. The actual maximum electric field at the drain and gate edges becomes less and another maximum electric field appears at the drain field plate and gate field plate, leading to a uniform electric field and potential distribution. The drain-field-plate structure has not been generally utilized in commercial GaN HEMTs, it leads to improved performance in high-power applications [14] consequently worthy of further investigation.

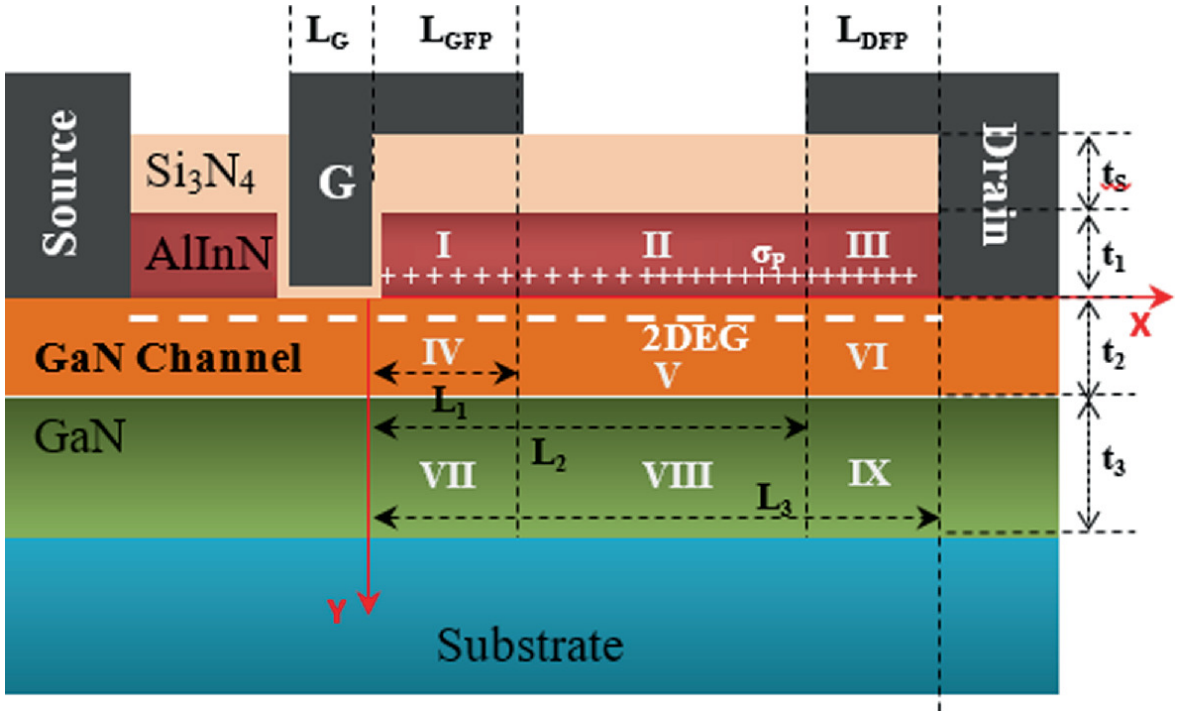

Fig. 1 Cross-sectional schematic view of AlInN/GaN HEMT with gate and drain field plates

3 Model Development

The substrate (SiC), buffer (GaN), channel (GaN), and barrier (AlInN) layers are depleted with the device's off-state biased condition $(V_{DS} > 0\,\text{V},\ V_{GS} = 0\,\text{V},\ V_S = 0\,\text{V})$. The GaN-buffer layer is considered as a *p*-type material due to the presence of the acceptor traps [15]. The depletion region of the potential distribution can be calculated by solving two-dimensional Poisson's equations in nine depletion regions. In the structure, the *x*-direction shows the lateral distance in relation to gate region's right edge and the *y*-direction shows the vertical distance in relation to AlInN/GaN hetero-interface. In addition, the heterointerface point at the right edge of the gate region is set to zero. The depletion region contains Si-substrate, GaN-buffer, GaN-channel, and AlGaN-barrier layers. These layers are categorized into three sections in lateral-distance *x*-direction due to the presence of gate-drain field plates. The limits are designated as $L_0, L_1, L_2,$ and L_3, respectively, with $L_0 = 0$ and $L_3 = L_{GD}$. The passivation layer (Si_3N_4) thickness is

represented as t_p. The AlInN-barrier, GaN-channel, and GaN-buffer layer thickness are represented as $t_1, t_2,$ and $t_3,$ respectively. The substrate depletion region thickness is represented as t_{sub}. The t_{sub} is derived from a general analytical modeling method by considering Eq. (1):

$$t_{\text{S}} = \left(\left(t_{\text{eff}}^2 + t_{\text{eff0}}^2\right)^{0.5} - t_{\text{eff}}\right)/2 \tag{1}$$

$$t_{\text{S}} = t_1/k_1 + (t_2 + t_3)/k_2 \quad \text{and}$$

$$t_{\text{eff0}}^2 = \left(2V_{\text{DS}}/q + t_1\left(N_1 t_1 - 2\left(Pt_3\sigma_p - N_2 t_2\right)\right)/k_1 + d_3\left(N_2 t_2 - 2Pt_3\right)/k_2 + Pt_3^2/k_2\right)/qP_{\text{sub}}$$

where $k_1 = \varepsilon_1/\varepsilon_p$, $k_2 = \varepsilon_2/\varepsilon_{\text{sub}}$. N_1 is background intrinsic carrier concentration of AlInN, N_1 is background intrinsic carrier concentration of GaN-channel, ε_1 and ε_1 are dielectric constants of the barrier- and channel-layer. The GaN-buffer-layer's charge density is considered to be invariant in model development and assumed to be $Q\left(2 \times 10^{13}\ \text{cm}^{-2}\right)$. Parameter P is the GaN buffer-layer equivalent concentration and is expressed as $P = Q/t_3$. ε_{sub} and P_{sub} are the dielectric constant and doping concentration of the substrate. σ_p is the charge density of polarization and it depends on the thickness and Al composition of the barrier material. In the simulation analysis, current continuity, drift–diffusion, and Poisson's equation physical models are used. These parameter models include the impact-ionization model for generation, the Shockley–Read–Hall model for recombination, carrier-statistic model, polarization- and mobility-model. The two-dimensional potential function is represented as $\varphi_{i,j}(x, y)\left(L_{j-1} < x < L_j,\ d_{i-1} < y < d_i;\ i, j = 1, 2, 3\right)$ all 9 regions with

$l_1 = L_1,\ l_2 = L_2 - L_1,\ l_3 = L_3 - L_2;\ d_0 = -t_1,\ d_1 = 0,\ d_2 = t_2,\ d_3 = t_2 + t_3$

. Since the fact that the device current is very small and can be negligible before occurring the breakdown. The charges are the fixed ionized charges which are presented in the depletion region of each layer [16]. The two-dimensional potential functions are obtained by calculating the Poisson's equations as

$$\frac{\partial^2 \varphi_{1,j}(x,y)}{\partial x^2} + \frac{\partial^2 \varphi_{1,j}(x,y)}{\partial y^2} = \frac{qN_1}{\varepsilon_1}, \quad j = 1,2,3 \tag{2}$$

$$\frac{\partial^2 \varphi_{1,j}(x,y)}{\partial x^2} + \frac{\partial^2 \varphi_{1,j}(x,y)}{\partial y^2} = \frac{qN_1}{\varepsilon_1}, \quad j = 1,2,3 \tag{3}$$

$$\frac{\partial^2 \varphi_{1,j}(x,y)}{\partial x^2} + \frac{\partial^2 \varphi_{1,j}(x,y)}{\partial y^2} = \frac{qN_1}{\varepsilon_1}, \quad j = 1,2,3 \tag{4}$$

The depletion region charges are separated in two parts to make the modeling simpler. The depletion region denoted as top and bottom regions are specified above and below AlInN/GaN heterointerface. By applying the equivalent potential method, depletion region charges are corresponding to the passivation layer of the surface potential and substrate boundaries [16]. So, the top and bottom regions of the charges are corresponding to the passivation layer of the surface potential and substrate, represented as V_{top} and V_{sub}, respectively.

$$V_{\text{top}} = q\sigma_p \left(\frac{t_1}{\varepsilon_1} + \frac{t_p}{\varepsilon_p} \right) + qN_1 \left(\frac{t_1^2}{2\varepsilon_1} + \frac{t_1 t_p}{\varepsilon_p} \right) \tag{5}$$

$$V_{\text{sub}} = qN_2 \left(\frac{t_2^2}{2\varepsilon_2} + \frac{t_2 t_3}{\varepsilon_2} + \frac{t_2 t_{\text{sub}}}{\varepsilon_{\text{sub}}} \right) - qN_3 \left(\frac{t_3^2}{2\varepsilon_3} + \frac{t_3 t_{\text{sub}}}{\varepsilon_{\text{sub}}} \right) - qN_{\text{sub}} \left(\frac{t_{\text{sub}}^2}{2\varepsilon_{\text{sub}}} \right) \tag{6}$$

The depletion layer is equivalent to a neutral semiconductor with respect to the mathematical equivalent potential method. So, Laplace equations are given as

$$\frac{\partial^2 \varphi_{i,j}(x,y)}{\partial x^2} + \frac{\partial^2 \varphi_{i,j}(x,y)}{\partial y^2} = 0, \quad i, j = 1, 2 \text{ and } 3. \tag{7}$$

The channel and buffer layer are considered as a combined layer due to the same GaN semiconductor material for easiness. The combined GaN layer of the potential function represented as

$$\varphi_{4,j}(x,y)\left(L_{j-1} < x < L_j, 0 < y < t_3,\ j = 1, 2, 3\right) \tag{8}$$

and it can be expressed as Eq. (9).

$$\frac{\partial^2 \varphi_{4,j}(x,y)}{\partial x^2} + \frac{\partial^2 \varphi_{4,j}(x,y)}{\partial y^2} = 0, \quad j = 1, 2, 3 \tag{9}$$

The boundary conditions are applied to solve Laplace expressions in the model development. These boundary conditions give with respect to continuity electric flux at passivation interface of AlInN/Si_3N_4 in the vertical direction as

$$-\varepsilon_1 \left.\frac{\partial \varphi_{1,j}(x,y)}{\partial y}\right|_{y=d_0} = \begin{cases} \varepsilon_p \frac{V_{\text{top}} + \varphi_f(x) - \varphi_{1,j}(x - t_1)}{t_p}, & i = 1, 3 \\ \varepsilon_p \frac{V_{\text{top}}}{t_p}, & i = 2 \end{cases} \tag{10}$$

where $\varphi_f(x) = V_G,\ L_0 \le x < L_1;\ \varphi_f(x) = V_{DS},\ L_2 \le x < L_3$. The electric field in the vertical direction is evaluated to zero when $L_1 \le x < L_2$. The electric flux and potential at the heterointerface of AlInN/GaN are constant in the vertical field and is represented as

$$-\varepsilon_1 \left.\frac{\partial \varphi_{1,j}(x,y)}{\partial y}\right|_{y=0} = -\varepsilon_2 \left.\frac{\partial \varphi_{4,j}(x,y)}{\partial y}\right|_{y=0} \quad j = 1, 2, 3 \tag{11}$$

(12)

$$\varphi_{1,j}(x,0) = \varphi_{4,j}(x,0) \qquad j = 1,2,3$$

Equation (13) can be calculated at the heterointerface by employing an equivalent potential method.

$$\left.\frac{\partial^2 \varphi_{1,j}(x,y)}{\partial x^2}\right|_{y=0} = \left.\frac{\partial^2 \varphi_{4,j}(x,y)}{\partial y^2}\right|_{y=0} \qquad j = 1,2,3 \tag{13}$$

Equation (14) can be calculated with respect to the continuity of electric flux at the buffer and substrate interface as

$$-\varepsilon_2 \left.\frac{\partial \varphi_{4,j}(x,y)}{\partial y}\right|_{x=t_3} = \varepsilon_{\text{sub}} \frac{\varphi_{4,j}(x,t_3) - V_{\text{sub}}}{t_{\text{sub}}} \qquad j = 1,2,3 \tag{14}$$

The potential-function $\varphi_{i,j}(x,y)$ is simplified with Taylor's expansion as a parabolic function and can be modeled as

$$\varphi_{i,j}(x,y) = a_{i,j} + b_{i,j}x^2, \qquad i = 1 \text{ and } 4, \qquad j = 1,2 \text{ and } 3 \tag{15}$$

Boundary conditions in the vertical direction are obtained using Eqs. (10)–(14) and substituted in Eq. (15) to calculate the relation between $\text{Al}_x\text{Ga}_{1-x}\text{N}$ as

$$2c_{1,j} = \frac{1}{T_j^2}\left(-a_{1,j} + V_j\right) \tag{16}$$

Here, a is a modification factor to consider the edge-effect due to Region III and Region I being near the drain and gate electrode edges [17]. $T_j\,(j = 1,2 \text{ and } 3)$ is the device thickness is determined through structural parameters and is stated as Eq. (17).

$$T_j = \begin{cases} \dfrac{\left(\left(t_1^2/2 + k_1 t_1 t_p\right) + \beta_j\left(d_3^2/2 + k_2 d_3 t_{\text{sub}}\right)\right)}{1+\beta_j}, & j = 1,3 \\ \dfrac{\left(\left(k_1 t_1 t_p\right) + \beta_2\left(d_3^2/2 + k_2 d_3 t_{\text{sub}}\right)\right)}{\beta_2}, & j = 2 \end{cases} \tag{17}$$

The partial differentiation function can be obtained by using Eqs. (16) and (17) in Eq. (7) at the condition of $y = 0$ is expressed as

$$\frac{\partial^2 \varphi_j(x,0)}{\partial x^2} - \frac{\varphi_j(x,0)}{T_j^2} = -\frac{V_j}{T_j^2}, \quad j = 1, 2 \text{ and } 3 \tag{18}$$

The potential at heterointerface of AlInN/GaN is stated as $\varphi_j(x,0) = \varphi_{1,j}(x,0) + \varphi_{4,j}(x,0)$, $j = 1, 2, 3$. Hence, the potential distribution can be written as

$$\varphi(x,0) = \begin{cases} V_{11}\sinh\frac{x}{T_1} + V_{12}\sinh\frac{L_1 - x}{T_1} + V_1 & L_0 \le x < L_1 \\ V_{21}\sinh\frac{x - L_1}{T_2} + V_{22}\sinh\frac{L_2 - x}{T_2} + V_2 & L_1 \le x < L_2 \\ V_{31}\sinh\frac{x - L_2}{T_3} + V_{32}\sinh\frac{L_3 - x}{T_3} + V_3 & L_2 \le x < L_3 \end{cases} \tag{19}$$

The potential drop is negligible at the gate dielectric due to the heterointerface and the gate electrode is very closely bounded. So, the potential of Region-I at the left edge is V_G and potential of Region-III at the right edge is V_{DS}.

$$\varphi_1(0,0) = V_G, \quad \varphi_3(L_2,0) = V_{\mathrm{DS}} \tag{20}$$

The potential at heterointerface and electric flux is constant in the lateral direction and produces

$$\left.\frac{\partial \varphi_j(x,0)}{\partial x}\right|_{x=L_j} = \left.\frac{\partial \varphi_{j+1}(x,0)}{\partial x}\right|_{x=L_j} \quad j = 1, 2 \tag{21}$$

$$\varphi_j\left(L_j, 0\right) = \varphi_{j+1}\left(L_j, 0\right) \quad j = 1, 2 \tag{22}$$

The parameter values of $V_{11}, V_{12}, V_{21}, V_{22}, V_{31}, \text{ and } V_{32}$ are obtained by substituting Eq. (19) into Eqs. (20)–(22). The analytical modeling is proposed without numerical simulation boundary conditions. So, this model can be able to utilize in developing a breakdown voltage model of AlInN/GaN HEMTs.

4 Electric Field at the Heterointerface

The electric field at heterointerface can be obtained by the potential distribution model, which shows a significant effect on the device physical characteristics. The avalanche breakdown is created in the proposed device by the unnecessary peaks of the electric field. This electric field distribution at heterointerface analysis is required to model the breakdown voltage of the device. The electric field distribution between drain and gate region is derived by Eq. (19) as follows:

$$E(x) = \begin{cases} \left(V_{11}\cosh\frac{x}{T_1} - V_{12}\cosh\frac{L_1-x}{T_1}\right)/T_1 & L_0 \le x < L_1 \\ \left(V_{21}\cosh\frac{x-L_1}{T_2} - V_{22}\cosh\frac{L_2-x}{T_2}\right)/T_2 & L_1 \le x < L_2 \\ \left(V_{31}\cosh\frac{x-L_2}{T_2} - V_{32}\cosh\frac{L_3-x}{T_3}\right)/T_3 & L_2 \le x < L_3 \end{cases} \tag{23}$$

Figure 2 shows the electric-field distribution and potential at heterointerface with respect to numerical simulation and analytical model results. From the figure, it is observed that the analytical model results and numerical simulation results are in good agreement. In Fig. 2a, the electric-field peaks are observed at the drain and gate region for conventional AlInN/GaN structure which are represented as E_D and E_G, respectively. By employing a field plate at drain and gate, the electric-field distribution is changed and peaks are observed at the drain and gate region which are represented as E_{DFP} and E_{GFP}, respectively. These peaks are created at the vale of the electric field by changing the E_D and E_G leading to a uniform distribution. The E_D, E_G, and E_{GFP} are increased to some extent and there is an important increase in E_{DFP} with the increase in V_{DS}. It is apparent that the increase in voltage is nearly sustained at the drain region of the field-plate edge. It is due to the potential at the heterointerface with the lateral electric-field integral. So, the breakdown in the lateral structure would occur most probably at the drain-field-plate edge. A significant potential increment is observed at the drain and gate edges of conventional structure from

Fig. 2b due to the large E_D and E_G as illustrated in Fig. 2a. Another side, the potential is almost constant at the valley of electric field in the conventional structure, which shows that the area can barely accept the voltage applied. The electric field of AlInN/GaN HEMT with field plate is increased at the valley, which leads to a constant potential distribution.

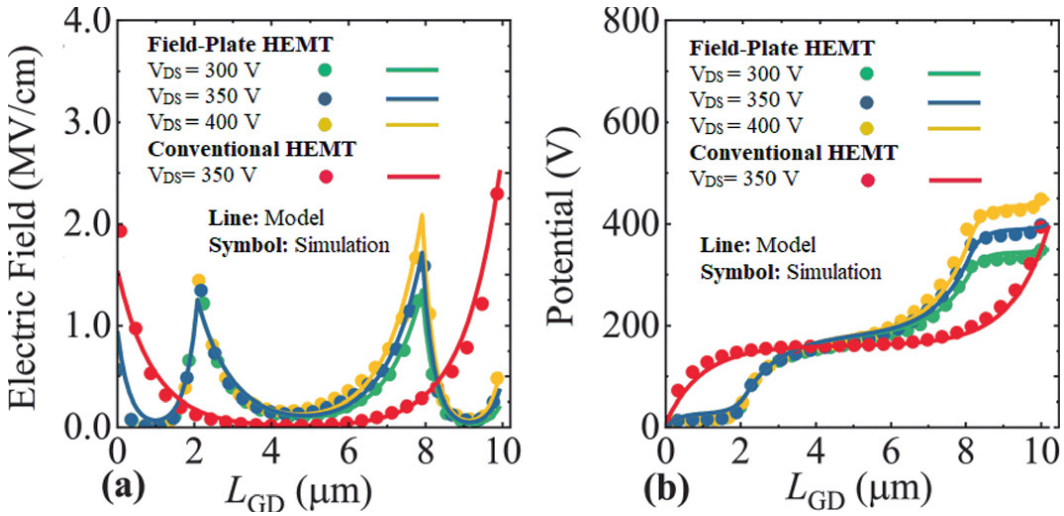

Fig. 2 Simulation (symbol) and model (line) results of **a** the electric field and **b** the potential at heterointerface with different drain voltages

The electric-field distribution with different thicknesses of the passivation layer of AlInN/GaN HEMT is shown in Fig. 3a.

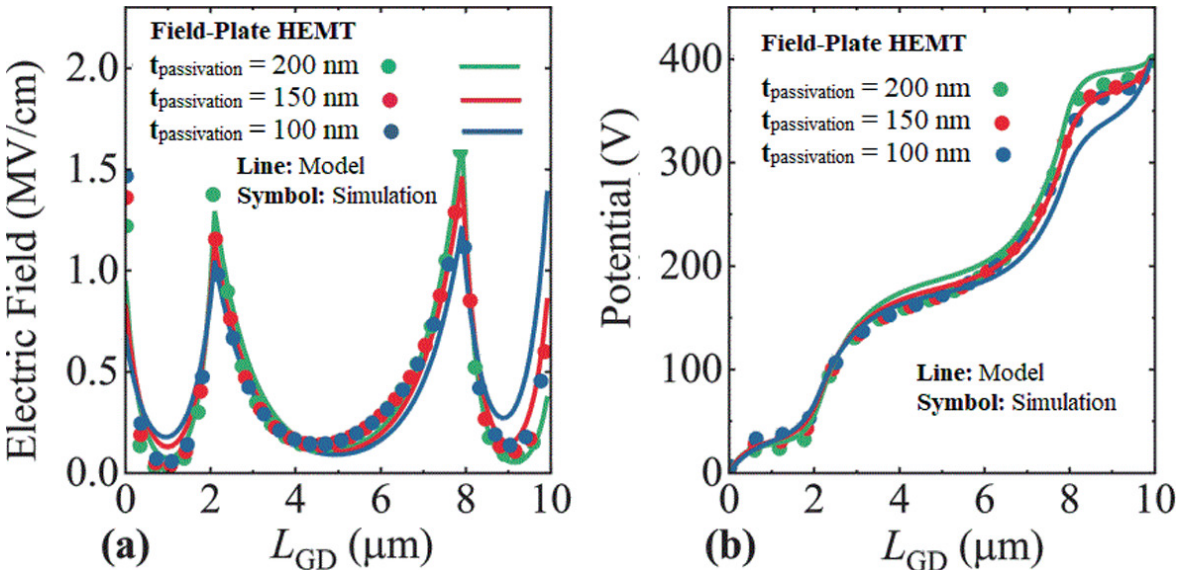

Fig. 3 Simulation (symbol) and model (line) results of **a** the electric field and **b** the potential at heterointerface with different passivation layer thicknesses

It is observed that the E_D and E_G slightly decreases and E_{DFP} and E_{GFP} significantly increase when the thickness of passivation layer decreases. This is due to decreasing the space with a thin passivation layer between heterointerface and field plates of the drain and gate. So, the field-plate technique gives a significant effect on electric-filed distribution. The potential distribution with different thicknesses of the passivation layer of AlInN/GaN HEMT is shown in Fig. 3b. It is observed that the analytical model results are well-matched with the numerical-simulation results. The potential distribution and electric field with drain and gate field plate are shown in Fig. 4. The positions of the E_{DFP} and E_{GFP} varies with different drain and gate field plates is shown in Fig. 4a. The applied voltage considered at the drain and gate field plates are shown in Fig. 4b. It is observed that the field plates need to be enhanced to achieve better performance.

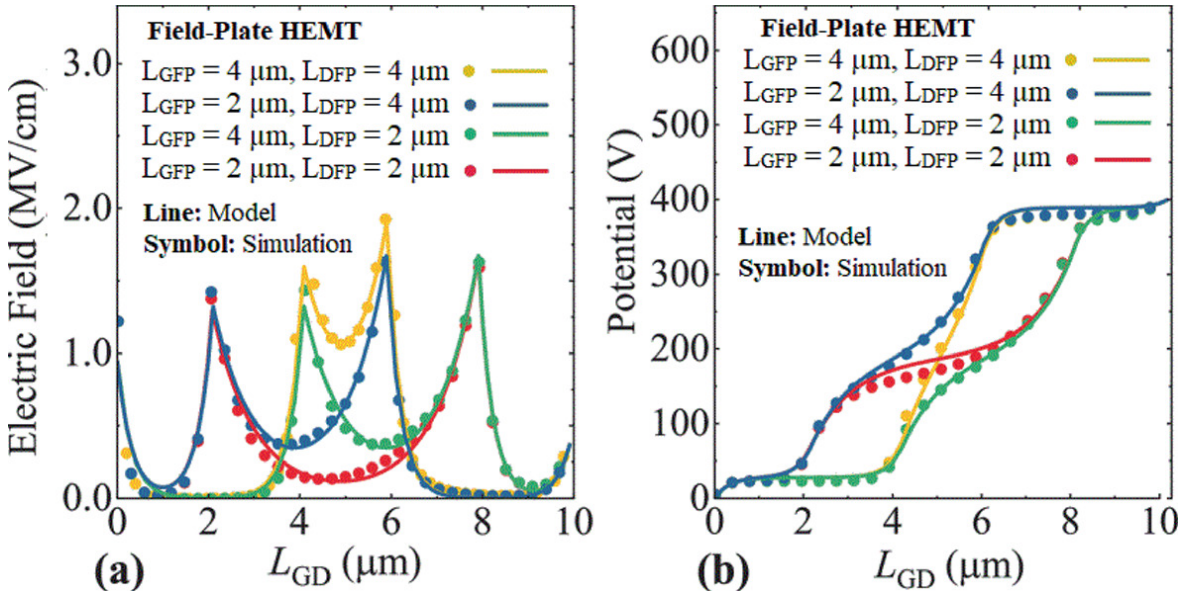

Fig. 4 Simulation (symbol) and model (line) results of **a** the electric-field and **b** the potential at heterointerface with different lengths of drain and gate field plates

5 Breakdown Voltage

The breakdown voltage occurring at two possible points are $L_0 = 0$ and $L_0 = 0$ in lateral HEMT structure with drain and gate field plates, respectively. In model development, the breakdown voltage is well defined through the electric field approaching the critical electric field [18]. The lateral breakdown voltage model is obtained with $E(x, 0) = E_C$ by substituting Eq. (23):

$$\begin{cases} BV_{\mathrm{GFP}} = \dfrac{(E_{\mathrm{GaN}}T_1 + V_{12})/\cosh(L_1/T_1) - \gamma_2}{\theta_1} \\ BV_{\mathrm{DFP}} = \dfrac{(E_{\mathrm{GaN}}T_1 + \gamma_2)/\cosh(L_3/T_1) - \gamma_3}{\theta_3 - \theta_2\cosh(L_3/T_1)} \end{cases} \tag{24}$$

The $\mathrm{BV_{DFP}}$ and $\mathrm{BV_{DFP}}$ are the breakdown voltages occurring at drain and gate field plate edges correspondingly and later breakdown voltage $(\mathrm{BV_{lat}})$ is the least point between them.

$$\mathrm{BV_{lat}} = \min(\mathrm{BV_{GFP}}, \mathrm{BV_{DFP}}) \tag{25}$$

The breakdown voltage ensues in the vertical structure of the interface of GaN/Si at the silicon side before the GaN buffer electric field reaches. This is due to continuity in electric flux at the interface of GaN and Si. So, this interface below the drain region is one probable location of breakdown voltage and it is modeled as

$$\begin{aligned} \mathrm{BV_{Si}} = {} & 2E_{\mathrm{Si}}^2 \frac{\varepsilon_{\mathrm{sub}}}{qN_{3,\mathrm{sub}}} + 2E_{\mathrm{Si}}\varepsilon_{\mathrm{sub}}\left(\frac{t_1}{\varepsilon_1} + \frac{t_2 + t_3}{\varepsilon_2}\right) \\ & + q\left(N_3 t_3\left(\frac{t_1}{\varepsilon_1} + \frac{2t_2 + t_3}{2\varepsilon_2}\right) - \sigma N_3 \frac{t_1}{\varepsilon_1} - N_2 t_2\left(\frac{t_1}{\varepsilon_1} + \frac{t_2}{2\varepsilon_2}\right)\right) \end{aligned} \tag{26}$$

Another probable breakdown voltage location is at AlInN/GaN heterointerface due to the maximum electric field present at the interface and it is modeled as

(27)

$$\mathrm{BV_{GaN}} = \frac{(\varepsilon_2 E_{\mathrm{GaN}} - qN_3t_3)^2}{2qN_{3,\mathrm{sub}}} + q\left(\frac{t_1\left(2\left(N_3t_3\sigma_p - N_2t_2\right) - N_1t_1\right)}{2k_1} + \frac{N_3t_3^2 - d_3\left(N_2t_2 - 2N_3t_3\right)}{2k_2} - N_3t_3t_{\mathrm{eff}}\right) + \varepsilon_2 E_{\mathrm{GaN}}t_{\mathrm{eff}}$$

The breakdown voltage in the vertical direction is calculated with $\mathrm{BV_{GaN}}$ and $\mathrm{BV_{Si}}$, and is given as

$$\mathrm{BV_{ver}} = \min\left\{\mathrm{BV_{GaN}}, \mathrm{BV_{Si}}\right\} \tag{28}$$

The P_{ferro} and t_{sub} are considered as 3×10^6 V/cm and $3 \times 10^6 \frac{\mathrm{V}}{\mathrm{cm}}$, respectively [19]. The breakdown voltage with field plates is restricted by the minimum breakdown voltage between $\mathrm{BV_{ver}}$ and $\mathrm{BV_{lat}}$ and is represented as

$$\mathrm{BV} = \min\left\{\mathrm{BV_{lat}}, \mathrm{BV_{ver}}\right\} \tag{29}$$

The breakdown voltage increases with L_{GD} increases and becomes saturated at a specific distance of drain-to-gate as shown in Fig. 5a and these results are in good settlement with available experimental results [20]. In Fig. 5a, the vertical device's breakdown occurs at 475 V and 640 V for the $1\ \mu\mathrm{m}$ and $1.5\ \mu\mathrm{m}$ thickness of GaN buffer layer, respectively, and shows that the breakdown voltage is high with thick GaN buffer layer. But, as the thickness of the buffer layer increases further the breakdown appears in the lateral structure instead of vertical structure. The L_{GD} is sufficiently long due to the increase in L_{GD} which leads to an increase in breakdown voltage. The breakdown voltage with $2\ \mu\mathrm{m}$ and $3\ \mu\mathrm{m}$ of GaN buffer layer saturates at $800\ \mathrm{V}$ and $1050\ \mathrm{V}$, respectively, and is shown in Fig. 5a. The figure-of-

merit (FoM) is obtained by $\mathrm{FoM} = \mathrm{BV}^2/R_{\mathrm{on}}$ with a breakdown voltage analytical model and is shown in Fig. 5b.

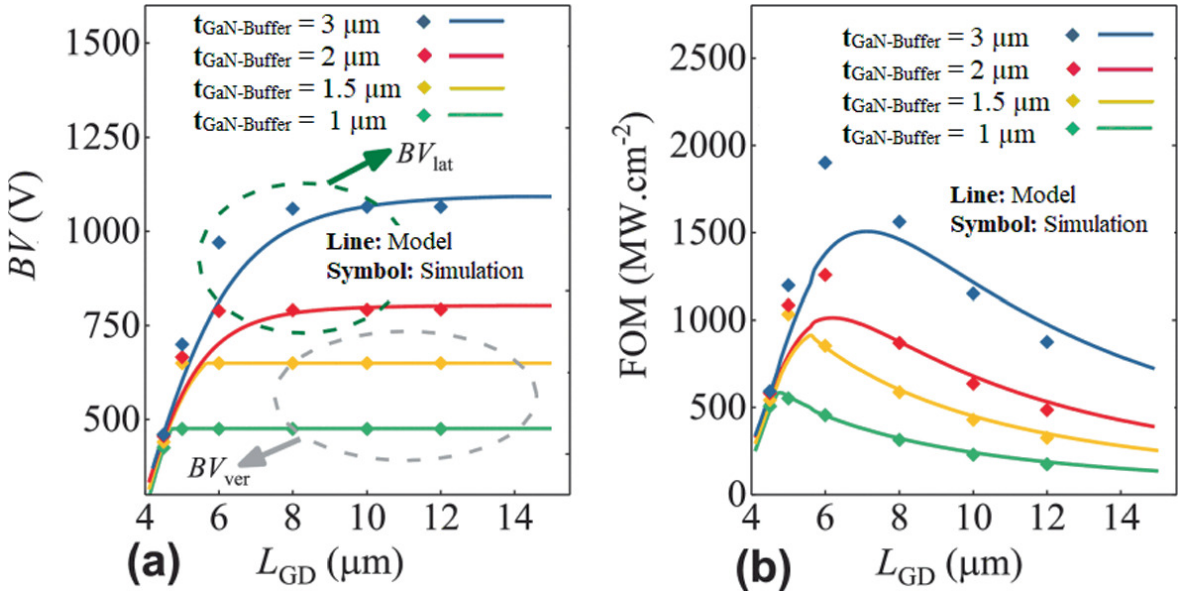

Fig. 5 Simulation (symbol) and model (line) results of **a** breakdown voltage and **b** figure-of-merit (FOM) with different distances of drain and gate

The maximum peaks are observed at $L_{\mathrm{GD}} = 4.8\ \mu\mathrm{m},\ 5.9\ \mu\mathrm{m},\ 6.4\ \mu\mathrm{m},$ and $7\ \mu\mathrm{m}$ with change in buffer thickness. The numerical and analytical simulation results are in good agreement. The peaks in FoM increase with a thick buffer layer. Also, the breakdown voltage saturates with an increase in L_{GD}. So, optimized buffer thickness and L_{GD} need to be chosen when the peaks in FoM occur.

Figure 6 indicates the breakdown voltage of the device with different field-plate parameters. In Fig. 6a, the breakdown creates in a vertical structure with a thin buffer layer and it is constant with changes in L_{GFP}. The breakdown voltage drops a little with L_{GFP} increases due to the breakdown that arises at the gate field-plate edge while the device is operated in full depletion condition. In Fig. 6b, the breakdown voltage

increases significantly with L_{GFP} increases when the thickness of the buffer layer increases.

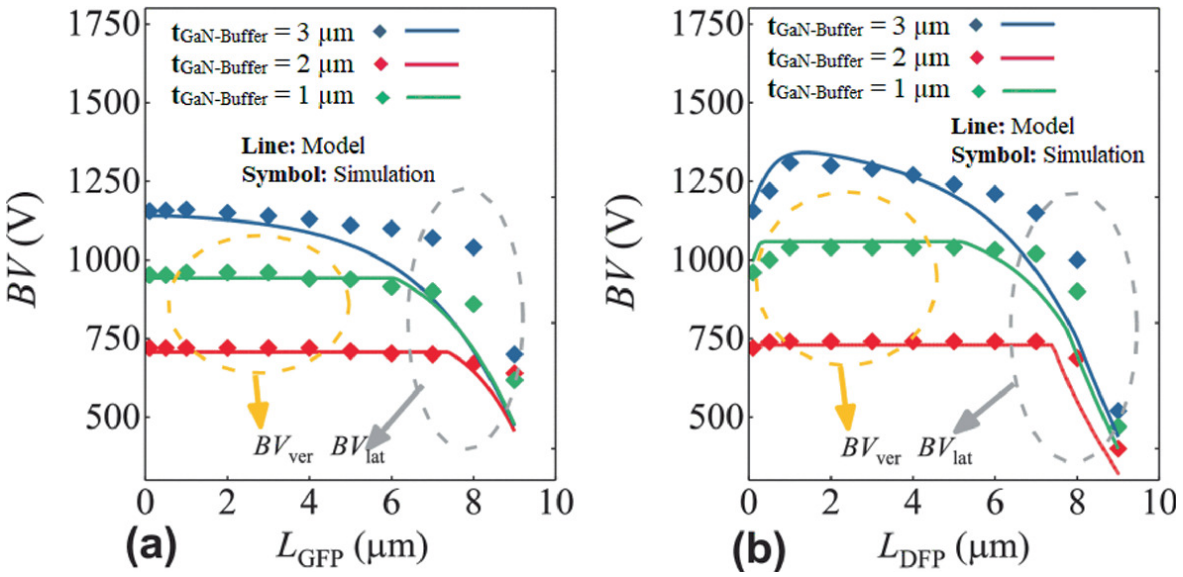

Fig. 6 Simulation (symbol) and model (line) results of breakdown voltage at **a** drain field plate of 0 μm and **b** gate field plate of 0 μm

This shows that the drain field plate is a more possible place for the breakdown to occur in lateral structure when the device is in a full-depletion region. The V_{br} is moderated and electric-field distribution is uniform with drain field plate leading to large breakdown voltage and it reduces significantly with L_{GFP} increases further. From this, the high breakdown voltage is achieved by optimizing the drain field plate with respect to GaN-buffer thickness.

6 Conclusion

An analytical model for the electric field, potential distribution, and breakdown voltage of AlInN/GaN HEMT with drain and gate field plates is presented. The analytical model is developed with the Laplace equation solution. For the justification, the analytical model results are compared with numerical simulation results and available experimental results, and are found to be in good agreement. A more accurate analytical model is developed by considering GaN buffer-layer and Si-

substrate material. The breakdown voltage analytical model gives a more physical understanding of the breakdown characteristics of the device, which are calculated by the simultaneous vertical and lateral breakdown. The breakdown voltage occurs in the vertical device when the GaN-buffer layer is sufficiently thin. Also, the breakdown voltage is constant when the gate-to-drain distance is increasing. So, achieving a large breakdown voltage is critical with a thin buffer layer. This vertical breakdown is difficult to occur with a thick buffer layer and consequences in lateral breakdown occur. To accomplish good performance, an optimized buffer thickness, field-plate thickness, and gate-to-drain distance are used.

References

1. S.H. Sohel et al., Polarization engineering of AlGaN/GaN HEMT with graded InGaN sub-channel for high-linearity X-band applications. IEEE Electron Device Lett. **40**(4), 522–525 (2019)

2. M. Alshahed et al., Low-dispersion, high-voltage, low leakage GaN HEMTs on native GaN substrates. IEEE Trans. Elect. Dev. **65**(7), 2939–2947 (2018)
[Crossref]

3. B. Kim, H. Fark, S. Eom, Kaband MMIC using AlGaN/GaN-on-Siwith recessed high-*k* dual MIS-structure. IEEE Electron Device Lett. **39**(7), 995–998 (2018)
[Crossref]

4. G. Amarnath, D.K. Panda, T.R. Lenka, Modeling and simulation of DC and microwave characteristics in AlInN(AlGaN)/AlN/GaN MOSHEMTs with different gate length. Int. J. Numer. Model. Electron. Netw. Dev. Fields **32**(1), e2456 (2019)

5. A. Rawat, V.K. Surana, M. Meer, N. Bhardwaj, S. Ganguly, D. Saha, Gate current reduction and improved DC/RF characteristics in GaN-based MOS-HEMTs using thermally grown TiO_2 as a dielectric. IEEE Trans. Electron Devices **66**(6), 2557–2562 (2019)
[Crossref]

6. S. Karmalkar, M.S. Shur, G. Simin, M.A. Khan, Fieldplate engineering for HFETs. IEEE Trans. Electron Devices **52**(12), 2534–2540 (2005)
[Crossref]

7. J.P. Ibbetson, P.T. Fini, K.D. Ness, S.P. DenBaars, J.S. Speck, U.K. Mishra, Polarization effects, surface states and the source of electrons in AlGaN/GaN heterostructure field-effect transistors. Appl. Phys. Lett. **77**(2), 250–252 (2000)
[Crossref]

8. Nao, W., et al.: A two-dimensional fullyanalytical model with polarizationeffect for off-state channel potential and electricfield distributions of GaN-based field-plated high electronmobility transistor. Chin. Phys. B **23**(8) (2014)

9. S. Karmalkar, N. Soudabi, A closed-form model of the drain voltage dependence of the off-state channel electric field in a HEMT with a field plate. IEEE Trans. Electron Devices **53**(10), 2430–2437 (2006)
[Crossref]

10. G. Amarnath, D. Sudha, D. Krishna, S. Ghanate, S. Karthik, A. Vinod, Analytical model development for channel potential in junction-less double-gate FETs, in *2020 IEEE International Conference on Advent Trends in Multidisciplinary Research and Innovation (ICATMRI)* (2020), pp. 1–5

11. L. Tang, B. Buan, Y. Wang, Analytical models or the electric-field and potential of AlGaN/GaN HEMT with partialsilicon doping. Superlattices Microstruct. **128**, 349–357 (2019)
[Crossref]

12. K. Nourad, A. Pelia, A. Toltani, Analytical modeling analysis of AlmGa1−mN/GaN HEMTs employing fieldplate and high-*k* dielectric stack high-voltage-operation. J. Comput. Electron. **12**(3), 501–510 (2013)
[Crossref]

13. J. Jiu et al., Analytical model for the potential and electric field distributions of AlGaN/GaN HEMTs with gate-connected FP based on equivalent potential method. Superlattices Microstruct. **138** (2019)

14. G. Amarnath, T.R. Lenka, Analytical model development for unified 2D electron gas sheet charge density of AlInN/GaN MOSHEMT. Int. J. Electron. Telecommun. **63**(4), 363–368 (2017)
[Crossref]

15. Y. Shi et al., Normally off GaN-on-Si MIS-HEMTs fabricated with LPCVD-SiNx passivation and high-temperature gate recess. IEEE Trans. Electron Devices **63**(2), 614–619 (2016)
[Crossref]

16. G. Amarnath, D.K. Panda, T.R. Lenka, Microwave frequency small-signal equivalent circuit parameter extraction for AlInN/GaN MOSHEMT. Int. J. RF Microwave Comput. Aided Eng. **28**(2), e21179 (2018)
[Crossref]

17. A. Soni, M. Shrivastava, Novel drain-connected field plate GaN HEMT designs for improved VBD–RON tradeoff and RF PA performance. IEEE Trans. Electron Devices **67**(4), 1718–1725 (2020)
[Crossref]

18. B. Jiao, Q. Jhou, J. Kin, Simulation of AlGaN/GaN HEMTs' breakdownvoltage enhancement using gate-field-plate, source-field-plate and drain-field plate. Electronics **8**(4), 1–11 (2019)

19. G. Amarnath, R. Swain, T.R. Lenka, Modeling and simulation of 2DEG density and intrinsic capacitances in AlInN/GaN MOSHEMT. Int. J. Numer. Model. Electron. Networks Devices Fields **31**(1), e2268 (2018)
[Crossref]

20. T. Jabemura, S. Veda, Y. Kawada, "Enhancement of breakdown-voltage in AlGaN/GaN HEMTs: Fieldplate plus high-*k* passivationlayer and high acceptor density buffer layer. IEEE Trans. Electron Devices **65**(9), 3848–3854 (2018)

T. R. Lenka, H. P. T. Nguyen (eds.), *HEMT Technology and Applications*, Springer Tracts in Electrical and Electronics Engineering
https://doi.org/10.1007/978-981-19-2165-0_6

Performance Analysis of HfO_2 and Si_3N_4 Dielectrics in β-Ga_2O_3 HEMT

Meenakshi Chauhan[1] ✉, Abdul Naim Khan[1] ✉, Raghuvir Tomar[1] ✉ and Kanjalochan Jena[1] ✉
(1) Department of Electronics and Communication Engineering, The LNM Institute of Information Technology, Jaipur, Rajasthan, 302031, India

✉ **Meenakshi Chauhan (Corresponding author)**
Email: 20pec006@lnmiit.ac.in

✉ **Abdul Naim Khan**
Email: 19pec001@lnmiit.ac.in

✉ **Raghuvir Tomar**
Email: rtomar@lnmiit.ac.in

✉ **Kanjalochan Jena**
Email: kanjalochan.jena@lnmiit.ac.in

Abstract
β-Ga_2O_3 HEMT with 10 nm AlN as a barrier layer is designed in this paper. The dielectric layer of Si_3N_4 and HfO_2 is introduced beneath the gate as a passivation layer. HfO_2 shows high thermal stability and high reliability while Si_3N_4 shows good interface attribute. The double gate of 0.2 µm and 0.5 µm with a gap of 50 nm aids in enhancing the 2DEG. The relation between dielectric constant and bandgap shows the

interdependence on diametric size of the material. The passivation layer controls the gate leakage current and improves the pinch-off characteristics of the device. The transfer characteristic, transconductance, and output conductance demonstrate the device tunability for application in power radio frequency and microwave.

Keywords Dielectric – AlN – β-Ga_2O_3 – Passivation – Bandgap

1 Introduction

The dawn of semiconductors initiated by Si, grew up to III–V group elements such as AlGaN/GaN, InGaAs/GaAs, AlGaN/GaN, and now Ga_2O_3 is paving the way to the pinnacle. Comparing the properties of GaN with the contemporary Ga_2O_3, the breakdown voltage for GaN is 3.3 MV/cm and for Ga_2O_3 is 8 MV/cm; the bandgap for GaN is 3.4 eV while for Ga_2O_3 lies between 4.5 and 4.9 eV; mobility for GaN is reported to be 1200 cm^2Vs^{-1} as compared to 300 cm^2Vs^{-1} for Ga_2O_3 [1]. β-Ga_2O_3 shows the potential to grow a large single crystal that is better, both quality-wise and economically. Due to some distinct properties, β-Ga_2O_3 has an edge over its counter compounds of III–V semiconductors and promises to find unparallel applications in power electronics. The researchers have great zeal in exhibiting monoclinic β-Ga_2O_3 as an efficient and reliable material for HEMT [2–4]. The β-Ga_2O_3 HEMT can be fabricated on single crystal and large diameter wafers can be produced using Float Zone and edge-defined field-fed growth techniques. The material is cheap and easily available, also the techniques are low cost and low energy consumption [5]. The β-Ga_2O_3 HEMT is finding application in high-voltage and high power RF and DC power switching applications [6, 7]. Scaling also plays an important role in enhancing RF characteristics and power added efficiency (PAE) [8, 9]. Gate scaling improves the DC and RF performance and frequency of the device [10]. Proper parameters help in improving the device sensitivity, gate leakage current and short channel effects, hence the device finds application as biosensor [11, 12]. Table 1 shows the standard value for material properties of β-Ga_2O_3 [13].

Table 1 Material properties OF β-Ga_2O_3

Parameters	**β-Ga_2O_3**
Bandgap (eV)	4.8–4.9
Electron mobility, μ_n (cm^2/Vs)	300
Relative dielectric constant, ε	10
Electron affinity, χ (eV)	4.0
Breakdown field, E_b (MV/cm)	8

The dielectric layer is employed beneath the gate to reduce gate leakage effects in HEMT. The dielectric plays a vital role in reducing gate leakage current and reducing power dissipation. Hence, the implementation of dielectric improves the performance of HEMT by enhancing gain and output resistance [14]. Various dielectric materials like Al_2O_3, HfO_2, and ZrO_2 have been implemented in HEMT but the percentage of reduction in gate leakage current and adherence are taken into consideration. In this paper, HfO_2 and Si_3N_4 are implemented as a dielectric layer in β-Ga_2O_3 HEMT. HfO_2 shows high thermal stability and high reliability while Si_3N_4 shows good interface attributes [15].

2 Device Architecture and Simulation

The substrate is taken to be unintentional doped Ga_2O_3, with uniform doping in depth but it reduces towards edge of the device [5]. The detailed device structure is shown in Fig. 1. The β-Ga_2O_3 substrate has a buffer layer, 50 nm of the same material with unintentional doping. The 2DEG channel is formed between the buffer and barrier layer of 10 nm. The AlN of 10 nm acts as a barrier layer. The oxide (HfO_2) or nitride layers (Si_3N_4) provide a surface passivation layer with the double gate of the same material. The dielectric constant for Si_3N_4 lies between 9.5 and 10.5, and for HfO_2 it lies between 20 and 25 [16]. The distance between source and gate L_{SG} is 0.2 µm, the distance between source and drain L_{SD} is 1.2 µm, and the distance between the gate and drain L_{GD} is 0.5 µm. The source and drain contact (Ti/Au/Ni) have fixed the work

function, Φ_m = 5.1 eV. The gate length is 0.2 µm and 0.5 µm, which reduces short channel effects and provides better electrostatic control in the channel region [17].

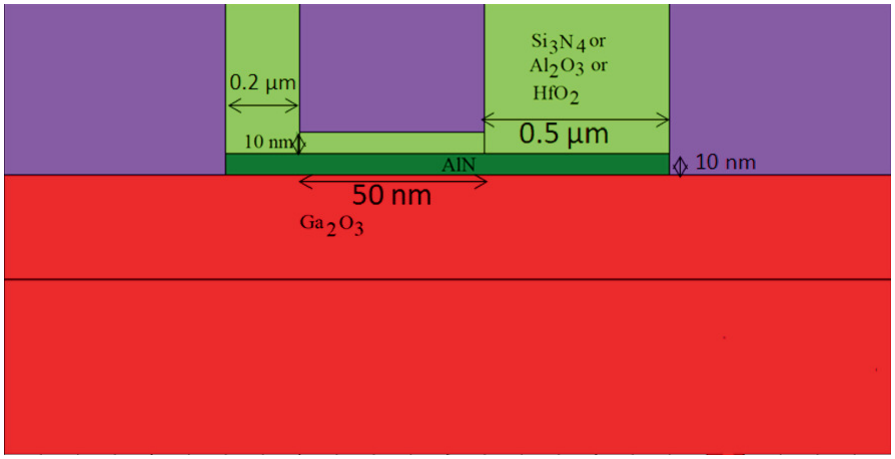

Fig. 1 Cross-section of dual-gate AlN/β-Ga_2O_3 HEMT

The dielectric material is used to reduce the gate leakage current and improve the efficiency and pinch-off characteristics of the device. The dielectric constant at room temperature is directly proportional to the bandgap of material as shown in Eq. (1). The relation between dielectric constant and susceptibility is given in [18].

$$\in(\infty) = \chi(\infty) + 1 \tag{1}$$

$$\chi(\infty) \propto \left[E_g(\infty)\right]^{-2}$$

$$\frac{\chi(D)}{\chi(\infty)} = \left[\frac{E_g(D)}{E_g(\infty)}\right]^{-2}$$

where $\chi(D)$ is electrical susceptibility, $E_g(D)$ is the bandgap for nanomaterials.

The dielectric constant is related to the movement of electrons from the conduction band to the valence band. Therefore, the dielectric constant is a consequence of bandgap and the phenomenon of motion of electrons from the ground state to the excited state [18].

$$\frac{\varepsilon(D)-1}{\varepsilon(\infty)-1}=\left[\frac{E_g(\chi)}{E_g(\infty)}\right]^{-2} \tag{2}$$

where $\varepsilon(D)$ and $\mathrm{BV_{Si}}$ are dielectric constants for nano and bulk materials, and D denotes the diametric size of the material.

Equation (2) shows the relation between the dielectric constant and bandgap of material, with dependence on the size of the crystal. This paper compares the performance of two dielectric materials, Si_3N_4 and HfO_2 implemented as passivation layers separately in β-Ga_2O_3 HEMT.

The parameters of dielectric material Si_3N_4 and HfO_2 enacted in the device are being compared in Table 2 [16].

Table 2 Comparison of parameters FOR Si_3N_4 and HfO_2

Parameter	**Si_3N_4**	**HfO_2**
Dielectric Constant (K)	7	25
Bandgap (eV)	5.3	5.8
CB offset (eV)	2.4	1.4
Permittivity (F/m)	9.5–10.5	20–25

3 Results and Discussion

The $I_d - V_d$ graph specifies the output characteristics for dielectric Si_3N_4 and HfO_2 at gate voltage $V_g = 5$ V as shown in Fig. 2. The I_{ds} is observed to be slightly higher for HfO_2 than Si_3N_4. The abrupt increase with lower drain biasing indicates the rise in the mobility of the 2DEG device. Thus, the significance of the proposed HEMT device is successful.

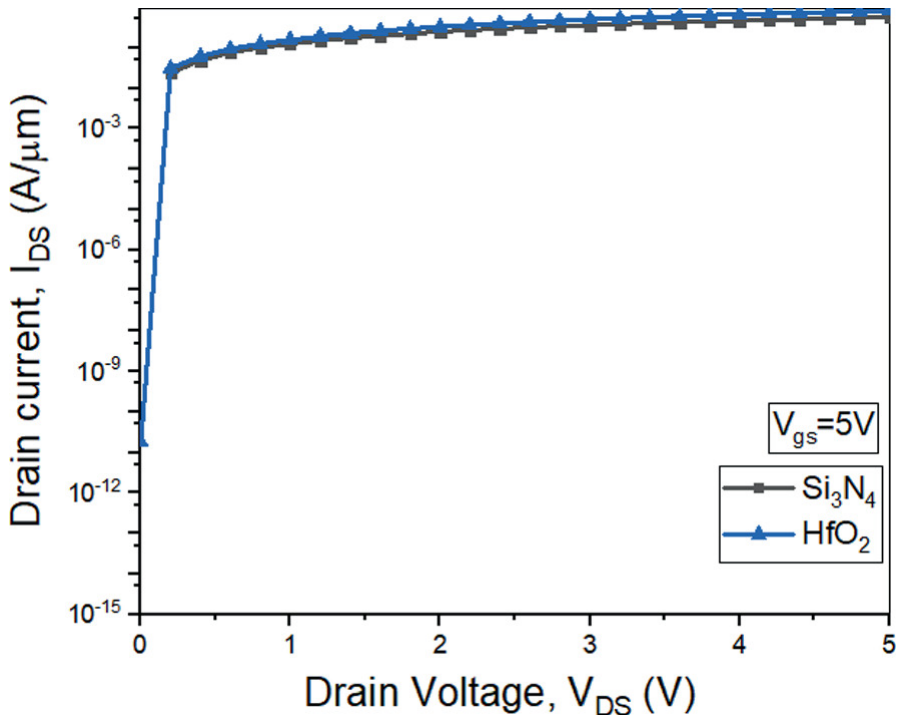

Fig. 2 Output characteristics of AlN/β-Ga_2O_3 HEMT

The transfer characteristics are analyzed using $I_{ds} - V_{gs}$ at $V_d = 5$ V for the dielectric Si_3N_4 and HfO_2. As shown in Fig. 3, the β-Ga_2O_3 HEMT with HfO_2 turns off at a higher gate bias than Si_3N_4. This is the consequence of the high permittivity of HfO_2, resulting in reduced charge carrier concentration and hence decreasing the V_{off}.

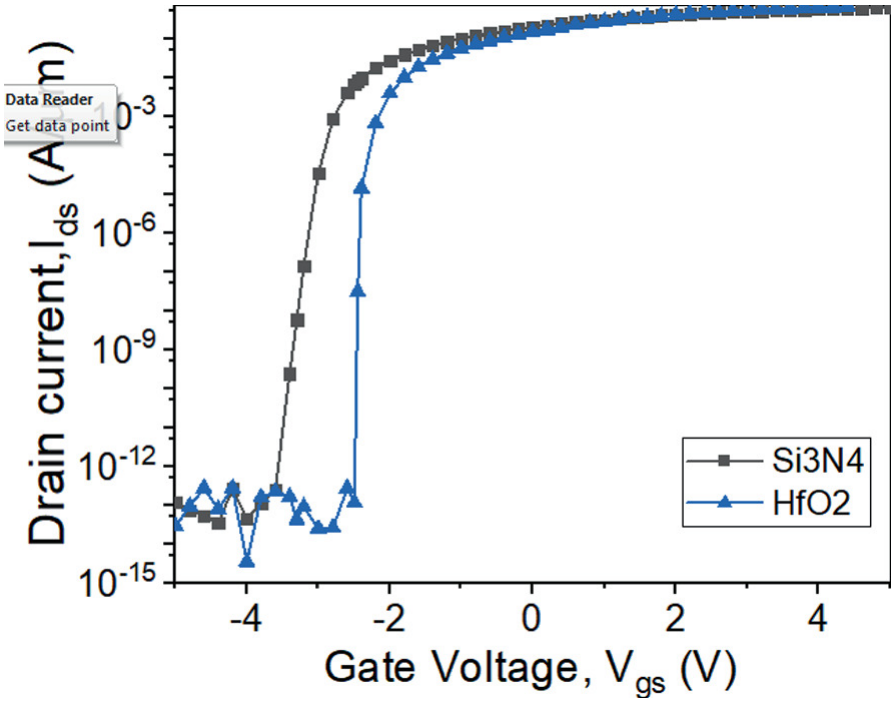

Fig. 3 Transfer characteristics of AlN/β-Ga_2O_3 HEMT with Si_3N_4 and HfO_2 as dielectric layer

The threshold voltage of the proposed device is plotted for different dielectric materials- HfO_2 and Si_3N_4.

The parameter transconductance (g_m) is defined as the differential of drain current with respect to gate voltage for constant drain voltage values. This crucial parameter, g_m is responsible for RF and linearity of the device [19]. The transconductance also plays an essential role in gain, cutoff frequency, and making the device work in a high-frequency range. Figure 4 compares the transconductance (g_m) versus gate voltage (V_g) for HfO_2 and Si_3N_4. Due to the shifting of threshold voltage on the right side in the case of HfO_2, the peak transconductance is observed at 2 V while for Si_3N_4, it is 1 V.

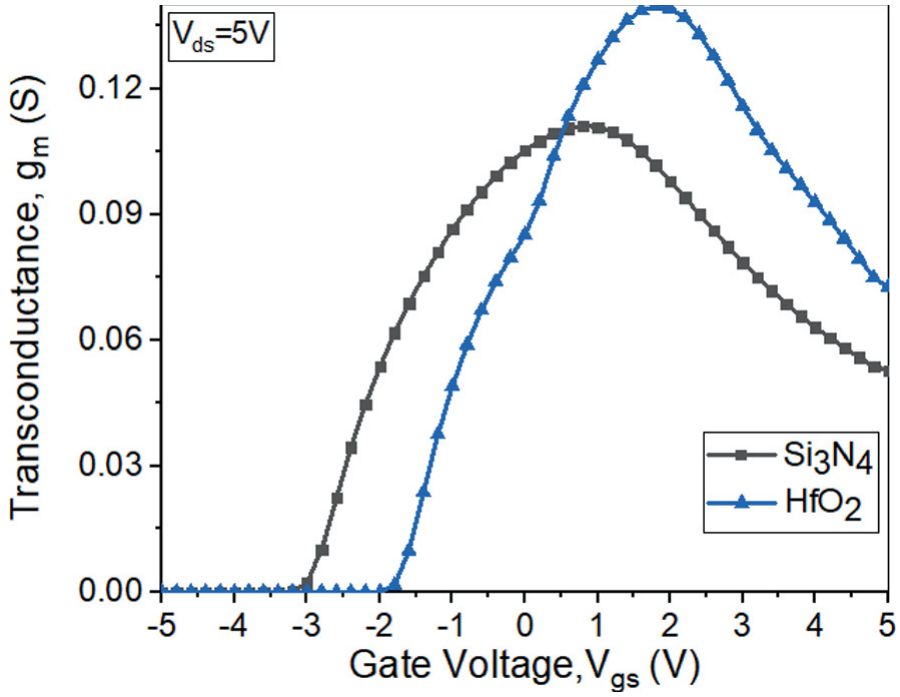

Fig. 4 Transconductance (g_m) versus gate voltage (V_g)

A higher value of g_m is depicted for a better response of the device. The g_m value of the proposed device is found to be 0.15S/μm (Fig. 4). Output conductance, g_0, is successive change in output current with respect to change in drain to source voltage, keeping gate-source voltage constant. g_0 must be as low as possible for better performance of the device. The graph (Fig. 5) indicates output conductance to be low for Si_3N_4 as compared to HfO_2.

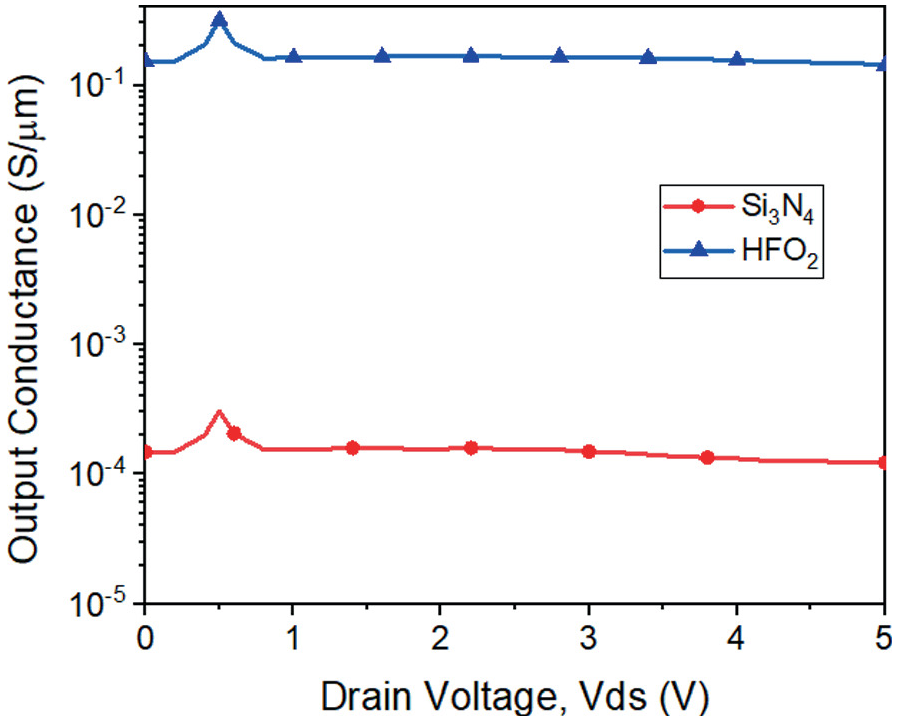

Fig. 5 Output conductance (S/μm) versus drain voltage (V_{ds})

The gate-to-gate capacitance is reduced for the increasing gate biasing and drain biasing values (V_{ds} = 5 V). The gate capacitance is responsible for the device's lower signal analysis and RF performance analysis of the proposed HEMT. Figure 6 shows the gate capacitance (C_{gg}) versus gate voltage (V_g) at V_{DS} = 5 V.

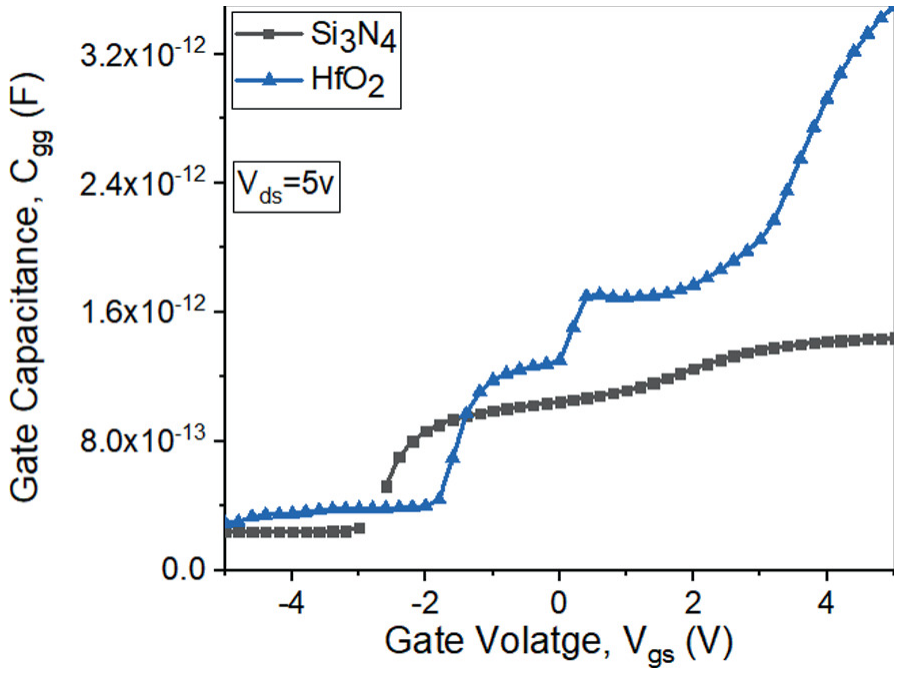

Fig. 6 Capacitance voltage characteristics of β-Ga_2O_3

G_{ds} is defined as the derivative of drain current and drain voltage. G_{ds} is also called output transconductance. For better performance of the device, G_{ds} should be high. It decides the ON-state resistance (R_{on}) of the device and is inversely proportional to G_{ds} [20]. Due to the larger drain current (I_d) in HfO_2-based device, the R_{on} is low and is shown in Fig. 7. It decides the ON-state resistance (R_{on}) of the device, which is inversely proportional to G_{ds}. Due to the larger drain current of HfO_2-based device, the R_{on} is low and is shown in Fig. 7. The proposed device I_{on}/I_{off} ratios acquired for different dielectric and passivation layers are demonstrated in Fig. 8. For all scenarios, a more significant I_{on}/I_{off} value of 10^9 is obtained that is reasonably required for various applications related to power devices.

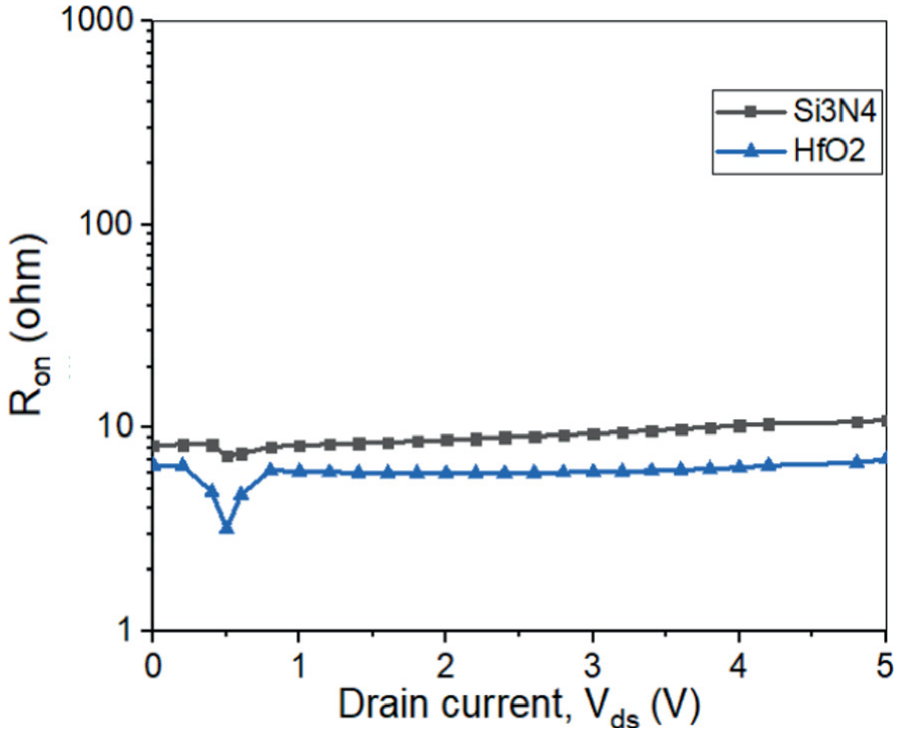

Fig. 7 R_{on} as a function of drain current

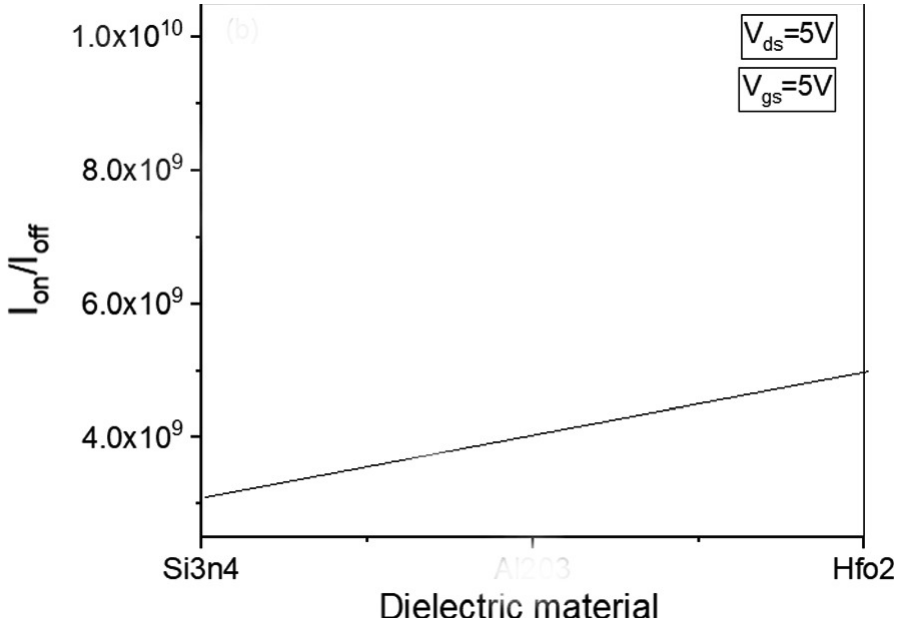

Fig. 8 I_{on}/I_{off} versus Dielectric material at V_{gs} = 5 V and V_{ds} = 5 V

The response of HfO_2-based device is faster than Si_3N_4. For better performance of the device, G_{ds} should be high.

4 Conclusion

The sky is the limit for research on β-Ga_2O_3 material with its distinct characteristics. The proposed β-Ga_2O_3 HEMT is simulated for Si_3N_4 and HfO_2 as a dielectric at the interface of AlN and the gate of the device. The transconductance is found to be steeply raised at lower drain biasing with higher mobility in 2DEG devices, which signifies the motive of the proposed HEMT device. The lower gate capacitance values ensured more preliminary signal analysis and RF performance analysis of the proposed HEMT in future microwave applications.

References

1. M. Higashiwaki, K. Sasaki, M. Kuramata, A. Hisahi, T. Masui, S. Yamakoshi, Recent progress in Ga_2O_3 power devices. Semicond. Sci. Technol. **31**(3) (2016)

2. GalliumOxide (Ga_2O_3) metal oxide field effect transistors on single crystal β-Ga_2O_3(010) substrates. Appl. Phys. Lett. **100**(013504) (2012)

3. T. Wadhera, G. Wadhwa, T.K. Bhardwaj, D. Kakkar, B. Raj, *Silicon*, 1–9 (2020)

4. T. Wadhera, D. Kakkar, G. Wadhwa, B. Raj, J. Electron. Mater. **48**(12), 7635–7646 (2019) [Crossref]

5. K. Sasaki, M. Higashiwaki, A. Kuramata, T. Masui, S. Yamakoshi, Ga_2O_3 Schottky barrier diodes fabricated by using single crystal β-Ga_2O_3 (010) substrates. IEEE Electron Device Lett. **34**(4), 493–495 (2013) [Crossref]

6. M. Higashiwaki, K. Sasaki, A. Kuramata, T. Masui, S. Yamakoshi, Gallium oxide(Ga_2O_3) metal oxide field effect transistors on single crystal β-Ga_2O_3(010) substrates. Appl. Phys. Lett. **100**(013504), 2012 (2013)

7. A.J. Green, K.D. Chabak, M. Baldini, N. Moser, R. Gilbert, R.C. Fitch, G. Wagner, Z. Galazka, J. McCandless, A. Crespo, K. Leedy, G.H. Jessen, Beta-Ga2O3 MOSFETs for radio frequency operation. IEEE Electron Device Lett. **38**(6), 790–793 (2017) [Crossref]

8. M. Singh, M.A. Casbon, M.J. Uren, J.W. Pomeroy, S. Dalcanale, S. Karboyan, P.J. Tasker, M.H. Wong, K. Sasaki, A. Kuramata, S. Yamakoshi, M. Higashiwaki, M. Kuball, Pulsed large signal RF performance of field-plated Ga_2O_3 MOSFETs. IEEE Electron Device Lett. **39**(10), 1572–1575 (2018) [Crossref]

9.

K. Shinohara et al., Scaling of GaN HEMTs and Schottky diodes for sub millimeter-wave MMIC applications. IEEE Trans. Electron Devices **60**(10), 2982–2996 (2013)
[Crossref]

10. M.J. Kumar, A. Chaudhry, IEEE Trans. Electron Devices **15**, 569–574 (2004)
[Crossref]

11. G. Wadhwa, B. Raj, J. Electron. Mater. **47**(8), 4683–4693 (2018)
[Crossref]

12. A. Chaudhry, M.J. Kumar, IEEE Trans. Device Mater. Reliab. **4**(1), 99–109 (2004)
[Crossref]

13. S. Kumar, R. Soman, A.S. Pratiyush, R. Muralidharan, D.N. Nath, A Performance comparison between beta-Ga_2O_3 and GaN HEMTs. IEEE Trans. Electron Devices **66**(8), 3310–3317 (2019)
[Crossref]

14. V. Sandeep, J.C. Pravin, J. Nano Electron. Phys. **13**(4) (2021)

15. J.C. Pravin, D. Nirmal, P. Prajoon, J. Ajayan, Physica E: Low Dimension Nanostructure 83.95 (2016)

16. J. Robertson, High Dielectric Constant Oxides. Eur. Phys. J. Appl. Phys. **28**, 265–291 (2004)
[Crossref]

17. U. Pachauri, P. Joshi, N. Arora, Theoretical Model for size, dimension and shape effect on behavior of semiconductor materials. Appl. Phys. A **126**, 253 (2020)
[Crossref]

18. T. Ishigaki, R. Tsuchiya, Y. Morita, H. Yoshimoto, N. Sugii, T. Iwamatsu, H. Oda, Y. Inoue, T. Ohta, T. Hiramoto, S. Kimura, Solid-State Electron. **53**(7), 717–722 (2009)
[Crossref]

19. A. Mohamed et al., RF performance of Trigate GaN HEMTs. IEEE Trans Electron Dev. **63**(11), 4255–4261 (2016)
[Crossref]

20. A.J. Green et al., 3.8-MV/cm breakdown strength of MOVPE-grown Sn-doped β-Ga2O3 MOSFETs. IEEE Electron Device Lett. **37**(7), 902–905 (2016)
[Crossref]

T. R. Lenka, H. P. T. Nguyen (eds.), *HEMT Technology and Applications*, Springer Tracts in Electrical and Electronics Engineering
https://doi.org/10.1007/978-981-19-2165-0_7

3D Simulation Study of Laterally Gated AlN/β-Ga_2O_3 HEMT Technology for RF and High-Power Nanoelectronics

Rajan Singh[1] ✉, Trupti Ranjan Lenka[1] ✉ and Hieu Pham Trung Nguyen[2] ✉

(1) Microelectronics and VLSI Design Group, Department of Electronics and Communication Engineering, National Institute of Technology Silchar, Silchar, Assam, 788010, India
(2) Department of Electrical and Computer Engineering, New Jersey Institute of Technology, Newark, New Jersey 07102, USA

✉ **Rajan Singh (Corresponding author)**
Email: rajan_rs@ece.nits.ac.in

✉ **Trupti Ranjan Lenka**
Email: trlenka@ieee.org

✉ **Hieu Pham Trung Nguyen**
Email: hieu.p.nguyen@njit.edu

Abstract
In this work, we present the effect of buried gate dimensions on electron mobility in a laterally gated AlN/β-Ga_2O_3 high-electron-mobility-transistor (HEMT) using 3D numerical simulations. The recessed parts of the gate laterally control the two-dimensional-electron-gas (2DEG) density in the channel as opposed to vertical control in the conventional planar HEMT. The constant low-field

mobility model accounting for lattice temperature and field-dependent mobility model accounting for negative differential carrier mobility are evoked to analyze the electric field and carrier concentration by varying the channel width (W_G). A maximum drain current density of 0.8 and ~1 A/mm is obtained using a constant low-field and field-dependent mobility model, respectively, in the device with a gate length (L_G) of 0.1 μm and channel width of 100 nm. It is found that with increasing bias voltage, electron mobility starts decreasing due to rising lattice temperature in the constant low-field mobility model, whereas higher electric field-led carrier velocity saturation is attributed to lower mobility in the field-dependent mobility model.

Keywords 3D Simulation – 2DEG – β-Ga_2O_3 – AlN – Linearity – Lateral-Gate HEMT

1 Introduction

Ultra-wide bandgap semiconductor material gallium-oxide (Ga_2O_3) has been garnering a lot of attention for its excellent material properties for high-voltage and high-frequency power applications. Due to being most thermally stable, the β-phase of Ga_2O_3 is most studied as well as reported, over its four other polymers. β-Ga_2O_3 has a large bandgap of ~4.9 eV, and an estimated critical field up to 8 MV/cm [1] provides enough room for lateral scaling of the small-scale devices for superior RF performances. Apart from the availability of high-quality inexpensive native substrates, a wide variety of n-type dopants with controllable doping concentrations in the range of 10^{15} to 10^{20} cm^{-3} provides β-Ga_2O_3 an edge over other existing wideband technologies [2]. However, multiple phonon scattering and large effective mass led to low electron mobility of ~200 cm^2 V^{-1} s^{-1} [3]. In addition, it has a low thermal conductivity and anisotropic values are reported around 0.16 and 0.21 W m^{-1} K^{-1} [4], which necessitates device-level thermal management for efficient and safe device operations at high voltages.

On the back of high mobility and large carrier density in the form of a 2DEG channel, GaN HEMT devices have shown tremendous performance in the field of high frequency and power electronics

applications. However, bias-dependent behavior of transconductance, i.e., sudden fall in E_g values with increasing V_{DS} restricts linearity of the transistors, and is widely reported [5–7]. This poor linearity is attributed to the dynamic access resistance, which increases with output drain current [5]. To circumvent the effect and improve the linearity, different structures like self-aligned [8], access-region-gap [9], graded as well as coupling channel HEMTs [10, 11] and 3D gate HEMTs [12] are proposed. Since electron mobility has a profound effect on device performance, it should be thoroughly investigated under different applicable mobility models. In the case of β-Ga_2O_3, lattice temperature increases at higher currents due to its low thermal conductivity and finally, mobility degrades. On the other hand, high-field transport in β-Ga_2O_3 shows negative differential conductivity beyond 200 kV/cm [13]. Analysis of electron mobility and the subsequent effect on output current under these two different transport characteristics lay the motivation of this work.

Herein, we propose AlN/β-Ga_2O_3 HEMT with a lateral gate structure, and the effect of two different mobility models on electron mobility are analyzed using 3D device simulations. Figure 1 shows the 3D schematic of laterally gated AlN/β-Ga_2O_3 HEMT. The gate metal is placed between drain and source contacts and rests on the AlN epitaxy, similar to the planer HEMT. The gate metal also extends up to the β-Ga_2O_3 buffer layer from both sides with lateral spacing or channel width (W_C) of 100 nm. The gate (head) length (L_G) of 100 nm is fixed for all types of analysis performed in this work. Gate metal width $d = W_C/2$ penetrates the β-Ga_2O_3 buffer layer up to a fixed depth of h = 200 nm. Nitride insulator (Si_3N_4) of thickness 100 nm is used for surface passivation. Strong polarized III-nitride—AlN material of thickness 22 nm is used as a highly scalable barrier layer, which ensures good 2DEG density in the order of 10^{13} cm^{-2}. Equal gate-source (L_{GS}) and gate-drain length (L_{GD}) of 0.7 μm are used to calibrate the simulation results with the reported experimental data [14]. Gate electrode is considered to be Schottky with a barrier height of 1.0 V and source/drain electrodes are set as ohmic with a contact resistance of 0.4 Ω mm as given in the experimental β-Ga_2O_3 device [15]. Source and

drain access regions are doped with n-type dopants having a Gaussian profile and concentration of 1×10^{19} cm^{-3}. A 2D schematic of the investigated device is shown in Fig. 2.

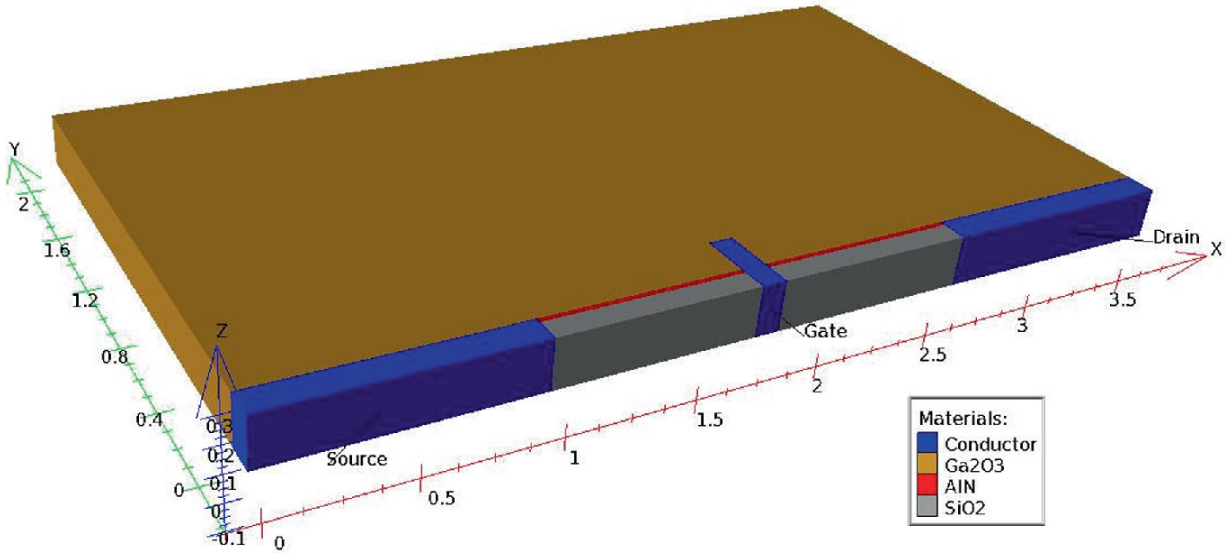

Fig. 1 3D schematic of the investigated laterally gated AlN/β-Ga_2O_3 HEMT

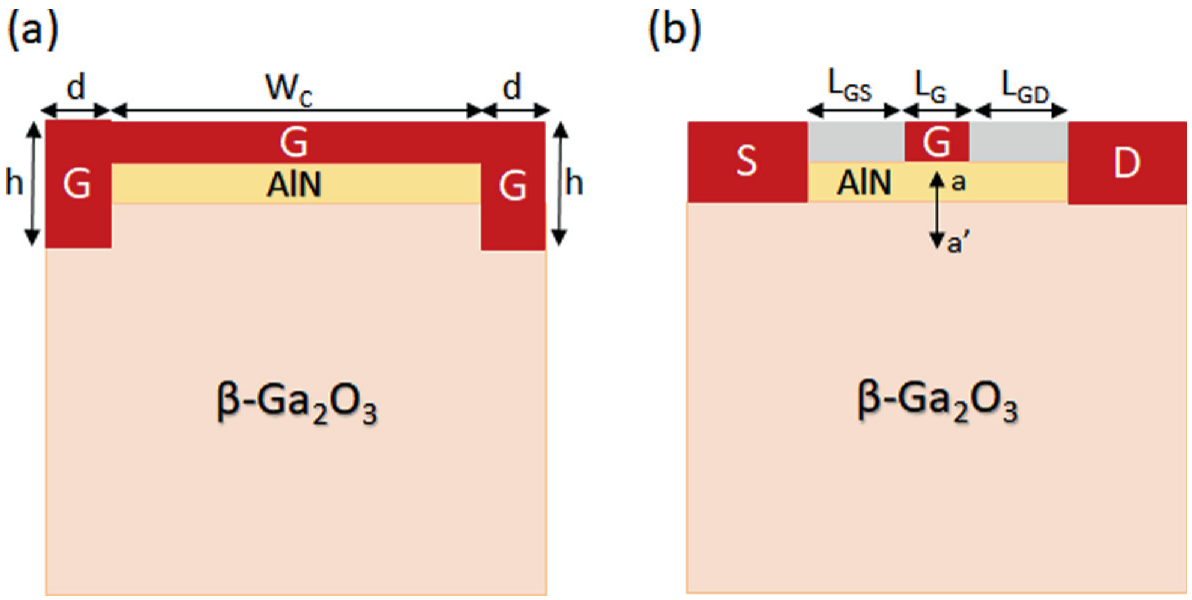

Fig. 2 2D schematic of the investigated device **a** *Y*–*Z* cut plane view with fixed position *X* = 1.75 µm, **b** *X*–*Y* cut plane view with fixed position *Z* = 0.1 µm

2 3D Simulation Framework and Mobility Models

The device structure file is designed as per the material epitaxial sequence, doping, and electrode specifications mentioned above. The β-Ga_2O_3 material is considered a user-defined material in ATLAS [16], and its different properties are calculated and taken from [17, 18]. Table 1 shows the β-Ga_2O_3 material property used in the simulations. The different physics-based models—Shockley–Read–Hall (SRH) for carrier recombination, Boltzmann statistics for carrier calculations. The two different mobility models—*LAT.TEMP* and *FLDMOB* accounting for heat flow in the device and negative differential conductivity (NDC), respectively, are evoked. The mobility models are described next mentioning all the user-defined model parameters used in simulations.

Table 1 Material property of β-Ga_2O_3 [17, 18]

Symbol	Quantity	Values
E_g	Energy bandgap	4.9 eV
χ	Electron affinity	3.15 eV
m_e	Electron effective mass	0.25 m_0
D	Density of states	1.045×10^{18} m^{-2} V^{-1}
N_C	Conduction band density	3.13×10^{18}
N_V	Valence band density	2.86×10^{18}
ε_r	Relative permittivity	10
a_0	Lattice constant	3.04
μ_{n0}	Electron mobility	140 cm^2 /Vs
μ_{p0}	Hole mobility	50 cm^2 /Vs

The default low-field mobility model [16] for electrons that takes account of heat flow in the investigated device is given as

(1)

$$\mu_{\mathrm{n0}}(T_{\mathrm{L}}) = \mathrm{mun}\left(\frac{T_{\mathrm{L}}}{300}\right)^{t\_\mathrm{mun}}$$

where T_{L} denotes the lattice temperature in degrees Kelvin and parameters $\mathrm{mun} = 140\ \mathrm{cm}^2/\mathrm{V\,s}$ [19] and $t\_\mathrm{mun} = 2.0$ [20]. The low thermal conductivity of β-Ga_2O_3 severely affects the high-voltage operations due to the rise in lattice temperature. To improve the device performance, the applied model provides temperature distribution across the lattice structure, which helps the efficient design of device-level thermal management systems.

The field-dependent mobility model [13] accounting for negative differential mobility is given as

$$\mu_n(E) = \frac{\mu_{n0} + \frac{v_{\mathrm{sat}\_n}}{E}\left(\frac{E}{E\_\mathrm{crit}\_n}\right)^{\gamma_n}}{1 + \left(\frac{E}{E\_\mathrm{crit}\_n}\right)^{\gamma_n}} \tag{2}$$

where $\mu_{n0} = 140\ \mathrm{cm}^2/\mathrm{V\,s}$ is the low-field electron mobility, $v_{\mathrm{sat}\_n} = 1.5 \times 10^7 \mathrm{cm/s}$ is the electron saturation velocity, constant $\gamma_n = 2.47$, and $E\_\mathrm{crit}\_n = 1.54 \times 10^5\ V/\mathrm{cm}$. All user-defined parameters for this model are taken from [13]. As electron mobility in bulk β-Ga_2O_3 single-crystal is reported quite low ~200 cm^2/Vs [3] however, reasonable high electron velocity ~1.5 × 10^7 cm/s in β-Ga_2O_3 FETs [19]. Furthermore, a peak velocity of 2 × 10^7 cm/s at an electric field of 200 kV/cm in β-Ga_2O_3 is reported and velocity-field characteristics exhibited velocity decreased after peaking out at 200 kV/cm [13]. This field-dependent mobility model efficiently captures these velocity features. Since the 2-DEG density is critical in HEMTs performance, the amount of band bending at the heterointerface is equally important. The higher the band alignment between heterostructure constituents, the higher value of confined 2-

DEG density is anticipated [2]. The study of band alignment and measurement of conduction band offset (CBO) ΔE_C in AlN/β-Ga_2O_3 heterostructure is widely reported in [21–23].

Here, for the analyzed device, the energy band diagram, band bending led CBO, and electron concentration at the heterointerface are shown in Fig. 3.

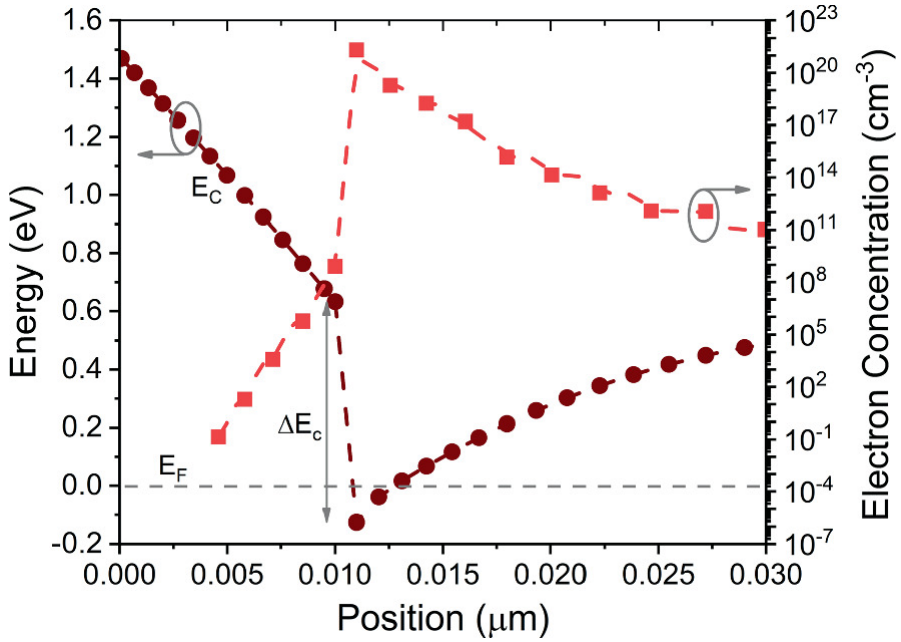

Fig. 3 Energy band diagram and electron concentration of AlN/β-Ga_2O_3 HEMT below the gate obtained along cutline a-a' shown in Fig. 2. Peak electron concentration of ~10^{21} cm^{-3}, and ΔE_C of ~0.8 eV is estimated

3 Results and Discussion

The device performance is investigated by applying two different mobility models. The model details and user-defined parameters are given in the previous section. The channel width W_C of the simulated device is increased from 100 to 200 nm in the step of 50 nm. The gate length L_G = 100 nm, and penetration depth h = 200 are kept fixed. The simulated I_D–V_G characteristics of the proposed device are shown in Figs. 4 and 5. As the W_C increases, the maximum drain current increases for both models, albeit with 25% higher currents in the field-dependent mobility model. Since L_G is fixed, threshold voltage (V_{OFF})

becomes more negative corresponding to higher W_C. It is due to reduced control of the gate over the channel.

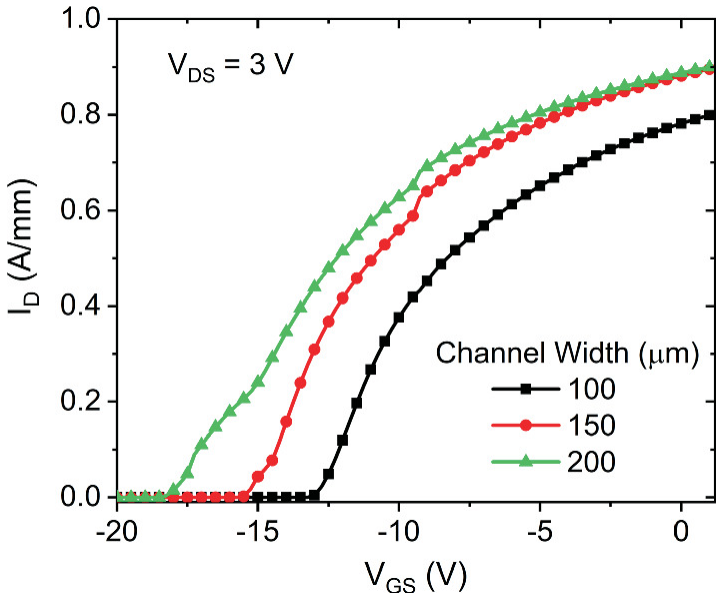

Fig. 4 Simulated transfer characteristics of the proposed AlN/β-Ga_2O_3 HEMT considering low-field mobility model accounting for heat flow in the structure

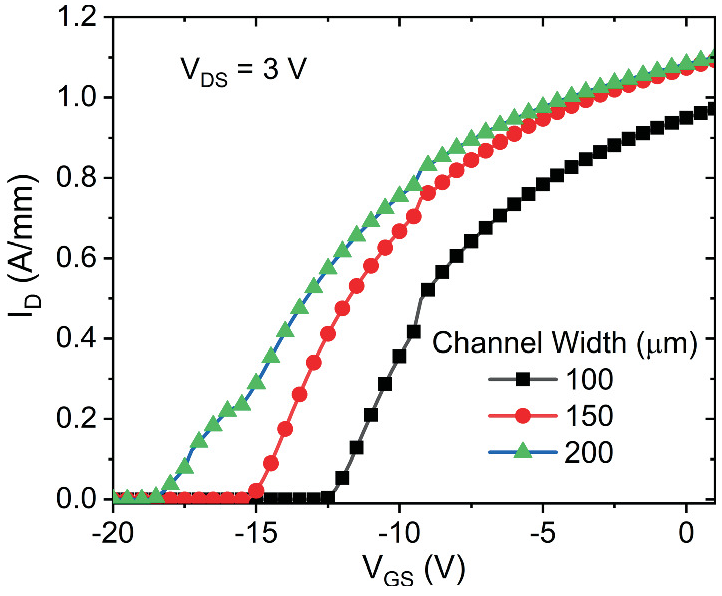

Fig. 5 Simulated transfer characteristics of the proposed AlN/β-Ga_2O_3 HEMT considering a high-field mobility model accounting for negative differential conductivity

Next, to analyze the effect of different mobility models on the electric field and electron concentration in the channel, both the

quantities are extracted in channel 10 nm below the interface from source to drain end. The peak electric field under the gate is estimated greater than 3 MV/cm for both the mobility models corresponding to $V_{GS} = 0$ V. As V_{GS} becomes more negative, lower values of peak electric field are estimated, and are equal to 0.5 and 0.75 MV/cm for low-field and field-dependent mobility models, respectively, corresponding to $V_{GS} = -15$ V. It is also observed that there is slight dispersion in peak electric values for lower values of V_{GS}. Figure 6 shows the electric field profile in the channel extracted from different structural files saved at $V_{GS} = 0, -5, -10, -15$ V. It is worth noting that for β-Ga_2O_3 electron velocity $\sim 1.5 \times 10^7$ cm/s peaks out at 200 kV/cm under high-field transport [13].

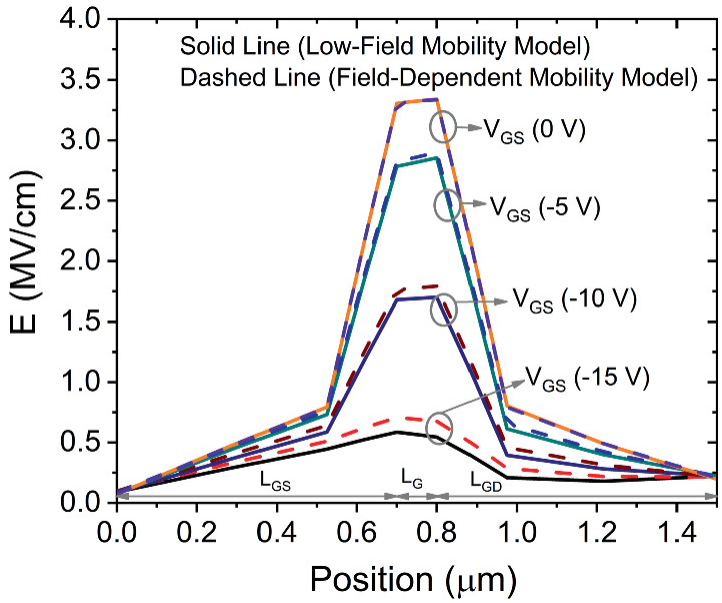

Fig. 6 Simulated electric field profile along the channel for different V_{GS}; peak values of the electric field under the gate and symmetrical profile under drain and source access region are observed ($V_{DS} = 3$ V)

Since output current is directly proportional to electric field across the channel and electron concentration in the channel. Next, electron concentration is extracted along the channel from the source to drain below 10 nm from the interface for both mobility models. Electron concentration profiles related to both the models are extracted at $V_{GS} = 0, -15$ V, and fixed V_{DS} of 3 V, shown in Fig. 7. Peak electron

concentration of ~10^{19}, ~10^{18} cm^{-3} is obtained at the source-, drain-gate end for both the mobility models. Symmetrical electron concentration profile about the gate—highest at the source and drain end and lowest under the gate is observed, however, the respective values are at least one order higher relating to the field-dependent mobility model over the low-field mobility model.

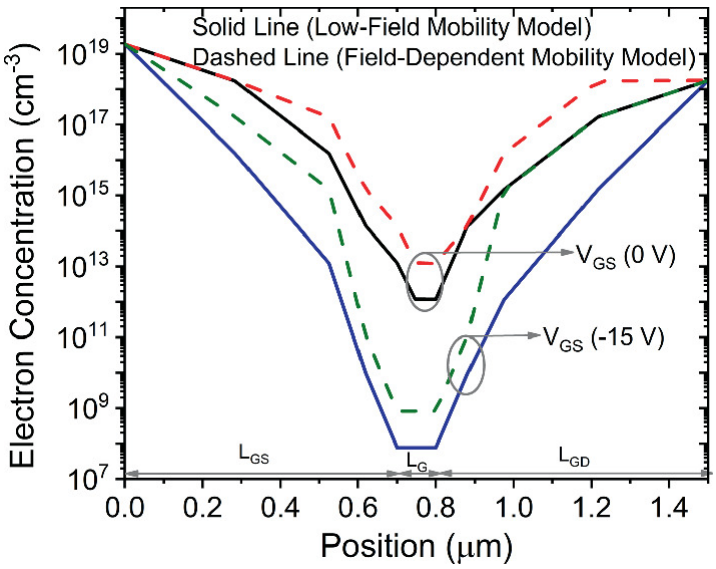

Fig. 7 Electron concentration extracted along the channel for V_{GS} = 0 and −15 V under two different mobility models (V_{DS} = 3 V)

It is worth noting that mobility degrades with increasing gate voltage for both mobility models, however, the underlying reasons are different. In the case of field-dependent mobility, average peak velocity starts decreasing beyond electric field ≥200 kV and hence mobility degrades [13]. On the other hand, for low-field mobility which accounts for lattice temperature, mobility decreases with rising lattice temperature as per relation (1).

The peak lattice temperature is extracted from the simulated structure files saved at different V_{GS} and are shown in Fig. 8. It can be seen that peak lattice temperature at V_{GS} = 0 V is the highest among other recorded values. At lower gate voltages, say V_{GS} = −15 V, there is almost a 4% drop in maximum temperature is estimated. In this way, results from (1) got validated from simulation results.

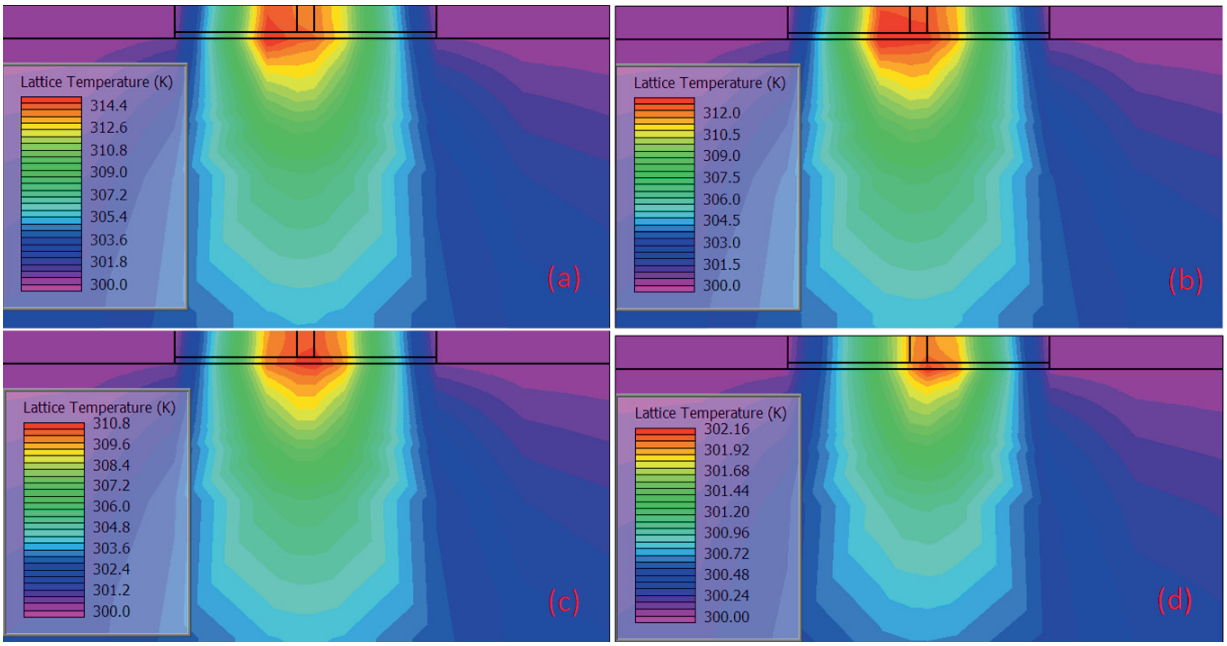

Fig. 8 Lattice temperature contours corresponding to device with L_G = 0.1 µm, W_C = 150 µm, extracted at V_{DS} = 3 V, and V_{GS} = 0 V (**a**), −5 V (**b**), −10 V (**c**), −15 V (**d**)

4 RF Characteristics

The small-signal high-frequency response of the proposed device is also analyzed, and cutoff frequency (f_T) as well as maximum oscillation frequency (f_{MAX}) are estimated. The device with gate-length L_G = 0.1 µm and channel width W_C = 0.1 µm. The drain bias V_{DS} = 3 V is kept fixed, while gate bias is equal to the corresponding peak transconductance value. As shown in Fig. 9, with respect to peak transconductance, V_{GS} is equal to −11, and −12 V for field-dependent and low-field models, respectively. Transconductance curves for both mobility models exhibit 'peaky' behavior, i.e., sudden fall from peak value as gate voltage increases. This nature of g_m versus V_{GS} is responsible for the poor linearity of HEMT devices, and is widely reported. Several studies attributed this nonlinearity to dynamic source resistance or source choking effect.

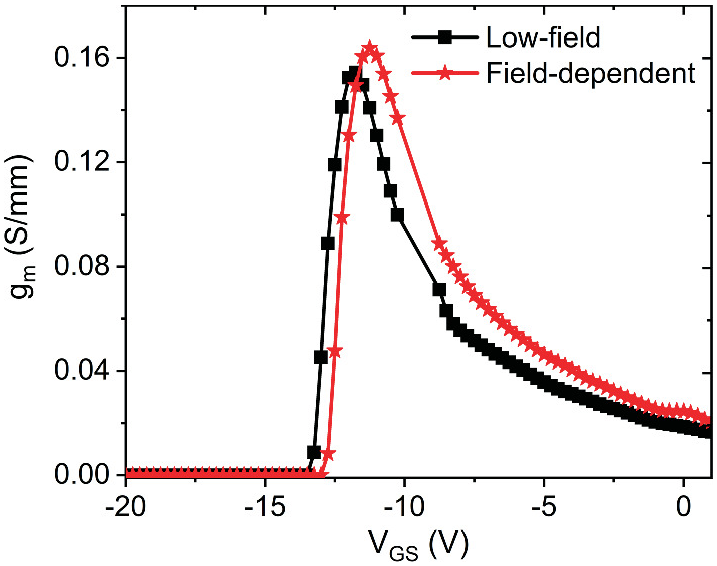

Fig. 9 Transconductance (g_m) versus gate voltage (V_{GS}) for the proposed device with low-field and field-dependent mobility models, and channel width (W_C) = 100 nm

The small-signal high-frequency response for the proposed device is investigated to estimate the cutoff frequency f_T and maximum frequency of oscillation f_{MAX} and is shown in Figs. 10 and 11 considering the field-dependent and low-field mobility models, respectively. From the 'Gain' versus 'Frequency' plots shown above, f_T is found to be 21 and 26 GHz, while f_{MAX} is equal to 40 and 61 GHz, respectively, for field-dependent and low-field mobility models. The estimated values here are in good agreement with values reported for the β-Ga_2O_3 experimental device [15]. However, these values are significantly lower than theoretically estimated values ~200 GHz for f_T [24], considering the saturation velocity $v_{sat} = 1.5 \times 10^7$ cm/s for β-Ga_2O_3 devices. Here, for the proposed device design, lateral depletion of the charge carriers under the gate in the channel reduces the channel conductance (Fig. 7). Furthermore, as source resistance RS increases with reduced carrier density ns in the channel, consequently, DC, as well as RF performances, are affected.

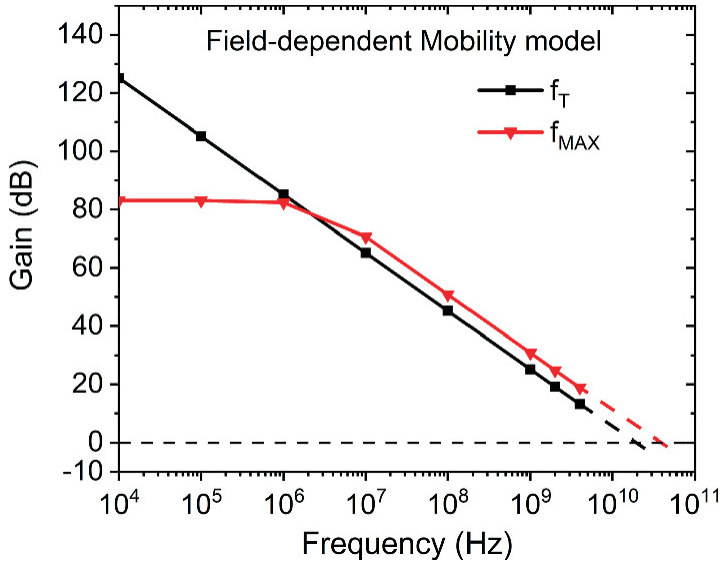

Fig. 10 Current gain (h_{21}) versus frequency (f) plot showing unity-gain cutoff frequency (f_T) and maximum oscillation frequency (f_{MAX}) for a field-dependent model

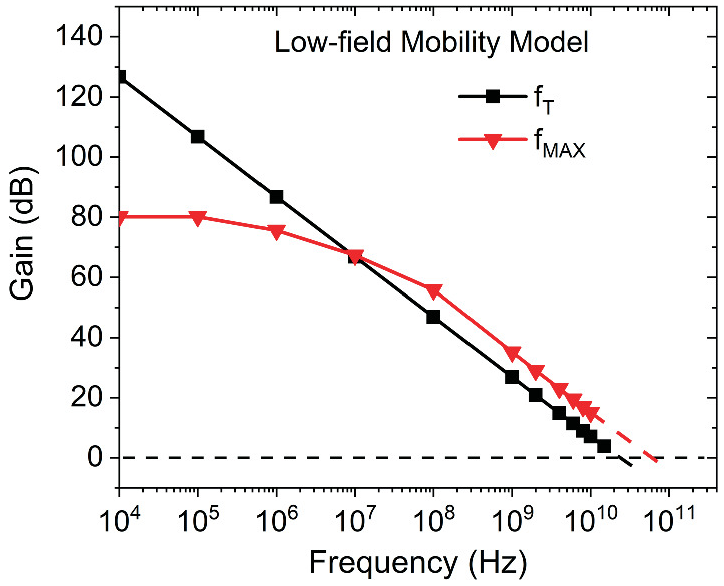

Fig. 11 Cutoff frequency (f_T) and maximum oscillation frequency (f_{MAX}) for the low-field mobility model

5 Conclusion

In conclusion, we reported DC and RF performance analysis of laterally gated AlN/β-Ga_2O_3 high-electron-mobility transistor using 3D numerical simulations under two different mobility models related to β-Ga_2O_3 material. Low-field mobility model accounting for heat flow in

the device and the field-dependent mobility model, which accounts for negative differential conductivity have been evoked to analyze the device performance. Transfer characteristics of the proposed device are analyzed corresponding to duo mobility models evoked individually under fixed gate length while varying the channel width. As channel width increases, lateral control of the gate abates and off-voltage of the transistor rises. Lateral depletion of carriers showed better gate control near the subthreshold region and led to the improved subthreshold slope. Related to each mobility model, electron concentration and electric field values are estimated along the channel by varying the gate-bias voltage and fixed V_{DS}. Small-signal high-frequency analyses are performed to estimate the cutoff and maximum oscillation frequency for the laterally gated AlN/β-Ga_2O_3 HEMT. It is observed that β-Ga_2O_3 poor thermal conductivity caused higher lattice temperature at increased voltages, and carrier velocity saturation at higher electric fields affected the device performance. These results would be helpful to understand the electron mobility in the emerging β-Ga_2O_3 device technology.

Acknowledgements

The authors acknowledge the National Institute of Technology Silchar for providing the necessary facilities to carry out the research with international collaboration with the New Jersey Institute of Technology, New Jersey, USA.

References

1. M. Higashiwaki, K. Sasaki, A. Kuramata, T. Masui, S. Yamakoshi, Gallium oxide (Ga_2O_3) metal-semiconductor field-effect transistors on single-crystal β-Ga_2O_3 (010) substrates. Appl. Phys. Lett. **100**(1), 3–6 (2012). https://doi.org/10.1063/1.3674287 [Crossref]

2. R. Singh et al., The dawn of Ga_2O_3 HEMTs for high power electronics—a review. Mater. Sci. Semicond. Process. **119**, 105216 (2020). https://doi.org/10.1016/j.mssp.2020.105216

3. N. Ma et al., Intrinsic electron mobility limits in β-Ga_2O_3. Appl. Phys. Lett. **109**(21), 212101 (2016). https://doi.org/10.1063/1.4968550 [Crossref]

4. M.D. Santia, N. Tandon, J.D. Albrecht, Lattice thermal conductivity in β-Ga_2O_3 from first principles. Appl. Phys. Lett. **107**(4) (2015). https://doi.org/10.1063/1.4927742

5. T. Palacios et al., Influence of the dynamic access resistance in the g_m and f_T linearity of AlGaN/GaN HEMTs. IEEE Trans. Electron Devices **52**(10), 2117–2122 (2005). https://doi.org/10.1109/TED.2005.856180
[Crossref]

6. T. Fang, R. Wang, G. Li, H. Xing, S. Rajan, D. Jena, Effect of optical phonon scattering on the performance limits of ultrafast GaN transistors. *Device Research Conference*, vol. 33(5) (2011), pp. 273–274. https://doi.org/10.1109/DRC.2011.5994529

7. C.H. Chen et al., The causes of GaN HEMT bell-shaped transconductance degradation. Solid. State. Electron. **126**, 115–124 (2016). https://doi.org/10.1016/j.sse.2016.09.005
[Crossref]

8. K. Shinohara et al., Self-aligned-gate GaN-HEMTs with heavily-doped n+-GaN ohmic contacts to 2DEG, in *2012 International Electron Devices Meeting* (2012), pp. 27.2.1–27.2.4. https://doi.org/10.1109/IEDM.2012.6479113

9. R. Singh, T.R. Lenka, H.P.T. Nguyen, Optimization of dynamic source resistance in a β-Ga_2O_3 HEMT and Its effect on electrical characteristics. J. Electron. Mater. **49**(9), 5266–5271 (2020). https://doi.org/10.1007/s11664-020-08261-0
[Crossref]

10. S. Bajaj et al., Graded AlGaN channel transistors for improved current and power gain linearity. IEEE Trans. Electron Devices **64**(8), 3114–3119 (2017). https://doi.org/10.1109/TED.2017.2713784
[Crossref]

11. H. Lu et al., AlN/GaN/InGaN coupling-channel HEMTs for improved g2098 and gain linearity. IEEE Trans. Electron Devices 1–6 (2021). https://doi.org/10.1109/TED.2021.3082104

12. O. Odabasi et al., AlGaN/GaN-based laterally gated high-electron-mobility transistors with optimized linearity. IEEE Trans. Electron Devices **68**(3), 1016–1023 (2021). https://doi.org/10.1109/TED.2021.3053221
[Crossref]

13. K. Ghosh, U. Singisetti, Ab initio velocity-field curves in monoclinic β-Ga_2O_3. J. Appl. Phys. **122**(3), 035702 (2017). https://doi.org/10.1063/1.4986174
[Crossref]

14. E. Ture et al., Performance and parasitic analysis of sub-micron scaled tri-gate AlGaN/GaN HEMT design. Eur. Microw. Week **2015**, 97–100 (2015). https://doi.org/10.1109/EuMIC.2015.7345077
[Crossref]

15. Z. Xia et al., β-Ga 2 O 3 Delta-doped field-effect transistors with current gain cutoff frequency of 27 GHz. IEEE Electron Device Lett. **40**(7), 1052–1055 (2019). https://doi.org/10.1109/LED.2019.2920366
[Crossref]

16. Device Simulation Software, *ATLAS User's manual* (Silvaco, Santa Clara, CA, USA, 2019)

17. A. Mock et al., Band-to-band transitions, selection rules, effective mass, and excitonic contributions in monoclinic β-Ga_2O_3. Phys. Rev. B **96**(24), 1–14 (2017). https://doi.org/10.1103/PhysRevB.96.245205
[Crossref]

18. S. Poncé, F. Giustino, Structural, electronic, elastic, power, and transport properties of β-Ga_2O_3 from first principles. Phys. Rev. Res. **2**(3), 033102 (2020)
[Crossref]

19. Y. Zhang et al., Evaluation of low-temperature saturation velocity in β-(AlxGa1−x)$2O_3$/Ga_2O_3 modulation-doped field-effect transistors. IEEE Trans. Electron Devices **66**(3), 1574–1578 (2019). https://doi.org/10.1109/TED.2018.2889573
[Crossref]

20. S.A.O. Russell et al., Heteroepitaxial Beta-Ga_2O_3 on 4H-SiC for an FET with reduced self heating. IEEE J. Electron Devices Soc. **5**(4), 256–261 (2017). https://doi.org/10.1109/JEDS.2017.2706321
[Crossref]

21. H. Sun et al., Valence and conduction band offsets of β-Ga_2O_3/AlN heterojunction. Appl. Phys. Lett. **111**(16), 162105 (2017). https://doi.org/10.1063/1.5003930
[Crossref]

22. J.-X. Chen et al., Band alignment of AlN/β-Ga_2O_3 heterojunction interface measured by x-ray photoelectron spectroscopy. Appl. Phys. Lett. **112**(26), 261602 (2018). https://doi.org/10.1063/1.5035372
[Crossref]

23. S. Lyu, A. Pasquarello, Band alignment at β-Ga_2O_3/III-N (III = Al, Ga) interfaces through hybrid functional calculations. Appl. Phys. Lett. **117**(10), 102103 (2020). https://doi.org/10.1063/5.0020442
[Crossref]

24. S. Kumar, R. Soman, A.S. Pratiyush, R. Muralidharan, D.N. Nath, A Performance Comparison Between β-Ga_2O_3 and GaN HEMTs. IEEE Trans. Electron Devices **66**(8), 3310–3317 (2019). https://doi.org/10.1109/TED.2019.2924453
[Crossref]

T. R. Lenka, H. P. T. Nguyen (eds.), *HEMT Technology and Applications*, Springer Tracts in Electrical and Electronics Engineering
https://doi.org/10.1007/978-981-19-2165-0_8

Operation Principle of AlGaN/GaN HEMT

G. Purnachandra Rao[1] ✉, Rajan Singh[1] ✉ and Trupti Ranjan Lenka[1] ✉
(1) Department of Electronics and Communication Engineering, National Institute of Technology Silchar, Silchar, Assam, 788010, India

✉ **G. Purnachandra Rao (Corresponding author)**
Email: gpurna_rs@ece.nits.ac.in

✉ **Rajan Singh**
Email: rajan_rs@ece.nits.ac.in

✉ **Trupti Ranjan Lenka**
Email: trlenka@ieee.org

Abstract

Nowadays, the development of wide bandgap-based devices in power electronics has become more prominent to ameliorate the energy capability of devices. Furthermore, it can help reduce the total energy wastage in the world. Presently, AlGaN/GaN high-electron-mobility transistors (HEMTs) have shown excellent performance on the back of their extraordinary attributes like higher carrier density, and higher channel mobility over traditional wide bandgap devices like AlGaAs/GaAs. Because of the outstanding characteristics of the GaN HEMTs and their composited materials, they are becoming promising devices for the upcoming generation of more power and highest frequency-based implements. This chapter will provide a complete overview of the "Operation Principle of AlGaN/GaN HEMT."

Keywords GaN – HEMT – 2DEG – Polarization

1 Introduction

During the past few years, High-Electron-Mobility Transistors (HEMTs) based on AlGaN/GaN have been meticulously studied due to their basic electrical properties making them captivates for the devices, where high-power applications are needed. Group III-nitrides (AlN, GaN, InN) have become the center of attraction for enormous research. The group III-nitrides have an ultra-large bandgap and can sustain higher temperatures. These attributes are not observed in traditional GaAs, Silicon, and germanium semiconductors. Therefore, GaN HEMTs can withstand higher operating temperatures without the acute need for thermal management.

GaN HEMTs have high carrier density confined in a triangular quantum well, which facilitates higher channel mobility and high saturated electron drift velocity. All these attractive attributes make the GaN-based HEMT devices next-generation high-frequency power devices. This chapter provides information on the working principle of AlGaN/GaN HEMT devices.

2 AlGaN/GaN HEMT Structure

A conventional HEMT design layout using AlGaN/GaN is shown in Fig. 1. It is also similar to the basic AlGaAs/GaAs HEMT. A majority of charge carriers are isolated from ionized impurities, and further heterojunction is formed between the AlGaN and GaN material. And this junction formation is because of their dissimilarities in AlGaN and GaN materials band gaps. This junction leads to the formation of a channel at the midpoint of the AlGaN/GaN heterojunction, shown in Fig. 1. But, AlGaN/GaN HEMT devices are not required for any additional doping [1–5]. In AlGaN/GaN HEMTs, the excess electrons will come from the top layer surface because of the phenomenon caused by wurtzite-shaped GaN, which is known as the creation of spontaneous polarization.

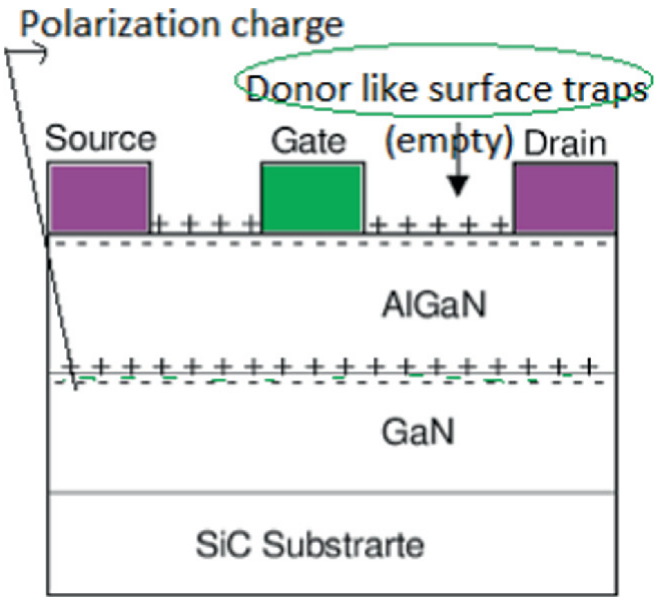

Fig. 1 Schematic representation of polarization charge of GaN-Based HEMT [6]

In the AlGaN HEMT, the top layer is AlGaN, the bottom is GaN, and there is the substrate that is the GaN or something else, which is based on the application of thermal management system [6–8]. The collection of free carriers creates a channel consisting of 2DEG. Figure 1 shows traps on the top layer and a positive charge induced by polarization at the interface of AlGaN/GaN. The 2DEG is confined to the third dimension and freely moves in two directions only. The creation of 2DEG in AlGaN/GaN HEMT is clearly explained with some suitable diagrams in the following sections. The 2DEG concentration is extremely large value of 2.7×10^{13} cm^{-2}, and it is almost 12-fold higher than the AlGaAs and InP-based HEMT devices [9, 10].

3 Polarization Effects

AlGaN/GaN HEMT has an outstanding feature, which can produce 2DEG without any additional doping procedure. This special feature is mainly due to the spontaneous polarization and piezoelectric attributes that originated in III-nitrides [11]. These distinctive qualities are due to the natural formation of the III-nitrides crystal arrangement. Because of an atom's more propensity nature, this can form a bonding between the III group elements with nitrogen. The atoms are being connected in the passion of tetrahedral, which is known by each atom being bonded with

another four atoms. The crystal formation of III-nitrides leads to create spontaneous polarization (PSP) [12–16]. This is mainly because of the powerful electronegativity variation among metal atoms and nitrogen, which impact spontaneous polarization. Epitaxially, GaN flake was accrued normal to exterior facet and has scantiness of inversion uniformity. This resulted in the formation of spontaneous polarization toward the <0001> direction. Figure 2 represents the different polarization fields in AlGaN/GaN HEMT.

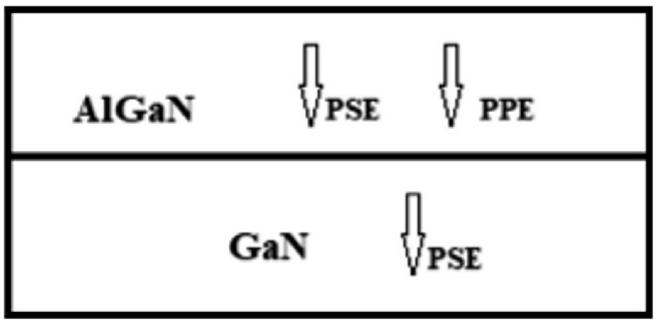

Fig. 2 Spontaneous and piezoelectric polarization fields in the AlGaN/GaN HEMT [11]

The other polarization effect is piezoelectric polarization (PPE), formed due to the strain in epitaxial layers. This piezoelectric field is emerging mainly because of the factors of mechanical deformation and the drawback of regularities. In general, the HEMT is comprised of AlGaN/GaN; the upper layer (AlGaN) is slender and thin when compared with the lower layer, which has GaN. It is assumed that the GaN layer is supposed to be placid sans any other polarization effects. One kind of stress is formed on the AlGaN flake because of the lattice mismatch between the upper and lower layers, resulting in one type of polarization called piezoelectric polarization. The following equation [11] expresses the mathematical representation for piezoelectric polarization.

$$P_{\mathrm{PE}} = 2\varepsilon_a \left(e_{31} - \frac{e_{33} c_{13}}{c_{33}} \right) \tag{1}$$

The above equation gives information about the piezoelectric field induced due to the stress caused by the mismatch in lattice values of AlGaN and GaN layers. In the above expression, "ε_1" is known by the

lattice constant of AlGaN, and e_{31}, e_{33} are the piezoelectric constants of AlGaN and GaN materials. The interface between the barrier (AlGaN layer) and buffer (GaN layer) will incite hiatuses in the polarization. The below expression gives the complete polarization outcome due to the AlGaN and GaN layers. AlGaN manifests positive polarization fields, whereas GaN shows the negative polarization filed at the joint interface surface.

$$\sigma = (P_{\text{SP, AlGaN}} + P_{\text{PE, AlGaN}}) - P_{\text{SP,GaN}} \tag{2}$$

From the above expression [11], it is clearly evident that at the heterointerface of AlGaN/GaN layers, a constant 2DEG can exist. This is due to the spontaneous polarization in the upper layer being more excellent value when compared with the lower material layer.

---

4 Two-Dimensional Electron Gas (2DEG)

2DEG is an acronym for two-dimensional electron gas, which can move in two directions and is limited to a third direction. Figure 3 depicts the band diagram of HEMT-based AlGaN/GaN. Due to its III-nitride intrinsic character called polarization, it can create a conduction path at the interface of the upper and lower material layers. As already discussed in the previous section, the dissimilarity at the joining layers of AlGaN and GaN will result in a net positive charge. The conduction band was dragged toward the bottom so that the electrons would move toward the interface of AlGaN and GaN layers. These electrons are confined and restricted in the potential well of a triangular shape. So finally conduction band is pulled upwards, and the polarization will shift the total negative charges in the plane's direction. The electrons jammed at the joining section are called 2DEG, and these charged particles can be used in the AlGaN/GaN channel [17, 18]. Figure 3 will give the complete pictorial representation of 2DEG formation.

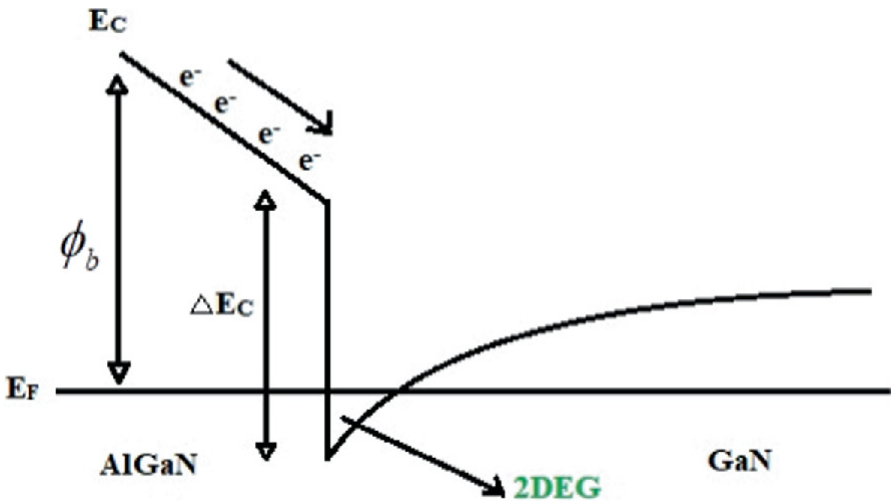

Fig. 3 Band diagram of AlGaN/GaN heterointerface [11]

The following equation [11] gives the mathematical expression for the 2DEG concentration:

$$n_s = \left(\frac{\sigma_{\text{int}}}{q}\right) - \left(\frac{\varepsilon_0 \varepsilon_{\text{r}}}{q^2 t_{\text{AlGaN}}}\right)(q\phi_{\text{b}} + E_{\text{F}} - \Delta E_{\text{C}}) \tag{3}$$

The bandgap energies of AlGaN and GaN materials are not equal due to the lattice difference between the two materials. In the above expression, ΔE_{C} is the energy variation of AlGaN and GaN material, N_1 is the Fermi level with respect to the conduction band of GaN material, $q\phi_{\text{b}}$ is giving the information about the contact of gate terminal Schottky barrier level height which can impact the threshold voltage, t_{AlGaN} is known by the width of the AlGaN material layer, ε_{r} is the dielectric constant, which can control the breakdown field strength, a is known by the charge of an electron and σ_{int} designated by the sheet charge at the joining section of AlGaN and GaN layers. The mathematical expression clearly shows that the sheet charge density is directly proportional to the polarization effect (σ). Mainly high-electronmobility transistors benefit from heteroconfiguration to form a potential well for charged particles; this configuration can create

benefits for electrons that can move in any constraint of two dimensions and are confined to the third direction [19, 20].

4.1 Origin of 2DEG in GaN-Based HEMT

AlGaN/GaN HEMT has an impressive unique behavior, which can develop 2DEG without any extra doping scheme. This distinct feature is mainly due to III-nitride qualities like spontaneous polarization and piezoelectric properties. These two attributes were utterly relying on the structure of III-nitride crystals. 2DEG is a bunch of electrons that are confined in a plane, they can propagate or move around in the *X*- and *Y*-direction, but they cannot propagate through the *Z*-direction so that there will be fewer scatterings from the bulk or any kind of dopants. This 2DEG is escaped from those scattering mechanisms caused by the impurities, and they can gain high mobility [21].

As shown in Fig. 4, GaN atomic structure looks like the wurtzite-shaped structure or crystal lattice. GaN has a non-centrosymmetric manner, which means the atoms surrounding the nitrogen atoms are not symmetry. There is a chance of pulling each other because nitrogen and gallium have different electronegativity. And by that electronegativity, there is a tendency to pull the electrons towards it.

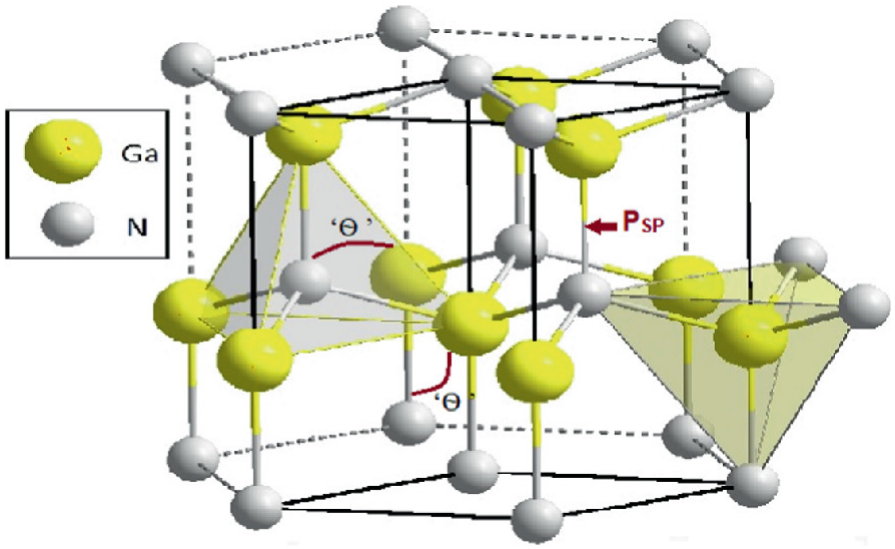

Fig. 4 Atomic Structure of GaN [26]

Due to the difference between electron negativities, the nitrogen is more negative compared to the gallium. This leads to some

spontaneous polarization vector created inside the structure. This polarization remains will be +ve charge and −ve charge. Those charges will be further apart from each other to the similarity of the dipole. This means they can't move around, but they create an electric field inside or an internal electric field. This is called spontaneous polarization. This is happening without applying any kind of pressure or mechanical stress [22].

If we apply some mechanical stress, the angle between those bonds of Gallium and Nitrogen atoms will change. The angle is denoted by "θ." This angle may be increasing or decreasing depending on the tensile stress or compressive stress. Depending upon the stress, there is another polarization vector that will be created. This additional polarization vector is known as the piezoelectric polarization. If the input is pressure or mechanical stress, the output will be some voltage or electric field. So, because of this strain, there will be two different kinds of polarization in GaN. One is piezoelectric, and another is spontaneous. And this whole process is a natural phenomenon [19].

4.2 Doped Barrier Layer

The energy band diagram of AlGaN is shown in Fig. 5. E_C is the conduction band, E_V is the valance band, and E_F is the Fermi level. Here AlGaN is doped with the *n*-type material to create the *n*-type heavily doped material. We can see that the Fermi level is very near the conduction band. The origin of electrons is from doping [12]. There will be a bunch of electrons in the conduction band. +ve and −ve charge in the surface; these charges are bound charges like a dipole.

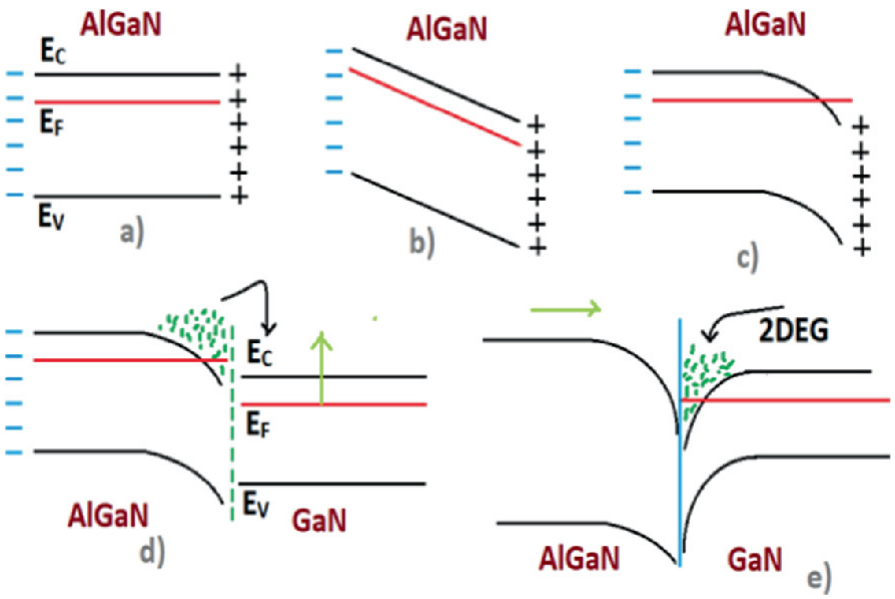

Fig. 5 Schematic diagram for 2DEG origin in doped GaN

These are created by the polarization vectors and existed in AlGaN, because AlGaN is placed on the GaN crystal. Their (AlGaN and GaN) lattice constants are not matched to each other. GaN inserts some kind of tensile strain on the AlGaN. So that there is some polarization because of the caused stress, and this leads to some kind of electric field. This electric field creates band bending at the interface of AlGaN with GaN as per Poisson's equation.

AlGaN is *n*-type doped material which is having high electrons on the top of the conduction band. These bunch of electrons will propagate toward the band bending or interface to make the device balanced so that it creates a −ve charge on the top of AlGaN and +ve charge on the bottom of the material.

When we grow on AlGaN on the GaN, the Fermi levels on both sides are not equally matched. But under thermal equilibrium, i.e., under any extra bias, the two Fermi levels will remain constant throughout the structure. So, therefore, the accumulated charges are collected at the interface. These are −ve electrons.

Because of a huge number of electrons coming from the AlGaN, they will move to the interface and are bent because some +ve charges exist at the interface. The Fermi levels are constant on both sides to make equilibrium. This region of electrons is known as 2DEG. This electron can move in two directions only and be confined to the other directions.

This will create another electric field that is opposite to the previous piezoelectric field.

4.3 Undoped Barrier Layer

In Fig. 6, AlGaN is not doped. So, E_F is in the middle of the conduction band and valance band. The creation of 2DEG doesn't need any kind of intentional doping. This is the primary key point in the GaN-structured HEMT devices. The operation's unique feature is that spontaneous and piezoelectric polarization would create the bending at the interface where we can collect electrons in that bending. AlGaN material has some trap charges on the top of the material. The Fermi level pinning at this trap site is full of electrons; whenever there is bending of bands, it gives the electrons to the conduction band. These electrons will be directed toward the interface of the AlGaN/GaN. These electrons will be accumulated over in the interface of AlGaN/GaN. The Fermi level is coming from the trap sites creates a constant through the region to become an equilibrium position. Here the accumulated electrons are called the 2DEG. These 2DEG or mobile electrons will be bound to the interface only. This means they cannot propagate through the *Z*-direction. But they can travel in the *X*- and *Y*-directions only [16, 23].

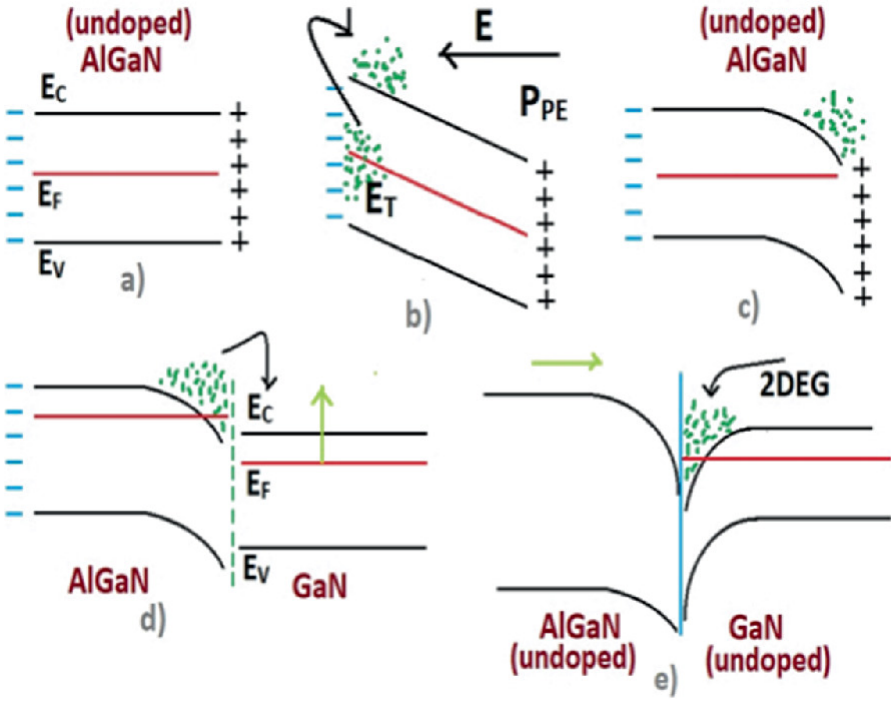

Fig. 6 Schematic diagram for 2DEG origin in undoped GaN

4.4 Energy Band Diagram

HEMTs are mainly using the principle of heterojunctions that are formed by semiconductors, which are having different band gaps between them. In the heterojunctions, the conduction band (E_C) and the valance band (E_V) at the junction point of the wider and narrowband should bend to get continuity in the Fermi level. Excess electrons will have in the upper material because of the heavily doped donor atoms (but in GAN-based HEMT, it is quite different because of the charge caused by polarization in the GaN material). The lower material has a narrow bandgap, lower energy, and no doping or less doping. So, the electrons will transfer from the high state to the lower state of having less energy to form the thermal equilibrium. Due to diffusion, an electric field will be induced between wide bandgap and narrow bandgap materials [17, 24].

This process will continue until concentration on both sides becomes equal, making a junction under thermal equilibrium conditions like in a PN junction. Ultimately, the undoped narrow bandgap material will get excess electrons at the interface, giving a high speed. These electrons can get high mobility because accumulated electrons are free from the scattering effects caused by the donor atoms, which are not in the undoped material. The dissimilarity at the interface of two junctions will form a notch at the center, and this notch can collect electrons from the upper material. The accumulated electrons can give a high level of current due to increased mobility in these HEMT devices. Figure 7 represents the band diagram of a heterojunction in the HEMT's model [7, 8, 25].

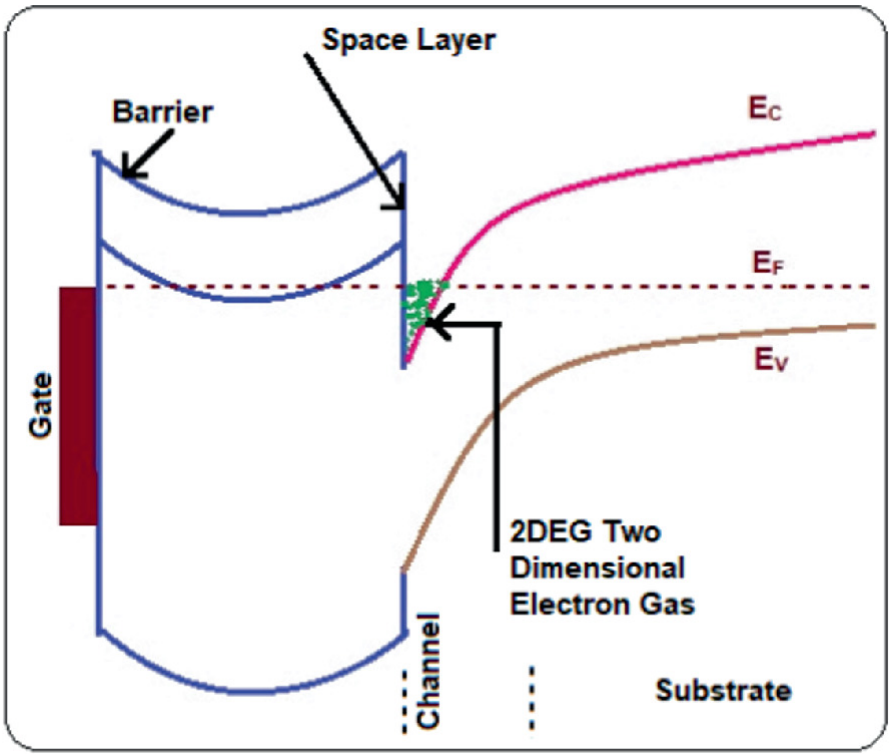

Fig. 7 Energy band diagram of HEMT structure [26]

5 Conclusion

AlGaN/GaN HEMT devices give significant promises for developing more powerful and rapid speed implements working at excessive temperatures compared to traditional devices. On the other side, because of heterojunction, HEMT devices can give a higher speed of charge particle transportation than the other field-effect transistor constructions. This chapter clearly explained the basic structure of HEMT and its working principle in different aspects. Due to the natural material characteristics and device characteristics, AlGaN/GaN HEMT is the best promising device for the next generation of excellent speed, more power, and extreme temperature operations.

References

1. T. Mimura, The early history of the High Electron Mobility Transistor (HEMT). IEEE Trans. Microw. Theory Tech. **50**(3), 780–782 (2002) [Crossref]
2.

T. Mimura, A new field-effect transistor with selectively doped GaAs/n-Al Ga As Heterojunctions. Jpn. J. Appl. Phys. **19**(5), 225–227 (1980)
[Crossref]

3. U.K. Mishra, P. Parikh, Y.-F. Wu, AlGaN/GaN HEMTs—an overview of device operation and applications. Proc. IEEE **90**, 1022–1031 (2002)
[Crossref]

4. C.G. Van de Walle, C. Stampfl, J. Neugebauer, Theory of doping and defects in III-V nitrides. J. Cryst. Growth **189**(190), 505–510 (1998)
[Crossref]

5. M. A. Khan, et al., Observation of a two-dimensional electron gas in low pressure metalorganic chemical vapor deposited GaN/AlGaN heterojunctions. Appl. Phys. Lett. **60**, 3027–3029 (1992)

6. U.K. Mishra, AlGaN/GaN HEMTs—an overview of device operation and applications. Proc. IEEE **90**(6), 1022–1031 (2002)
[Crossref]

7. J.P. Ibbetson, P.T. Fini, K.D. Ness, S.P. DenBaars, J.S. Speck, U.K. Mishra, Polarization effects, surface states, and the source of electrons in AlGaN/GaN heterostructure field effect transistors. Appl. Phys. Lett. **77**, 250–252 (2000)
[Crossref]

8. L. Hsu, W. Walukiewicz, Effect of polarization fields on transport properties in AlGaN/GaN heterostructures. J. Appl. Phys. **89**, 1783–1789 (2001)
[Crossref]

9. M. Li, Y. Wang, 2D analytical model for current–voltage characteristics and transconductance of AlGaN/GaN MODFETs. IEEE Trans. Electron Devices **55**(1), 261–267 (2008)
[Crossref]

10. A. Zhang, L. Zhang, Z. Tang, X. Cheng, Y. Wang, K.J. Chen, M. Chan, Analytical modeling of capacitances for GaN HEMTs, including parasitic components. IEEE Trans. Electron Devices **61**(3) (2014)

11. A.S.A. Fletcher, D. Nirmal, A survey of gallium nitrate HEMT for RF and high power applications. Superlattices Microstruct. (2017). https://doi.org/10.1016/j.spmi.2017.05.042
[Crossref]

12. Ambacher, Two dimensional electron gases induced by spontaneous and piezoelectric polarization in undoped and doped AlGaN/GaN heterostructures. J. Appl. Phys. **87**, 334 (2000)

13. O. Ambacher, Growth and applications of group III-nitrides. J. Appl. Phys. **31**(20), 2653 (1998)

14. S. Keller, Metal organic chemical vapour deposition of group III nitrides—a discussion of critical issues. J. Cryst. Growth **248**, 479–486 (2003)
[Crossref]

15. D.A. Neumayer, Growth of group III nitrides. A review of precursors and techniques. J. Chem. Mater. **8**(1), 9–25 (1996)

[Crossref]

16. S.C. Jain, III–nitrides: Growth, characterization, and properties. J. Appl. Phys. **87**(3), 965–1006 (2000)
[Crossref]

17. B.K. Jebalin, S. Rekh, Prajoon, N. Mohankumar, D. Nirmal, Unique model of polarization engineered AlGaN/GaN based HEMTs for high power applications. Superlattices Microstruct. **78**, 210–223 (2015)

18. T.R. Lenka, A.K. Panda, Characteristics study of 2DEG transport properties of AlGaN/GaN and AlGaAs/GaAs-based HEMT. Semiconductors **45**(5), 660–665 (2014)

19. Z.H. Feng, Enhanced thermal stability of the two dimensional electron gas in GaN/AlGaN/GaN heterostructures by Si_3N_4 surface passivation induced strain solidification. Appl. Phys. **85**(22), 5248–5250 (2004)

20. A. Tyagi, Partial strain relaxation via misfit dislocation generation at hetero interfaces in (Al, In) GaN epitaxial layers grown on semi polar ($112^{-}2$) GaN free standing substrates. Appl. Phys. **95**(25), 251905 (2009)

21. T.R. Lenka, G.N. Dash, A.K. Panda, 2DEG Transport characteristics by self-consistent subband calculations of Schrödinger and Poisson equations in InAlN/GaN HEMT, *IEEE Nanotechnology Materials and Devices Conference* (IEEE, Aci Castello, Italy, 2014) pp. 124–127. https://doi.org/10.1109/NMDC.2014.6997438

22. S. Khandelwal, N. Goyal, T.A. Fjeldly, A physics-based analytical model for 2DEG charge density in AlGaN/GaN HEMT devices. IEEE Trans. Electron Devices **58**(10), 3622–3625 (2011)
[Crossref]

23. Chen, Room-temperature mobility above 2200 cm2/V_s of two-dimensional electron gas in a sharp-interface AlGaN/GaN heterostructure. Appl. Phys. Lett. **106** (2015)

24. Pengelly, A review of GaN on SiC high electron-mobility power transistors and MMICs. IEEE Trans. Microw. Theory Tech. **60**, 1764 (2012)

25. M.N.A. Aadit, S.G. Kirtania, F Afrin, M.K Alam, Q.D.M. Khosru, High Electron Mobility Transistors: Performance Analysis, Research Trend and Applications. (Intech open science) https://doi.org/10.5772/67796

26. https://en.wikipedia.org/

T. R. Lenka, H. P. T. Nguyen (eds.), *HEMT Technology and Applications*, Springer Tracts in Electrical and Electronics Engineering
https://doi.org/10.1007/978-981-19-2165-0_9

Multigate MOS-HEMT

Atanu Kundu[1] and Mousiki Kar[1] ✉
(1) Department of Electronics and Communication Engineering, Heritage Institute of Technology, Kolkata, India

✉ **Mousiki Kar (Corresponding author)**
Email: mousikikar@gmail.com
Email: mousiki.kar@heritageit.edu

Abstract
Gallium nitride (GaN) based High-Electron-Mobility Transistors (HEMTs), and in particular, aluminum gallium nitride (AlGaN)/GaN devices have become a popular choice due to their ability to produce higher power densities at higher frequencies as compared to their silicon (Si) and gallium arsenide (GaAs) based counterparts. GaN-based HEMTs have also proven to be excellent candidates for amplifiers operating at higher power levels, high temperatures, and in robust environments. This chapter discusses how the performance of such GaN-based HEMTs can be enhanced by introducing a gate oxide and an underlapped structure. The chapter also delves into the advantages of multigate structures and the use of quaternary indium aluminum gallium nitride (InAlGaN) compound to deliver higher breakdown voltage.

Keywords MOS-HEMT – DG GaN HEMT – Underlap structure

1 Introduction

Low power dissipating, high speed, and high-frequency devices having small dimensions are the fundamental requirements for the Very Large Scale Integrated (VLSI) circuits [1–4]. Silicon was considered the most suitable material for CMOS technology, therefore it has been dominating for the past 50 years in the VLSI industry [5, 6]. Due to the numerous inherent advantages, viz. reliability, ease of use, and low cost, silicon has been used for the fabrication of discrete devices and integrated circuits in the VLSI industry [5, 7, 8].

Conventional MOSFETs have comparatively slower performance due to impurity scattering, which ultimately causes unwanted heating and loss [9, 10]. However, as per the current requirements of the semiconductor industry and applications, silicon has certain limitations [11, 12]. Silicon being indirect bandgap material, it is difficult to make optical devices. It is inappropriate for designing terahertz frequency application devices. It is unsuitable for high-voltage and high-temperature electronics applications [8–12].

Silicon-based devices are not operable where temperature rises above 200 °C and is not appropriate for cryogenic semiconductor applications that operate at 4.2 K and below for space instruments [13, 14]. Devices working in a harsh environment should be immune to water, oxygen, and hydrogen, which can deteriorate and modify the electrical characteristics with time. III-N materials like gallium nitride (GaN) show exceptional performance for analog, high-frequency, high-power applications [15, 16]. Therefore, it has a wide range of applications like space, radio astronomy, military applications, cryogenic low-noise systems, satellite broadcasting receivers, cell-phone handsets, radio telescopes, and entertainment applications in broadcasting satellite receivers [17, 18]. Besides, GaN-based devices show good agreement for power conversion and control-based SOC devices [19, 20].

With innovative device structure, GaN/AlGaN HEMT has been considered appropriate as solid-state transistors for amplification as well as low to high (900 V) voltage range operations, which includes a major share of the consumer electronic market, viz. audio amplifiers, converters for electric vehicles (EV) inverters for renewable energy and hybrid electric vehicles (HEV), and power supplies [18–21]. In the high-voltage regime, GaN devices are likely to be better at coexisting with SiC

and act as the backbone for electrical grid systems, converting power [21, 22].

On account of the high breakdown voltage, GaN transistors can withstand high drain voltages, high-saturation current densities, and higher output impedance per watt of RF power [9, 11, 12, 20]. This causes lower loss matching circuits and lower parasitic capacitances per watt of output power making GaN transistors an appropriate choice for high-speed amplifiers. As GaN is ten times faster than silicon, GaN-based transistors can operate in the terahertz frequency regime, which makes it suitable for 5G technology and wideband applications [23–25].

Novel device processing technology ensures to integrate GaN-based devices with existing Si technology, where with this heterogeneous integration both the advantages of Si and GaN can be achieved. RFIC design requires the integration of an RF circuit by proper choice of radio architecture, the existing device technology, crosstalk, parasitics, cost, and time-to-market which can be managed properly by this heterogeneous integration [26, 27]. The assortment of superior efficiency, higher power density, lower noise figure, and robustness gives new potential in the designing of radar transceivers for 5G wireless communication and space applications [28–30].

GaN has inherent properties like large bandgap, high carrier mobility, and saturation velocity with a high critical electric field. It enables high sheet carrier concentration without extrinsic doping, due to the spontaneous and piezoelectric polarization. The high bandgap helps to tolerate high voltage and without extrinsic doping nonuniform dopant distribution and dopant scattering effect can be avoided. These features help in achieving up to $f_t/f_{\max}$ around 500 GHz in the nanoscaled HEMTs and high-voltage, high-power rectifiers and transistors capable of handling voltages up to 1500 V [31, 32].

Overall, GaN-based III–V materials show great promise in electronics circuit applications. The introduction of various innovative device structures, viz. multigate, double gate (DG), underlap MOS-HEMT can work as perfect power amplifiers at microwave frequencies, amplifiers with gain control, and show good agreement as terahertz devices. They are also good candidates as a magnetic semiconductor for spintronics device materials by proper doping with appropriate transition metal [33–35].

2 GaN HEMT

The challenges like low noise, high breakdown voltage, high-temperature operation and thermal conductivity, high mobility, high cutoff frequency, and reliability for use in the extreme environment have been overcome in the straddling-based heterojunction AlGaN/GaN HEMT. Therefore, it is preferred for high-speed and high-power electronic devices over conventional MOSFETs [36, 37]. A basic AlGaN/GaN HEMT structure has been depicted in Fig. 1. It consists of an AlGaN barrier layer grown on a GaN channel layer.

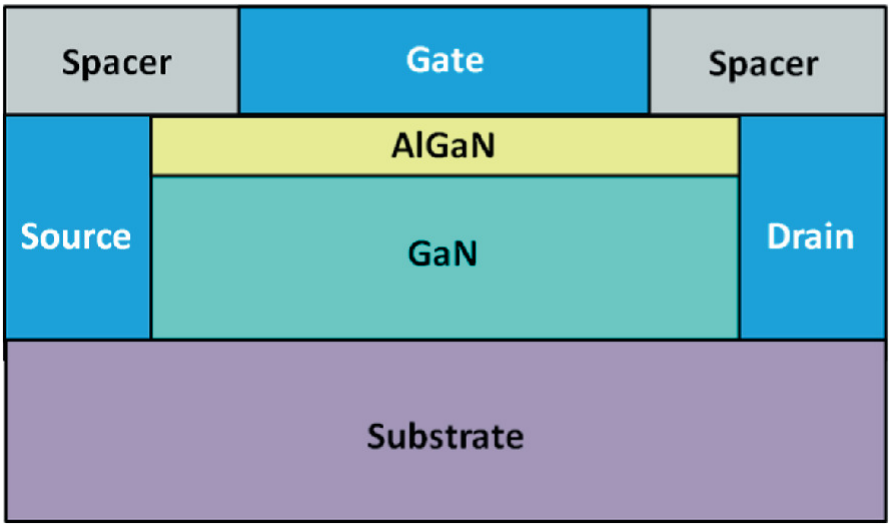

Fig. 1 A basic AlGaN/GaN HEMT

These device structures are usually grown on a substrate material which can be semi-insulating silicon carbide (SiC), sapphire, or Si. In order to make the device reliable and manufacturing cost-effective, the substrates have lattice constants that differ from the GaN layer. There is a lattice mismatch existing between the substrate and the GaN epilayers induces strain leading to defect areas.

Wide bandgap of GaN, which is an inherent material property, provides high breakdown and high operational temperature. The large lattice mismatch between AlN and GaN introduces strain in the junction interface, which leads to generating piezoelectric effect [38]. Due to this piezoelectric field, high conduction band offset leads to a very high-

density sheet charge, which results in high current and higher carrier mobility [39].

In AlGaN/GaN structures sapphire is used as the substrate which gives excellent thermal conductivity, high operating temperature up to 1800 °C, and is naturally the second hardest material which can even leave a scratch on diamond. When the junction is formed between a high and low bandgap material, the electron in the conduction band of high bandgap material diffuses automatically to the conduction band of low bandgap material so as to acquire minimum energy. This leads to high electron concentration on GaN side and low electron concentration on the AlGaN side of the junction. The conduction band of GaN material near the junction comes closer to the Fermi level and the AlGaN conduction band distance increases from the Fermi level.

Thus, two-dimensional electron gas (2DEG) is formed in the quantum well. There exists a difference in electronegativity between Al–N and Ga-N bonds, which are highly ionic and are strong dipoles in nature. This feature of the III-nitride materials leads to creating five times more spontaneous polarization in III–V semiconductors. As piezoelectric and spontaneous polarizations occur in the AlGaN/GaN material system of the AlGaN layer, these two different polarization vectors result in the formation of dipole sheet charges at the AlGaN/GaN junction [35, 37–39]. Due to the low-loss switching capability in AlGaN/GaN technology, it is possible to fabricate an entire transceiver on a single chip.

High-power amplifiers (HPA) require wide bandwidth and high linearity at low power consumption. GaN HEMTs meet all the requirements and are considered the best choice. Conventionally for designing high-power amplifier devices, gallium arsenide HEMT or LDMOS devices were used, but it has been seen that GaN-based HEMTs provide higher power-added efficiency (PAE) for high-power amplifiers (HPAs). Higher PAE saves electrical power usage (OPEX) as well as lessens the dimension and cost of high-power amplifiers (HPAs). In case of amplifiers, higher PAE also reduces the launch cost of a satellite [3, 7, 8, 11]. Adverse effects such as trapping are major drawback for AlGaN/GaN HEMTs, which cause reliability issues. Due to this, it is difficult to use GaN-based HEMT transistors for high-voltage, high-temperature, and high-power applications. The performance of the

device majorly degrades when it operates at high voltage because the electrons get trapped in various locations in the device [11, 17, 18, 40].

3 GaN MOS-HEMT

In order to effectively increase gate swing and suppress the gate leakage current, the Schottky gate is replaced by the metal–oxide–semiconductor (MOS) structure in the DG GaN-HEMT gate to form the MOS-HEMT. The introduction of a dielectric between the Schottky-gate and the semiconductor of the GaN HEMT reduces the gate leakage current to a great extent and thus leads to a higher input impedance, higher cutoff frequency, and superior breakdown voltage. Also, the device can operate in a large range of gate biases. The GaN MOS-HEMTs were developed by Khan et al. for the first time using SiO_2 deposited by plasma-enhanced chemical vapor deposition [41]. MOS-HEMT devices remain stable under RF power stress even at temperatures as high as 400 °C [42] (Fig. 2).

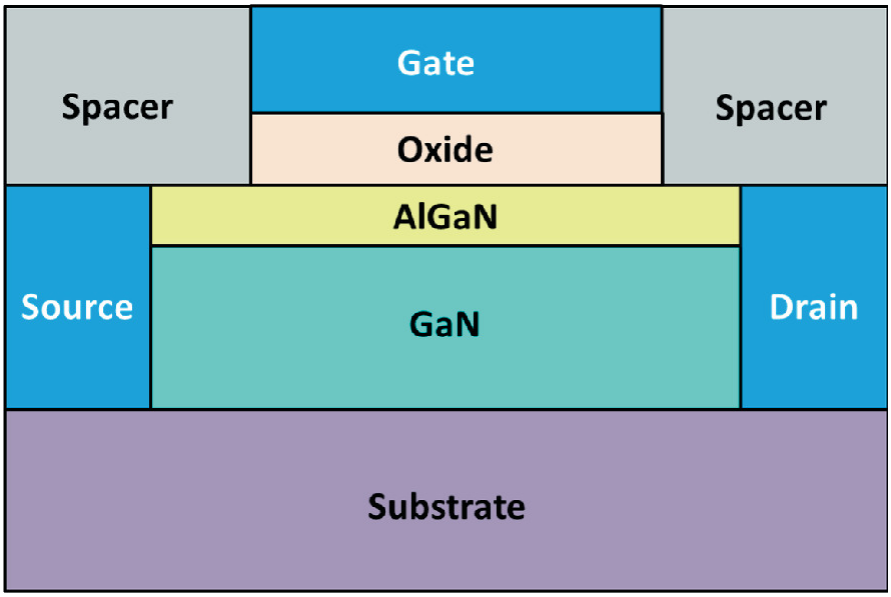

Fig. 2 A basic AlGaN/GaN MOS-HEMT

MOS-HEMT devices maintain relatively high-power output and low gate leakage current with long-term RF stress, whereas the HEMTs exhibit visible degradation in power and gate leakage current [43]. High-power density, cutoff frequency, maximum-oscillation frequency,

and low-noise figure are essential factors for high-power/high-frequency microwave devices. This enables compact die sizes and simple input and output matching networks. Higher power-added efficiency (PAE) saves electrical power consumption and reduces the cost and size of HPAs due to the low heat dissipation [41, 43].

MOS-HEMT devices operate at a higher supply voltage similar to the power feeder voltage range, which is generally used for radar and satellite communication equipment. GaN-based MOS-HEMTs show higher impedance than other devices [44]. HPA designers can utilize the advantages of MOS-HEMTs in order to increase the performance of HPAs with a wide coverage of frequency bands and higher PAE [41–44].

MOS-HEMTs are preferred over the Schottky-HEMTs because they have higher gate capacitance, higher input impedance, lower leakage current, higher drive current capacity, and are better candidates for high-frequency RF applications. Tremendous improvements in solid-state transistor speed has been achieved. Integrated circuits demonstrated up to a few terahertz in GaN/AlGaN DG MOS-HEMT IC amplifiers. DG HEMTs exhibit an evidently superior frequency performance with an added higher immunity to short-channel effects due to the reduced parasitic resistances and lower drain conductance in their extrinsic form. When the gate length reduces below 100 nm in single-gate HEMT (SG HEMT), it leads to a fall in transconductance (g_m), resulting in a reduction of voltage gain (g_m/g_d) of the device. Thus, the maximum frequency of oscillation ($f_{\max}$) reduces [15, 17, 18, 37].

While fabricating MOS-HEMT, it was found that the choice of materials ensures good thermal stability. The use of high-κ dielectrics helps to reduce leakage current, while the inclusion of a nucleation layer reduces stress and lattice mismatch. The barrier layer thickness is capable of proper confinement of carriers within the quantum-well at the heterointerface. The selection of the substrate material is important for the overall device behavior. One of the highly used substrate materials is silicon due to its excellent property of high resistivity, low cost, abundance in nature, and good thermal conductivity.

F. Medjdoub et al. presented a MOS-HEMT that is normally off based on AIN/GaN on a 0.1 μm silicon substrate [45]. A thermal dry oxidized AlN (AlON) has been grown that has been reported to be highly selective toward the silicon nitride layer, which depleted the 2DEG, in

turn, resulting in a normally off operation. When this fabricated MOS-HEMT is compared with an identical but non-oxidized MOS-HEMT, it displayed a drastic positive shift in its threshold voltage, with a drop in drain leakage by three-four times in favor of the former. Thus, the fabricated MOS-HEMT is suited for high-power applications [43–45].

J. Ma et al. have presented a high-performance GaN power MOS-HEMTs on silicon, where the results favored the potential of these devices for power applications [44–46]. M. Tao et al. reported low current collapse by a normally off GaN MOS-HEMT on a silicon substrate. The structure displayed a very high breakdown voltage (~1528 V), and 356 mA/mm drain current and a positive threshold voltage with a leakage current of 5 μA/mm [28]. The gate insulator or gate oxide selection is one of the most important materials, whose selection has been discussed for device performance analysis. Different innovative device structures are showing good agreement in a normally off AlGaN/GaN MOS-HEMT with silicon dioxide (SiO_2) dielectric [46, 47].

It is also possible to achieve high breakdown voltage in a new silicon dioxide deposition scheme based on RF Magnetron sputtering and plasma enhanced chemical vapor deposition (PECVD) for an AlGaN/GaN MOS-HEMT for high-power applications [48, 49]. The mobility characteristics in the channel of a SiO_2/GaN hybrid MOS-HEMT stay under accumulation operating condition. The mobility model developed shows the negative dependence of peak mobility on temperature. This happened due to the effects of phonon and Coulomb scattering [50].

A comparative study between a passivated MOS-HEMT, an unpassivated HEMT, and a passivated HEMT device was presented by Basu et al. [51]. The use of Al_2O_3 thin film as an oxide dielectric as well as an insulator layer was found to promote the reduction in device performance degradation by reducing current collapse effects in MOS-HEMTs [28, 40].

Annealing is effective on the electrical characteristics of an InAlN/GaN MOS-HEMT having an Al_2O_3 insulating film. The leakage current was reduced 7 times as compared to HEMT structures without the insulating film [52]. The effect of channel mobility and threshold

voltage engineering in an Al_2O_3/AlGaN interface in GaN MOS-HEMTs for power switching applications was presented by Bajaj et al. [53].

The outcome of post oxidation annealing (POA) process on the hydrogen peroxide (H_2O_2)-based oxide growth layer in an Al_2O_3/AlGaN/GaN MOS-HEMT was investigated by Liu et al. [54]. The traps in the device were reduced, thereby improving its electrical characteristics [45, 54]. The authors have also presented the fabrication of an E-mode AlGaN/GaN MOS-HEMT s and it has been reported that the Cl doped Al_2O_3 MOS-HEMT exhibited higher gate leakage than with undoped Al_2O_3 [55].

---

4 Multigate GaN MOS-HEMT

The inability of the device to maintain the desired channel aspect ratio (α) accounts for the reduction in gm with gate length in single-gate HEMT. Double-gate HEMT (DG-HEMT) overcomes the shortcomings of SG HEMT by virtue of its double-gate structure. Also, it requires the same supply voltage to operate and gates can be controlled independently depending on applications.

On the introduction of a new gate in the MOS-HEMT on the backside, named as a back gate, the modified device is denoted as double-gate MOS-HEMT (DG MOS-HEMT) shown in Fig. 3. The extra gate improves gate control and doubles ON current that can be attained in the device because of double oxide capacitances [15, 18, 36]. Gate oxide capacitances improve on current and reduce off current. Thus, it improves gate controllability.

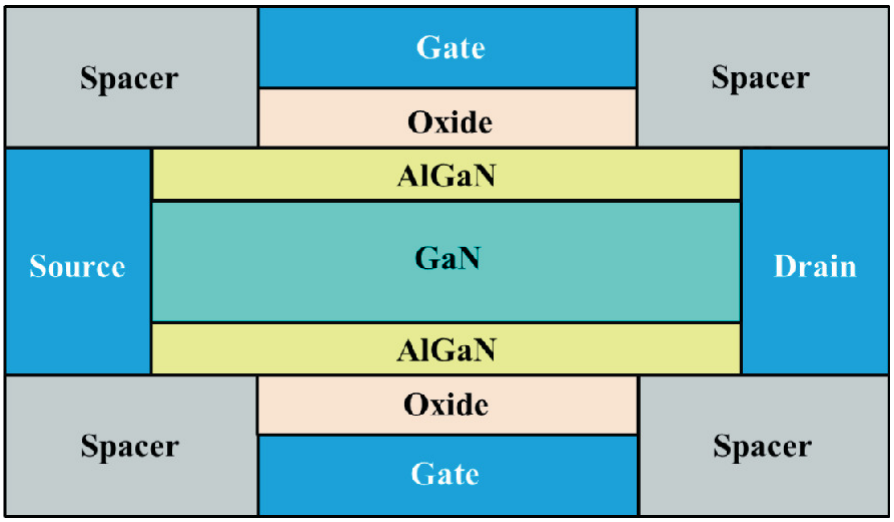

Fig. 3 A basic AlGaN/GaN double-gate MOS-HEMT

Since there is no capacitive potential division between the top and bottom gate, in case both the gates, are shorted and the electrical field lines are being shielded by the bottom gate, the DIBL is minimized and SCE is reduced in the double-gate structure. In addition, the short channel effect control is very good by virtue of a thin fully depleted body and gate shielding of drain fringing electric field lines from penetrating the body from both sides. Hence, SCE improved and the improved subthreshold slope closer can be achieved.

Due to the action of two gates, the device can now be scaled to shorter gate lengths for the same body and oxide thickness. The threshold voltage of the device further can be controlled by the gate metal work function. However, DG MOS-HEMTs suffer from several drawbacks. The fabrication process is very complex and gate alignment is difficult which may add parasitic source/drain overlap capacitances [9, 11].

5 Advantage of Underlapped Structure

To overcome the parasitic capacitances associated with the conventional overlapped devices underlap structure has been introduced. The overlapped gate-source/drain (G-S/D) double-gate MOS-HEMT structure is shown in Fig. 4a. The non-overlapped or underlapped gate-source/drain (G-S/D) double-gate MOS-HEMT structure is depicted in Fig. 4b.

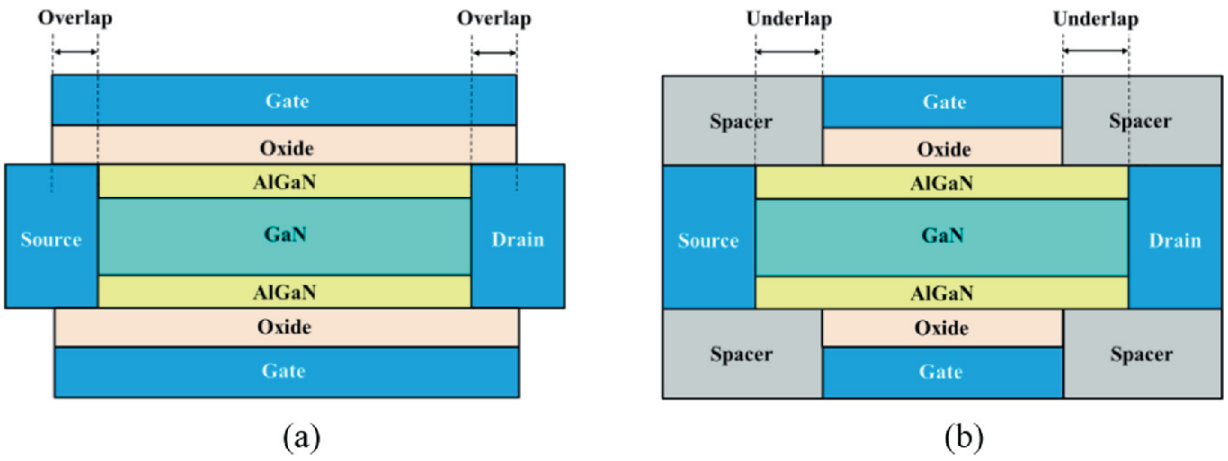

Fig. 4 Cross-sectional view of **a** Overlapped double-gate MOS-HEMT. **b** Underlapped double-gate MOS-HEMT

The non-overlapped or underlapped gate-source/drain (G-S/D) structure is used to overcome the problem of SCE and DIBL of the scaled transistors [15, 18, 36, 37]. The SCEs in conventionally scaled bulk-Si transistors were predominantly controlled by the high-channel doping. However, due to the difficulty of nonuniform dopant distribution, which leads to multiple threshold voltage, the ultra-thin body (UTB) of the DG FETs is left undoped and the doping is also avoided in HEMT devices. Thus, it is required to have underlap regions for acceptable SCE control. The underlap region on the drain side increases the distance between the channel and drain regions. Thus, the effect of the induced drain voltage on gate barrier lowering is minimized. The underlap structure, due to the absence of overlap gate-source/drain capacitance, reduces the gate overlap capacitance. Although, it reduces the on-state current due to the increased series resistances added to the device for the underlap regions [56–58].

However, optimum performance can be achieved by optimum underlap length and the improved device performances have been achieved by the use of high dielectric constant (k) spacer material. This effect of increased series resistance is less in case of these power transistors as they operate at a higher voltage. The use of a high dielectric constant (k) spacer material increases the on current of the device as the fringing field density inside the high-k spacer material improves, which improves the potential barrier reduction in DG MOS-HEMTs. Though high-k spacers can improve performance, it also

reduces the intrinsic gain of the device which can be optimized by optimum use of *k* value of the spacer materials and other parameters [59].

6 Quaternary InAlGaN/GaN DG-MOS HEMT

In order to enhance the output power density of a device keeping the working voltage constant, an increase in the drain current and breakdown voltage must be achieved. This leads to an increase in 2DEG concentration, carrier mobility, and drain current density. A better analog performance is derived from the device.

The critical barrier thickness of the AlGaN layer is reduced by the increased Al composition, causing an increase in its radio frequency performances. However, the growth of Al in the AlGaN layer or direct use of the AlN interlayer has its limits as the tensile stress that is brought about by the lattice mismatch between AlGaN and GaN severely deteriorates the crystal quality of heterostructures [60].

However, indium (In) is found to be advantageous over aluminum (Al) in this respect. Replacing AlGaN with an InAlN layer with 18% indium is lattice-matched to GaN and provides very high spontaneous polarization. This also yields almost double 2DEG values with respect to the former [56, 58]. It is difficult to grow high-quality ternary InAlN because of its immiscibility, composition non-homogeneity, and the presence of pits in the film corresponding to the dislocation defects in the GaN buffer. Figure 5 shows the structure of a basic InAlGaN/GaN double-gate MOS-HEMT. Quaternary InAlGaN is a better candidate for barrier material providing high electron sheet density in the quantum well, as well as proving to be much more miscible [56, 60].

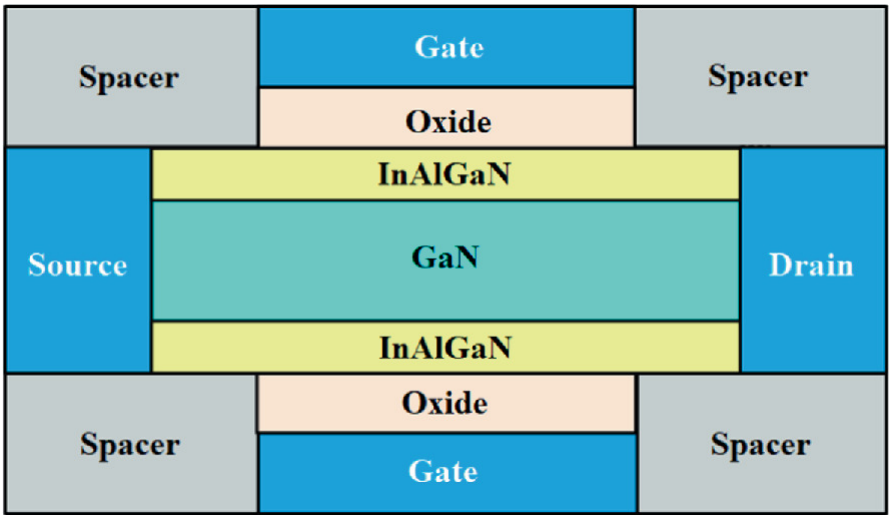

Fig. 5 A basic InAlGaN/GaN double-gate MOS-HEMT

Using quaternary InAlGaN barrier layers in GaN-based HEMTs allows the realization of depletion mode (d-mode) and enhancement mode (e-mode) operation. Their composition can be altered leading to a change in the spontaneous and piezoelectric polarization in a pseudo-morphically grown InAlGaN layer, one can control the polarization difference between the InAlGaN barrier and the GaN buffer [60].

Lattice-matched pure AlInN and tensile strained InAlGaN layers with high Al contents both contribute high two-dimensional electron gas (2DEG) densities [61]. However, high In content leads to inferior crystal quality with limited device performance. Effects such as relaxation and In pulling, are exhibited by barrier layers under high compressive strain which degrade device characteristics [62].

Quaternary InAlGaN having a considerably higher bandgap than ternary AlGaN can deliver higher breakdown voltage, further allowing its application in the high-frequency, high-power electronics domain. After careful evaluation of their analog, RF and power performances InAlGaN/GaN has been established as a better choice than the conventional AlGaN/GaN in MOS-HEMT devices. When the quaternary barrier width increases, the 2DEG values are also enhanced due to an increase in both its spontaneous and piezoelectric polarization charge, thus improving the device's drain current density. When the barrier thickness is reduced, control of the gate over the channel is strengthened making the device highly sensitive. This leads to a rise in the high-frequency input power swing as it turns ON.

References

1. S.K. Saha, *FinFET Devices for VLSI Circuits and Systems* (CRC Press, 2020)

2. C. Bhargava, G.M. Khanal, *Advanced VLSI Technology Technical Questions and Solutions* (River Publishers, 2020)

3. R. Qu, W. Zhang, Q. Lv, M. Zhang, Research on security evaluation of space used very large scale integration (VLSI), in *The 2nd International Conference on Computing and Data Science* (2021), pp. 1–5

4. V.K. Sharma, Design and simulation of FinFET circuits at different technologies, in *2021 6th International Conference on Inventive Computation Technologies (ICICT)* (IEEE, 2021), pp. 1–6

5. T. Mikolajick, U. Schroeder, S. Slesazeck, The past, the present, and the future of ferroelectric memories. IEEE Trans. Electron Devices **67**(4), 1434–1443 (2020) [Crossref]

6. D. Xie, E. Simoen, H. Chen, H. Arimura, N. Horiguchi, Impact of dummy gate removal and a silicon cap on the low-frequency noise performance of Germanium nFinFETs. IEEE Trans. Electron Devices **67**(11), 4713–4719 (2020) [Crossref]

7. F.U. Ahmed, Z.T. Sandhie, L. Ali, M.H. Chowdhury, A brief overview of on-chip voltage regulation in high-performance and high-density integrated circuits. IEEE Access (2020)

8. A. Amirsoleimani, F. Alibart, V. Yon, J. Xu, M.R. Pazhouhandeh, S. Ecoffey, Y. Beilliard, R. Genov, D. Drouin, Memory vector-matrix multiplication in monolithic complementary metal–oxide–semiconductor-memristor integrated circuits: design choices, challenges, and perspectives. Adv. Intell. Syst. **2**(11), 2000115 (2020)

9. H. Mukherjee, R. Dasgupta, M. Kar, A. Kundu, A comparative analysis of analog performances of underlapped dual gate AlGaN/GaN based MOS-HEMT and Schottky-HEMT, in *2020 IEEE Calcutta Conference (CALCON)* (IEEE, 2020), pp. 412–416

10. A. Lavasani, D. Bulmash, S.D. Sarma, Wiedemann-Franz law and Fermi liquids. Phys. Rev. B **99**(8), 085104 (2019)

11. B. Syamal, A. Kundu, AlGaN/GaN HEMT modeling and simulation, in *Handbook for III–V High Electron Mobility Transistor Technologies* (CRC Press, 2019), pp. 251–273

12. A. Kundu, S. Roy, C.K. Ghosh, C.K. Sarkar, Micro/nanoelectromechanical systems, in *Nanotechnology* (CRC Press, 2017), pp. 297–318

13. R. Chen, F.F. Wang, SiC and GaN devices with cryogenic cooling. IEEE Open J. Power Electron. **2**, 315–326 (2021) [Crossref]

14. S.M. Abd El-Azeem, S.M. El-Ghanam, Comparative study of gallium nitride and silicon carbide

MOSFETs as power switching applications under cryogenic conditions. Cryogenics **107**, 103071 (2020)

15. A. Mondal, A. Roy, R. Mitra, A. Kundu, Comparative study of variations in gate oxide material of a novel underlap DG MOS-HEMT for analog/RF and high power applications. Silicon **12**(9), 2251–2257 (2020)
[Crossref]

16. R. Sun, J. Lai, W. Chen, B. Zhang, GaN power integration for high frequency and high efficiency power applications: a review. IEEE Access **8**, 15529–15542 (2020)

17. M.A. Khan, X. Hu, G. Sumin, A. Lunev, J. Yang, R. Gaska, M.S. Shur, AlGaN/GaN metal oxide semiconductor heterostructure field effect transistor. IEEE Electron Device Lett. **21**(2), 63–65 (2000)
[Crossref]

18. R. Mitra, A. Roy, A. Mondal, A. Kundu, Influence of symmetric underlap on analog, RF and power applications for DG AlGaN/GaN MOS-HEMT. Silicon, 1–8 (2021)

19. M.A. Khan, G. Simin, J. Yang, J. Zhang, A. Koudymov, M.S. Shur, R. Gaska, X. Hu, A. Tarakji, Insulating gate III–N heterostructure field-effect transistors for high-power microwave and switching applications. IEEE Trans. Microw. Theory Tech. **51**(2), 624–633 (2003)

20. P. Kordoš, D. Gregušová, R. Stoklas, K. Čičo, J. Novák, Improved transport properties of Al_2O_3/AlGaN/GaN metal-oxide-semiconductor heterostructure field-effect transistor. Appl. Phys. Lett. **90**(12), 123513 (2007)
[Crossref]

21. X. Ding, Y. Zhou, J. Cheng, A review of gallium nitride power device and its applications in motor drive. CES Trans. Electr. Mach. Syst. **3**(1), 54–64 (2019)
[Crossref]

22. A. Avila, M. Lucu, A. Garcia-Bediaga, U. Ibarguren, I. Gandiaga, A. Rujas, Hybrid energy storage system based on Li-Ion and Li-S battery modules and GaN-based DC–DC converter. IEEE Access **9**, 132342–132353 (2021)
[Crossref]

23. A. Acharyya, Gallium nitride-based solid-state devices for terahertz applications. Adv. Mater. Future Terahertz Devices Circuits Syst. **727**, 9 (2021)
[Crossref]

24. R.K. Kaneriya, G. Rastogi, P.K. Basu, R.B. Upadhyay, A.N. Bhattacharya, Intersubband device modeling of gallium nitride high electron mobility transistor for terahertz applications. Radio Sci. **54**(12), 1172–1180 (2019)

25. A.S.A. Fletcher, D. Nirmal, A survey of gallium nitride HEMT for RF and high power applications. Superlattices Microstruct. **109**, 519–537 (2017)

26. L.-H. Hsu, Y.-Y. Lai, P.-T. Tu, C. Langpoklakpam, Y.-T. Chang, Y.-W. Huang, W.-C. Lee et al., Development of GaN HEMTs fabricated on silicon, silicon-on-insulator, and engineered substrates and the heterogeneous integration. Micromachines **12**(10), 1159 (2021)

27. F. Meng, D. Disney, B. Liu, Y.B. Volkan, A. Zhou, Z. Liang, X. Yi et al., Heterogeneous integration of GaN and BCD technologies and its applications to high conversion-ratio DC–DC boost converter IC. IEEE Trans. Power Electron. **34**(3), 1993–1996 (2018)

28. A. Chini et al., Experimental and numerical correlation between current-collapse and Fe-doping profiles in GaN HEMTs, in *IEEE International Reliability Physics Symposium Proceedings* (2012), pp. 2–5

29. B. Syamal, X. Zhou, S.B. Chiah, A.M. Jesudas, S. Arulkumaran, G.I. Ng, A comprehensive compact model for GaN HEMTs, including quasi-steady-state and transient trap-charge effects. IEEE Trans. Electron Devices **63**(4), 1478–1485 (2016)
[Crossref]

30. R. Ma, K.H. Teo, S. Shinjo, K. Yamanaka, P.M. Asbeck, A GaN PA for 4G LTE-advanced and 5G: meeting the telecommunication needs of various vertical sectors including automobiles, robotics, health care, factory automation, agriculture, education, and more. IEEE Microw. Mag. **18**(7), 77–85 (2017)

31. C. Jiang, T. Liu, C. Du, X. Huang, M. Liu, Z. Zhao, L. Li et al., Piezotronic effect tuned AlGaN/GaN high electron mobility transistor. Nanotechnology **28**(45), 455203 (2017)

32. W.E. Muhea, F.M. Yigletu, R. Cabre-Rodon, B. Iniguez, Analytical model for Schottky barrier height and threshold voltage of AlGaN/GaN HEMTs with piezoelectric effect. IEEE Trans. Electron Devices **65**(3), 901–907 (2018)

33. Z. Cui, K. Bai, X. Wang, E. Li, J. Zheng, Electronic, magnetism, and optical properties of transition metals adsorbed g-GaN. Physica E **118**, 113871 (2020)
[Crossref]

34. J. Li, H. Liu, Magnetism investigation of GaN monolayer doped with group VIII B transition metals. J. Mater. Sci. **53**(23), 15986–15994 (2018)
[Crossref]

35. E. Vetter, M. Biliroglu, D. Seyitliyev, P. Reddy, R. Kirste, Z. Sitar, R. Collazo, K. Gundogdu, D. Sun, Observation of carrier concentration dependent spintronic terahertz emission from n-GaN/NiFe heterostructures. Appl. Phys. Lett. **117**(9), 093502 (2020)
[Crossref]

36. A. Roy, R. Mitra, A. Mondal, A. Kundu, Analog/RF and power performance analysis of an underlap DG AlGaN/GaN based high-*k* dielectric MOS-HEMT. Silicon, 1–8 (2021)

37. R. Mitra, A. Roy, A. Kundu, M. Kar, Impact of AlGaN doping concentration on the analog/RF performance of a double gate underlap n-AlGaN/GaN MOSHEMT, in *2020 International Symposium on Devices, Circuits and Systems (ISDCS)* (IEEE, 2020), pp. 1–4

38. G. Hansdah, M. Raul, Pyroelectricity with an extra-polarization effect in AlN/GaN heterostructures. Mater. Today Proc. (2021)

39. M.K. Chattopadhyay, K.T. Upadhyay, Unified analytical model for charge density and plasmonic waves in the quaternary AlInGaN/AlN/GaN heterostructures, in *Microelectronics, Circuits and Systems* (Springer, Singapore, 2021), pp. 167–177

40.

E. Conwell, V.F. Weisskopf, Theory of impurity scattering in semiconductors. Phys. Rev. **77**(3), 388–390 (1949). S.A. Sleiman, A. Di Carlo, G. Verzellesi, G. Meneghesso, E. Zanoni, Current collapse associated with surface states in GaN-based HEMT's. theoretical/experimental investigations. Simul. Semicond. Process. Devices, 81–84 (2004)

41. X. Hu, S. Hwang, K. Hussain, R. Floyd, S. Mollah, F. Asif, G. Simin, A. Khan, Doped barrier $Al_{0.65}Ga_{0.35}N/Al_{0.40}Ga_{0.60}N$ MOSHFET with SiO_2 gate-insulator and Zr-based ohmic contacts. IEEE Electron Device Lett. **39**(10), 1568–1571 (2018)
[Crossref]

42. K. Nishiguchi, S. Kaneki, S. Ozaki, T. Hashizume, Current linearity and operation stability in Al_2O_3-gate AlGaN/GaN MOS high electron mobility transistors. Jpn. J. Appl. Phys. **56**(10), 101001 (2017)
[Crossref]

43. J.D. Albrecht, R.P. Wang, P.P. Ruden, M. Farahmand, K.F. Brennan, Electron transport characteristics of GaN for high temperature device modeling. J. Appl. Phys. **83**(9), 4777 (1998)
[Crossref]

44. R.S. Pengelly, S.M. Wood, J.W. Milligan, S.T. Sheppard, W.L. Pribble, A review of GaN on SiC high electron-mobility power transistors and MMICs. IEEE Trans. Microw. Theory Tech. **60**(6 Part 2), 1764–1783 (2012)

45. S. Kumar, N. Remesh, S.B. Dolmanan, S. Tripathy, S. Raghavan, R. Muralidharan, D.N. Nath, Interface traps at Al_2O_3/InAlN/GaN MOS-HEMT-on-200 mm Si. Solid-State Electron. **137**, 117–122 (2017)

46. M. Zhu, J. Ma, E. Matioli. Investigation of p-GaN tri-gate normally-off GaN power MOSHEMTs, in *2020 32nd International Symposium on Power Semiconductor Devices and ICs (ISPSD)* (IEEE, 2020), pp. 345–348

47. Z.-S. Kim, H.-S. Lee, J. Na, S.-B. Bae, E. Nam, J.-W. Lim, Ultra-low rate dry etching conditions for fabricating normally-off field effect transistors on AlGaN/GaN heterostructures. Solid-State Electron. **140**, 12–17 (2018)
[Crossref]

48. A. Malmros, *Advanced III-Nitride Technology for mm-Wave Applications* (Chalmers Tekniska Hogskola, Sweden, 2019)

49. F. Azam, AlGaN/GaN MOSHFETs using ALD dielectrics: a study in performance and reliability. Ph.D. dissertation. North Carolina State University (2018)

50. P. Fiorenza, G. Greco, F. Iucolano, A. Patti, F. Roccaforte, Channel mobility in GaN hybrid MOS-HEMT using SiO_2 as gate insulator. IEEE Trans. Electron Devices **64**(7), 2893–2899 (2017)
[Crossref]

51. S. Basu, P.K. Singh, S.-K. Lin, P.-W. Sze, Y.-H. Wang, Effects of short-term DC-bias-induced stress on n-GaN/AlGaN/GaN MOSHEMTs with liquid-phase-deposited Al_2O_3 as a gate dielectric. IEEE Trans. Electron Devices **57**(11), 2978–2987 (2010)

[Crossref]

52. Z.H. Liu, G.I. Ng, H. Zhou, S. Arulkumaran, Y.K.T. Maung, Reduced surface leakage current and trapping effects in AlGaN/GaN high electron mobility transistors on silicon with SiN/Al_2O_3 passivation. Appl. Phys. Lett. **98**(11), 113506 (2011)
[Crossref]

53. S. Bajaj, T.-H. Hung, F. Akyol, D. Nath, S. Rajan, Modeling of high composition AlGaN channel high electron mobility transistors with large threshold voltage. Appl. Phys. Lett. **105**(26), 263503 (2014)
[Crossref]

54. H.-Y. Liu, W.-C. Ou, W.-C. Hsu, Investigation of post oxidation annealing effect on H_2O_2-grown-Al_2O_3/AlGaN/GaN MOSHEMTs. IEEE J. Electron Devices Soc. **4**(5), 358–364 (2016)
[Crossref]

55. H.-Y. Liu, C.-W. Lin, C.-S. Lee, W.-C. Hsu, Threshold voltage engineering of enhancement-mode AlGaN/GaN metal-oxide-semiconductor high electron mobility transistors with different doping concentration of in situ Cl–doped Al_2O_3. ECS J. Solid State Sci. Technol. **10**(7), 075005 (2021)
[Crossref]

56. A. Roy, R. Mitra, A. Kundu, Influence of channel thickness on analog and RF performance enhancement of an underlap DG AlGaN/GaN based MOS-HEMT device, in *2019 Devices for Integrated Circuit (DevIC)* (IEEE, 2019), pp. 186–190

57. S. Adak, S.K. Swain, Impact of high-*K* dielectric materials on performance analysis of underlap $In_{0.17}Al_{0.83}N$/GaN DG-MOSHEMTs. Nano **14**(05), 1950060 (2019)

58. S. Kumar, M. Ali, R. Kumar, R. Mitra, A. Kundu, M. Kar, Impact of source and drain underlap on analog performance of double-gate AlGaN/GaN MOS-HEMT, in *2020 IEEE Calcutta Conference (CALCON)* (IEEE, 2020), pp. 378–381

59. K. Koley, A. Dutta, B. Syamal, S.K. Saha, C.K. Sarkar, Subthreshold analog/RF performance enhancement of underlap DG FETs with high-*k* spacer for low power applications. IEEE Trans. Electron Devices **60**(1), 63–69 (2012)

60. M. Hrit, K. Mousiki, K. Atanu, Enhancement in Analog/RF and power performance of underlapped dual gate GaN based MOSHEMTs with quaternary InAlGaN barrier of varying widths. J. Electron. Mater. (2021). https://doi.org/10.1007/s11664-021-09324-6
[Crossref]

61. B. Reuters, A. Wille, N. Ketteniss, H. Hahn, B. Holländer, M. Heuken, H. Kalisch, A. Vescan, Polarization-engineered enhancement-mode high-electron-mobility transistors using quaternary AlInGaN barrier layers. J. Electron. Mater. **42**(5), 826–832 (2013)

62. S. Turuvekere, N. Karumuri, A.A. Rahman, A. Bhattacharya, A.D. Gupta, N.D. Gupta, Gate leakage mechanisms in AlGaN/GaN and AlInN/GaN HEMTs: comparison and modeling. IEEE Trans. Electron Devices **60**(10), 3157–3165 (2013)

T. R. Lenka, H. P. T. Nguyen (eds.), *HEMT Technology and Applications*, Springer Tracts in Electrical and Electronics Engineering
https://doi.org/10.1007/978-981-19-2165-0_10

Enhancement-Mode MOSHEMT

Raghunandan Swain[1] ✉ and Trupti Ranjan Lenka[2] ✉
(1) Department of Electronics and Telecommunication Engineering, Parala Maharaja Engineering College, Berhampur, Odisha, 761003, India
(2) Department of Electronics and Communication Engineering, National Institute of Technology, Silchar, Assam, 788010, India

✉ **Raghunandan Swain (Corresponding author)**
Email: raghu.etc@pmec.ac.in

✉ **Trupti Ranjan Lenka**
Email: trlenka@ieee.org

Abstract
The enhancement-mode (E-mode) High-Electron-Mobility Transistors (HEMTs) and Metal–Oxide Semiconductor High-Electron-Mobility Transistors (MOSHEMTs) play a major role in power electronic applications for fail-safe operation. However, due to the formation of two-dimensional electron gas (2DEG), these devices operate in depletion mode and the realization of normally off MOSHEMT has become a challenge among the researchers. In this chapter, first attempt is made to investigate the effect of oxide layer parameters such as thickness and dielectric constant through analytical modeling of oxide-dependent 2DEG and threshold voltage. It is also verified through mathematical modeling that the inclusion of oxide/barrier interface density of states (DOS) into the existing HEMT models and considering thin subcritical barrier thickness can satisfy the modeling challenges of the DC characteristics of this device. Moreover, oxide barrier interface

charges also affect the shift in threshold voltage toward the positive *X*-axis of transfer characteristics up to a larger extent.

Keywords 2DEG – Enhancement mode – HEMT – MOSHEMT – Normally off

1 Introduction

The two major sectors which highly depend on GaN over the conventional silicon counterpart are power and ICT (Information and Communications Technology) sectors. The current power electronics industry employs GaN for both power management and switching applications. Power management operation includes IT and consumer market bearing applications in various home appliances and computing, while switching operation includes applications in the automotive industry and different energy conversion systems. The basic requirements of power electronics devices are low switching loss, high ON state peak current, high OFF state breakdown voltage, and high-frequency operation by reducing the loss due to passive components. Moreover, they should tolerate higher temperatures by avoiding the use of external heat sinks, thereby decreasing the size of the devices. The increased energy loss is manifested with higher power and higher operating frequencies. So, high-performance conversion devices are substantial to perform efficiently and save energy. However, the emerging GaN technology has some unique advantages over silicon such as high bandgap (3.4 eV), high electron mobility (900 cm^2/V s), high breakdown electric field (3 MV/m), high thermal conductivity (1.5 W/cm K), high-temperature sustainability (up to 700 °C), high Baliga Figure of Merit (385,000) [1]. GaN HEMTs possess superior characteristics and there is a consistent research effort to obtain high blockage voltage, normally off behavior, and low on-resistance (Ron) highly suitable for power electronic applications [2, 3]. Although, blocking voltage as high as 1.8 kV for GaN on Si HEMT [4] and Ron as low as 4.8 Ω [5] have already been achieved, realizing E-mode operation is still under active research because, in general, GaN HEMTs operate in normally-on mode due to formation of 2DEG. Moreover, GaN E-mode HEMTs are highly essential to replace the conventional Si-FETs

used in power electronics circuits [6]. Therefore, in this chapter, the primary focus is on realizing normally off operation in MOSHEMTs through the most convenient methods and verifying it through compact modeling and TCAD (technology computer-aided design) simulations.

2 Model Development and Simulation

2.1 Effect of Oxide Layer on 2DEG

One of the approaches to realize electric field (E_{well}) in the triangular well region across the barrier/GaN junction is to obtain and use the 2DEG concentration (n_s) while solving Poisson's equation. Another approach is to measure potential at barrier/GaN junction and then obtain n_s and E_{well} from it. The second method is used here due to its less complexity.

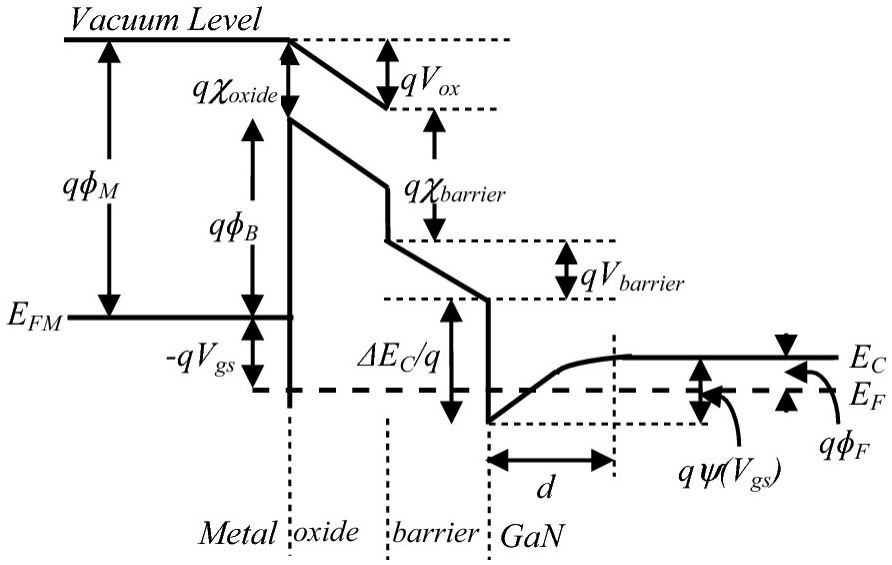

Fig. 1 Energy band bending in MOSHEMT showing the formation of quantum well

The energy band bending compensates the difference in work function between metal to semiconductor and applied gate voltage. Potential is dropped at GaN surface due to 2DEG, in barrier layer due to piezoelectric and spontaneous polarization charges and in oxide layer due to fabrication process lead unintentional charges. The potential drop equation on both sides of the oxide layer can be written as (Fig. 1)

(1)

$$\varphi_{\mathrm{M}} + V_{\mathrm{gs}} = V_{\mathrm{ox}} + V_{\mathrm{barrier}} + \chi_{\mathrm{barrier}} + \Delta E_C/e - \Psi\left(V_{\mathrm{gs}}\right) + \varphi_{\mathrm{F}}$$

$$\varphi_{\mathrm{MS}} + V_{\mathrm{gs}} = V_{\mathrm{ox}} + V_{\mathrm{barrier}} - \Psi\left(V_{\mathrm{gs}}\right) \tag{2}$$

where φ_{MS} is metal to GaN work function difference, ΔE_{C} is the discontinuity in conduction band at quantum well, e is the electronic charge, φ_{F} is Fermi potential in GaN, χ_{barrier} is the electron affinity of barrier, (σ) and V_{barrier} are the voltage drop at the oxide and barrier layer respectively due to application of gate voltage V_{gs}, $\Psi\left(V_{\mathrm{gs}}\right)$ is the potential at GaN surface, φ_{B} is the barrier between metal and oxide. The potential at the GaN surface is

$$\varphi_{\mathrm{MS}} + V_{\mathrm{gs}} = V_{\mathrm{ox}} + V_{\mathrm{barrier}} - \Psi\left(V_{\mathrm{gs}}\right) \tag{3}$$

The voltage drop in the oxide layer is given by

$$V_{\mathrm{ox}} = \frac{Q_{\mathrm{ox}} + Q_{\mathrm{it}}}{C_{\mathrm{ox}}} \tag{4}$$

where C_{ox} is capacitance due to oxide dielectric per unit area, $\varepsilon_{\mathrm{sub}}$ and Q_{it} are the charges present in the oxide layer and oxide/barrier interface, respectively.

These charges occupy interface energy levels having a central charge neutrality level (E_{CNL}). Acceptor levels are present above E_{CNL} and donor levels are present below it [7]. Negative and positive charges are formed due to ionized acceptor and donor states, respectively, at equilibrium depending on the position of Fermi level (E_{F0}) above (in Al_2O_3, SiO_2) [7] and below (in HfO_2) [8] E_{CNL} as shown in Fig. 2.

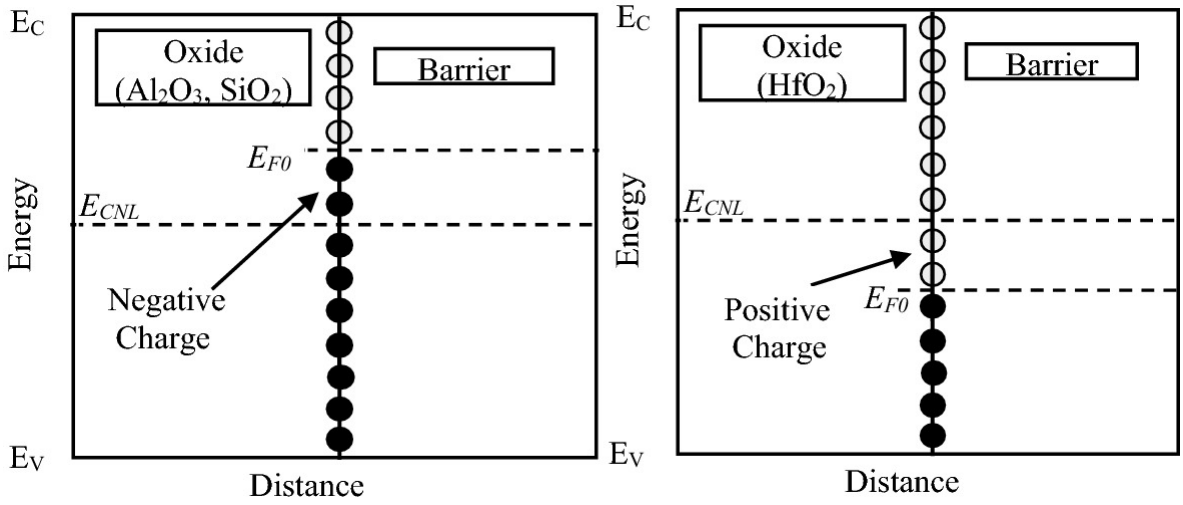

Fig. 2 Fermi energy level position-dependent on positive and negative charges at V_{gs} = 0 V

Now Q_{it} is given by

$$Q_{it} = D_{it} \cdot (E_{F0} - E_{CNL} + q \cdot V_{gs}) = Q_{it0} + D_{it} \cdot q \cdot V_{gs} \tag{5}$$

where $Q_{it0} = D_{it} \cdot (E_{F0} - E_{CNL})$ is the oxide/barrier interface charge at V_{gs} = 0 V.

$V_{barrier}$ is given by

$$V_{barrier} = \frac{q \cdot \sigma_{pol} \cdot t_{barrier}}{\varepsilon_{barrier}} \tag{6}$$

I_{max} is the net polarisation charge, $\varepsilon_{barrier}$ and $t_{barrier}$ are the electrical permittivity and thickness of barrier layer.

The expression for surface potential can be found by putting Eqs. (4), (5) and (6) in Eq. (3) as follows:

$$\Psi\left(V_{gs}\right) = \frac{Q_{ox} + Q_{it0}}{C_{ox}} + \frac{q \cdot \sigma_{pol} \cdot t_{barrier}}{\varepsilon_{barrier}} - \varphi_{MS} - \left(1 - \frac{q \cdot D_{it}}{C_{ox}}\right) \cdot V_{gs} \tag{7}$$

The inversion layer width (d) at GaN surface at V_{gs} = 0 V can be expressed as [9]:

(8)

$$d = \sqrt{2\varepsilon_{GaN} \cdot \Psi_s / qN_{GaN}}$$

where ε_{GaN} is electrical permittivity of GaN, N_{GaN} is unintentional doping in GaN [6]. At moderate inversion *i.e.* $\Psi_s = 2\varphi_F$ and $V_{gs} = 0$ V, E_{well} can be expressed as

$$E_{well} = \frac{\left(\varphi_{MS} - \frac{(Q_{ox}+Q_{it0})\cdot t_{ox}}{\varepsilon_{ox}} - \frac{q\cdot\sigma_{pol}\cdot t_{barrier}}{\varepsilon_{barrier}}\right)}{\sqrt{\frac{4\varepsilon_{GaN}\cdot\varphi_F}{qN_{GaN}}}} \quad (9)$$

Here, the quantum well is approximated in a triangular shape as the slope of the potential function is constant. Electrons are quantized at specific energy levels when confined in a quantum well. The expression of quantized energy level can be written as follows [10]:

$$E_n = \left(\frac{\hbar^2}{2m_n^*}\right)^{1/3} \left(\frac{3}{2}\pi q E_{well}\right)^{2/3} \left(n + \frac{3}{4}\right)^{2/3} \quad (10)$$

where σ_p is the effective mass of electron in GaN, $\hbar = \frac{h}{2\pi}$ is modified Plank's constant, and a can be 0, 1, 2, 3, 4 ...

The 2DEG concentration can be obtained by using three energy subbands in the triangular quantum well, 2D density of states function *D*, and Fermi–Dirac probability distribution function [11].

$$n_s = D\int_{E_0}^{E_1} \frac{dE}{1+e^{\left(\frac{q(E-E_F)}{KT}\right)}} + 2D\int_{E_1}^{E_2} \frac{dE}{1+e^{\left(\frac{q(E-E_F)}{KT}\right)}} + 3D\int_{E_2}^{\infty} \frac{dE}{1+e^{\left(\frac{q(E-E_F)}{KT}\right)}} \quad (11)$$

It is assumed here that the Fermi level is constant inside the quantum well and the 2DEG is analyzed at zero gate bias [12].

Equation (11) upon solving and neglecting higher-order energy terms can be written as

$$n_s = \frac{DKT}{q} \log\left[\left(1 + e^{\frac{q(E_F - E_0)}{KT}}\right) \cdot \left(1 + e^{\frac{q(E_F - E_1)}{KT}}\right) \cdot \left(1 + e^{\frac{q(E_F - E_2)}{KT}}\right)\right] \quad (12)$$

At low temperature, the above equation reduces to

$$n_s = D(E_1 - E_0) + 2D(E_2 - E_1) + 3D(E_F - E_2) \quad (13)$$

According to the developed model, the 2DEG concentration is dependent on the thickness and charge of the oxide layer. The variation of 2DEG concentration with oxide thickness for an AlGaN/GaN MOSHEMT is plotted in Fig. 3. The 2DEG concentration increases with oxide thickness in case of HfO_2 and decreases with oxide thickness in case of SiO_2 and Al_2O_3. For negative oxide/barrier interface charge (SiO_2 and Al_2O_3), E_{well} increases with oxide thickness and so as the Eigen energy values. This reduces the difference between the Eigen energy and Fermi energy and hence n_s. The reverse phenomenon happens in case of HfO_2 due to the presence of positive interface charges.

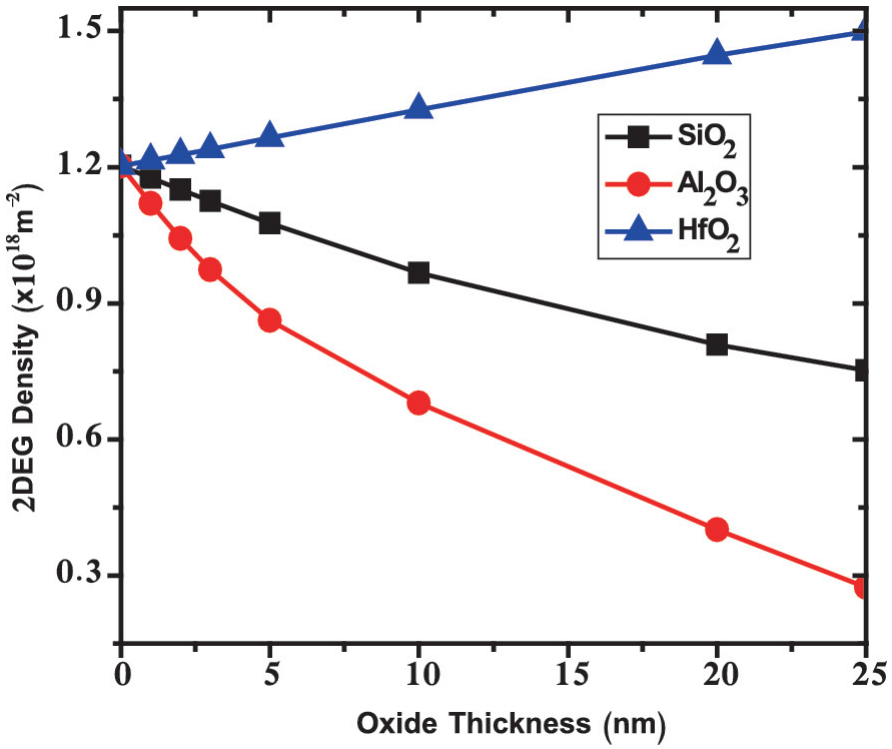

Fig. 3 Variation of n_s with the thickness of three different oxides (Al_2O_3, HfO_2, and SiO_2) [12]

2.2 Oxide Interfacial Charge Effect on the Threshold Voltage

The conduction band profile and charges formed at different interfaces across the MOSHEMT structure are shown in Fig. 4. The total charge at the oxide/barrier interface is due to barrier surface donor trap charges (Q_d), barrier polarization charges (σ_{pol}) due to σ_1 and σ_2, fixed oxide/barrier interfacial charge (Q_{ox}) and gate bias dependent variable oxide/barrier interface charge (Q_{it}) [13, 14]. Among all, Q_d is always positive due to empty donor traps present at the surface of the barrier and becomes a source of electrons inside the 2DEG [15]. Q_{ox} is positive for HfO_2 and negative for SiO_2 and Al_2O_3 [16]. A minor amount of charges present at the bulk of oxide can be ignored.

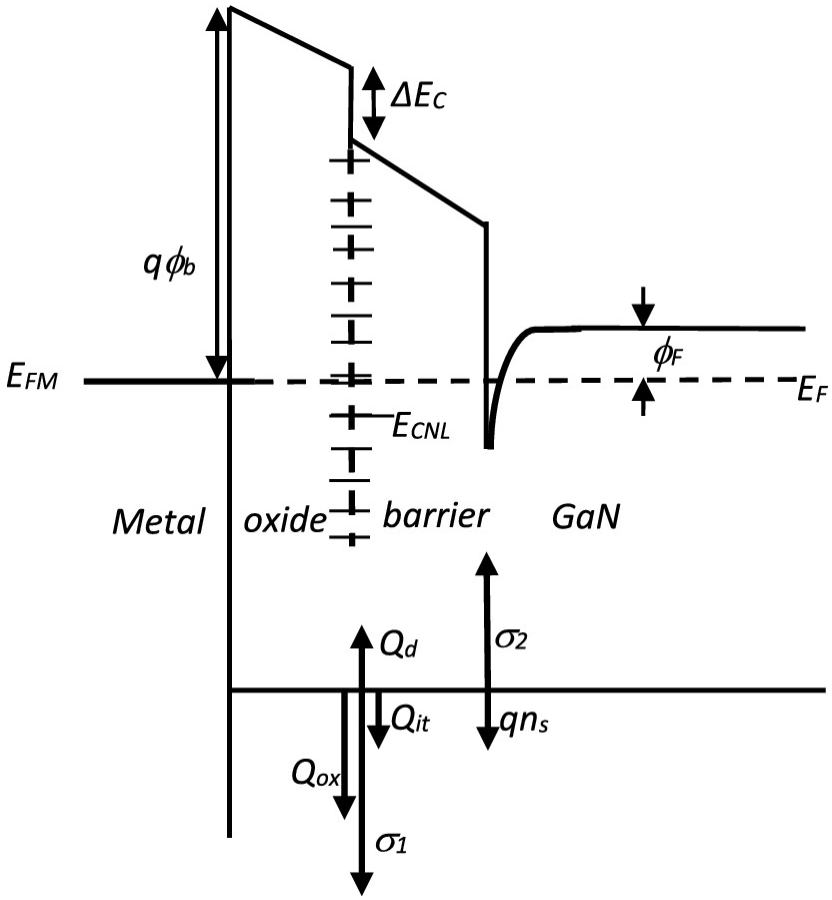

Fig. 4 Charge distribution along AlGaN/GaN MOSHEMT

So the V_T expression for this structure can be written as

$$V_T = \varphi_b - \Delta E_c - \varphi_F - \frac{t_{ox}}{\varepsilon_{ox}}\sigma_{pol} - \frac{t_b}{\varepsilon_b}\sigma_2 - \frac{t_{ox}}{\varepsilon_{ox}}(Q_d + Q_{it}(E_F) + Q_{ox}) \quad (14)$$

Equation (14) signifies that threshold voltage is a function of oxide interfacial charge and it can be rewritten as

$$V_T = K - \frac{t_{ox}}{\varepsilon_{ox}}(\sigma_1 + \sigma_2) - \frac{t_{ox}}{\varepsilon_{ox}}(Q_{ox} + Q_d + Q_{it}(E_F)) \quad (15)$$

$$K = \varphi_b - \Delta E_c - \varphi_F - \frac{t_b}{\varepsilon_b}\sigma_2 \quad (16)$$

Equation (15) represents inverse proportionality of V_T with respect to Q_{ox} at constant t_{ox}. Further for very small t_{ox}, the last term of Eq. (15) can be neglected and V_T becomes independent of Q_{ox}. Moreover, V_T decreases with an increase in t_{ox} at constant Q_{ox}. If t_{ox} is less, V_T moves toward positive for positive Q_{ox} and vice versa.

The formation of positive/negative interfacial charges and 2DEG can be represented by demonstrating the movement of barrier surface electrons as shown in Fig. 5. In case of HfO_2, the barrier surface donors provide electrons to GaN surface quantum well, hence empty donors found below E_{CNL} form positive charges. Similarly, in SiO_2 and Al_2O_3 barrier surface donors provide electrons to the acceptor states present above E_{CNL} forming negative charges.

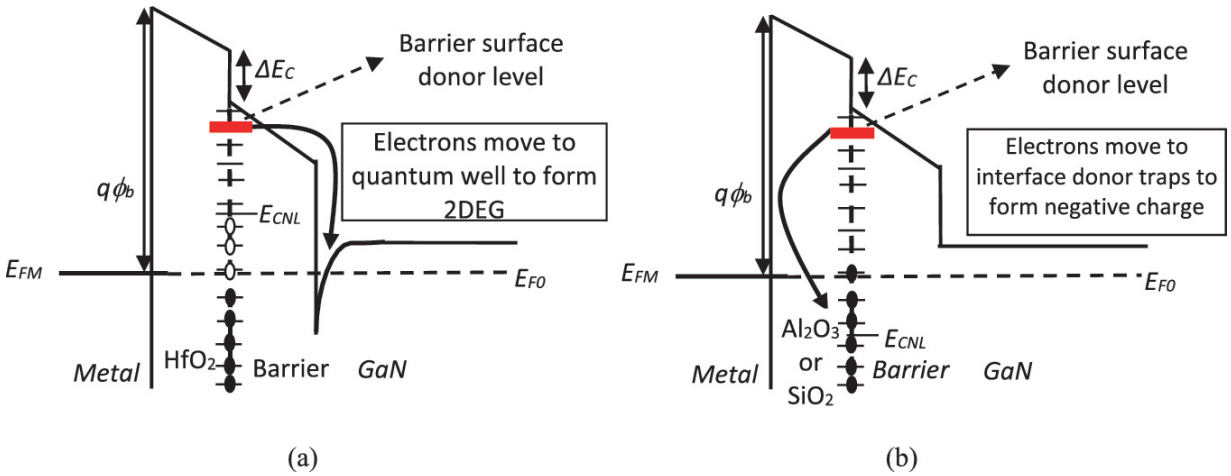

Fig. 5 Migration of electrons **a** from barrier to GaN forming 2DEG and positive interfacial charge, **b** from barrier to oxide/barrier interface forming negative interfacial charge [17]

Further, in order to validate this the transfer characteristics after TCAD simulation of an AlN/GaN MOSHEMT with 2 nm thick oxide and corresponding oxide interface charges are shown in Fig. 6. It is observed here that, in case of HfO_2 negative V_t is obtained due to a positive interfacial charge and in case of SiO_2 and Al_2O_3, positive V_t is obtained due to a negative interfacial charge. However, a higher amount of current is obtained in Al_2O_3 as higher negative charges form high 2DEG concentration at the well. V_t increases for negative Q_{ox} and decreases for positive Q_{ox}.

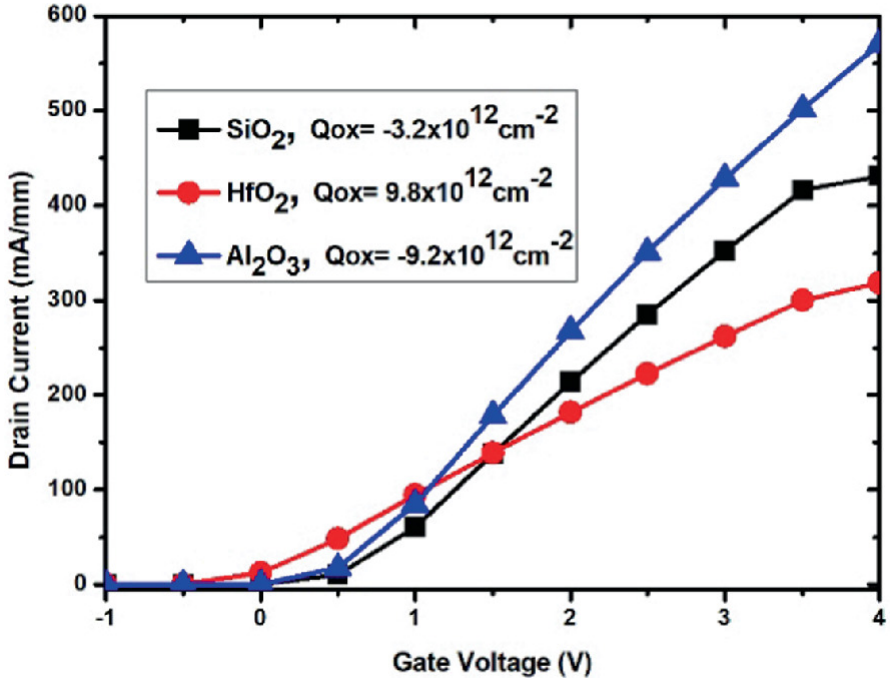

Fig. 6 Transfer characteristics of AlN/GaN MOSHEMT with 2 nm thick oxide layer

3 Conclusion

In this chapter, the effect of oxide parameters such as the amount and nature of charges and thickness on 2DEG concentration and the threshold voltage is explained through necessary modeling. It is concluded here that lower oxide thickness without compromising

leakage current and negative oxide/barrier interfacial charge can be an option to realize enhancement mode operation in MOSHEMTs.

References

1. T. Imada, M. Kanamura, T. Kikkawa, Enhancement-mode GaN MISHEMTs for power supplies. IEEE Power Electron. Conf. 1027–1033 (2010)

2. S.L. Zhao, B. Hou, W.W. Chen, M.H. Mi, J.X. Zheng, J.C. Zhang, X.H. Ma, Y. Hao, Analysis of the breakdown characterization method in GaN-based HEMTs. IEEE Trans. Power Electron. **31**, 1517–1527 (2016)
[Crossref]

3. H. Hahn et al., Threshold voltage engineering in GaN-based HFETs: A systematic study with the threshold voltage reaching more than 2V. IEEE Trans. Electron Devices **62**(2), 538–545 (2015)
[Crossref]

4. N. Ikeda, S. Kaya, J. Li, Y. Sato, S. Kato, S. Yoshida, High power AlGaN/GaN HFET with a high breakdown voltage of over 1.8 kV on 4 inch Si substrates and the suppression of current collapse, in *20th International Symposium Power Semiconductor Devices IC's* (2008), pp. 287–290

5. Y. Suzuki, K. Tone, J.T. Asubar, H. Tokuda, M. Kuzuhara, High drain current and low on-resistance in AlGaN/GaN HEMTs with Au-plated ohmic electrodes. IEEE Int. Meet. Future Electron Devices (2015)

6. P. Parikh, Y. Wu, L. Shen, Commercialization of High 600V GaN-on-silicon power HEMTs and diodes. Mater. Sci. Forum 1174–1179 (2013)

7. M. Tapajna, J. Kuzmík, A comprehensive analytical model for threshold voltage calculation in GaN based metal-oxide-semiconductor high-electron-mobility transistors. Appl. Phys. Lett. **100**, 113509 (2012)
[Crossref]

8. Y. Hayashi, S. Sugiura, S. Kishimoto, T. Mizutani, AlGaN/GaN MOSHFETs with HfO_2 gate oxide: A simulation study. Solid-State Electron. **54**, 1367–1371 (2010)
[Crossref]

9. Y. Tsividis, *Operation and Modeling of the MOS Transistor*, 2nd ed. (Oxford University Press, 2010)

10. F. Stengel, S. Noor Mohammad, H. Morkoc, Theoretical investigation of electrical characteristics of AlGaN/GaN modulation doped field-effect transistors. J. Appl. Phys. **80**, 3031–3042 (1996)

11. D. Delagebeaudeuf, N.T. Linh, Metal-(n) AIGaAs-GaAs two-dimensional electron gas FET. IEEE Trans. Electron Devices **29**, 955–960 (1982)
[Crossref]

12. S.S. Li, *Semiconductor Physical Electronics*, 1st ed. (Plenum Press, 1993)

13. R. Swain, J. panda, K. Jena, T.R. Lenka, Modeling and simulation of oxide dependent 2DEG sheet charge density in AlGaN/GaN MOSHEMT. J. Comput. Electron. **14** (03), 754–761 (2015)

14. X. Qin et al., A comparative study of atomic layer deposition of Al_2O_3 and HfO_2 on AlGaN/GaN. J. Mater. Sci. Mater. Electron. **26**, 4638–4643 (2015)

15. J.P. Ibbetson, P.T. Fini, K.D. Ness, S.P. DenBaars, J.S. Speck, U.K. Mishra, Polarization effects, surface states, and the source of electrons in AlGaN/GaN heterostructure field effect transistors. Appl. Phys. Lett. **77**(2), 250–252 (2000)
[Crossref]

16. M. Tapajna, J. Kuzmık, Control of threshold voltage in GaN based metal–oxide–semiconductor high-electron mobility transistors towards the normally-off operation. Jpn. J. Appl. Phy. **52**, 08JN08 (2013)

17. R. Swain, K. Jena, T.R. Lenka, Oxide interfacial charge engineering towards normally-off AlN/GaN MOSHEMT. Mater. Sci. Semicond. Process. **53**, 66–71 (2016)
[Crossref]

T. R. Lenka, H. P. T. Nguyen (eds.), *HEMT Technology and Applications*, Springer Tracts in Electrical and Electronics Engineering
https://doi.org/10.1007/978-981-19-2165-0_11

Performance Analysis of AlGaN/GaN HEMT for RF and Microwave Nanoelectronics Applications

G. Purnachandra Rao[1] ✉, Rajan Singh[1] ✉ and Trupti Ranjan Lenka[1] ✉
(1) Department of Electronics and Communication Engineering, National Institute of Technology Silchar, Assam, 788010, India

✉ **G. Purnachandra Rao (Corresponding author)**
Email: gpurna_rs@ece.nits.ac.in

✉ **Rajan Singh**
Email: rajan_rs@ece.nits.ac.in

✉ **Trupti Ranjan Lenka**
Email: trlenka@ieee.org

Abstract

In recent days, wide bandgap semiconductor materials constructed with GaN are exhibiting incredible performances in developing devices that are handling applications like high power, high frequency, high reliability in switching speeds, etc. This device became most promising due to its matchless properties over the conventional technologies which use Si-based materials, specifically with their impressive electrical management features demonstrating in HEMT (High Electron Mobility Transistor) based on GaN material. This review reports the detailed study on performance analysis of GaN-based HEMTs, preferably in RF and Microwave Nanoelectronics applications, along with various aspects of the issues related to the device function.

Keywords GaN – HEMT – 2DEG – Polarization – Traps – Current collapse

1 Introduction

The day-by-day improved technology devices are not matching their performance with the use of Si. This leads to the replacement of current devices with more reliable and sophisticated improvements. Which are also to be expected to exhibit veracity and accuracy, and more sensible to electrical energy. Therefore, all these requirements are preceded forward to find the new technology christened HEMT (high electron mobility transistor).

AlGaN/GaN HEMTs are highly recommended for RF and Microwave applications owing to their extraordinary feature of the wide bandgap. A higher bandgap of GaN gives the improved drain current and substantial breakdown voltage, which in turn the GaN to be a promising device for monolithic microwave integrated circuits (MMICs) and RF amplifiers. The movement of free electrons in HEMTs was explored in the year of 1969. But the primary RF model came to accessible in the mid of 1980. In the initial days, the cost associated with a RF model is very high, resulting in limited usage of HEMT. Now the device price is moderately reduced and frequently used in RF applications, in cellular communications, satellite communication and radio astronomy. The AlGaN/GaN HEMT is preferable for RF applications, that needs less noise, broad bandwidth range and workable in more power range. In the initial days, HEMTs are produced in individual transistors, but now it is developing compactly. These Compact Integrated circuits are MMIC's, generally employed in the burgeoning of RF models where remarkable performance is necessitated. HEMTs are widely becoming outstanding devices for an upcoming generation where the applications involving in high power. The scientist named E. J. Lum demonstrated the superior advantage of HEMT, presenting three folds of more power density as compared with MESFET, which leads to reduction in chip size. The HEMTs based on GaAs and InP were achieved in improved corner frequencies, but these HEMTs offer small breakdown fields. Therefore, these kinds of devices based on GaAs and InP are preferred for small voltages.

But in contrast, HEMT based on GaN provides remarkable RF performance against traditional HEMTs based on GaAs and InP materials. The distinctive feature of GaN material with a larger bandgap resulting in high breakdown voltage with excessive handling temperature. GaN material has one more stupendous advantage of spontaneous polarization, which carries a cloud of 2DEG solidity (n_s) of 6×10^{13} cm^{-2}. This beneficial feature of HEMT based on AlGaN/GaN is drawing the attention of aspirational researchers in the direction of GaN material over AlGaAs/GaAs devices. Several improved mechanisms are adopted to ameliorate the device performance. The field plate mechanism can enhance the device characteristics by decreasing unwanted spikes that emerged in the gate area. Hence, the breakdown voltage strength of the device could be increased. One more way to enhance the device performance is by placing a slender AlN barrier flake between the interface of AlGaN and GaN channel. This arrangement gives an improved carrier charge thickness and diminishes the compound scattering dislocations and finally yields increased mobility. Additionally, it improves the device's operating frequency, and dual heterojunction formation can offer increased 2DEG concentration.

In this report, it reviews the developments and withstanding of AlGaN/GaN from the initial stage to recent days covering the following sections. First, the basic idea behind HEMT and operation with structure will be discussed. Then performance analysis is carried out with some available literature followed by different factors influencing the performance of the device.

---

2 Motivation Towards HEMT

In the present day, the requirement for the high switching speed demanded in various fields like RF and Microwave communications technologies urged transistors to expand with the help of improved electron mobility and preferred transport features. The devices with high-speed electron mobility devices are invented by T. Mimura, who had conducted profound research work in the domain of mixed semiconductors of III-V materials at Fujitsu Laboratories Ltd, Kobe, Japan [1].

Conventional MOSFET devices and MESFET devices designed with the scaled channel lengths can lead to a scattering mechanism resulting in mobility decrement [2]. The conventional transistors are not only facing mobility problems but also suffering with many other factors such as, short channel effects, current leakage and power dissipation at the gate terminal, ionizing impurities, lattice and impurity scattering, threshold voltage shift in the negative direction, larger subthreshold slope, etc. These effects can degrade the device performance drastically. But fortunately, there is a preventive solution to ameliorate the device performance with the help of increment in doping concentration levels. However, some mentioned issues were solved with the rise in doping, but increased doping concentration is not a perfect choice for improving mobility. Some of the problems with raised doping levels are discussed as follows [3].

Figure 1 gives the effect of increment in doping concentration. From this Fig. 1, we can notice that if the doping is hiked, then the mobility will decrease. In this case, columbic scatterings will dominate the electron mobility so that it will lead to lesser speed. This is an untoward action, so the rise in doping option is not a good choice for this situation. Then, what is the alternative to overcome all these effects.

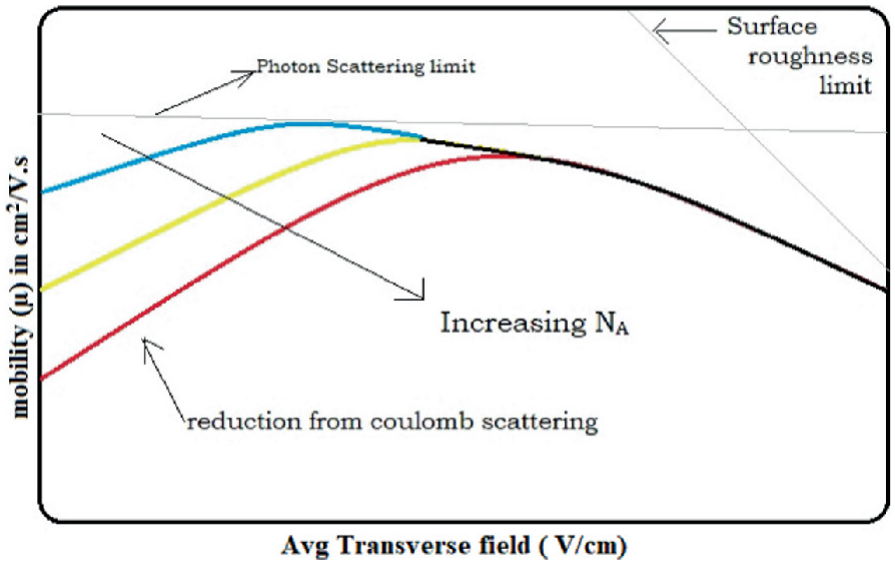

Fig. 1 Mobility variation with Average transverse field [4]

To get high mobility, one solution is known by a device based on HEMT. The HEMT contains heterojunction between two distinct

bandgap materials where charged electrons are confined in the quantum well and free from scatterings caused by impurity atoms. Therefore, the classical MOSFET limitations may be overcomed by this heterojunction principle.

The junction between two different materials having different bandgaps is known as a heterojunction. But there is one requirement to form the heterojunctions; when we grow one material on another, there should be a lattice match between those two materials. In this sense, the lattice constant must be comparable. If we want to grow silicon on germanium, there is a problem because the lattice constant is quite different in silicon and germanium. Where Si has 5.43 and Ge is having 5.65. But on the other hand, if we want to grow GaAs on Ge, there is no difficulty because the lattice constant matches [4, 5].

Now a days, the AlGaN/GaN HEMT became a splendid device that can work in a very high range of frequencies with high breakdown voltage ability and possess high electron speed in saturation. GaN exhibits extreme piezoelectric polarization, which supports the collection of huge charge carriers at the interface of AlGaN/GaN. So, therefore without extra doping in the AlGaN material, it can give the cloud of electrons to the interface. Therefore, AlGaN type devices giving more freedom in designing them. In this report, we review the GaN and its affiliate compositions with clear and in-depth explanations.

It is very clear from Table 1, where GaN has a high bandgap, high breakdown field and more saturation velocity among all the listed semiconductors. These features will give that GaN can be operated in high frequencies and higher voltage levels. Figure 2 provides a relation between cut-off frequency and break down voltage [6, 7].

Table 1 Physical parameters of different compound semiconductors [6]

Parameter	**Si**	**4HSiC**	**InP (InGaAs)**	**GaAs**	**GaN**
Bandgap (eV) @27 °C	**1.11**	3.02	1.35	1.43	*3.29*
Saturation velocity of electron ($\times 10^7$ cm/s)	**1.0**	*2.7*	2.5	2.0	*2.7*
Mobility of electron (cm^2/V s) @27 °C	1500	**700**	*15,000 (InGaAs)*	8500	*900*
Breakdown field (($\times 10^5$ V/cm)	**3.0**	25	7.5	6.5	*33*

Parameter	Si	4HSiC	InP (InGaAs)	GaAs	GaN
Thermal management conductivity (W/cm K)	1.5	*4.9*	0.68	**0.54**	1.3

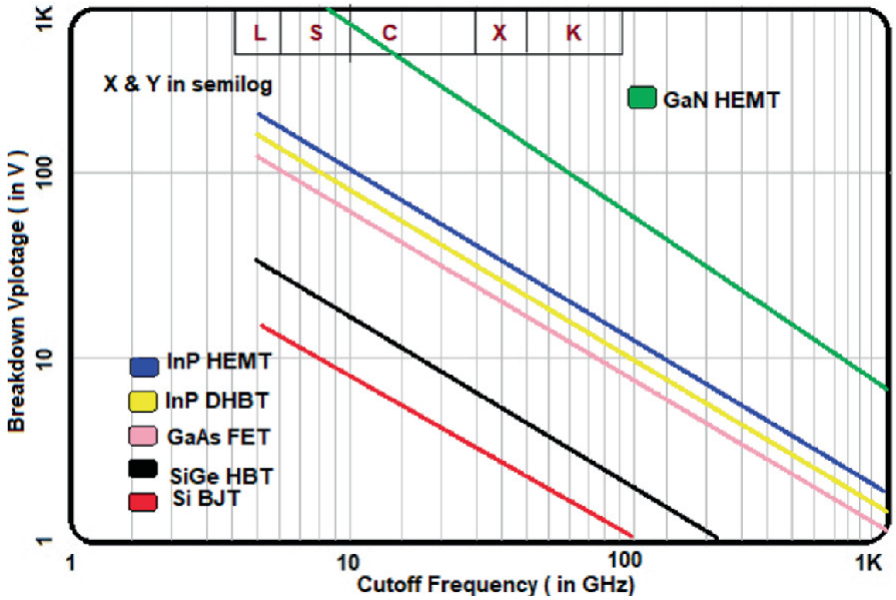

Fig. 2 Relationship between cutoff frequency and breakdown voltage [6]

Khan [8] was the first person who demonstrated the functional behaviour and the existence of 2DEG at the interface junction of AlGaN/GaN HEMT. The channel quality will be improved by reducing the defects in the manufacturing process. SiN passivation and charge controlling at the surface are going to diminish the effect of parasitic inconsistencies.

Figure 3 explains the relation between the operating voltage and power density on the output side. From Fig. 3, we can notice power density of GaN is four–six folds higher than the GaAs FET and SiC MESFET, and GaN has a high impedance. This unique feature leads to identify the GaN as the most promising material for communications.

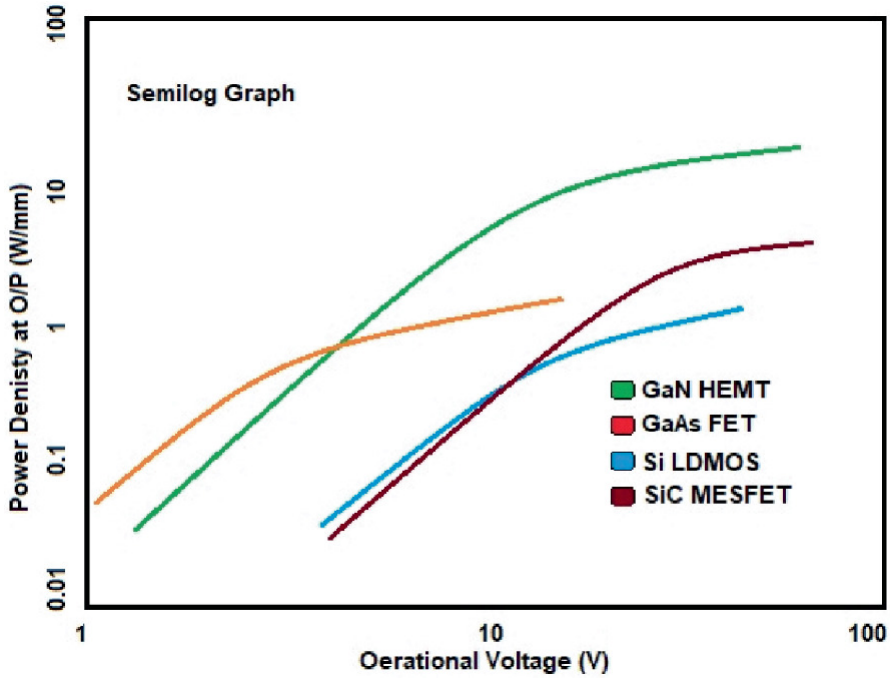

Fig. 3 Operation voltage versus output power density [6]

3 AlGaN/GaN HEMT Structure

Figure 4 depicts the HEMT based on AlGaN/GaN device, which is constructed on a silicon substrate. It has a huge concentration of 2DEG density due to its intrinsic properties like spontaneous polarization and piezoelectric effects. The concentration is almost equal to 2.7×10^{13} cm^{-2}, which is twelve folds higher than HEMTs based on AlGaAs/GaAs materials.

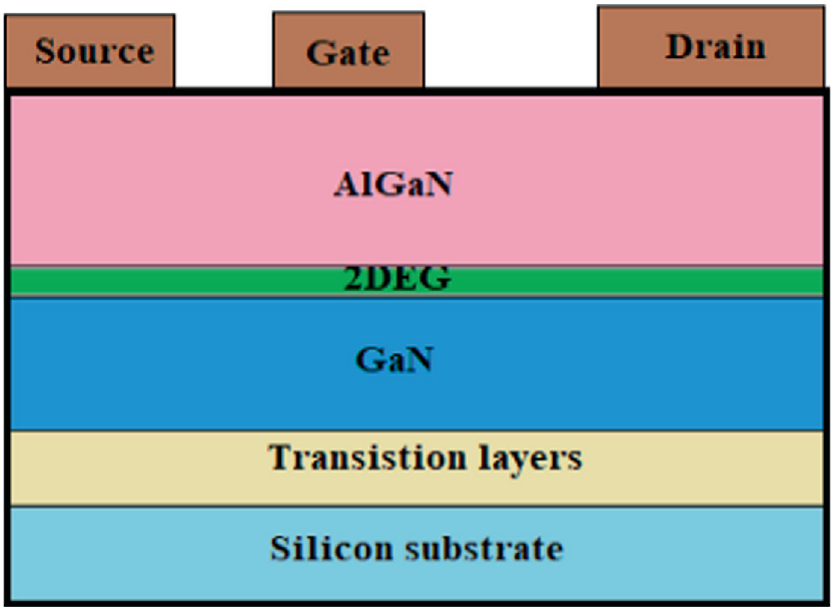

Fig. 4 Structure of AlGaN/GaN HEMT [43]

The mobility of the 2DEG at the intersection of AlGaN and GaN layers is very high, and its value is almost equal to 2000 cm^2/vs. The primary key to achieve this mobility is the existence of the concept of a 2DEG sheet charge at the junction point. This particular character makes the AlGaN/GaN-based HEMT as the most suitable device for RF and microwave applications [9–13].

4 Performance Analysis of AlGaN/GaN HEMT

AlGaN/GaN HEMT devices are becoming more and more popular for their unique nature in providing less noise, high breakdown voltage and promised speed. So, many aspirational researchers and companies are looking towards HEMT; this leads to more inspection and research on HEMT designs. Here, some of the existing literature reports of GaN HEMTs are discussed.

4.1 The Control of Charge Employed with 2D Distributive Design for I–V Characteristics

Mario [14] successfully developed a traditional charge control model in which elucidation of well-known one dimensional Schrödinger equation utilized with Robin boundary constraints in the short

horizontal field and velocity saturation key unravelled for 2D Poisson's expression. Feasible eigenvalues are introduced in expanding the solution of given Poisson's equations. Additionally, it acquired a more polarization effect by employing a doped 22 nm AlGaN flake on the top of the undoped AlGaN layer. Furthermore, they proposed an altered mobility prototype named Polyakov-Schwierz. Figure 5 depicts the relation of drain current (mA) and V_{DS} (V) with distinct voltages applied at the gate terminals.

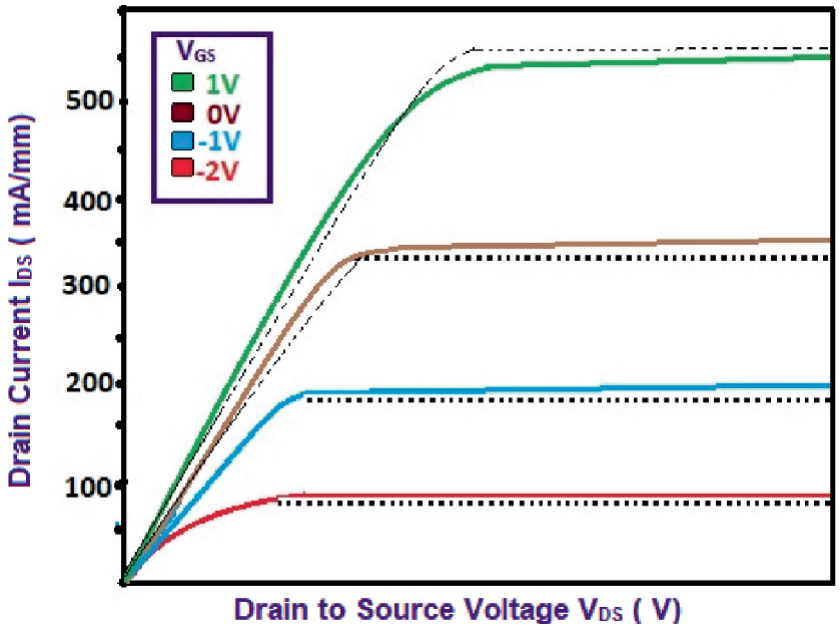

Fig. 5 Voltage–current characteristics for AlGaN (Al:15% and Ga: 85%)/GaN HEMT at distinct gate bias [16]

4.2 Surface Charge Relying on Parasitic Components

In [15], it mainly focused on the stability of congenital charges and capacitance parameters by expounding a solution for charged sheet solidity inside the movement of change particles. As a result, the outcome of modified HEMT is acquainted with parasitic modules. Therefore, surface potential is depending on latent parasitic elements formed by terminal charges. Figure 6 is clearly illustrated with donor traps and acceptor traps in HIGH and LOW positions of the device with the developed model [16]. This arrangement is finally constituted with tri terminal charges accompanied by several trans capacitances.

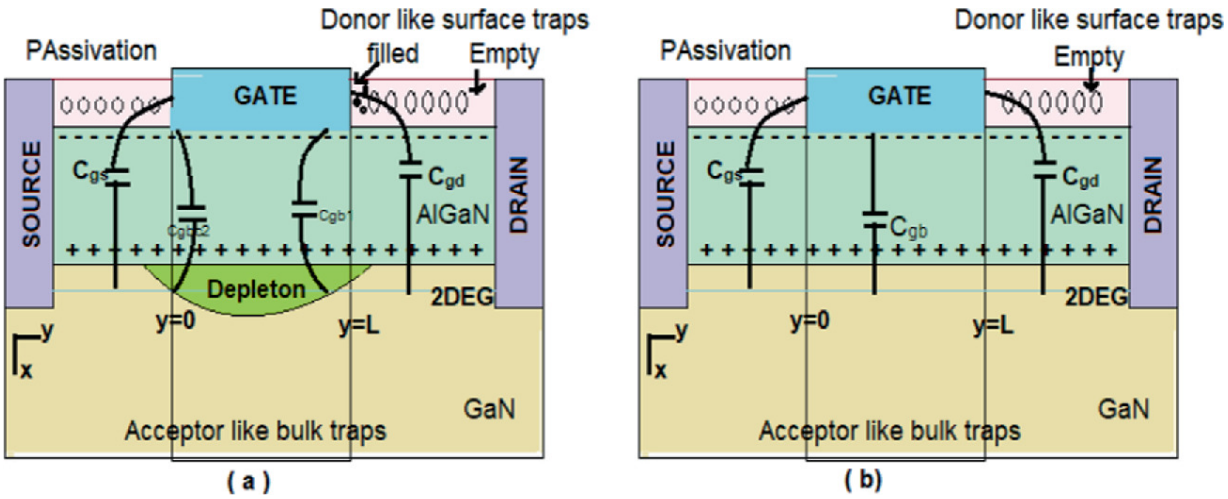

Fig. 6 Simplified schematic view of an AlGaN/GaN HEMT and its capacitance regions consisting of intrinsic and fringing **a** OFF state and **b** ON state [16]

4.3 Control of Gate Voltage Over the Crucial 2DEG Concentration

Many kinds of researches explained the mutual relation between 2DEG and Fermi level. This mechanism is demonstrated by Khandelwal et al. in [17] by taking some experimental setup in which the density of 2DEG composition is compared in separate dual regions. Here, the first region is assumed as a sub-band, is just above the Fermi level, and the second region is sub-band just below the Fermi level. So that, a novel model is developed by adding the above two areas and solving primary device characteristics equations, and clubbed them together without any extra parameters. This arrangement illustrated the variation in density of 2DEG composition in proportion with applied gate bias (Fig. 7).

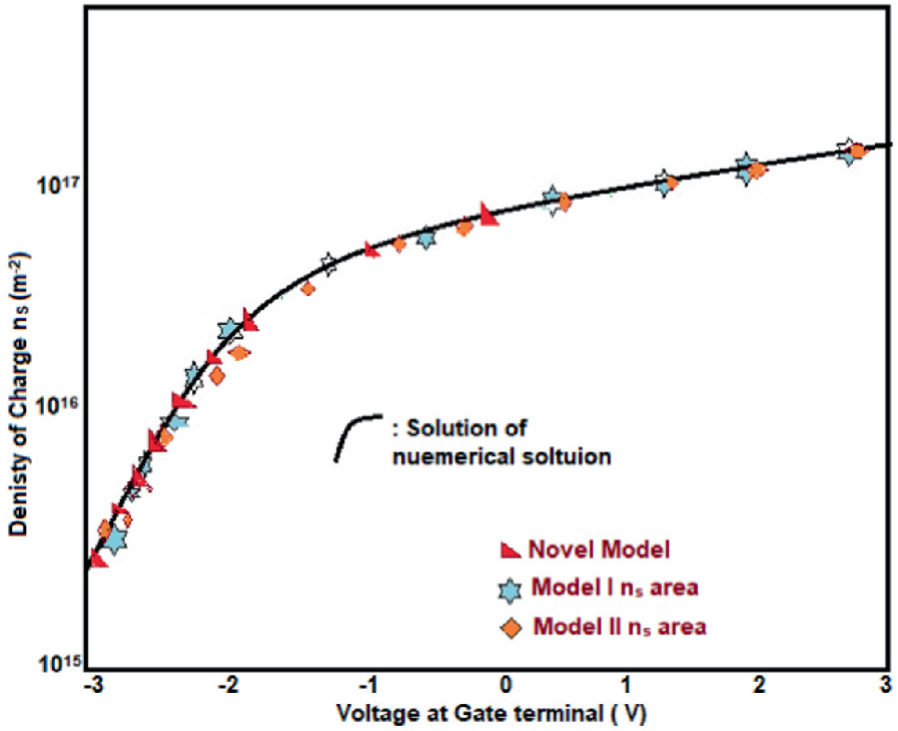

Fig. 7 Comparison of novel model and regions with gate bias [15]

4.4 Dual Gate AlGaN/GaN HEMT

In the year of 2013, Guohao offered a new kind of HEMT structure. This construction is constituted of two gates. The secondary gate electrode could enclose the primary gate and stretch towards the source and drain electrodes by the protrusion. The complete schematic of the novel dual-gate HEMT picture is shown in Fig. 8 [18, 19].

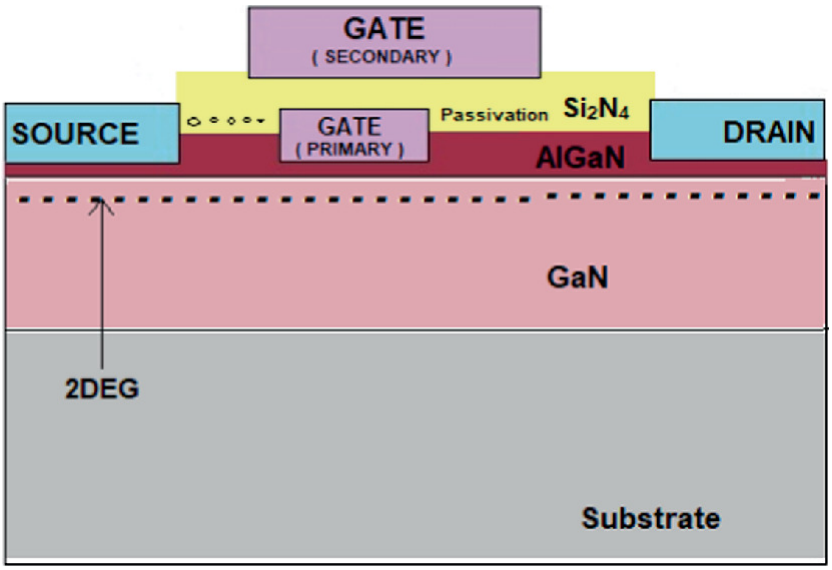

Fig. 8 Representation of an AlGaN/GaN double gate HEMT structure [16]

If we observe, the structure of dual Gate HEMT is almost equal to single gate HEMT except for the buffer layer, which is situated on the top and bottom sides. Dual Gate HEMT provides excellent benefits over traditional single gate HEMT devices. Dual gate devices prevent intrusion of charge carriers to buffer side and provide enhanced pinch-off characteristics and amplified g_m.

4.5 Role of Temperature

It is also one of the crucial factors which affect the HEMT device. For higher temperatures, the device can't stick to its promises. It couldn't deliver the optimal performance in such incidents. Therefore, a thermal design model is needed for understanding device performance status in high temperatures. Bangall et al. [20] introduced one such design which can handle thermal effects very efficiently. The configuration developed by Bangall is shown in Fig. 9. The proposed design comprises of heat sinks placed within several layers. Several mathematical models are applied to solve the setup with the help of the Fourier series and proclaimed with well-known spectra.

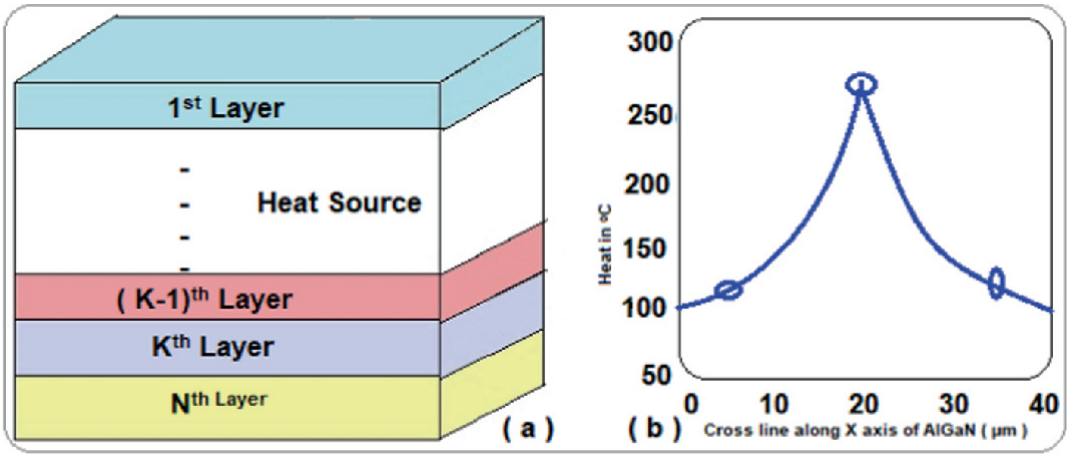

Fig. 9 **a** HEMT design based on (**b**) Distribution of temperature index. Heat source arrangement [20] in AlGaN/GaN HEMT [20]

5 Factors Affecting the Performance of GaN HEMT

5.1 Trapping Effects

The primary cause of effects is the production of nearby active energy states within the semiconductor energy—gap, which emanates from the direction of the channel and gate terminal as a consequence of traps that will be formed. It leads to a powerful jolt on the device's static and dynamic performances. Trapping effects are mainly due to the formation of parasitic elements. Generally, parasitic effects are developed in GaN HEMT due to asymmetry in crystal and impurities within the device layer due to atom dislocations [21]. The device's performance weakened due to engulfed trapping phenomena. Applying viable and feasible electric fields can eradicate the above said unwanted occurrence. Two main dominant causes of trapping effects are the current collapse in output current and the kink effect [22]. Let us see how the kink effect is forming; it is the abrupt change of drain current because of the demure trapping effect on lesser drain bias. The kink effect is thrived on lower drain voltage (V_{ds}) and disappeared on the higher electric field, which concomitant to an unpredicted increase in current at drain due to higher negative in a pinch-off voltage. Consequently, ON resistance along with transconductance (g_m) is also affected [23].

Traps that are being occupied on the top region of the energy bandgap are known by acceptors, and those existed on the bottom place of bands are known as donors, will dominate the performance of the device. Traps are scrambled at the AlGaN barrier because the Fermi level is placed above the surface trap index. The AlGaN barrier used is very thin; hence traps are easily moved to the channel on account of the unique polarization process in AlGaN [24]. Arrhenius [25] proposed and developed an equation for emission rate at the trap level. Which is given by

$$e = AT^2 \exp\left(-\frac{E_F}{kT}\right) \tag{1}$$

$$\Delta \emptyset_{PF} = \left(\frac{q^3}{\pi}\right)^{1/2} \sqrt{F} + \beta \sqrt{F} \tag{2}$$

$$E_{\mathrm{i}}(F) = E_{\mathrm{i}}(0) - \beta\sqrt{F} \tag{3}$$

The barrier (^{a}) is diminishing with the changes in the electric field (F). Here $E_{\mathrm{i}}(F)$ is the ionization energy of a function, and the symbols are their usual meanings. Therefore, traps formed at AlGaN surface proximity can influence the channel reduction and plummet in drain current [26].

5.2 Surface Passivation

The unwanted interaction of outside signals and chemical responses is detached from transistor devices with the help of situating an oxide layer above the HEMT. This arrangement stabilizes the electrical performance, refines breakdown voltage, reduces the undesired leakage current and improves power consumption [27]. The compound material Si_3N_4 can curtail the impact of trap states. In earlier developed devices, silicon dioxide is widely used to fulfil the desired activity. It demonstrated in [28], silicon dioxide passivation exhibited an excellent result of lowering in leakage current (0.009 A) when passivation is inspected with silicon nitride (Si_3N_4) on the identical and same wafer. But, Silicon Nitride exhibits considerable output current by 700 mA and a subtle increase in leakage current. Bruce [29] reported that high voltage transitions with Si_3N_4 passivation could give the outstanding minimization of on resistance value.

In another research by Chu [30] exhibited passivation by Si_3N_4, ALD and including filed around 1200 V, augmentation in drain current, decrease in C_{gd} to 3 pF accompanied by diminishing in trap effects. If La_2O_3, including Si3N4, used in passivation could develop a drastic increase in the breakdown voltage of HEMT. Surprisingly, Nicolas Herbecq [31] reported a matchless increased withstand voltage of 3000 V by passivation with MOCVD SiN formed on AlGaN/GaN HEMT besides extinguishing substrate parasitic conduction.

A Slender ALN film is passivated on the surface with the help of PEALD could result in the pruning of ON resistance value in the region of high-stress electric fields. Huang [32] examined passivation by AlN

PEALD gives nominal leakage current but allows output current to 350 mA. Generally, the solidness of the passivation layer should maintain in the range of 50–100 nm with encompassing manifold field plates. CF Lo developed a distinct HEMT [33] of having mobility 1900 cm^2/Vs and an impressive output current of 1.25 A by incorporating the passivation with AlN with the help of ozone gate advance technology.

5.3 Field Plate Arrangement

Many types of researches and experiments were noticed that the optimized performance characteristics of GaN HEMT with the aid of field plates. Brannick [34] suggested the attachment of field plates around gate and source points can deliver improved power attributes of the device, and extending the length of the field plate can reduce the degradation of the device positively. It is distinctly deciphered that the trap effect decreased by aligning lengthy field plates in some research.

Here, one main difference in arrangement can give the best results, i.e. field plate at gate terminal bestows good and acceptable breakdown voltage escorted by subjugating current collapse. But field plates in the source terminal's proximity can quickly introduce more unwanted traps into the gate region. Multiple field plate layer structures are taken into consideration in the analysis of boosting device performance. It yields remarkable performance by eliminating lag at the drain, dwindling in current collapse. Double field gates can exhibit dealing in sharing applied voltage in an identical manner, which is not observed in the devices having a single field plate connection.

In [35], the author proved the magnified performance of the device by examining 0.6 μm and 0.5 μm lengths of gate and field late, respectively. Ahmet Toprak [35] stated GAN could give five folds better power handling capacity (33%) at the drain terminal against the same setup with GaAs. One more advantage also identified in some more research papers is handling self-hotness, one of the essential factors for managing power gadgets. We know that if the device's temperature increases, it will affect the working and gives unaccepted results. But this kind of complication issue related to self-heat is also curtailed with the service of field plates. This improvement is explained by Šodan [36]; in this paper, some experimental setup is made to compare two

devices with the same properties with different field plate configurations. It has shown that reduced thermal resistance was achieved in field plate arrangement.

But some kinds of limitations are restricted to the length of the plates; otherwise, some disturbance would cause in breakdown voltage of the device. The remedy for improving breakdown voltage is improving the dimension over drain and gate node described in [35]; it also achieved appreciable mobility of the value 1310 $cm^2\ V^{-1}\ s^{-1}$. So from all these works of literature [34–38], different lengths of field plates have almost the same breakdown voltage, reduced current collapse and vanish the traps at the gate surface. But the difference is clearly visible in ON resistance, i.e. stretched field plates can diminish ON resistance value.

5.4 Dominance Caused by the Back-Barrier Layer

There is one more primary factor that affects the performance of GaN HEMT is known as the back barrier. It is possible to procure high speed by decreasing gate length; consequently, meticulous pinch-off voltage features eluding from the upper part of the barrier in the presence of more drain voltage. This will leads to short channel effects raised in the device. Therefore curtailing gate length has some limitations. In [39], it has instigated the pivotal concept of back barrier with AlGaN in GaN HEMT with suitable gate length. The setup with the back barrier is successfully enclosing the 2DEG in the allotted channel. Mobility of the transistor increased thoroughly sans touching pinch-off characteristics. Whilst, astonishing polarization sequel also rose drastically.

Here, one point should be remembered for polarization, which also escalates when Al's content is increased but leads to degradation of the device by forming traps with stretching Al content. As we discussed earlier, the kink effect known by an abrupt spike in current at meagre source voltage will come into the picture [40]. At more V_{DS}, hot electrons are performing detrapping effects with the help of included back barrier. So in the process of controlling electrons in the top region, the barrier lost its control over electron blocking in the lower barrier layer.

So, to conquer the situation, an additional substitution of the hindmost barrier layer within the device. Now device performance is

remarkable with augmented breakdown voltage, amplified 2DEG concentration, reduction of current collapse, and interestingly DIBL subjugated. With some experimental setup by Chunjiang [41] demonstrated the largest output current 1. 3 A, and acceptable breakdown voltage accompanied with the back-barrier layer. In [42], it is developed with a twin barrier layer in the bottom side with few changes in gate length, exhibited a truncated ON resistance followed by the fabulous breakdown voltage of 2200 V.

So, from all these results and discussions, the bottom barrier layer in GAN HEMT plays a vital role in enhancing the performance characteristics (2DEG, current collapse, trap removal, pinch-off voltage) of the device.

---

6 Conclusion

This report shows a detailed review of the performance analysis of AlGaN/GaN-based HEMT. These devices are an excellent choice for applications involved in RF and Microwave Nanoelectronics due to their distinctive character of wide bandgap, extensive frequency range and high breakdown voltage of operation. The review started with a brief acquaints with the fundamental need of HEMT devices and explained basic working principles with primary structure. Mainly, it furnished the several factors which can impact the performance of the AlGaN/GaN HEMT device in an understandable fashion. This paper demonstrated various primary issues, and key remedies for GaN-based HEMT's are discussed with the existed literature of several research papers. This review work presents a direction in the future advancement of HEMT to aspirant researchers of a similar domain.

References

1. T. Mimura, The early history of the high electron mobility transistor (HEMT). IEEE Trans. Microwave Theory Tech. **50**(3), 780–782 (2002)
[Crossref]

2. T. Mimura, A new field-effect transistor with selectively doped GaAs/n-Al Ga As heterojunctions. Jpn. J. Appl. Phys. **19**(5), 225–227 (1980)
[Crossref]

3.

U.K. Mishra, P. Parikh, Y.-F. Wu, AlGaN/GaN HEMTs—An overview of device operation and applications. Proc. IEEE **90**, 1022–1031 (2002)
[Crossref]

4. C.G. Van de Walle, C. Stampfl, J. Neugebauer, Theory of doping and defects in III–V nitrides. J. Cryst. Growth **189**(190), 505–510 (1998)
[Crossref]

5. G. Snider, *1D Poisson Band Diagram Calculator* (University of Notre Dame Press, South Bend, IN)

6. S. Nakajima, *Compound Semiconductor IC's*. 0-7803-889-17/05/$20.0002 005 lEEE

7. E.O. Johnson, RCA Rev. **26**, 163 (1965)

8. M.A. Khan, et al., Observation of a two-dimensional electron gas in low pressure metalorganic chemical vapour deposited GaN/AlGaN heterojunctions. Appl. Phvs. Lett. **60**, 3027–3029 (1992)

9. U.K. Mishra, AlGaN/GaN HEMTs an overview of device operation and applications. Proc. IEEE **90**(6), 1022–1031 (2002)
[Crossref]

10. Wang, Maximizing the performance of 650-V p-GaN gate HEMTs: Dynamic RON degradation and circuit design considerations. IEEE Trans. Power Electron **32** (7), 5539–5549 (2016)

11. J.P. Ibbetson, P.T. Fini, K.D. Ness, S.P. DenBaars, J.S. Speck, U.K. Mishra, Polarization effects, surface states, and the source of electrons in AlGaN/GaN heterostructure field effect transistors. Appl. Phys. Lett **77**, 250–252 (2000)
[Crossref]

12. L. Hsu, W. Walukiewicz, Effect of polarization fields on transport properties in AlGaN/GaN heterostructures. J. Appl. Phys **89**, 1783–1789 (2001)
[Crossref]

13. T.R. Lenka, A.K. Panda, Characteristics study of 2DEG transport properties of AlGaN/GaN and AlGaAs/GaAs-based HEMT. Semiconductors **45** (5), 660–665 (2011). (Springer) [IF: 0.739 (2014), JCR-Thomson Reuters, SCI]

14. M. Li, Y. Wang, 2D analytical model for current–voltage characteristics and transconductance of AlGaN/GaN MODFETs. IEEE Trans. Electron Devices **55**(1), 261–267 (2008)
[Crossref]

15. A. Zhang, L. Zhang, Z. Tang, X. Cheng, Y. Wang, K.J. Chen, M. Chan, "Analytical modeling of capacitances for GaN HEMTs," including parasitic components. IEEE Trans. Electron Devices **61** (3) (Mar 2014)

16. J. Shanthi, P. Vimala, High electron mobility transistor: A review on analytical models. IJIRST Int. J. Innov. Res. Sci. Technol. **3** (05) (Oct 2016) ISSN (online): 2349-6010

17. S. Khandelwal, N. Goyal, T.A. Fjeldly, A physics-based analytical model for 2DEG charge density in AlGaN/GaN HEMT devices. IEEE Trans. Electron Devices **58**(10), 3622–3625 (2011)

[Crossref]

18. G. Yu, Y. Wang, Y. Cai, Z. Dong, C. Zeng, B.Zhang, Dynamic "characterizations of AlGaN/GaN HEMTs with field plates using a double-gate structure. IEEE Electron Device Lett. **34** (2) (Feb 2013)

19. S. Zafar* (a, b), A. Kashifa, S. Hussain (b), N. Akhtar (a), N. Bhatti (a), M. Imran (a), Designing of double gate HEMT in TCAD for THz applications. In: Proceedings of 2013 10th International Bhurban Conference on Applied Sciences & Technology (IBCAST), Islamabad, Pakistan (15th–19th January, 2013)

20. K.R. Bagnall, O.I. Saadat, T. Palacios, E.N. Wang, Analytical thermal model for HEMTs with complex epitaxial structures. In: 2014 IEEE Intersociety Conference on Thermal and Thermomechanical Phenomena in Electronic Systems (ITherm), Orlando, FL, USA. IEEE (27–30 May 2014), pp. 947–958

21. Zanoni, Trapping mechanisms in GaN-based MIS-HEMTs grown on silicon substrate. Phys. Status Solidi Appl. Mater. **212**, 1122–1129 (2015)

22. G. Meneghesso, Anomalous Kink effect in GaN high electron mobility transistors. IEEE Electron Device Lett. **30**(2), 100–102 (2009)
[Crossref]

23. Meneghesso, Reliability and parasitic issues in GaN-based power HEMTs: A review. Semicond. Sci. Technol. **31**, 093004 (2016)

24. J.B. Shealy, 0.9 W/mm, 76% P.A.E. (7 GHz) GaInAs/InP composite channel HEMTs. In: International Conference on Indium Phosphide and Related Materials (1997), pp. 20–23

25. J.L. Jimenez, Recent advances on the understanding of the physics of failure of GaN on SiC FET technology. In: Proceedings of IEEE International Reliability Physics Symposium, Phoenix, USA, pp. 429–435 (2008)

26. A.S.A. Fletchera, D. Nirmalb, A survey of gallium nitrate HEMT for RF and high power applications. Superlattices Microstruct. https://doi.org/10.1016/j.spmi.2017.05.042

27. T.R. Lenka, A.K. Panda, AlGaN/GaN-based HEMT on SiC-substrate for microwave characteristics using different passivation layers. Pramana J. Phys. **79** (1), 151–163 (2012) (Springer) [IF: 0.649 (2014), JCR-Thomson Reuters]

28. N. Kumar, Characterization of parasitic resistances of AlN/GaN/AlGaN HEMTs through TCAD-based device simulations and on-wafer measurements. IEEE Trans. Microwave Theor. **64**(5), 1351–1358 (2016)
[Crossref]

29. B.M. Green, The effect of surface passivation on the microwave characteristics of undoped AlGaN/GaN HEMTs. IEEE Electron Device Lett. **21**(6), 268–270 (2000)
[Crossref]

30. R. Chu, 1200-V normally off GaN-on-Si field-effect transistors with low dynamic onresistance. IEEE Electron Device Lett. **32**(5), 632–634 (2011)
[Crossref]

31. N. Herbecq, Above 2000V breakdown voltage at 600 K GaN-on-silicon high electron mobility transistors. Phys. Status Solidi A **213** (4), 873–877 (2016)

32. S. Huang, Effective passivation of AlGaN/GaN HEMTs by ALD-grown AlN thin film. IEEE Electron Device Lett. **33**(4), 516–518 (2012)
[Crossref]

33. C.F. Lo, Passivation of AlN/GaN high electron mobility transistor using ozone treatment. J. Vac. Sci. Technol. B: Nanotechnol. Microelectron. Mater. Process. Meas. Phenom. **28**, 52 (2010)
[Crossref]

34. A. Brannick, Influence of field plate on the transient operation of the AlGaN/GaN HEMT. IEEE Electron Device Lett. **30**, 436–438 (2009)
[Crossref]

35. A. Toprak, Structural field plate length optimization for high power applications. In: Proceedings of the 9th European Microwave Integrated Circuits Conference (2014)

36. V. Šodan, Influence of field-plate configuration on power dissipation and temperature profiles in AlGaN/GaN on silicon HEMTs. IEEE Trans. Electron Devices **62** (8) (2015)

37. T. Horii, High-breakdown-voltage GaN vertical Schottky barrier diodes with field plate structure. Mater. Sci. Forum **615–617**, 963–966 (2009)
[Crossref]

38. H. Xing, High breakdown voltage AlGaN–GaN HEMTs achieved by multiple field plates. IEEE Electron Device Lett. **25** (4) (2004)

39. M. Micovic, GaN double heterojunction field effect transistor for microwave and millimeter wave power applications. Int. Electron Device Meet. **4**, 807 (2004)

40. M. Xiao-Hua, Kink effect in current–voltage characteristics of a GaN-based high electron mobility transistor with an AlGaN back barrier. China. Phys. B **23** (2) (2014)

41. R. Chunjiang, GaN HEMT with AlGaN back barrier for high power MMIC switch application. J. Semicond. **36** (1) (2015)

42. A. Tzou, An investigation of carbon-doping-induced current collapse in GaN-on-Si high electron mobility transistors. Electronics **2** (5) (2016)

43. https://en.wikipedia.org/

T. R. Lenka, H. P. T. Nguyen (eds.), *HEMT Technology and Applications*, Springer Tracts in Electrical and Electronics Engineering
https://doi.org/10.1007/978-981-19-2165-0_12

High Electron Mobility Transistor: Physics-Based TCAD Simulation and Performance Analysis

Kalyan Biswas[1] ✉, Rachita Ghoshhajra[2] and Angsuman Sarkar[3] ✉
(1) ECE Department, MCKV Institute of Engineering, Liluah, Howrah, WB, India
(2) CSE Department, MCKV Institute of Engineering, Liluah, Howrah, WB, India
(3) ECE Department, Kalyani Government Engineering College, Kalyani, Nadia, WB, India

✉ **Kalyan Biswas (Corresponding author)**
Email: kalyan.b.2006@ieee.org

✉ **Angsuman Sarkar**
Email: angsumansarkar@ieee.org

Abstract

High Electron Mobility Transistor (HEMT) attained great interest because of its superior electron transport making it suitable for applications in high-speed circuits and high power requirements. These devices are finding special interest to replace conventional field-effect transistors having outstanding performance in the domain of high-frequency applications. In HEMT, the high mobility of electrons and highly confined characteristics of the two-dimensional electron gas made sure that modulation doping could be utilized to have high-speed field-effect transistors having brilliant “Short Channel Effects” (SCEs) and excessive scope of scaling. However, lack of existing experimental

results of such a device, designers require a dependable tool for simulation and analysis of the device characteristics in less time and low cost before device is fabricated for commercial use. Therefore, physics-based device simulator for design and performance prediction of the semiconductor device are very important. This book chapter describes an overview of the HEMT device and its physics-based simulation for performance analysis.

Keywords HEMT – Heterojunction – 2DEG – GaN – InGaAs/InP – TCAD simulation

---

1 Introduction

The growing demand of higher switching speed which is the basic requirement in the microwave communications field and RF technology, made it crucial for transistors to go forward with high electron mobility and greater transport characteristics. In order to cater the necessity of high power, high frequency, and low noise applications, traditional MOSFETs and related devices have requirement of a very short length of channel so that most of the carriers experience the least impurity scattering which causes degradation of performance. HEMT device was first developed and presented by Mimura and his team at Fujitsu Labs of Japan in the year 1980 [1]. Many composite materials have a much higher mobility than silicon, that is why devices are made using composite semiconductors and those devices show better performance in high-frequency operation. Modulation doping is one of the most significant developments that really augmented the importance of compound semiconductors. Modulation doping offers an important benefit of the free carrier concentration within the semiconductor layer. “High Electron Mobility Transistor” (HEMT) is a special type of FET based on this principle, which has a junction of two materials having different bandgaps (known as heterojunction) and acts as a channel as a substitute for a doped region (modulation doping). Heterojunction along with modulation doping rise the channel mobility in the HEMT device.

In microwave circuit applications HEMTs device are considerably important. With the advancement in HEMT device technology, many areas are found for its application, especially at millimeter and submillimeter wave frequencies. However, a substantial challenge for low-visibility, medical imaging, and security in addition to telecommunications applications still exists. The first generation most common materials used AlGaAs/GaAs lattice-matched HEMTs, later on, many material systems have been considered for the fabrication of HEMT device. In recent years, because of the technology generation below 22-nm, a lot of hypotheses have been created at the end line of the silicon device roadmap. A lot of attempts are being made on different materials having high channel mobility, among them HEMT-like structures are the most probable candidate.

"High Electron Mobility Transistor" is also recognized as "modulation-doped-FET" (MODFET) or heterostructure FET (HFET). There are lots of HEMT structures reported in literature. The fundamental principle of HEMT devices is the formation of heterostructure which consists of a doped wide bandgap energy material (barrier) and an undoped narrow energy bandgap material (channel) which form heterojunction [2].

This chapter begins with a brief discussion on working principle of HEMT devices. Then different common structures and material combinations used to realize HEMT devices are presented in Sect. 2. TCAD device simulation methodology along with different physics-based models are also introduced in Sect. 3. Basics of TCAD simulation methodology are presented in Sect. 4. Performance analysis of HEMT and MOS-HEMT devices are explained in Sect. 5. In Sect. 6, some of the applications of HEMT in communication, space applications, and biomedical sensor field is highlighted. Finally, a conclusion is made in Sect. 7.

---

2 Basic Principles

In HEMTs, heterojunctions are created by different semiconductors having a difference in bandgaps which requires the conduction band (CB) and valence band (VB) right through the material to bend to have a continuous level. In the formation of heterostructure with a material

having a wide bandgap and a narrow bandgap, the alignment of the bandgap energies is very essential. Based on the alignments of the bandgap, there may be different types of structure that exists depending on material combinations. Different possible bandgap alignments are shown in Fig. 1, namely, Straddling (a), Staggered (b), and Broken (c). Heterojunctions can also be classified based on the conductivity of materials forming heterojunction. There are two types of heterojunctions based on conductivity, one is isotype and another one is anisotype heterojunction. Isotype heterojunctions are those which are formed between the semiconductor having the same conductivity (N–n or p–P), where the capital letter represents the larger bandgap materials and small letter represents the low bandgap materials. However, anisotype heterojunctions formed between the semiconductor materials having different conductivity (N–p or n–P).

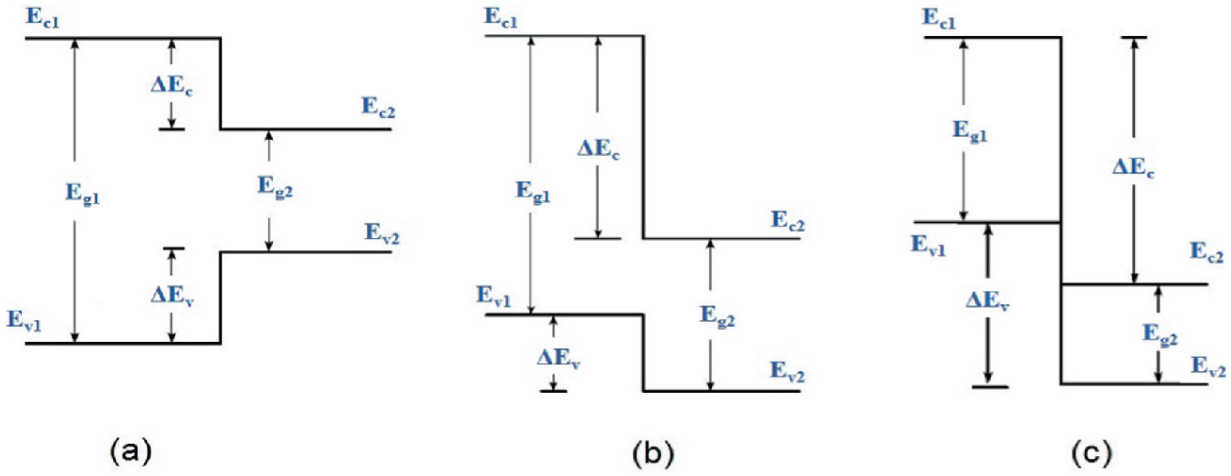

Fig. 1 Different possible bandgap alignments

The Straddling type heterojunction is the most important for the creation of the high mobility of electron in the channel of HEMT. The conduction band offset formed depends on the electron affinity difference of the semiconductors used.

When forming a heterojunction, the bending of band is necessary to have a continuous level. Excess electrons of doped wide bandgap materials diffuse toward the adjacent lower bandgap materials containing lower energy states. Thus, potential difference will be caused because of the movement of electrons which in turn produce an electric field between the two materials. Drift in electrons is caused by

this electric field to bring back to the conduction band (CB) of the larger bandgap material. These processes of drift/diffusion will be continued till they stabilize each other and create a junction at the equilibrium. It's worth mentioning that the smaller bandgap material which is undoped has an excess of majority carriers. As the material with lower bandgap is undoped, it has no donor atoms to create scattering as a result having high mobility. In HEMT, the most interesting aspect is the band discontinuities at the valance and conduction band which can be adjusted to control the flow of careers to and from the device. Because of this diffusion of the carriers, an electron accumulation is created inside the narrow bandgap material along the boundary of the two regions. A very large current in these devices can be generated because of the accumulation of electrons. The region of high electron density is generated as a result of accumulated electrons and is also known as 2D electron gas (2DEG). Figure 2 presents the schematic representation of a general band diagram shaped at the heterojunction for usual HEMTs [3].

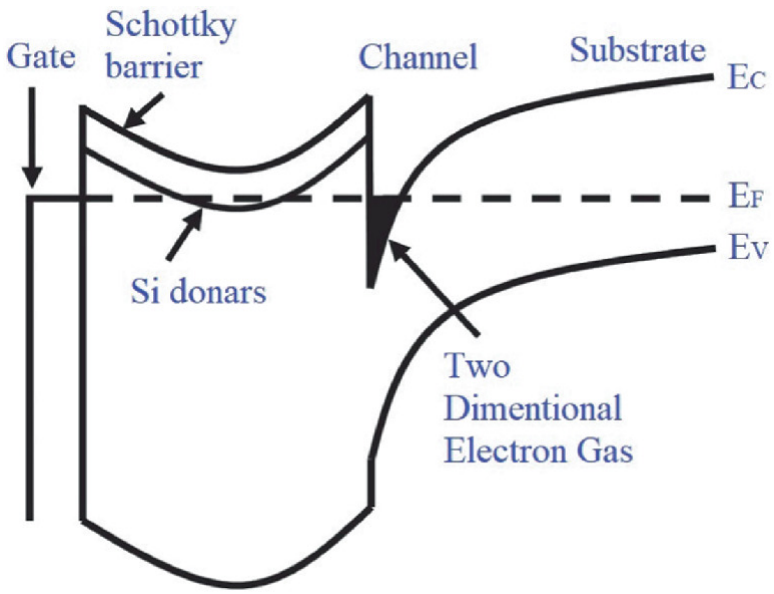

Fig. 2 Schematic band diagram of HEMTs

3 Different HEMT Structures

3.1 GaN-Based HEMTs

Other than optoelectronics domain, GaN finds applications in power electronics also because of its capability of high temperature and high frequency operations. Silicon Carbide (SiC) and Gallium Arsenide (GaAs) are also competing materials for use in high power electronics [4] apart from GaN. Different parameters of various semiconductor materials relevant to power devices are compared and shown in Table 1 [5]. From this table, it can be understood that both GaN and SiC are advantageous than GaAs and Si when bandgap and critical electric fields are considered. This allows these materials to have much higher breakdown voltage as well as much higher blocking capability enabling it to handle high power devices [5]. III–V group materials have been emerging as a strong alternative materials for applications in the domain of high power, high frequency applications in the recent times [6]. Even though the effective electron mass in the device using GaN is higher in comparison to GaAs technology, there are a few notable advantages which have made this a more favorable technology. Structure of GaN HEMTs consists of a layered structure similar to usual GaAs-based HEMTs and is depicted in Fig. 3. The first attraction is the large bandgap having very high breakdown voltage that lends this device for specialized applications. The second important characteristic of the III–V nitrides is the heterostructure technology which can provide Quantum well, heterojunction structure, and modulation-doped heterointerface all can be created in this system.

Table 1 Properties of semiconductor material

Material	**Bandgap, E_g (eV)**	**Relative dielectric Constant, ε_r**	**κ (W °Kcm^{-1})**	**E_c (V cm^{-1})**
Silicon (Si)	1.12	11.8	1.5	3×10^5
Gallium arsenide (GaAs)	1.42	12.5	0.54	4×10^5
Indium phosphide (InP)	1.33	12.4	0.67	4.5×10^5
3C–SiC	2.24	9.7	4.0	1.8×10^6
4H–SiC	3.23	10.0	4.0	3.5×10^6
6H–SiC	2.86	10.0	4.0	3.8×10^6

Material	Bandgap, E_g (eV)	Relative dielectric Constant, ε_r	κ (W °Kcm^{-1})	E_c (V cm^{-1})
Diamond	5.6	5.5	20.0–30.0	5×10^6
Gallium nitride (GaN)	3.4	9.5	1.3	3.3×10^6

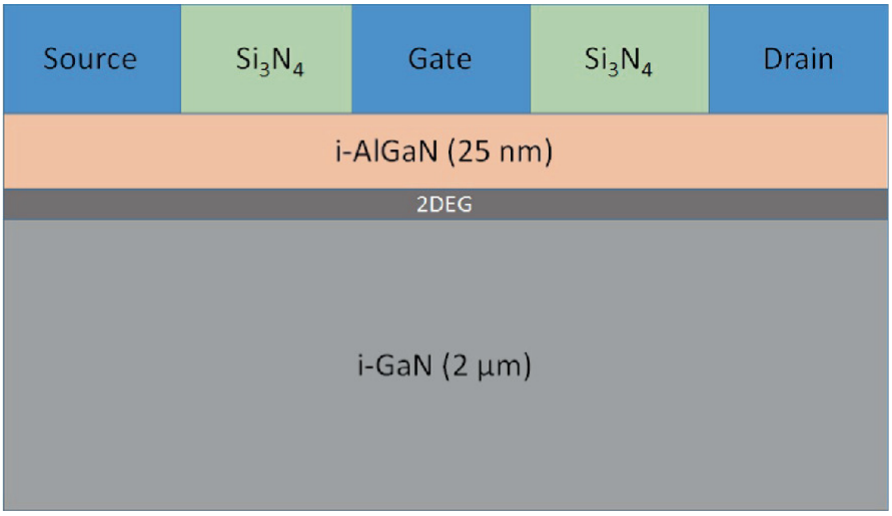

Fig. 3 Schematic representation of GaN-based HEMT

Fabrication process for GaN HEMT involves epitaxial growth on non-native substrates like SiC, Si, sapphire, and diamond. GaN substrates are very costly, due to difficulty to grow and available in small sizes which are not viable for large-scale production, thus GaN epitaxial layers are grown on non-native or foreign substrates. To evade vertical breakdown, the substrate is semi-insulated electrically and should be thermally conductive to dissipate heat generated at the channel. Lattice constant of GaN and the substrate material should be closely matched in order to reduce the effects of stress and grow epitaxial layers of superior quality.

3.2 Ga–As-Based HEMTs

A general structure of GaAs material-based HEMT is shown in Fig. 4. A heterostructure is formed in between AlGaAs having wide bandgap and GaAs, the smaller bandgap to detach the majority carriers from the ionized impurities. The material having a wider bandgap has a doping density of the order of 5×10^{17} cm^{-3}. As a consequence, a channel layer

is produced along the interface of GaAs and AlGaAs. A very thin layer of AlGaAs may be utilized as a spacer layer is kept undoped to reduce the scattering effect. At the underneath of the structure, the Si or GaAs is used as a substrate material.

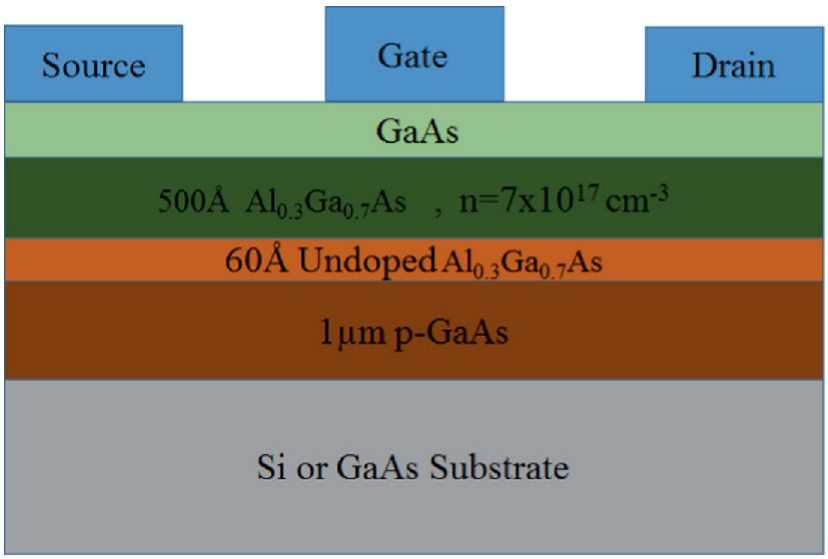

Fig. 4 Schematic of GaAs-based HEMTs

3.3 InP-Based HEMTs

Indium Phosphide (InP) is one of the attractive materials for optoelectronics and electronic device like HEMTs, photo-detectors, laser diodes, and solar cells. The advantage of InP-based devices are high carrier densities, high mobility of electrons and high saturation velocity at room temperature. In comparison to GaAs-based HEMT, InP-based HEMT results in lesser effective mass of electron in the InGaAs channel. Relatively, large conduction band offset (about 0.5 eV) in-between the channel layer and the neighboring barrier layer, InAlAs is formed in these types of devices [7, 8]. Therefore, InP-based HEMTs have high concentration of electrons and demonstrate high electron mobility and higher saturation velocity. A general structure of InP material based-HEMT is shown in Fig. 5.

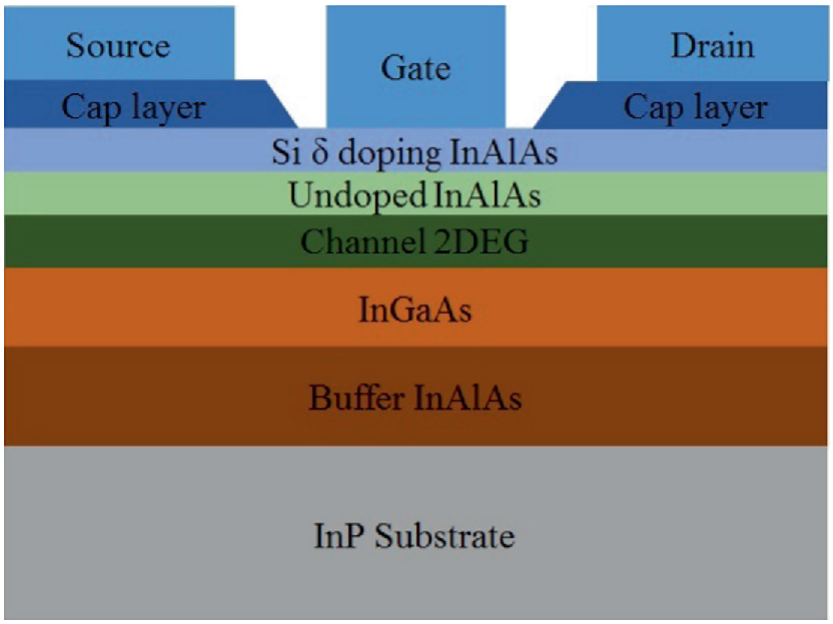

Fig. 5 Schematic of InP based HEMT

4 TCAD Simulations

With the increasing demand of HEMT technology for its acceptance in the areas of high frequency and high power applications, researchers show lots of interest in these devices in recent times. Because of the lack of exiting experimental results of such a device designers want a trustworthy tool to predict performance of the device in advance within little time and less cost before it is fabricated for commercial use. Therefore, physics-based device simulators for design and performance prediction of the semiconductor device are very important. Though many analytical models are already reported in the literature by the researchers to study and analyze the characteristics of HEMTS and to enhance device performance, TCAD device simulators are much more convenient to use for rapid developments [9]. Physics-based models are developed by considering the specific material properties focused on energy band diagram, polarization effect, piezoelectricity, etc. The specific models are developed consisting of a set of primary equations, which connect the carrier densities as well as the electrostatic potential using some simulation domain. Those fundamental equations need to be obtained from Maxwell's equation consisting of Poisson's equation, transport equations, continuity equations, etc. By solving those

equations, distribution of electron/hole densities as a consequence of transport as well as generation and recombination process are obtained. In TCAD simulation software, the structure is separated to a huge amount of mesh and grid points known as “nodes.” In these “nodes,” different electrical parameters of the device like current, voltage, transconductance, resistance, etc., are worked out by the software using the numerical simulations. This meshing process is very important and plays a major role in the simulation results accuracy. If the mesh density is increased in the simulation, the precision of calculation also enhances, but that in turn increases the duration of simulation. It is therefore very critical to compromise between the requirement of accuracy and affordable simulation duration in order to realize the extreme advantage from physical simulation. A general simulation methodology used by TCAD software is shown in Fig. 6.

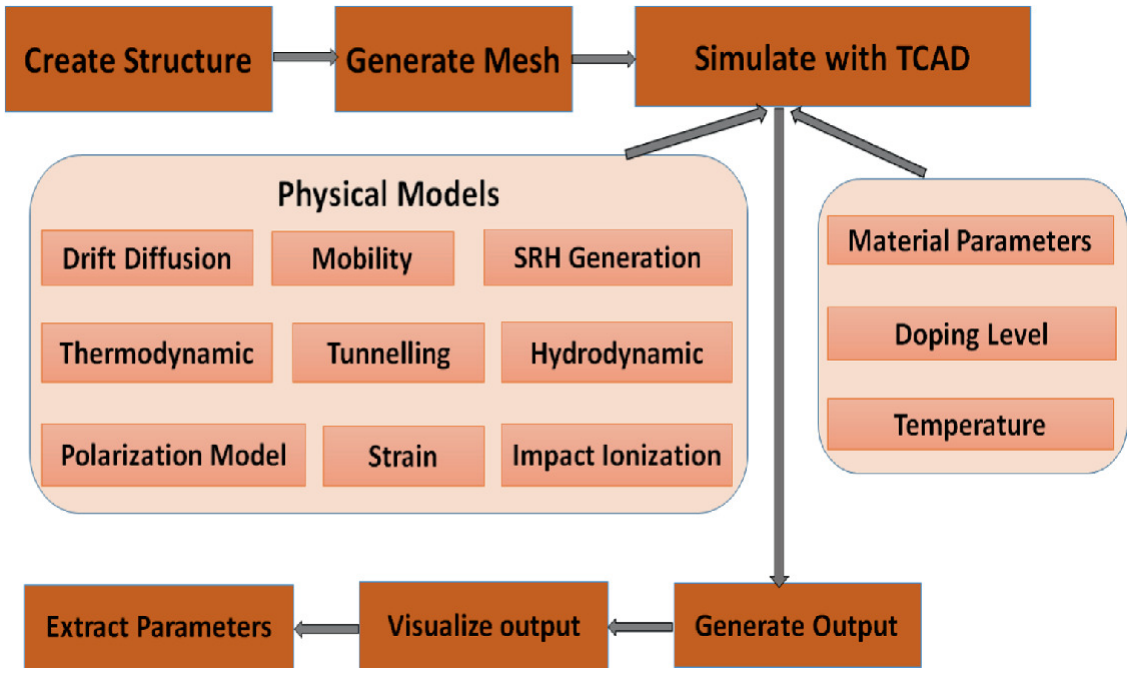

Fig. 6 Physical simulation methodology adopted in TCAD software

TCAD software offers many transport models for consideration of behavior of semiconductor physics [9, 10]. For proper calculation/prediction of the device characteristics, researchers need to include such device models in the simulation process correctly. In this section, different physical models available in popular TCAD software for the device modeling is presented. The physical simulation method

of a typical TCAD software is highlighted in Fig. 6. Different physical models offered by TCAD software are briefly described here.

4.1 Transport Model

Poisons equations describe the movement of carrier charges in semiconductor materials and used to solve the electrostatic potential from the continuity equations of carriers and electro and hole concentrations [9, 10]. Attainment of solution of the Poison's equation is needed for calculation of current densities from charge concentrations and electrostatic potential. That can obtained by using transport models.

4.2 "Drift–Diffusion" Transport Model

The "drift–diffusion" current relations are obtained by using conditions of charge carriers which are in thermal equilibrium and can be used for most of the device simulations in submicron regime. Current densities can be obtained through derivations using Boltzmann's theory. Drift–diffusion (DD) model integrated in TCAD software solves "Poisson's equations" as well as the "current continuity equation" numerically and gets electron concentrations, hole concentrations, electrostatic potentials, etc., at all the nodes which are defined during meshing. The current caused owing to the drift of carriers because of external electric field applied is known as Drift current whereas the current associated with diffusion of carriers is known as Diffusion current.

4.3 Thermodynamic Model

By using thermodynamic model self-heating effect of the device may be simulated by consideration of the equations related to lattice heat flow along with current continuity. This enables to calculate the effect of temperature gradient on current densities for the lattice temperature of the device. For GaN, InGaAs-based HEMT, this simulation model is very important as lots of heat is generated inside the device due its operating conditions.

4.4 Hydrodynamic Model

The hydrodynamic model is important for the simulation and analysis of semiconductor devices. This model can provide their average energy

and average energy flux along with the carrier concentration and current density. Continuity equation, energy balance equations, and the self-consistent Poisson's equations are solved by using this model for charge carriers and the lattice. Hydrodynamic model is more precise compared to drift–diffusion model though hydrodynamic model requires more computing resources that faces difficulty in convergence.

4.5 Generation-Recombination Process

Generation of Carrier is a method where pairs of "electron" and "hole" are produced by stimulating an "electron" in the valence band and transferring it to the conduction band leaving a "hole" there. On the other hand, when electrons and holes recombine and are annihilated known as recombination process. This eventually causes the disappearance of both carriers in this process. In semiconductor, several Generation-Recombination Process exists such as "Shockley–Read–Hall (SRH) generation/recombination," "Auger generation/recombination," or three-particle transitions, along with "impact ionization" process. The model for SRH [11] describes the electrons and holes recombination by the trapping process.

The Auger recombination model determines a recombination of hole and electron for a transition from band to band. The energy as a result of this mechanism is transported to another electron or hole and, consequently, the implication of the third particle impacts the recombination rate. In TCAD, standard models are available to choose proper description of the Generation-Recombination Process.

4.6 High-Field Saturation Model

With the application of high electric fields, a condition appears when the electron velocity due to drift in the channel is no longer proportional to the electric field in the channel. This results in the velocity to saturate to a finite speed v_{sat}. The high-field mobility model is obtained based on the low-field mobility with additional extensions to consider the high-field phenomenon. Three different models such as the "actual mobility model," "driving force model," and "velocity saturation model" are available. These models may be incorporated with few constraints.

4.7 Density Gradient Model

The wave nature of charge carriers need to be considered for MOSFET and GaN-based HEMT when their channel length and thickness of oxide are of quantum–mechanical scales. Moreover, for AlGaN/GaN materials-based HEMT devices, the discontinuity in bandgap at the interface results in a 2D electron gas (2DEG) to confine the electrons. This causes the quantization of energy levels inside a 2DEG channel. Hence, it is crucial to take account of this model for the simulation process to calculate the electron distribution accurately inside the channel.

---

5 Performance Analysis Using TCAD-Based Simulations: Some Recent Studies

5.1 Performance Analysis of AlGaN/GaN HEMT

Numerical studies based on inherent device physics of HEMTs have been done to analyze the influence of material combinations and other device parameters [12–18] in the recent past. Some common numerical simulation models reviewed from available literatures are summarized here.

5.1.1 GaN/AlGaN Heterojunction HEMT

One of the most interesting device structures developed in the recent years is the AlGaN/GaN-based HEMT. In this system, modulation doping was first used and demonstrated in 1992 and a working transistor was first reported in 1993 [13]. The wide bandgap of GaN makes a high breakdown voltage enabling the device to be used in high voltage operation. Another advantage is the higher saturation velocity of electrons in GaN in comparison to its Si counterpart which enables the device for high-frequency applications. Also, HEMT structure ensures a high concentration of electron induced at the AlGaN/GaN interface resulting high current. All these important factors together helps in these devices with exceptional power amplification characteristics at frequencies up to the millimeter wave regime.

5.1.2 Hybrid Electrothermal Model

Behavior of Gallium Nitride-based HEMTs has been studied and analyzed by means of a hybrid electrothermal approach where the solution of the problem is obtained by combining an effective model for electrical parameters simulation together with a 3D "Finite Element Model" (FEM) for the thermal simulation [14]. The assessment of the drain current has been done by analyzing pulsed measurements having different delays. This is required to get rid of the difficulties faced due to the nonuniform temperature distribution as the self-heating effect is present. The output characteristics are shown to be considerably affected by the "self-heating effect" for delay times also. Detailed physical effects like the existence of a TBR along the GaN/SiC interface, was involved and fully investigated by this method. The simulation approach is validated by comparing results with the measurement results.

5.1.3 Analysis of AlGaN/GaN HEMT

A 2-D simulation for device structure has been studied by using Silvaco Atlas tool and is presented by Khan et al. [15]. Because of the polarization effect in III–V compound material, it stores greater density of charges at the heterointerface. Low field mobility model in simulation setup is used to study and analyze this device. The simulation results show that and in I–V characteristics, the saturation current in the linear region decreases with temperature because of the degradation of carrier mobility. However, 2DEG sheet density and the threshold voltage both increases with rise in temperature. The deterioration in carrier mobility is the principal reason for degradation of device performance.

5.1.4 Analysis of Shear Stress in High Temperature

Hirose et al. [16] presented a report based on numerical simulation for "AlGaN/GaN HEMT" devices in which shear stress is generated because of the inverse piezoelectric effect. A device model used for numerical simulation and designing of trustworthy AlGaN/GaN structures. The estimated shear stress value is compared with the experimental results obtained for several "AlGaN/GaN HEMT" devices. From the comparative analysis, it is seen that structures which passed the test have shear stress value smaller than 0.19 GPa at the test conditions. The designed

structure intended for Ka-band passed the necessary test. Reported results point to the fact that the model may be used for designing stable "AlGaN/GaN HEMT" devices.

5.1.5 Effect of Self-Heating

In this work self-heating effect for the AlGaN/GaN model was simulated using Silvaco TCAD simulator. The contacts used for the source contact and drain contact are both ohmic in nature where as the gate was set as Schottky contact. For mobility description, "concentration dependent mobility model" (conmob) and "electric-field-dependent mobility" (fldmob) model was adopted. "Shockley–Read–Hall Recombination" model is utilized together with Boltzmann statistical model. The effect of piezoelectricity was considered along with spontaneous polarization effect for this simulation. Self-heating phenomena were included using the "lattice heating model" (lat. temp). Considering the self-heating effect, it is shown that the saturation current reduces with considering self-heating. Additionally, a bend in the curves for drain currents is observed. Heating may speed up electrical migration which is the cause of performance degradation for the gate, and create reliability issues [17].

5.1.6 Modeling of Recessed-Gate GaN HEMT

Electrical performance parameters of GaN-based HEMTs with and without recessed gate structure was reported by Sharbati et al. [18] and compared with non-recessed gate structure. Using the simulation model, it has been shown that 2DEG density, on resistance and breakdown voltage may be controlled by controlling Al content and barrier thickness. In case of recessed gate structure, the recessed height was controlled to attain improved performance of the HEMT for its application in power electronics domain. Reported simulation results are in good match with the results obtained experimentally. Simulated and experimental graph of the drain current vs gate voltage of GaN HEMTs for recessed gate and non-recessed gate structures and the corresponding transconductance values are shown in Fig. 7.

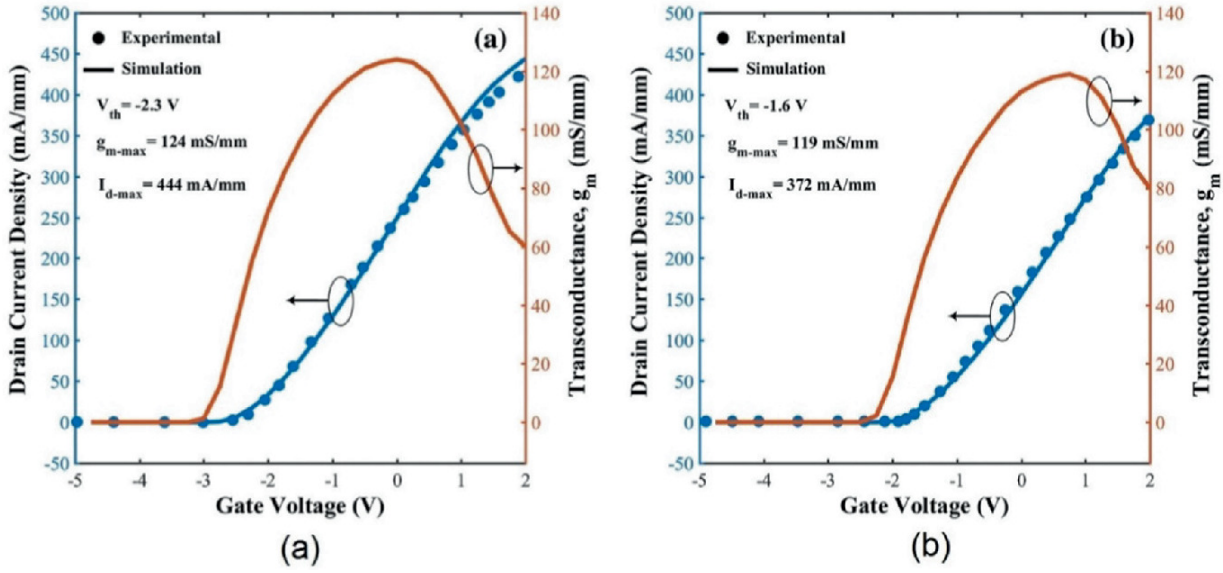

Fig. 7 Transfer characteristics plot of **a** non-recessed and **b** 3-nm recessed-gate GaN HEMT [18]

5.2 Performance Analysis of Nanoscale DG Heterostructure MOS-HEMT

HEMT gates consisted of a Schottky barrier which is not exceptionally effective at suppressing gate leakage, especially as devices are scaled-down. Therefore in recent years, research has gone into adding an additional insulating layer in between the metal gate contact and the semiconductor material layers. In most cases, the insulators used are oxides, creating a "metal–oxide–semiconductor HEMT (MOS-HEMT)" structure. A typical cross-sectional representation of the MOS-HEMT model is presented in Fig. 8. Al_2O_3 [19, 20] is a frequently chosen oxide used in MOS-HEMT devices because of its large bandgap, high breakdown voltage, high thermal and chemical stability, and ease of deposition, although others have been and continue to be explored. Excellent performance is demonstrated by researchers utilizing TiO_2 [21], HfO_2 [22], SiO_2 [23] and Pr_2O_3 [24] as the gate dielectric. There are many works based on TCAD simulation of MOS-HEMT devices available in literature [25–29].

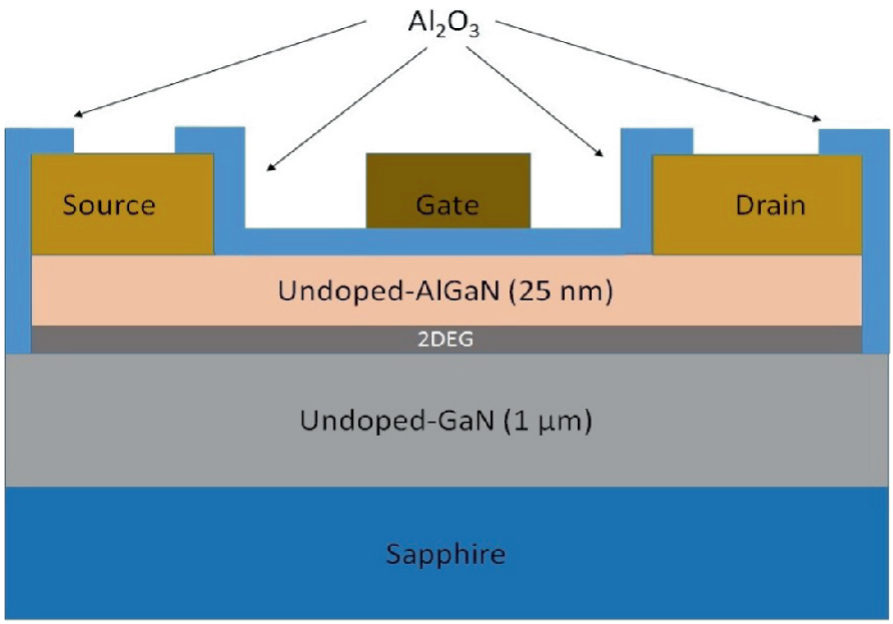

Fig. 8 Cross-section of Al_2O_3/AlGaN/GaN MOS-HEMT

5.2.1 Structure of Device and Simulation Setup

The schematic illustration of an InGaAs/InP-based Double Gate nanoscale MOSFET device is depicted in Fig. 9. Among III–V group compound semiconductors, "Indium-Gallium-Arsenide (InGaAs)" has been extensively studied as a prospective material for high mobility channel n-MOSFETs of future generation due to its enhanced channel mobility [30]. In literature, many works have been reported by researchers for its applications in digital, RF, and analog circuits [31–40]. The device structure composed of an InGaAs channel sandwiched between two InP barrier layers. The channel length is considered as 12 nm and the Source/Drain region length is fixed at 2 nm. Thickness of the channel (t_{ch}) is considered as 2 nm. To study the effect of barrier thickness, InP barrier layer thickness is varied in a range of 1–4 nm. High-k gate dielectric material HfO_2 having "Equivalent-Oxide-Thickness" (EOT) of 1.2 nm is used in order to accomplish robust vertical confinement vital to have higher transconductance and suitably low "drain-induced barrier lowering (DIBL)." The use of high-k gate dielectric helps to reduce gate leakage current. Highly doped source region and drain region of the device are n-type having doping density of the order of 10^{20} cm^{-3}. Channel region is lightly p-type doped having

density of doping $10^{16}/cm^3$. As channel, $In_{0.53}Ga_{0.47}As$ material is considered as it offers superb electron mobility.

Fig. 9 Schematic diagram of the InGaAs/InP based DG MOS-HEMT

The structure of the device as shown in Fig. 9 has been considered and simulated using the TCAD software SILVACO ATLAS [41]. 2-D numerical simulations using drift–diffusion carrier transport model have been performed in detail. In "drift–diffusion" mechanism, the fundamental equations comprise of carrier continuity equations and Poisson equation and, where the current is generated by either "drift" or from "diffusion" process. "Newton" numerical method is utilized for simulation in the model and 300 K has been set as temperature value. Field-dependent mobility model (fldmob) is incorporated in the simulation setup. For recombination, the "Shockley–Read–Hall (SRH)" model is engaged to deliberate effects essential for calculating the carrier mobility [42]. Density of mesh in the device design is chosen properly for the precise simulation results and also improves the computational efficiency. The simulation model has been initially calibrated with the results available in literature. The calibrated model is then used to calculate different electric parameters *of* the device for its performance evaluation.

5.2.2 Investigation of Device Performance for Different Barrier Thickness

In this segment, the different parameters important for analog performance analysis like transconductance (g_m), output resistance R_o, and intrinsic gain ($g_m R_o$) are calculated [43]. The importance of barrier

layer thickness for the analog performance is examined primarily by TCAD simulation. Sheet carrier density and electron mobility are the significant parameters of the heterostructure device. The separation between gate and channel has an impact on the gate control of the conduction layers and is a real way to command the basic physics governing the confinement of electrons inside the channel. This helps to reduce "Short Channel Effects" (SCEs). A better carrier modulation by the gate bias under high drain voltage occurs due to higher carrier confinement results a greater control of drain current. Thus, transconductance (g_m), gate capacitances, and frequency parameters of the device is directly influenced by the change in barrier layer thickness [44]. The thickness of barrier layer decides the space between the gates and the 2DEG [45]. Increase of 2DEG density with an increase in thickness of the barrier matches well with earlier reported results [46]. The thickness of the barrier is varied from 1 to 4 nm while channel width is 12 nm. The drain current variation with different values of barrier thickness is depicted in Fig. 10a.

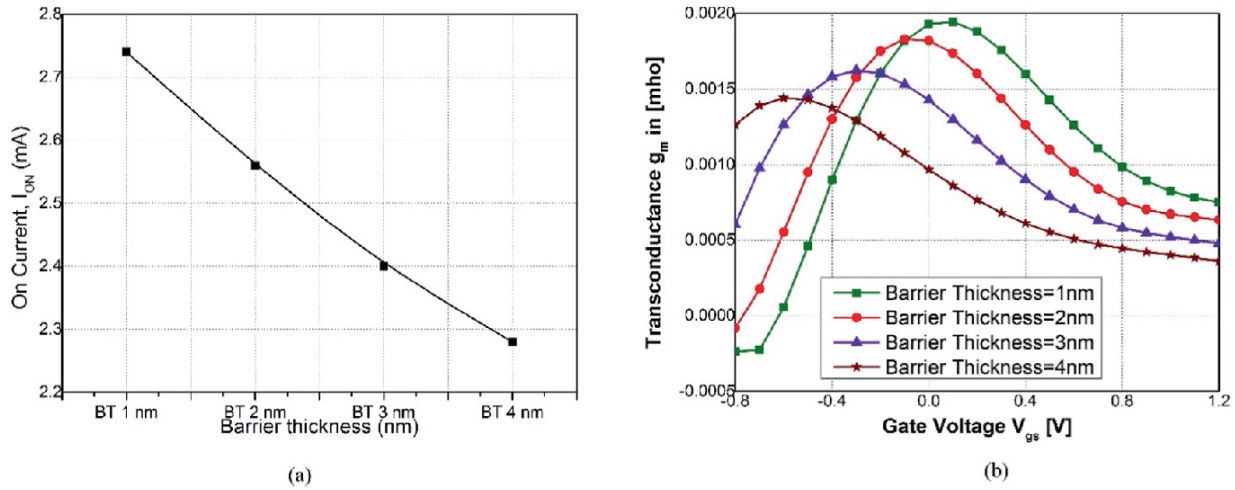

Fig. 10 Variation of on current (I_{ON}) for different barrier thickness and transconductance with V_{gs} for different values of barrier thickness

Figure 10b, shows the change in transconductance with gate voltage (V_{gs}) for various barrier thickness. Figure 10b exposes that a significant enhancement in g_m is witnessed for a device having a reduced barrier thickness.

The output resistance (R_o) obtained from the simulation and corresponding intrinsic gain ($g_m R_o$) of the device are presented in Fig. 11a and b, respectively.

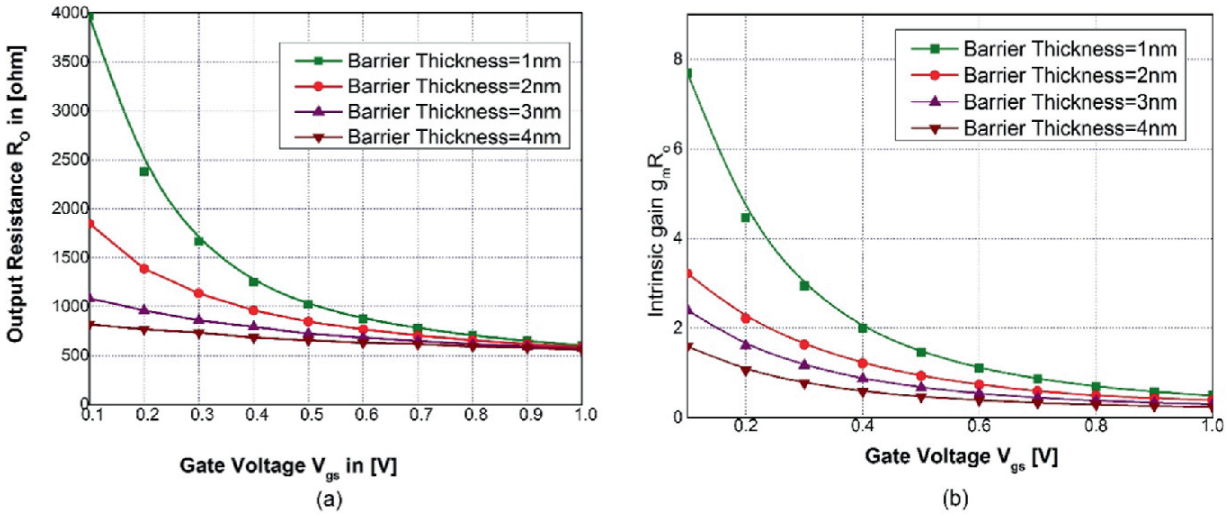

Fig. 11 Plot of **a** output resistance (R_o) for different barrier thickness and **b** intrinsic gain $g_m R_o$ for different barrier thickness

From Fig. 11a, it seems that a thin layer of barrier consequences a higher value of output resistance. The channel region moves far away from the interface of insulator–semiconductor for a thicker barrier and carriers inside the channel face less surface-roughness scattering, which in turn results in an improvement in its mobility to make a reduction in output resistance. In contrast, a reduction of barrier thickness results a reduction of charge density because of induced greater electric fields acting upon the barrier which causes superior depletion of the 2DEG. That's why lower value of current and higher value of sheet resistance as well as output resistance is observed with thinner barrier layer.

The two most significant parameters evaluated to identify the applicability of the device for RF circuits are the cut-off frequency (f_T) and the maximum oscillation frequency (f_{max}). The f_T represents the frequency for which the unity current gain is attained, whereas f_{max} stands for the frequency corresponding to the unity power gain of the device. f_T and f_{max} can be calculated as follows [36, 40]:

(1)

$$f_{\mathrm{T}} = \frac{g_{\mathrm{m}}}{2\pi(C_{\mathrm{gd}} + C_{\mathrm{gs}})}$$

where g_{m} denotes the transconductance, C_{gs}, and C_{gd} represents the capacitances for gate-source and gate-drain region, respectively.

$$f_{\max} = \frac{g_{\mathrm{m}}}{2\pi C_{\mathrm{gs}} \sqrt{4 \times (R_{\mathrm{s}} + R_{\mathrm{i}} + R_{\mathrm{g}}) \times \left(g_{\mathrm{ds}} + g_{\mathrm{m}} \frac{C_{\mathrm{gd}}}{C_{\mathrm{gs}}}\right)}} \tag{2}$$

where R_{g}, is the gate resistance, R_{s}, source resistance, and R_{i} is the intrinsic channel resistances. g_{ds} denotes the output conductance.

The plot of extracted values of f_{T} and $f_{\max}$ for different barrier thickness is illustrated in Fig. 12a and b, respectively. In Fig. 12, it is indicated that RF performances may be enhanced by reducing the thickness of the barrier, which is in agreement with the results published earlier [47, 48]. Value of $f_{\max}$ which indicates the power gain cut-off frequency is a more sensible measure for high-frequency characteristics of the device. To improve the value of f_{T} and $f_{\max}$ of the device the parameters in the denominator of Eq. (2) should be diminished.

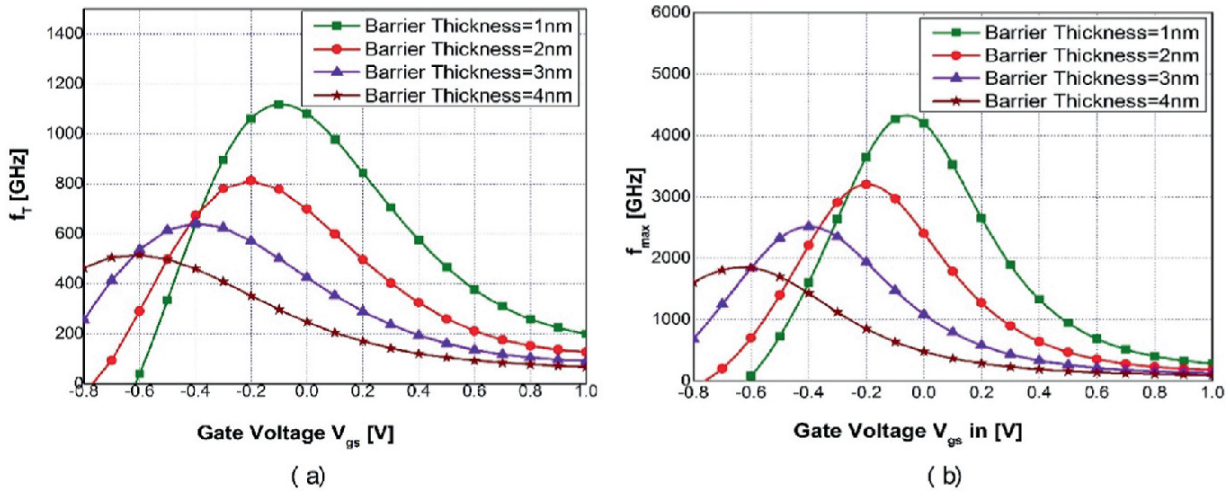

Fig. 12 Comparison of the **a** cutoff frequency (f_{T}) and **b** maximum frequency of oscillation ($f_{\max}$) as a function of the gate bias (V_{gs}) for different barrier thickness

5.2.3 Effect of Varying Channel Composition

The Indium mole fraction in the channel of the heterostructure MOS-HEMT ($In_xGa_{1-x}As$) is studied in this section [49]. Device performance is assessed by calculating various electrical performance parameters for its application on RF/Analog circuits. Change in drain current of the device under study and the transconductance variation with different gate voltage (V_{gs}) for various Indium concentration in the channel is shown in Fig. 13. It is understood that the drain current of the MOS-HEMT device under study improves with increase in *In* content in the channel and indicates that InAs channel allows maximum current. Transconductance of the device also improves with increment of In content. The f_T and f_{max} of the device is also calculated using TCAD simulation and plotted. Figure 14 displays the extracted f_T and f_{max} with varying gate voltage for various *In* contents in the InGaAs layer. The device with higher *In* percentage in the channel exhibits higher value of f_T and $f_{max.}$ Although, InGaAs material with more *In* is preferred as the channel material for better device performance but that rises the lattice constant of the material which in turn rises the mismatch in lattice constant with InP material.

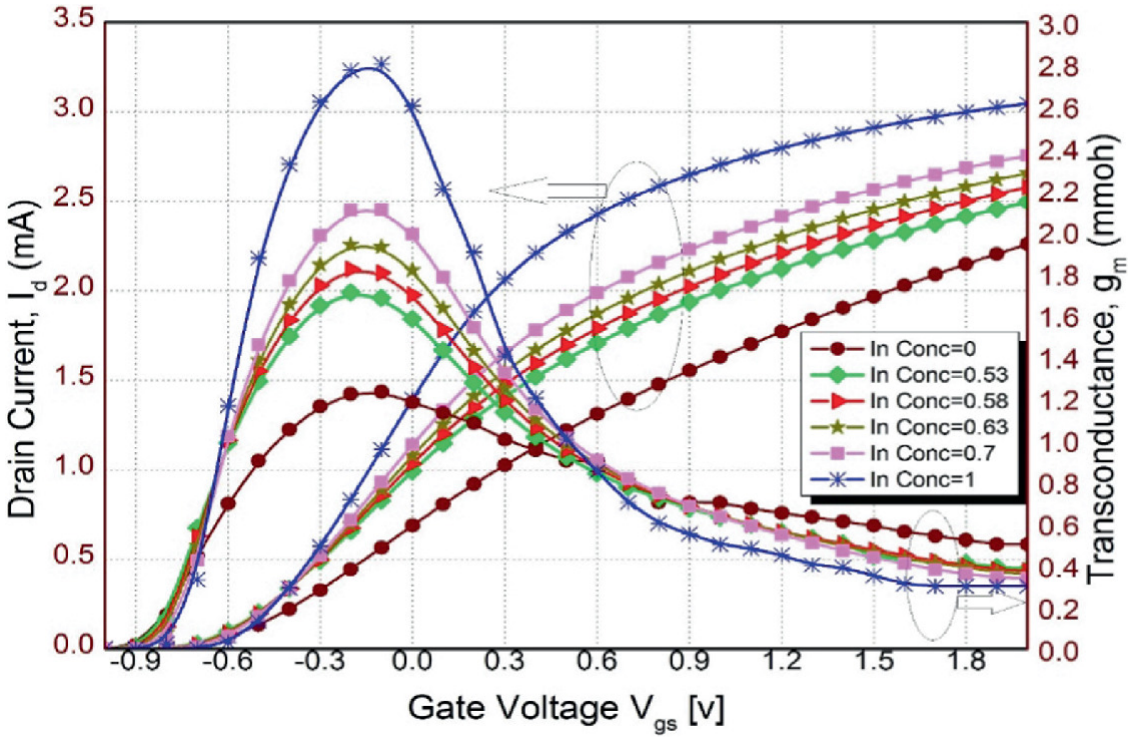

Fig. 13 Variation of ON current (I_{ON}) for different barrier thickness and transconductance with V_{gs} for various thickness of barrier layer

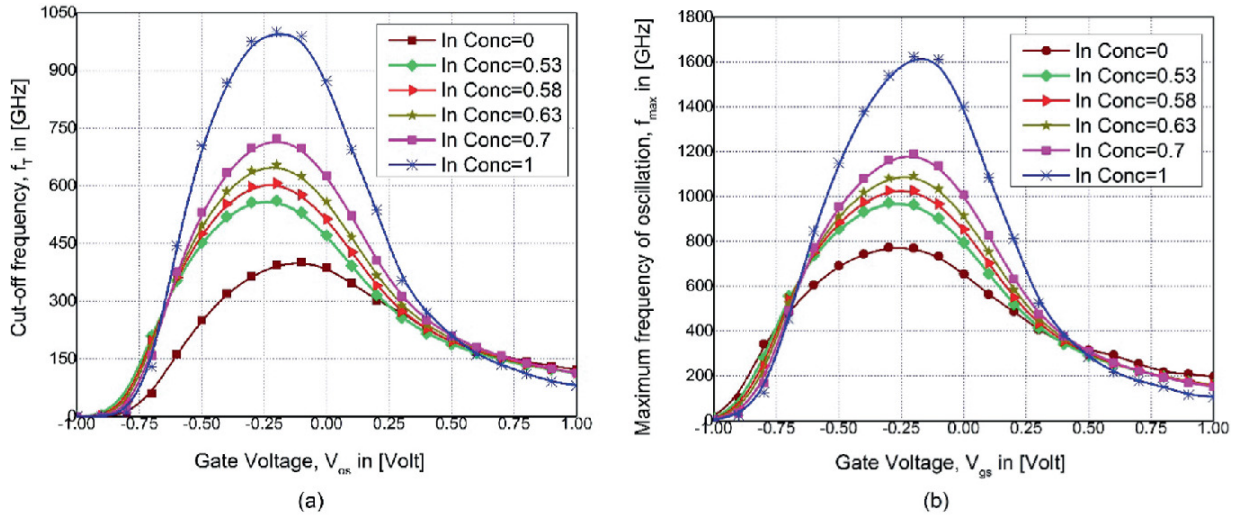

Fig. 14 **a** Cutoff frequency (f_T) and **b** maximum oscillation frequency (f_{max}) with different gate bias (V_{gs}) for different *In* concentration

5.2.4 Circuit Performance Analysis

Applicability of the device in the circuit was evaluated by using the MOS-HEMT device in a circuit such as "Cascode Amplifier" [49, 50]. The schematic representation of a cascode amplifier is depicted in Fig. 15a which contains two transistors and input is applied in the gate terminal of MOSFET 1. The output characteristic was obtained by mixed-mode simulation in Silvaco ATLAS TCAD device simulator for the circuit, built using the device of interest is shown in Fig. 15b. The change in the output characteristics of the circuit with various Indium concentration is observed in this figure. In simulation domain, the devices were defined by 1 μm width and 0.6 V was used as reference voltage. Figure 15b indicates that the higher differential gain of the circuit is obtained with the device which consists of lower mole fraction.

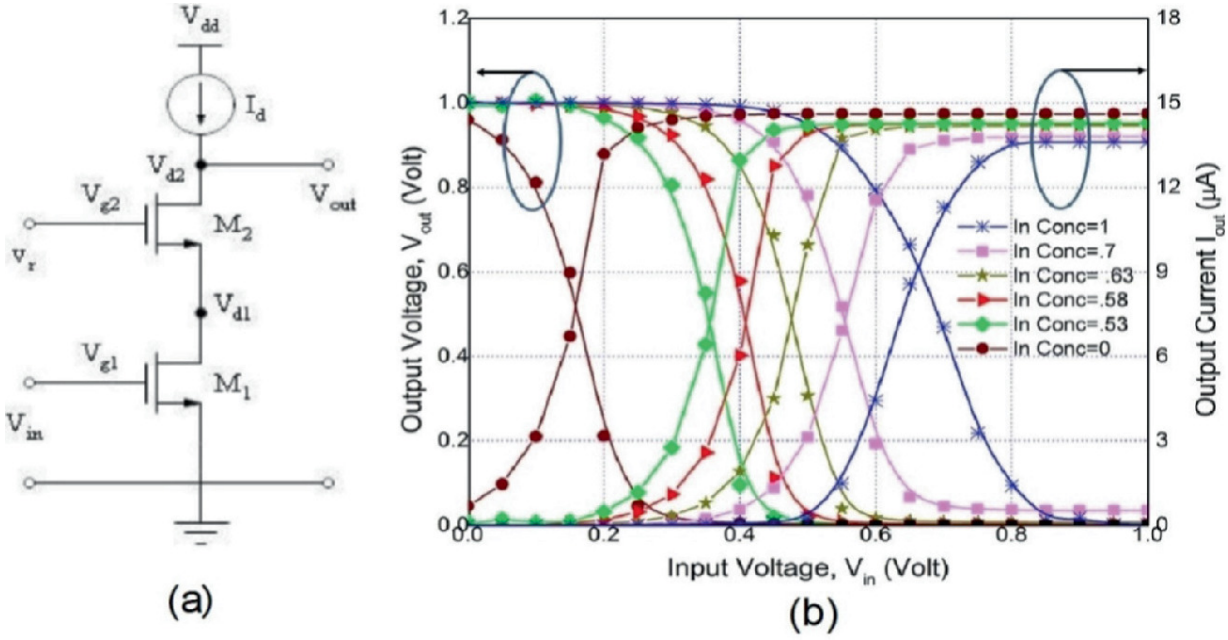

Fig. 15 **a** Schematic diagram of a cascode amplifier **b** Output characteristics of the cascode amplifier circuit with variation of *In* concentrations

5.2.5 Findings from Simulation and Analysis

In this section, it is demonstrated that device and circuit performance of a MOS-HEMT can be analyzed using TCAD device simulation. The consequence of barrier thickness variation on the Analog/RF Figure of merits of an InGaAs/InP based device is presented. In simulation results and from its analysis, it is very much clear that the related performance parameters of the device have significant improvement when thickness of barrier decreases. Effect of changing *In* percentages in the channel for RF and analogue performance characteristics of the device have also been examined. Improvement in ON current and transconductance with growing *In* content is also witnessed. Device with higher *In* mole fraction displays improved f_T and f_{max}. For a multistage circuit like cascode amplifier, the differential gain declines with higher *In* mole fraction.

---

6 Applications of HEMT

As Internet and Broadband communications have been developed around the globe, the need of capacity rise in high-speed communication network has been the basic demand. HEMT-based

devices attract the most interests from researchers for cracking the required limit of speed, having high gain as well as low noise mechanism. As many new areas of applications are suggested in recent times, many new companies are developing and offering HEMT-based solutions. Some of the attractive areas of applications are highlighted below.

6.1 Cellular Communication

HEMT devices finds major area of applications in Cellular Communications. The growing demands in bandwidth for a fixed level of power is very crucial. Linearity may also be improved with the same power level. AlGaN/GaN-based HEMT replacing Si-based devices for power amplifier and power switching applications. Filters that are capable of tuning electrically or reconfigurable filters utilizing RF-MEMS were developed by Pelliccia et al. [51]. In that work, quality factors of approximately 1000 and frequency tunability of approximately 5% are claimed by the researchers. An RF-MEMS tuned cavity oscillator for the application in X-band was reported by Horberg et al. [52]. GaN-HEMT MMIC technology was used to implement the active part of the oscillator.

6.2 Satellite Communication

Microwave equipment normally used in satellite communication is relatively costly as these devices require extra care for protection and proven reliability records from harsh environment in space for survival. A very efficient and having large output power amplifier using GaN for L-band space application is reported by Chi et al. [53]. It is revealed that GaN may be exploited to fabricate transistors for different purposes such as high-voltage converters [54]. A high-gain and high power amplifier and module were developed and reported by Quay et al. [55] for 90 GHz frequency having up to 400 mW of output power.

Another high efficiency and high power GaN-based HEMT which are compatible to be applied for navigation satellite or communication satellite are developed recently. The level of power of 200 W under CW conditions was reported [56]. These devices passed a space qualification test (SQT) on the GaN HEMT in accordance with the

standard space qualification procedures based on MIL-PRF-19500, a global standard.

6.3 Power Amplifiers

GaN HEMT is a preferred choice for application in radar components because of its availability in high gain and very low noise amplifiers. Recently, a power amplifier using GaN HEMT for X-band is developed and described with a detailed analysis of performance parameters [57]. An output power range of 47.5–48.7dBm can be achieved using this amplifier. This type of amplifier may be used to build electronic systems that need satellite transmitters or airborne phased radar array. Broadband gallium nitride (GaN-HEMT) power amplifier with push–pull technique and shunt-feedback is presented by Kim et al. [58].

6.4 Various Sensors

HEMT devices find applications in miniaturized sensors such as chemical and gas sensors which are proficient for operation in harsh environments. Fabrication methodology and testing results of an AlGaN/GaN HEMT device were reported recently [59]. Very good sensing characteristics were shown for H_2S, NO_2 gas. AnotherAlGaN/GaN-based nitrogen dioxide (NO_2) sensor using a tungsten trioxide (WO_3) film adapted as a gate was reported [60]. Ionic pollutants in solution was also detected by "differential extended gate (DEG)-AlGaN/GaN HEMT" [61]. These devices may be used for environmental monitoring. Recently, a pH sensor system based on AlGaN/GaN MOS-HEMT utilizing the "resistive coupling effect" is reported to overcome the Nernst limit [62]. This pH sensor is likely to be freely included in circuits with large transmission bandwidth, high power, and high temperature in a biosensor design with very high sensitivity. Another "extended-gate (EG) AlGaN/GaN HEMT" based pH sensor was reported recently [63]. The EG is implemented to develop the device as a disposable biosensor. The EG which acts as a sensing membrane, may be destroyed after it is contaminated and can be reused. 57.6 mV/pH sensitivity level was achieved by the device which is near to the Nernst limit, and a very good linearity of 98.93%. It was also reported that AlGaN/GaN HEMTs display great potential for the

making of sensor systems for pharmaceutical, bio-molecular and medical applications. "AlGaN/GaN HEMT" based DNA hybridization sensor was also available in literature [64]. Biosensor based on GaN MOS-HEMT is also reported recently for finding biomolecules like protein, streptavidin, and Uricase [65].

7 Conclusion

In this chapter, HEMT device characteristics and TCAD-based simulation and analysis have been discussed. These devices are finding special interest to replace conventional field-effect transistors having outstanding performance. After a brief outline, different device structures and basic principle is also presented. Basic simulation methodology along with different physical models appropriate for HEMT devices and commonly offered by the TCAD simulation software are presented in detail. Some noticeable analytical modeling and numerical research works on HEMTs device have also been presented in this chapter. Applications based on different HEMT structures in the areas of broadband communications, radar communications, satellite communication, and sensor are also introduced. This chapter is intended to provide researchers with various avenues to continue their research using TCAD-based simulation and analysis in a direction of further development of HEMT devices with potential applications.

References

1. T. Mimura, S. Hiyamizu, T. Fujii, K. Nanbu, A new field-effect transistor with selectively doped GaAs/n-AlxGa1-xAs heterojunctions. Jpn. J. Appl. Phys. **19**(5), 225–227 (1980) [Crossref]

2. D.A. Neamen, *Semiconductor Physics and Devices: Basic Principles* (Mcgraw-Hill, 2003)

3. M.N.A. Aadit, S. Kirtania, F. Afrin, M.K. Alam, Q.D.M. Khosru, High electron mobility transistors: Performance analysis, research trend and applications, in *Different Types of Field-Effect Transistors-Theory and Applications* (Chap. 3) (InTech, 2017). https://doi.org/10.5772/67796

4. R. Szweda, *Gallium Nitride and Related Bandgap Materials and Devices* (Elsevier Science, 2000)

5. R.J. Trew, M.W. Shin, V. Gatto, High power applications for GaN-based devices. Solid State

Electron. **41**(10), 1561–1567 (1997)
[Crossref]

6. S.R. Bahl, J. Joh, L. Fu, A. Sasikumar, T. Chatterjee, S. Pendharkar, Application reliability validation of GaN power devices, in *Proceedings of the International Electron Devices Meeting (IEDM)*, San Francisco, CA, USA, 3–7 Dec 2016, pp. 20.5.1–20.5.4.

7. K. Shinohara, T. Matsui, Y. Yamashita, A. Endoh, K. Hikosaka, T. Mimura, S. Hiyamizu, Simple and high-precision asymmetric gate-recess process for ultrafast InP-based high electron mobility transistors. J. Vac. Sci. Technol. B Microelectron. Nanometer Struct. **20**, 2096–2100 (2002). https://doi.org/10.1116/1.1510527
[Crossref]

8. K. Shinohara, T. Matsui, Nano-gate transistor-world's fastest InP-HEMT. J. Natl. Inst. Inf. Commun. Technol. **51**, 95–102 (2004)

9. C.K. Sarkar, *Technology Computer Aided Design: Simulation for VLSI MOSFET* (CRC Press, 2016)

10. C.K. Maiti, *Computer Aided Design of Micro- and Nanoelectronic Devices* (WorldScientific, 2016)

11. W. Shockley, W.T. Read, Statistics of the recombinations of holes and electrons. Phys. Rev. **87**(5), 835–842 (1952)
[Crossref]

12. N. Chand, S.K. Swain, S.M. Biswal, A. Sarkar, S. Adak, Comparative study on analog and RF parameter of InAlN/AlN/GaN normally off HEMTs with and without AlGaN back barrier. Devices Integr. Circ. (DevIC) **2021**, 616–620 (2021). https://doi.org/10.1109/DevIC50843.2021.9455877
[Crossref]

13. M. Asif Khan, A. Bhattarai, J.N. Kuznia, D.T. Olson, High electron mobility transistor based on a GaN-AlxGa1−xN heterojunction. Appl. Phys. Lett. **63**, 1214 (1993). https://doi.org/10.1063/1.109775

14. A. Valletta et al., Hybrid electrothermal simulations of GaN HEMT devices based on self-heating free virtual electrical characteristics. IEEE Trans. Electron Devices **68**(8), 3740–3747 (2021). https://doi.org/10.1109/TED.2021.3084547
[Crossref]

15. A.B. Khan, M. Sharma, M.J. Siddiqui et al., Performance analysis of AC and DC characteristics of AlGaN/GaN HEMT at various temperatures. Trans. Electr. Electron. Mater. **19**, 90–95 (2018). https://doi.org/10.1007/s42341-018-0018-8
[Crossref]

16. M. Hirose, K. Matsushita, K. Takagi, K. Tsuda, Numerical device model for reliable AlGaN/GaN HEMT structure design based on shear stress. IEEE Compound Semicond. Integr. Circ. Symp. (CSICS) **2013**, 1–4 (2013). https://doi.org/10.1109/CSICS.2013.6659242
[Crossref]

17. Z. Fang, The study of self-heating effect of AlGaN/GaN high electron mobility transistors based

on TCAD. J. Phys. Conf. Ser. **1699** (1) (Article ID 012006) (Nov 2020)

18. S. Sharbati, I. Gharibshahian, T. Ebel et al., Analytical model for two-dimensional electron gas charge density in recessed-gate GaN high-electron-mobility transistors. J. Elec. Materi. **50**, 3923–3929 (2021). https://doi.org/10.1007/s11664-021-08842-7 [Crossref]

19. H. Liu, B. Chou, W. Hsu, C. Lee, J. Sheu, C. Ho, Enhanced AlGaN/GaN MOS-HEMT performance by using hydrogen peroxide oxidation technique. IEEE Trans. Electron Devices **60**(1), 213–220 (2013) [Crossref]

20. Y. Hori1, Z. Yatabe1, T. Hashizume, Characterization of interface states in Al_2O_3/AlGaN/GaN structures for improved performance of high-electron-mobility transistors. J. Appl. Phys. **114**, 244503 (2013)

21. Z. Dong, J. Wang, C.P. Wen, D. Gong, Y. Li, M. Yu et al., High breakdown AlGaN/GaN MOSHEMT with thermal oxidized Ni/Ti as gate insulator. Solid State Electron. **54**, 1339–1342 (2010) [Crossref]

22. C.-S. Lee, Y.-H. Liao, B.-Y. Chou, H.-Y. Liu, W.-C. Hsu, Composite HfO_2/Al_2O_3-dielectric AlGaAs/InGaAs MOS-HEMTs by using RF sputtering/ozone water oxidation. Superlattice. Microst. **72**, 194–203 (2014)

23. C.-H. Hsu, W.-C. Shih, Y.-C. Lin, H.-T. Hsu, H.-H. Hsu, Y.-X. Huang, et al., Improved linearity and reliability in GaN metal–oxide–semiconductor high-electron-mobility transistors using nanolaminate La_2O_3/SiO_2 gate dielectric. Jpn. J. Appl. Phys. **55**, 04EG04 (2016)

24. H.-C. Chiu, C.-W. Yang, Y.-H. Lin, R.-M. Lin, L.-B. Chang, K.-Y. Horng, Device characteristics of AlGaN/GaN MOS-HEMTs using high-praseodymium oxide layer. IEEE Trans. Electron. Dev. **55**, 3305–3309 (2008)

25. S. Mondal, S. Paul, A. Sarkar, Investigation of the effect of barrier layer engineering on DC and RF performance of gate-recessed AlGaN/GaN HEMT, in *Methodologies and Application Issues of Contemporary Computing Framework* ed. by J. Mandal, S. Mukhopadhyay, P. Dutta, K. Dasgupta (Springer, Singapore, 2018). https://doi.org/10.1007/978-981-13-2345-4_14

26. S. Paul, S. Mondal, A. Sarkar, Characterization and analysis of low-noise GaN-HEMT based inverter circuits. Microsyst. Technol. **27**, 3957–3965 (2021) [Crossref]

27. S. Adak, N. Chand, S.K. Swain, A. Sarkar, Effect of AlGaN back barrier on InAlN/AlN/GaN E-mode HEMTs. Devices Integr. Circ. (DevIC) **2019**, 156–160 (2019). https://doi.org/10.1109/DEVIC.2019.8783383 [Crossref]

28. K. Biswas, A. Sarkar, C.K. Sarkar, Assessment of dielectrics and channel doping impact in nanoscale double gate III–V MOSFET with heavily doped source/drain region. ASP Mater. Focus **6**(2), 116–120 (2017) [Crossref]

29.

A. Roy, R. Mitra, A. Mondal, A. Kundu, Analog/RF and power performance analysis of an underlap DG AlGaN/GaN based high-K dielectric MOS-HEMT. Silicon, 1–8 (2021). https://doi.org/10.1007/s12633-021-01020-8

30. Y. Xuan, Y.Q. Wu, P.D. Ye, High-performance inversion-type enhancement-mode InGaAs MOSFET with maximum drain current exceeding 1 A/mm. IEEE Electron Device Lett. **29**(4), 294–296 (2008)
[Crossref]

31. P.H. Woerlee, M.J. Knitel, R. van Langevelde, Member, IEEE, D.B. Klaassen, L.F. Tiemeijer, A.J. Scholten, A.T. Zegers-van Duijnhoven, RF-CMOS performance trends. IEEE Trans Electron Devices **48** (8), 1776–1782 (Aug, 2001)

32. A. Nandi, A.K. Saxena, S. Dasgupta, Impact of dual-k spacer on analog performance of underlap FinFET. Microelectron. J. **43**, 883–887 (2012)

33. B. Murmann, P. Nikaeen, D.J. Connelly, R.W. Dutton, Impact of scaling on analog performance and associated modelling needs. IEEE Trans. Electron Devices **53** (9), 2160–2167 (Sept 2006)

34. A. Sarkar, R. Jana, The influence of gate underlap on analog and RF performance of III-V heterostructure double gate MOSFET. Superlattices Microstruct. (2014). https://doi.org/10.1016/j.spmi.2014.05.038
[Crossref]

35. L. Morassi, G. Verzellesi, H. Zhao, J.C. Lee, D. Veksler, G. Bersuker, Errors limiting split-CV mobility extraction accuracy in buried-channel InGaAs MOSFETs. IEEE Trans. Electron Devices **59** (4), 1068–1075 (Apr 2012)

36. N. Mohankumar, B. Syamal, C.K. Sarkar, Influence of Channel and Gate Engineering on the Analog and RF Performance of DG MOSFETs. IEEE Trans. Electron Devices **57** (4), 820–826 (Apr 2010)

37. H. Pardeshi, S.K. Pati, G. Raj, N. Mohankumar, C.K. Sarkar, Investigation of asymmetric effects due to gate misalignment, gate bias and underlap length in III–V heterostructure underlap DGMOSFET. Physica E **46**, 61–67 (2012)
[Crossref]

38. S. Tewari, A. Biswas, A. Mallik, Study of InGaAs-channel MOSFETs for analog/mixed-signal system-on-chip applications. IEEE Electron Device Lett. **33** (3), 372–374 (Mar 2012)

39. K.P. Pradhan, S.K. Mohapatra, P.K. Sahu, D.K. Behera, Impact of high-k gate dielectric on analog and RF performance of nanoscale DG-MOSFET. Microelectron. J. **45**, 144–151 (2014)
[Crossref]

40. A. Sarkar, A.K. Das, S. De, C.K. Sarkar, Effect of gate engineering in double-gate MOSFETs for analog/RF applications. Microelectron. J. **43**, 873–882 (2012)
[Crossref]

41. Device simulator ATLAS User manual. Silvaco Int., Santa Clara, CA, May 2011 [Online]. Available: http://www.silvaco.com

42. S.K. Pati, H. Pardeshi, G. Raj, N. Mohan Kumar, C.K. Sarkar, Impact of gate length and barrier

thickness on performance of InP/InGaAs based double gate metal–oxide-semiconductor heterostructure field-effect transistor (DG MOS-HFET). Superlattices Microstruct. **55**, 8–15 (2013)

43. K. Biswas, A. Sarkar, C.K. Sarkar, Impact of barrier thickness on analog, RF and linearity performance of nanoscale DG heterostructure MOSFET. Superlattices Microstruct. **86**, 95–104 (2015). ISSN 0749-6036. https://doi.org/10.1016/j.spmi.2015.06.047

44. L. Yang, A. Asenov, J.R. Watling, M. Boriçi, J.R. Barker, S. Roy, K. Elgaid, I. Thayne, T. Hackbarth, Impact of device geometry and doping strategy on linearity and RF performance in Si/SiGe MODFETs. Microelectron. Reliab. **44** (7), 1101–1107 (2004)

45. B.R. Bennett, R. Magno, J.B. Boos, W. Kruppa, M.G. Ancona, Antimonide-based compound semiconductors for electronic devices: A review. Solid-State Electron. **49**(12), 1875–1895 (2005)
[Crossref]

46. A. Adikimenakis, K.E. Aretouli, E. Iliopoulos, A. Kostopoulos, K. Tsagaraki, G. Konstantinidis, A. Georgakilas, High electron mobility transistors based on the AlN/GaN heterojunction. Microelectron. Eng. **86**(4–6), 1071–1073 (2009)
[Crossref]

47. G. Gu, Y. Cai, Z. Feng, B. Liu, C. Zeng, G. Yu, Z. Dong, B. Zhang, Enhancement-mode InAlN/GaN MISHEMT with low gate leakage current. J. Semicond. **33**, 064004-1-064004–3 (2012)

48. D.S. Lee, J.W. Chung, H. Wang, 245-GHz InAlN/GaN HEMTs with oxygen plasma treatment. IEEE Electron Device Lett. **32**, 755–757 (2011)
[Crossref]

49. K. Biswas, A. Sarkar, C.K. Sarkar, Effect of varying indium concentration of InGaAs channel on device and circuit performance of nanoscale double gate heterostructure MOSFET. Micro Nano Lett. **13** (5) (Feb 2018). https://doi.org/10.1049/mnl.2017.0884

50. S. Paul, S. Mondal, A. Sarkar, A novel GaN-HEMT based inverter and cascode amplifier. IEEE Electron Devices Kolkata Conf. (EDKCON) **2018**, 465–469 (2018). https://doi.org/10.1109/EDKCON.2018.8770510
[Crossref]

51. L. Pelliccia, F. Cacciamani, P. Farinelli, R. Sorrentino, High-Q tunable waveguide filters using ohmic RF MEMS switches. IEEE Trans. Microw. Theory Tech. **63**(10), 3381–3390 (2015). https://doi.org/10.1109/TMTT.2015.2459689
[Crossref]

52. M. Hörberg, T. Emanuelsson, P. Ligander, S. Lai, H. Zirath, D. Kuylenstierna, RF-MEMS tuned GaN HEMT based cavity oscillator for X-band. IEEE Microwave Wirel. Compon. Lett. **27**(1), 46–48 (2017). https://doi.org/10.1109/LMWC.2016.2629973
[Crossref]

53. C. Chi, C. Jun, W. Lei, L-band high efficiency GaN HEMT power amplifier for space application. IET Conf. Proc. 0687–0687 (2013). https://doi.org/10.1049/cp.2013.0455 IET Digit. Libr. https://digitallibrary.theiet.org/content/conferences/10.1049/cp.2013.0455

54.

P. Waltereit, W. Bronner, R. Quay, M. Dammann, M. Cäsar, S. Müller, R. Reiner, P. Brückner, R. Kiefer, F. Raay, J. Kühn, M. Musser, C. Haupt, M. Mikulla, O. Ambacher, GaN HEMTs and MMICs for space applications. Semicond. Sci. Technol. **28**, 074010 (2013). https://doi.org/10.1088/0268-1242/28/7/074010

55. R. Quay et al., Submicron-AlGaN/GaN MMICs for space applications. IEEE MTT-S Int. Microwave Symp. Digest (MTT) **2013**, 1–4 (2013). https://doi.org/10.1109/MWSYM.2013.6697533
[Crossref]

56. T. Satoh, K. Osawa, A. Nitta, GaN HEMT for space applications, in *2018 IEEE BiCMOS and Compound Semiconductor Integrated Circuits and Technology Symposium (BCICTS)*, pp. 136–139 (2018). https://doi.org/10.1109/BCICTS.2018.8551070

57. H. Tao, W. Hong, B. Zhang, X. Yu, A compact 60W X-band GaN HEMT power amplifier MMIC. IEEE Microwave Wirel. Compon. Lett. **27**(1), 73–75 (2017). https://doi.org/10.1109/LMWC.2016.2630926
[Crossref]

58. J. Kim et al., A 20-W wide bandwidth GaN HEMT power amplifier for VHF/UHF applications. IEEE Trans. Industr. Electron. **67**(12), 10905–10910 (2020). https://doi.org/10.1109/TIE.2019.2960749
[Crossref]

59. R. Sokolovskij, J. Zhang, Y. Jiang, G. Chen, G.Q. Zhang, H. Yu, AlGaN/GaN HEMT micro-sensor technology for gas sensing applications, in *2018 14th IEEE International Conference on Solid-State and Integrated Circuit Technology (ICSICT)*, pp. 1–4 (2018). https://doi.org/10.1109/ICSICT.2018.8564904

60. J. Sun, R. Sokolovskij, E. Iervolino, Z. Liu, P.M. Sarro, G.Q. Zhang, Suspended AlGaN/GaN HEMT NO_2 gas sensor integrated with micro-heater. J. Microelectromech. Syst. 1–8 (2019). https://doi.org/10.1109/JMEMS.2019.2943403

61. L. Zhao, X. Liu, B. Miao, Z. Gu, J. Wang, H. Peng, B. Zeng, J. Zhang, J. Li, Differential extended gate-AlGaN/GaN HEMT sensor for real-time detection of ion pollutants. Anal. Methods **11** (2019). https://doi.org/10.1039/C9AY01019J

62. S.-K. Cho, W.-J. Cho, High-sensitivity pH sensor based on coplanar gate AlGaN/GaN metal-oxide-semiconductor high electron mobility transistor. Chemosensors 9 (3), 42 (2021). https://doi.org/10.3390/chemosensors903004

63. J.-Y. Pyo, J.-H. Jeon, Y. Koh, C. Cho, H.-H. Park, K.-H. Park, S.W. Lee, W.-J. Cho, AlGaN/GaN high-electron-mobility transistor pH sensor with extended gate platform. AIP Adv. **8**, 085106 (2018) https://doi.org/10.1063/1.5041847

64. S. Schwarz, S. Linkohr, P. Lorenz, S. Krischok, T. Nakamura, V. Cimalla, C. Nebel, O. Ambacher, DNA-sensor based on AlGaN/GaN high electron mobility transistor. Phys. Status Solidi (a). **208** (2011). https://doi.org/10.1002/pssa.201001041

65. Shaveta, H.M. Ahmed, R. Chaujar, Rapid detection of biomolecules in a dielectric modulated GaN MOSHEMT. J. Mater. Sci. Mater. Electron **31**, 16609–16615 (2020). https://doi.org/10.

1007/s10854-020-04216-7

T. R. Lenka, H. P. T. Nguyen (eds.), *HEMT Technology and Applications*, Springer Tracts in Electrical and Electronics Engineering
https://doi.org/10.1007/978-981-19-2165-0_13

Emerging Device Architectures for Space Electronics

Khushwant Sehra[1] ✉, Samriddhi Raut[2] ✉, D. S. Rawal[3] ✉ and Manoj Saxena[4] ✉

(1) Department of Electronic Science, University of Delhi South Campus, New Delhi, India
(2) Department of ECE, Maharaja Surajmal Institute of Technology, Guru Gobind Singh Indraprastha University, New Delhi, India
(3) MMIC Fabrication Division, Solid State Physics Laboratory, Defence Research & Development Organization, New Delhi, India
(4) Department of Electronics, Deen Dayal Upadhyaya College, University of Delhi, New Delhi, India

✉ **Khushwant Sehra**
Email: ksehra@electronics.du.ac.in

✉ **Samriddhi Raut**
Email: samriddhiraut@ieee.org

✉ **D. S. Rawal**
Email: ds-rawal.sspl@gov.in

✉ **Manoj Saxena (Corresponding author)**
Email: msaxena@ddu.du.ac.in

Abstract

Gallium Nitride HEMT technology has been in focus for several decades due to its exemplary intrinsic properties. It provides a viable solution for the RF and high power Applications. The strong bonding nature of

such III–V binary and ternary compounds ensures robustness to ionizing radiations for Space Electronics. In this regard, GaN has established itself as the dominating material for fulfilling the needs of future RF and high power applications. This article brings a brief overview of the current technology trends in HEMTs for next-generation Space Electronics with a deliberate focus toward TCAD-based studies.

Keywords HEMT – 2DEG – Single event transients – Proton fluence

1 Introduction

Gallium Nitride has seen unprecedented development ever since it was proposed by Khan et al. [1] as a possible candidate for high frequency and high power applications over the traditional AlGaAs/GaAs systems discovered by Mimura et al. [2]. GaN devices have since evolved into a dominating technology which have captured the world interest for various defense applications [3–5]. Their superior device quality and unique intrinsic properties [6, 7] make it possible for the devices to deliver high power and exhibit low noise characteristics [8–10]. Accordingly, in an attempt to target mm-wave applications, GaN HEMTs have experienced significant changes to the epi-layer stacks [11–15], which have matured their growth technology over the years [16–19]. In this regard, the GaN devices, which were earlier realized on a SiC substrate, have now been reported to offer exceptional performance on low-cost Silicon substrates [15, 20–23]. This has consequently laid down the pathway for the integration of GaN on Si MMICs with Silicon-based CMOS circuits [24, 25].

GaN is a polar crystal with a wide bandgap and a high melting point which makes it possible for operating the devices at high temperatures [26–28]. In addition to this, the ternary alloy AlGaN with its binary counterpart GaN forming a heterostructure system is robust enough to withstand the harsh conditions experienced in space environments [27, 29–31]. This is possible due to their strong bonding nature [32–34]. These properties, make GaN-based devices desirable for space electronics. Accordingly, there have been numerous attempts to make both qualitative and quantitative assessments of different radiation

sources and their impact on the device performance [27, 29–31]. Several research groups have also ventured into the reliability aspects of the material systems post-irradiation [35–40] in order to investigate the changes in the base material. This consequently helps in identifying the sensitive areas of the device and opens up the avenues for improving the robustness of the device for space electronics. In one instance, Zhang et al. [41] have proposed the utilization of an AlGaN interlayer in limiting the Electron Hole Pair (EHP) generation in AlGaN/GaN HEMTs post heavy ion particle strike. The structure as reported, has a high Single Event Burnout (SEB) threshold in comparison to the conventional HEMT architecture. A similar concept has also been demonstrated by Zhang et al. [42] in terms of a composite channel to improve the robustness of the InP HEMTs against the incident proton fluence. In yet another work, a p-GaN HEMT has been identified to provide a robust operation against the ionizing X-Rays [43], thus qualifying the structure for possible space applications.

Apart from the material and device level studies pertaining to the robustness of the GaN HEMT devices under different radiation sources, it is imperative to investigate the performance of the device for actual circuit-level applications. In this regard, several research groups have made an effort to explore the robustness claimed in GaN devices for circuit-level applications. In one such instance, Raut et al. [44] have explored the robustness of the buffer- free architecture proposed by Chen et al. [45] under proton radiation environment. The architecture was subsequently explored by realizing Power Amplifiers, and investigating the performance under different fluence levels. In yet another attempt, Tang et al. [46] demonstrate a wireless power system based on an enhancement mode p-GaN HEMT, and subsequently explored the system performance using a 100 kGy irradiated device.

As pointed out in the above discussions, there is a need to bridge the gap between the experimental reports and their possible applications. However, carrying out such studies is often difficult since the radiation facilities and test structures are not available readily, as pointed out by Sehra et al. [32]. Further, most of the radiation species result in a permanent damage to the device [27, 29, 30, 37] which makes it unviable to fabricate and optimize devices in an iterative fashion. Accordingly, this calls for a low-cost solution involving

preliminary studies through the TCAD tools as demonstrated through author's previous works [32, 40, 44, 47, 48]. This article aims to expand on the above knowledge by providing supplementary information regarding the two robust device architectures explored by the author for possible space applications. The focus has been kept toward the TCAD simulations in line with the above discussions. The device architectures are explained briefly in Sect. 2. The simulation methodology for carrying out such analysis through TCAD is presented in Sect. 3. Additional supplementary information for gaining deeper insights into the robustness of the device architectures under test is given in Sect. 4, and finally, the article is summarized in Sect. 5.

---

2 Device Architectures Under Consideration

This section of the article aims to give a comprehensive view of the two emerging device architectures and gives a detailed insight to the issues that led to the development of the *Π*-shaped Gate and a Buffer-Free architecture for GaN HEMTs.

2.1 A *Π*-Shaped AlGaN/GaN HEMT

The GaN HEMTs have evolved ever since the field effect concept was demonstrated on the AlGaAs/GaAs system by Mimura et al. [2] and adopted for an AlGaN/GaN system by Khan et al. [49]. Accordingly, the reliability issues and the failure mechanisms observed for AlGaAs/GaAs systems were also observed in the AlGaN/GaN systems [50, 51] since their development was stemmed from the experiments performed by Mimura et al. [2]. In this regard, hot electron-induced device aging becomes a serious issue for GaN HEMTs [52], primarily due to their operating capabilities at high voltages. Further, in an attempt to push the device operation for mm-wave applications, the gate geometries have been continuously scaled down in submicrometer regimes [52–57]. The aggressive scaling of the gate geometries in submicrometer regimes reaching below 0.1 μm node, and coupled with high electric fields arising due to the high voltage operation results in the departure from the expected performance. Accordingly, several studies have been performed to study, identify, and mitigate the hot-electron degradation in GaN HEMTs through a combination of DC-Stress Tests and

Electroluminescence (EL) Characterizations [52, 58–65]. It has also been identified that gate engineering could help mitigate such reliability issues by minimizing the peak electric fields at the gate edge near the drain side of the terminal [61].

Consequently, a *Π*-shaped Gate architecture was proposed by Rey et al. [67] to minimize the hot-electron-induced degradation in GaN HEMTs. The idea behind such a gate architecture was to modify the electric field profiles at the heterointerface, in order to limit the kinetic energy of the energetic carriers by accelerating them through a stepped profile [67]. The proposed device, as reported exhibits modest trade-offs to the device RF performance. The authors also demonstrate an asymmetric *Π*-Gate to optimize the scattering rates to further reduce the kinetic energy. The proposed gate architecture was further studied for low noise applications by Sehra et al. [10, 68, 69] where the improved scattering rates of an asymmetric *Π*-Gate were exploited to achieve a lower noise figure by reducing the contribution from thermal noise [70, 71].

The abovementioned advantages proposed by Rey et al. [67] and further extended by Sehra et al. [10, 68, 69] evince the superior capabilities of the *Π*-shaped Gate for Space Applications. In this regard, Sehra et al. [48] further extended the study to investigate the performance of the said architecture for Single Event Transients (SETs) under the influence of heavy ion particle strike. The authors, also propose and validate for the first time the process recipe for the fabrication of *Π*-shaped Gate. The tool used for validation is Victory Process provided by Silvaco [66].

The process recipe at each major step realized through Silvaco's Victory Process is shown in Fig. 1. Initially, the desired epi-layer stack is grown on a six- inch substrate of semi-insulating SiC-4H through Metal Organic Chemical Vapor Deposition (MOCVD) technique. For the present case, the epi-layer stack was prepared in accordance with the experimental stack of a Conventional HEMT involving $Al_{0.23}Ga_{0.77}$ N barrier of 24 nm and a GaN buffer of 2.4 μm thickness [48]. Post-standard wafer cleaning procedure, the Ohmic contacts are defined with the help of photolithography technique for marking the Source and Drain windows and with *e*-beam evaporated Titanium(Ti)/Aluminum(Al)/Nickel(Ni)/Gold(Au) stack with thickness

of (300/1500/400/1000) $^{\circ}$A. This is followed up by standard lift-off procedures and Rapid Thermal Annealing (RTA) at 830 °C for 1 min in Nitrogen (N_2) ambient for Alloying. This is illustrated in Fig. 1a. The samples are then passivated by the dielectric deposition of Silicon Nitride (SiN_x) through Plasma Enhanced Chemical Vapor Deposition (PECVD) at 300 °C as shown in Fig. 1b. To realize the *Π*-shaped Gate, a two-step electron–beam lithography technique is used [48, 72]. This first involves the definition of the *Π*.

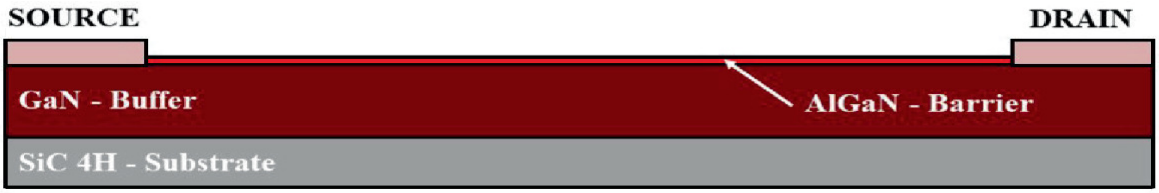

(a) Ohmic Contact Definition

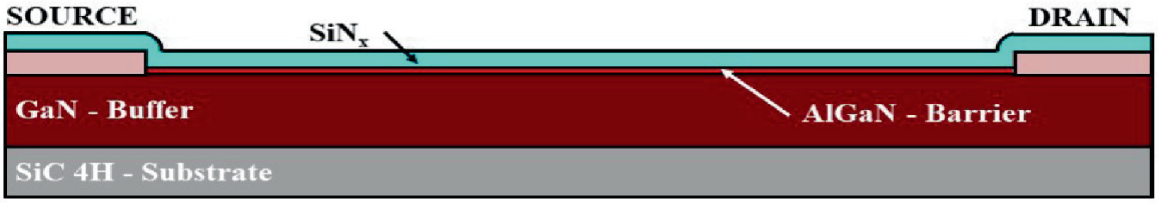

(b) Silicon Nitride growth using PECVD

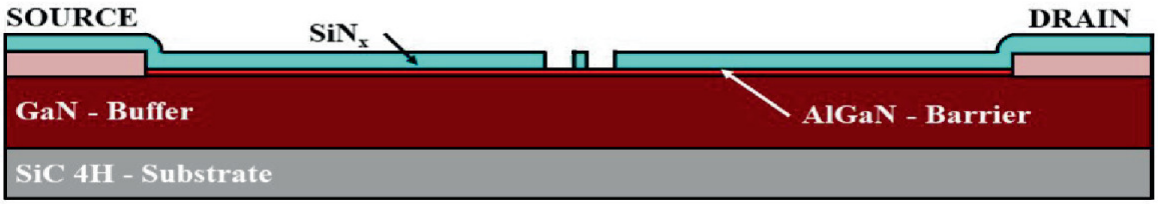

(c) Definition of Π - legs using Electron Beam Lithography

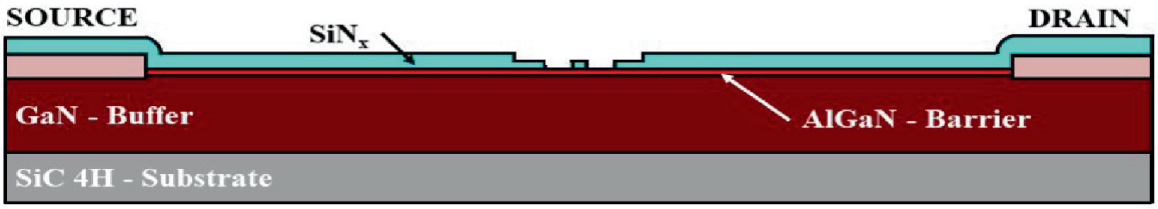

(d) Definition of Π - head using Electron Beam Lithography

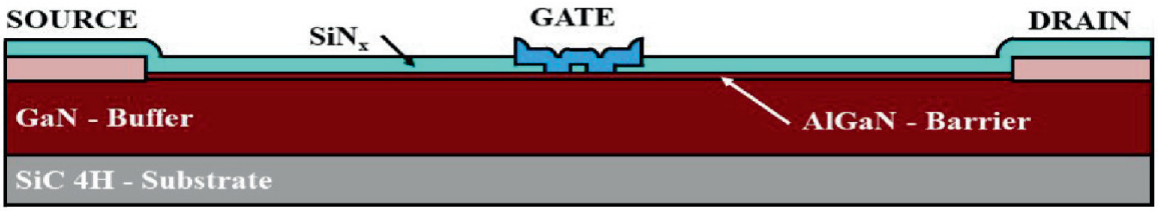

(e) Schottky Gate formation through e - beam evaporated Au/Ni Stack

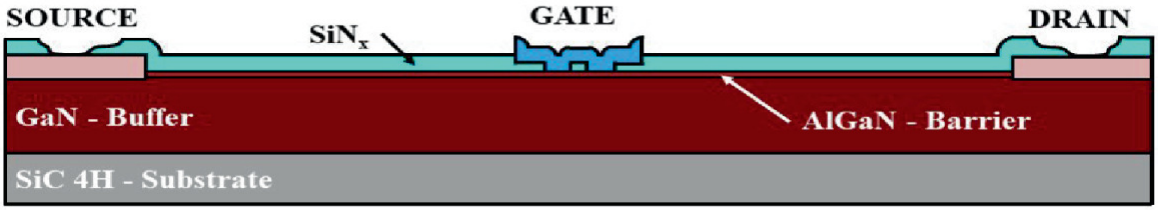

(f) Silicon Nitride etching from pad areas to get the metal contacts

Fig. 1 Describes the major steps for the fabrication of *Π*-Gate HEMT through Silvaco's process simulation [66]

Gate legs through Electron Beam Lithography (EBL) and followed by the etching of the deposited SiN_x dielectric through dry etching using BCl_3/Cl_2-based Inductively Coupled Plasma–Reactive Ion Etching (ICP–RIE). The steps are again repeated to define the head of the *Π*-structure through a different set of masks followed by partial etching of the SiN_x dielectric layer. The contact window etched out for the *Π*-structure is depicted in Fig. 1 c–d.

The schottky gate contact is then realized by depositing e-beam evaporated Nickel(Ni)/Gold(Au) stack with thickness of (400/2000) Å and standard lift-off procedures as shown in Fig. 1e. In the end, the SiN_x dielectric at the Drain/Source terminals is etched out to get the metallic contacts (Fig. 1f). The virtually fabricated *Π*-Gate is then compared with its Conventional counterpart to test the robustness against the heavy ion particle strikes. This article aims to provide deeper insights in the *Π*-architecture through a series of electron concentration contour plots in the later sections.

2.2 Buffer-Free AlGaN/GaN HEMTs

The wide bandgap semiconductors belonging to group III-nitrides, have been observed to exhibit trap-related dispersive effects that lead to the departure from the expected RF performance [1]. The electron trapping in the buffer and barrier regions or at the surface states on AlGaN barrier results in a collapse of the output current density and hence a compression of the output power density [73–75]. Accordingly, several techniques have been demonstrated to mitigate the trap-related dispersive effects through passivation techniques [76], employing field plate technology [77], or by modifying the gate architectures [75] to suppress the virtual gate formation. In this regard, it has been observed that a highly resistive (HR) GaN buffer would limit the buffer leakage and suppress the short channel effects to a large extent, thereby improving the overall breakdown characteristics of the device [78, 79]. This is expected to improve the overall PA performance of the device and can be achieved by various methods including deliberately

introducing intrinsic growth defects at the cost of crystal quality [80]. An alternative method, however, is by introducing dopants in GaN buffer during growth, where the commonly used dopants are iron (Fe) [81–84] and carbon (C) [74, 85–87]. These dopants, however, have other implications on the device performance such as the memory effects in iron (Fe) [88], or the floating buffer-induced channel pinch-off [88] in the case of carbon (C) doping. Further, there are several trade-offs in the performance metrics and these require critical design guidelines [85, 89–92] which causes a concern regarding the reliability issues.

One of the best alternatives to the above-stated issues is to adopt thin GaN buffers. These, however, have issues regarding the 2DEG confinement and are usually used along with back barriers such as the AlN. Previous reports on such a system resulted in high dislocations density (threading dislocation density) and poor carrier mobility (μ_n) at the quantum well [93–95]. In this regard, Chen et al. [45] redefined the concept of "buffer-free" by demonstrating AlGaN/GaN HEMTs using a 250 nm GaN buffer supported by a 60 nm thick AlN nucleation layer acting as the back-barrier for the 2DEG confinement. The device schematic is shown in Fig. 2. The structure as reported, demonstrates exceptionally good 2DEG properties reported for the first time on a thin GaN buffer (virtually buffer-free) along with an AlN back-barrier. The fabricated structure exhibits high carrier mobility (μ_n) of 2030 cm^2/Vs along with a high sheet carrier density (n_s) of 1.16×10^{13} cm^{-2} [45]. Further, the fabricated structures demonstrate a lower dispersion than their iron (Fe)-doped counterparts at gate lengths (L_G) of 200 and 100 nm. In addition to this, the group reports competitive RF and Power Amplifier (PA) performance of the buffer-free HEMT compared to their iron (Fe)-doped counterparts [45].

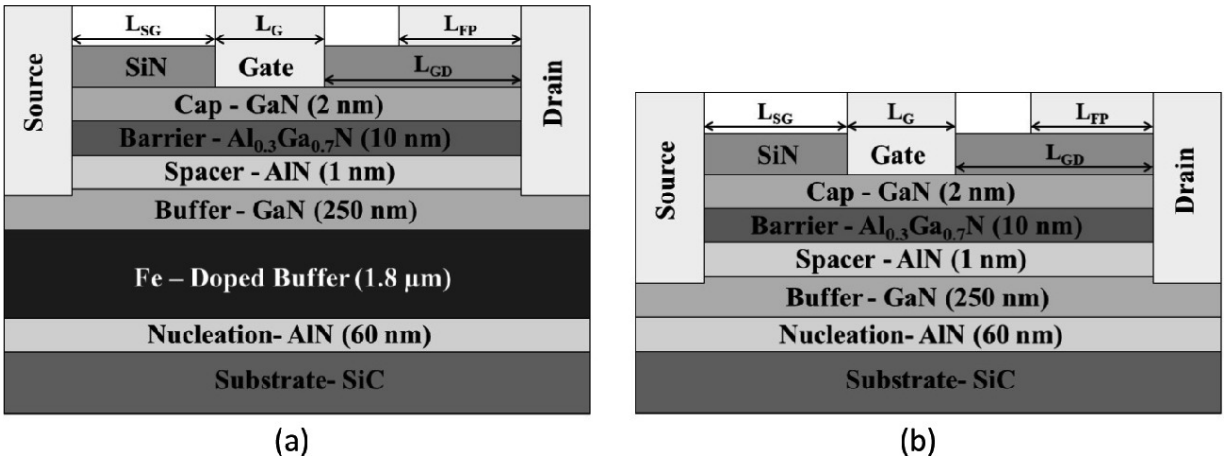

Fig. 2 Cross-sectional view of the **a** Fe-doped buffer, and **b** Buffer-free HEMT architecture. The geometrical specifications are: L_G = 200 nm/100 nm, L_{SD} = 2.75 µm/1.75 µm, L_{GD} = 1.75 µm/0.95 µm, L_{FP} = 0.25 µm/0.15 µm. The dimensions are as per [45] and the fabricated architecture has 2 × 50 µm arrangement

It is to be noted, that the high performance claimed by Chen et al. [45] on thin GaN buffers is possible due to the high quality, grain boundary-free AlN nucleation layer acting as the back-barrier. The growth technologies for the grain-free AlN was optimized by Lu et al. [16] and Chen et al. [17] to realize test structures with improved critical fields (E_C) and breakdown voltages (V_{Br}). Accordingly, the group achieved a high critical breakdown (V_{Br}) of 80 V and 50 V, respectively, at gate lengths (L_G) of 200 nm and 100 nm, respectively, which translates to provide high output power levels and efficiency.

The "buffer—free" concept put forward by Chen et al. [45] was consequently tested for space electronics under proton radiation environment by Raut et al. [44]. The structure was compared against the iron (Fe)-doped HEMTs for different proton fluence for Power Amplifier (PA) performance. This article aims to provide deeper insights into the performance of the two-device architectures under proton radiation through a series of Load Pull contours in the later sections.

3 Radiation Environment and Simulation Methodology

In order to emulate the radiation environment and thus investigate the impact of foreign environment on the performance metrics, Silvaco's Victory TCAD suite [66] was used. This section gives a brief overview of the simulation methodology adopted to carry out the analysis for Space Electronics.

3.1 Single Event Transients

To study the Single Event Transients post heavy ion particles strike, the Single Event Upset (SEU) model of Silvaco's Victory TCAD Suite is used [66]. Silvaco models the charge generation along the track length post heavy ion particle strike-through both spatial and time dependence. The spatial generation of the electron–hole pairs (EHP) along the track length can be specified by the *Entry Point* and *Exit Point* parameters of the SEU model. The model also has provisions to capture the recoils post-collision events through both *Axial* and *Radial* parameters [66]. The time dependence of the EHP generation along the track is modeled through parameters T_0 and T_C [40, 41, 66]. These parameters together define the instant charge generation that takes place (T_0) and the width of the Gaussian function that dictates the peak charge generation (T_C).

Accordingly, it is possible to replicate the damage profiles through the TCAD tools and thus investigate the performance of the device. The heavy ion particle strikes are commonly characterized through a Linear Energy Transfer (LET) value which is an estimate of the energy lost by the energetic particle as it undergoes several collisions within the lattice post penetration. It can also be defined as the energy deposited by the energetic particle per unit path length along its track [96]. In this regard, the LET value is commonly specified in units of MeV cm^2/mg. The SEU model in Silvaco's Victory TCAD Suite works on a Linear Charge Deposition (LCD) value in line with several experimental studies [41, 97, 98] and is specified in units of pc/μm. Accordingly, one may utilize the formulations given by Weatherford et al. [99] for interconversion between pc/μm and MeV cm^2/mg.

3.2 Proton Radiation Effects

To study the impact of proton radiation on the device performance, the Radiation Effects Module (REM) of Silvaco's Victory TCAD Suite is used

[66]. The energy transfer from the energetic protons to the crystal lattice on collision may result in displacement damage [29–31, 100]. The displacement damage is often characterized by the interaction of the energetic species with the nucleus, which results in lattice defects [29, 30]. Such an interaction does not ionize the atom but instead, the energy from collision displaces it from its original lattice position, thereby creating vacancies. Accordingly, the displacement damage caused is characterized by that component of Stopping Power ($S(E) = \partial E/\partial x$) that is disjoint from ionizing interactions [30]. It is generally called as Non-Ionizing Energy Loss (NIEL) and specified in units of MeV cm^2/(gram of particle). The displaced atom may acquire sufficient energy to cause subsequent displacement to form clusters [101] or may occupy an interstitial site as depicted by Sehra et al. [47]. The vacancies evolved as a result of interaction of proton fluence with the device architecture, acts as trapping centers and degrades the device performance.

Silvaco's Radiation Module captures the degradation caused by such displacements by calculating the density of defect states. Consequently, the density is a function of several parameters including the *damage factor* (α_D), the *NIEL Component* (E_L), and the *Particle Fluence* (no. of species/cm^2) of the interacting species [66]. Additionally, one may provide additional details to describe the defect states acting as the trapping centers by specifying the density and tail-state parameters (capture cross-sections) [66] to accurately capture the carrier interactions with the evolved defect states.

4 Results and Discussions

This section aims to give additional physical insights into the operation of the two device architectures under radiation environment to qualify devices for Space Electronics. In this regard, supplementary results from the author's previous works [44, 48] have been used for further analysis.

4.1 Robustness Against Heavy Ion Particle Stikes

The proposal for a *Π*-shaped Gate for the AlGaN/GaN HEMT against the Conventional architecture as discussed in Sect. 2.1 was to improve the hot electron reliability of the resulting device architectures by modifying the electric field profiles to improve the scattering rates. Since, the device as proposed by Rey et al. [67] and further extended by Sehra et al. [10] is capable to provide competitive performance for both Power and Low Noise applications, it is imperative to test the device architectures for the robustness against radiation under foreign environments. This section gives an insight into the robustness of the said device architectures against the Single Event Effects (SEEs) post-Heavy Ion Particle Strikes.

4.1.1 TCAD Setup for Heavy Ion Particle Damage Using SRIM

To investigate the device architectures for robustness against the heavy ion species, Silvaco's Single Event Upset (SEU) model [64] is invoked as described in Sect. 3.1. Author's previous work gives the details regarding the formulations of different parameters so considered for analysis [48]. A well-calibrated simulation deck of Conventional AlGaN/GaN HEMT calibrated against the in-house fabricated test structures is used for realizing the *Π*-Gate HEMT. Initial analysis is carried out through the open-source tool SRIM [102] to estimate the beam radius and the LET values required to model the SET effect. The SRIM Tool [102] is based on a Monte Carlo approach and is capable of accurately capturing the particle interactions. Accordingly, it has been used excessively to investigate the damage profiles in GaN HEMTs [30, 31, 48, 98, 103, 104] for various applications.

The SET model setup by Sehra et al. [48] relies on a beam radius of 0.07 μm as identified through the damage profiles generated through SRIM [102], in contrast to the 0.05 μm value used by Zerarka et al. [97, 98]. A comparison of the damage profiles generated by SRIM for the two device architectures at different magnification scales considering a 200 meV Xenon (Xe) source is shown in Fig. 3a–f The choice for heavy ion and its corresponding energy source has been taken to align with earlier experimental reports [41, 97, 98, 104–108]. Further, the T_0 and T_C values taken are in accordance with the longer SET experiments performed by Rostewitz et al. [105].

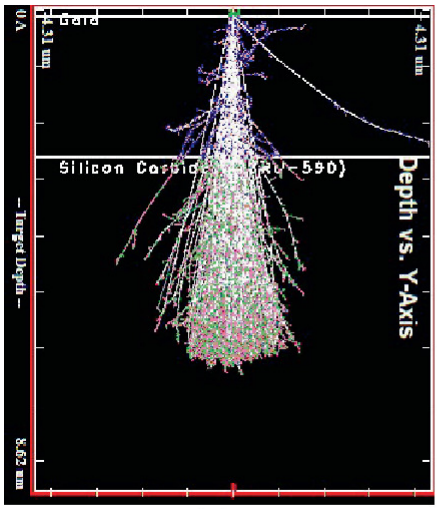
Gold
4.31 um
Silicon Carbid
Depth vs. Y-Axis
0 A
– Target Depth –
8.62 um

(a)

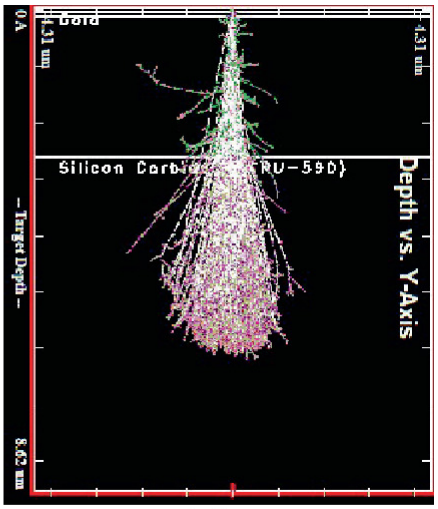
Gold
4.31 um
Silicon Carbi
Depth vs. Y-Axis
0 A
– Target Depth –
8.62 um

(b)

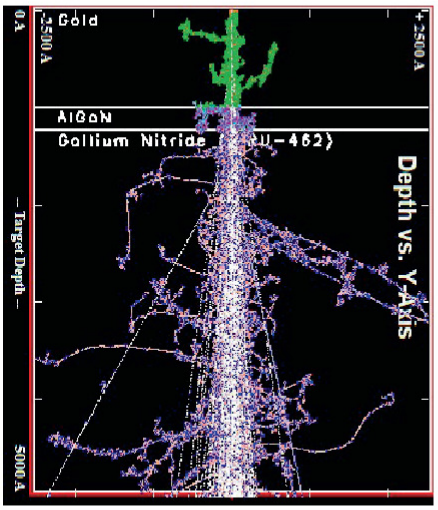
Gold
-2500 A
+2500 A
AlGaN
Gallium Nitride
Depth vs. Y-Axis
0 A
– Target Depth –
5000 A

(c)

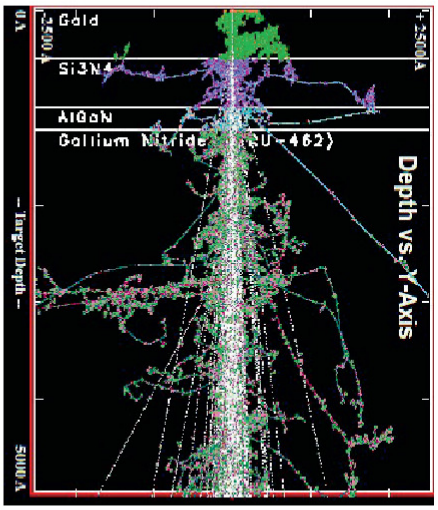
Gold
-2500 A
+2500 A
Si3N4
AlGaN
Gallium Nitride
Depth vs. Y-Axis
0 A
– Target Depth –
5000 A

(d)

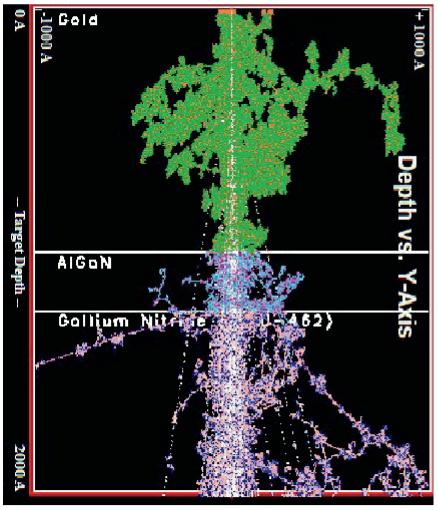
Gold
-1000 A
+1000 A
AlGaN
Depth vs. Y-Axis
0 A
– Target Depth –
2000 A

(e)

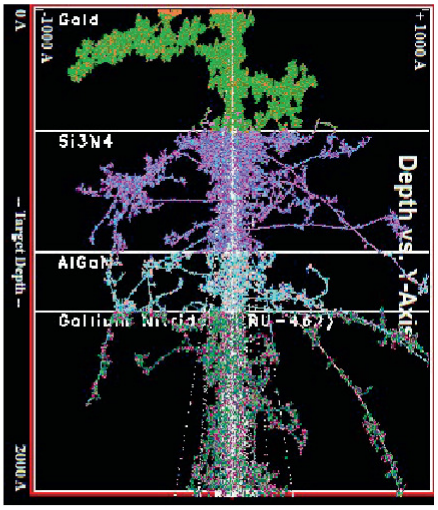
Gold
-1000 A
+1000 A
Si3N4
AlGaN
Depth vs. Y-Axis
0 A
– Target Depth –
2000 A

(f)

Fig. 3 The damage profiles generated through SRIM for SEU strike at the center of the gate for conventional HEMT [(**a**), (**c**), (**e**)] and *Π*-Gate HEMT [(**b**), (**d**), (**f**)]. Profiles generated in (**c**), (**e**) for the Conventional and (**d**), (**f**) for the *Π*-Gate have been simulated again to depict a close-up view of the resulting damage profiles for the two DUTs

To investigate the track length generated through a particle strike on the epi layer stacks of both the Conventional and *Π*-Gate HEMT, SRIM-based Monte Carlo simulations are used. The SRIM profiles depicted in Fig. 3 demonstrate a track length of 5 μm as a result of 200 meV Xenon (Xe) strike with an LET of 47.36 meV cm^2/mg at the center of the two DUTs. Therefore, in order to emulate SET conditions similar to the ones generated through SRIM, a track length of 5 μm was taken for all TCAD simulations. Further, the range of energetic ions so considered and as estimated by SRIM [48, 102] is sufficient enough to cross the active area of the device.

4.1.2 Impact on Conventional and Π-Gate

On careful observation, it is revealed from the damage profiles of Fig. 3c–d and e–f that a significant chunk of incident particle energy is absorbed by the extra Silicon Nitride layer beneath the MOS architecture of the *Π*-shaped Gate which increases the contribution of the Nuclear Stopping Power ($S(E)_n = \partial E_n/\partial x$). Using the above formulations for SEU particle strikes, Fig. 4 depicts the resulting contour plots of the electron concentrations (in cm^{-3}) for the two device architectures under study so recorded under ON-state conditions for an LET of 47.36 meV cm^2/mg (or 0.4 pC/μm [99]).

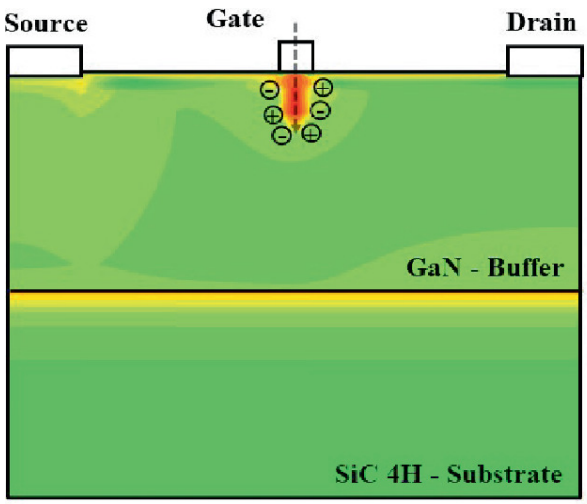
Source
Gate
Drain
GaN - Buffer
SiC 4H - Substrate

(a)

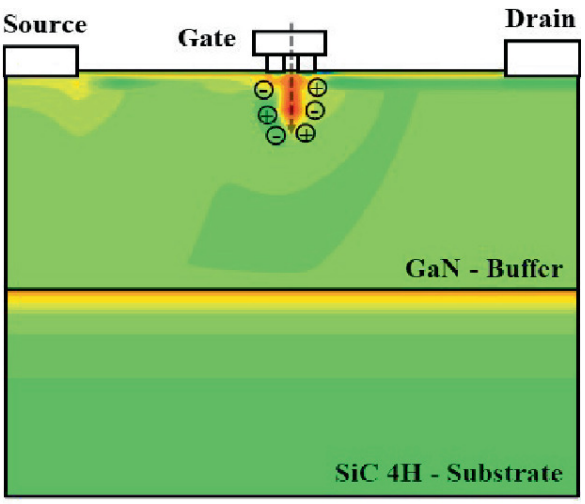
Source
Gate
Drain
GaN - Buffer
SiC 4H - Substrate

(b)

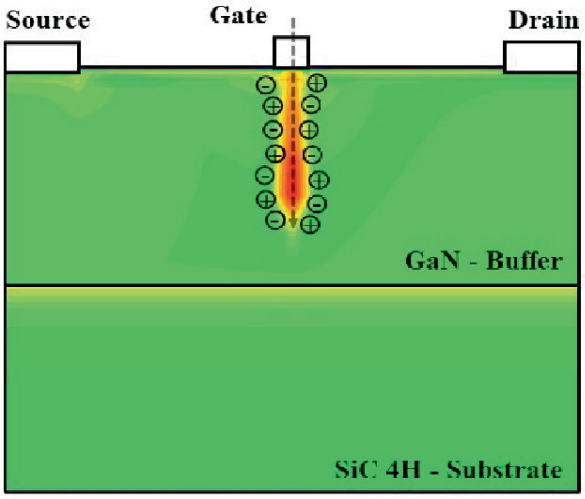
Source
Gate
Drain
GaN - Buffer
SiC 4H - Substrate

(c)

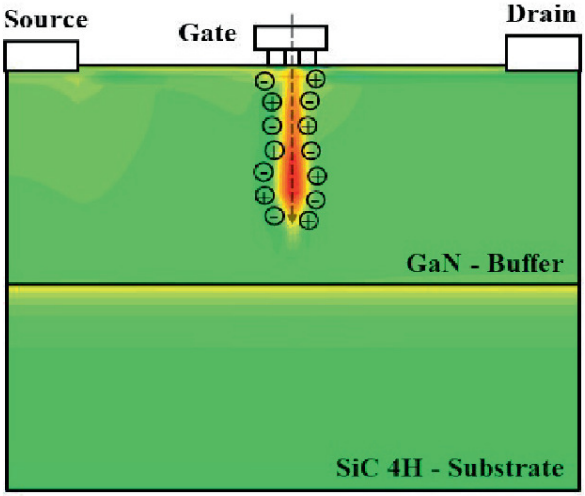
Source
Gate
Drain
GaN - Buffer
SiC 4H - Substrate

(d)

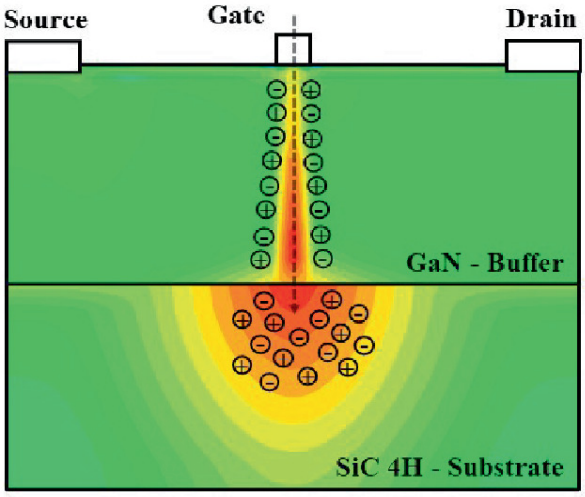
Source
Gate
Drain
GaN - Buffer
SiC 4H - Substrate

(e)

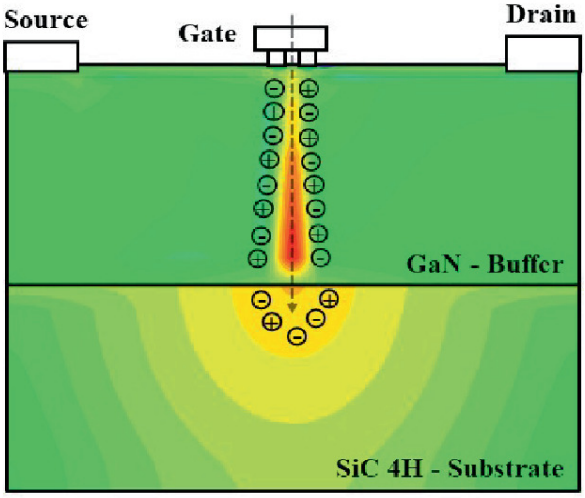
Source
Gate
Drain
GaN - Buffer
SiC 4H - Substrate

(f)

Fig. 4 Evolution of electron concentration (in cm^{-3}) contour plots of Conventional and *Π*-Gate as heavy ion passes through GaN buffer at a depth of **a**, **b** 0.5 μm, **c**, **d** 1.5 *μm*, and **e**, **f** 2.5 μm. LET value of Heavy Ion is 47.36 meV cm^2/mg. The devices are biased in ON-state conditions with V_{GS} = 0 V and V_{DS} = 10 V

It is evident from the contour plots of Fig. 4, the *Π*-Gate architecture is resistant toward such particle strikes due to the presence of MOS architecture that increases the contribution of nuclear stopping power ($S(E)_n = \partial E_n/\partial x$). This is validated through the plots of collision events for both the device architectures as given in Fig. 5. It is evident that the total number of vacancies generated in both the AlGaN barrier and GaN buffer is lower in *Π*-Gate (Fig. 5b) compared to its conventional counterpart (Fig. 5a). Further, the EHP generation is also depicted in Fig. 4 alongside the electron concentration to demonstrate the difference in charge generation (or EHP) for the two devices along the SEU track (depicted by $\rightarrow$).

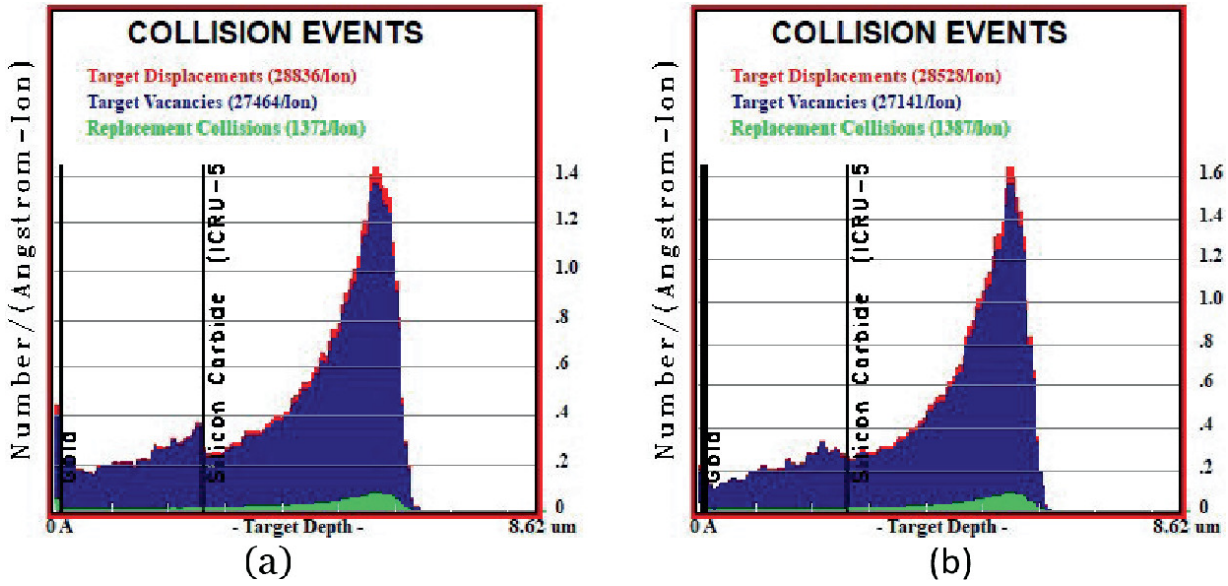

Fig. 5 Summary of collision events for **a** Conventional, and **b** *Π*-Gate AlGaN/GaN HEMT as a result of SEU particle strike corresponding to an LET of 47.36 meV cm^2/mg

When the device is radiated with heavy ion particle strikes, the incident particles start colliding with the lattice atoms of the epi-layer stack present in AlGaN/GaN HEMTs. In course of their action, the particles transfer their energy to lattice sites through which they pass,

causing them to shift from their initial position and create vacancies. This is accompanied by energy loss of the incident particle and such collisions may result them to deviate from their initial path as depicted in Fig. 3. Generally, a particle collides multiple times with several lattice sites before coming to complete rest, and in this process, several vacancies are generated until the energy of the incident particle is less than the binding energy of the lattice with which it is interacting. This phenomenon is depicted for the two DUTs in Fig. 5. Further, the elastic collisions that occur due to such particle strikes may result in such events, wherein the displaced lattice atoms acquire sufficient energy to collide with other lattice atoms to create secondary vacancies. This is depicted in damage profiles presented in Fig. 3. The tracks associated with *white color* in Fig. 3, correspond to the incident particle strike, while that of *green color* correspond to the displaced atoms from gate electrode, *purple color* tracks refer to the atoms displaced from GaN layer (for Conventional HEMT) and nitride layer (for *Π*-Gate HEMT), *sky blue* colored tracks are associated with the displacements in AlGaN barrier layers, and *dark green color* is associated with the displacements in GaN layer for the *Π*-Gate architecture. It is evident from both Figs. 3 and 5 that the *Π*-Gate architecture is resistant toward vacancy generation and lattice displacements as the damage profiles (Fig. 3b, d, f) are mainly crowded due to the tracks generated through the incident particle strikes. This is again validated through the abrupt change in collision events depicted in Fig. 5 for the Conventional HEMT at GaN/SiC interface which is also observed in the electron concentration contour plots depicted in Fig. 4.

It is worthwhile to mention that the EHP generated along the track length as depicted in Fig. 4 gets redistributed due to the electric field set up in the AlGaN/GaN system as a result of the applied bias. Accordingly, the redistribution may include majority of electrons to be accumulated near the drain electrode, which sets off specific events for the activation of the parasitic bipolar transistor. There is also a possibility of the holes being accumulated below the Gate region, which consequently sets off peculiar environment for the back-channel effects. These effects have been widely reported in many experimental reports [109–111] and a visual representation of the same is provided by Sehra et al. [48].

These effects are more pronounced at specific conditions and can be individually visualized by considering the impact of angled strike at the Gate electrode. Two strike conditions are considered, where the incident particle strikes the Gate electrode at an angle of − 60° and + 60°. The resulting electron concentration contour plots for the two device architectures is depicted in Fig. 6. It is observed from Fig. 6a–b, that the impact of ion strike is closer to the drain electrode. Accordingly, the redistribution of EHP under the applied bias results in holes to traverse a longer distance towards the source, which consequently lowers the barrier potential at the Gate region, for enhanced electron injection from the Source terminal. These events constitute the back-channel effects. The resulting Single Event Transients (SETs) recorded by Sehra et al. [48] demonstrate robustness of *Π*-shaped gate to such events due to the presence of an MOS architecture. This can also be visualized from the contour plots of Fig. 6a–b. The parasitic bipolar effect can be visualized from the particle strike at an angle of + 60° as shown in Fig. 6c–d. Under these conditions, the impact is near the Source electrode, and the excessive hole accumulation kicks off the bipolar effects. The change in current associated with these effects is thus small as demonstrated by Sehra et al. [48].

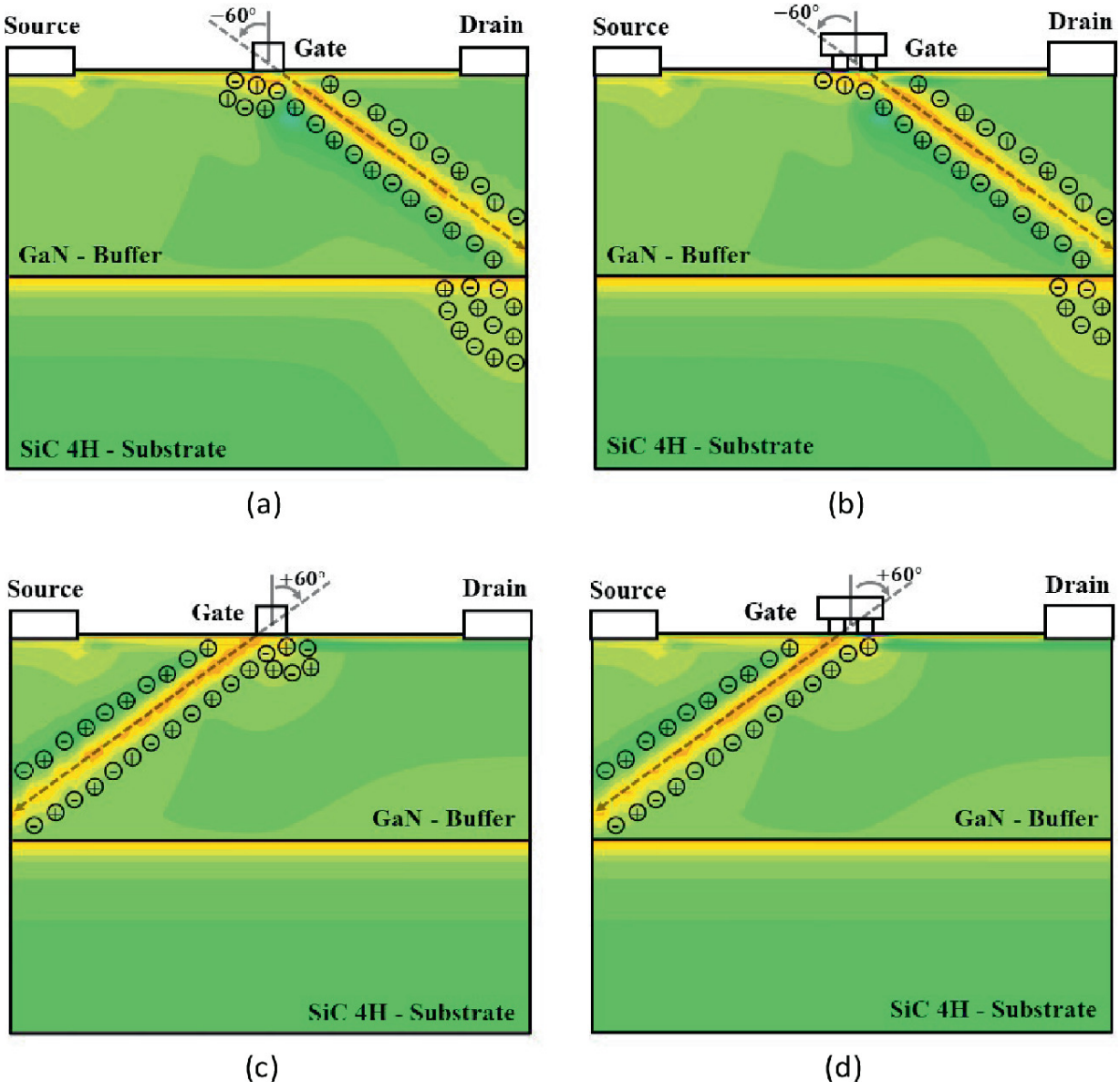

Fig. 6 Impact of angled particle strike on electron concentration (in cm^{-3}) of Conventional and *Π*-Gate for **a**, **b** −60°, and **c**, **d** + 60°. LET value of heavy ion is 47.36 meV cm^2/mg. The devices are biased in ON-state conditions with V_{GS} = 0 V and V_{DS} = 10 V

The discussions presented above, through a combination of damage profiles (generated from SRIM [102]) and electron concentration contour plots (generated from Victory [66]) brings deeper insights into the robustness of the *Π*-shaped Gate against the SETs induced by heavy ion particle strikes, and thus evinces the superiority of *Π*-shaped Gates for Space Electronics.

4.2 Proton Irradiation Effects on Buffer-Free HEMT

The buffer-free architecture for the AlGaN/GaN HEMT was proposed and optimized by Chen et al. [45] to suppress the trap-related buffer dispersion and improve the Large Signal Performance, as discussed in Sect. 2.2. This was achieved by optimizing the growth technology of a thin GaN buffer with a high -quality grain boundary-free AlN nucleation layer acting as the back-barrier [16, 17]. The device, as reported, exhibits a lower buffer dispersion and similar RF performance compared to its Iron (Fe) doped counterpart. Accordingly, proposed device design was further investigated by Raut et al. [44] to test the robustness of the buffer-free architecture under proton radiation environment. The authors also present a detailed description of the proton irradiation effects on the PA performance for both Buffer-Free and Iron (Fe) doped architecture. This section gives additional insights into the robustness of the said architectures.

4.2.1 Impact on DC Characteristics

To investigate the proton irradiation effects on the device architectures under test, Silvaco's Radiation Effects Module (REM) [66] was invoked as described in Sect. 3.2. Author's previous work [44] gives details regarding the formulations of the *fluence model* used for investigating the effects.

Authors make use of the well-calibrated simulation decks of buffer-free and iron (Fe)-doped architectures in order to mimic the actual behavior of the device. The experimental data and the device geometries were adapted from Chen et al. [45].

Initial analysis for this work also involved preliminary investigation using the SRIM Simulations [102]. The epi-layer stack of the device was defined and investigated under a 1.8 meV Proton source. The choice for the energy is in accordance with the Bragg's curve for producing maximum damage in the device [30, 112, 113]. In this regard, the corresponding NIEL values obtained from the SRIM Simulations were given as input (E_L) to the *fluence model*. Further, it is evident from the damage profiles that the trajectories of the incident protons post penetration are high enough to penetrate the SiC substrate [47, 112, 113]. Accordingly, the incident protons can easily interact with the active area of the device. The proton fluence considered in the

investigation ranges from 1×10^{11} protons/cm^2 to 1×10^{14} protons/cm^2 with a decade change in the particle fluence. This aligns with several experimental reports on similar radiation species [114–116]. The value of *damage factor* (α_D) was determined by calculating the total number of vacancies generated in the epi layer stack from the SRIM Simulations [102] for each fluence in accordance with the methodology presented by Pearton et al. [30]. The number of vacancies increases linearly with the proton fluence suggesting that the displacement damage is proportional to the particle's NIEL as also summarized in various experimental reports [30, 117, 118].

The DC characteristics of the two device architectures were compared under the proton environment using the *fluence model* as described above. The impact on transfer and transconductance profiles is depicted in Fig. 7a and b, respectively. A superficial look at the profiles depicted in Fig. 7 demonstrates a higher degradation in Iron (Fe) doped architecture in comparison to the Buffer-Free HEMT.

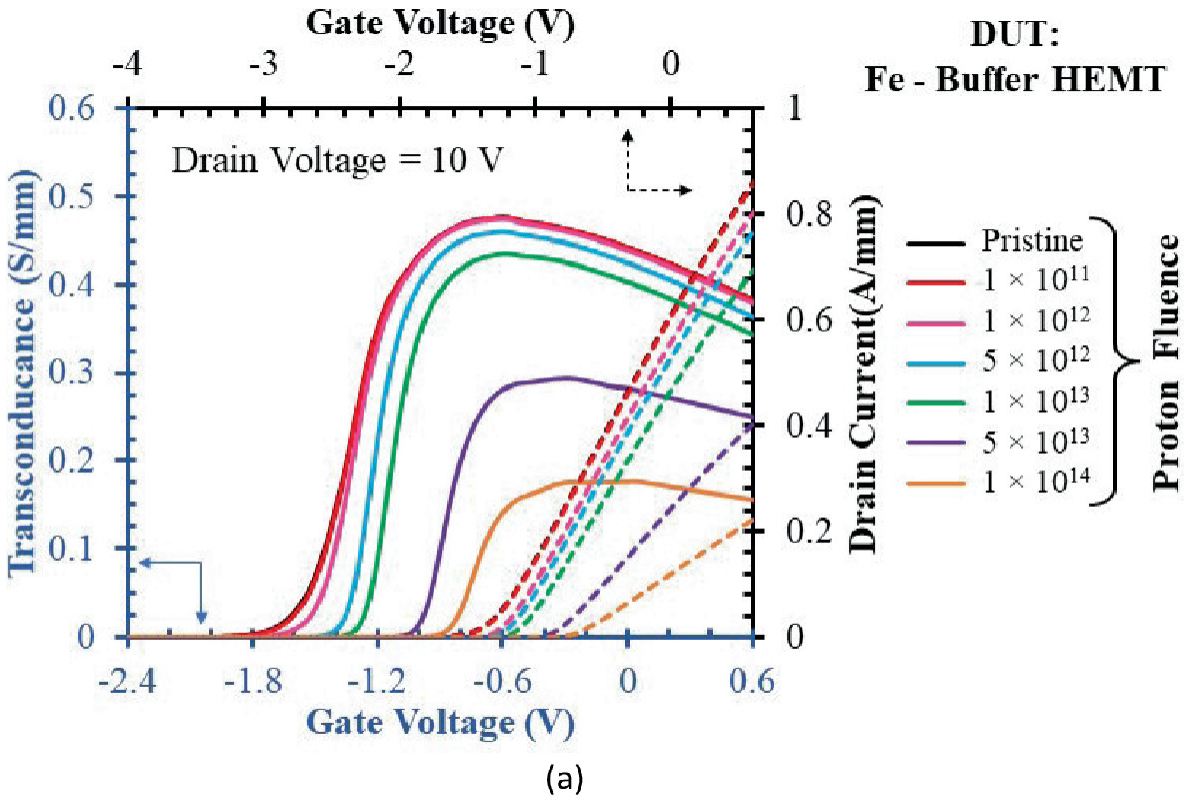

(a)

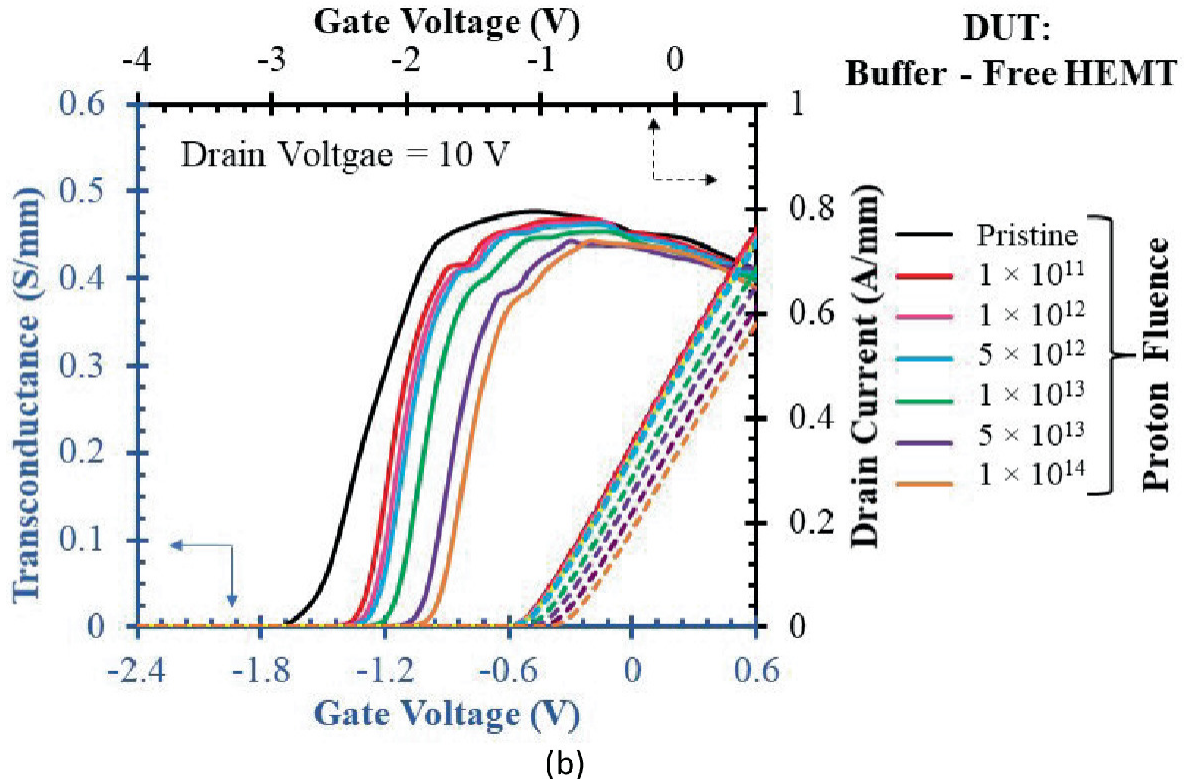

(b)

Fig. 7 Impact of 1.8 meV proton source on the transfer and transconductance profiles of **a** Fe-buffer HEMT, and **b** Buffer-Free HEMT

A general observation, from the results presented in Fig. 7, point toward the roll-off in both the maximum drain current ($I_{D(Max)}$) and the peak transconductance ($g_{m(Max)}$) values. This is in addition to the positive shift observed in the device pinch-off voltage. These effects point toward the fact that the proton fluence-induced displacement damage generates acceptor type vacancies [29–31, 42, 119]. Further, it has also been observed that the proton-induced trapping centers may in fact be linked to the carrier scattering which is ultimately responsible for the degradation of carrier mobility (μ_n) as recorded in the author's previous works [44] and on similar lines to several experimental reports [47, 115, 120]. The degradation of carrier mobility, as a result is responsible for the deterioration observed in ON-state current.

The change (in %) associated with various performance metrics of the iron (Fe)-doped buffer and the Buffer-Free HEMT with respect to pristine conditions is summarized in Tables 1 and 2, respectively.

Table 1 Percentage change in device metrics of an Fe-Buffer HEMT under different proton fluence

Metrics	**Change (in %) with proton fluence (/cm^2)**					
	1×10^{11}	**1×10^{12}**	**5×10^{12}**	**1×10^{13}**	**5×10^{13}**	**1×10^{14}**
Maximum drain current	2.97	4.80	7.70	12.86	41.23	72.27
Peak transconductance	1.98	4.06	12.40	22.27	52.31	63.26
Electron density (*ns*)	0.19	0.27	2.68	4.74	22.13	36.07
Peak electric field	0.13	0.25	0.62	0.82	7.95	11.83
Threshold voltage ($V_{T\,h}$)	0.00	6.06	19.39	24.24	42.42	56.36
Peak lattice temperature	0.31	0.62	1.08	1.54	3.70	20.59
2DEG mobility (μn)	0.55	0.69	1.70	10.89	54.07	65.32
Cut—off frequency (*f*T)	0.66	1.59	8.15	11.15	53.14	64.67
Max. oscillation Freq. (*f*Max)	0.66	1.60	5.82	9.96	30.08	46.53

Table 2 Percentage change in device metrics of a buffer—free HEMT under different proton fluence

Metrics	**Change (in %) with proton fluence (/cm^2)**

Metrics	Change (in %) with proton fluence (/cm^2)					
	1×10^{11}	1×10^{12}	5×10^{12}	1×10^{13}	5×10^{13}	1×10^{14}
Maximum drain current	0.11	1.32	1.77	3.10	12.18	18.68
Peak transconductance	2.04	2.54	2.73	2.53	5.93	10.41
Electron density (ns)	0.41	0.40	0.74	1.06	13.06	25.95
Peak electric field	-0.07	0.16	0.20	0.29	2.85	9.17
Threshold voltage ($V_{\mathrm{T\,h}}$)	2.43	2.43	2.43	2.43	14.63	26.82
Peak lattice temperature	0.16	0.32	0.64	0.97	1.29	7.78
2DEG mobility (μn)	0.42	0.52	0.95	10.83	23.27	38.90
Cut—off frequency (fT)	0.07	0.17	0.37	0.66	8.45	16.38
Max. oscillation Freq. (fMax)	0.17	0.41	1.31	1.98	5.11	7.22

It is observed that the percentage change associated with each performance metric at a specific proton fluence is considerably higher in case of iron (Fe)-doped HEMT compared to the Buffer-Free architecture. For the buffer-free architecture, a smaller change in $I_{\mathrm{D(Max)}}$ can be linked to the enhanced 2DEG confinement courtesy of the wide bandgap AlN—nucleation layer acting as the back-barrier for the thin GaN buffer. A suppressed roll-off in the $g_{\mathrm{m(Max)}}$ values in case of buffer-free architecture, can be linked to the enhanced gate control over the thin GaN channel in comparison to the thick iron (Fe)-doped buffer. Accordingly, as the proton particles penetrate deep within the device, displacement damage is spread across the device in a large volume in a thick GaN buffer compared to the buffer-free architecture. This can be verified from the vacancy plot as a function of proton fluence for the GaN buffer obtained from SRIM Simulations [102]. The spread of displacement damage and subsequently its effect on the device performance can be visualized by monitoring the shift in the device pinch-off voltage (V_{Th}) recorded at 1 mA/mm. Due to a thinner buffer and better 2DEG confinement, the gate control is much pronounced in a buffer-free HEMT which counters the deleterious effects of the radiation-induced defects. As a result, the V_{Th} shift associated with the said architecture is much lower than the conventional Iron (Fe) doped

buffer. Also, there is a considerable difference in the number of vacancies generated for an iron (Fe)-doped buffer compared to the Buffer-Free architecture, which consequently gets reflected in the percentage change of n_s for the two devices. The number of vacancies generated also has a direct consequence in degrading the carrier mobility (μ_n) at the 2DEG channel which is significantly lower for a buffer-free HEMT.

The discussions presented above for the results compiled in Tables 1 and 2, point toward the fact that the RF performance of the buffer-free architecture will be tolerant against the ill-effects of the radiation-induced traps. This is in conjunction to the small degradation recorded in $g_{m(Max)}$ for the buffer-free HEMT in comparison to the iron (Fe)-doped buffer, which consequently limits the deterioration in the Current Gain and the Unilateral Power Gain metrics along with f_T and f_{Max}.

4.2.2 RF Performance Under Proton Radiation

This section presents the RF performance comparison of the Buffer-Free and iron (Fe)-doped HEMT to test the applicability under space environment. The devices were calibrated with transfer characteristics and S—parameters in Keysight ADS [121] suite using ASM HEMT model card [122]. The calibrated models were then used to design a Class F Power Amplifier for X-band application (8–12 GHz). The author's previous work [44] was based on 3 GHz and an extension for Microwave X–band is presented in this article.

Harmonic balance simulation setup was employed for the Class F Power Amplifier analysis. At first, a suitable bias point of interest is determined and system' stability is constantly monitored. This is followed by designing of output matching network (OMN) and input matching networks (IMN) through iterative process of load optimization in load-pull and source pull simulations respectively. During load/source pull simulation, given constant input power, output/input load is varied to have maximum power-added efficiency (P_{AE}), optimum power delivered (P_{DEL}), gain, and linearity. Figure 8 shows the output of load-pull simulation where an optimum load is determined at the point where optimum output power and maximum

PAE are delivered. From P_{DEL} and PAE contours, the maximum P_{DEL} of 22 dBm and PAE of 73.08% is obtained after three iterations.

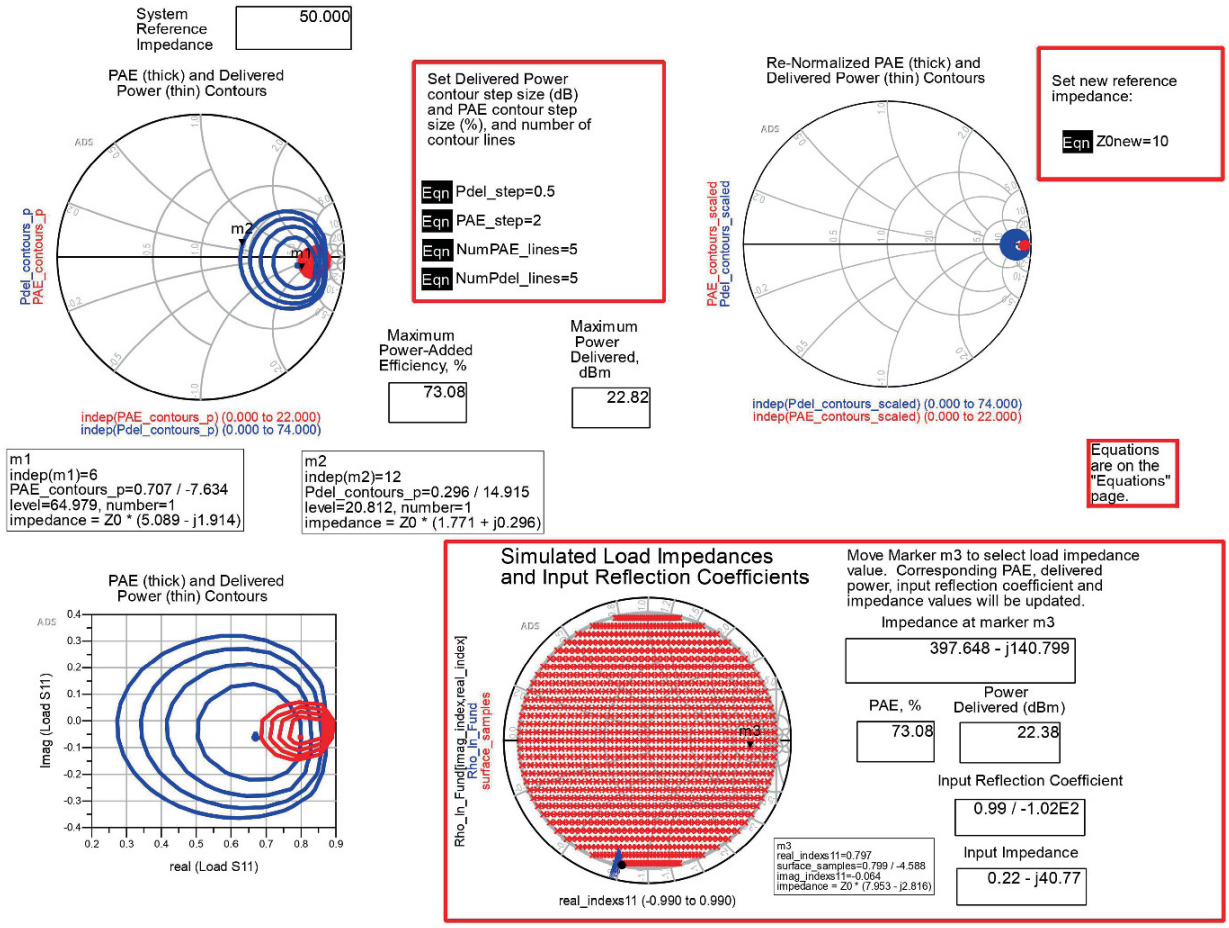

Fig. 8 Load pull simulation result after three iterations for Fe–buffer HEMT under pristine condition

The complete methodology for load optimization and PA design is adapted from the author's previous works [44].

Buffer-Free structure despite of lacking highly doped buffer layer shows competitive RF performance. When exposed to high energy proton radiation, rate of performance deterioration in iron (Fe)-doped buffer HEMT is significantly higher than Buffer-Free structure which directs higher radiation sensitivity in buffered configuration. Figure 9a and b illustrate the Output Power (P_{OUT}), Power Added Efficiency (P_{AE}), and Gain obtained through the Harmonic Balance Simulation at 10 GHz for system biased at $V_{\mathrm{GS}} = -1$ V and $V_{\mathrm{DS}} = 10$ V. The change (in %) on the various figure of metrics of Power Amplifier for the Iron (Fe) doped

buffer and Buffer-Free HEMT with respect to pristine conditions is summarized in Tables 3 and 4, respectively. As discussed in previous section, the impact of radiation is not so pronounced at lower fluence values. However, at higher fluences, due to larger number of vacancies and defect sites generated in Iron (Fe) doped buffer compared to Buffer-Free structure, higher amount of dispersion effects, higher 2DEG degradation, and hence, reduced gate control overcharge carriers is observed in case of buffered configuration. This has consequent impact on power extraction capability which can be referred from reduced power delivered and gain. Moreover, lower distortion and better linearity in case of Buffer-free HEMT can be concluded from trend of P1dB and third-order intercept (TOI). This is in conjunction to the DC results presented in Sect. 4.2.1. To conclude, Buffer-Free HEMT tends to have much higher resistance to radiation hence directs better suitability in high-power and space applications.

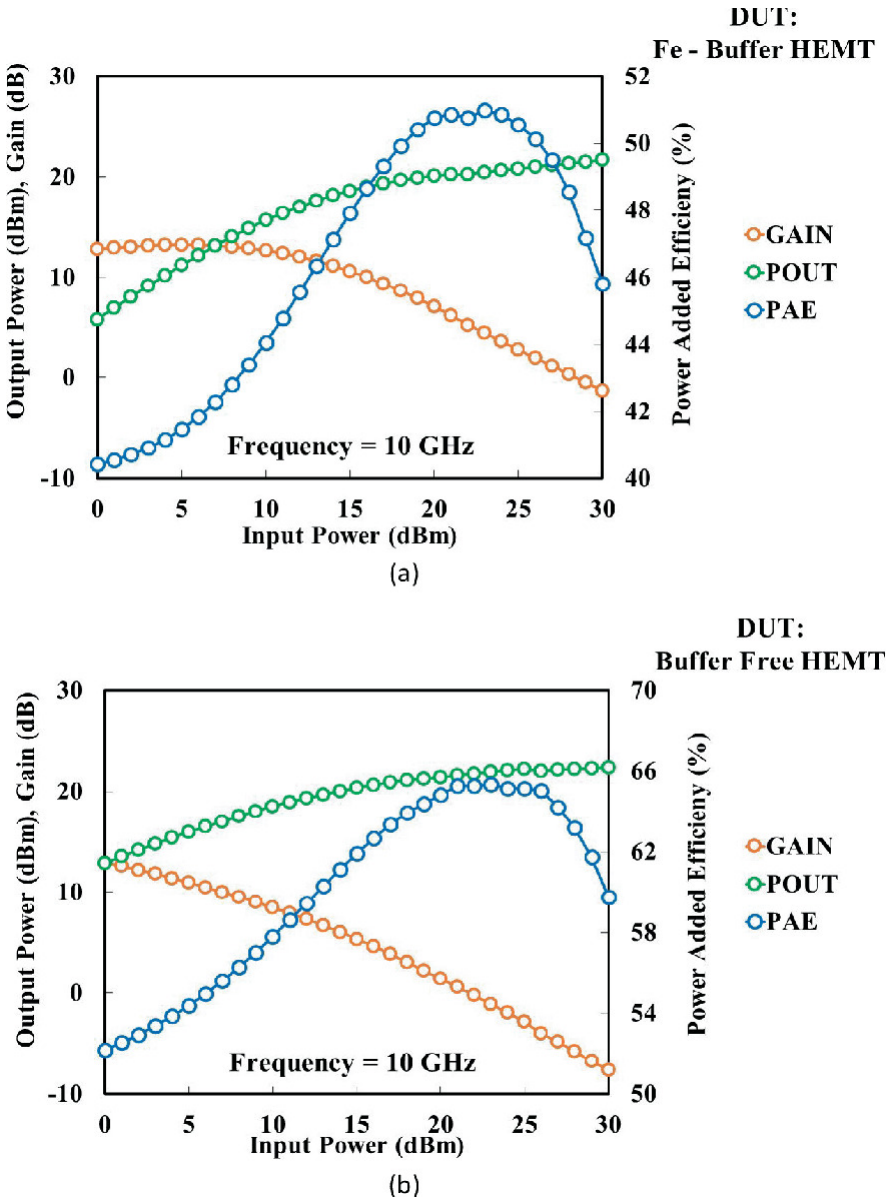

Fig. 9 Power amplifier key figure of metrics under pristine condition: Output power, gain, and power added efficiency (PAE) for **a** Fe-buffer HEMT, and **b** Buffer- free HEMT

Table 3 Percentage change in class-F power amplifier figure of merits based on buffer-free HEMT under different proton fluence

Metrics	**Change (in %) with proton fluence (/cm^2)**			
	1×10^{11}	**1×10^{12}**	**1×10^{13}**	**1×10^{14}**
Maximum output power	1.08	1.84	5.46	8.56
Maximum gain	1.26	3.09	6.82	50.86
Maximum P1dB	1.59	2.14	7.36	12.99

Metrics	Change (in %) with proton fluence ($/cm^2$)			
	1×10^{11}	1×10^{12}	1×10^{13}	1×10^{14}
Maximum PAE	0.01	1.28	1.40	5.08
3rd order intercept (TOI)	0.73	1.93	3.67	11.78

Table 4 Percentage change in class-F power amplifier figure of merits based on Fe-buffer HEMT under different proton fluence

Metrics	Change (in %) with proton fluence ($/cm^2$)			
	1×10^{11}	1×10^{12}	1×10^{13}	1×10^{14}
Maximum output power	1.55	4.17	7.29	9.40
Maximum gain	3.52	20.189	54.86	92.07
Maximum P1dB	1.10	1.85	13.83	31.03
Maximum PAE	10.99	21.33	23.66	29.81
3rd order intercept (TOI)	2.06	7.36	10.20	27.54

5 Conclusions

This work presents TCAD-based detailed analysis of emerging GaN HEMT devices under different radiation phenomena for assessing the device performance for Space Electronics. Modifying the gate architecture and layer stack can significantly help in increasing the robustness against the harmful effects of the different radiation sources. In this regard, the TCAD-based studies can help the device engineers optimize the device design for a robust operation under a foreign environment. Accordingly, this will be a viable approach to analyze the reliability of the fabricated test structures to save both time and cost of production.

Acknowledgements

The authors wish to acknowledge DBT Star College Laboratory at Deen Dayal Upadhyaya College, University of Delhi; Semiconductor Device Research Laboratory (SDRL) at the Department of Electronic Science, University of Delhi South Campus for providing the necessary tools and financial assistance for completion of this work.

References

1. M.A. Khan, M.S. Shur, Q. Chen, J. Kuznia, Current/voltage characteristic collapse in AlGaN/GaN heterostructure insulated gate field effect transistors at high drain bias. Electron. Lett. **30**(25), 2175–2176 (1994)

2. T. Mimura, S. Hiyamizu, T. Fujii, K. Nanbu, A new field-effect transistor with selectively doped GaAs/n-Al*x*Ga1−*x*As heterojunctions. Jpn. J. Appl. Phys. **19**(5), L225 (1980)

3. G. Gauthier, F. Reptin, KORRIGAN: development of GaN HEMT technology in Europe. CS Mantech Conf. 49–51 (Citeseer, 2006)

4. M.J. Rosker, J.D. Albrecht, E. Cohen, J. Hodiak, T.H. Chang, DARPA's GaN technology thrust, in *2010 IEEE MTT-S International Microwave Symposium* (IEEE, 2010), pp. 1214–1217

5. D.S. Green, C.L. Dohrman, J. Demmin, Y. Zheng, T.H. Chang, A revolution on the horizon from DARPA: Heterogeneous integration for revolutionary microwave/millimeter-wave circuits at DARPA: Progress and future directions. IEEE Microwave Mag. **18**(2), 44–59 (2017)

6. O. Ambacher, J. Smart, J. Shealy, N. Weimann, K. Chu, M. Murphy, W. Schaff, L. Eastman, R. Dimitrov, L. Wittmer et al., Two-dimensional electron gases induced by spontaneous and piezoelectric polarization charges in N-and Ga-face AlGaN/GaN heterostructures. J. Appl. Phys. **85**(6), 3222–3233 (1999)

7. O. Ambacher, B. Foutz, J. Smart, J. Shealy, N. Weimann, K. Chu, M. Murphy, A. Sierakowski, W. Schaff, L. Eastman et al., Two dimensional electron gases induced by spontaneous and piezoelectric polarization in undoped and doped AlGaN/GaN heterostructures. J. Appl. Phys. **87**(1), 334–344 (2000)

8. M. Su, C. Chen, S. Rajan, Prospects for the application of GaN power devices in hybrid electric vehicle drive systems. Semicond. Sci. Technol. **28**(7), 074012 (2013)

9. R.S. Pengelly, S.M. Wood, J.W. Milligan, S.T. Sheppard, W.L. Pribble, A review of GaN on SiC high electron-mobility power transistors and MMICs. IEEE Trans. Microw. Theory Tech. **60**(6), 1764–1783 (2012)

10. K. Sehra, V. Kumari, M. Gupta, M. Mishra, D. Rawal, M. Saxena, Optimization of π–gate AlGaN/AlN/GaN HEMTs for low noise and high gain applications. Silicon 1–12 (2020)

11. S. Dhakad, N. Sharma, C. Periasamy, N. Chaturvedi, Optimization of ohmic contacts on thick and thin AlGaN/GaN HEMTs structures. Superlattices Microstruct. **111**, 922–926 (2017)

12. N. Remesh, H. Chandrasekar, A. Venugopalrao, S. Raghavan, M. Rangarajan, D.N. Nath, Re-engineering transition layers in AlGaN/GaN HEMT on Si for high voltage applications. J. Appl. Phys. **130**(7), 075702 (2021)

13. A.K. Visvkarma, K. Sehra, R. Laishram, D. Rawal, M. Saxena, Advances in DC/RF performance of AlGaN/GaN MIS-HEMT by incorporating dual metal gate architecture. IETE Tech. Rev. 1–9 (2020)

14. F. Heinz, F. Thome, A. Leuther, O. Ambacher, A 50-nm gate-length metamorphic HEMT technology optimized for cryogenic ultra-low-noise operation. IEEE Trans. Microwave

Theory Tech. (2021)

15. Y. Wu, W. Zhang, J. Zhang, S. Zhao, J. Luo, X. Tan, W. Mao, C. Zhang, Y. Zhang, K. Cheng, et al., Au-free Al0.4Ga0.6N/Al0.1G0.9N HEMTs on silicon substrate with high reverse blocking voltage of 2 kv. IEEE Trans. Electron Devices **68**(9), 4543–4549 (2021)

16. J. Lu, J.T. Chen, M. Dahlqvist, R. Kabouche, F. Medjdoub, J. Rosen, O. Kordina, L. Hultman, Transmorphic epitaxial growth of AlN nucleation layers on SiC substrates for high-breakdown thin GaN transistors. Appl. Phys. Lett. **115**(22), 221601 (2019)

17. J.T. Chen, J. Bergsten, J. Lu, E. Janz´en, M. Thorsell, L. Hultman, N. Rorsman, O. Kordina, A GaN–SiC hybrid material for high-frequency and power electronics. Appl. Phys. Lett. **113** (4), 041605 (2018)

18. J.H. Lee, K.S. Im, Growth of high quality GaN on Si (111) substrate by using two-step growth method for vertical power devices application. Curr. Comput. Aided Drug Des. **11**(3), 234 (2021)

19. Y. Feng, H. Sun, X. Yang, K. Liu, J. Zhang, J. Shen, D. Liu, Z. Cai, F. Xu, N. Tang et al., High quality GaN-on-SiC with low thermal boundary resistance by employing an ultrathin AlGaN buffer layer. Appl. Phys. Lett. **118**(5), 052104 (2021)

20. A. Dadgar, F. Schulze, M. Wienecke, A. Gadanecz, J. Bl¨asing, P. Veit, T. Hempel, A. Diez, J. Christen, A. Krost, Epitaxy of GaN on silicon—impact of symmetry and surface reconstruction. New J. Phys. **9** (10), 389 (2007)

21. A. Dadgar, T. Hempel, J. Bl¨asing, O. Schulz, S. Fritze, J. Christen, A. Krost, Improving GaN-on-silicon properties for GaN device epitaxy. Phys. Status Solidi C **8** (5), 1503–1508 (2011)

22. J. Jeong, Y. Jang, J. Kim, S. Kim, W. Kim, Design of W-band GaN-on-silicon power amplifier using low impedance lines. Appl. Sci. **11**(19), 9017 (2021)

23. Y. Wang, X. Lin, A high power X-band GaN solid-state power amplifier with 55% PAE, in *2021 9th International Symposium on Next Generation Electronics (ISNE)*. IEEE (2021), pp. 1–3

24. H. Xie, Z. Liu, Y. Gao, K.E. Lee, G.I. Ng, 100 nm T-gate GaN-on-Si HEMTs fabricated with CMOS-compatible metallization for microwave and mm-wave applications, in *2021 5th IEEE Electron Devices Technology & Manufacturing Conference (EDTM)*, IEEE (2021), pp. 1–3

25. S. Warnock, C.L. Chen, J. Knechtl, R. Molnar, et al., InAlN/GaN-on-Si HEMT with 4.5 W/mm in a 200-mm CMOS-compatible MMIC process for 3D integration, in *2020 IEEE/MTT-S International Microwave Symposium (IMS)*. IEEE (2020), pp. 1–4

26. Z. Xu, W. Zhang, F. Xu, F. Wang, L.M. Tolbert, B.J. Blalock, Investigation of 600 V GaN HEMTs for high efficiency and high temperature applications, in *2014 IEEE Applied Power Electronics Conference and Exposition-APEC 2014*. IEEE (2014), pp. 131–136

27. S. Pearton, F. Ren, A. Zhang, G. Dang, X. Cao, K. Lee, H. Cho, B. Gila, J. Johnson, C. Monier et al., GaN electronics for high power, high temperature applications. Mater. Sci. Eng. B **82**(1–3), 227–231 (2001)

28. P. Palacios, T. Zweipfennig, A. Ottaviani, M. Saeed, C. Beckmann, M. Alomari, G. Lukens, H.

Kalisch, J. Burghartz, A. Vescan, et al., 3D Integrated 300 °C tunable RF oscillator exploiting AlGaN/GaN HEMT for high temperature applications, in *2021 IEEE MTT-S International Microwave Symposium (IMS)*. IEEE (2021), pp. 519–522

29. S.J. Pearton, R. Deist, F. Ren, L. Liu, A.Y. Polyakov, J. Kim, Review of radiation damage in GaN-based materials and devices. J. Vac. Sci. Technol. A Vac. Surf. Films **31**(5), 050801 (2013)

30. S. Pearton, F. Ren, E. Patrick, M. Law, A.Y. Polyakov, Ionizing radiation damage effects on GaN devices. ECS J. Solid State Sci. Technol. **5**(2), Q35 (2015)

31. S. Pearton, A. Aitkaliyeva, M. Xian, F. Ren, A. Khachatrian, A. Ildefonso, Z. Islam, M.A.J. Rasel, A. Haque, A. Polyakov et al., Radiation damage in wide and ultra-wide bandgap semiconductors. ECS J. Solid State Sci. Technol. **10**(5), 055008 (2021)

32. K. Sehra, V. Kumari, M. Gupta, M. Mishra, D.S. Rawal, M. Saxena, TCAD investigation of total ionizing dose (TID) effects on gallium nitride HEMTs. Silvaco's simulation standard, Silvaco Inc. **31** (1) (2021). Available at: https://silvaco.com/simulation-standard/tcad-investigation-of-total-ionizing-dose-tid-effects-on-gallium-nitride-hemts/

33. A.I. Nedelcescu, C. Carlone, A. Houdayer, H.V. Bardeleben, J.L. Cantin, S. Raymond, Radiation hardness of gallium nitride. IEEE Trans. Nucl. Sci. **49**(6), 2733–2738 (2002)

34. A.Y. Polyakov, S.J. Pearton, P. Frenzer, F. Ren, L. Liu, J. Kim, Radiation effects in GaN materials and devices. J. Mater. Chem. C **1**(5), 877–887 (2012)

35. C. Sharma, A.K. Visvkarma, R. Laishram, A. Malik, K. Narang, S. Vinayak, R. Singh, Cumulative dose γ-irradiation effects on material properties of AlGaN/GaN hetero-structures and electrical properties of HEMT devices. Semicond. Sci. Technol. **34**(6), 065024 (2019)

36. A.K. Visvkarma, C. Sharma, C. Saraswat, D. Rawal, S. Vinayak, M. Saxena, Improvement in Schottky barrier inhomogeneities of Ni/AlGaN/GaN Schottky diodes after cumulative γ-ray irradiation. Semicond. Sci. Technol. **36**(6), 065012 (2021)

37. S. Pearton, A. Haque, A. Khachatrian, A. Ildefonso, L. Chernyak, F. Ren, Opportunities in single event effects in radiation-exposed SiC and GaN power electronics. ECS J. Solid State Sci. Technol. **10**(7), 075004 (2021)

38. D.S. Kim, J.G. Kim, J.H. Lee, Y.S. Hwang, Y.J. Yoon, J.S. Lee, Y. Bae, J.H. Lee, Mechanism of proton-induced electrical degradation of AlGaN/GaN high electron mobility transistors. Solid-State Electron. **175**, 107957 (2021)

39. A. Khachatrian, A. Ildefonso, Z. Islam, M.A.J. Rasel, A. Haque, J. Kim, F. Ren, M. Xian, S.J. Pearton, Total dose effects and single event upsets during radiation damage of GaN and SiC. ECS Trans. **104**(7), 13 (2021)

40. S. Das, V. Kumari, K. Sehra, M. Gupta, M. Saxena, TCAD based investigation of single event transient effect in double channel AlGaN/GaN HEMT. IEEE Trans. Device Mater. Reliab. **21**(3), 416–423 (2021)

41. F. Zhang, Y. Wang, X. Wu, F. Cao, An SEB hardened AlGaN/GaN HEMT with barrier interlayer. IEEE Access **8**, 12445–12451 (2020)

42.

Zhang, J.J., Ding, P., Jin, Y.N., Meng, S.H., Zhao, X.Q., Hu, Y.F., Zhong, Y.H., Jin, Z.: A comparative study on radiation reliability of composite channel InP high electron mobility transistors. Chinese Physics B (2021)

43. Q. Yongle, W. Denggui, Z. Jianjun, K. Zhang, K. Yuechan, W. Suzhen, T. Chen, Effect of X-ray irradiation on threshold voltage of AlGaN/GaN HEMTs with p-GaN and MIS gates. Nanotechnol. Precis. Eng. **3**(241), 241–243 (2020)

44. S. Raut, K. Sehra, M. Mishra, D. Rawal, M. Gupta, M. Saxena, Proton irradiation effects on buffer-free gallium nitride on silicon carbide high electron mobility transistor-based radio frequency power amplifier. Semicond. Sci. Technol. **36**(4), 045019 (2021)

45. D.Y. Chen, A. Malmros, M. Thorsell, H. Hjelmgren, O. Kordina, J.T. Chen, N. Rorsman, Microwave performance of 'buffer-free'GaN-on-SiC high electron mobility transistors. IEEE Electron Device Lett. **41**(6), 828–831 (2020)

46. S.W. Tang, P.Y. Yao, D.S. Chao, T.L. Wu, H.M. Hsu, Stability of wireless power transfer using gamma-ray irradiated GaN power HEMTs. Microelectron. Reliab. 114425 (2021)

47. K. Sehra, V. Kumari, M. Gupta, M. Mishra, D. Rawal, M. Saxena, Degradation mechanisms in a proton irradiated HEMT with 3DEG conduction and 3DHG as a back barrier, in *2021 IEEE 21st International Conference on Nanotechnology (NANO)*. IEEE (2021), pp. 173–176

48. K. Sehra, V. Kumari, M. Gupta, M. Mishra, D. Rawal, M. Saxena, Impact of heavy ion particle strike induced single event transients on conventional and π-gate AlGaN/GaN HEMTs. Semicond. Sci. Technol. **36**(3), 035009 (2021)

49. M. Asif Khan, A. Bhattarai, J. Kuznia, D. Olson, High electron mobility transistor based on a GaN-Al*x*Ga1−*x*N heterojunction. Appl. Phys. Lett. **63**(9), 1214–1215 (1993)

50. A. Watanabe, K. Fujimoto, M. Oda, T. Nakatsuka, A. Tamura, Rapid degradation of WSi self-aligned gate GaAs MESFET by hot carrier effect, in *30th Annual Proceedings Reliability Physics 1992*. IEEE (1992), pp. 127–130

51. C. Tedesco, C. Canali, F. Magistrali, A. Paccagnella, E. Zanoni, Hot-electron induced degradation in AlGaAs/GaAs HEMTs. Microelectron. Eng. **19**(1–4), 405–408 (1992)

52. G. Meneghesso, G. Verzellesi, F. Danesin, F. Rampazzo, F. Zanon, A. Tazzoli, M. Meneghini, E. Zanoni, Reliability of GaN high-electron-mobility transistors: State of the art and perspectives. IEEE Trans. Device Mater. Reliab. **8**(2), 332–343 (2008)

53. M. Micovic, D. Brown, D. Regan, J. Wong, Y. Tang, F. Herrault, D. Santos, S. Burnham, J. Tai, E. Prophet, et al., High frequency GaN HEMTs for RF MMIC applications, in *2016 IEEE International Electron Devices Meeting (IEDM)*. IEEE (2016), pp. 3–3

54. A. Hassan, M. Ali, A. Trigui, Y. Savaria, M. Sawan, A GaN-based wireless monitoring system for high-temperature applications. Sensors **19**(8), 1785 (2019)

55. H.B. Jo, S.W. Yun, J.G. Kim, D.Y. Yun, I.G. Lee, D.H. Kim, T.W. Kim, S.K. Kim, J. Yun, T. Kim, et al., Lg = 19 nm In0.8Ga0.2As composite-channel HEMTs with fT = 738 GHz and fmax= 492 GHz, in *2020 IEEE International Electron Devices Meeting (IEDM)*. IEEE (2020), pp. 8–4

56.

J.S. Moon, B. Grabar, J. Wong, D. Chuong, E. Arkun, D.V. Morales, P. Chen, C. Malek, D. Fanning, N. Venkatesan et al., Power scaling of graded-channel GaN HEMTs with mini-field-plate T-gate and 156 GHz f*T*. IEEE Electron Device Lett. **42**(6), 796–799 (2021)

57. T. Iwamoto, S. Akiyama, K. Horio, Passivation-layer thickness and field-plate optimization to obtain high breakdown voltage in AlGaN/GaN HEMTs with short gate-to-drain distance. Microelectron. Reliab. **121**, 114153 (2021)

58. E. Zanoni, M. Meneghini, G. Meneghesso, F. Rampazzo, D. Marcon, V.G. Zhan, F. Chiocchetta, A. Graff, F. Altmann, M. Simon-Najasek, et al., Reliability physics of GaN HEMT microwave devices: The age of scaling, in *2020 IEEE International Reliability Physics Symposium (IRPS)*. IEEE (2020), pp. 1–10

59. A. Minetto, N. Modolo, M. Meneghini, E. Zanoni, L. Sayadi, S. Sicre, B. Deutschmann, O. Haberlen, Hot electron effects in AlGaN/GaN HEMTs during hard-switching events. Microelectron. Reliabil. 114208 (2021)

60. M. Meneghini, N. Ronchi, A. Stocco, G. Meneghesso, U.K. Mishra, Y. Pei, E. Zanoni, Investigation of trapping and hot-electron effects in GaN HEMTs by means of a combined electrooptical method. IEEE Trans. Electron Devices **58**(9), 2996–3003 (2011)

61. J.A. del Alamo, J. Joh, GaN HEMT reliability. Microelectron. Reliabil. **49**(9–11), 1200–1206 (2009)

62. M. Ruzzarin, M. Meneghini, I. Rossetto, M. Van Hove, S. Stoffels, T.L. Wu, S. Decoutere, G. Meneghesso, E. Zanoni, Evidence of hot-electron degradation in GaN-based MIS-HEMTs submitted to high temperature constant source current stress. IEEE Electron Device Lett. **37**(11), 1415–1417 (2016)

63. G. Meneghesso, M. Meneghini, A. Stocco, D. Bisi, C. De Santi, I. Rossetto, A. Zanandrea, F. Rampazzo, E. Zanoni, Degradation of AlGaN/GaN HEMT devices: Role of reverse-bias and hot electron stress. Microelectron. Eng. **109**, 257–261 (2013)

64. Y. Puzyrev, T. Roy, M. Beck, B. Tuttle, R. Schrimpf, D. Fleetwood, S. Pantelides, Dehydrogenation of defects and hot-electron degradation in GaN high-electron-mobility transistors. J. Appl. Phys. **109**(3), 034501 (2011)

65. Y. Puzyrev, S. Mukherjee, J. Chen, T. Roy, M. Silvestri, R.D. Schrimpf, D.M. Fleetwood, J. Singh, J.M. Hinckley, A. Paccagnella et al., Gate bias dependence of defect-mediated hot-carrier degradation in GaN HEMTs. IEEE Trans. Electron Devices **61**(5), 1316–1320 (2014)

66. Silvaco Victory TCAD Tool Ver. 1.12.1.R. Available at: https://www.silvaco.com

67. A.D.L. Rey, J.D. Albrecht, M. Saraniti, A *Π*—shaped gate design for reducing hot-electron generation in GaN HEMTs. IEEE Trans. Electron Devices **65**(10), 4263–4270 (2018)

68. K. Sehra, V. Kumari, V. Nath, M. Gupta, D. Rawal, M. Saxena, Comparison of linearity and intermodulation distortion metrics for T-and Pi-gate HEMT, in *2019 International Conference on Electrical, Electronics and Computer Engineering (UPCON)*. IEEE (2019), pp. 1–6

69. K. Sehra, V. Kumari, V. Nath, M. Gupta, M. Saxena, Optimization of asymmetric π gate HEMT

for improved reliability and frequency applications, in *2019 IEEE 9th International Nanoelectronics Conferences (INEC)*. IEEE (2019), pp. 1–4

70. A. Van der Ziel, E. Wu, Thermal noise in high electron mobility transistors. Solid-State Electron. **26**(5), 383–384 (1983)

71. A. Dasgupta, S. Khandelwal, Y.S. Chauhan, Surface potential based modeling of thermal noise for HEMT circuit simulation. IEEE Microwave Wirel. Compon. Lett. **25**(6), 376–378 (2015)

72. Y. Chen, K. Peng, Z. Cui, Fabrication of ultra-short T gates by a two—step electron beam lithography process. Microelectron. Eng. **73**, 662–665 (2004)

73. J.M. Tirado, J.L. Sanchez-Rojas, J.I. Izpura, Trapping effects in the transient response of AlGaN/GaN HEMT devices. IEEE Trans. Electron Devices **54**(3), 410–417 (2007)

74. S. Gustafsson, J.T. Chen, J. Bergsten, U. Forsberg, M. Thorsell, E. Janz´en, N. Rorsman, Dispersive effects in microwave AlGaN/AlN/GaN HEMTs with carbon-doped buffer. IEEE Trans. Electron Devices **62** (7), 2162–2169 (2015)

75. K. Sehra, V. Kumari, M. Gupta, M. Mishra, D. Rawal, M. Saxena, TCAD investigation of gate-lag measurements on conventional and π-gate AlGaN/GaN HEMTs, in *2020 IEEE 20th International Conference on Nanotechnology (IEEE- NANO)*. IEEE (2020), pp. 128–133

76. B.M. Green, K.K. Chu, E.M. Chumbes, J.A. Smart, J.R. Shealy, L.F. Eastman, The effect of surface passivation on the microwave characteristics of undoped AlGaN/GaN HEMTs. IEEE Electron Device Lett. **21**(6), 268–270 (2000)

77. Y.F. Wu, A. Saxler, M. Moore, R. Smith, S. Sheppard, P. Chavarkar, T. Wisleder, U. Mishra, P. Parikh, 30-W/mm GaN HEMTs by field plate optimization. IEEE Electron Device Lett. **25**(3), 117–119 (2004)

78. M.J. Uren, D. Hayes, R. Balmer, D. Wallis, K. Hilton, J. Maclean, T. Martin, C. Roff, P. McGovern, J. Benedikt, et al., Control of short-channel effects in GaN/AlGaN HFETs, in *2006 European Microwave Integrated Circuits Conference*. IEEE (2006), pp. 65–68

79. M. Uren, K. Nash, R.S. Balmer, T. Martin, E. Morvan, N. Caillas, S.L. Delage, D. Ducatteau, B. Grimbert, J.C. De Jaeger, Punch-through in short—channel AlGaN/GaN HFETs. IEEE Trans. Electron Devices **53**(2), 395–398 (2006)

80. P. Klein, J. Freitas Jr., S. Binari, A. Wickenden, Observation of deep traps responsible for current collapse in GaN metal–semiconductor field-effect transistors. Appl. Phys. Lett. **75**(25), 4016–4018 (1999)

81. S. Heikman, S. Keller, T. Mates, S. DenBaars, U. Mishra, Growth and characteristics of Fe-doped GaN. J. Cryst. Growth **248**, 513–517 (2003)

82. Z. Bougrioua, M. Azize, P. Lorenzini, M. Lau¨gt, H. Haas, Some benefits of Fe doped less dislocated GaN templates for AlGaN/GaN HEMTs grown by MOVPE. Physica Status Solidi (a) **202** (4), 536–544 (2005)

83. A. Corrion, F. Wu, T. Mates, C. Gallinat, C. Poblenz, J. Speck, Growth of Fe-doped GaN by RF plasma-assisted molecular beam epitaxy. J. Cryst. Growth **289**(2), 587–595 (2006)

84. W. Lee, J.H. Ryou, D. Yoo, J. Limb, R. Dupuis, D. Hanser, E. Preble, N. Williams, K. Evans, Optimization of Fe doping at the regrowth interface of GaN for applications to III-nitride-based heterostructure field-effect transistors. Appl. Phys. Lett. **90**(9), 093509 (2007)

85. C. Poblenz, P. Waltereit, S. Rajan, S. Heikman, U. Mishra, J. Speck, Effect of carbon doping on buffer leakage in AlGaN/GaN high electron mobility transistors. J. Vac. Sci. Technol. B: Microelectron. Nanometer Struct. Process. Measur. Phenom. **22**(3), 1145–1149 (2004)

86. S. Haffouz, H. Tang, J. Bardwell, E. Hsu, J. Webb, S. Rolfe, AlGaN/GaN field effect transistors with C-doped GaN buffer layer as an electrical isolation template grown by molecular beam epitaxy. Solid-State Electron. **49**(5), 802–807 (2005)

87. J. Bergsten, M. Thorsell, D. Adolph, J.T. Chen, O. Kordina, E.Ö. Sveinbjörnsson, N. Rorsman, Electron trapping in extended defects in microwave AlGaN/GaN HEMTs with carbon-doped buffers. IEEE Trans. Electron Devices **65** (6), 2446–2453 (2018)

88. S. Heikman, S. Keller, S.P. DenBaars, U.K. Mishra, Growth of Fe doped semi-insulating GaN by metalorganic chemical vapor deposition. Appl. Phys. Lett. **81**(3), 439–441 (2002)

89. E. Bahat-Treidel, F. Brunner, O. Hilt, E. Cho, J. Wurfl, G. Trankle, AlGaN/GaN/GaN: C back-barrier HFETs with breakdown voltage of over 1 kV and low $R_{\mathrm{ON}} \times A$. IEEE Trans. Electron Devices **57**(11), 3050–3058 (2010)

90. V. Desmaris, M. Rudzinski, N. Rorsman, P. Hageman, P. Larsen, H. Zirath, T. Rodle, H. Jos, Comparison of the DC and microwave performance of AlGaN/GaN HEMTs grown on SiC by MOCVD with Fe-doped or unintentionally doped GaN buffer layers. IEEE Trans. Electron Devices **53**(9), 2413–2417 (2006)

91. M. Meneghini, I. Rossetto, D. Bisi, A. Stocco, A. Cester, G. Meneghesso, E. Zanoni, A. Chini, A. Pantellini, C. Lanzieri, Role of buffer doping and pre-existing trap states in the current collapse and degradation of AlGaN/GaN HEMTs, in *2014 IEEE International Reliability Physics Symposium*. IEEE (2014), pp. 6C–6

92. S. Rajan, A. Chakraborty, U.K. Mishra, C. Poblenz, P. Waltereit, J.S. Speck, MBE-grown AIGaN/GaN HEMTs on SiC, in *High Performance Devices* (World Scientific, 2005), pp. 108–113

93. S. Mathis, A. Romanov, L. Chen, G. Beltz, W. Pompe, J. Speck, Modeling of threading dislocation reduction in growing GaN layers. J. Cryst. Growth **231**(3), 371–390 (2001)

94. J.P. Ao, T. Wang, D. Kikuta, Y.H. Liu, S. Sakai, Y. Ohno, AlGaN/GaN high electron mobility transistor with thin buffer layers. Jpn. J. Appl. Phys. **42**(4R), 1588 (2003)

95. P. Herfurth, D. Maier, L. Lugani, J.F. Carlin, R. Rosch, Y. Men, N. Grandjean, E. Kohn, Ultrathin body InAlN/GaN HEMTs for high-temperature (600 °C) electronics. IEEE Electron Device Lett. **34**(4), 496–498 (2013)

96. V. Zajic, P. Thieberger, Heavy ion linear energy transfer measurements during single event upset testing of electronic devices. IEEE Trans. Nucl. Sci. **46**(1), 59–69 (1999)

97. M. Zerarka, P. Austin, A. Bensoussan, F. Morancho, A. Durier, TCAD simulation of the single

event effects in normally-OFF GaN transistors after heavy ion radiation. IEEE Trans. Nucl. Sci. **64**(8), 2242–2249 (2017)

98. M. Zerarka, O. Crepel, Radiation robustness of normally-off GaN/HEMT power transistors (COTS). Microelectron. Reliab. **88**, 984–991 (2018)

99. T.R. Weatherford, Radiation effects in high speed III–V integrated circuits. Int. J. High Speed Electron. Syst. **13**(01), 277–292 (2003)

100. A.Y. Polyakov, S. Pearton, P. Frenzer, F. Ren, L. Liu, J. Kim, Radiation effects in GaN materials and devices. J. Mater. Chem. C **1**(5), 877–887 (2013)

101. B. Chatterjee, D. Shoemaker, Y. Song, T. Shi, H.L. Huang, D. Keum, A. Krishnan, B.M. Foley, I. Jovanovic, J. Hwang et al., Cumulative impacts of proton irradiation on the self-heating of AlGaN/GaN HEMTs. ACS Appl. Electron. Mater. **2**(4), 980–991 (2020)

102. J.F. Ziegler, M.D. Ziegler, J.P. Biersack, SRIM–The stopping and range of ions in matter (2010). Nucl. Instrum. Methods Phys. Res. Sect. B **268**(11–12), 1818–1823 (2010)

103. H. Sasaki, T. Hisaka, K. Kadoiwa, T. Oku, S. Onoda, T. Ohshima, E. Taguchi, H. Yasuda, Ultra-high voltage electron microscopy investigation of irradiation induced displacement defects on AlGaN/GaN HEMTs. Microelectron. Reliab. **81**, 312–319 (2018)

104. S. Mateos-Angulo, R. Rodr´ıguez, J. Del Pino, B. Gonz´alez, S. Khemchandani, Single event effects analysis and charge collection mechanisms on AlGaN/GaN HEMTs. Semicond. Sci. Technol. **34** (3), 035029 (2019)

105. M. Rostewitz, K. Hirche, J. L¨atti, E. Jutzi, Single event effect analysis on DC and RF operated AlGaN/GaN HEMTs. IEEE Trans. Nuclear Sci. **60** (4), 2525–2529 (2013)

106. A. Bensoussan, R. Marec, J. Muraro, L. Portal, P. Calvel, C. Barillot, M. Perichaud, L. Marchand, G. Vignon, GaAs P-HEMT MMIC processes behavior under multiple heavy ion radiation stress conditions combined with DC and RF biasing. Microelectron. Reliab. **53**(9–11), 1466–1470 (2013)

107. S. Kuboyama, A. Maru, H. Shindou, N. Ikeda, T. Hirao, H. Abe, T. Tamura, Single-event damages caused by heavy ions observed in AlGaN/GaN HEMTs. IEEE Trans. Nucl. Sci. **58**(6), 2734–2738 (2011)

108. B.D. Olson, J.D. Ingalls, C.H. Rice, C.C. Hedge, P.L. Cole, A.R. Duncan, S.E. Armstrong, Leakage current degradation of gallium nitride transistors due to heavy ion tests, in *2015 IEEE Radiation Effects Data Workshop (REDW)*. IEEE (2015), pp. 1–10

109. S. Onoda, A. Hasuike, Y. Nabeshima, H. Sasaki, K. Yajima, S. Sato, T. Ohshima, Enhanced charge collection by single ion strike in AlGaN/GaN HEMTs. IEEE Trans. Nuclear Sci. **60** (6), 4446–4450 (2013)

110. D. McMorrow, A.R. Knudson, J.B. Boos, D. Park, J.S. Melinger, Ionization—induced carrier transport in InAlAs/InGaAs high electron mobility transistors. IEEE Trans. Nucl. Sci. **51**(5), 2857–2864 (2004)

111. D. McMorrow, J.S. Melinger, A.R. Knudson, S. Buchner, L.H. Tran, A. Campbell, W. Curtice,

Charge-enhancement mechanisms of GaAs field-effect transistors: Experiment and simulation, in *RADECS 97. Fourth European Conference on Radiation and its Effects on Components and Systems (Cat. No. 97TH8294)*. IEEE (1997), pp. 346–352

112. X. Hu, A.P. Karmarkar, B. Jun, D.M. Fleetwood, R.D. Schrimpf, R.D. Geil, R.A. Weller, B.D. White, M. Bataiev, L.J. Brillson et al., Proton-irradiation effects on AlGaN/AlN/GaN high electron mobility transistors. IEEE Trans. Nucl. Sci. **50**(6), 1791–1796 (2003)

113. J.M. Osheroff, J.M. Lauenstein, R.L. Ladbury, LET and range characteristics of proton recoil ions in gallium nitride (GaN). IEEE Trans. Nucl. Sci. **68**(5), 597–602 (2021)

114. D.M. Keum, H.Y. Cha, H. Kim, Proton bombardment effects on normally—off AlGaN/GaN-on-Si recessed MIS heterostructure FETs. IEEE Trans. Nucl. Sci. **62**(6), 3362–3368 (2015)

115. S. Yue, Z. Lei, C. Peng, X. Zhong, J. Wang, Z. Zhang, Y. En, Y. Wang, L. Hu, High-fluence proton-induced degradation on AlGaN/GaN high-electron—Mobility transistors. IEEE Trans. Nucl. Sci. **67**(7), 1339–1344 (2020)

116. N.E. Ives, J. Chen, A.F. Witulski, R.D. Schrimpf, D.M. Fleetwood, R.W. Bruce, M.W. McCurdy, E.X. Zhang, L.W. Massengill, Effects of proton—Induced displacement damage on gallium nitride HEMTs in RF power amplifier applications. IEEE Trans. Nucl. Sci. **62**(6), 2417–2422 (2015)

117. S.R. Messenger, E.A. Burke, M.A. Xapsos, G.P. Summers, R.J. Walters, I. Jun, T. Jordan, NIEL for heavy ions: An analytical approach. IEEE Trans. Nucl. Sci. **50**(6), 1919–1923 (2003)

118. J. Srour, J. Palko, A framework for understanding displacement damage mechanisms in irradiated silicon devices. IEEE Trans. Nucl. Sci. **53**(6), 3610–3620 (2006)

119. X. Hu, B.K. Choi, H.J. Barnaby, D.M. Fleetwood, R.D. Schrimpf, S. Lee, S. Shojah-Ardalan, R. Wilkins, U.K. Mishra, R.W. Dettmer, The energy dependence of proton-induced degradation in AlGaN/GaN high electron mobility transistors. IEEE Trans. Nucl. Sci. **51**(2), 293–297 (2004)

120. A.P. Karmarkar, B. Jun, D.M. Fleetwood, R.D. Schrimpf, R.A. Weller, B.D. White, L.J. Brillson, U.K. Mishra, Proton irradiation effects on GaN-based high electron-mobility transistors with Si-doped Al/sub x/Ga/sub 1–x/N and thick GaN cap layers. IEEE Trans. Nucl. Sci. **51**(6), 3801–3806 (2004)

121. Keysight ADS (2021). Available at: www.keysight.com

122. S. Khandelwal, Y.S. Chauhan, T.A. Fjeldly, S. Ghosh, A. Pampori, D. Mahajan, R. Dangi, S.A. Ahsan, ASM GaN: Industry standard model for GaN RF and power devices—Part 1: DC, CV, and RF model. IEEE Trans. Electron Devices **66**(1), 80–86 (2018)

T. R. Lenka, H. P. T. Nguyen (eds.), *HEMT Technology and Applications*, Springer Tracts in Electrical and Electronics Engineering
https://doi.org/10.1007/978-981-19-2165-0_14

Evolution and Present State-of-Art Gallium Oxide HEMTs–*The Key Takeaways*

Rajan Singh[1] ✉, Trupti Ranjan Lenka[1] ✉ and Hieu Pham Trung Nguyen[2] ✉

(1) Microelectronics and VLSI Design Group, Department of Electronics and Communication Engineering, National Institute of Technology Silchar, Silchar, Assam, 788010, India
(2) Department of Electrical and Computer Engineering, New Jersey Institute of Technology, Newark, New Jersey 07102, USA

✉ **Rajan Singh (Corresponding author)**
Email: rajan_rs@ece.nits.ac.in

✉ **Trupti Ranjan Lenka**
Email: trlenka@ieee.org

✉ **Hieu Pham Trung Nguyen**
Email: hieu.p.nguyen@njit.edu

Abstract

On the back of the large energy bandgap, ultrawide bandgap (UWBG) materials have shown superior figures of merit for device performance in high-power and high-frequency applications. Among emerging UWBG semiconductors of interest, gallium oxide (Ga_2O_3) has a distinctive advantage over its peers mainly due to the availability of high-quality bulk crystals grown using cost-effective melt-based techniques. Furthermore, bandgap energy of ~5 eV makes Ga_2O_3 highly

suitable for high-voltage devices. Related to high-speed device technologies, high-electron-mobility-transistors (HEMTs) have shown capabilities beyond existing lightly doped metal–oxide–semiconductor (LDMOS) for high-power applications, and GaN-based power devices ~600 V are currently commercially available. However, emerging areas like charging stations for electric vehicles (EVs) and electric power trains demand ultra-high-power switching >1 kW. Going by what Ga_2O_3 promises, it can be considered as a viable candidate for these emerging as well as existing power electronics areas. Large bandgap-led high critical field of β-Ga_2O_3 ensures superior performance in high voltage rectifiers and E-mode MOSFETs over GaN and SiC. Furthermore, β-Ga_2O_3 HEMTs also outperform GaN HEMTs in terms of X-band RF output power. However, low electron mobility coupled with poor thermal conductivity of β-Ga_2O_3 limits its dc power switching performance and demand device level thermal management. In this paper, we present the evolution of β-Ga_2O_3 HEMTs and overview the high power RF and dc switching performance of the latest reported β-$(Al_xGa_{1-x})_2O_3$/β-Ga_2O_3 MODFETs and AlN/β-Ga_2O_3 HEMTs. These results have been discussed to gauge the capabilities of β-Ga_2O_3 technology and potential applications in RF and high power electronics applications.

Keywords Gallium oxide (Ga_2O_3) – β-$(Al_xGa_{1-x})_2O_3$/β-Ga_2O_3 MODFETs – AlN/β-Ga_2O_3 HEMTs – High-power – Heterostructure – Power switch – Ultrawide bandgap (UWBG) semiconductors

1 Introduction

The lifecycle of a particular semiconductor material technology generally goes through key phases: evolution, growth, and maturity. Since the invention of the Si- and Ge-based transistors in 1947, the latter half of the twentieth century in the microelectronics industry was focused on Si material technology. Going forward through the development and growth phases, material physical limits finally overweigh over the devices' performance, especially for high-voltage and high-power applications. Another breakthrough in the electronics

industry was the growth of AlGaAs/GaAs heterojunctions for high-speed electronics. This device technology allowed band-gap engineering which further facilitated charge accumulation in the form of two-dimensional electron gas (2DEG) and enabled the first AlGaAs/GaAs high-electron-mobility transistors (HEMTs). This further pushed the interest in wide bandgap (WBG) semiconductors like GaN and SiC for power device applications. Over the last decades, both GaN and SiC technologies have also seen their growth and development cycle, and are currently in the final development stage for commercial use [1]. It also looks like these existing technologies have hit their performance peak and extended their life cycle.

During the last few years, ultra-wide bandgap (UWBG) semiconductors like the diamond, high-Al AlGaN, AlN, and Ga_2O_3 have garnered a lot of attention based on theoretical characteristics such as high-voltage operation, large blocking voltage, high-temperature suitability, and fast-switching. Furthermore, due to the higher bandgap of UWBG over WBG semiconductors, several figures-of-merit (FOM) for device performance already indicated superior performance related to UWBG materials [2]. Among these emerging UWBG semiconductors, researchers are giving more favor to Ga_2O_3 mainly due to its attractive material properties for power electronic applications. Moreover, the availability of high-quality single-crystal substrates is like icing on the cake. Surprisingly, these Ga_2O_3 bulk-crystals are generally grown using melt-based crystal-growth techniques, hence cost is expected to be competitive if not lower than existing GaN technology [3]. Moreover, as Ga_2O_3 substrates size increases, a further drop in the price is predicted, which would make Ga_2O_3 devices even more competitive and viable for power electronics. In Table 1, we summarize key physical properties of the main UWBG (AlN, Ga_2O_3, and Diamond) and WBG (GaN, SiC) materials along with important metrics for device applications. These matrices include substrate quality accessed based on dislocation density and substrate diameter, and doping capabilities (both n- and p-type) [2]. Others include critical electrical field E_C for high-voltage operations, electron mobility μ_n for high-speed, and thermal conductivity for high-temperature operations. As it is evident, each one of these UWBG materials presently has its point of concern in at least

one of the various matrices. For example, to date, Ga_2O_3 has shown poor p-type conductivity mainly due to the large effective mass of holes and very low thermal conductivity necessitates device-level thermal management for Ga_2O_3 devices. On the other hand, diamond, having best-in-class thermal conductivity and electron mobility, but, suffers from poor-quality small-size substrates.

Table 1 Material properties and important technological metrics for device applications of the selected UWBG and WBG semiconductor materials [2]

Properties	**UWBG**			**WBG**	
	***β*-Ga2O3**	**AlN**	**Diamond**	**4H-SiC**	**GaN**
Energy bandgap (eV)	4.9	6.2	5.5	3.26	3.4
Critical Electric Field (MV/cm)	8	12	10	2.2	3.2
Relative dielectric constant	10	10	5.7	9.7	9
Electron mobility (cm^2/V. s)	140	310	4500	900	1150
Saturation velocity (×107 cm/s)	1.5	1.5	1.5	2.2	1.5
Substrate quality (dislocation cm−2)	≈104	≈104	≈105	≈102	≈104
Substrate diameter (inches)	4	2	1	8	8 (on Si)
Doping capability (*n*-/*p*-type)	Good/No	Moderate/Poor	Moderate/Good	Good/Good	Good/Good
Thermal conductivity (W/m. K)	11–27	250–310	2200–3500	370	253

Based on the properties given above, various Figures-of-merit (FOM) are calculated to envisage the performance capabilities of these semiconductor materials. As can be seen from Table 2, some FOM values increase nonlinearly with rising energy bandgap from WBG to UWBG semiconductors. It is worth noting that, out of five crystals of Ga_2O_3, the monoclinic *β*-phase is most stable at room temperature, and is most widely explored and widely reported. Here, also, we have

focused on β-Ga_2O_3 polymorph, its material properties, and β-Ga_2O_3-based devices especially HEMTs.

Table 2 Different FOMs for power device applications based on β-Ga_2O_3, GaN, and 4H-SiC material technology at room temperature (300 K)

Figures-of-merit	**Si**	**4H-SiC**	**GaN**	**β-Ga_2O_3**
Baliga's FOM ($\mu n.\varepsilon r.Ec3$)	1	216	649	1665
Johnson's FOM ($Ec.vs/2\pi$)	1	7	6.9	17.3
Baliga High Frequency's FOM ($\mu.Ec2$)	1	36	97.3	74
Keyes' FOM ($\lambda.c.vs/4\pi.\varepsilon r$)	1	4.63	0.709	0.009

FOM values are normalized with those for Silicon. *Note:* For Si material, E_g = 1.12 eV, μ_n = 1350 cm^2/Vs, ε_r = 11.7, $v_s = 2.3 \times 10^7$ cm/s, E_C = 0.3 MV/cm, and λ = 1.48 W/cmK resulted to BFOM = 4305×10^{17} V^2/cm.s, JFOM = 1.1×10^{12} V/s, BHFFOM = 121 V/cm.s, KFOM = 1.17×10^{15} W/deg.s

So, as per various FOMs: Baliga's FOM predicting DC conduction losses and Johnson's FOM (JFOM) showing suitability for RF amplification, it can be said that β-Ga_2O_3 has enough potential for high-voltage, as well as, for low power switching in a high-frequency regime. On the other hand, FOM which takes thermal conductivity in its calculation shows poor performance of β-Ga_2O_3 devices, as shown by Keyes' FOM. Additionally, being an emerging material technology, various known as well as unknown challenges exist for Ga_2O_3 also, and would need required interest from potential organizations like defense and military institutions for enormous research and sustained funding. Here, we will give an outlook on the evolution of Ga_2O_3 HEMTs in the context of its suitability for existing power-electronic applications which are currently inaccessible with existing GaN/SiC technologies, and for emerging areas like electric vehicles (EVs) and associated infrastructure, robotics, and sensors.

As far as β-Ga_2O_3 devices are concerned, various power devices like Schottky diodes [4–7], FETs, MESFETs, MOSFETs (both enhancement- and depletion-mode) [8–13], and MODFETs/HEMTs [14–18] with

superior DC and RF performance have been already reported. Regarding β-Ga_2O_3 HEMTs, the majority of the work reported to date focused on the development of growing ternary alloys to make β-$(Al_xGa_{1-x})_2O_3$/β-Ga_2O_3 heterostructures. While these heterostructures showed good DC and RF performance, looking at the β-Ga_2O_3 material properties and indications of different FOMs, further improvement could be possible. Also, these results do not match with the existing although, rather a mature GaN technology. Some of the key issues in the β-$(Al_xGa_{1-x})_2O_3$/Ga_2O_3 heterostructures like small band bending led small band offsets and parasitic channel in the β-$(Al_xGa_{1-x})_2O_3$ barrier layer are already identified [19]. Furthermore, in absence of any polarization properties in β-Ga_2O_3, two-dimensional electron gas (2-DEG) density is also one order less than GaN HEMT counterparts. Nevertheless, like an effective and efficient use of III-nitrides (GaN, AlN, InN) in GaN technology, the same can also be explored for β-Ga_2O_3, as successful growth of III-N (III = Al, Ga)/β-Ga_2O_3 heterostructures are already reported.

In the following section, we discuss briefly the achievements and issues of the β-$(Al_xGa_{1-x})_2$/Ga_2O_3 heterostructures reported to date. The next section reviews the major developments reported for the evolution of the III-nitrides (AlN, GaN, InN)/β-Ga_2O_3 heterostructures focusing on the growing technology and band offset measurements. Then, the performance of the latest (AlN, GaN)/β-Ga_2O_3 HEMTs is discussed, followed by conclusions.

---

2 β-$(Al_xGa_{1-x})_2O_3$/β-Ga_2O_3 Heterostructures

In the year 2009, successful demonstration of molecular beam epitaxy (MBE) technology for the growth of homoepitaxial β-Ga_2O_3 films facilitated the growth of ternary alloys β-(Al, Ga)$_2O_3$ and β-(In, Ga)$_2O_3$ and bandgap engineering in resulting heterostructures. This was the major technological breakthrough and opened new potential applications for β-Ga_2O_3. Subsequently, β-$(Al_xGa_{1-x})_2O_3$/Ga_2O_3 or β-

(AGO/GO) MODFETs were developed which resembled characteristics like band offset led charge confinement in the form of 2-DEG density, similar to the GaN HEMTs.

Figure 1 shows key technological breakthroughs in the process of growth of β-$(Al_xGa_{1-x})_2O_3/Ga_2O_3$ heterostructures. Earlier efforts to grow ternary alloys β-$(Al, Ga)_2O_3$ or β-$(In, Ga)_2O_3$ faced major challenges like solubility limit of β-Ga_2O_3 and surface morphology between binary and ternary β-Ga_2O_3 materials. Oshima et al. [20] demonstrated the first-time growth of β-$(AlGa)_2O_3$ thin films on a (010) β-Ga_2O_3 substrate using plasma-assisted MBE (PA-MBE). This type of development helped the growth of future β-(AGO/GO) heterostructures. Subsequent developments involved carrier confinement at the interface of β-(AGO/GO) heterostructures and growth of the first β-$(Al_xGa_{1-x})_2O_3/Ga_2O_3$ (AGO/GO) heterostructure by Kaun et al. [21]. However, poor available technology-led interface abruptness hampered carrier confinement at the interface. Validation of carrier confinement in heterojunction FETs (HFETs or MODFETs) was another big achievement, and demonstrated by two author groups [14, 22]. While Wong et al. [22] attributed it to the Si unintentional dopants accumulated during melt-growth of β-Ga_2O_3 substrates, Ahmadi et al. [14] used intentional doping of Ge in the AGO barrier to achieving carrier confinement at the heterointerface. In other means to achieve higher 2-DEG density, Si-delta doping was used in the β-AGO barrier, and high mobility of 180 cm^2/Vs in β-$(Al_xGa_{1-x})_2O_3/Ga_2O_3$ MODFET [16]. Recently, Tadjer et al. [18] demonstrated first-time use of ozone-MBE in the growth of β-$(Al_xGa_{1-x})_2O_3/Ga_2O_3$ HFETs and showed breakdown voltage of 900 V. Figure 2 shows schematics of the main β-$(Al_xGa_{1-x})_2O_3/Ga_2O_3$ HFETs/MODFETs demonstrated recently.

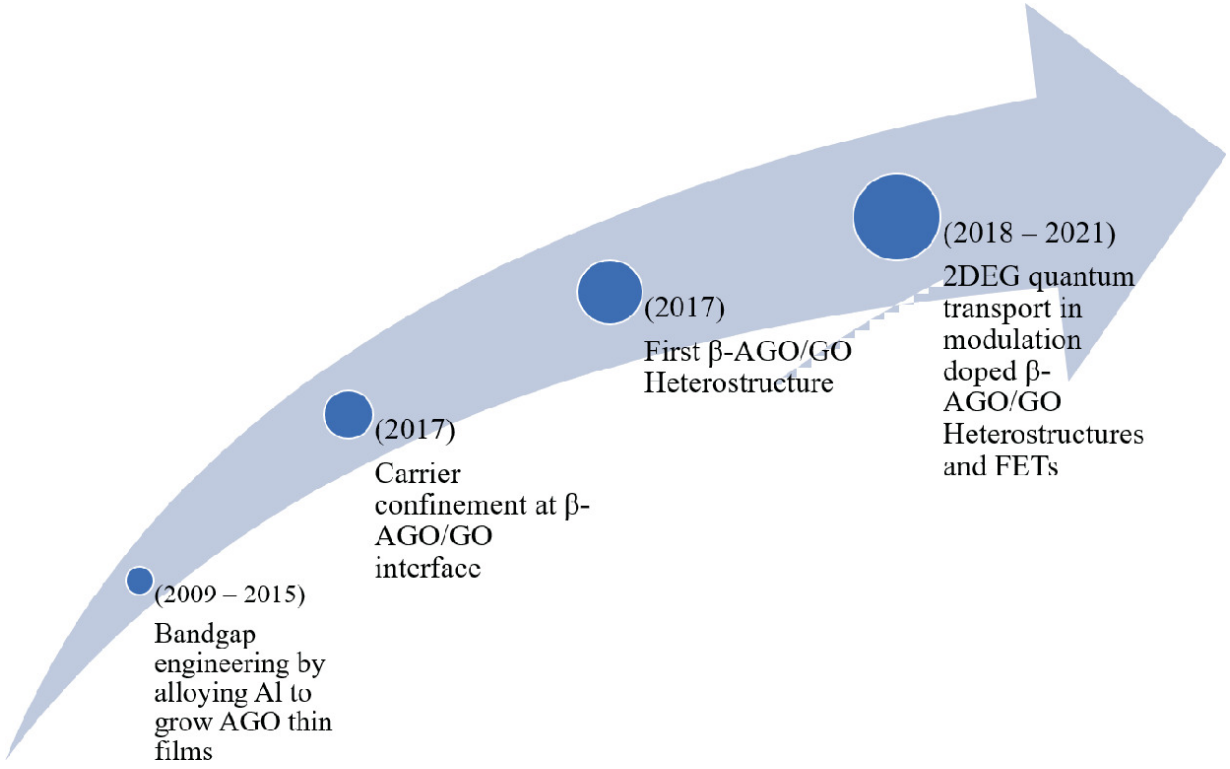

Fig. 1 Major experimental developments during realization of β-AGO/GO MODFETs/HEMTs

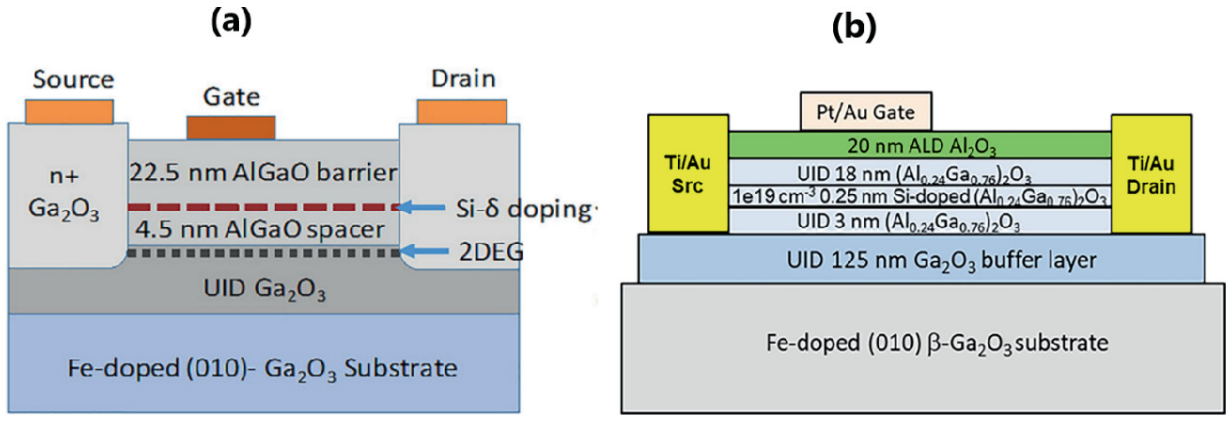

Fig. 2 Schematic epitaxial layers of Si delta-doped β-(AGO)/GO heterostructures **a** MODFET structure grown using PA-MBE method and having highly doped S/D contact regions with contact resistance as low as 4.9 Ω mm [16], **b** HFET structure grown using ozone-MBE technique [18]

In summary, β-$(Al_xGa_{1-x})_2O_3/Ga_2O_3$ HFETs/MODFETs achieved superior DC and RF performance. However, 2DEG density was limited to ~10^{12} cm^{-2} mainly due to small conduction band offset (CBO) ~0.4–0.6 eV due to the small bandgap difference between AGO and GO materials. Key parameters of two different delta-doped β-

$(Al_xGa_{1-x})_2O_3/Ga_2O_3$ heterostructure grown using plasma-assisted molecular beam epitaxy (PA-MBE) and ozone-assisted MBE (O-MBE) are shown in Fig. 3. The later device achieved higher 2DEG density on the back of more advanced MBE process technology. However, higher contact resistances limit the maximum achievable output current. It is worth noting that, these devices suffer from secondary channels formed in the barrier layer. Nevertheless, the development of AlN, GaN/β-Ga_2O_3 heterostructures has made possible bandgap engineering and higher band offsets, and higher 2DEG density is anticipated. Next, the evolution of III-nitrides/β-Ga_2O_3 heterostructure and recently reported β-Ga_2O_3-based HEMTs are discussed.

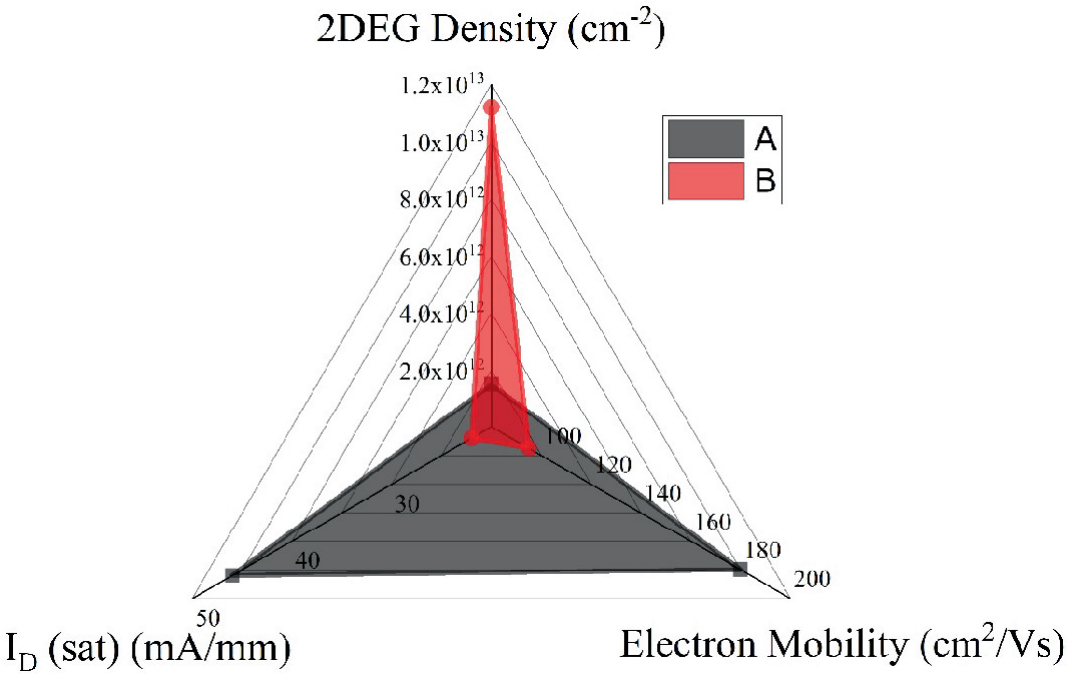

Fig. 3 Comparison of key parameters for delta-doped β-$(Al_xGa_{1-x})_2O_3/Ga_2O_3$ MODFETs grown using **a** plasma-assisted MBE, and **b** ozone-assisted MBE.

3 III-N (III = Ga, Al, In)/β-Ga_2O_3 Heterojunction

Large band offsets and higher charge density were the key motivations for developing III-nitride/β-Ga_2O_3 heterostructure. Low lattice mismatch and advanced process technology led to realize a high-quality

epitaxial layer of AlN, GaN on β-Ga_2O_3 or vice versa [23]. Since band offsets have a large impact on transport properties in heterojunction, several experimental and computational studies measuring band offsets in AlN, GaN/β-Ga_2O_3 heterostructures have been presented. Band alignments between AlN and β-Ga_2O_3 are found as type I (straddling) and type II (staggered), and conduction band offset (CBO), ΔEC in the range of 0.58–1.9 eV was reported. This variation in measurement values is attributed to different measurement methodologies and depositions techniques. Various attributes of AlN/β-Ga_2O_3 band offset measurements reported are given in Table 3.

Table 3 Band alignment values, type of alignment, and methodology to grow in AlN/β-Ga_2O_3 heterojunctions

Interfaces	CBO (eV)/type of alignment	Deposition method	Methodology	References
β-Ga_2O_3/AlN	1.75/type-II	MOCVD	Experimental	[24]
	2.43/type-II	–	Computational	[25]
AlN/β-Ga_2O_3	1.90/type-II	–		[25]
	1.39/type-I	PEALD	Experimental	[26]
	0.58/type-II	T-ALD		[26]

The development of AlN/β-Ga_2O_3 heterostructure and band offsets measurement facilitated bandgap engineering and modulation doping in potential β-Ga_2O_3 power devices. This breakthrough in β-Ga_2O_3 device technology-led various state-of-art β-Ga_2O_3 power devices including AlN/β-Ga_2O_3 HEMT and E-mode β-Ga_2O_3 MOSFET. In one of our previous works, we demonstrated novel AlN/β-Ga_2O_3 HEMT and estimated record RF output power of 2.91 W/mm in X-band [27]. Recently, Song et al. [23] demonstrated the use of p-GAN to achieve E-mode operation in AlN/β-Ga_2O_3 HEMT. The device schematic and energy band diagram at thermal equilibrium for AlN/β-Ga_2O_3 HEMT [27] are shown in Fig. 4.

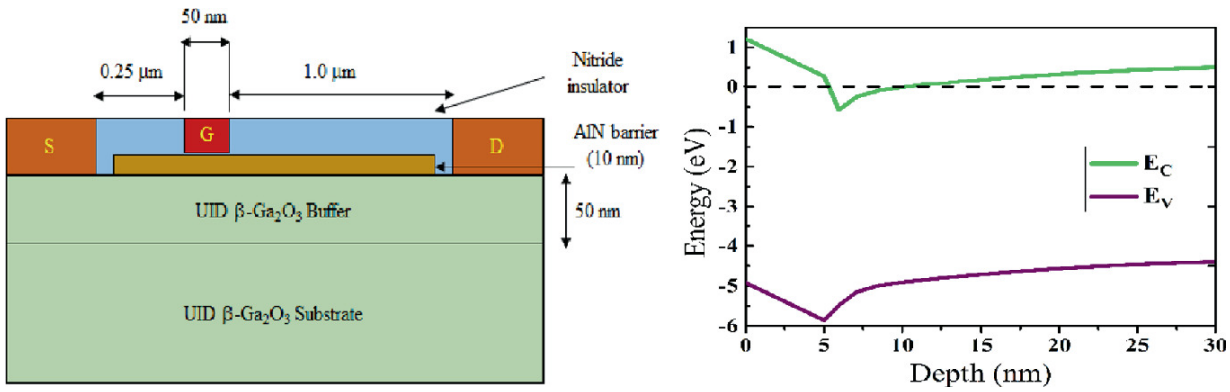

Fig. 4 Device schematic of AlN/β-Ga_2O_3 HEMT, and energy band diagram at zero bias showing band offsets at the heterostructure below the gate, figures adopted from [27]

Higher bandgap difference between AlN and β-Ga_2O_3 materials facilitated large CBO in the range of 0.65–2.5 eV, and polarization induced doping in AlN/β-Ga_2O_3 HEMTs helped to achieve 2DEG density in the range of (4.5–5.23) × 10^{13} cm^{-2}. These values were reported in [28], in which we demonstrated the effect of band parameters on conduction band offsets, and the effect on 2DEG density in AlN/β-Ga_2O_3 HEMT is estimated. Furthermore, excellent dc electrical parameters and record RF output power P_{OUT} of 2.91 W/mm at 10 GHz are estimated in AlN/β-Ga_2O_3 HEMT [27].

In summary, initial investigations of AlN/β-Ga_2O_3 HEMTs revealed their capabilities to outperform delta-doped AGO/GO MODFETs. Some of the important parameters for recently reported AlN/β-Ga_2O_3 HEMTs [23, 27] are compared in Fig. 5. Looking at this technological progress of III-nitrides/β-Ga_2O_3 heterostructure, more state-of-art β-Ga_2O_3 HEMTs with excellent dc and RF performance are expected in near future.

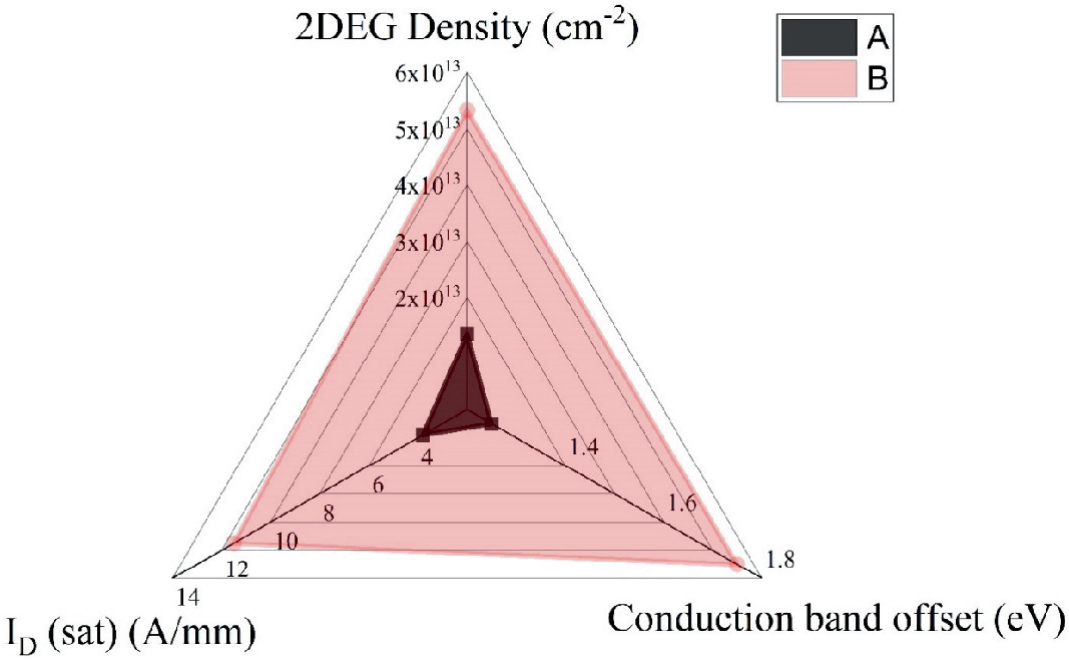

Fig. 5 Comparison of important parameters for recently reported **a** AlN/β-Ga_2O_3 polarization-induced-doped FET [23], and **b** AlN/β-Ga_2O_3 HEMT [27]

4 Conclusion

The evolution of III-nitrides/β-Ga_2O_3 heterostructures and device performance of AlN/β-Ga_2O_3 HEMTs are presented. These devices achieved superior performance over delta-doped AGO/GO MODFETs by taking advantage of the polarization-induced doping in the channel and higher charge density in the form of 2DEG. Although the experimental demonstration of III-nitrides//β-Ga_2O_3 heterostructures has shown the potential of β-Ga_2O_3 material technology, lattice mismatch led to challenges as growing high-quality epitaxial layers persist. High-quality and defect-free interfaces could be achieved by significant improvement in growth optimization to achieve III-nitrides/β-Ga_2O_3 heterostructures based high-performance transistors. Although the maximum achievable cut-off frequency in β-Ga_2O_3 HEMTs is lower than the GaN counterpart, higher RF output power is estimated for β-Ga_2O_3 HEMTs up to the X-band frequency range. Furthermore, higher 2DEG mobility in AGO/GO MODFETs could stem from suppressed scattering and smooth interface, and can significantly improve the switching

speed of β-Ga_2O_3 power devices. However, the low thermal conductivity of β-Ga_2O_3 will demand device-level and integrated thermal management for effective heat removal to avoid performance degradation. Looking at the all-around progress of the process, processing, and device technology of β-Ga_2O_3 material, it has shown enough pieces of evidence to cater to emerging power electronics applications apart from supplementing existing technologies.

Acknowledgements

The authors acknowledge the National Institute of Technology Silchar for providing necessary facilities to carry out the research with international collaboration with New Jersey Institute of Technology, New Jersey, USA.

References

1. E. Ahmadi, Y. Oshima, Materials issues and devices of α- And β-Ga_2O_3, J. Appl. Phys. **126**(16) (2019). https://doi.org/10.1063/1.5123213

2. J.Y. Tsao et al., Ultrawide-Bandgap semiconductors: research opportunities and challenges, Adv. Electron. Mater. **4**(1) (2018). https://doi.org/10.1002/aelm.201600501

3. S.J. Pearton, F. Ren, M. Tadjer, J. Kim, Perspective: Ga_2O_3 for ultra-high power rectifiers and MOSFETS, J. Appl. Phys. **124**(22) (2018). https://doi.org/10.1063/1.5062841

4. M. Mohamed, K. Irmscher, C. Janowitz, Z. Galazka, R. Manzke, R. Fornari, Schottky barrier height of Au on the transparent semiconducting oxide β-Ga_2O_3. Appl. Phys. Lett. **101**(13), 3–8 (2012). https://doi.org/10.1063/1.4755770
[Crossref]

5. J. Yang, F. Ren, M. Tadjer, S.J. Pearton, A. Kuramata, Ga_2O_3 Schottky rectifiers with 1 ampere forward current, 650 v reverse breakdown and 26.5 MW.cm-2 figure-of-merit, AIP Adv. **8**(5) (2018). https://doi.org/10.1063/1.5034444

6. X. Lu, X. Zhang, H. Jiang, X. Zou, K.M. Lau, G. Wang, Vertical β-Ga_2O_3 Schottky Barrier diodes with enhanced breakdown voltage and high switching performance. Phys. Status Solidi Appl. Mater. Sci. **217**(3), 3–7 (2020). https://doi.org/10.1002/pssa.201900497
[Crossref]

7. Y. Wei et al., Experimental study on static and dynamic characteristics of Ga_2O_3 Schottky barrier diodes with compound termination. IEEE Trans. Power Electron. **36**(10), 10976–10980 (2021). https://doi.org/10.1109/TPEL.2021.3069918
[Crossref]

8. M. Higashiwaki et al., Depletion-mode Ga_2O_3 metal-oxide-semiconductor field-effect transistors on β-Ga_2O_3 (010) substrates and temperature dependence of their device characteristics. Appl. Phys. Lett. **103**(12), 1–5 (2013). https://doi.org/10.1063/1.4821858 [Crossref]

9. A.J. Green et al., 3.8-MV/cm breakdown strength of MOVPE-grown Sn-Doped β-Ga_2O_3 MOSFETs. IEEE Electron Device Lett. **37**(7), 902–905 (2016). https://doi.org/10.1109/LED.2016.2568139 [Crossref]

10. M.H. Wong, Y. Nakata, A. Kuramata, S. Yamakoshi, and M. Higashiwaki, Enhancement-mode Ga_2O_3 MOSFETs with Si-ion-implanted source and drain, Appl. Phys. Express **10**(4) (2017). https://doi.org/10.7567/APEX.10.041101

11. S. Krishnamoorthy, Z. Xia, S. Bajaj, M. Brenner, S. Rajan, Delta-doped β-gallium oxide field-effect transistor. Appl. Phys. Express **10**(5), 051102 (2017). https://doi.org/10.7567/APEX.10.051102 [Crossref]

12. J.K. Mun, K. Cho, W. Chang, H.-W. Jung, J. Do, Editors' choice—2.32 kV breakdown voltage lateral β-Ga_2O_3 MOSFETs with source-connected field plate. ECS J. Solid State Sci. Technol. **8**(7), Q3079–Q3082 (2019). https://doi.org/10.1149/2.0151907jss [Crossref]

13. Z. Feng et al., Design and fabrication of field-plated normally off β-Ga_2O_3MOSFET with laminated-ferroelectric charge storage gate for high power application. Appl. Phys. Lett. **116**(24), 1–6 (2020). https://doi.org/10.1063/5.0010561 [Crossref]

14. E. Ahmadi et al., Demonstration of β-$(Al_xGa_{1-x})_2O_3$/β-Ga_2O_3 modulation doped field-effect transistors with Ge as dopant grown via plasma-assisted molecular beam epitaxy. Appl. Phys. Express **10**(7), 071101 (2017). https://doi.org/10.7567/APEX.10.071101 [Crossref]

15. S. Krishnamoorthy et al., Modulation-doped β-$(Al\ 0.2\ Ga\ 0.8)_2O_3$/Ga_2O_3 field-effect transistor, Appl. Phys. Lett. **111**(2), 023502 (2017). https://doi.org/10.1063/1.4993569

16. Y. Zhang et al., Demonstration of high mobility and quantum transport in modulation-doped β-$(Al_xGa_{1-x})_2O_3$/Ga_2O_3 heterostructures. Appl. Phys. Lett. **112**(17), 1–6 (2018). https://doi.org/10.1063/1.5025704 [Crossref]

17. M.A. Mastro, M.J. Tadjer, J. Kim, F. Ren, S.J. Pearton, Design of Ga_2O_3 modulation doped field effect transistors. J. Vac. Sci. Technol. A **39**(2), 023412 (2021). https://doi.org/10.1116/6.0000825 [Crossref]

18. M.J. Tadjer et al., Delta-doped β-$(Al_xGa_{1-x})_2O_3$/Ga_2O_3 heterostructure field-effect

transistors by ozone molecular beam epitaxy. J. Vac. Sci. Technol. A **39**(3), 033402 (2021). https://doi.org/10.1116/6.0000932
[Crossref]

19. R. Singh et al., The dawn of Ga_2O_3 HEMTs for high power electronics—A review, Mater. Sci. Semicond. Process. **119**(September) (2019), 105216 (2020). https://doi.org/10.1016/j.mssp.2020.105216

20. T. Oshima, T. Okuno, N. Arai, Y. Kobayashi, S. Fujita, β-$Al_{2x}Ga_{2-2x}O_3$ thin film growth by molecular beam epitaxy, Jpn. J. Appl. Phys. **48**(7) PART 1, 7–10 (2009). https://doi.org/10.1143/JJAP.48.070202

21. S.W. Kaun, F. Wu, J.S. Speck, β -$(Al_xGa_{1-x})_2O_3$/Ga_2O_3 (010) heterostructures grown on β-Ga_2O_3 (010) substrates by plasma-assisted molecular beam epitaxy, J. Vac. Sci. Technol. A Vacuum, Surfaces, Film. **33**(4), 041508, (2015). https://doi.org/10.1116/1.4922340

22. M.H. Wong, K. Sasaki, A. Kuramata, S. Yamakoshi, M. Higashiwaki, Electron channel mobility in silicon-doped Ga_2O_3 MOSFETs with a resistive buffer layer, Jpn. J. Appl. Phys. **55**(12) (2016). https://doi.org/10.7567/JJAP.55.1202B9

23. K. Song, H. Zhang, H. Fu, C. Yang, R. Singh, Normally-off AlN/β -Ga_2O_3 field-effect transistors using polarization-induced (2020)

24. H. Sun et al., Valence and conduction band offsets of β-Ga_2O_3/AlN heterojunction. Appl. Phys. Lett. **111**(16), 162105 (2017). https://doi.org/10.1063/1.5003930
[Crossref]

25. S. Lyu, A. Pasquarello, Band alignment at β-Ga_2O_3/III-N (III = Al, Ga) interfaces through hybrid functional calculations. Appl. Phys. Lett. **117**(10), 102103 (2020). https://doi.org/10.1063/5.0020442
[Crossref]

26. J.-X. Chen et al., Band alignment of AlN/ β-Ga_2O_3 heterojunction interface measured by x-ray photoelectron spectroscopy. Appl. Phys. Lett. **112**(26), 261602 (2018). https://doi.org/10.1063/1.5035372
[Crossref]

27. R. Singh, T.R. Lenka, R.T. Velpula, B. Jain, H.Q.T. Bui, H.P.T. Nguyen, A novel β-Ga2O3 HEMT with fT of 166 GHz and X-band POUT of 2.91 W/mm, Int. J. Numer. Model. Electron. Networks, Devices Fields **34**(1), 1–11 (2021). https://doi.org/10.1002/jnm.2794

28. R. Singh, T.R. Lenka, H. Pham, T. Nguyen, Analytical study of effect of energy band parameters and lattice temperature on conduction band offset in AlN/Ga_2O_3 HEMT, Electronics and Energetics **34**(3), 323–332 (2021). https://doi.org/10.2298/FUEE2103323S

T. R. Lenka, H. P. T. Nguyen (eds.), *HEMT Technology and Applications*, Springer Tracts in Electrical and Electronics Engineering
https://doi.org/10.1007/978-981-19-2165-0_15

Linearity Analysis of AlN/β-Ga_2O_3 HEMT for RFIC Design

Yogesh Kumar Verma[1] ✉, Varun Mishra[2] ✉, Rajan Singh[3] ✉, Trupti Ranjan Lenka[3] ✉ and Santosh Kumar Gupta[4] ✉

(1) School of Electronics and Electrical Engineering, Lovely Professional University, Jalandhar, Punjab, 144411, India
(2) Department of Electronics and Electrical Engineering, Graphic Era (Deemed to be University), Dehradun, Uttarakhand, 248002, India
(3) Microelectronics and VLSI Design Group, Department of Electronics and Communication Engineering, National Institute of Technology Silchar, Silchar, Assam, 788010, India
(4) Department of Electronics and Communication Engineering, Motilal Nehru National Institute of Technology, Allahabad, Uttar Pradesh, 211004, India

✉ **Yogesh Kumar Verma (Corresponding author)**
Email: yogesh.25263@lpu.co.in

✉ **Varun Mishra**
Email: varunmishra.ece@geu.ac.in

✉ **Rajan Singh**
Email: rajan_rs@ece.nits.ac.in

✉ **Trupti Ranjan Lenka**
Email: trlenka@ieee.org

✉ **Santosh Kumar Gupta**

Email: skg@mnnit.ac.in

Abstract
In this work, the different figures-of-merit for AlN/β-Ga_2O_3 High Electron Mobility Transistor (HEMT) are computed using TCAD. The first and second-order derivatives of transconductance, output-conductance (g_d), intrinsic-gain (dB), gate-source capacitance (C_{gs}), gate-drain capacitance (C_{gd}), transconductance-generation factor (TGF), transconductance-frequency product (*TFP*), 1-dB compression-point, extrapolated input voltages (VIP_2 and VIP_3), third-order input intercept point (IIP_3), third-order intermodulation distortion (IMD_3), and gain-transconductance frequency product (GTFP) are computed to predict the linearity performance and minimize intermodulation distortion. The present analysis is beneficial for optimizing the device bias point required for RFIC design.

Keywords AlN – β-Ga_2O_3 – HEMT – 2DEG – TCAD

1 Introduction

The (N)-polar AlN on β-Ga_2O_3 form the two-dimensional electron gas (2-DEG) concentration of a much larger magnitude than conventional metal-polar AlN/GaN hetero-interface [1]. The β-Ga_2O_3 epilayers have been grown by several research groups on different substrates [2]. These advanced growth techniques offer versatile hetero-structures with precise control over the interface. Zhang et al. [3] revealed the formation of 2-DEG at the interface of β-$(Al_xGa_{1-x})_2O_3$ and Ga_2O_3 analogues to the formation of 2-DEG in MgZnO/ZnO, AlGaN/GaN, and AlGaAs/GaAs heterostructures [4–10]. However, β-Ga_2O_3/AlN heterojunction induces higher 2-DEG density in comparison to conventional β-$(Al_xGa_{1-x})_2O_3$/Ga_2O_3 heterostructures. There exist better transport properties as mobility greater than 200 cm^2/V.sec, saturation velocity of 2×10^7 cm/sec, large energy bandgap of 4.7 eV, and breakdown field of 8 MV/cm in β-Ga_2O_3 material [3]. Sun et al. [1] calculated the valence band offset and conduction band offset of β-

Ga_2O_3/AlN heterojunction as −0.55 eV and −1.75 eV respectively using HR-*X*-ray photoemission spectroscopy. The combination of wide energy bandgap and ability to control the conductivity by doping in Ga_2O_3 material finds application to high power MESFETs and MOSFETs [1, 11–14].

It is essential to characterize device linearity in order to minimize linearizer design complexity of communication systems [15]. The linearity is defined as the property of a device where output of the device is directly proportional to the input. The devices are typically linear only over a certain input power range. The operation of a device in the non-linear region can create distortion in the form of harmonics and intermodulation products. The harmonics are copies of a signal appearing at integer multiples of the fundamental signal. The amplitude of a harmonic usually decreases as the harmonic order increases. Intermodulation occurs when two (or more) signals mix in a non-linear device. The mixing produces new signals at the sum and difference of their two frequencies. The order of harmonics and intermodulation is the sum of their (unsigned) coefficients. The harmonic and intermodulation products are undesired signals due to the creation of leakage into adjacent channels, noise or distortion, etc. The undesired intermodulation is often referred to as intermodulation distortion. The higher order harmonics have very low amplitudes and can usually be ignored. The third-order intermodulation products present an additional complication; where for every 1 dB increase in the fundamental (useful) signal, the third-order (unwanted) intermodulation products increase in level by 3 dB. The intermodulation distortion occurs basically due to the mixing of multiple input signals inside the receiver often due to non-linearity in the receiver. The third-order intermodulation distortion (IMD_3) lies close to fundamental frequencies thereby causing in-band problems.

2 Device Structure and Its Physics

The Ga and O atoms in β-Ga_2O_3 and the Al and N atoms in AlN are both arranged in a hexagonal pattern but with slightly different sizes of hexagons [1]. The two-dimensional electron gas (2DEG) is formed at

the heterointerface of AlN and β-Ga_2O_3 due to polarization charges. This 2-DEG typically features both high charge carrier density and mobility and can serve as an active layer in HEMT. Figures 1 and 2 represent the AlN/β-Ga_2O_3 hetero-interface and the structure of β-Ga_2O_3/AlN HEMT, respectively. The length of gate, thickness of AlN layer, order of doping concentration, and thickness of SiO_2 layer is 50 nm, 10 nm, 10^{19} cm^{-3}, and 20 nm respectively. Table 1 and 2 represent the symbols and relations used in the present work.

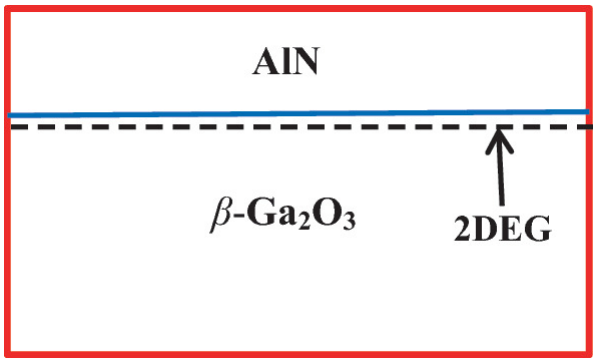

Fig. 1 Formation of 2-DEG at the interface of AlN and β-Ga_2O_3

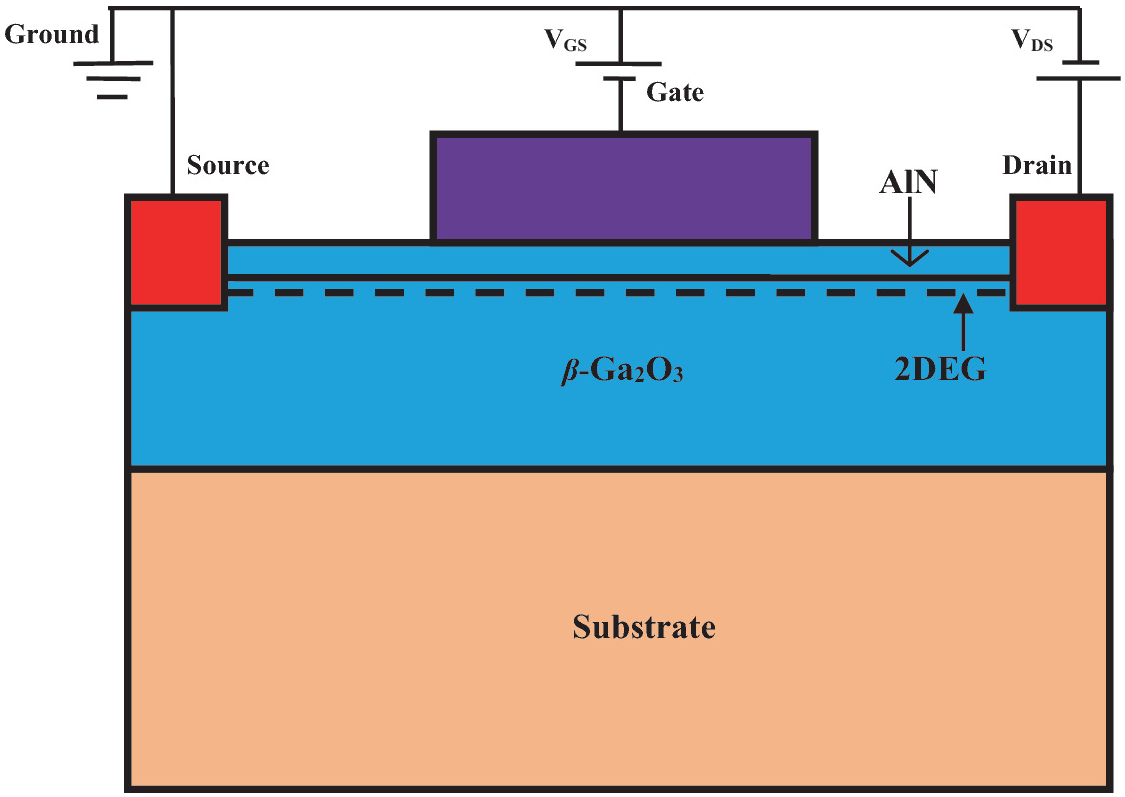

Fig. 2 Structure of AlN/β-Ga_2O_3 HEMT

Table 1 Symbols used

V_D or V_{DS}	Drain voltage
V_G or V_{GS}	Gate voltage
I_D or I_{DS}	Drain current
V_{OFF}	Threshold-voltage
C_{gs}, C_{gd}	Gate-source and gate-drain capacitance respectively
R_S	Source-resistance (50 Ω)

Table 2 Symbols and Relations Used [16, 17]

Symbol	Quantity	Unit	Relations used
g_{m1}	Transconductance	$A\mu^{-1}\,m\,V^{-1}$	$g_{m1} = [\partial I_{DS}/\partial V_{GS}]$
g_{m2}	First-order derivative of transconductance	$A\mu^{-1}\,m\,V^{-1}$	$g_{m2} = (1/2!)\left[\partial^2 I_{DS}/\partial V_{GS}^2\right]$
g_{m3}	Second-order derivative of transconductance	$A\mu^{-1}\,m\,V^{-1}$	$g_{m2} = (1/2!)\left[\partial^2 I_{DS}/\partial V_{GS}^2\right]$
g_d	Output Conductance	$A\mu^{-1}\,m\,V^{-1}$	$g_d = [\partial I_{DS}/\partial V_{DS}]$
A_v	Intrinsic-Gain	dB	$A_v = (g_{m1}/g_d)$
TGF	Transconductance Generation Factor	V-1	$\mathrm{TGF} = (g_{m1}/I_D)$
TFP	Transconductance Frequency Product	HzV-1	$\mathrm{TFP} = (g_{m1}/I_D)\,.f_T$
1-dB Compression Point	1-dB Compression Point	dBm	$1\text{ dB Compression Point} = 0.22 \times \sqrt{\frac{g_{m1}}{g_{m3}}}$
VIP_2, VIP_3	Distortion characteristic parameters	Volt	$\mathrm{VIP}_2 = 4 \times (g_{m1}/g_{m2})$ $\mathrm{VIP}_3 = \sqrt{(24 g_{m1})/g_{m3}}$
IIP_3	Third-order input intercept point	dBm	$\mathrm{IIP}_3 = (2 \times g_{m1}) / (3 \times g_{m3} \times R_s)$
IMD_3	Third-order intermodulation distortion	dBm	$\mathrm{IMD}_3 = \left[4.5 \times (VIP_3)^3 \times g_{m3}\right]^2 \times R_s$

Symbol	Quantity	Unit	Relations used
GTFP	Gain transconductance frequency product	HzV-1	$\mathrm{GTFP} = (g_{m1}/g_d) \cdot (g_{m1}/I_D) \cdot f_T$

3 Results and Discussions

The energy level difference between Fermi energy level (E_F) and position of first sub-band (E_0) predicts the presence of 2DEG density (n_s) in the triangular potential well. The increase in V_G causes an increase in ($E_F - E_0$); which consequently cause increase in n_s. Figure 3 represents the relative positions of ($E_F - E_0$) w.r.t. V_G. The higher order derivatives of transconductance deteriorate the linearity of communication systems and need to be suppressed. Figure 4 represents the calculation of g_{m1}, g_{m2}, and g_{m3} at $V_D = 1$ V corresponding to a range of V_G from −20 V to 0 V. The value of g_{m1} is calculated as 1.367×10^{-11} and 0.0052 corresponding to $V_G = -20$ V and $V_G = 0$ V respectively. The peak value of g_{m1} having magnitude 0.325 occurs at −12 V. As V_G increases the ($E_F - E_0$) continuously increases and there occurs maximum probability of the electrons to be confined in the triangular quantum well, as a result n_s increases and consequently g_{m1} is increased. The value of g_{m2} is calculated as -8.138×10^{-12} and 1.51972×10^{-5} corresponding to $V_G = -20$ V and $V_G = 0$ V respectively. The peak value of g_{m2} equivalent to 0.16228 occurs at −13 V. The magnitude of g_{m2} increases with an increase in V_G from −20 V to −13 V, thereby it decreases with increase in V_G from −14 V to 0 V. The value of g_{m3} is calculated as 0.0647 and 0.018 corresponding to $V_G = -20$ V and $V_G = 0$ V, respectively. The peak value of g_{m3} equivalent to 0.04854 occurs at −10 V. The magnitude of g_{m3} increases with increase in V_G from −20 V to −10 V, thereby it decreases with increase in V_G from −11 V to 0 V.

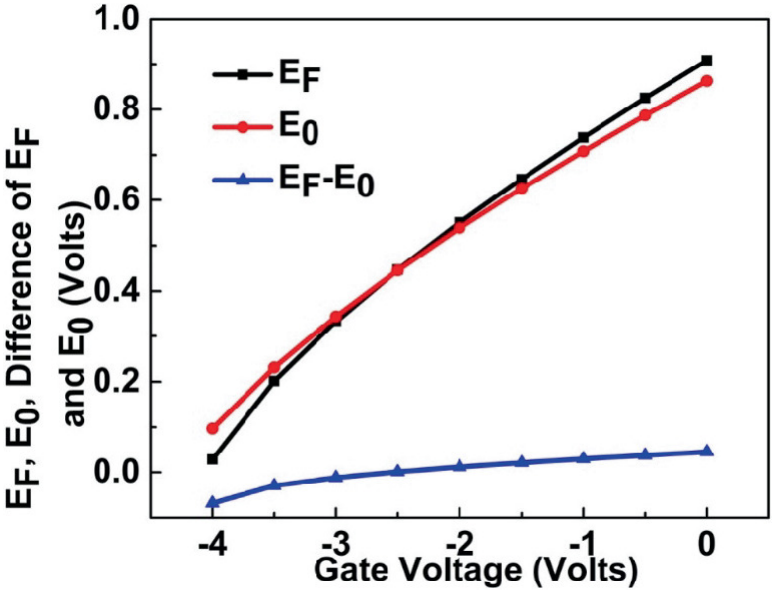

Fig. 3 Calculation of E_F, E_0, and Difference of E_F and E_0 (Volts)

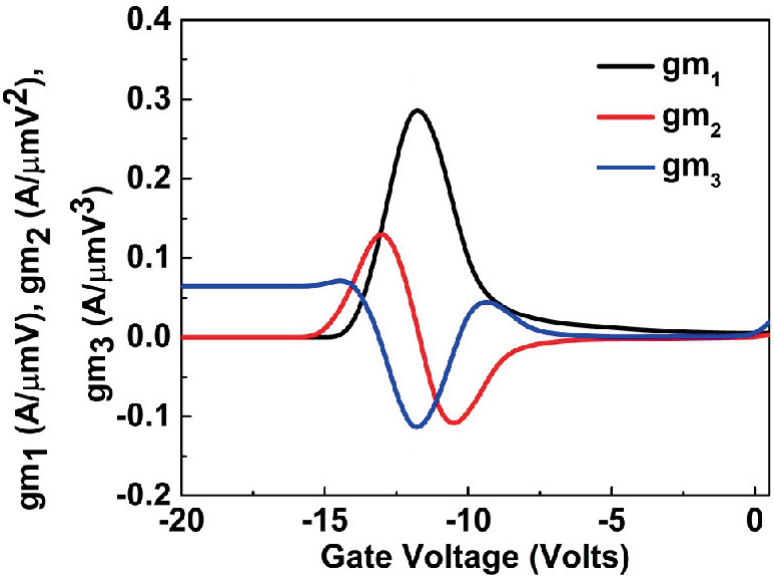

Fig. 4 Calculation of g_{m1}, g_{m2}, and g_{m3}

Table 3 represents the calculation of g_d corresponding to a range of V_D from 0 to 1 V for $V_G = -13$ V, $V_G = V_{OFF}$, and $V_G = 0.5$ V. As the output conductance decreases, it results in an increased output resistance due to which the driving capability of the device is improved. The value of g_d is calculated as 1.11×10^{-5} and 5.398×10^{-5} corresponding to $V_D =$ 0 V and $V_D = 1$ V respectively at $V_G = -13$ V. The value of g_d decreases

continuously with increase in V_D from 0 V to 0.1 V, thereby it increases corresponding to a range of V_D from 0.2 V to 1 V at $V_G = -13$ V. The value of g_d is calculated as 0.015 and 0.024 corresponding to $V_D = 0$ V and $V_D = 1$ V, respectively at $V_G = V_{OFF}$. The value of g_d decreases continuously with increase in V_D from 0 V to 0.1 V, thereby it increases corresponding to a range of V_D from 0.2 V to 1 V at $V_G = V_{OFF}$. The value of g_d is calculated as 0.923 and 0.936 corresponding to $V_D = 0$ V and $V_D = 1$ V, respectively, at $V_G = 0.5$ V. The value of g_d decreases continuously with increase in V_D from 0 V to 0.3 V, thereby it increases corresponding to a range of V_D from 0.4 V to 1 V at $V_G = 0.5$ V.

Table 3 Calculation of g_d ($A\mu^{-1}\,m^{-1}\,V^{-1}$) w.r.t. V_D

V_D (Volts)	$V_G = -13$ V	$V_G = V_{OFF}$	$V_G = 0.5$ V
0	1.11E-5	0.015	0.923
0.1	5.777E-6	0.008	0.920
0.2	6.944E-6	0.009	0.918
0.3	9.168E-6	0.011	0.917
0.4	1.213E-5	0.013	0.917
0.5	1.594E-5	0.015	0.919
0.6	2.072E-5	0.017	0.925
0.7	2.674E-5	0.019	0.927
0.8	3.431E-5	0.021	0.929
0.9	4.372E-5	0.0229	0.933
1	5.398E-5	0.024	0.936

The gate voltage acts as the source of pulling energy required to pull up the ground state toward Fermi energy level. The higher the magnitude of $(E_F - E_0)$, higher will be the operable gate voltage and consequently higher will be the linear operable region of the transistor. The derivative of $(E_F - E_0)$ with respect to V_G gives the measurement of linearity. Figure 5 represents the calculation of g_d and intrinsic gain with respect to V_G at $V_{DS} = 1$ V. The magnitude of $(E_F - E_0)$ increases

with increase in V_G and consequently, g_d is increased. The value of g_d is calculated as 1.563×10^{-9} and 0.933 corresponding to $V_G = -20$ V and $V_G = 0$ V respectively. The magnitude of g_d increases continuously with increase in V_G from −20 V to 0 V. The peak value of g_d equal to 0.933 occurs at $V_G = 0$ V. The value of intrinsic gain is calculated as 20.582 and 22.79 corresponding to $V_G = -20$ V and $V_G = 0$ V respectively. The peak value of gain equal to 34.133 occurs at $V_G = -14$ V.

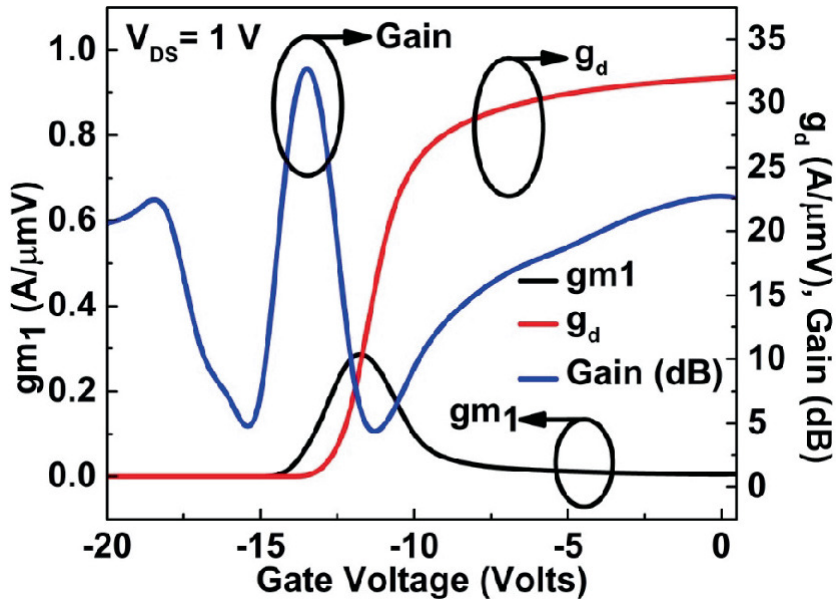

Fig. 5 Calculation of g_d and intrinsic gain with respect to V_G at $V_{DS} = 1$ V

Figure 6 represents the calculation of C_{gs} and C_{gd} corresponding to a range of V_G from −20 V to 0 V. The value of C_{gs} is calculated as 1.096×10^{-13} and 3.528×10^{-13} corresponding to $V_G = -20$ V and $V_G = 0$ V, respectively. The magnitude of C_{gs} increases continuously with increase in V_G from −20 V to 0 V. The value of C_{gd} is calculated as 1.098×10^{-13} and 1.147×10^{-13} corresponding to $V_G = -20$ V and $V_G = 0$ V, respectively. The peak value of C_{gd} equal to 1.457×10^{-13} occurs at $V_G = -11$ V. The magnitude of C_{gd} increases with increase in V_G from −20 V to −11 V, thereby it decreases with increase in V_G from −10 V to 0 V.

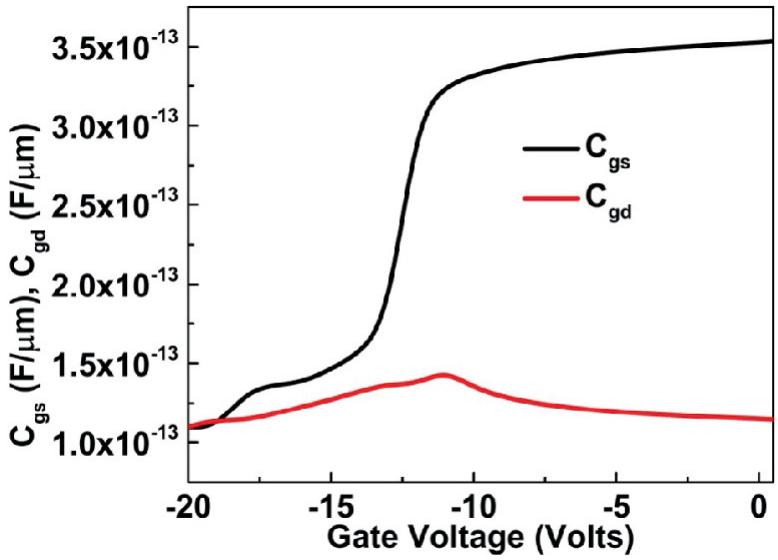

Fig. 6 Calculation of C_{gs} and C_{gd} with respect to V_G

Table 4 represents the calculation of TFP and 1 dB compression point corresponding to a range of V_G from −20 V to 0 V. The value of TFP is calculated as 0.529 and 8.909×10^6 corresponding to $V_G = -20$ V and $V_G = 0$ V, respectively. The peak magnitude of TFP equal to 4.116×10^{14} occurs at −13 V. The value of 1 dB compression point is calculated as 1.499×10^{-6} and 0.054 corresponding to $V_G = -20$ V and $V_G = 0$ V, respectively. The two peak values of 1 dB compression point equal to 0.709 and 0.647 occur at $V_G = -13$ V and $V_G = -5$ V, respectively. 1-dB compression point predicts the upper limit of linear operation.

Table 4 Calculation of TFP and 1 dB Compression Point w.r.t. V_G

V_G (Volts)	*TFP*	1 dB Comp. point
−20	0.529	1.4993E-6
−19	0.08072	9.5397E-7
−18	0.31651	1.3713E-6
−17	8.9367	3.262E-6
−16	61.725	5.7396E-6
−15	1076.9	1.3651E-5
−14	2.2092E10	0.00116
−13	4.1159E14	0.70957

V_G (Volts)	*TFP*	1 dB Comp. point
−12	1.4625E11	0.15558
−11	3.2072E10	0.17987
−10	2.7476E9	0.13082
−9	6.8114E8	0.09572
−8	2.6808E8	0.16229
−7	1.32E8	0.22144
−6	8.3356E7	0.33076
−5	5.643E7	0.64729
−4	3.2783E7	0.43744
−3	1.9822E7	0.33021
−2	1.3606E7	0.34776
−1	1.0168E7	0.33435
0	8.9086E6	0.17435

Figure 7 represents VIP_2 and VIP_3 corresponding to a range of V_G from −20 V to 0 V. The value of VIP_2 is calculated as 6.721 and 39 corresponding to $V_G = -20$ V and $V_G = 0$ V, respectively. The three peak values of VIP_2 equal to 19.803, 21.894, and 37.298 occurs at $V_G = -19$ V, $V_G = -12$ V, and $V_G = -1$ V, respectively. The value of VIP_3 is calculated as 7.118×10^{-5} and 8.277 corresponding to $V_G = -20$ V and $V_G = 0$ V, respectively. The two peak values of VIP_3 equal to 33.687 and 30.731 occurs at $V_G = -13$ V and $V_G = -5$ V, respectively.

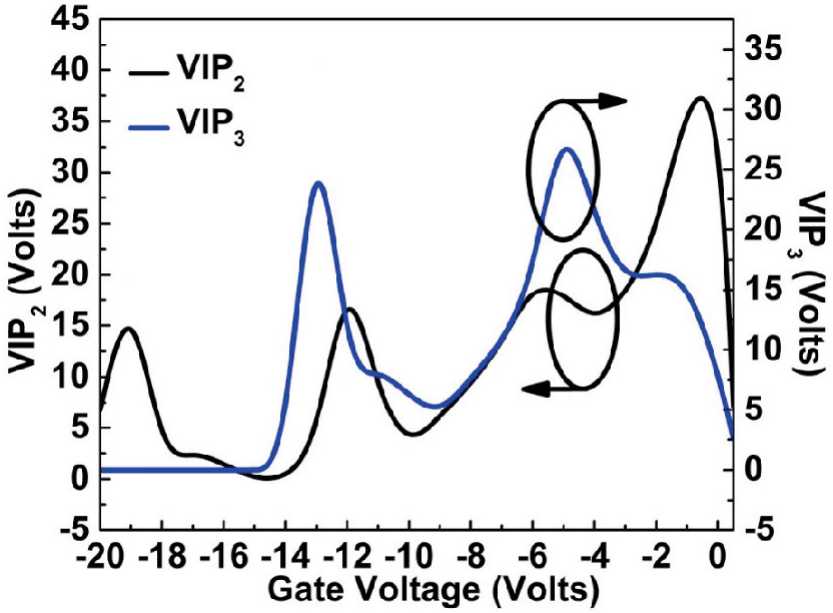

Fig. 7 Calculation of VIP_2 and VIP_3 w.r.t. V_G

Figure 8 represents the calculation of IIP_3 and IMD_3 corresponding to a range of V_G from −20 V to 0 V. The value of IIP_3 is calculated as −85.505 and 15.805 corresponding to $V_G = -20$ V and $V_G = 0$ V, respectively. The magnitude of IIP_3 increases sharply with increase in V_G from −20 V to −11 V, thereby it varies gradually with increase in V_G from −10 V to 0 V. The value of IMD_3 is calculated as −212.58 and 59.837 corresponding to $V_G = -20$ V and $V_G = 0$ V respectively. The magnitude of IMD_3 increases sharply with increase in V_G from −20 V to −11 V, thereby it varies gradually with increase in V_G from −10 V to 0 V.

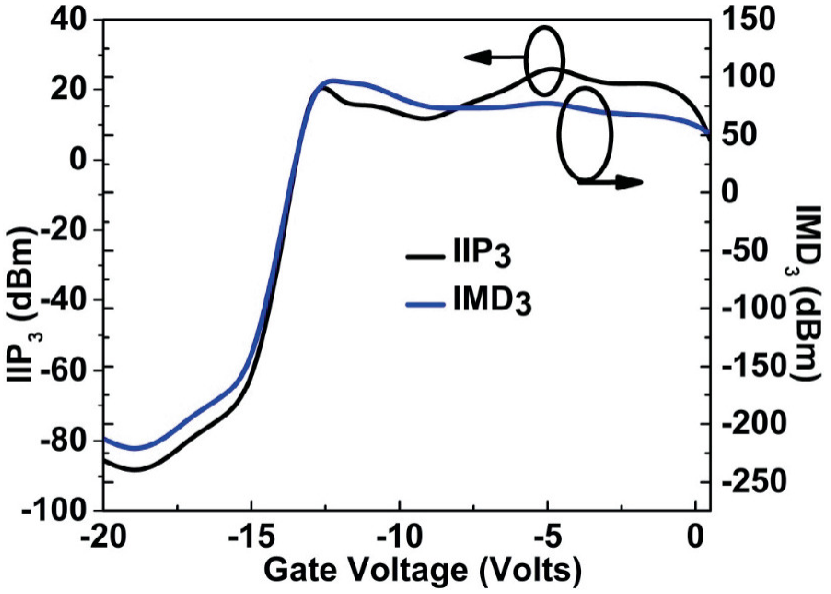

Fig. 8 Calculation of IIP_3 and IMD_3 corresponding to a range of V_G from −20 V to 0 V

Figure 9 represents the calculation of GTFP and its reciprocal corresponding to a range of V_G from −20 V to 0 V. The value of GTFP is calculated as 0.005 and 4.68×10^4 corresponding to $V_G = -20$ V and $V_G = 0$ V, respectively. The peak value of GTFP equal to 9.875×10^{17} occurs at $V_G = -13$ V. The reciprocate value of GTFP is calculated as 216.5 and 2.135×10^{-5} corresponding to $V_G = -20$ V and $V_G = 0$ V, respectively. The peak value of 1/GTFP equal to 1661.4 occurs at $V_G = -19$ V.

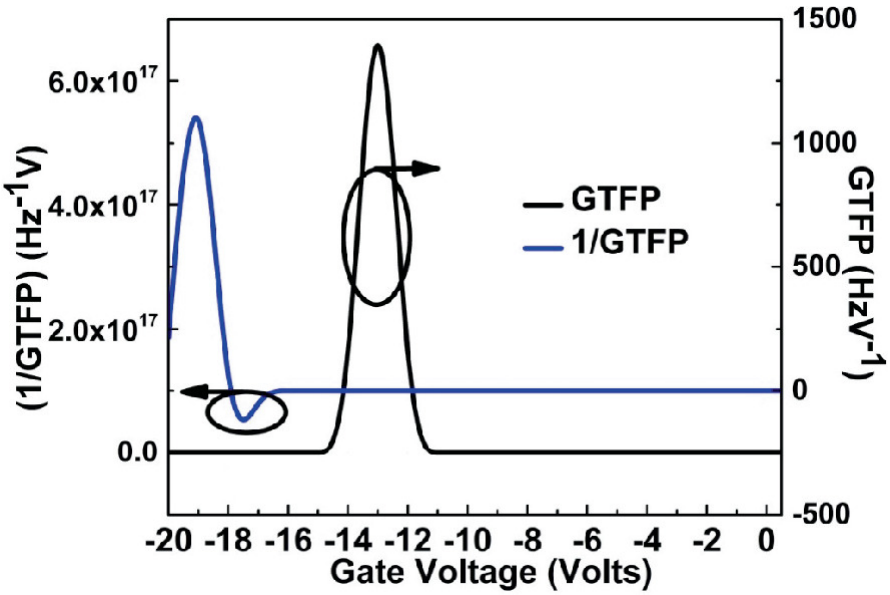

Fig. 9 Calculation of *GTFP* and its reciprocal corresponding to a range of V_G from −20 V to 0 V

4 Conclusion

In this work, the different figures-of-merit for AlN/β-Ga_2O_3 HEMT are computed considering its depletion mode of operation. The RF characteristics highlight that AlN/β-Ga_2O_3 HEMT provides TFP = 8.909 × 10^6 HzV^{-1} and GTFP = 4.68 × 10^4 HzV^{-1} at gate voltage (V_G) = 0 V augmenting its utility in high-speed RF applications. The analog parameters g_{m1}, g_{m2}, and g_{m3} are calculated as 0.0052 A/μmV, 0.0029 A/μmV^2, and 0.018 A/μmV^3 respectively at V_G = 0 V. The value of g_d decreases with increase in V_D from 0 V to 0.12 V, thereby it increases continuously corresponding to a range of V_D from 0.14 V to 1 V at V_G = V_{OFF}. The drain current, TGF, 1-dB compression point, VIP_2, VIP_3, and IIP_3 are calculated as 0.921 A/μm, 0.005 V^{-1}, 0.054 dBm, 39 V, 8.277 V, and 15.805 dBm at V_G = 0 V concluding that AlN/β-Ga_2O_3 HEMT is a potential contender inherently equipped with high 2DEG charge density for high-power and analog/RF applications.

References

1. H. Sun et al., Valence and conduction band offsets of β-Ga_2O_3/AlN heterojunction. Appl. Phys. Lett. **111**(16), 162105 (2017) [Crossref]
2. V. Gottschalch et al., Growth of β-Ga_2O_3 on Al_2O_3 and GaAs using metal-organic vapor-phase epitaxy. Phys. status solidi **206**(2), 243–249 (2009) [Crossref]
3. Y. Zhang et al., Demonstration of high mobility and quantum transport in modulation-doped β-$(Al_xGa_{1-x})_2O_3$/Ga_2O_3 heterostructures. Appl. Phys. Lett. **112**(17), 173502 (2018) [Crossref]
4. Y.K. Verma, V. Mishra, S.K. Gupta, A physics based analytical model for MgZnO/ZnO HEMT, J. Circuits, Syst. Comput. (2019)
5. S. Ghosh, A. Dasgupta, S. Khandelwal, S. Agnihotri, Y.S. Chauhan, Surface-potential-based compact modeling of gate current in AlGaN/GaN HEMTs. IEEE Trans. Electron Devices **62**(2), 443–448 (2015). https://doi.org/10.1109/TED.2014.2360420

[Crossref]

6. S. Khandelwal, Y.S. Chauhan, T.A. Fjeldly, Analytical modeling of surface-potential and intrinsic charges in AlGaN/GaN HEMT devices. IEEE Trans. Electron Devices **59**(10), 2856–2860 (2012). https://doi.org/10.1109/TED.2012.2209654
[Crossref]

7. Y.K. Verma, V. Mishra, P.K. Verma, S.K. Gupta, Analytical modelling and electrical characterisation of ZnO based HEMTs, Int. J. Electron. **106**(5), 707–720 (2019)https://doi.org/10.1080/00207217.2018.1545931

8. S. Krishnamoorthy, Z. Xia, S. Bajaj, M. Brenner, S. Rajan, Delta-doped β-gallium oxide field-effect transistor. Appl. Phys. Express **10**(5), 51102 (2017)
[Crossref]

9. J. Zhang, B. Syamal, X. Zhou, S. Arulkumaran, G.I. Ng, A compact model for generic Mis-hemts based on the unified 2deg density expression. IEEE Trans. Electron Devices **61**(2), 314–323 (2014). https://doi.org/10.1109/TED.2013.2295400
[Crossref]

10. S. Krishnamoorthy et al., Modulation-doped β-$(Al_{0.2}Ga_{0.8})_2O_3/Ga_2O_3$ field-effect transistor, Appl. Phys. Lett. **111**(2), 23502 (2017)

11. B.W. Krueger, C.S. Dandeneau, E.M. Nelson, S.T. Dunham, F.S. Ohuchi, M.A. Olmstead, Variation of Band Gap and Lattice Parameters of β-$(Al_xGa_{1-x})_2O_3$ powder produced by solution combustion synthesis. J. Am. Ceram. Soc. **99**(7), 2467–2473 (2016)
[Crossref]

12. Z. Hu et al., Enhancement-mode Ga_2O_3 vertical transistors with breakdown voltage >1 kV. IEEE Electron Device Lett. **39**(6), 869–872 (2018)
[Crossref]

13. Z. Xia et al., β-Ga_2O_3 delta-doped field-effect transistors with current gain cutoff frequency of 27 GHz. IEEE Electron Device Lett. **40**(7), 1052–1055 (2019)
[Crossref]

14. S.W. Kaun, F. Wu, J.S. Speck, β-$(Al_xGa_{1-x})_2O_3/Ga_2O_3$ (010) heterostructures grown on β-Ga_2O_3 (010) substrates by plasma-assisted molecular beam epitaxy, J. Vac. Sci. Technol. A Vacuum, Surfaces, Film. **33**(4), 41508 (2015)

15. S. Kumar, R. Soman, A.S. Pratiyush, R. Muralidharan, D.N. Nath, A performance comparison between beta-Ga_2O_3 and GaN HEMTs. IEEE Trans. Electron Devices **66**(8), 3310–3317 (2019)
[Crossref]

16. Y.K. Verma, S.K. Gupta, Center potential based analysis of Si and III-V gate all around field effect transistors (GAA-FETs), Silicon, 1–17 (2020)

17. S.K. Gupta, A.S. Rawat, Y.K. Verma, V. Mishra, Linearity distortion analysis of junctionless quadruple gate MOSFETs for analog applications, Silicon, 1–9 (2018). https://doi.org/10.

1007/s12633-018-9850-z

T. R. Lenka, H. P. T. Nguyen (eds.), *HEMT Technology and Applications*, Springer Tracts in Electrical and Electronics Engineering
https://doi.org/10.1007/978-981-19-2165-0_16

HEMT for Biosensing Applications

Deepak Kumar Panda[1] ✉ and Trupti Ranjan Lenka[2] ✉
(1) Microelectronics and VLSI Design Group, School of Electronics, VIT-AP University, Amaravati, Andhra Pradesh, 522237, India
(2) Microelectronics and VLSI Design Group, Department of Electronics & Communication Engineering, National Institute of Technology Silchar, Silchar, Assam, 788010, India

✉ **Deepak Kumar Panda (Corresponding author)**
Email: deepak.panda@vitap.ac.in

✉ **Trupti Ranjan Lenka**
Email: trlenka@ieee.org

Abstract
Among various types of biological sensors, the semiconductor biosensors gathered attraction due to their superior advantage in the process of integration, multifunction, and miniaturization. ISFET's based sensor has been processed for the very same as they deliver faster response, higher sensitivity, higher resolution, and label-free detection. The major drawback of these types of sensors it lacks because of its material degradation of the gate insulators and longer-term drift performance which possess instability in solution. Field-Effect Transistors (FET) based biosensors provide easy signal read-out capabilities, lower detection limit, and higher sensitivity. At the same time, the occurrence of Debye or Charge screening when exposed in high salt concentration suchlike as physiological fluids restrict in ground of clinical applications as assay requirements that includes expansive sample pre-treatment process steps, this technology suffer

from noise signals which restrict their detection limit. Upon the introduction of a few external change around surface conditions, i.e., linking of biomolecules in the underlap area of gate region results in significant variation in the piezoelectric-induced carrier density inside channel region of the device results in variation in drain current. Henceforth, comparatively HEMT-based biosensor facilitates higher sensitivity upon immobilization of biomolecules. Therefore these demerits could be overcome by implementation of GaN HEMT biosensor that bears the built-in properties like stability in aqueous solutions, biocompatibility, and are more sensitive to surrounding surface charge as the 2DEG channel concentration at the heterointerface layer which changes due to its existing surface charge variations by capacitive coupling.

Keywords 2DEG – Biosensor – Dielectrics – GaN HEMT – MOSHEMT – Sensitivity

1 Introduction

A major advantage of third-generation semiconductor material depicted by wide-bandgap GaN delivers stable material properties, higher thermal and chemical stability in solution, superior biocompatibility, higher sensitivity toward surface charge modifies the 2DEG channel which moves closer toward surface, the resulting higher bond strength of GaN-based semiconductor materials restricts chemical attack, used for transduction as its highly sensitive, thermally stable, have good chemical resistivity, high-temperature tolerance, and excellent electrical properties, allows the detection of a wide range of molecules, higher bandgap, sensitivity, lower power consumption, and faster responses. In addition, the use of GaN HEMT-based biosensor devices permits single microcircuits to operate a whole diagnostic laboratory, radio-frequency system for delivering data to a stationary computer [1].

The key factors which limit the performance degradation and reliability performance of AlGaN/GaN high electron mobility transistors (HEMT) biosensors in field of high-power radio-frequency (RF) applications is its greater gate leakage current. To eradicate this

problem, the Metal-Insulator-Semiconductor (MIS) structure is introduced to the GaN HEMT gate region to form the MIS-HEMT. The previous review literature focuses on a wide category of insulation dielectrics for semiconductor devices that includes oxides that are insulated in the form of the metal oxide semiconductor (MOS) structure, i.e., MOSHEMT [2]. This chapter deals with different types of HEMTs consisting of oxide and biomolecules forming cavity underlap gate area are referred to as MOSHEMTs biosensor, with MISHEMTs as a designation of insulated gate HEMTs biosensors. A list of experiments conducted predicts that N-polar GaN MOSHEMT biosensor devices can improve on current, reduce off current, improve sensitivity. A brief introduction focusing on HEMT as a biosensor with different structures, different materials, and different characteristics is focused on in this manuscript.

1.1 Characteristic of Biosensor

Sensitivity: The minimal amount of analyte which could be recognized by a biosensor determines its detection limit (Figs. 1 and 2).

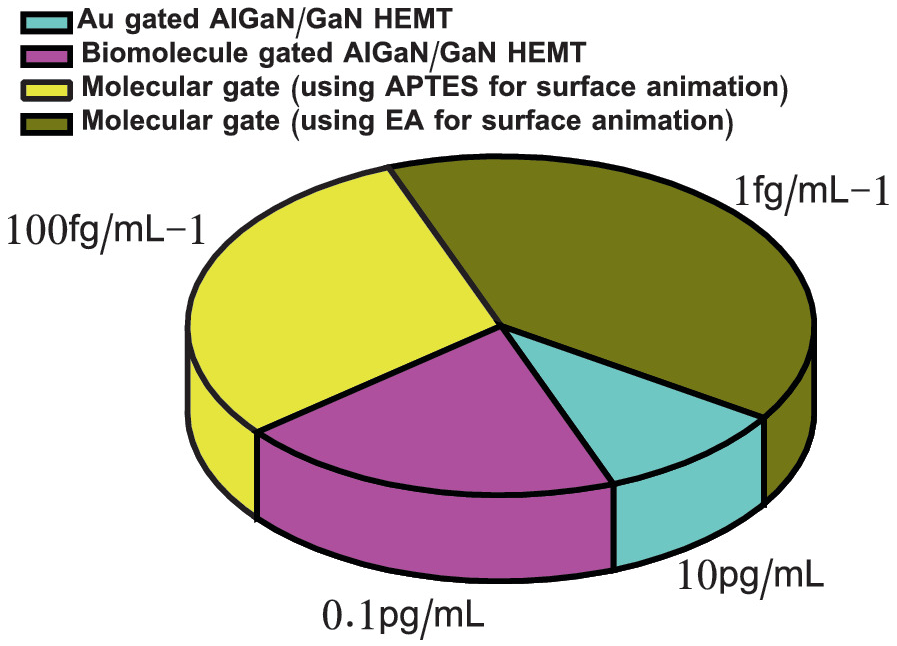

Fig. 1 Detection limit for different AlGaN-based HEMT

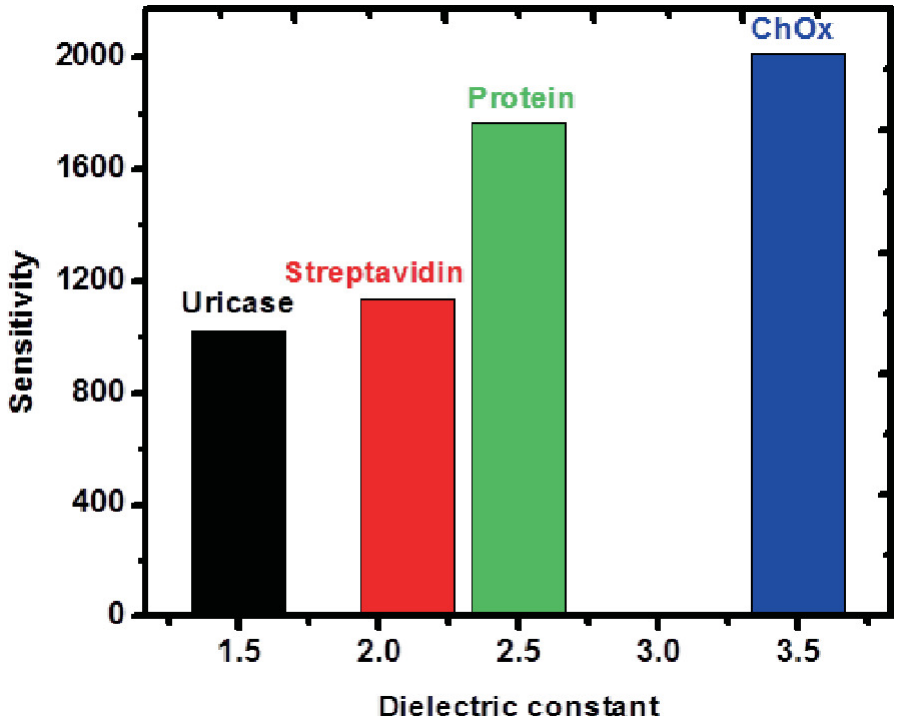

Fig. 2 Sensitivity parameter value variation upon exposure to various biomolecules are immobilized inside the cavity

Selectivity: It's stated as a limit to which the method could be used to analyze particular analytes in a matrix or mixture without its interference from any other components which are of similar behavior.

Specificity: It's defined as capability to examine unequivocally the analyte presence consisting components which are expected to come out. Generally the aforementioned include matrix, degradants, impurities, etc.

Linearity: It's the attribute that proves the accuracy of the concerned measured response (for a given set of measurements with various analyte concentrations) to a given straight line.

1.2 Working Principle of HEMT as Biosensor

Dielectric modulation is used to engrave/etch a part of the gate oxide under the gate electrode forming a nanocavity region, which is then filled up with many types of biomolecules. The biomolecules permittivity inside the cavity change (i.e., different biomolecules having various permittivity values) the electrical characteristics of the device which gets reflected in the values of transfer curve and sensitivity. Due to its less cost and easy operation, dielectric modulation is mostly

applied in biosensors. The working principle of dielectric modulation functions on different biomarkers and immobilization of biomolecules occurring inside the device. Therefore, the involvement of different types of biomarkers (aptamer, antibody, molecules, genes, enzymes) could bind more samples. Once both get to interact with each other there is a higher increase value in biomolecules concentration leading to a greater change in terms of the electrical properties of the device, i.e., threshold voltage, drain current, and electron concentration, etc. At last, these sensors could predict how speed operating device can perform its work, i.e., in terms of sensitivity, sensing speed, stability, and selectivity [3–11] (Fig. 3).

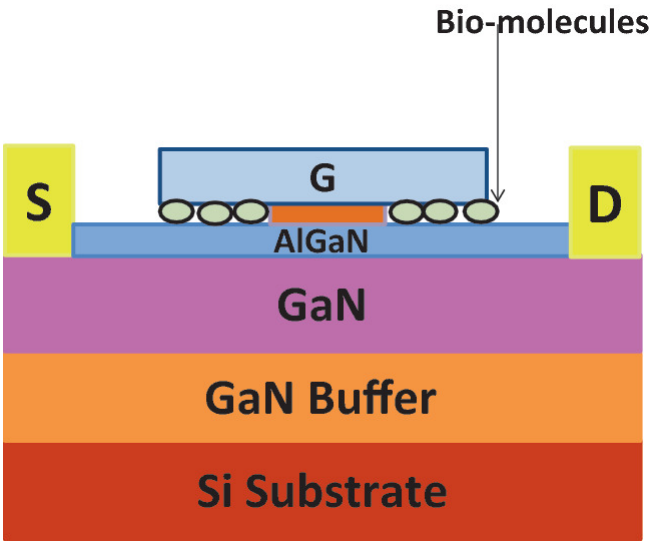

Fig. 3 Cross-sectional view of dielectric modulated HEMT-based biosensor [1]

2 MOSHEMT Structure and Characteristics

See Fig. 4.

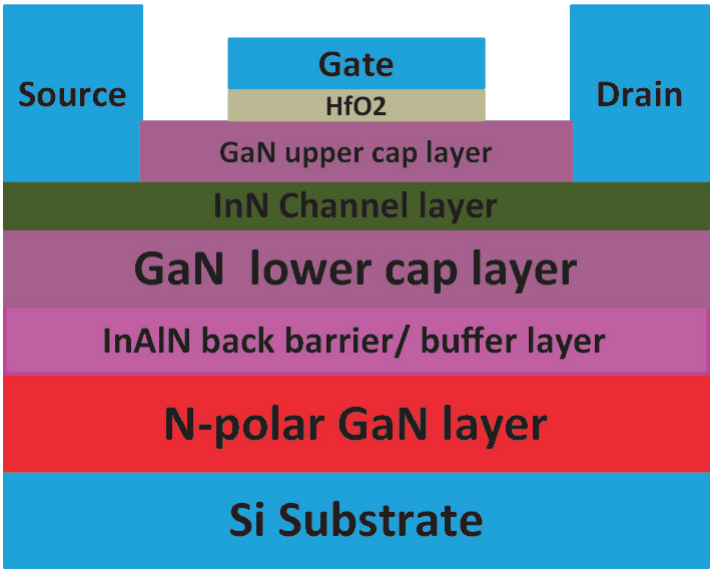

Fig. 4 Cross-sectional view of N-polar GaN MISHEMT-based biosensor [2]

The above schematic picture for GaN MOSHEMT biosensor with different barrier layers of AlInN, AlGaN, and AlN is shown in fig depicts the implemented device for N-polar GaN/$In_{0.9}Al_{0.1}$ N/InN MISHEMT. This proposed device structure composed stacked-layer N-polar GaN layer of 0.6 nm, accompanied through comfortable 1 μm $In_{0.9}Al_{0.1}$ N buffer layer/back-barrier which was grown by MOCVD process with an appropriate experimental performance as given by David et al., accompanied by an N-polar GaN layer which was formed upon Si substrate, followed by a GaN spacer layer of 0.4 nm is formed above this layer resulting in confinement of electrons to decrease scattering effect. Next, the formation of $In_{0.9}Al_{0.1}$ N back/buffer layer enhances the conductivity in channel of N-polar GaN HEMT. A gate insulator is formed using high-k material dielectric layer, i.e., HfO_2 (where $K = 21$) for decreasing the gate leakage current. To perform a dielectric modulation technique on N-polar GaN MISHEMT biosensor forming two separate cavities in the underlap area by the process of etching the insulator layer. At first whole area is covered with the HfO_2 insulator and thereafter later forms corresponding two separate cavities resulting into region-I&III as presented in below fig. Finally, these are formed above GaN cap layer. This corresponding cavity consisting of biomolecules such as streptavidin, uricase, ChOx, protein results in subsequent changes into various electric parameters which are

analyzed. The different permittivity values of biomolecules are represented in Table.1 [2].

Table 1 The permittivity values for various biomolecules [2]

Biomolecules	Dielectric constant
Protein	2.5
Streptavidin	2.1
ChOx	3.5
Uricase	1.5

AlGaN/GaN MOSHEMT biosensor structure comprises of the 2DEG forming piezoelectric and spontaneous polarization effects in heterointerface of AlGaN and GaN layer. Upon downscaling device dimensions gate lengths and oxide thickness are being reduced, where scaling of barrier thickness comes into effect. AlGaN barrier layer thickness is reduced to restrict the limitations of SCE's, the sheet carrier density reduces because of proximity at the heterointerface layer as it possesses negatively charged surface. On further increasing the 2DEG density the breakdown field in AlGaN HEMT biosensor devices higher Aluminium mole fraction is advantageous for raising the power of polarization, which in turn results in poor transport properties. To eradicate this issue a thin layer of lattice-matched AlInN layer is formed on top of GaN layer, which in turn reduces the strain present in conventional AlGaN-based MOSHEMT biosensor. The bandgap formed of AlInN is greater than the AlGaN layer which results in a more spontaneous polarization charge. This higher bandgap resulting in a greater increase in the electron carrier confinement value inside quantum well, to maintain the output resistance to be high. These huge carriers form accumulation inside the 2DEG layer resulting in a higher sheet carrier density which corresponds in higher current, power densities over conventional systems. To recover these problems, AlN/GaN MOSHEMT biosensor is used to serve as an alternate for next-generation high-power applications. However, resulting surface sensitivity and higher leakage current in AlN-based devices may result in poor device performance [12–14].

Figure 5 depicts the dependence of gate voltage on the drain current for an identical geometry structure of MOSHEMTs and HEMTs. This drain current obtained is nearly 150% more in case of MOSHEMTs device, whereby it reaches a greater value of nearly 0.45 A/mm. Using this equation $I_{ds} = e.n_s.v_{sat}.W$, one can predict that the maximum sheet carrier density $n_s = 6 \times 10^{12}/cm^2$ which is expected for the case of an undoped AlGaN/GaN two-dimensional channel density where, $v_{sat} = 6 \times 10^6$ cm/s.

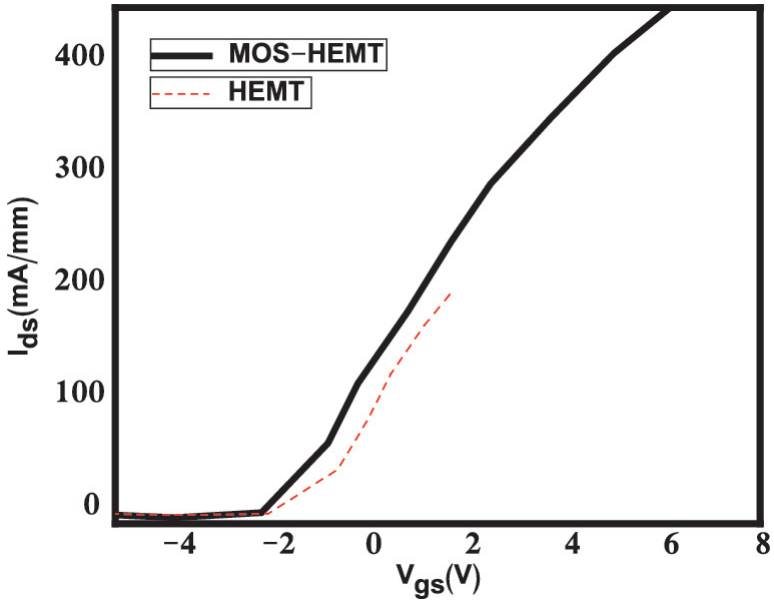

Fig. 5 Drain-current versus gate bias voltage in saturation region when Vds is given 10 V and here for the case of MOSHEMT (represented by a solid line), and whereas for the baseline HEMT (represented by a dashed line) where gate length $L_g = 5$ μm

Figure 6 depicts variation in the threshold voltage for different biomolecules. The above figure states that the threshold voltage rises upon adding neutrally charged biomolecules inside the cavity as well as a greater spreading in drain current value. This voltage is a valuable sensing metric for the device, that states applied gate voltage to attain its threshold inversion point.

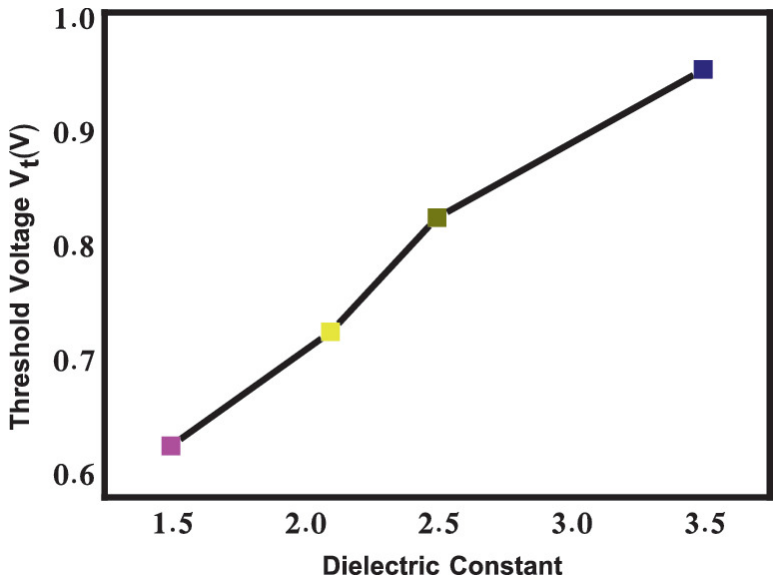

Fig. 6 Variation in Threshold voltage parameter upon immobilization of biomolecules inside the cavity

Figure 7 depicts shifting in change in threshold voltage is taken as one of the good sensing parameters in the identification and optimization of biomolecules inside the device. There are two key factors that is taken to be considered in change of ΔVt is permittivity. Greater variation in threshold voltage leads in sensitivity enhancement.

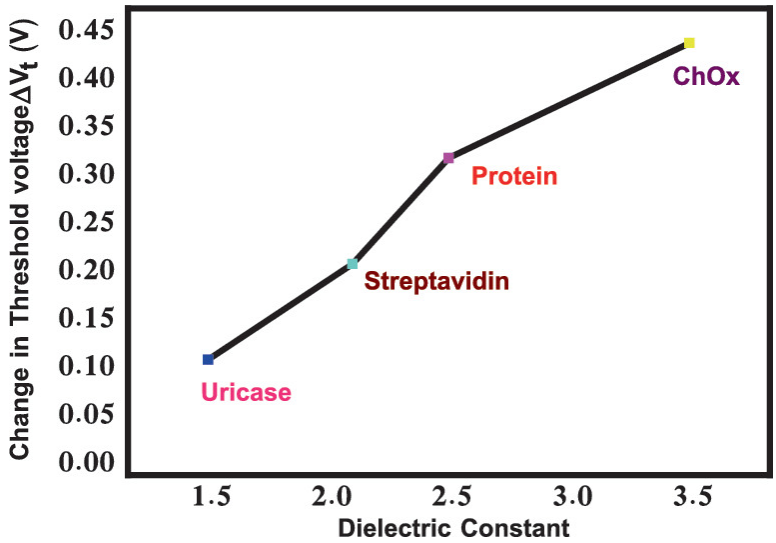

Fig. 7 Change in threshold voltage parameter upon introducing biomolecules inside the cavity

3 State-Of-Art Research of GaN MOSHEMT with Different Material Systems

By introducing a dielectric between the Schottky-gate and the semiconductor of the GaN HEMT forming an MIS-HEMT which in turn reduces the gate leakage current, thus resulting in a higher breakdown voltage and a larger range of gate bias within which the device can operate. Both the positive as well as negative gate voltage swing of the MIS-HEMT increases, owing to the negative shift in the threshold voltage value induced by increasing gate-to-channel spacing and gate forward turn-on voltage with the introduction of the gate dielectric. Although there is a decrease in transconductance peak value, it remains relatively comparing the larger range of gate voltage with greater improved linearity, behind there as on for which MIS-HEMTs enjoy good linearity in microwave power applications. The layer of gate dielectric could act as the layer of surface passivation to stabilize surface states of the semiconductor material, thus resulting in suppression of current collapse, improvement of the microwave power properties, and long-term reliability of the device [2].

First GaN MOSHEMTs were developed by Khan et al. using SiO2 deposited by the method of plasma-enhanced chemical vapor deposition. The higher gate dielectric constant value can increase the value of gate capacitance, thereby resulting in both as better control of the channel charge and a lesser deleterious effect of the gate dielectric value introduction on transconductance as well as a noticeable advantage in device scaling [18].

In recent years, there have been ongoing studies on the application of the MIS structure in N-polar GaNHEMTs. N-polar GaN heterostructures possess lower ohmic contact resistance and better quantum confinement but suffer from substantial point defects in GaN resulting in a larger gate leakage current value; therefore, the introduction of the MIS structure can greatly enhance the device properties. MIS-HEMTs have become one of the important categories of nitride semiconductor electronic devices. But in comparison to Ga-polar devices, N-polar based devices offers meritious effects in the field of better electron confinement in the channel, the increased gate-

channel capacitance value, lower access and contact (source and drain)resistance, offers enhancement mode of operation, advantages of reverse polarization direction, and decrease in short channel effects(SCS's) due to its back-barrier structure. Also, these devices have proven an increased RF, noise performance, and DC in comparison aforementioned Ga polar devices. We can obtain a highly scaled enhancement mode device by using this n-polar technology with better properties such as cut-off frequency and transconductance [15–19].

Eickhoff et al. firstly performed an AlGaN/GaN high electron mobility transistor (HEMT) biosensor for detection of pH wherein GaN oxidized surface serves as sensing membrane which contacts available hydrogen ions. The author Fan et al. utilized gold material for gate region of AlGaN/GaN HEMT based biosensor that has widened detection area relating to AlGaN/GaN HEMT based biosensors, which realized successfully for the detection of ions, DNA, and protein. Furthermore, these are further implemented for different inorganic materials which serve as sensing membranes that broadened the range of application for AlGaN/GaN HEMT biosensors improving its sensitivity value. Although, higher-energy Au deposition progress, some inorganic materials activate native oxide which results in lowering instability of the device decreasing performance response [33].

For prostate-specific antigen detection an AlGaN/GaN HEMTs biosensor formed using gold-coated gates thioglycolic acid-modified was implemented. Although, gold deposited layer not only increases processing cost but also reduces the sensitive detection of the sensors. In comparison to Au-gated AlGaN/GaN HEMT biosensors, these devices attain a better lower detection limit. Millimeter-graded biomolecule-gate AlGaN/GaN HEMT acts as a transducer that offers two main benefits which include both a lesser number of steps for the fabrication process of the sensor as well as potentially attained a lesser detection limit where the target biomarker moves closer to the 2DEG [20, 21].

To recover these problems, here we have implemented molecular gated-AlGaN/GaN HEMT-based biosensor tests potentiality in pH detection, prostate-specific antigen, Hg^{2+}, and TNT. Although it offers better performance, relatively low sensitivity limited its application in real detection. Zhiqi et al. have also demonstrated a more effective surface changing strategy based on HEMT devices, where ethanolamine

(EA) is applied over GaN surface which gave amphoteric amine groups for the case of immobilization of probe molecular for applying in bioassay. Another surface modification strategy using ethanolamine was used to solve the lower sensitivity problem faced by molecular-gated AlGaN/GaN HEMT biosensors. Although clinical applications gets limited due to the nature of these sensors that can get easily contaminated in the biological environment. Therefore to recover this problem Gate-pulsed AlGaN/GaN HEMT structure was implemented, but their design makes it more complicated due to the subsequent modification. The biggest advantage of this device is sensing structures comprising a different sensitive membrane, which overcomes demerit for being contaminated around the surrounding biochemical environment [22].

ZnO nanostructures offer better merits in the field of biotechnology, i.e., electrochemical activity, chemical stability, higher specific surface area, biocompatibility, and featuring communication of electron. In addition to that, these materials act as an absolute choice for adsorbing organic molecules as they possessess a relatively higher isoelectric point (IEP) value 9.5. The use of Zinc oxide (ZnO) nanostructures in the HEMT gate areas is the path for the process of biosensors fabrication. The process of adsorbing enzyme and transfer function, i.e., vary in electrochemical properties in gate region of the surface, these materials possessing transport property, higher compatibility are in greater need [23–31].

The inclusion of doped Silicon GaAs cap layer on AlGaAs layer improves both the chemical stability of the gate as well as carrier transport property in cap layer. Additionally, these electrons inside AlGaAs/GaAs HEMTs could be overactivated easily over AlGaN/GaN HEMTs due to its lesser energy bandgap of GaAs(=1.42 eV) than GaN(=3.44 eV). Finally, we have opted for GaAs substrate for the construction of the HEMT device to increase the sensor sensitivity as well as also for achieving a lower detection limit [32–34].

4 List of Sensitivity Parameters

Table 2 represents the important parameters metrics and methods for detection used which affects the sensitivity parameter of the device

such as channel potential, nanogap cavity, conductance, current gain, gate length, on current, transconductance, channel conductance, change in threshold voltage for biomolecules detection, and thin barrier. The device sensitivity is increased by improving parameters, i.e., length, gate length, width, and nanogap cavity.

Table 2 Review on various detection method and their performance metrics

Method of Detection	Sensitivity parameter
Charge deduction based sensitivity method [14]	Glucose oxidase enzyme is $\frac{\Delta g_{ds}}{I_{ds}}$ MIG from serum is $\Delta E(x)$ KIM-I from urine is Δch_{pot}
Ethanolamine surface functionalization technique [24]	Prostrate-Specific Antigen from serum is Δg_d
Charge control based sensor model [35]	CerB-2 from saliva is the ΔI_D
Dielectric Modulation [36]	Threshold voltage, change in threshold voltage, drain current
Aptamer Functionalization technique [37]	Change in drain current
Dielectric modulation [38]	Change in drain current
MIS structure with extended gate [39]	Shift of V_R
Electrical double layer gated technique [40]	Change in drain current

5 Advantages of MOSHEMT

The compound semiconductor device technologies advances in microwave devices applied in military radar systems and high power electromagnetic are being altered with semiconductor power amplifiers. Wider bandgap semiconductor microwave devices like GaN-based MOSHEMTs which carry the potential for operating at power densities more times larger than Si-LDMOS, silicon carbide (SiC), and GaAsFET devices. MOSHEMTs also have other merits like higher saturation electron velocity, higher breakdown voltage(>200 V), better thermal conductivity, low turn-on resistances, lower parasitic capacitances and, higher cut-off frequencies. Also, these GaN-based MOSHEMTs have been considered to be the prime choice in order to

realize superior performance in high power amplifiers (HPAs) designs. Recently, these HPAs have become essential for wider bandwidth operation and high linearity operations at lower power consumption. While LDMOS or HEMT have initially been broadly used as high-power amplifier devices, MOSHEMT provides the following advantages. First, higher power-added efficiency (PAE), which saves electrical power consumption and reduces the cost and size of HPAs due to the small amount of heat dissipation. Next, high operating voltage, MOSHEMT operates at higher supply voltage similar to power feeder voltage range which is generally used for radar and satellite communication equipment. Generally, the design of the amplifier becomes more critical as the low device impedances. GaN-based MOSHEMTs show higher impedance than different devices. Thus, the HPA designers can utilize the advantages of MOSHEMTs to increase the performance of HPAs with a wide coverage of frequency bands and higher PAE with respect to the required HPA performance. In comparison with HEMT, GaN MOSHEMT devices offer better advantages of higher electron mobility in both lower as well as higher transverse field, high breakdown voltage, and reduced gate leakage current density.

---

6 Conclusion

This chapter deals with many varieties of biosensors focused on various heterostructures, i.e., AlGaAs/GaAs, AlGaN/GaN, InGaAs, AlInN/AlN, ZnO based high electron mobility transistors (HEMTs). Also, the choice of these corresponding materials has gained immense potential in different fields because of their widespread properties such as good selectivity, higher sensitivity, reliability, specificity, good repeatability, chemical and thermal stability, stability, linearity, small device size, and high electron mobility. This technology offers lesser cost, easier for integrating into portable systems, time-effective, and depicts signs for excellence in future in case of point-of-care diagnostics.

References

1. V. Hemaja, D.K. Panda, A comprehensive review on high electron mobility transistor (HEMT)

based biosensors: Recent advances and future prospects and its comparison with si-based biosensor. Silicon (2021). https://doi.org/10.1007/s12633-020-00937-w
[Crossref]

2. V. Hemaja, D.K. Panda, Dielectric modulated enhancement mode N-polar GaN MIS-HEMT biosensor for label free detection. ECS J. Solid State Sci. Technol. (2021). https://doi.org/10.1149/2162-8777/abea5c
[Crossref]

3. A.G. Gudkov, S.V. Agaseiva, V.G. Tikhomirov, V.V. Zherdeva, D.V. Klinov, V.D. Sasurin, Perspective in the development of biosensors based on AlGaN/GaN HEMT. Biomed. Eng. **53**(3), 196–200 (2019)
[Crossref]

4. R. Narang, K.V.Sashidhar Reddy, M. Saxena, R.S. Gupta, M. Gupta, A dielectric modulated tunnel-FET-based biosensor for label-free detection: Analytical modeling study and sensitivity analysis, IEEE Electron Dev. Lett. **59**(10), 2809–2817 (2012)

5. R. Narang, M. Saxena, R.S. Gupta, M. Gupta, Dielectric modulated tunnel-field-effect-transistor-A biomolecule sensor. IEEE Electron Dev. Lett. **33**(2), 266–268 (2012)

6. R. Narang, M. Saxena, M. Gupta, Drain current model of a four-gate dielectric modulated MOSFET for application as a biosensor. IEEE Electron Dev. Lett. **62**, 2636–2644 (2015)
[Crossref]

7. Ajay, R. Narang, M. Saxena, M. Gupta, Investigation of dielectric modulated (DM) double gate (DG) junctionless MOSFETs for application as biosensor. Superlattices Microstruct. **85**, 557–572, (2015)

8. R.K. Paswan, D.K. Panda, T.R. Lenka, Dielectric modulated AlGaAs/GaAs HEMT for label-free detection of biomolecules. International Workshop on the Physics of Semiconductor and Devices, pp. 709–715 (2017)

9. E. Rahman, A. Sadman, Q.D.M. Khosru, Effect of biomolecule position and fill in factor on the sensitivity of a dielectric modulated double gate junctionless MOSFET biosensor. Sens. Bio-Sensing Res. **13**, 49–54 (2017)

10. Shaveta, H.M. Maali Ahmed, R. Chaujar, Rapid detection of biomolecules in a dielectric modulated GaN MOSHEMT, J Mater Sci. Mater Electron (2020)

11. S. Kalra, M. Jagdesh Kumar, A. Dhawan, Dielectric modulated filed effect transistors for DNA detection: Impact of DNA orientation, IEEE Electron Dev. Lett. **37**(11), 1485–1488 (2016)

12. E. Rahman, A. Sadman, Q.D.M. Khosru, Effect of biomolecule position and fill in factor on sensitivity of a dielectric modulated double gate junctionless MOSFET biosensor, Sens. Bio-sensing Res. **13**, 49–54 (2017)

13. P. Pal, Y. Pratap, M. Gupta, S. Kabra, Modeling and simulation of AlGaN/GaN MOSHEMT for biosensor applications, 1–7 (2018)

14. A. Varghese, C. Periasamy, L. Bhargava, Fabrication and charge deduction based sensitivity analysis of GaN MOSHEMT device for glucose, MIG, C-erbB-2, KIM-1, and PSA detection. IEEE

Trans. Nanotechnol. **18**, 747–755 (2019)
[Crossref]

15. P. Pal, Y. Pratap, M. Gupta, S. Kabra, Modeling and simulation of AlGaN/GaN MOSHEMT for biosensor application. IEEE Sensors 1–7 (2018)

16. D.K. Panda, T.R. Lenka, Analytical model development of channel potential, electric field, threshold voltage and drain current for gate workfunction engineered short channel E-mode N-polar GaN MOSHEMT. Microsyst. Technol. 1–8 (2019)

17. D.K. Panda, G. Amarnath, T.R. Lenka, Small signal parameter extraction of E-mode N-polar GaN MOSHEMT using optimization algorithms and its comparison. J. Semconductors **39**(7), 074001 (1–9) (2018)

18. A. Rakoski, S. Diez, H. Li, S. Keller, E. Ahmedi, C. Kurdak, Electron transport in N-Polar GaN-based heterostructures. Appl. Phys. Lett. **114**, 162102 (2019)

19. D.K. Panda, T.R. Lenka, Compact thermal noise model for enhancement mode N-polar GaN MOSHEMT including 2DEG density solution with two sub-bands, IET Circuits Devices and Systems, 1–7 (2018)

20. D.K. Panda, T.R. Lenka, Analytical model development of channel potential, electric field, threshold voltage and drain current for gate workfunction engineered short channel E-mode N polar GaN MOSHEMT. Microsyst. Technol. 1–8 (2019)

21. B.S. Kang, H.T. Wang, T.P. Lele, Y. Tseng, F. Ren, S.J. Pearton, J.W. Johnson, P. Rajagopal, J.C. Roberts, E.L. Piner, K.J. Linthcum, Prostate specific antigen detection using AlGaN/GaN high electron mobility transistors. Appl. Phys. Lett. **91**, 112106 (2007)
[Crossref]

22. J.D. Li, J.-J. Chang, B. Miao, X.-W. Wei, J. Xie, J.C. Zhang, Z.-Q. Zhang, H.-W. Li, D.M. Wu, Label free electrical detection of prostrate specific antigen with millimeter grade biomolecule-gated AlGaN/GaN high electron mobility transistor (Springer, 2014)

23. J.-D. Li, J.-J. Chang, B. Miao, X.-W. Wei, J. Xie, J.-C. Zhang, Z.-Q. Zhang, D.-M. Wu, Detection of prostrate specific antigen with biomolecule-gated AlGaN/GaN high electron mobility transistors, J. Micromech. Microeng. **24**, 075023 (2014)

24. Z. Gu, J. Wang, B. Miao, L. Zhao, X. Liu, D. Wu, J. Li, Highly sensitive AlGaN/GaN HEMT biosensors using an ethanolamine modification strategy for bioassay applications. RSC Adv. **9**,15341(2019)

25. Md A. Khan, P. Kumar, G. Siddharth, M. Das, S. Mukherjee, Analysis of drain current in polycrystalline MgZnO/ZnO and MgZnO/CdZnO HFET, IEEE Trans. Electron Dev. **66**(12), 5097–5102 (2019)

26. Y.K. Verma, V. Mishra, S.K. Gupta, A physics based analytical model for MgZnO/ZnO HEMT. J. Circuits, Syst. Comput. (2019)

27. S.-H. Park, W.-P. Hong, J.-J. Kim, Theoretical Studies on the two dimensional electron gas properties of MgZnO/MgO/ ZnO heterostructures. J. Korean Phys. Soc. **69**(1), 96–98 (2016)
[Crossref]

28. B.H. Chu, B.S. Kang, H.T. Wang, C.Y. Chang, T. Lele, Y. Tseng, A. Goh, A. Sciullo, W.S. Wu, J.N. Lin, B.P. Gila, S.J. Pearton, J.W. Johnson, E.L. Piner, K.J. Linthicum, F. Ren, AlGaN/GaN HEMT and ZnO nanorod-based sensor for chemical and bio-applications 7216, 72162A1-10 (2009)

29. Y. Song, Y. Lie, X. Yan, Y. Zhang, Y. Liu, Biosensors of ZnO nanotetrapods and HEMT for detecting uric acid, IEEE, pp. 345–346 (2012)

30. S. Ma, Q. Liao, H. Liu, Y. song, P. Li, Y. Huang, Y. Zhang, An excellent enzymatic lactic acid biosensor with ZnO nanowires-gated AlGaAs/GaAs high electron mobility transistor. Royal Soc. Chem 6415–6418 (2012)

31. R. Singh, Md.A. Khan, S. Mukherjee, A. Kranti, Analytical model for 2DEG density in graded MgZnO/ZnO Heterostructures with cap layer. IEEE Trans. Electron Devices **64**(9), 3661–3667 (2017)

32. K. Ding, C. Wang, B. Zhang, Y. Zhang, M. Guan, L. Cui, Y. Zhang, Y. Zeng, Z. Lin, F. Huang, Specific detection of alpha-fetoprotein using algaas/gaas high electron mobility transistors, IEEE Electron Device Lett. **35**(3) (2014)

33. X.-M. Zhan, M.-L. Hao, Q. Wang, W. Li, H.-L. Xiao, C. Feng, L.-J. Jiang, C.-M. Wang, X.-L. Wang, Z.-G. Wang, Highly sensitive detection of deoxyribonucleic acid hybridization using Au-gated AlInN/GaN high electron mobility transistor-based sensors, Chin. Phys. Lett 34(4), 047301(2017)

34. Y. Song, X. Zhang, X. Yan, Q. Liao, Z. Wang, Y. Zhang, An enzymatic biosensor based on three-dimensional ZnO nanotetrapods spatial net modified AlGaAs/GaAs high electron mobility transistors. Appl. Phys. Lett 105, 213703 (2014)

35. A. Varghese, C. Periasamy, L. Bhargava, Analytical modeling and simulation-based investigation of AlGaN/AlN/GaN Bio-HEMT Sensor for C-erbB-2 Detection. IEEE Sens. J. **18**(23), 9595–9603 (2018)
[Crossref]

36. S.N. Mishra, K. Jena, A dielectric-modulated normally-Off AlGaN / GaN MOSHEMT for bio-sensing application: Analytical modeling study and sensitivity analysis**74**(4) (2019)

37. T.Y. Tai, A. Sinha, I. Sarangadharan, A.K. Pulikkathodi, S.L. Wang, S.C. Shiesh, Y.L. Wang, Aptamer-functionalized AlGaN/GaN high-electron-mobility transistor for rapid diagnosis of fibrinogen in human plasma, Sens. Mater. (2018)

38. B.H. Chu, B.S. Kang, C.Y. Chang, F. Ren, A. Goh, A. Sciullo, K.J. Linthicum, AlGaN/GaN high electron mobility transistors integrated into wireless detection system for glucose and pH in exhaled breath condensate. ECS Trans. **19**(3), 85–97 (2019)
[Crossref]

39. J.Y. Pyo, J.H. Jeon, Y. Koh, C.Y. Cho, H.H. Park, K.H. Park, W.J. Cho, AlGaN/GaN high-electron-mobility transistor pH sensor with extended gate platform. AIP Adv. **8**(8), 1–6 (2018)

40. I. Sarangadharan, A. Regmi, Y.W. Chen, C.P. Hsu, P.C. Chen, W.H. Chang, Y. L. Wang, High sensitivity cardiac troponinI detection in physiological environment using AlGaN/GaN High Electron Mobility Transistor (HEMT) biosensors. Biosens Bioelectron (2018)